Elena Ciappi · Sergio De Rosa
Francesco Franco · Jean-Louis Guyader
Stephen A. Hambric *Editors*

Flinovia - Flow Induced Noise and Vibration Issues and Aspects

A Focus on Measurement, Modeling, Simulation and Reproduction of the Flow Excitation and Flow Induced Response

Springer

Flinovia - Flow Induced Noise and Vibration Issues and Aspects

Elena Ciappi · Sergio De Rosa
Francesco Franco · Jean-Louis Guyader
Stephen A. Hambric
Editors

Flinovia - Flow Induced Noise and Vibration Issues and Aspects

A Focus on Measurement, Modeling, Simulation and Reproduction of the Flow Excitation and Flow Induced Response

Springer

Editors
Elena Ciappi
INSEAN
Marine Technology Research Institute
National Research Council of Italy
Rome
Italy

Sergio De Rosa
Francesco Franco
Department of Industrial Engineering,
Aerospace Section
Università degli Studi di Napoli Federico II
Napoli
Italy

Jean-Louis Guyader
Laboratoire Vibrations Acoustique
INSA-Lyon
Villeurbanne Cedex
France

Stephen A. Hambric
Penn State Center for Acoustics
and Vibration
The Pennsylvania State University
State College, PA
USA

ISBN 978-3-319-09712-1 ISBN 978-3-319-09713-8 (eBook)
DOI 10.1007/978-3-319-09713-8

Library of Congress Control Number: 2014951334

Springer Cham Heidelberg New York Dordrecht London

Printed on acid-free paper

Springer is part of Springer Science+Business Media (www.springer.com)

Preface

The first international symposium on **Fl**ow **I**nduced **N**oise and **Vi**bration Issues and **A**spects (flinovia) was held in November 2013 over 3 days in Rome, hosted by our friends at the Italian Consiglio Nazionale delle Ricerche (CNR). This book contains the recent work of 17 contributors from Italy, France, United States of America, Canada, and China.

The proceedings of the conference truly span most issues and aspects of flow-induced vibration and noise. Several authors describe experimental and numerical methods for characterizing fluctuating wall pressures induced by turbulent fluid flows, focusing primarily on turbulent boundary layers. Several other authors examine the resulting vibrations of flow-excited structures. Finally, some authors use structural vibrations to infer the behavior of the exciting flow.

The volume consists of 16 full chapters and a single extended abstract that summarizes the interactions among the presenters and attendees and the mutual refinements gained through oral presentations and discussions. That summary succinctly reflects a shared vision of the field and its specific topics.

The following are the main areas in which the presentations can be categorized, even if only for the sake of convenience, since most of the papers are largely interdisciplinary. Only the last name of the first author of each chapter is used for identification in this listing.

Opening Lecture

The flinovia keynote speaker, Dr. William Blake, opened the symposium with a survey of papers by several authors who have examined the nature of TBL flow over rough surfaces. Blake summarized both experimental and numerical studies, including the use of time-accurate Large Eddy Simulation (LES) techniques.

Source Characterization

Many authors have investigated TBL wall pressures over the past 50 years.

Juvé provides an overview of previous attempts to compute wall pressure auto- and cross-spectra using computational fluid dynamics (CFD) methods. He also emphasizes the importance of considering pressure gradients, which decelerate or accelerate the flow, altering the boundary layer shape and resulting wall pressures.

Moeller also address pressure gradient effects, providing new measurements that demonstrate the significant effects of adverse pressure gradients on boundary layer shape, and therefore on the wall pressures. Their measurements also show the dispersive nature of low frequency convecting wall pressures, establishing that group velocities, not phase velocities, should be used in TBL wall pressure models.

Camussi provides a summary of both experimental and numerical investigations of supersonic TBL flow wall pressures. While supersonic wall pressure autospectra seem to scale similarly to subsonic spectra, there is still a need for more investigations into the cross-spectra of TBL wall pressures, which span the shock cells that appear in supersonic flow.

Using LES to simulate large-scale turbulent eddies, combined with Reynolds Averaged Navier–Stokes (RANS) modeling for smaller turbulence, is becoming quite common.

Juvé shows that these methods, as well as rigorous Direct Numerical Simulation (DNS), are able to simulate accurate wall pressure spectra beneath simple TBL flows.

Caro describes how time-accurate CFD combined with RANS, commonly called Hybrid RANS-LES methods, are applied using the commercial software Star-CD to simulate complex flows around automobiles. Caro shows that simply applying boundary layer parameters in empirical models (such as that of Chase) to estimate TBL wall pressure models, does not work well in complicated flows.

De Luca presents a simulation of the turbulent synthetic jets, which can have important industrial applications in designing specific actuators.

Direct and Inverse Methods

Along with direct measurement and simulation methods, some authors are pursuing inverse methods to either infer or synthesize TBL wall pressure fluctuations using traversing microphones and panel vibrations. The goal is to synthesize the effective TBL wall pressures in a test facility without moving fluid, usually using wave-number filtering and an assumed field of partially correlated plane wave sources.

Aucejo and Robin describe approaches for simulating TBL wall pressures with a single traversing source, using the acoustic holography technique or surface plane wave decomposition. Different techniques were used demonstrating that the main difficulty lies in the use of a large array of sensors. The decisive advantage of the

proposed methods is associated with the synthetic antenna concept where one moving sensor is used instead of an array.

Totaro attempts to use vibration measurements to identify the wall pressure fluctuations responsible for a panel's vibration. The method gives good results for deterministic excitation even if the ill-conditioning, common in inverse methods, must be corrected through regularization. For random excitation like TBL, the method must still be improved to overcome limitations due to acoustic background noise in test facilities.

Structural Vibration and Noise

Once turbulent sources are characterized, they must be applied to models of underlying structures so that vibration, stresses, and radiated noise may be simulated.

Chevalier outlined the importance of flow-induced noise for underwater structures, and by other authors, including Ichchou, for aerospace structures.

Several frequency-domain approaches for modeling flow-induced vibration are summarized by Maxit, who also shows the effects of structural ribs on the resulting vibration.

While the usual structural modeling approach is to use finite elements (FE), FE becomes computationally infeasible for large structures excited by slowly moving fluid due to the exorbitant mesh sizes required.

Ichchou suggests using energy methods to allow for coarser meshes, while still providing sufficient spatial distribution of the results to visualize structural vibration and energy distribution.

The overall structural response to TBL flow can also be used to infer equivalent distributed source forcing functions. Similar in some extent to the synthetic array methods described earlier, De Rosa pursues reconstructing the effective structural forcing functions based on structural vibrations. The approach requires the underlying modal response functions to be represented properly. The underlying response functions, combined with the spatial cross-correlation of the wall pressure fluctuations, form the well-known joint acceptance functions of a structure and a source; this latter can be approximated by using equivalent pseudo deterministic excitation.

Ciappi uses dimensional analysis with flow and structural variables to collapse a large series of disparate structural vibration measurements into a somewhat universal curve. Her proposed scaling function normalizes structural response by the autospectrum of the wall pressures, effectively providing the integration of the joint acceptance functions.

While most investigators analyze flow-induced vibration and noise in the frequency domain, sometimes time-domain analyses are required, particularly for flows that are not statistically stationary or ergodic, or for cases where the acoustic and/or structural waves couple with the flow.

Leung describes the interaction of duct flow with liner vibration and acoustic waveguide propagation, as he tries to explain experimental observations of reduced duct silencer performance.

Finally, Hambric shows that time-domain calculations of fluctuating stress, along with mean stresses, are required when assessing fatigue damage of structural materials.

In the appendix, one more abstract is reported involving a contribution whose full paper was not available to be included in this book. It belongs to Ceccio, who investigated TBL flow under varying pressure gradients, but on the suction side of lifting surfaces at very high Reynolds numbers. The lifting surface flows separate from the trailing edge, generating another important turbulent source—shed vortices.

Summary

The first flinovia was a great opportunity to gather together a diverse group of international investigators of flow-induced vibrations and noise in an intimate setting, with a single continuous session. This workshop model allowed for lively discussion among all participants, both during the presentations, and during breaks and social events.

Several authors mentioned ongoing efforts in flow-induced vibrations and noise, showing that this field is still being investigated, and remains of great importance to an impressive number of crucial communities, including the world's navies, the automotive industry, and the air and space industries.

We, the organizers, are hopeful that future flinovias will be held so that the state of the art will continue to be discussed, and that we all may benefit from mutual exchanges of discoveries and ideas. We want also to recognize and thank all the CNR-INSEAN persons who greatly collaborated before, during, and after the symposium to attain its best outcome.

June 2014

Elena Ciappi
Sergio De Rosa
Francesco Franco
Jean-Louis Guyader
Stephen A. Hambric

Committees

Conference Days

11–13 November 2013, CNR, Consiglio Nazionale Ricerche
Piazzale Aldo Moro, Roma, Italy

Supporting Institutions Committee

(*) CNR-INSEAN, The Italian Ship Model Basin, Rome, Italy, www.insean.cnr.it
(§) Pasta-lab, Department of Industrial Engineering, Aerospace Section, University of Naples Federico II, Italy www.pastalab.unina.it
(+) CELYA, Lyon Acoustics Centre, University of Lyon, France, celya.universite-lyon.fr

International Organizing and Editors Committee

Elena Ciappi CNR-INSEAN, Marine Technology Research Institute, National Research Council of Italy, Rome, Italy
Sergio De Rosa and Francesco Franco, Department of Industrial Engineering, Aerospace Section, University of Naples Federico II, Italy
Jean-Louis Guyader Laboratoire Vibrations Acoustique, INSA-Lyon, Villeurbanne Cedex, France
Stephen A. Hambric CAV, Center for Acoustics and Vibration, Pennsylvania State University, University Park, PA, USA

Local Organizing Committee

(*) Giovanni Aloisio, Elena Ciappi, Enrico De Bernardis, Massimo Miozzi, Silvano Grizzi
(§) Sergio De Rosa and Francesco Franco

Contents

Contributors

Jason M. Anderson Naval Surface Warfare Center, Bethesda, MD, USA

Mathieu Aucejo Structural Mechanics and Coupled Systems Laboratory, Cnam Paris, Paris, France

Christian Audoly DCNS Research, Rond-point de l'Artillerie de la Marine, Toulon, France

Olivier Bareille LTDS, Ecole Centrale de Lyon, UMR CNRS 5513, Ecully Cedex, France

Alain Berry Université de Sherbrooke, Sherbrooke, Canada

Marion Berton Laboratoire de Mécanique des Fluides et d'Acoustique, UMR CNRS 5509, Ecole Centrale de Lyon, Ecully Cedex, France

William K. Blake Naval Surface Warfare Center, Bethesda, MD, USA; Department of Aerospace and Mechanical Engineering, University of Notre Dame, South Bend, IN, USA

Robert L. Campbell Applied Research Lab, Penn State University, State College, PA, USA

Roberto Camussi University Roma TRE, Rome, Italy

Stéphane Caro CD-adapco, Lyon Office, Lyon, France

Frédérique Chevalier DCNS Lorient, Lorient, France

Fabien Chevillotte Matelys, Vaulx-en-Velin, France

Matteo Chiatto Von Karman Institute, Rhode-St-Genese, Belgium

Dimitrios Chronopoulos Nottingham University, Nottingham, UK

Elena Ciappi CNR-INSEAN, Marine Technology Research Institute, National Research Council of Italy, Rome, Italy

Stephen C. Conlon Applied Research Lab, Penn State University, State College, PA, USA

Gennaro Coppola Department of Industrial Engineering, Aerospace Section, Universita' degli Studi di Napoli, Naples, Italy

Vincent Cotoni CD-adapco, Lyon Office, Lyon, France

Luigi de Luca Department of Industrial Engineering, Aerospace Section, Universita' degli Studi di Napoli, Naples, Italy

Marie De Rochambeau LTDS, Ecole Centrale de Lyon, UMR CNRS 5513, Ecully Cedex, France

Sergio De Rosa Pasta-Lab, Department of Industrial Engineering, Aerospace Section, Università Degli Studi Di Napoli "Federico II", Naples, Italy

Richard G. DeJong Engineering Department, Calvin College, Grand Rapids, MI, USA

Alessandro Di Marco University Roma TRE, Rome, Italy

Harris K.H. Fan Department of Mechanical Engineering, The Hong Kong Polytechnic University, Kowloon, Hong Kong

Francesco Franco Pasta-Lab, Department of Industrial Engineering, Aerospace Section, Università Degli Studi Di Napoli "Federico II", Naples, Italy

Michele Girfoglio Department of Industrial Engineering, Aerospace Section, Universita' degli Studi di Napoli, Naples, Italy

Jean-Louis Guyader Laboratoire Vibrations Acoustique, INSA-Lyon, Villeurbanne Cedex, France

Stephen A. Hambric Applied Research Lab, Penn State University, State College, PA, USA

Bastien Hiverniau LTDS, Ecole Centrale de Lyon, UMR CNRS 5513, Ecully Cedex, France

Mohamed N. Ichchou LTDS, Ecole Centrale de Lyon, UMR CNRS 5513, Ecully Cedex, France

Daniel Juvé Laboratoire de Mécanique des Fluides et d'Acoustique, UMR CNRS 5509, Ecole Centrale de Lyon, Ecully Cedex, France

Garret C.Y. Lam Department of Mechanical Engineering, The Hong Kong Polytechnic University, Kowloon, Hong Kong

Quentin Leclère Laboratoire Vibrations Acoustique, INSA-Lyon, Villeurbanne Cedex, France

Damien Lecoq LUNAM Université, Université du Maine, CNRS UMR 6613, LAUM-ENSIM, Le Mans Cedex 9, France

Randolph C.K. Leung Department of Mechanical Engineering, The Hong Kong Polytechnic University, Kowloon, Hong Kong

Laurent Maxit Laboratoire Vibrations Acoustique, INSA-Lyon, Villeurbanne Cedex, France

Fred Mendonça CD-adapco, Lyon, France

Teresa S. Miller Bombardier Aerospace, Wichita, KS, USA

Mark J. Moeller Newmarket, NH, USA

Stéphane Moreau Université de Sherbrooke, Sherbrooke, Canada

Charles Pézerat LUNAM université, Université du Maine, CNRS UMR 6613, LAUM-ENSIM, Le Mans Cedex 9, France

Olivier Robin Université de Sherbrooke, Sherbrooke, Canada

Edouard Salze Laboratoire de Mécanique des Fluides et d'Acoustique, UMR CNRS 5509, Ecole Centrale de Lyon, Ecully Cedex, France

Matthew Shaw Applied Research Lab, Penn State University, State College, PA, USA

Phil Shorter CD-adapco, Lyon Office, Lyon, France

Nicolas Totaro Laboratoire Vibrations Acoustique, INSA-Lyon, Villeurbanne Cedex, France

Bernard Troclet LMT Cachan, Ecole Normale Supérieur de Cachan and EADS Defense and Space, Cachan Cedex, France

The Acoustics of Flow over Rough Elastic Surfaces

William K. Blake and Jason M. Anderson

Abstract This paper summarizes an analytical model approach for calculating flow induced sound from either elastic or rigid surfaces with small roughness. The analytical approach used here provides a result for both the wave number-frequency spectrum of the structure's excitation pressure and the structure's response to that pressure and can be applied to many types of uneven surfaces, such as those on which are dispersed 2 or 3 dimensional deterministic or random geometric shape irregularities. This paper is focused on 3 dimensional distributed roughness elements. The shape of the unevenness protrudes into the boundary layer above it, acting as a flow spoiler and generating forces and wakes in the immediate region of the roughness element. It is assumed that these shapes are small and in the range of 10 to several hundred viscous scales. We will discuss the effects of surface elasticity on the ability of these sources to produce sound in regions both above the surface (on the flow side for both elastic and inelastic surfaces) and below the surface on the quiescent fluid side (in the case of elastic surfaces). A method for modeling forcing functions will also be presented in the context of the overall theory. The unevenness is presumed to be small enough, or of such a nature, as to not affect the basic elasticity of the surface. In the subject case of rough walls, analytical results will be compared with both aero-acoustics measurements made in multiple facilities and large eddy simulations. All research was made possible by a recent program sponsored by the U.S. Navy's Office of Naval Research.

W.K. Blake (✉) · J.M. Anderson
Naval Surface Warfare Center, Bethesda, MD, USA
e-mail: hydroacoustics@aol.com

W.K. Blake
Department of Aerospace and Mechanical Engineering,
University of Notre Dame, South Bend, IN, USA

E. Ciappi et al. (eds.), *Flinovia - Flow Induced Noise and Vibration Issues and Aspects*, DOI 10.1007/978-3-319-09713-8_1

1 Background

The subject of sound radiated by rough-wall turbulent boundary layers, and over nonuniform surfaces in general, has been given sporadic study for many years. In 2007 a focused program to understand the essential physics of radiated sound from rough-wall turbulent boundary layers on elastic or rigid surfaces was begun under ONR sponsorship with a funded partnership of the Naval Surface Warfare Ctr., Virginia Tech, Florida Atlantic University, and the University of Notre Dame as principal investigators. Thus multi-institution team approach resulted in a sequence of numerical and physical models of a series of canonical rough surfaces for which experimental numerical and analytical work was conducted. These numerical simulations and the matching physical experiments were designed by the team collaboration.

We will use the rough wall turbulent boundary layer as a particular example of the more general problem of unevenness. In work prior to 2007, our knowledge base for rough-wall turbulent boundary layer noise was under-pinned by experimental observations in air of Hersh [19] and of Farabee and Geib [13], as well as the analytical modeling of roughness on a rigid surface by Howe [22, 23]. Until 2007 predictions of roughness noise were constrained by the lack of a fundamental understanding of how the roughness elements and the above boundary layer interact to produce sound and how the elasticity of the surface beneath them modified the sound. According to the premise of Howe [23], the roughness elements on the rigid surface were represented as a spatial distribution of small aeroacoustic scatterers beneath the turbulent boundary layer. It was assumed that the interstitial flow around the roughness elements was of low enough magnitude that the flow-surface interactions that might exist there were sufficiently overwhelmed by another mechanism by which the pressure field induced by the upper flow was just diffracted by these elements. The roughness elements in this semi-quiescent under-layer produce pressure scattering sites to subsonically-convected hydrodynamic pressure due to the turbulence above causing a diffuse set of dipoles at the roughness elements. In this process the interactions are essentially inviscid and the experiments of Hersh [19], conducted some years earlier, were used to evaluate certain numerical factors pertaining to the incident field for which the theory was unable to account. Although the experiments of Farabee and Geib [13], also on a rigid surface in air, expanded the empirical database for the characteristics of wall pressure generated by roughness, with regard to roughness noise the database did not seem firm enough to add much to the already existing Howe-Hersh representation of the sound. So, given the data that was reported, the Howe theory of diffraction did not appear to account for the measured acoustic levels. Furthermore, given the measurement and numerical capabilities of the day, the requisite measurements and associated computations needed to fully clarify mechanisms would not have been practical.

Large eddy simulations (LES) of Yang and Wang [31–34] were conducted for a fully-developed turbulent channel flow with rigid walls and regular geometric patterns of roughness elements. The region of the flow that was most active in the creation of

the roughness dipoles was that due to the turbulence-element interaction within an inner layer of the flow. In the parallel work of Hong et al. [20, 21, 34], stereoscopic observations disclosed 2 distinct layers which were characterized by spatial wave number scales, either convected in the outer boundary layer or formed in an inner layer by the roughness elements and their interstices. The general conclusion to be reached from the combined results of Yang and Wang and of Hong et al. is a view of a rough-wall turbulent boundary layer that is made up of two layers: an inner layer that is dominated by roughness-scale eddies and direct turbulence-element interaction, and an outer layer dominated by a larger scale convected turbulent field for which similarity rules are classically known and which is augmented over smooth wall intensity by the roughness-activated turbulence from below. This "double-deck" structure of roughness noise regimes is illustrated in Fig. 1, which depicts the element-dominated flow near the wall and the outer flow with a blend region that extends from 2 to 5 roughness heights above the wall. Extension of this view to the surface forcing suggests a wave number spectrum that contains contributions to these pressures at the mean flow convection near $k = k_c$, and a high wave number, for k near $(k_g)^{-1}$, and a low wave number acoustic domain caused by direct hydrodynamic lift and drag.

This view of the turbulence actually is anticipated by some of the earlier work. The diffraction model of Howe was developed to account for the interaction of the outer flow with the roughness elements and a local flow-spoiler model applies to the direct roughness-scale interactions occurring at the roughness elements near the wall. An accompanying empirical study using array-based measurement technology undertaken by Glegg et al. [16], Glegg and Devenport [17], Devenport et al. [10, 11], and Grissom et al. [18] and designed to support an empirical confirmation of some of the LES results, also provided extensions to the results in the form of measured radiated sound for larger parameter sets for other roughness distributions and configurations than could be simulated on the computer. Additionally, experimental measurements of similar scope and detail by Anderson et al. [1] provided direct corroboration of the LES results for radiated sound from the roughness patches that were designed to match the geometries used in the computational simulations.

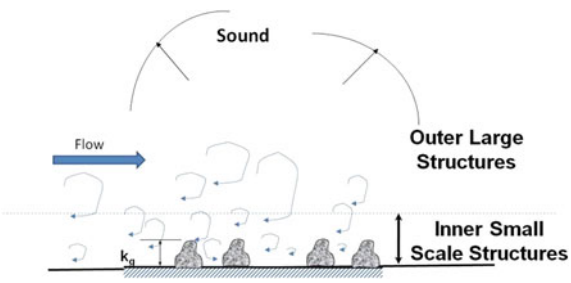

Fig. 1 Illustration of the rough-wall turbulent boundary layer suggesting a double-deck structure of the acoustic source distribution

The experiments also extended the results to parameter values that were beyond those practical for computation. In turn, the computational simulations allowed the conduct of numerical experiments that were not possible in the physical arrangements.

This paper presents a comprehensive review of the major results of both physical and numerical aspects of this work with extensions to the problems of elastic plates and shells with uneven flow surfaces. The analytical formulation of Sect. 2 provides an outline of structural response and acoustic radiation from the elastic plate with small-scale roughness; Sect. 3 develops a forcing model specific for roughness that is based on the collective observations made with LES and physical experiments; Sect. 4 presents a specific analytical model result to illustrate the sound power that might be radiated in a physical simulation using parameters that have been used both experimentally and computationally in the past researches.

2 Analytical Formulation

2.1 Overview

With this prior work as background, see Blake and Anderson [7] and Anderson and Blake (2013), the body of recent work provides a theory and modeling approach for radiated sound from single protuberances and randomly distributed rough surfaces, specifically, but straightforward extensions are possible to regular geometries of non-uniformities, e.g. grooves and steps. As discussed in the introduction, the double-deck structure of the sources pose a source structure of inner and outer flow that separates mechanisms due to both direct turbulence-element interaction in the inner layer and interaction of the outer flow turbulence pressure field with the roughened surface including diffraction. In both cases, as far as the elastic structure is concerned, an elemental flow-driven force F_n drives the fluid loaded plate locally as depicted in the alternative structural model frameworks shown in Fig. 2.

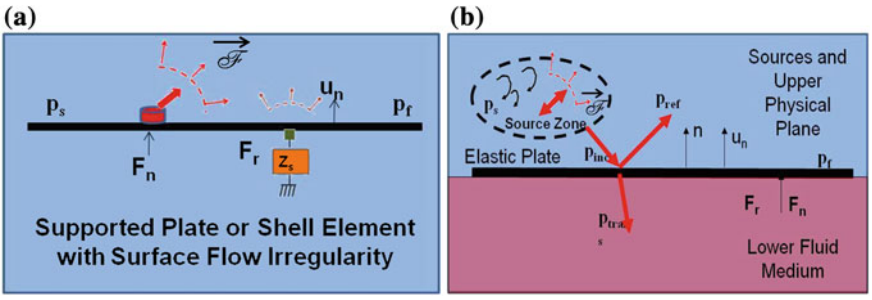

Fig. 2 Fluid-structure interaction components for analytical model of the fluid-loaded plate driven by flow over its irregular surface. **a** Mechanical system. **b** Structural-acoustic system

It is assumed in the following that flow exists only on the upper side of the plate or shell, the acoustic medium is contained always on the upper side and may be on the quiescent lower side. The effects of surface impedance, roughness size, and statistical roughness size distribution are to be accounted for in the model. The flow-induced drivers of the modeled sound are depicted as due to multiple contributions: a pressure field on the interstitial surface pressure among the elements due to the outer flow, a dipole source strength on the elements themselves due to diffraction of the outer flow pressure by the roughness elements, and direct element forces due to turbulence—element interaction. The sound will be calculated as an incoherent superposition of all three contributions, although the assumption of incoherence is really a convenience that allows a clear presentation here, and provides a more clear separation of source types than would otherwise be permitted. The role played by the surface to the acoustic medium and the elements dipoles will be as a finite impedance reflector which serves to alter the radiated sound on the flow side and create transmitted sound to the quiescent-fluid inner space. It is assumed that the Mach number of the outer flow is small enough that convective wave effects can be neglected in the fluid. The theory also provides for the additional effects of structural constraints and structural boundaries; these are provided for notionally through inclusion of a point attachment of impedance, Z_s, in our analysis. However a simple example of the roughened, fluid-loaded, simple-supported elastic plate will be presented in Sect. 4. The roughness elements are assumed to be rigid and rigidly attached to the structure.

The problem at hand is to calculate the sound radiated by the fluid system shown in Fig. 1, when it is attached to an elastic plate with fluid loading on both sides as depicted in Fig. 2. Accordingly, a system of localized and spatially-distributed pressures and plate normal velocity, u_n, are determined under influence of drive from the roughness element which imposes a localized force, F_n, on the plate at the element. The plate is assumed to be mechanically constrained in some way; this is conceptualized here with a point attachment of impedance, Z_r, which applies a point force F_r.[1] Distributed pressures, p_s, are applied to the remainder of the (essentially flat) surface as well. These pressures have 3 contributions: the first is imposed by the volume distribution of pressure sources consisting of both the non-frozen convected turbulence in the interstitial flow and in that the outer flow; the second is due to fluid-borne (essentially acoustic) pressures emitted by both the force dipoles in the fluid momentum at the elements in the inner layer and the forces directly-applied by the elements on the plate; the third source is due to the fluid reaction on the plate that is due to the out-of-plane motion of the plate, u_n. The combined methods of Ffowcs Williams [14, 15], Powell [28], Maidanik and Kerwin [27], Blake [5], and Skelton and James [29] are used to determine the generalized Fourier transform in frequency, ω, and planar wave number, $k_{1,3}$, where k_1 is streamwise and k_3 is transverse. We consider here the acoustics of a flat supported plate, but the

[1] Note that depending on the lateral correlation length of the surface pressure on a forward or backward-facing step, see Sect. 5, one may require adjustment of these results to a line rather than a point force response.

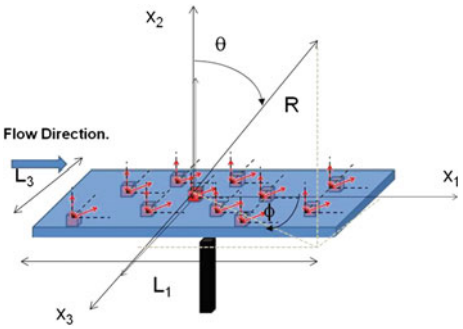

Fig. 3 Coordinate system used for expressing sound radiated from a roughness patch on a planar wall

analysis is straightforwardly transformable to other geometries as desired. All the acoustic sources in the turbulence of the fluid medium and the flow-element forces, F_n, are assumed to be unaffected by the motion of the elastic surface. First, ignoring the effect of the stiffener, (i.e. letting $Z_r = 0$) the solution for the spectrum of sound pressure, $\Phi_{\text{rad}}(y,\omega)$, above the plate due to a patch of N_{elements}, as illustrated in Fig. 3, is (see Blake and Anderson [7] for detail)

$$\begin{aligned}\Phi_{\text{rad}}(\vec{y},\omega) \approx \Phi_{\text{quadrupole}}(\vec{y},\omega) + \left|1+R(\tilde{k},\omega)\right|^2\left(\frac{k_o}{4\pi|\vec{y}-\vec{x}|}\right)^2 \times \cdots \\ \cdots \times N_{\text{elements}}\left(\Phi_{f1}(\omega)\cos^2\ \varphi\ \sin^2\ \theta + \Phi_{f3}(\omega)\sin^2\ \varphi\ \sin^2\ \theta\right) + \cdots \\ \cdots + \left(\left|1-R(\tilde{k},\omega)\right|^2\left(\frac{k_o}{4\pi|\vec{y}-\vec{x}|}\right)^2\right) \times \cdots \\ \cdots \times \left(4\cdot N_{\text{elements}}\Phi_{f2}(\omega) + \left[\frac{Z_r g(\vec{x}_a)}{1+Z_r g(0)}\right]^2 \Phi_{s\infty}\left(\left|\vec{k}_{1,3}=k_p,\omega\right|\right)\right)\cos^2\ \theta\end{aligned} \tag{1}$$

In this expression, $\Phi_{\text{quadrupole}}(y,\omega)$ is the net quadrupole sound from the turbulence swarm above the plate, k_o is acoustic wave number, ω/c_o, ϕ and θ are spherical coordinates with θ measured off the normal to the plate and $\phi = 0$ the flow direction looking downstream. The spectrum $\Phi_{s\infty}\left(k_{1,3},\omega\right)$ is the blocked pressure spectrum on the surface. The coordinate in the patch of N_{element} roughness elements is x on the plate, and y is the off-plate observer location, which is assumed to be in the far field with $|y| \gg$ dimension of the patch. $R(k,\omega)$ is the reflection coefficient from the plate:

$$R(\tilde{k}_{1,3},\omega) = \left(\frac{Z_s(\tilde{k}_{1,3},\omega) + Z_{fl}(\tilde{k}_{1,3},\omega) - Z_{fu}(\tilde{k}_{1,3},\omega)}{Z_s(\tilde{k}_{1,3},\omega) + Z_{fu}(\tilde{k}_{1,3},\omega) + Z_{fl}(\tilde{k}_{1,3},\omega)}\right) \tag{2}$$

and

$$\tilde{k}_{1,3} = (k_o\cos\phi\sin\theta, k_o\sin\phi\sin\theta) \tag{3}$$

is the acoustic trace wave number in the plane of the plate.

The expressions for the fluid and structural impedances are

$$Z_{fu}(k_{1,3},\omega) = (\rho_o c_o)_u \frac{k_{ou}}{\sqrt{k_{ou}^2 - k_{1,3}^2}} \quad \text{and} \quad Z_{fl}(k_{1,3},\omega) = (\rho_o c_o)_l \frac{k_{ol}}{\sqrt{k_{ol}^2 - k_{1,3}^2}} \tag{4}$$

and

$$Z_s(k_{1,3},\omega) = \rho_s h\omega \cdot Z(k_{1,3},\omega) \tag{5}$$

With $Z(k_{1,3},\omega)$ representing the frequency-wave number behavior of the structure *in vacuo*. We leave this impedance in this general form because specific evaluations will be outside the scope of this paper. What is relevant is the scaling on structural mass density mass as expressed by the leading term $\rho_s h\omega$, where h is plate thickness.

The case of a rigid plate is that for which $Z_f/Z_s = 0$. In the context of our double-deck fluid model, the quadrupole sources, T and T^i, are due to the net effect of the non-frozen convected upper-layer and interstitial turbulence as would be included in application of a Chase-type [8] model for the quadrupoles. The dipole strengths include the diffraction-loading on the elements due to interaction with imposed pressure from the outer flow as would have been predicted by Howe [23] and, more recently, Glegg et al. [16], Glegg and Devenpor [17], plus the directly-applied flow-element forces that constitute the roughness-scale inner flow. It is this force mechanism that also drives the plate directly as a "rain-on-the-roof" stochastic forcing. All space-time characteristics are, of course embedded in the natures of the transforms in $(k_{1,3},\omega)$.

The contribution due to the induced force dipole from the structural attachment, which also conveniently represents the notional effect of constraining boundary conditions, is

$$\Phi_{\text{rad,attach}}(k_{1,3} = k_p,\omega) = \left(\frac{Z_r g(\vec{x}_a)}{1 + Z_r g(0)}\right)^2 \Phi_{s\infty}(k_{1,3} = k_p,\omega) \tag{6}$$

and the net "blocked" pressure spectrum on the surface of the plate from all contributions is of the form

$$\begin{aligned}\Phi_{s\infty}(k_{1,3},\omega) = &\left\{\Phi_{\text{quadrupole}}\right\}_{\text{rigid}} + \cdots \\ &\cdots + \frac{N_{\text{elements}}}{(2\pi)^4}\Phi_{f_2}(\omega)\frac{\sin(k_1 h/2)\sin(k_3 h/2)}{k_1^2 k_3^2 h^2/4} + \cdots \\ &\cdots + \frac{N_{\text{elements}}}{(2\pi)^4}\frac{k_1^2\cdot\Phi_{f_1}(\omega) + k_3^2\cdot\Phi_{f_3}(\omega)}{k_0^2 - k_{1,3}^2}\end{aligned} \tag{7}$$

where $\Phi_{f1}(\omega)$, $\Phi_{f2}(\omega)$, and $\Phi_{f3}(\omega)$, are stream-wise, normal, and transverse force frequency-spectra on the elements, respectively. The explicit functional form

appearing in the second component of Eq. (7) arises by assuming a square base of the roughness element of dimension h. The rigid-wall form of Eq. (1) is

$$\Phi_{\mathrm{rad}}(\vec{y},\omega) = \Phi_{\mathrm{quadrupole}}(\vec{y},\omega) + \cdots \\ \cdots + 4\left[\frac{k_o}{4\pi|\vec{y}-\vec{x}|}\right]^2 N_{\mathrm{elements}}\left(\Phi_{f1}(\omega)\cos^2\phi\sin^2\theta + \Phi_{f3}(\omega)\sin^2\phi\sin^2\theta\right) \tag{8}$$

Equations (1) and (8) are the essential results for this section. They show the essential components of the sound and clarify the specific roles of surface impedance in weighting the roles of the structure both as reflector to hydroacoustic sources and scatterer due to structural inhomogeneity. When the surface is essentially rigid, $Z_s \gg Z_f$, then Eq. (6) gives a classical result that the sound is concentrated to the plane of the plate, $\theta = \pi/2$; normal dipoles being relegated to quadrupole rank of order $(k_o k_g)^2$ times the dipole components due to specular reflection at the plate surface where k_g is the height of protuberance or spoiler. The quadrupole term includes contributions from both the outer flow and the interstitial flow in the inner flow, but sustained by the essentially flat sections of the wall particularly interstices. The dipoles contain both the direct flow-induced inner-layer forces as well as the diffraction-induced forces caused by element scattering of outer-flow hydrodynamic scale pressures.

2.2 General Characteristics of Acoustic Response

In this section we consider the intrinsic structural-acoustic response characteristics that are common to all elastic structures with an attached spoiler dipole. For illustration and to baseline parameters for discussion, we consider a plate-fluid system in which a fluid dipole is just above the plate and oriented with its axis to 45° relative to the plate plane. This is a dipole couple that, therefore, consists of equal in-phase dipoles, one normal to the plate plane, the other parallel to it. At one extreme of structural parameters, when the plate is effectively rigid, i.e. $Z_s \gg Z_{fu}$ and Z_{fl} in Eq. (2), $R(k,\omega) = +1$, and all terms in Eq. (1) except the first 2 vanish leaving a $\sin^2\theta$ directivity pattern. This is illustrated by the polar wave number-azimuth plot in Fig. 4 for the sound field in the upper-half fluid region above the plate and a force dipole of unit strength representing a single roughness element aligned 45° with the surface. The null in the acoustic radiation at 0° is due to the nearly exact extinction of the normal ("lift") dipole component by the acoustic reflection of the plate. This is the case of aeroacoustic application, particularly as typically encountered in wind tunnels, where the surface that supports the turbulent boundary layer is rigid.

In the opposite extreme of the same dipole attached to an effectively transparent (R = 0) elastic plate with fluid on both sides, depicted in Fig. 5, the acoustic field can change substantially. The plate is now not a perfect reflector of the surface irregularity's dipole. Since the plate is assumed to be infinite, and since the plate's

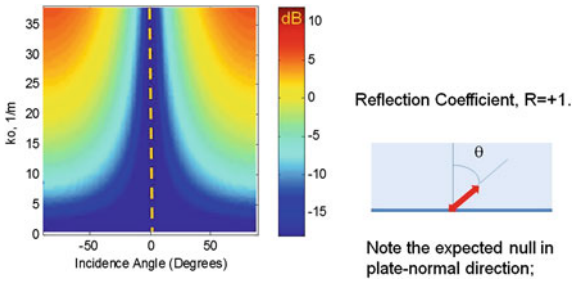

Fig. 4 Wave number-azimuth plot of sound radiated above an effectively-rigid surface which supports a force dipole at $\theta = 45°$ to the plate-normal

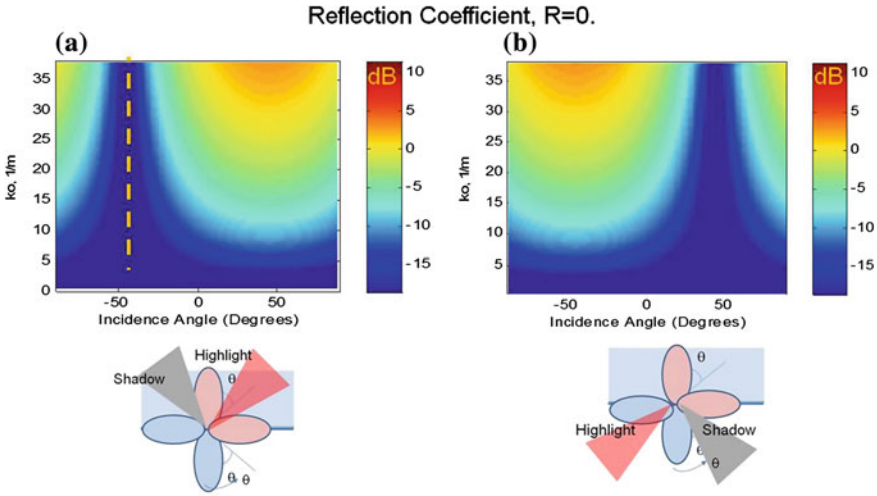

Fig. 5 Acoustic radiation to the fluid above, $x_2 > 0$, (**a**) and below, $x_2 < 0$, (**b**) a single roughness element above an Aluminum plate 1.25 cm thick as in Fig. 3, The dipole is oriented to 45° of the plate normal. Both plots show the wave number-azimuth characteristics and the *sketches below* show the directivity pattern of the dipole showing its resolution along the coordinate (x_1, x_2) axes and the resulting highlight zones. These lie along the ±45° axes. The calculation is made for an Aluminum plate, h = 1.252 cm, in water

response is below its acoustic coincidence frequency, there are no resonance effects depicted in this example. The null in the radiated sound in the upper fluid, $x_2 > 0$, has now shifted to be aligned with that of the original dipole. Below the surface in the quiescent fluid, $x_2 < 0$, the null in the radiated sound shifts 180° in accordance with the directivity of the exciting dipole. All the calculations in Figs. 4, 5 and 6 were made for the dipole's strength set to $\Phi_{f1}(\omega) = \Phi_{f2}(\omega) = 1$, and all plots of the sound are to the same scale and reference value. Therefore, comparison of the figures shows that the values of radiated sound on the main lobe of directivity are

generally comparable in all cases shown. However, on the upper side, as the plate impedance increases at higher frequencies the directivity fills in due to contribution from direct reflection of the dipoles on this side. Essentially, at other frequencies the sound on both sides of the plate is due to the acoustically-slow bending waves induced on the plate by the direct drive from the attached dipole force element. We shall see that the characteristics of plate response in this region of frequency will be changed by the presence of boundaries and structural attachments.

Figure 6 shows another case depicting a transition between transparent and reflective behavior, depending on frequency. In this case the plate might be Aluminum or glass reinforced composite plate with a thickness of h = 0.038 mm in air. In this case as the inverse of the fluid loading factor, which is defined as

$$\beta^{-1} = m_s\omega/\rho_o c_o \tag{9}$$

transitions from 2 to 3, the plate's response shifts from transparent (heavy fluid loading) to reflecting (light fluid loading). We shall return to this point later when we examine a more specific example of the roughness-driven aeroacoustic response of a finite plate in air. Equation (6) shows that the contribution of sound radiated by the structural supports or attachments to the plate is proportional to the spectrum of the blocked pressure on the surface. This pressure is essentially that on the rigid wall and is of the form given by Eq. (7). In the next section we will develop the nature of this spectrum as generated by hydrodynamically subsonic flow.

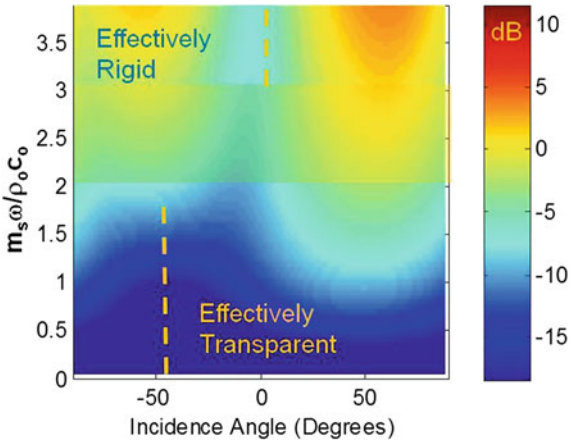

Fig. 6 Acoustic radiation to the fluid above the plate-roughness system, $x_2 > 0$ of Fig. 3, for a dipole oriented to 45° of the plate normal. The plot shows sound level on the *upper (flow) side* of the plate as function of fluid loading factor and azimuth. The highlights shift in angle as the frequency is increased

3 Forcing Functions for Walls with Distributed 3-Dimensional Roughness

3.1 Dipole Source Strengths and Construction of a Spectrum for Blocked Wall Pressure

3.1.1 Results of Large Eddy Simulations

The LES results of Yang and Wang [31–34] used simulations of geometric patterns of 40 hemispheres and cubes arranged in body-centered patterns on a wall of a turbulent channel flow as illustrated in Fig. 7. The results include the calculation of forces on the individual elements, space-time correlations of those forces, and radiated sound. Among other configurations, they used a roughness patch of 40 elements (10 transverse rows of 4 elements each) for which it was found that the sound could be characterized by 40 statistically independent roughness dipoles lying in the surface. The strengths of the dipoles were found to vary slightly (say by 3 dB, maximum) row by row with distance from the leading edge, but downstream of the first row the dipole strengths had a nearly fixed value. The outer flow of the roughness elements appeared in the simulation to be fed by large-scale disturbances ejected from the interstitial flow among the roughness elements.

The viscous-scaled roughness size, $k^+ = k_g U\tau/\nu$, is ~ 168 for these calculations. The sound was wholly due to direct flow-element interaction that included contributions from both upstream roughness scale turbulent flow and wakes generated by the elements, not diffraction, Yang and Wang [31]. Within limits it was found that the mean square forces on all elements were comparable even though differences did remain between elements in the first row compared with those downstream. Figure 8 shows a comparison of the spectra of forces on an individual element and in the population downstream of the first 4 rows for the three roughness shapes.

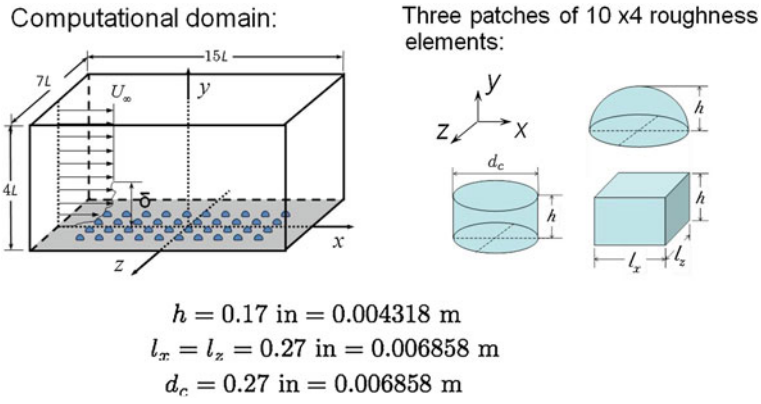

Fig. 7 Large eddy simulation set-up, Yang and Wang [31–34]. *Note* $h = k_g$ in this subsection

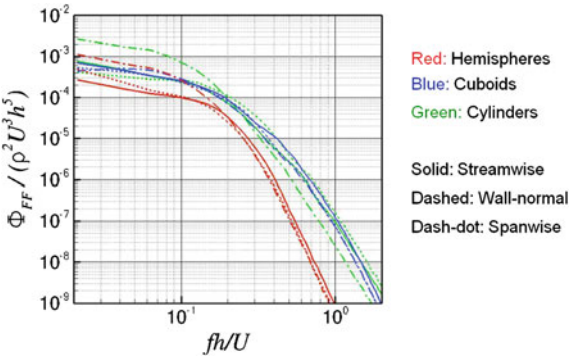

Fig. 8 Non-dimensionalized spectral density of net, per element forces obtained by large eddy simulation in air for U_o = 13.7 m/s; Yang and Wang [31–34]

Forces exerted on the cube and cylinder elements significantly exceed those on the hemispherical elements at normalized frequencies above 0.3, with only slight difference between transverse and stream-wise forces on the cubes. Figure 9 compares the exact calculation of sound by Yang et al with spectra of sound using Eq. (10) in a flyover plane 45° off the plane normal to and downstream of the center of the patch. The points represent results obtained using large eddy simulation, the lines were obtained using analytical expressions for the force spectra using a curve fit expressions for the results of Fig. 8. For example, the one for cuboid elements is Eq. (11) of the next section. The model for the radiated sound as Eq. (8) with the direct

$$\begin{aligned}\Phi_{\mathrm{rad}}(\vec{y},\omega) = \iint_S 4\left[\frac{k_o}{4\pi|\vec{y}-\vec{x}|}\right]^2 \frac{\mathrm{d}N_{\mathrm{elements}}}{S} x \cdots \\ \cdots \left(\Phi_{f1}(\omega)\cos^2\varphi(\vec{x},\vec{y})\sin^2\theta(\vec{x},\vec{y})\right. \\ \left.+\Phi_{f3}(\omega)\sin^2\varphi(\vec{x},\vec{y})\sin^2\theta(\vec{x},\vec{y})\right)\mathrm{d}S(\vec{x})\end{aligned} \tag{10}$$

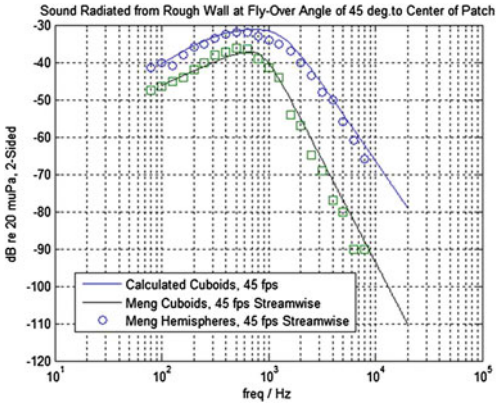

Fig. 9 Calculated frequency spectral density of sound pressure emitted from LES flow over cube and hemisphere roughness patches comparing the result of Yang and Wang [34] with relationships of this paper; in air for U_o = 13.7 m/s; the Curle-Powell relationship for dipole sound was used to calculate the sound

quadrupole sound ignored giving Eq. (10). Also ignored are row-by-row variations in the forces in the implementation of Eq. (10). In this form, the location of the field point $\vec{y}$ in the roughness patch is not in the geometric far field of all points $\vec{x}$ on the surface. Thus the integration includes the coordinate-accurate polar and azimuthal angles between each element of integration in the plate plane and the observer's field point. Furthermore, the force spectrum has been assumed to be independent of position in the patch. Clearly the calculated sound spectra in Fig. 9 for the two roughness types follow differences in the force spectra in Fig. 8. Subject to these statistical approximations we have introduced the concept of a distributed mean spectral density per roughness element in Eq. (10).

3.1.2 Results of Physical Experiments

The companion aeroacoustic experimental programs conducted as part of the study. The first of these was conducted in the NSWCCD anechoic flow facility Anderson et al. [1] and the second in Virginia Tech's facility Grissom et al. [18], Devenport et al. [10, 11]. Both of these studies provided radiated sound from turbulent-flow roughness patches on rigid surfaces within anechoic environments. These experimental studies were designed collaboratively with the LES team and discussed in detail by these references and summarized by Anderson and Blake [3]. In addition to general corroboration of the numerical simulations, these experiments substantially extended the application of knowledge gained for sound from rough-wall turbulent boundary layers.

Figure 10 shows a pair of example spectra of sound radiated from a patch of cubes: 0.17 in. on a side separated stream-wise and transversely by 1 in. for 8 × 32 elements arranged in a body-centered pattern. The sound was measured at a sideline microphone in the wall approx 0.7 m transversely from the center of the patch at

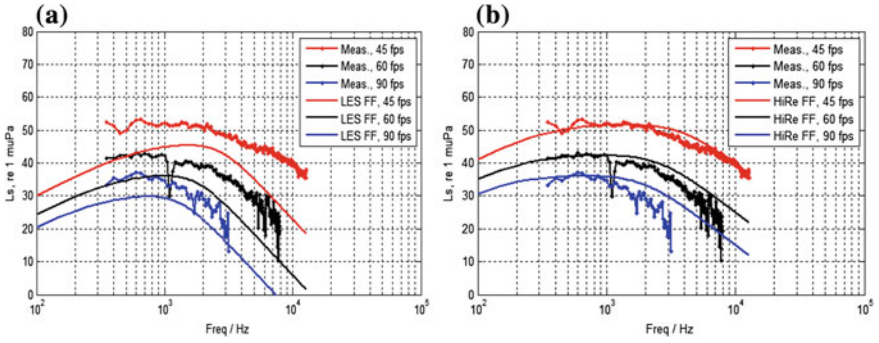

Fig. 10 Measured radiated sound from an 8 × 32 element patch in air compared with estimates using Eq. (1) for the *large* patch of cubes, neglecting the quadrupoles, for an observer to the side line of the patch a distance 0.7 m to the right hand side of the flow direction. The lines were calculated with Eq. (10) using Eqs. (11) and (12) for graphs (**a**) and (**b**) respectively. **a** Measurement and sound calculated with LES force spectrum, Eq. (11). **b** Measurement and sound calculated with inferred force spectrum Eq. (12)

multiple tunnel speeds and is shown in both the right and left of the figure, see Anderson et al. [1] for detail. The calculated sound is obtained using Eq. (10) and alternative analytical functions for the force spectra: either Eq. (11) on the left or Eq. (12) on the right. On the left the force spectrum is that provided by LES computation already shown the cuboids in Fig. 9. On the right the comparison is made with a force spectrum that was derived specifically to fit the results at 92 ft/s and used to calculate other speeds. This spectrum model will be referred to as the high Reynolds number ("HiRe") force regression and the former the "LES" force spectrum which was for the lowest Reynolds number of the physical experiment. Recall that the LES results for both the sharp-edged cube and sharp-edged cylindrical elements provided similar force spectra, recall Fig. 8. The designation as a "high Reynolds number" force regression is so-named because of its determination by the higher Reynolds number measurement in the experiment compared with the LES case. Examination of Fig. 10a shows that the LES force spectrum is in closer agreement by shape, although $\sim$4 dB lower, compared with the measured sound at 45 ft/s than it is at the highest speed. Conversely, Eq. (12) gives better agreement with data at high velocity shown in Fig. 10b. The "LES" regression is

$$\frac{\Phi_f(f) \times U_o/k_g}{\left[\rho_o U_o^2 k_g^2\right]^2} = \frac{6.055 \times 10^{-4}}{1 + 101.3(fk_g/U_o)^2 + 2{,}632(fk_g/U_o)^{6.15}} \tag{11}$$

and the "HiRe" regression is

$$\frac{\Phi_f(f) \times U_o/k_g}{\left[\rho_o U_o^2 k_g^2\right]^2} = \frac{81 \times 10^{-4}}{1 + 375(fk_g/U_o)^2 + 1{,}646(fk_g/U_o)^5} \tag{12}$$

Figure 11 shows the radiated sound nondimensionalized on the measured wall pressure spectrum for roughness patches that include measurements from Anderson et al. [1] and Devenport et al. [10, 11]. The ordinate uses local free-stream Mach number, roughness size, number of elements, and range from the center of the roughness patch to the observer used in each measurement, i.e.:

$$\frac{\Phi_{\text{rad}}(\omega)}{\Phi_{\text{wall}}(\omega)(U_o/c_o)^2 N_{\text{elements}}(k_g/R)^2} \tag{13}$$

This form of non-dimensionalization was introduced in earlier papers by Blake et al. [6], Anderson et al. [1], and Devenport et al. [10, 11] and isolates the essential dependence of the radiated sound on the dipole strengths of the roughness elements. The ratio ignores any differences in directivity since the measurements in both facilities were on or within 45° of the main lobe of directivity in the far field of the roughness patch. The straight diagonal line in the figure is a theoretical line, $\sim k_o^2$, drawn using a regression for the empirically inferred proportionality between frequency spectra of element force, $\Phi_f(\omega)$, and wall pressure spectrum $\Phi_p(\omega)$, given below in Eq. (14)

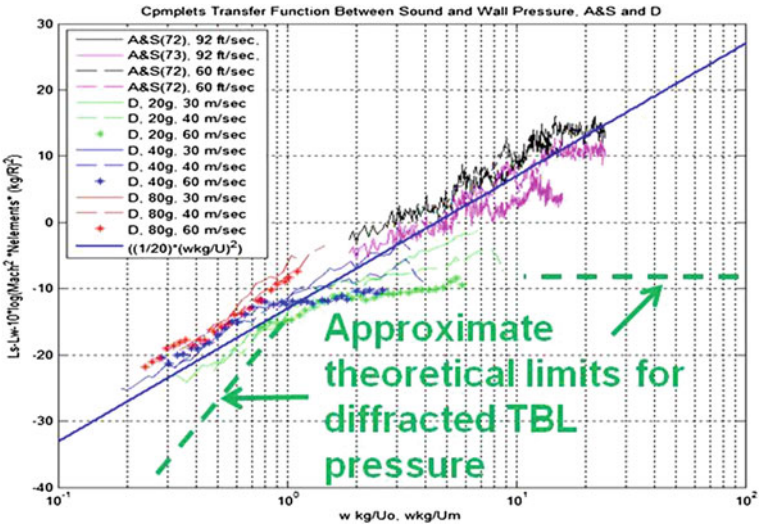

Fig. 11 The radiated sound nondimensionalized on the measured wall pressure spectrum for a series of roughness patches that include measurements from Anderson et al. [1] and Devenport et al. [10, 11], and Smith et al. [30]

$$\frac{\Phi_f(\omega)U_o/k_g}{\left[\rho_o U_o^2 k_g^2\right]^2} = 4\frac{\Phi_p(\omega)U_o/k_g}{\left[\rho_o U_o^2\right]^2} \tag{14}$$

where the wall pressure spectrum is measured between elements. The dependence as k_o^2 is a direct consequence of the dipole radiation mechanism being dominant as in Eq. (8) vs. Eq. (10). The close trend of all the experimental results to this line also points to the efficacy of Eq. (14) in (at least roughly) characterizing the dipole source strength of the roughness. The spread in the dimensionless values shown is likely due to 3 factors. First as noted above, although measurement field points in the experiments of Devenport et al. and Anderson et al. were above the surface and not in the fly-over plane of the roughness patch, they were not made at the same field points in directivity (θ, ϕ). Second, Eq. (11) represents an approximation to the force spectra on the elements. Third, variability at frequencies above roughly $\omega k_g/U > \sim 2\pi$ may be due to diffraction of hydrodynamic wave numbers by the roughness elements as scattering sites. Forth, the flow in the interstitial region of the roughness is inhomogeneous making a clear definition wall pressure spectrum there difficult. As discussed by Devenport et al. [10, 11] the breakpoint in measured sound occurring in the vicinity of $\omega k_g/U_o = 1$ to 10 is a consequence of the geometric scale equivalence between hydrodynamic wave length and roughness element dimension.

The dotted lines in the figure represents 2 asymptotic relationships for the diffraction-generated contribution due to the pressure field of the outer flow scattering off roughness elements as predicted by Howe's [22] diffraction model. The frequency in this graph is normalized on the geometric roughness size and free stream

velocity. For dimensionless frequencies below unity, the scattering is determined by element interaction with hydrodynamic pressure induced by upper-layer turbulence as compact dipoles where flow velocity determines the spatial scale of the pressure component interacting with the roughness element. At higher dimensionless frequencies the scattering elements are not hydrodynamically-compact and this causes the diffracted component to flatten as shown. In applying the diffraction theory of Howe [22], Chase's factors for boundary layer-induced wall pressure were used but numerically altered to match parameters of the rough wall boundary layer. The measurements shown in the figure were obtained over a wide range of roughness Reynolds numbers k_g^+. This plot suggests that the diffraction contribution from the rough wall forms a lower bound threshold above which is a contribution due to the direct flow-element interaction forces. Note that in the work of Glegg and Devenport [17] the diffraction contribution was indicated to be dominant for 2 dimensional small k_g^+ wavy walls, however where coherent scattering of k_c wave numbers from the 2d pattern of riblets created patterns in the radiated sound.

At very low wave numbers bounded by the acoustic wave number in the fluid medium there is a contribution due to sound emitted from forces on the elements propagating along the plate surface, this is labeled as the dipole acoustic region in Fig. 12. Superimposed on these two contributions is one that is due to the direct flow-element interaction forces that are applied to the plate in the normal direction. The wave number spectrum of this contribution is limited by the size of the roughness projected on the plate surface and is marked in Fig. 12 as $2\pi/k_g$.

The illustrations in Fig. 13 compare the calculated wall pressure spectra for the rough wall to that of the smooth wall using reasonable parameters listed in Table 1 for the boundary layer. The boundary layer displacement thicknesses are taken as identical to both wall types to eliminate that parameter from the comparison. What separates the rough from the smooth wall in the illustration are the wall shear stress coefficient, C_f, and the roughness size, k_g, because both of these determine the

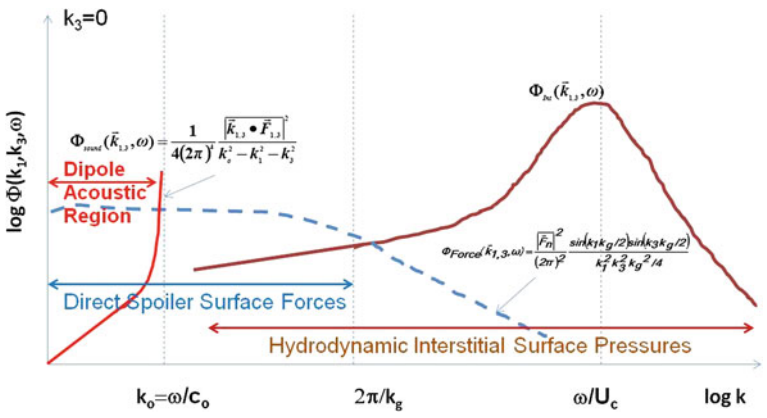

Fig. 12 The "blocked" wall pressure on the rigid wall: the wave number-frequency spectrum function of rigid-wall surface pressure

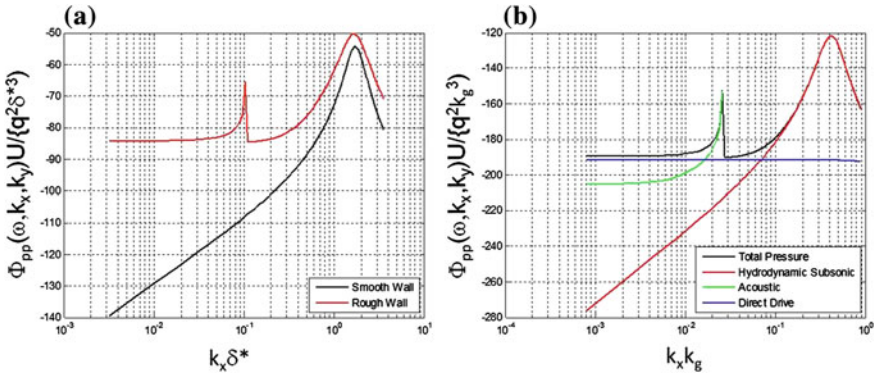

Fig. 13 Examples of the "blocked" wall pressure on rigid smooth and rough walls; **a** comparison of smooth and rough wall cases normalized on δ^*, **b** the contributions of the rough wall pressure spectrum normalized on k_g. For this example the acoustic wave number is $k_o\delta^* = 0.1$ or $k_o k_g = 0.027$

Table 1 Illustrative properties of rough and smooth wall turbulant boundary layers

U	29.9 m/s
δ^*	3.2 mm
c_f, smooth	0.0024
k_g	0.95 mm
C_f, rough	0.0136

strengths of the momentum dipoles attached to the roughness elements. The hydrodynamic subsonic component is calculated using the expression of Chase [8] using parameters for the rough wall appearing in Blake [4] for smooth and rough walls. The pressure spectrum for the rough wall was used in the simulations of elastic response that will be discussed in Sect. 4. Note that the range of $k_x k_g$ shown in Fig. 13b is less than 2π so does not show the fall-off at high wave numbers shown for the direct forcing in Fig. 12.

4 An Illustration of Acoustic Response of a Simply-Supported Plate with Irregular Surface

We assemble the results of the previous sections using, as an example, the sound from a flow-driven rough rectangular elastic panel. We consider the rectangular panel to be roughened with a uniformly random distribution of small elements that extend over a larger planar region that supports the panel and forming a rough-wall turbulent boundary layer. The problem of forced vibration of a simply-supported flat plate solved via modal expansion is a classical way for illustration of the dominant behavior mechanisms often modeled by other techniques in engineering

use. The method, developed originally by Lyon [26] and Dyer [12] is well-known and described elsewhere; see e.g. Blake [5] and Skelton and James [29].

Assume now that the plate isolated in Fig. 3 is actually a panel of dimensions L_1 and L_3 of a larger stiffened structure. We assume that this panel can respond independently of all others and that the remainder of the structure acts as a rigid acoustic baffling surface. Equation (1) provides all the contributions to the sound emitted by this plate element. The first term represents the quadrupoles (soon to be neglected compared with all the others for this low Mach number case), the second term accounts for the direct radiation from the flow dipoles associated with the $N_{elements}$ of roughness on the plate, and the third term represents the sound from the forced vibration. So under the assumption that the distance from the observer to the plate center, r, satisfies the restriction that $r \gg L_1, L_3$, this problem Eq. (1) takes on the form

$$\begin{aligned}\Phi_{\text{rad}}(\vec{y},\omega) \approx \Phi_{\text{quadrupole}}(\vec{y},\omega) + \left|1+R(\tilde{k},\omega)\right|^2\left(\frac{k_o}{4\pi|r|}\right)^2 \times \cdots \\ \cdots \times N_{\text{elements}}\left(\Phi_{f1}(\omega)\cos^2\varphi\sin^2\theta + \Phi_{f3}(\omega)\sin^2\varphi\sin^2\theta\right) + \cdots \\ \cdots + \Phi_{\text{Vib}}(\vec{y},\omega)\end{aligned} \tag{15}$$

where

$$\frac{\Phi_{\text{Vib}}(\vec{y}\cdot\omega)}{\Phi_{pp}(\omega)} = \sum_{m,n}\frac{[\Phi_{\text{rad}}(\vec{y},\omega)]_{m,n}}{\Phi_{pp}(\omega)} \tag{16a}$$

$$[\Phi_{\text{rad}}(\vec{y},\omega)]_{m,n} = \left[\frac{\rho_o c_o}{m_s\omega}\right]^2\left[\frac{k_o^2}{2\pi|r|^2}\right]\Phi_{pp}(\vec{k}_{m,n},\omega)\left[\frac{(2\pi)^2}{A_p}\right]\frac{\left|S_{m,n}(\bar{\gamma}_{1,3})\right|^2}{\left|\mathscr{L}(k_{m,n},k_o)\right|^2} \tag{16b}$$

is the contribution to the sound from the flow-induced vibration with $\Phi_{\text{pp}}(\omega)$ the auto-spectrum of wall pressure between the roughness elements. The various factors appearing in Eq. (16) are the trace wave numbers in the plane of the plate,

$$\bar{\gamma}_1 = k_o\sin\theta\cos\varphi, \bar{\gamma}_3 = k_o\sin\theta\sin\varphi \tag{17}$$

the Fourier wave number transform of the mode shape of the m, n mode

$$S_{m,n}(\vec{k}_{m,n}) = 2k_m k_n e^{i(k_1L_1+k_3L_3)/2}\left[\frac{\left(1-(-1)^m e^{ik_1L_1}\right)\left(1-(-1)^n e^{ik_3L_3}\right)}{\left(k_m^2-k_1^2\right)\left(k_n^2-k_3^2\right)}\right] \tag{18}$$

the impedance function for the plate, also evaluated at the trace wave number,

$$\mathscr{Y}(k_{m,n},k_o)=\left[\left(\frac{k_{m,n}}{k_p}\right)^4+i\eta_{m,n}\left(\frac{k_{m,n}}{k_p}\right)^2-\left[1+\frac{\rho_0 c_o}{m_s\omega}\frac{k_o}{\sqrt{k_{m,n}^2-k_o^2}}\right]\right] \tag{19}$$

as well as assorted physical parameters fluid density, ρ_o, and sound speed, c_o, and area density of plate material, m_s. For the simply-supported plate, the modal wave numbers are, respectively, $m\pi/L_1$, and $n\pi/L_3$. $A_p = L_1L_3$. The wave number of blocked surface pressure is as given by Eq. (7) and is illustrated in Figs. 12 and 13. The last term of interest is the reflection coefficient, $R\left(k_{1,3},\omega\right)$; this was given by Eq. (2) and it, too, is evaluated at the trace wave number of the acoustic medium on the plate.

Figure 8 shows that for a given roughness geometry, to acceptable accuracy, say 3 dB in representing the measured dipole strengths of the rough surface on the rigid wall with the theory, the forces in all three vector directions (normal, transverse, and stream-wise) may be taken as effectively equal, and that the autospectrum of these forces is related to the autospectrum of wall

$$\begin{aligned}\frac{\Phi_{\text{rad}}(\vec{y},\omega)}{\Phi_{pp}(\omega)}\approx\sum_{m,n}\frac{[\Phi_{\text{rad}}(\vec{y},\omega)]_{m,n}}{\Phi_{pp}(\omega)}+\cdots\\ \cdots+\Big[\left|1+R(k_o,k_p)\right|^2\left(\cos^2\varphi\sin^2\theta+\sin^2\varphi\sin^2\theta\right)\\ +4\times\left|1-R(k_o,k_p)\right|^2\cos^2\varphi\Big]\times\cdots\\ \cdots\times N_{\text{elements}}\left[\frac{k_oL_1}{4\pi R}\right]^2\left[\frac{\Phi_{FF}(\omega)}{L_1^2\Phi_{pp}(\omega)}\right].\end{aligned} \tag{20}$$

pressure in the roughness interstices by Eq. (14) so that the blocked pressure excitation spectrum is usefully represented in proportion to $\Phi_p(\omega)$. The radiated sound from the flow-excited vibration normalized on $\Phi_{pp}(\omega)$ is given by the expression.

Figure 14 illustrates all contributions to this expression for a flow-excited plate with fluid on both sides in the context of 2 example plates. These examples are selected because they are identical to those considered experimentally and analytically by Davies [9] for a smooth wall. At that time an analytical approach, basic to that used here, was validated by experiment, See Davies [9] and Blake [4]. This calculation used the structural parameters of Davies experiment and the geometric arrangement of Yang et al.'s 40-element roughness pattern scaled to the size in Table 1. The analysis includes all direct acoustic radiation source components and contributions from plate response to this notional structure and rough-wall turbulent boundary layer. The figure shows that modal response to the normal forcing from the elements controls the low frequencies whereas the directly radiated sound from the fluid dipoles contributing to these forces accounts for the sound at higher frequencies.

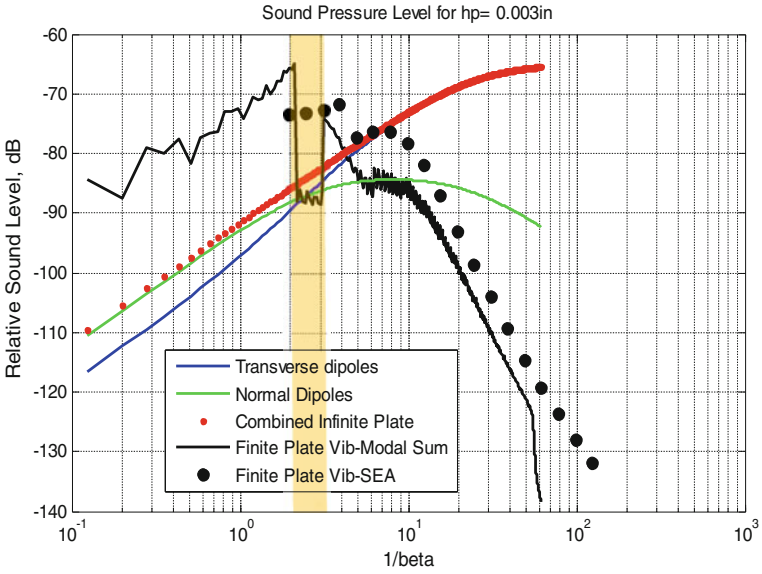

Fig. 14 An example calculation of sound from the combined direct and reflected dipoles, and induced vibration in heavy fluid on 2 sides. The directly radiated sound from the transverse and normal force components on the roughness is evaluated at the angles of maximum acoustic response. Sound is calculated on the flow side of the 0.076 mm thick steel plate in air

The example uses the rough wall parameters in Table 1 and the plate area is defined by $L_1 = 0.2792$ m and $L_3 = 0.3299$ m. These calculations illustrate that the $m_s\omega/\rho_o c_o \sim 2-3$ limit for vibration-controlled sound may be too restrictive for finite-plate modal response and may extend to somewhat higher values. At low frequencies, sound will be dominated by flow-induced vibration while at higher frequencies above this transition value, sound will be dominated by surface dipoles as modified by surface reflection from plate as an effectively-infinite structure. At all frequencies, both transverse and normal dipoles will contribute to driving the plate-fluid system.

5 Conclusions

In this paper, we have constructed a general model of the sound emitted by flow over either elastic or in-elastic surfaces. In the case examined of the elastic wall with surface irregularities, the excitation of the plate is by a superposition of direct forcing by the flow-driven forces on the protuberance and acoustic pressures due to the dipoles of the fluid unsteady momentum around the protuberance. Radiated sound is a superposition of both direct dipoles and elastic response. The roles of the

structure's fluid loading parameter, $\rho_o c_o/m_s\omega$, and of the acoustically-scaled dimension $k_o L$ of the elastic region of a flow-driven surface has been clarified in this process for which the turbulent boundary layer has 2 physically-different source mechanisms. What differentiates the elastic surface from the rigid wall, particularly at low free-stream Mach number, is the importance of the surface-normal forces on the elements. For low Mach number flow these normal forces provide the excitation of the elastic surface that are made essentially extinct in the rigid-wall case by perfect reflection from the surface. The role of finiteness of extent of the elastic surface, or of attachments, comes as the modal response for which modeling approaches have been well-known for many years. This contribution from flow-excited vibration, though dominant for the smooth wall, is shown here to be relatively irrelevant in the case of the rough or irregular wall when $\rho_o c_o/m_s\omega$ is sufficiently small.

Although the discussion presented herein makes specific reference to the rough wall, the analysis presented here was introduced as being relevant to all manner of wall with geometric imperfections and irregularities. The LES work of Yang and Wang [31–34] on rough walls and, for example, of Ji and Wang [25] for walls with forward-facing steps supports this general picture of dipoles as common physics of the flow source contributions for walls with geometric unevenness that fit the notions portrayed in Figs. 1 and 2 of this paper. Those results disclose an inner flow which generates the essential dipole system at the step that lies beneath an outer flow which generates sound by diffraction. The experimental observations of Hong et al. [20, 21] for rough walls would seem to suggest this double-deck structure for the broader class of turbulent boundary layers over generally-uneven surfaces. The major differences among walls with differing surface irregularity shapes seems to lie principally in the spatial dimensionality of wall pressure statistics and relative orientations with respect to the flow direction of the flow dipoles that are generated. These, in turn, are determined by the interaction of inner and outer flow dynamics which determine the relative strengths of the vector dipoles on the surface. The surface structural acoustics then determines how these dipoles are filtered to create the sound.

The focus in specifics in this work involved sound from rough patches made up of geometrically-regular grids of roughness elements for which all elements were nearly the same size. Although this selection of geometry maintained a geometric similarity across the three component researches of this study, the results beg the question of what might happen if the roughness elements were of a more random nature in size and spacing. In spite of this we now have a much clearer view of the multitude of physical processes taking place within the boundary layer and how those processes produce sound. With such knowledge, a systematic approach could be developed that provides structure to the calculation and scaling of sound for both aeroacoustic and hydroacoustic engineering applications.

References

1. J.M. Anderson, D.O. Stewart, W.K. Blake, Experimental investigations of sound from flow over rough surfaces, in *ASME Meeting, IMECE2009−11445* (2009)
2. J.M. Anderson, W.K. Blake, Aero-structural acoustics of uneven surfaces part 2: a specific forcing by a rough wall boundary layer, in *20th AIAA/CEAS Aeroacoustics Conference*, Atlanta, GA, 16–20 June 2014
3. J.M. Anderson, W.K. Blake, D.O. Stewart, Aero-structural acoustics of uneven surfaces part 2: a specific forcing by a rough wall boundary layer, in *To Be Published at the 20th AIAA/CEAS Aeroacoustics Conference*, Atlanta, GA 16–20 June 2014 2013
4. W.K. Blake, Aero-Hydroacoustics for Ship. DTNSRDC Report 84/010, June 1984
5. W.K. Blake, *Mechanics of Flow Induced Sound and Vibration* (Academic Press, New York, 1986)
6. W.K. Blake, K.H. Kim, M. Goody, M. Wang, W. Devenport, S. Glegg, Investigations of roughness-generated TBL sound using coupled physical-computational experiments in conjunction with theoretical development, in *Second ASA-EAA Joint Conference*, Paris, France, 29 June–4 July 2008
7. W.K. Blake, J.M. Anderson, Aero-structural acoustics of uneven surfaces part 1: a general model approach to radiated sound, in *20th AIAA/CEAS Aeroacoustics Conference*, Atlanta, GA, 16–20 June 2014
8. D.M. Chase, The character of the turbulent wall pressure spectrum at subconvective wavenumbers and a comprehensive model. J. Sound Vib. **112**, 125–147 (1987)
9. H.G. Davies, Sound from turbulent-boundary-layer-excited panels. J. Acoust. Soc. Am. **49**, 878–889 (1971)
10. W. Devenport, D. Grissom, W. Alexander, B. Smith, S. Glegg, Measurements of roughness noise. J. Sound Vib. **330**, 4250–4273 (2011). doi:10.1016/j.jsv.2011.03.017
11. W. Devenport, E. Wahl, S. Glegg, W. Alexander, D. Grissom, Measuring surface pressure with far field acoustics. J. Sound Vib. **329**, 3958–3971 (2010). doi:10.1016/j.jsv.2010.03.012
12. I. Dyer, Response of plated to a decaying and convecting random pressure field. J. Acoust. Soc. Am. **31**, 922–928 (1959)
13. T.M. Farabee, F.E. Geib, Measurements of boundary layer pressure fluctuations at low wavenumbers on smooth and rough walls, in *Flow Noise Modeling Measurements and Control*. ASME NCA, vol. 11 (1991), pp. 55–68
14. J.E. Ffowcs Williams, Sound radiation from turbulent boundary layers formed on compliant surfaces. J. Fluid Mech. **22**(2), 347–358 (1965)
15. J.E. Ffowcs Williams, The influence of simple supports on the radiation from turbulent flow near a plane compliant surface. J. Fluid Mech. **26**, 641–649 (1966)
16. S. Glegg, W. Devenport, D. Grissom, D, Rough wall boundary layer noise: theoretical predictions, in *13th AIAA/CEAS Aeroacoustics Conference*, Rome, Italy, AIAA-2007–3417, 20–23 May 2007
17. S. Glegg, W. Devenport, The far-field sound from rough wall boundary layers, in *Proceedings of the Royal Society* A, vol 465 (2009), pp. 1717–1734. doi:10.1098/rspa.2008.0318
18. D. Grissom, B. Smith, W. Devenport, S. Glegg, Rough wall boundary layer noise: an experimental investigation, in *13th AIAA/CEAS Aeroacoustics Conference*, Rome, Italy, AIAA-2007-3418, 20–23 May 2007
19. A.S. Hersh, Surface roughness generated flow noise, in *AIAA 8th Aeroacoustics Conference*, Atlanta GA, AIAA-83-0786, 11–13 April 1983
20. J. Hong, J. Katz, M.P. Schultz, Near-wall turbulence statistics and flow structures over three-dimensional roughness in a turbulent channel flow. J. Fluid Mech. **667**, 1–37 (2011)
21. J. Hong, J. Katz, C. Meneveau, M.P. Schultz, Coherent structures and associated subgrid-scale energy transfer in a rough-wall turbulent channel flow. J. Fluid Mech., (2012) (in Press)
22. M. Howe, On the generation of sound by turbulent boundary layer flow over a rough wall, in *Proceedings of the Royal Society*. A, vol. 395 (1984), pp. 247–263

23. M. Howe, The influence of viscous surface stress on the production of sound by turbulent boundary layer flow over a rough wall. J. Sound Vib. **104**, 29–39 (1986)
24. M. Howe, *Acoustics of Fluid-Structure Interaction* (Cambridge University Press, Cambridge, 1998)
25. M. Ji, M. Wang, LES of turbulent flow over steps: wall pressure fluctuations and flow-induced noise, in *14th AIAA/CEAS Aeroacoustics Conference*, Vancouver, Canada, AIAA Paper 2008-3052, 5–7 May 2008
26. R.H. Lyon, Response of strings to random noise fields. J. Acoust. Soc. Am. **28**, 391–398 (1956)
27. G. Maidanik, E.M. Kerwin, *The Influence of Fluid Loading in the Radiation from Infinite Plates Below the Critical Frequency* (Bolt Beranek and Newman, Report, 1965). 1320
28. A. Powell, Aerodynamic noise and the plane boundary. J. Acoust. Soc. Am. **36**, 982–990 (1964)
29. E.A. Skelton, J.H. James, *Theoretical Acoustics of Underwater Structures*, (Imperial College Press., London 1997)
30. B. Smith, W. Alexander, W. Devenport, S. Glegg, Grissom, The relationship between roughness noise and the near-field pressure spectrum, D., in *AIAA/CEAS 14th Aeroacoustics Conference*, Vancouver BC, AIAA-2008-2904, 5–8 May 2008
31. Q. Yang, M. Wang, Computational study of boundary-layer noise due to surface roughness, in *14th AIAA/CEAS Aeroacoustics Conference*, Vancouver, Canada, AIAA Paper 2008-2905, 5–7 May 2008
32. Q. Yang, M. Wang, Computational study of roughness-induced boundary-layer noise. AIAA J. **47**(10), 2417–2429 (2009)
33. Q. Yang, M. Wang, Boundary-layer noise induced by a roughness patch, in *16th AIAA/CEAS Aeroacoustics Conference*, Stockholm, Sweden, AIAA Paper 2010-3772, 7–9 June 2010
34. Q. Yang, M. Wang, Statistical analysis of acoustic source-field in rough-wall boundary layers, in *17th AIAA/CEAS Aeroacoustics Conference*, Portland, Oregon, AIAA Paper 2011-2738, 5–8 June 2011

Part I
Source Characterization

Predicting the vibroacoustic response of a structure under turbulent wall-pressure fluctuations requires turbulent boundary layer (TBL) frequency or wavenumber spectra. These wall-pressure characteristics are commonly obtained using empirical or semi-empirical models, which are usually based on large experimental databases. Unfortunately, these TBL models are accurate only for a few simple configurations. Only numerical simulations can address complex geometries, as in real transportation systems, with a broad range of speeds. Alternatively, TBL characterization can be carried out through specific experimental setups, which are extremely expensive.

This section reports many attempts to compute auto- and cross-spectra of wall pressure fluctuations using computational fluid dynamics. Use of the Large Eddy Simulation (LES) method to simulate large-scale turbulent eddies, combined with that of the Reynolds Averaged Navier–Stokes (RANS) method for smaller turbulence, is discussed. Attention is also paid to Direct Navier–Stokes (DNS) simulation and Hybrid RANS-LES methods. In addition, we analyze the importance of pressure gradients, which decelerate or accelerate the flow, on the TBL shape and wall pressures.

Moreover, the complexity and the relevance of experimental measurements are considered in this section. New measurements, also dealing with supersonic TBL flow wall pressures, are presented and the need for more experimental investigations is highlighted. Finally, we present a simulation of turbulent synthetic jets, for industrial applications, compared to some experimental results.

Spectral Properties of Wall-Pressure Fluctuations and Their Estimation from Computational Fluid Dynamics

Daniel Juvé, Marion Berton and Edouard Salze

Abstract The various methods to obtain 1-point and 2-point statistical properties of wall-pressure fluctuations from CFD are described and discussed. If only averaged flow quantities are available through Reynolds Averaged Navier Stokes computations, empirical models or sophisticated statistical modeling have to be used to estimate wall-pressure spectra and spatial correlations. While very useful at design stage, their applicability to complex flows or geometries seems quite limited. Considering the rapid growth of computational power, it seems clear that the main pathway for the near future is to rely on time-dependent flow simulations, typically Large Eddy Simulations, and to estimate the pressure statistics through a posteriori signal processing. It seems also possible, at the moment only for relatively high Mach number flows, to estimate not only the hydrodynamic part but also the tiny acoustic contribution. Examples of computations of this acoustic contribution to wall-pressure are given together with related experiments.

1 Introduction

Estimating the statistical properties of the wall-pressure fluctuations induced by a turbulent flow is a necessary step to predict the vibroacoustic response of a structure. Typical examples are found in transportation systems, with a range of speeds varying from a few meters per second (for marine applications) to several hundred of meters per second (for aircraft applications). Classically, frequency spectra as

D. Juvé (✉) · M. Berton · E. Salze
Laboratoire de Mécanique des Fluides et d'Acoustique, UMR CNRS 5509, Ecole Centrale de Lyon, 36 Avenue Guy de Collongue, 69134 Ecully Cedex, France
e-mail: daniel.juve@ec-lyon.fr

M. Berton
e-mail: marion.berton@ec-lyon.fr

E. Salze
e-mail: edouard.salze@ec-lyon.fr

E. Ciappi et al. (eds.), *Flinovia - Flow Induced Noise and Vibration Issues and Aspects*, DOI 10.1007/978-3-319-09713-8_2

well as wave-number spectra are obtained using empirical models in which the global parameters of the flow enter and are evaluated using semi-analytical models (for example the boundary layer thickness is estimated using a simple flat plate formula). For the more complex geometries encountered in real configurations, it seems logical to rely on numerical simulations to obtain the required information. Today, Reynolds Averaged Navier Stokes (RANS) computations are performed routinely and are able to estimate accurately the global flow parameters at a reasonable computational cost. One important question is then: are the classical empirical models used to estimate the wall pressure statistical properties sufficient to predict for example the excitation of structures by flows under the influence of favorable or adverse pressure gradients or by detached flows induced by geometrical singularities of the surface?

To obtain more versatile models it seems desirable to rely more on numerical simulations at an earlier stage. Various approaches are possible depending on the nature of the numerical simulations. If only RANS simulations are available, a statistical model can be constructed in order to estimate the pressure spectra from the relatively poor information given by the RANS approach (typically a local value of the kinetic turbulent energy and of the dissipation rate). If unsteady computations are performed (such as Direct Numerical Simulations -DNS- or Large Eddy Simulations -LES-) a direct estimation of the time-evolution of the pressure fluctuations is possible from which statistical properties can be deduced by signal post-processing. Even with time-dependent simulations, a final and important difficulty persists if it is desirable to obtain not only the hydrodynamic contribution to wall-pressure but also the acoustic (compressible) contribution. In this case high fidelity compressible simulations are to be performed, and this is a particularly difficult task for low Mach number flows.

In aeroacoustics all these methods have been developed over the years and nearly routine unsteady computations are now performed to compute for example the noise generated by subsonic and supersonic aircraft propulsive jets [4, 5]. While the situation is clearly more difficult for wall bounded flows, such computations are already feasible for a number of applications or they will be feasible in a near future, due to the combination of rapidly growing available computational power and to the implementation of the high fidelity algorithms used in aeroacoustics.

In this paper we will give a short (and of course incomplete) review of the various approaches used to estimate wall pressure statistical properties with some illustration of today possibilities and shortcomings.

2 Fluid Dynamics and Wall-Pressure Fluctuations

To begin with, it may be useful to recall why the estimation of wall-pressure fluctuations is much more complicated than the determination of mean and turbulent velocity profiles.

The equations governing the flow are of course the Navier–Stokes equations. They are given by (we limit ourselves to incompressible flow for the moment):

$$\frac{\partial U_i}{\partial t} + U_j \frac{\partial U_i}{\partial x_j} = -\frac{1}{\rho}\frac{\partial p}{\partial x_i} + \nu \frac{\partial^2 U_i}{\partial x_i \partial x_j} \tag{1}$$

where U is the time-dependent local flow velocity, p the time-dependent local pressure, and ρ and ν the fluid density and kinematic viscosity.

It is natural to introduce the Reynolds decomposition of any time-dependent field as the sum of a mean part and a fluctuating part:

$$U_i = \bar{U}_i + u_i'; p = p_0 + p'$$

It is easily shown that the fluctuating pressure is then solution of a Poisson equation:

$$\frac{1}{\rho}\nabla^2 p' = -2\frac{\partial \bar{U}_i}{\partial x_j}\frac{\partial u_j'}{\partial x_i} - \frac{\partial^2}{\partial x_i \partial x_j}\left(u_i' u_j' - \bar{u}_i' u_j'\right) \tag{2}$$

The RHS of this equation can be considered as a forcing term involving the product of the gradient of the mean and of the fluctuating velocity and the double divergence of the centered product of velocity fluctuations; in other terms the sum of a linear contribution with respect to fluctuating quantities (or shear noise) and a non linear one (or self noise). Formally the solution of this equation can be written as the convolution product of the source term (ST) with an appropriate Green's function G:

$$p' = \rho G \times \mathrm{ST} \tag{3}$$

In the presence of a flat plate (regarded as infinite), G is chosen as the half space Green's function

$$G = \frac{1}{2\pi}\frac{1}{|\mathbf{x} - \mathbf{y}|} \tag{4}$$

These formula emphasize the fact that the pressure at a given point depends on the whole velocity field around it, with a weighting function decreasing only slowly with the distance between the source and the receiver. In this sense the pressure can be considered as a non-local variable and it is the main reason why its statistical modeling is much more difficult than for velocity fluctuations.

To take into account compressibility effects (the acoustic part of the pressure fluctuations), the Poisson equation has to be replaced by the wave equation and the appropriate Green's function is simply the fundamental solution for the wave equation in half space (obtained for example by the method of images).

If a time-dependent fluid dynamics code can be used, the pressure fluctuations can be computed as a function of time using the Poisson equation in differential or integral form for incompressible flow. For compressible flow, one has to solve simultaneously the Navier-Stokes equations and an energy equation. Post-processing will give access (in principle at least) to all the needed statistical quantities. If only the Reynolds Averaged Navier-Stokes equations are solved a very difficult step of statistical modeling has to be performed. This is why today the large majority of the estimations of wall pressure statistical characteristics are based on empirical models, with RANS computations only used to determine the global flow properties.

3 Semi-empirical Models and RANS Computations

Let us have a look at the frequency-spectra first. The model which is considered as reproducing in the best way experimental data has been developed by Goody [13]. It is clearly an empirical model (as stated by Goody himself) even if it is based on earlier theoretical development by Chase and Howe; the overall form of the spectrum and its level have been adjusted to obtain the best possible fit with experimental data measured for a relatively large range of Reynolds number, but only for boundary layers without any external pressure gradient. Its form is as follows:

$$\frac{\Phi(\omega)}{{\tau_w}^2\delta} = \frac{C_2(\omega\delta/U_e)^2}{\left[(\omega\delta/U_e)^{0.75}+C_1\right]^{3.7}+\left[C_3(\omega\delta/U_e)\right]^7} \tag{5}$$

In this formula, C_1, C_2 and C_3 are 3 empirical constants; by fitting a large number of experimental data, Goody obtained $C_1 = 0.5$, $C_2 = 3$ while connecting C_3 to a sort of Reynolds number R_T

$$C_3 = 0.11R_T^{-0.57}; \quad R_T = R_\tau \frac{u_\tau}{U_e}$$

u_τ is the friction velocity and R_τ the Reynolds number based on this friction velocity and on the boundary layer thickness δ. U_e is the external flow velocity and τ_w the wall shear stress ($\tau_w = \rho u_\tau^2$).

The excellent agreement between Goody's formula and measured frequency spectra is illustrated on Fig. 1, were mixed variables have been used to normalize the spectra.

In the formula developed by Goody only global flow characteristics are used, and they can be easily obtained through a standard RANS computation. It is then tempting to use the same formula for flows (slightly) more complex than the TBL on a flat plate, but in view of the calibration process one can have some doubt about the validity of this approach.

One important case for practical applications is the development of a TBL in the presence of accelerating or decelerating flows induced by external pressure gradients

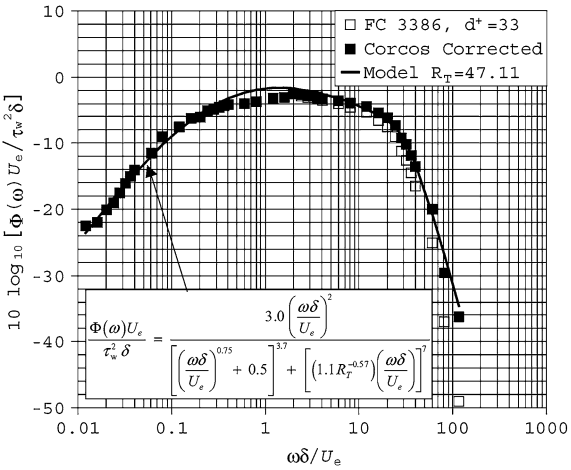

Fig. 1 Comparison of Goody's model with the data of Farabee and Casarella; $Re_\theta = 3{,}386$. Figure reproduced from Ref. [13] with permission

or by curvature effects. Some years ago an experiment was conducted at ECLyon in order to study the influence of external pressure gradients created in a wind tunnel with an adjustable upper wall (ENABLE European program [23]). The geometry of the wind tunnel, placed in an anechoic environment, is shown in Fig. 2. To test Goody's model in this configuration, we have run a RANS code (Ansys-Fluent $k-\omega$ or $k-\varepsilon$) and compared estimated spectra with the measured ones in different test sections to highlight the influence of the mean pressure gradient.

The comparisons were made for an inflow velocity equal to 50 m/s, the experimental spectra having been decontaminated from parasitic acoustic waves. A partial view of the computational mesh is shown in Fig. 3 together with computed velocity contours. A very fine mesh near the wall has been used in order to reproduce accurately the near wall region of the flow; the first point of the mesh in the direction normal to the lower wall was located at a distance of the order of 2–3

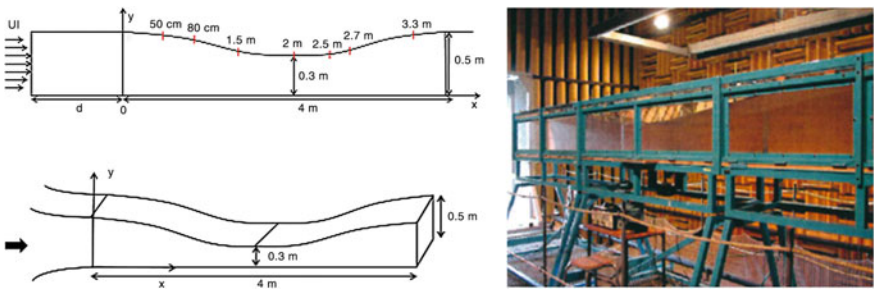

Fig. 2 Geometry and photograph of the wind tunnel with adjustable upper wall used in the ENABLE experiment

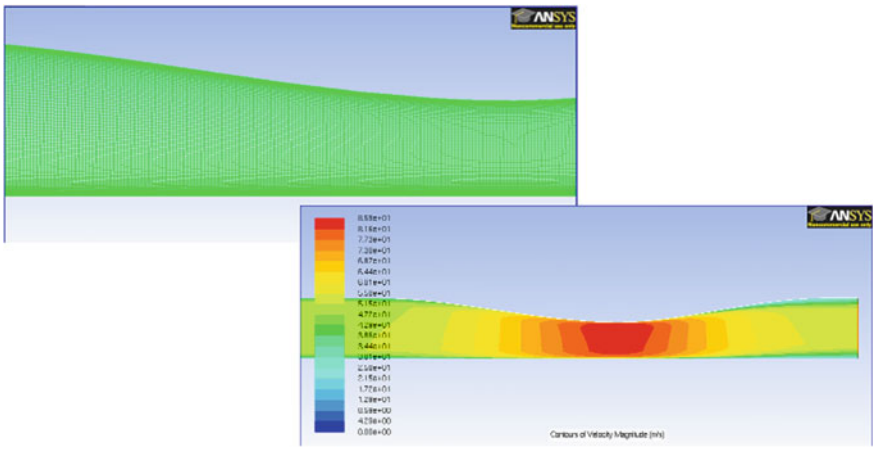

Fig. 3 Partial view of the numerical mesh and velocity contours computed in the RANS simulation of the ENABLE experiment

wall units only. A comparison of measured and calculated velocity profiles is given in Fig. 4 to demonstrate the very good agreement obtained; agreement with measured values of the wall shear-stress along the duct was also excellent.

Figure 5 displays the spectra measured and computed using Goody's formula at $x = 0.5$ m, where the external pressure gradient is very nearly zero (ZPG case). It can be shown that Goody's model does a very good job, reproducing both overall shape and level (within 1–2 dB). But in the diverging part of the wind tunnel (decelerating flow, Adverse Pressure Gradient), things are radically different (Fig. 6). The estimated spectrum is quite far from the experimental one and it underestimates the low-medium part of the spectrum by up to 12 dB!. It is also to be noted that the predicted general shape is also completely at variance with the

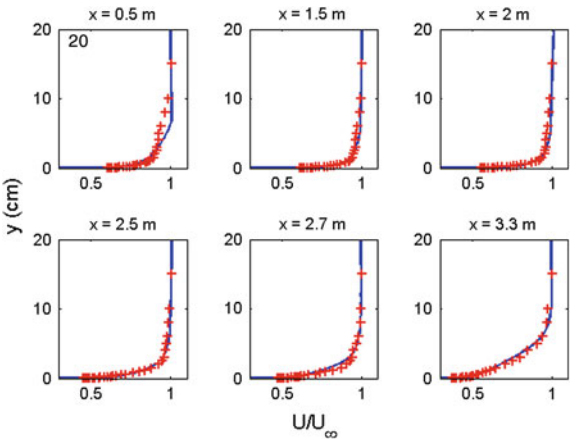

Fig. 4 Comparison between measured and computed velocity profiles along the ENABLE wind tunnel

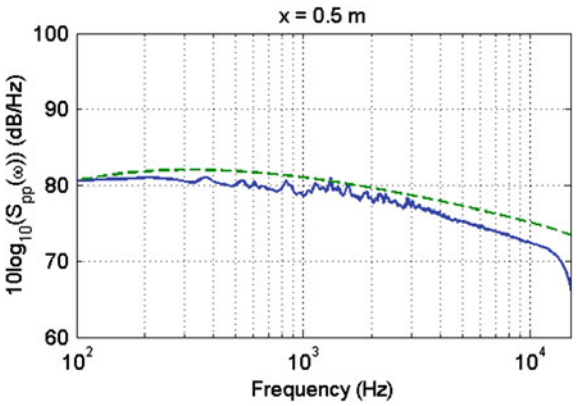

Fig. 5 Comparison between measured and estimated wall pressure spectrum using Goody's model and RANS flow computation for the ENABLE experiment; Zero Pressure Gradient case (in *continuous blue line* experimental data; in *green dashed line* Goody's model)

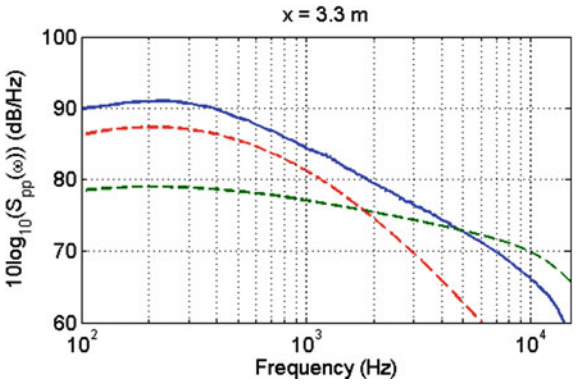

Fig. 6 Comparison between measured and estimated wall pressure spectrum using Goody's model and RANS flow computation for the ENABLE experiment; Adverse Pressure Gradient case (in *continuous blue line* experimental data; in *green dashed line* Goody's model; in *red dashed line* Rozenberg's model)

measured one. This lack of validity of Goody's formula in APG conditions has been already noted by other researchers and recently Rozenberg et al. [24] have proposed a modification of the initial model to deal with APG encountered on airfoils near the trailing edge. The result of Rozenberg's model is also shown on Fig. 6, and it is clear that it does a far better job than the classical one even if significant differences are noted at high frequency. Unfortunately the empirical character of the new model is even more pronounced than the model by Goody and its applicability in situations with different values of the pressure gradient is questionable. When trying to use it in the first part of the wind tunnel where the flow is accelerated (Favorable Pressure Gradient) we obtained very bad results; in fact the quality of the estimation

was worse than with Goody's model. In Fig. 7 we have plotted only the comparison of Goody's formula with experimental data; in this case the model overestimates the measured spectrum level by 5 dB typically.

The main conclusion at this stage is that empirical models do a good job when applied to classical configurations (for which they have been calibrated!) but are unable to be predictive in slightly different situations as exemplified for TBL with external pressure gradients, a case encountered in most practical applications in transportation systems. It seems clear that this difficulty of using empirical models for frequency spectra will be increased when 2-point statistical quantities, such as space-time cross-correlations of wave-number spectra, have to be estimated for computing flow induced vibration and noise.

Certainly the most used formula for evaluating the 2D wave-number spectrum of pressure fluctuations is the Chase model [6, 7]. This model is highly empirical and involves up to 7 adjustable coefficients when extrapolated to cover both the hydrodynamic region and the acoustic domain (plus another parameter controlling the level of the spectral peak at $k = k_0$, see for example Howe [16]). We give below the form limited to the hydrodynamic domain, depending on 4 adjustable coefficients.

$$\frac{\Phi(k,\omega)}{\rho^2 u_\tau^3 \delta^3} = \frac{1}{\left[(k_+\delta)^2 + 1/b^2\right]^{5/2}} \left[C_M (k_1\delta)^2 + C_T (k\delta)^2 \frac{(k_+\delta)^2 + 1/b^2}{(k\delta)^2 + 1/b^2} \right] \tag{6}$$

$$k_+{}^2 = (\omega - U_c k_1)^2/(hu_\tau)^2 + k^2$$

$$M = U/c_0 \ll 1; \quad k \gg \omega/c_0; \quad \omega\delta/U > 1$$

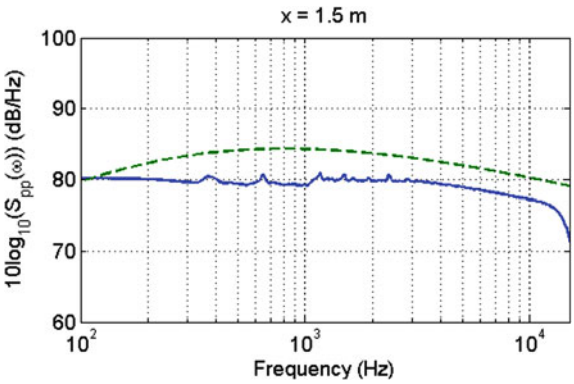

Fig. 7 Comparison between measured and estimated wall pressure spectrum using Goody's model and RANS flow computation for the ENABLE experiment; Favorable Pressure Gradient case (in *continuous blue line* experimental data; in *green dashed line* Goody's model)

The adjustable coefficients have been fixed by comparison with experiment and the recommended values are

$$b \approx 0.75; \quad C_M \approx 0.1553; \quad C_T \approx 0.0047; \quad h \approx 3$$

C_M and C_T correspond to the contributions to wall pressure fluctuations of the shear and self terms respectively.

Experiments in which wave-number spectra have been measured are very rare, so that this formula (and other empirical ones) can be considered as reliable only near the convective ridge; there are some doubts about its validity in the subconvective region, and the situation is even worse in the acoustic domain where the validity of the complete formula has not been confirmed by experiment. Moreover it is doubtful that such models can be applied in the presence of external pressure gradients, curvature effects or rough surfaces. It is then clearly desirable to develop a less empirical approach relying on more detailed flow computations.

3.1 Statistical Modeling

In aeroacoustics, the purely empirical approach has been progressively abandoned and methods based on a statistical modeling of jet noise are now used routinely for example with the MGB code or some other code based on the work by Tam and Auriault [28] for example. For wall-pressure fluctuations the only paper dealing with this approach is due to Peltier and Hambric [22]. There are good reasons for the very limited amount of work done along that line. Compared to jet free flows, wall-bounded flows are much more complicated to model; they are highly non homogeneous and anisotropic and the range of involved turbulent eddies is very large. Another reason is the close vicinity between sources and observation point; it is then not possible to use any asymptotic expansion of the Green's function (a near-field situation as opposed to a far-field situation, common in aeroacoustics applications).

To compute wall-pressure spectra it is necessary to estimate correlation functions or their equivalent in Fourier space (wave-number spectra). Starting with the equation for the fluctuating pressure (Eq. 2), it is possible to build a formula for space-time correlation functions; in a very symbolic form (and assuming dependence only on space and time separations) it can be written as:

$$R_{p'p'}(\Delta \mathbf{x_s}, \tau) \propto \int \int \left(U_i U_j R_{u'_k u'_l} + R_{u'_i u'_j u'_k u'_j} \right) \mathrm{d}y \mathrm{d}y' \tag{7}$$

with $\mathbf{x}_s = (x_1, x_2)$ denoting coordinates in the wall plane (x_1 is aligned with the mean flow).

The wave-number frequency spectrum is then obtained by a Fourier transform with regard to space and time:

$$\Phi_{p'p'}(\mathbf{k},\omega) = FT_{\Delta\mathbf{x}_s,\tau}\left[R_{p'p'}(\Delta\mathbf{x}_s,\tau)\right] \tag{8}$$

with $\mathbf{k} = (k_1, k_2)$ the conjugate coordinate of $\mathbf{x}_s$ in the wall plane.

This formula involves the double volume integration of two spatial correlation functions of velocity fluctuations; one is a second order correlation tensor (involving gradients of the mean flow velocity, a Mean Flow-Turbulence interaction or shear-noise term) and the second one is a fourth order correlation tensor (Turbulence-Turbulence interaction term or self-noise). It should be kept in mind that the available information given by RANS computations for the turbulent fluctuations is very limited. Usually only the local values of the turbulent kinetic energy k and of the dissipation rate ε are available ($k-\varepsilon$ model). It is then necessary to perform a large modeling effort to link the needed cross-correlations to these values. Typically one has to reduce 2-point correlations to 1-point information by assuming a given shape of the space and time correlations (a Gaussian shape in general) and to estimate the time and length scales defining the decay rate of these correlations by using dimensional arguments:

$$L \propto \frac{\varepsilon}{k^{3/2}}; \quad T \propto \frac{\varepsilon}{k^2} \tag{9}$$

The proportionality coefficients are obtained by fitting experimental data obtained in TBL flows. In fact the situation is quite complex as the turbulence is highly non homogeneous and non isotropic. The modeling has to be accurate for a very large range of turbulent scales in terms of non dimensional wall units $y^+ = yu_\tau/\nu$ (y is here the distance normal to the surface). Let us take a simple numerical example for a TBL in air with an external velocity of and a plate of length 1 m; this gives a boundary thickness of the order of 2 cm and a viscous length scale of only 10 μm; as the peak of turbulent intensity occurs for $y^+ \approx 20$ (see the review paper by Smits et al. [27]), the modeling has to cover correctly a range of several hundred of wall units. Details of the modeling approach will be found in the paper by Peltier and Hambric [22] in which point frequency spectra are computed and compared to Schloemer's data for APG and FPG as well as ZPG conditions. The authors obtained good agreement with Schloemer's data [26] after tuning their model, and the influence of APG and FPG is relatively well captured (Fig. 8).

In principle the approach developed by Peltier and Hambric is able to estimate not only point frequency spectra but also space-time correlations of wall pressure fluctuations, but no attempt has been done in the cited paper nor in other work, to the best of our knowledge.

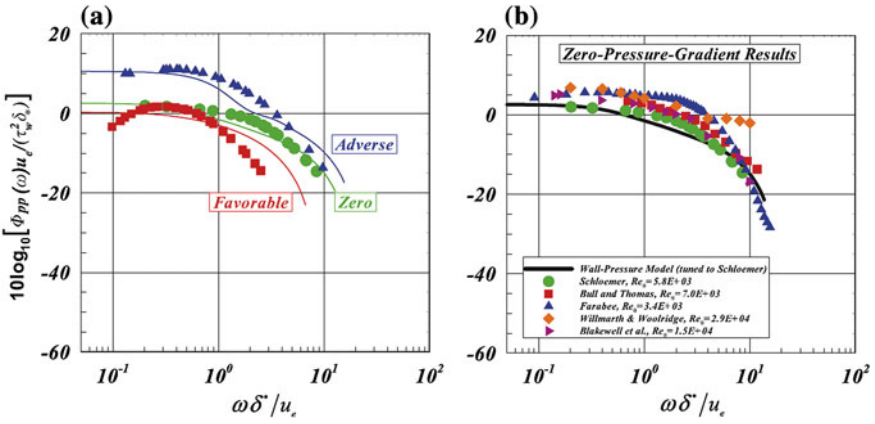

Fig. 8 Predicted wall-pressure spectra using statistical modeling compared to **a** Schloemer's data for favorable, zero and adverse pressure gradients, and **b** to data of several authors for zero pressure gradient conditions. Figure reproduced from Peltier and Hambric [22] with permission

4 Time-Resolved Incompressible CFD and Wall-Pressure Fluctuations

Due to the intrinsic limitations of empirical models and even of statistical modeling based on RANS computations, a number of authors have tried to estimate wall pressure fluctuations directly from time-dependent numerical simulations. One of the main difficulties is the range of turbulent scales to be computed and for this reason most of the published results do not consider true boundary layers, but fully developed channel flows; they are less demanding in terms of computational power as periodic boundary conditions and spectral methods in the 3 directions can be used (at least for incompressible flow).

4.1 Direct Numerical and Large Eddy Simulations

When speaking of time-dependent Navier-Stokes computations, two main possibilities exist, the Direct Numerical Simulation (DNS) and the Large Eddy Simulation (LES). In DNS the numerical mesh has to resolve all the turbulent scales from the largest ones to the ultimate Kolmogorov scale, where viscosity effects become dominant. In LES, only the most energetic scales are resolved and the influence of the smaller scales (or subgrid scales) is modeled via typically a turbulent viscosity approach. DNS is exact as no modeling of turbulence is needed, but extremely demanding in terms of computational power and thus limited to relatively low Reynolds number flows, whereas LES is less demanding and thus can be applied (with care!) to more realistic flows. The numerical cost is however important even

in LES as in the direction normal to the wall it is necessary to use a very refined mesh in order to capture the most energetic region, located very close to the wall for moderate to high values of the Reynolds number.

A final, and important, point is the choice between incompressible or compressible computations. Most of the published papers are dealing with incompressible flow, which is very reasonable from the purely fluid mechanics point of view, the Mach number being in general quite low. But we, acousticians, know that in a number of practical cases it is necessary to estimate also the acoustic contribution to the wave-number spectrum. This is clearly needed if the sound generated by the TBL has to be computed (aerodynamic noise in the sense of Lighthill), but this is also often the case to determine flow induced vibrations and the noise generated by these vibrations. An instructive discussion and numerical examples can be found for example in the excellent papers by Graham [14, 15]. Computing the tiny acoustic contribution (as compared to the incompressible or hydrodynamic contribution) is a very difficult challenge. Great progress has been made in recent years in aeroacoustics in the computation of the noise generated by jets and airfoils, but the application to TBL has only been attempted very recently.

4.2 Progress in Numerical Estimation of Wall Pressure Fluctuations

The first estimations of the statistical properties of wall pressure fluctuations date back to the end of the 80s (Kim [19], Choi and Moin [8]). The data base used by Choi and Moin was obtained from a DNS of a channel flow, for a small value of the Reynolds number based on the center-line velocity and on the channel half height ($Re_h = 3,200$) or for the more relevant Reynolds number based on the boundary layer momentum thickness, $Re_\theta = 287$; these values are typically 10–100 times lower than those measured in classical experiments. Point-spectra, correlations and wave-number spectra were displayed and compared to experimental data. The number of grid points was of the order of 2 millions and the resolution of frequency spectra was typically limited to values of the reduced frequency $\omega\theta/U_e$ of order unity. The main problem with DNS is that the relation between the Reynolds number and the number of required grid points is $N \propto Re^{9/4}$. So multiplying the Reynolds number by a factor of 10 requires multiplying the number of grid points by nearly 200!

In the following years the range of simulated frequencies has only slowly evolved, in direct relation with the increase of available computational power. Na and Moin [21] in 1998 for example studied a separated boundary layer, using 13 million grid points, and more recently (in 2006), Hu et al. [17] performed a huge computation of a channel flow with 520 million grid points. They were able to simulate channel flow up to $Re_\tau = 1,400$ (Reynolds number based on the friction velocity), a value comparable to the experimental ones. One of their typical result is

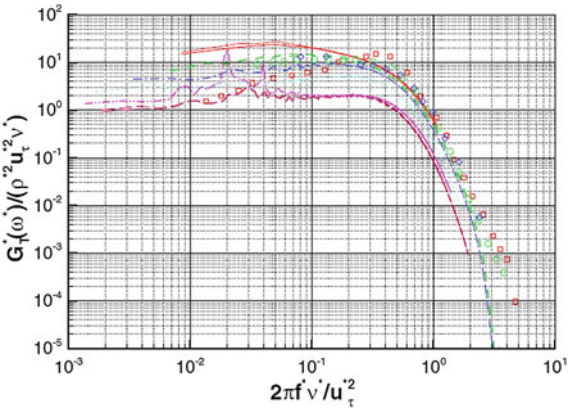

Fig. 9 Point spectrum of wall pressure fluctuations evaluated from a DNS computation and compared with experiments. Channel flow simulation for $Re_\tau = 720$, $Re_\theta = 1{,}343$. Figure reproduced from Hu et al. [17] with permission

displayed in Fig. 9. The comparison of spectra shows a good agreement for the overall shape, but the numerical simulations seem to underestimate the levels (for comparable values of the Reynolds number). It is very surprising, and quite unfortunate considering the huge data base available, that the authors do not mention any 2-point results, such as wave-number frequency spectra.

At this stage two important points need attention: is it possible to simulate a true boundary layer flow at a reasonably high value of the Reynolds number? And, is it possible to do that with compressibility taken into account, in order to estimate the acoustic contribution to wall pressure statistics?

5 The Acoustic Contribution to Wall-Pressure Fluctuations

The estimation of the full wave-number spectrum is a formidable task both from the experimental point of view and from the numerical one. The number of experiments in which at least a 1-D spectrum is available is quite limited, not to speak of 2-D spectra.

5.1 Experimental Results

Obtaining the wave-number spectrum can be done directly (using 2D arrays of sensors) or indirectly by computing first cross-correlations and then taking a spatial Fourier transform. The first approach is nearly out of reach due to the very large number of sensors needed to cover both high spatial frequencies (hydrodynamic

contribution) and low spatial frequencies (acoustic contribution). 1D spectra can be obtained using a linear array of sensors (aligned with the mean flow) but it should be kept in mind that 1D spectra integrate the contributions of all wave-vectors projected along the array direction. Example of direct measurement of the 1D streamwise spectra can be found in the paper by Abraham and Keith [1] who used a linear array of 48 microphones. The quality of the measurements far from the convective ridge was limited by aliasing and array side lobes; comparison with the Corcos [9] and Chase [7] models was nevertheless possible, and a relatively good agreement with the latter was obtained in the subconvective region. The acoustic region was not specifically studied in this paper.

Recently an experiment was developed at ECLyon (in collaboration with Renault) in order to estimate the 2D wave-number spectrum both in the convective region and in the acoustic domain. For automotive applications it is indeed thought that the (very small) acoustic contribution to the wall pressure field can nevertheless contribute significantly to vehicle interior noise as it is considerably less filtered out by the windshield than the hydrodynamic contribution in a certain range of audible frequencies. The experimental details and the main results are to be found in a PhD Thesis [2] and in a JASA paper [3].

A linear array of 63 microphones was mounted on a rotating disk (see Fig. 10), and the cross-spectra were measured for 63 angular positions; the flow speed was varied from 33 to 54 m/s. The wave-number frequency spectrum was then obtained through a 2D discrete spatial Fourier transform for a useful range of frequencies extending approximately from 500 Hz to 5 kHz. One of the main results of the study by Arguillat [2] concerns the ratio of the acoustic Power Spectral Density (PSD) to the hydrodynamic PSD; it was found to be of the order of 3 % (−15 dB) with very little variations with frequency (Fig. 11). This value seems a bit high (but we just do not have any reference value available, theoretically or experimentally), may be due to confinement in the wind tunnel cross-section.

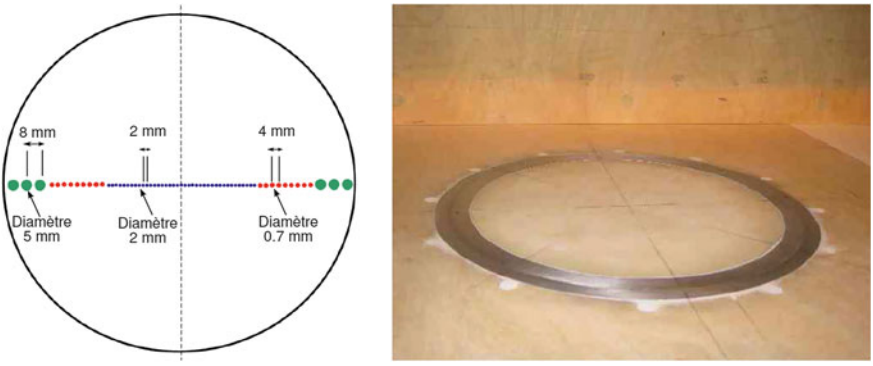

Fig. 10 Arrangement of the linear array used in the Arguillat experiment [2] and of the rotating disk inserted in the lower wall of the wind tunnel

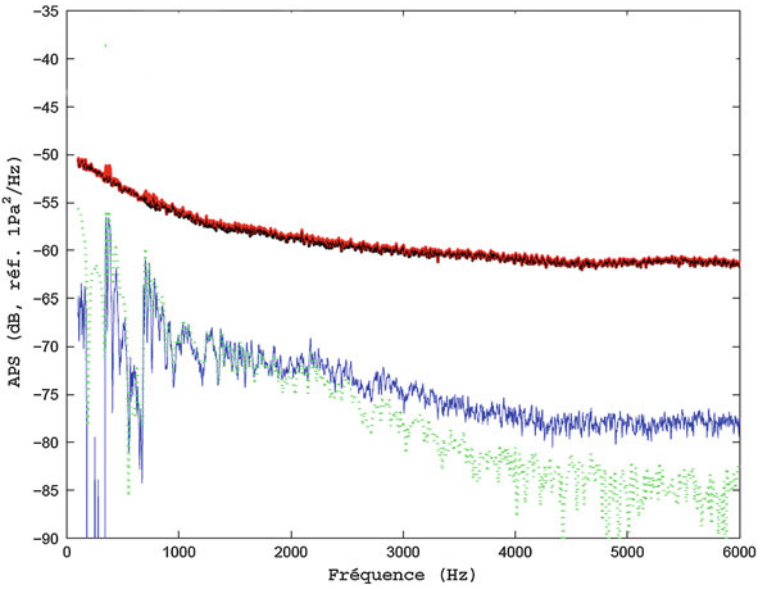

Fig. 11 Estimation of the relative contribution of the acoustic and hydrodynamic regions to the wall pressure spectrum in the experiment by Arguillat. The full spectrum and the hydrodynamic contribution are nearly undiscernable (*upper curves*) and the acoustic contribution is some 15 dB lower whatever the frequency; the acoustic contribution has been evaluated by integration of the 2D wave-number spectrum over the radiation disk (*blue line*) and by fitting a Corcos-like model to the data (*green line*)

To verify this, and to extend the range of applications, a new experimental set-up was designed at ECLyon. The objectives were first to enhance signal processing relative to the Arguillat experiment; a larger disk was used and a different arrangement of the microphones along the array was chosen in order to increase the array resolution and to reduce side lobes; potential contamination by parasitic acoustic noise was reduced by installing acoustic liners inside parts of the wind tunnel. The second goal was to study the influence of external pressure gradients (APG and FPG) generated by tilting part of the upper wall, and this up to a maximum velocity of around 100 m/s (details can be found in [25]). In parallel numerical simulations are performed by *X*. Gloerfelt using high fidelity compressible LES (ANR SONOBL program). The experiments are on their way, but preliminary results are very encouraging; as an example we show on Fig. 12 two k_1-k_2 wave-number spectra obtained for an external velocity of 45 m/s at 500 and 1,000 Hz respectively. The color maps are much cleaner than in the Arguillat experiment, with the influence of side lobes being considerably reduced; as a result the acoustic disk as well as the convective region are clearly visible.

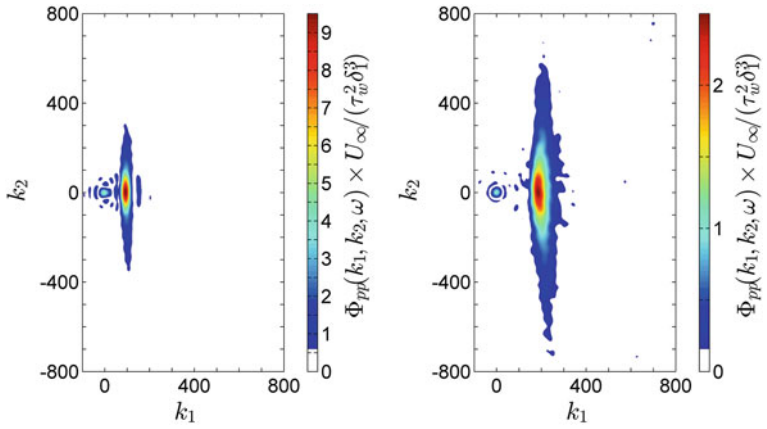

Fig. 12 Normalised 2D wave-number spectra of wall pressure fluctuations measured in the SONOBL experiment for two frequencies, $f = 500$ Hz (*left*) and $f = 1{,}000$ Hz (*right*). Incoming velocity $U_e = 45$ m/s; Zero Pressure Gradient case. More details will be found in [25]

5.2 Numerical Simulations

Numerical simulations mimicking the SONOBL experiment are still in progress. However Gloerfelt and Berland [12] have very recently published results for a spatially developing TBL for a higher value of the Mach number (0.5 instead of 0.1–0.3 in our experiments). They used high order, high precision algorithms to solve the 3D fully compressible Navier-Stokes equations, and were able to compute both the noise radiated outside the boundary layer and the wall pressure fluctuations. Three figures will illustrate this very original and interesting work.

Figure 13 displays a point frequency spectrum scaled by inner variables, and compared to experimental data and to Goody's model. Up to the frequency cut-off of the LES (imposed by the numerical grid, with 54 millions of points) the computed spectrum agrees very well with the data, in shape and level. Figure 14 displays a cut at $k_2 = 0$ of 2D wave-number spectra (not to be confused with the spanwise spectrum measured by 1D arrays) obtained for various values of the reduced frequency $\omega\theta/U_e$. The evolution with the frequency of the convective ridge is very apparent with a maximum around $k_1 = \omega/U_c$ ($U_c = 0.8U_e$ is the convection velocity), but, much more important, a peak associated to acoustic disturbances is clearly seen around $k_1 = \omega/c_{\text{eff}}$, especially for the two higher frequencies (c_{eff} is an effective sound speed accounting for the convection of acoustic waves by the rapid mean flow). And finally we display a color map of $\Phi_{pp}(k_1, k_2 = 0, \omega)$ on Fig. 15.

The hydrodynamic part is clearly seen with its well-known non symmetric pattern toward the subconvective or superconvective regions, but much more

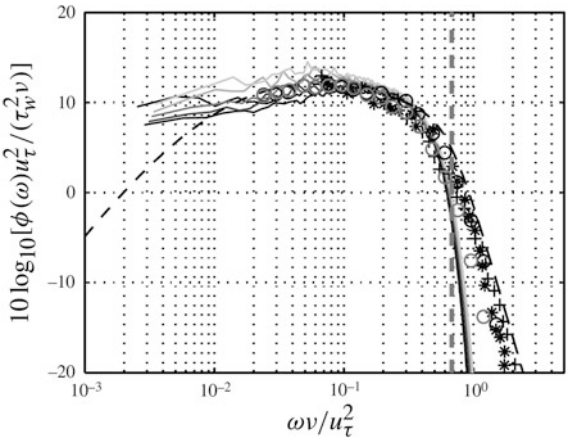

Fig. 13 Frequency power spectra of wall pressure fluctuations computed from a LES of a spatially developing TBL (*solid line*) and compared to various experimental data sets (*symbols*) and to Goody's model (*dashed line*). The *vertical dashed line* indicates the frequency cut-off of the LES. Figure reproduced from Gloerfelt and Berland [12] with permission

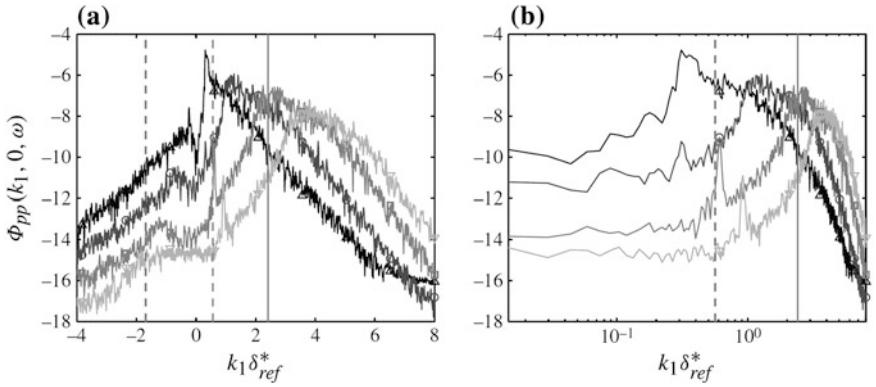

Fig. 14 Wavenumber-frequency spectra computed from LES for different non-dimensional frequencies (δ^* denotes the boundary layer displacement thickness). The *solid vertical line* indicates the convective wavenumber and the *vertical dashed line* the convected acoustic wavenumber; they are associated with the curve corresponding to the third highest frequency, for which a very distinct peak is seen near the acoustic wavenumber. Figure reproduced from Gloerfelt and Berland [12] with permission

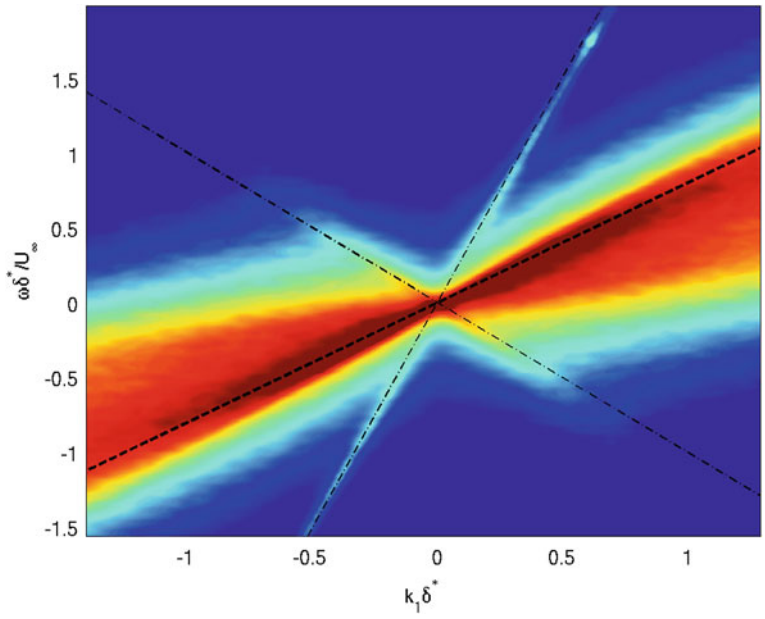

Fig. 15 Color map of the wavenumber-frequency spectrum (dB scale) computed from LES for a large range of non-dimensional frequencies. The *thick dashed line* represents the convection of turbulent structures ($k_c = \omega/U_c$; $U_c = 0.6U_e$) and the *light dashed lines* correspond to acoustic waves convected by the mean flow ($k_+ = \omega/(U_e + c_0)$ and $k_- = \omega/(U_e - c_0)$). Figure courtesy of *X*. Gloerfelt

important are the characteristic lines showing the acoustic contribution convected upstream and downstream with effective velocities equal to $c_0 - U_e$ and $c_0 + U_e$ respectively.

6 Conclusion

In this paper we have given a rapid description of the various methods used to estimate the statistical properties of wall pressure fluctuations from CFD data: empirical models fed by RANS global flow characteristics, statistical modeling relying on local values of turbulent intensity and turbulent space and time scales, and finally time-dependent Navier-Stokes simulations (DNS or LES).

Empirical models are clearly useful at a first design stage, but their applicability is limited to the cases where they have been calibrated, i.e. typically turbulent boundary layers over flat surfaces; even the relatively simple extension of TBL in the presence of an external pressure gradient necessitates non trivial adjustments of the models for point frequency spectra. The statistical modeling of Peltier and Hambric [22] is attractive but, up to now, it has been developed only for the

estimation of point spectra, not for 2-point correlations. One possible extension would be to use LES instead of RANS computations to inform the statistical model, an approach recently put forward for jet noise computation [18].

It seems however that the time-dependent computation of pressure fluctuations by solving the Navier-Stokes equations is the main pathway for the (near) future. Considering the range of Reynolds numbers encountered in the applications, LES is certainly to be preferred to DNS, at the expense of not being able to compute the influence of the smaller turbulent scales (introducing a high frequency cut-off). For applications in which the Mach number is not too small, a compressible computation will even be possible to determine the acoustic contribution to wall pressure fluctuations (this is already possible for high Mach number flows). In this context it should be noted that an alternative computational method, the Lattice Boltzmann Method, has shown also a great potential. Of course new experimental data, more precise and in well-controlled conditions, are needed to validate the computations (but it should be kept in mind that in some cases numerical simulations can be more appropriate than experiments!). Very recently a number of teams have been working in this direction, developing new facilities and new measurement techniques [10, 11, 20]. It can thus be expected that this combined effort in the numerical and experimental directions will shed some new light in a near future on this old and difficult problem.

Acknowledgments The authors have benefited from fruitful discussions with and inputs by Christophe Bailly, Xavier Gloerfelt and Gilles Robert. This work was performed within the framework of the Labex CeLyA of Université de Lyon, operated by the French National Research Agency (ANR-10-LABX-0060/ANR-11-IDEX-0007). Financial support of Marion Berton by DCNS Research is also acknowledged.

References

1. B.M. Abraham, W.L. Keith, Direct measurements of turbulent boundary layer wall pressure wavenumber-frequency spectra. J. Fluid Eng. **120**, 29–39 (1998)
2. B. Arguillat, Etude expérimentale et numérique de champs de pression pariétale dans l'espace des nombres d'onde, avec application aux vitrages automobiles, Ph.D. thesis, Ecole centrale de Lyon, 2006, pp. 2006–2014
3. B. Arguillat, D. Ricot, C. Bailly, G. Robert, Measured wavenumber-frequency spectrum associated with acoustic and aerodynamic wall pressure fluctuations. J. Acoust. Soc. Am. **128** (4), 1647–1655 (2010)
4. C. Bailly, C. Bogey, O. Marsden, Progress in direct noise computation. Int. J. Aeroacoustics **9** (1–2), 123–143 (2011)
5. C. Bogey, O. Marsden, C. Bailly, Influence of initial turbulence level on the flow and sound fields of a subsonic jet at a diameter-based Reynolds number of 10^5. J. Fluid Mech. **701**, 352–385 (2012)
6. D.M. Chase, Modeling the wavevector-frequency spectrum of turbulent boundary layer wall pressure. J. Sound Vib. **70**(1), 29–67 (1980)
7. D.M. Chase, The character of turbulent wall pressure spectrum at subconvective wavenumbers and a suggested comprehensive model. J. Sound Vib. **112**, 125–147 (1987)

8. H. Choi, P. Moin, On the space-time characteristics of wall pressure fluctuations. Phys. Fluids A **2**, 1450–1460 (1990)
9. G.M. Corcos, The structure of turbulent pressure field in boundary layer flows. J. Fluid Mech. **18**(3), 353–378 (1964)
10. K. Ehrenfried, L. Koop, Experimental study of pressure fluctuations beneath a compressible turbulent boundary layer. In: 14th AIAA/CEASAeroacoustics Conference, AIAA Paper (2008), pp. 2008–2800
11. C. Gabriel, S. Müller, F. Ullrich, R. Lerch, A new kind of sensor array for measuring spatial coherence of surface pressure on a car's side window. J. Sound Vib. **333**, 901–915 (2014)
12. X. Gloerfelt, J. Berland, Turbulent boundary layer noise: direct radiation at Mach number 0.5. J. Fluid Mech. **723**, 318–351 (2013)
13. M. Goody, Empirical spectral model of surface pressure fluctuations. AIAA J. **42**(9), 1788–1794 (2004)
14. W.R. Graham, Boundary layer induced noise in aircraft, part I: the flat plate model. J. Sound Vib. **192**(1), 101–120 (1996)
15. W.R. Graham, A comparison of models for the wavenumber-frequency spectrum of turbulent boundary layer pressures. J. Sound Vib. **206**(4), 541–565 (1997)
16. M.S. Howe, *Acoustics of Fluid Structure Interactions* (Cambridge University Press, Cambridge, 1998)
17. Z.W. Hu, C.L. Morfey, N.D. Sandham, Wall pressure and shear stress spectra from direct simulations of channel flow. AIAA J. **44**(7), 1541–1549 (2006)
18. S.A. Karabasov, M.Z. Afsar, T.P. Hynes, A.P. Dowling, W.A. McMullan, C.D. Pokora, G.J. Page, J.J. McGuirk, Jet noise: acoustic analogy informed by large eddy simulation. AIAA J. **48** (7), 1312–1325 (2010)
19. J. Kim, On the structure of pressure fluctuations in simulated turbulent channel flow. J. Fluid Mech. **205**, 421–451 (1989)
20. D. Lecoq, C. Pézerat, J.-H. Thomas, W.P. Bi, Extraction of the acoustic component of turbulent flow exciting a plate by inverting the vibration problem. J. Sound Vib. **333**(2), 2505–92519 (2014)
21. Y. Na, P. Moin, Direct numerical simulation of a separated turbulent boundary layer. J. Fluid Mech. **374**, 379–405 (1998)
22. L.J. Peltier, S.A. Hambric, Estimating turbulent boundary layer wall pressure spectra from CFD RANS solutions. J. Fluids Struct. **23**, 920–937 (2007)
23. G. Robert, Experimental data base for the pressure gradient effect, EU Contract ENABLE, G4RD-CT-2000-00223 (2002)
24. Y. Rozenberg, G. Robert, S. Moreau, Wall pressure spectral model including the adverse pressure gradient effects. AIAA J. **50**(10), 2168–2179 (2012)
25. E. Salze, C. Bailly, O. Marsden, E. Jondeau, D. Juvé, An experimental characterization of wall pressure wavevector-frequency spectra in the presence of pressure gradients. In: 20th AIAA/CEAS Aeroacoustics Conference, AIAA Paper 2014–2909 (2014)
26. H.H. Schloemer, Effects of pressure gradients on turbulent boundary layer wall pressure fluctuations. J. Acoust. Soc. Am. **43**(1), 93–113 (1967)
27. A.J. Smits, B.J. McKeon, I. Marusic, High-Reynolds number wall turbulence. Annu. Rev. Fluid Mech. **43**, 353–375 (2011)
28. C.K. Tam, L. Auriault, Jet mixing noise from fine scale turbulence. AIAA J. **37**(2), 145–153 (1999)

Effect of Developing Pressure Gradients on TBL Wall Pressure Spectrums

Mark J. Moeller, Teresa S. Miller and Richard G. DeJong

Abstract The effects of favorable and adverse pressure gradients on the shape and pressure spectra of turbulent boundary layers are investigated. A contracting and then expanding wind tunnel test section is used for this investigation. Favorable (negative) pressure gradients are found to cause a modest reduction in the pressure spectrum levels compared to equilibrium flows. Adverse (positive) pressure gradients are found to dramatically increase the pressure spectrum levels and decrease the phase velocity.

1 Introduction

Turbulent boundary layers (TBL) are a significant source of vibration and noise for vehicles moving through a fluid medium. An extensive review of wall pressure fluctuations beneath an equilibrium TBL research can be found in Bull [1]. Recent reviews of equilibrium TBL models can be found in Graham [2] and Miller et al. [3]. Although large areas of vehicles can be approximated by flat plates and the corresponding equilibrium TBL, the areas of most interest acoustically are represented by non-equilibrium TBLs. Early work investigating the effect of pressure gradients on wall pressure fluctuation was accomplished by Schloemer [4] in 1967. He found that spectral levels were increased for positive pressure gradient boundary layers. A more recent study on the effect of adverse pressure gradients on wall pressure spectral

M.J. Moeller (✉)
27 Lubberland Drive, Newmarket, NH 03857, USA
e-mail: mmoeller33@gmail.com

T.S. Miller
Bombardier Aerospace, One Learjet Way, Wichita, KS 67277, USA
e-mail: terri.miller@aero.bombardier.com

R.G. DeJong
Engineering Department, Calvin College, 1712 Knollcrest Circle,
Grand Rapids, MI 49546, USA
e-mail: dejong@calvin.edu

E. Ciappi et al. (eds.), *Flinovia - Flow Induced Noise and Vibration Issues and Aspects*, DOI 10.1007/978-3-319-09713-8_3

models is given by Rozenberg et al. [5]. They found that the effect of an adverse pressure gradient cannot be neglected because it leads to an under-estimation of the wall pressure spectrum. This present study is an extension of the work accomplished by DeJong and Kuiper [6] which investigated the effects of both positive and negative pressure gradients on pressure fluctuations under TBL. This previous work suggested that a pressure gradient has a significant effect on the TBL pressure spectrum, more so for positive (adverse) gradients than negative (favorable) pressure gradients.

2 Mean Flow Characterization

Tests were performed in the Calvin Engineering Low Speed Wind Tunnel, illustrated in Fig. 1, measuring the TBL pressure spectrum levels in flows with positive and negative pressure gradients. The wind tunnel was driven by a variable speed 15 kW, 12 bladed fan, producing flow speeds up to $M = 0.3$ in the closed loop configuration with a variable area test cross section, 3.0 m long. The test section was preceded by a 30 to 1 area contraction. This was preceded by a flow straightener section using soda straws and 4 screens to provide a smooth flow with turbulence levels at the inlet to the test section less than 0.1 % of the mean flow. Substantial sound absorption was provided in the remainder of the flow loop to minimize the extraneous noise levels.

The top of the test section was a 30 mm thick composite wood panel with a Formica surface. The bottom panel was a 30 mm composite panel with a Formica

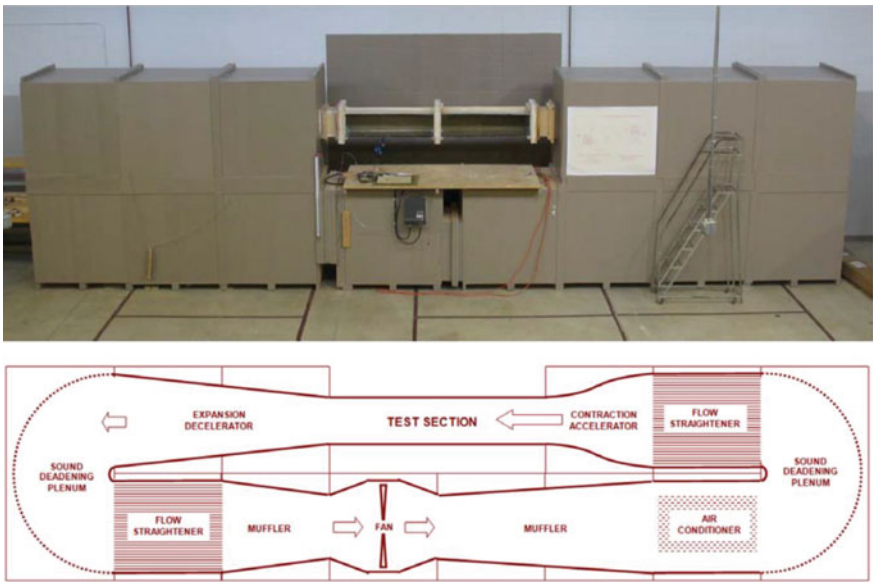

Fig. 1 Calvin engineering low speed wind tunnel

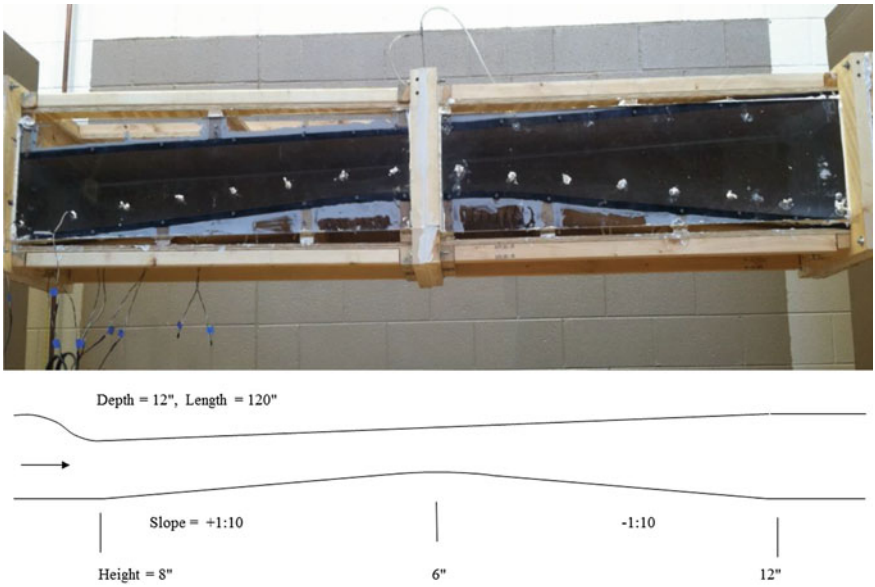

Fig. 2 Modified wind tunnel test section

surface that was formed to achieve a complex curve shown in Fig. 2. The side panels were made of 25 mm thick Plexiglas.

The flow was allowed to develop on the bottom surface of the test section. Measurements were taken at sixteen stations evenly spaced every 15.24 cm along the bottom surface to characterize the flow. The measurements included static pressure, velocity gradient, boundary layer profiles and unsteady pressure measurements with electret microphones. Three microphones were recorded and analyzed at each station. The first was on the centerline of the test section at the station location, the second was 2.54 cm downstream of the first microphone and the third was located in the test section wall to monitor the background noise.

The boundary layer profiles were integrated to determine the displacement thickness, $\delta^* = \int_0^\delta (1 - \frac{u(y)}{U_\infty})\mathrm{d}y$ and momentum thickness, $\theta = \int_0^\delta \frac{u(y)}{U_\infty}(1 - \frac{u(y)}{U_\infty})dy$. The shape factor, $H = \frac{\delta^*}{\theta}$ was calculated from the result. The boundary later thickness δ was set by the traverse location where the velocity was 0.99 times the local free stream velocity.

The wall shear stress was estimated by fitting the boundary layer profile to the 'Law of the Wall'. Coles law of the wall was used. A typical result is shown in Fig. 3 for station 6.

$$\frac{u(y)}{U_\tau} = \frac{1}{0.41}\ln(y^+) + 5.0 \tag{1}$$

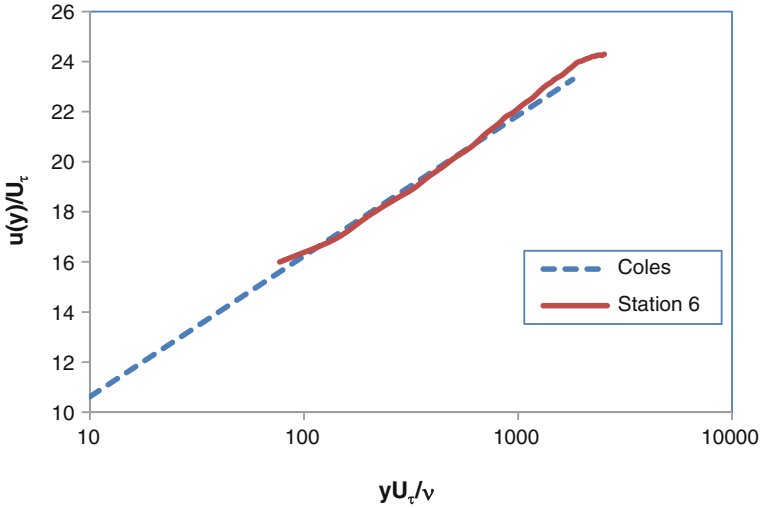

Fig. 3 Law of the wall station 6

$$y^+ = \frac{yU_\tau}{\nu}, \quad U_\tau = \sqrt{\frac{\tau_w}{\rho}} \tag{2}$$

The station wise results are summarized in Table 1, Boundary Layer Properties, and illustrated in Fig. 4. The first eight stations are in the favorable gradient region.

Table 1 Boundary layer properties

Station	U	δ^*	ϑ	H	τ_w
1	43.764	1.13E−03	7.27E−04	1.551	4.395
2	46.56	1.33E−03	8.67E−04	1.539	4.487
3	47.897	1.56E−03	1.03E−03	1.507	4.487
4	50.256	1.72E−03	1.18E−03	1.455	4.959
5	53.305	1.75E−03	1.22E−03	1.438	5.557
6	56.6	1.70E−03	1.19E−03	1.433	6.406
7	60.863	1.65E−03	1.15E−03	1.431	7.375
8	61.55	1.63E−03	1.17E−03	1.394	7.794
9	61.585	3.31E−03	2.29E−03	1.445	5.204
10	57.67	4.59E−03	3.04E−03	1.512	3.614
11	52.75	6.80E−03	4.23E−03	1.609	2.151
12	47.456	0.01	5.62E−03	1.83	1.18
13	44.385	0.015	7.46E−03	1.99	0.7
14	42.297	0.02	8.66E−03	2.261	0.425
15	40.931	0.027	0.011	2.379	0.272
16	40.518	0.026	0.01	2.47	0.261

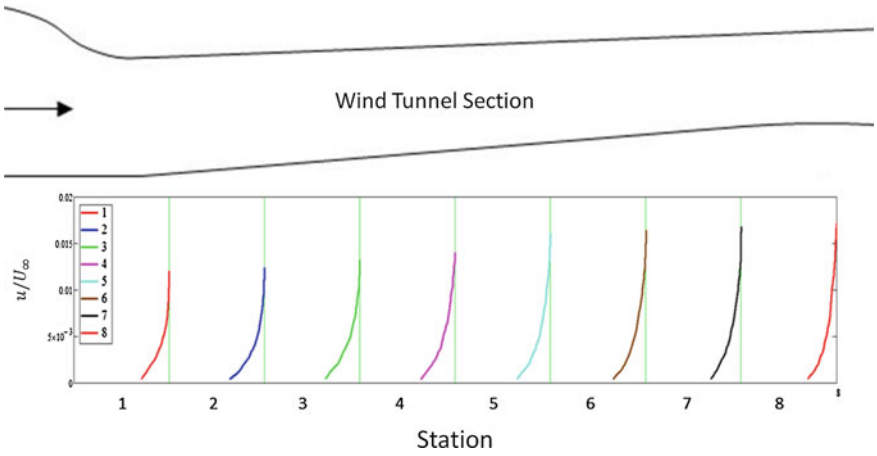

Fig. 4 Favorable gradient velocity profiles

The velocity increases from 44 to 65 m/s. The boundary layer thickness initially increases and then slowly decreases in this region. The initial shape factor was 1.51 decreasing to 1.4. The wall shear stress increases monotonically in this region.

From station 9 to 16 the area opens up and there is an adverse pressure gradient. The free stream velocity decreases from 65 to 40.5 m/s and the boundary layer grows dramatically. The velocity profiles are shown in Fig. 5. Note the scale is four times larger than for the favorable gradient figure. The wall shear stress decreases from 7.8 to 0.26 N. The shape factor increases from 1.4 to 2.47.

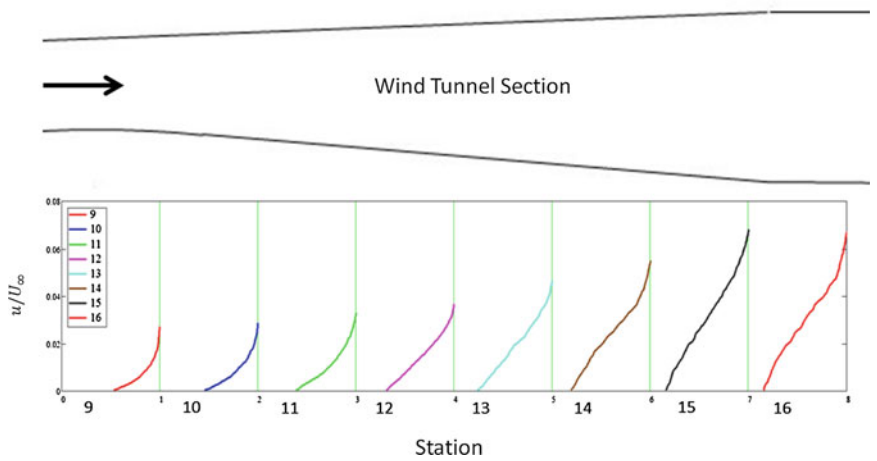

Fig. 5 Adverse gradient velocity profiles

The resulting flow represents an attached turbulent boundary layer that experiences a favorable pressure gradient and then an adverse pressure gradient. The mean flow properties were characterized for use in unsteady pressure data reduction. The evolution of the flow can be seen in Fig. 6. This experiment provided a platform for investigating both favorable and adverse gradient TBL flows.

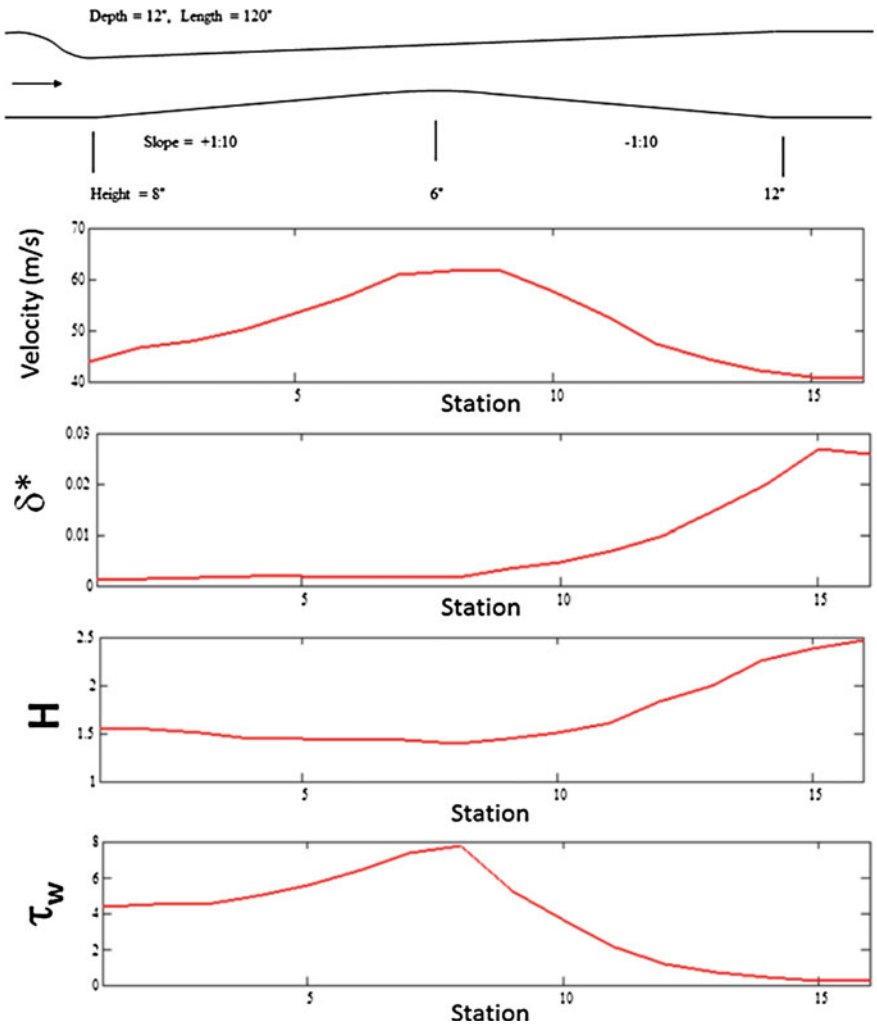

Fig. 6 Boundary layer properties

3 Unsteady Pressure Measurements

The unsteady pressure was sensed using a pair of electret microphones. The electret microphones were 6.0 mm in diameter, spaced 25.4 mm apart along the center line of the bottom surface and located at each of the sixteen stations in the test section. Each microphone sensed the TBL pressure through a 1.6 mm diameter pin hole, 3.2 mm long, which minimized the disturbance to the surface shear stress. In order to cancel the acoustic background noise in the wind tunnel, a microphone was mounted in the adjacent side wall and the coherent pressure was subtracted from the array pressures. The mounting technique is illustrated in Fig. 7.

The raw data for the unsteady pressure measurements are illustrated in Fig. 8 using station six as an example. At station six the flow velocity was 56.6 m/s, wall shear stress 6.41 N, and the displacement thickness 1.71×10^{-3} m with a shape factor of 1.43. The measurements include the spectrum levels in Pa^2/Hz and the cross spectrum. The cross spectrum and spectrum levels were used to calculate the coherence and the phase. It can be seen that there is a lot of low frequency energy in the spectrum. Also the coherence is low above 5 kHz. Due to the low coherence, the phase was not calculated above 5 kHz. The phase is seen to be wrapped i.e. between plus and minus π. The phase was median smoothed for later post processing. Data were collected for all sixteen stations.

The mean square pressure was calculated by summing the spectrum levels and multiplying by the analysis bandwidth as shown in Eq. 6. The low frequency content was included in this computation.

$$\langle p^2 \rangle = \sum S_{\mathrm{pp}}(f) * bw \tag{3}$$

The mean square pressure was normalized by the wall shear stress and is shown in Fig. 9. The expected result for an equilibrium boundary layer at the same Reynolds number is 6.62. These experimental results are consistently above that even for the favorable pressure gradient region.

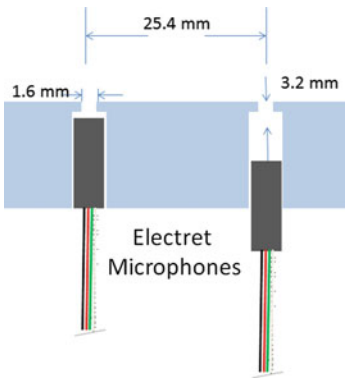

Fig. 7 Microphone mounting technique

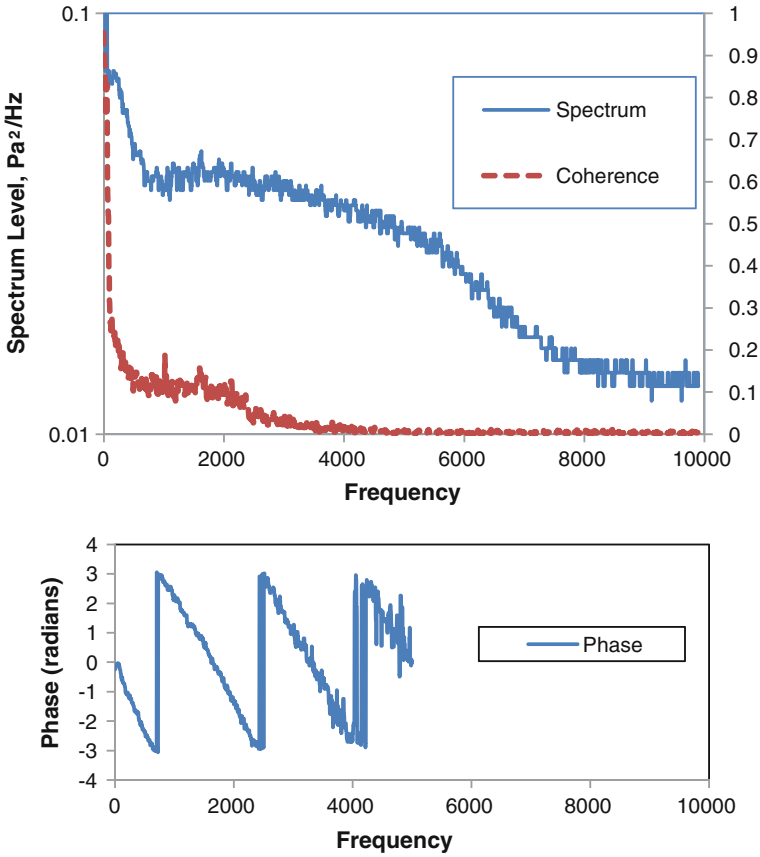

Fig. 8 Unsteady pressure measurements station 6

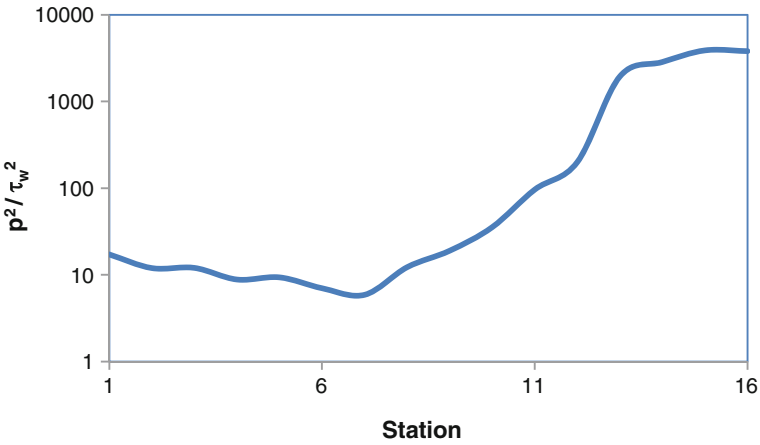

Fig. 9 Normalized means square pressure, $\frac{\sum S_{pp}(f)*bw}{\tau_w^2}$

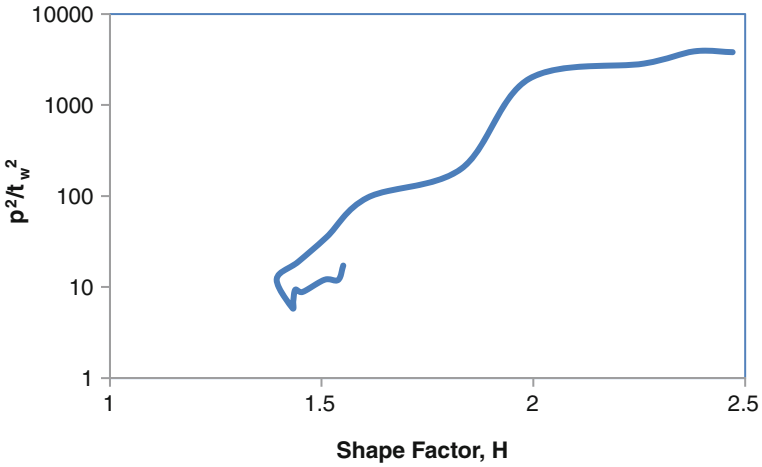

Fig. 10 Normalized mean square plotted versus shape factor

The normalized mean square pressure is plotted against shape factor in Fig. 10. The normalized mean square pressure seems to correlate with shape factor. This is plotted on a log scale. In the adverse gradient region the wall pressure is increasing dramatically and the wall shear stress is significantly reduced.

4 Unsteady Pressure Measurements

One way to better understand the data set is to compare the results to other data in the literature. Much of the data in the literature is for equilibrium boundary layers and the data sets tend to be normalized to facilitate comparison. A review of single point wall pressure spectra can be found in Bull [1], Keith et al. [7] or Miller et al. [3]. There are many nondimensionalizations possible. Three explored here include outer variable, inner variable and Chase-Howe mixed variable nondimensionalization, summarized in Table 2.

The outer variable normalizations tend to collapse the low frequencies. To get a general collapse requires a mixed variable normalization such as Goody [8]. The current data for station 6 is compared to Finnveden et al. [9] equilibrium TBL in Fig. 11. The result is high and has more high frequency content.

Table 2 Spectral normalizations

	Frequency	Spectrum level
Outer	$\omega\delta^*/U_\infty$	$10*\log(\phi_{pp}(\omega)/(q^2\delta^*/U_\infty))$
Inner	$\omega\nu/u_\tau^2$	$10*\log(\phi_{pp}(\omega)\ u_\tau^2/(\tau_w^2)\ \nu)$
Chase-Howe	$\omega\delta^*/U_\infty$	$10*\log(\phi_{pp}(\omega)\ U_\infty/(\tau_w^2\delta^*))$

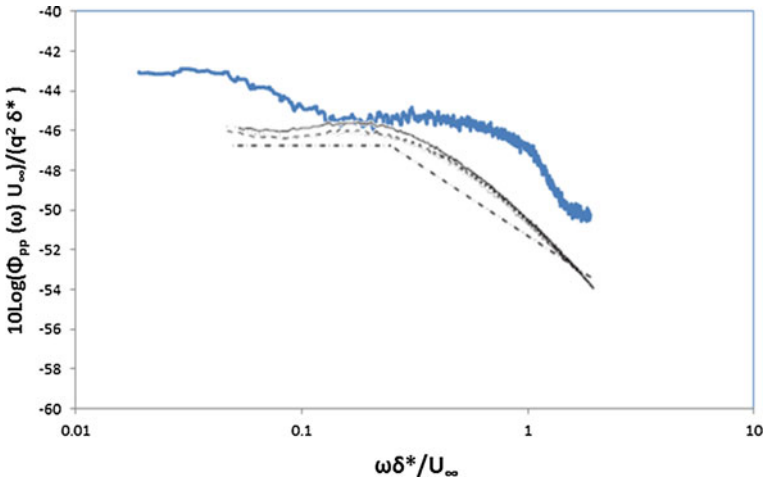

Fig. 11 Outer variable normalization compared to Finnveden et al. [9]

The collapse on Chase-Howe mixed variables is shown in Fig. 12. The current data set is shown in red and is compatible with the previously reported spectral levels. The comparison data was reported in Ciopollo [10].

The inner variable collapse is shown in Fig. 13 and compared to results reported by Ciopollo [10]. Station 6 is shown and it is for a favorable pressure gradient. The spectral levels are higher than the Zero pressure gradient results they reported.

The favorable gradient results, station 1 through station 8 are shown in Fig. 14. The spectral levels start high at station 1 and are gradually decreasing up to station 7. At station 8 the levels start increasing again.

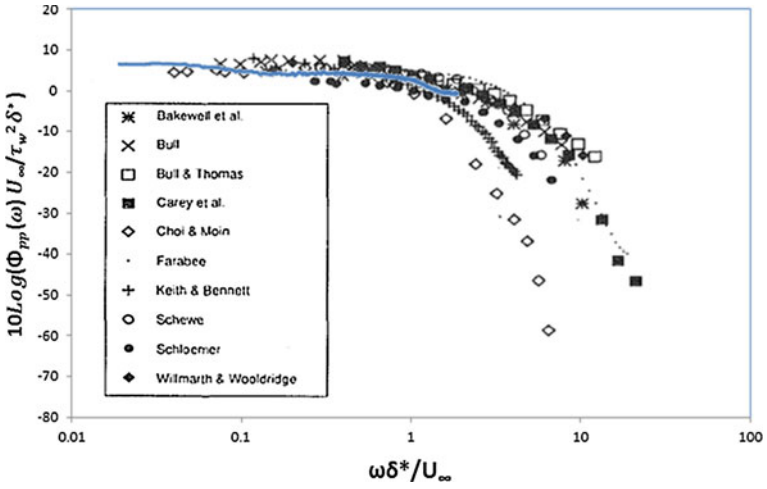

Fig. 12 Comparison to Chase-Howe

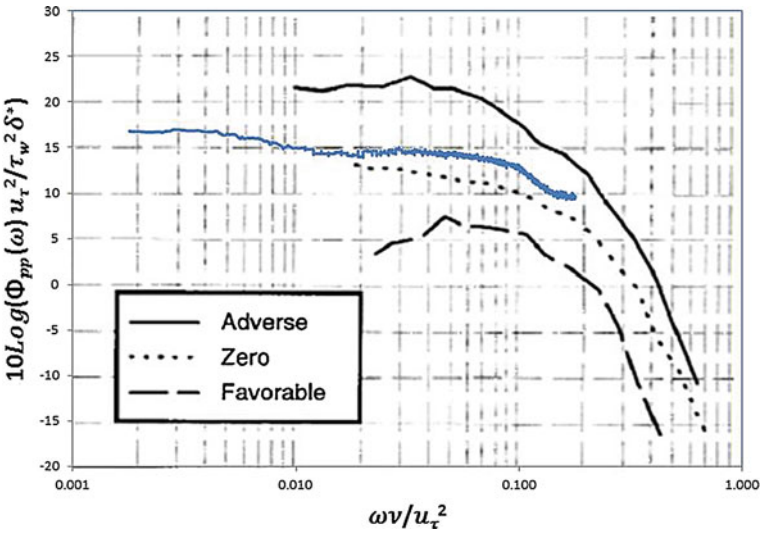

Fig. 13 Inner variable collapse

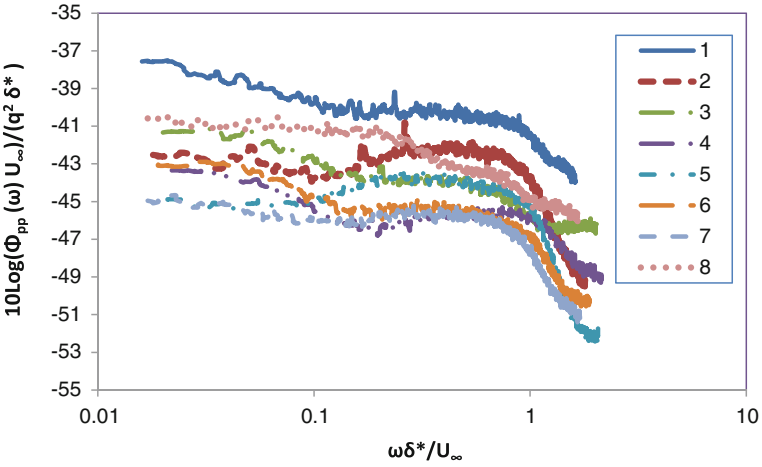

Fig. 14 Favorable gradient outer variable normalized pressure spectra

The outer variable normalized results for the adverse gradient portion, station 9 to station 16 are shown in Fig. 15. The effect of the adverse gradient is profound. As the boundary layer gets closer to separation, the low frequency content is greatly increased.

The Chase-Howe mixed variable results are shown in Fig. 16 and the inner variable results are shown in Fig. 17.

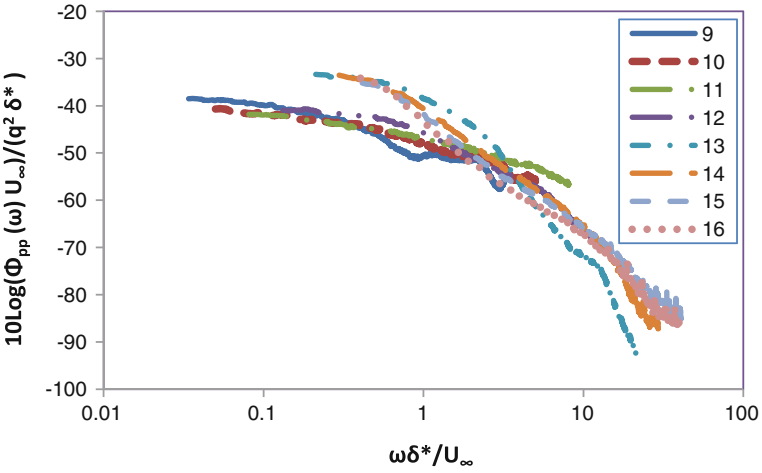

Fig. 15 Adverse gradient outer variable normalized pressure spectra

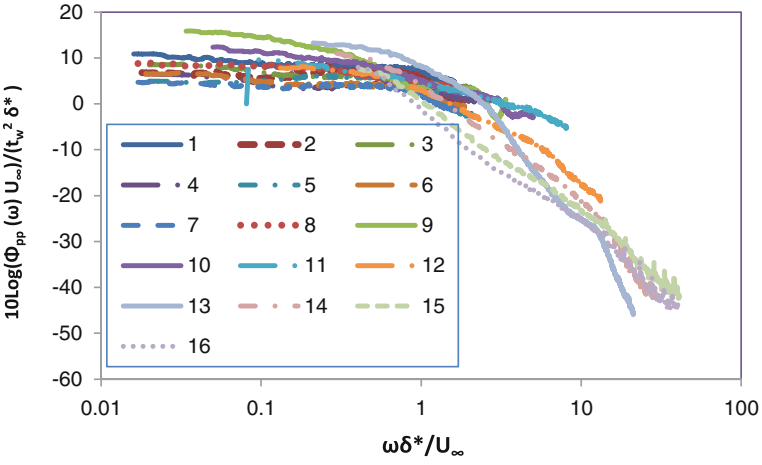

Fig. 16 Chase-Howe normalization

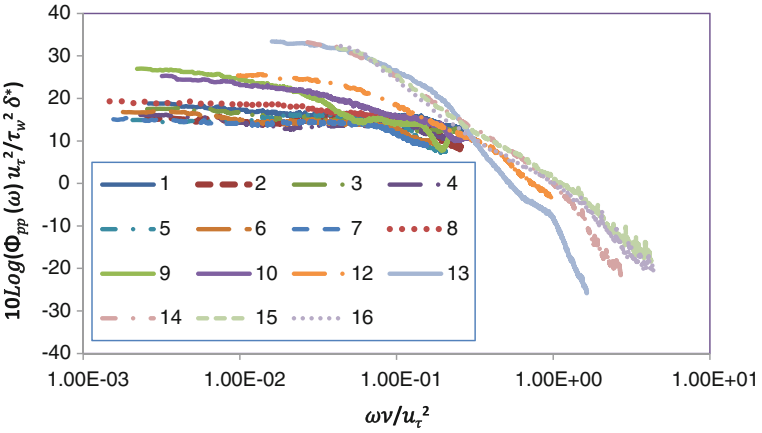

Fig. 17 Inner variable normalization

5 Phase Data

The cross spectrum can be processed into phase and coherence. The phase delay between two points provides insight into how fast the disturbances are traveling. The first step is to unwrap the phase as shown in Fig. 18. The phase is corrected to have a smooth decrease in phase as frequency increases and then median smoothed.

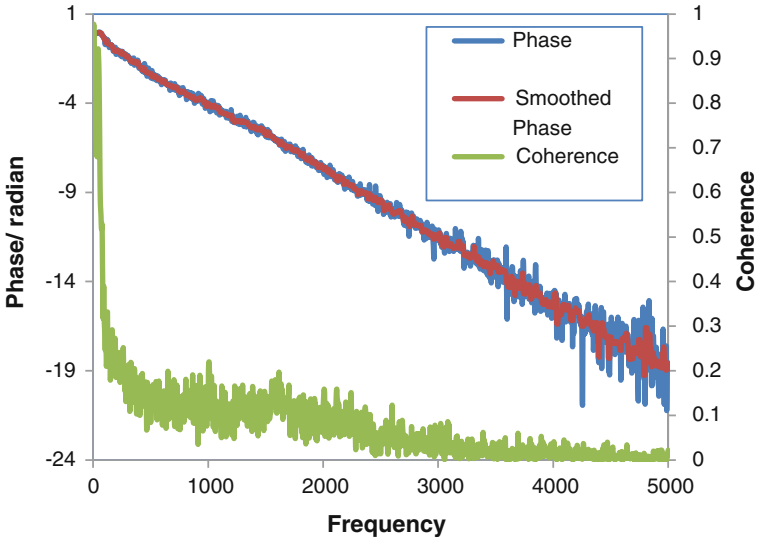

Fig. 18 Unwrapped phase

The coherence is shown and at high frequency the phase estimate is degraded due to the low coherence.

The phase can be converted to a phase velocity via Eq. 4. The phase velocity has been reported by many other investigators including Blake [11], Efimtsov [12], LeClerq and Bohineust [13] and Miller and Moeller [14]. All report that the phase velocity is dependent on the separation between the two transducers used to infer the phase, but all separations tend to have similar shape.

$$C_p = \frac{-\omega \Delta x}{\varphi} \tag{4}$$

The phase velocity for station 6 is shown in Fig. 19 and is compared to the results of Miller and Moeller [14]. The Miller experiments were conducted in a constant area duct and so had a slightly favorable pressure gradient due to the growth of the boundary layer. These results are fairly typical of the data in the literature in that the phase velocity at low frequency rises monotonically with frequency and then peaks and slowly reduces at high frequency. Miller curve fit the phase velocity in a fashion similar to Efimtsov [12] as in Eq. 5.

$$\frac{C_p}{U_\infty} = 1.25\left(\frac{\omega\delta^*}{U_\infty}\right)^{0.5}\left[\frac{1+\left(0.1\left(\frac{\omega\delta^*}{U_\infty}\right)\right)^2}{1+\left(4\left(\frac{\omega\delta^*}{U_\infty}\right)\right)^4}\right]^{0.15} + 0.18 \tag{5}$$

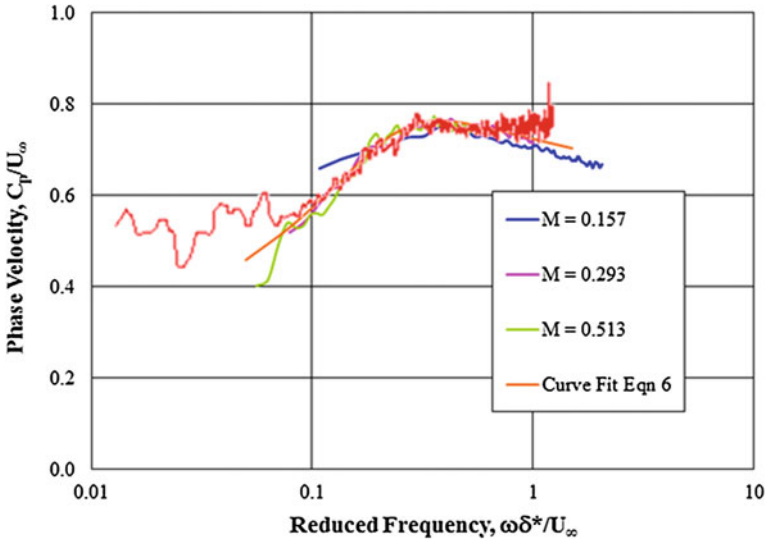

Fig. 19 Phase velocity station 6, miller and fit

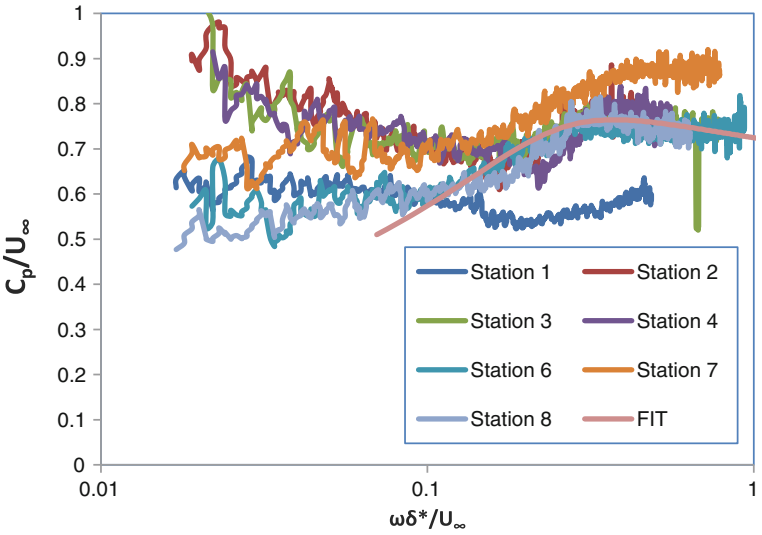

Fig. 20 Phase velocity favorable gradient

The phase velocities for the favorable gradient stations are compared to the curve fit by Miller in Fig. 20. Station 5 had poor coherence and a phase velocity was not recovered there. One thing to note is that the phase velocity at station 1 is low. Station 7 has a higher phase velocity and station eight has relaxed to more typical of the other stations. All stations have different low frequency behavior.

Miller noted that there was a discrepancy between the phase velocity and the array measured convection velocities reported in Abraham and Keith [15] and Arguillat et al. [16]. The phase velocities are concave with frequency and the convection velocities are largely convex. Both are measures of the velocity of the disturbances. Smol'yakov [17] reports this curve fit (Eq. 6) to Abraham and Keith and recommends using it in wavenumber frequency models.

$$\frac{U_c}{U_\infty} = \frac{1.6\left(\frac{\omega\delta^*}{U_\infty}\right)}{1 + 16\left(\frac{\omega\delta^*}{U_\infty}\right)^2} + 0.6 \tag{6}$$

The measured phase velocities show a different trend with frequency as compared to the array measured convection velocities. The phase velocity and group velocity are related by Eq. 7.

$$C_g = \frac{\partial\omega}{\partial k} \tag{7}$$

Blake [11] provided this result for calculating the normalized group velocity from the phase velocity in Eq. 8.

$$\frac{C_g}{U_\infty} = \frac{\left(\frac{C_p}{U_\infty}\right)^2}{\frac{C_p}{U_\infty} - \left(\frac{\omega\delta^*}{U_\infty}\right)\left(\frac{\partial\frac{C_p}{U_\infty}}{\partial\frac{\omega\delta^*}{U_\infty}}\right)} \tag{8}$$

The phase velocity, group velocity and array measured convection velocity fit by Smol'yakov [17] are shown in Fig. 21. The group velocity can be recognized as similar to the array measured convection velocity. So the phase velocity is not an appropriate estimate of the convection velocity when the process is dispersive.

It is clear that below $\omega\delta^*/U_\infty$ of 0.3 the Taylor's frozen turbulence hypothesis cannot be correct because the dispersion will change the turbulence as it propagates. Above that value, the hypothesis is plausible as the process is essentially nondispersive with the phase and group velocities being roughly equal. However the decay rates are high in that region and so only a short time picture of the turbulence can be inferred.

Of interest is what happens at low frequency. Both the phase velocities and group velocities tend to zero as frequency tends to zero. Further as in Efimtsov [12], Finnveden et al. [9] and Miller and Moeller [14] the decay rates increase with

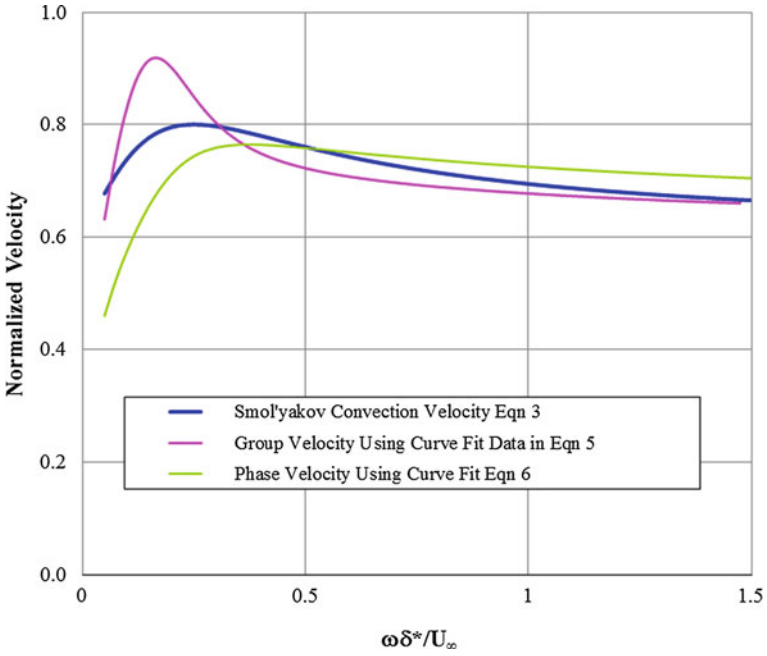

Fig. 21 Normailzed group and phase velocities

decreasing frequency. This implies that these boundary layers do not support the propagation of large low frequency structures.

Landahl [18] speculated that the turbulent boundary layer can be described as a waveguide with the turbulent propagation described by the Orr-Sommerfeld equation. The favorable gradient and equilibrium turbulent boundary layers are stable and he calculated a convection velocity by finding the least stable eigenvalues of the boundary layer profile. These estimates were concave with frequency and consistent with the array measured convection velocities.

In the adverse gradient portion of this flow, the results are dramatically different than in the favorable gradient region. The waveguide view of the boundary layer provides some insight into these dynamics. The adverse gradient boundary layers have an inflection point and this implies they also have unstable eigenvalues resulting in rapidly growing disturbances. This in turn leads to rapidly growing boundary layer thickness and much larger mean square pressures. Both of which are observed in this data set.

The propagation process is also fundamentally different than the favorable and equilibrium boundary layers as can be observed from their phase velocities in Fig. 22. Only the stations with good coherence are reported here. We did not repeat the experiment to try to recover the missing data. One thing to note is that the phase velocity is much slower than the favorable gradient stations.

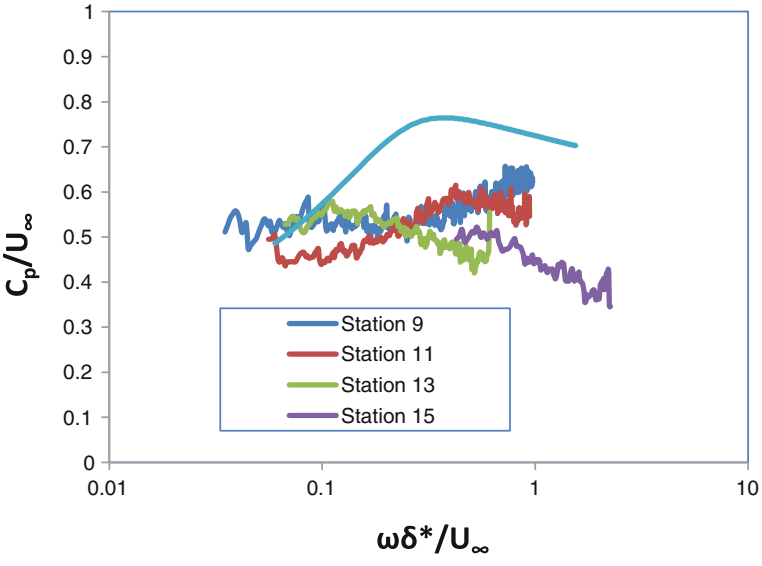

Fig. 22 Phase velocity in adverse gradient flows

6 Observations

There is some evidence of an anomaly at the inlet to the test section. There is a relatively high shape factor, low phase velocity and high spectral levels at low frequencies at station 1. These effects die out in the favorable gradient region. The source of this is unknown at this time. This may be due to an irregularity at the outlet of the contraction section or to the sudden change in the bottom slope just before station 1, causing a stagnation point.

7 Conclusions

The effects of favorable and adverse pressure gradients on the shape and pressure spectra of turbulent boundary layers have been investigated. Favorable (negative) pressure gradients cause a modest reduction in the pressure spectrum levels compared to equilibrium flows. Adverse (positive) pressure gradients dramatically increase the pressure spectrum levels and decrease the phase velocity.

References

1. M.K. Bull, Wall-pressure fluctuations beneath turbulent boundary layers: some reflections on forty years of research. J. Sound Vib. **190**(3), 299–315 (1996)
2. W.R. Graham, A comparison of models for the wavenumber-frequency spectrum of turbulent boundary layer pressures. J. Sound Vib. **206**(4), 541–565 (1997)
3. T.S. Miller, J.M. Gallman, M.J. Moeller, Review of turbulent boundary layer models for acoustic analysis. *J. Aircr.* **49**(6), 1739–1754 (2012)
4. H.H. Schloemer, Effects of pressure gradients on turbulent-boundary-layer-wall-pressure fluctuations. J. Acoust. Soc. Am. **42**(1), 93–113 (1967)
5. Y. Rozenberg, G. Robert, S. Moreau, Wall-pressure spectral model including the adverse pressure gradient effects. AIAA J. **50**(10), 2168–2179 (2012)
6. R.G. DeJong, I.J. Kuiper, Pressure gradient effects on turbulent pressure spectrum, in *Inter-Noise 2012,* New York City, USA, 19-22 Aug 2012
7. W.L. Keith, D.A. Hurdis, B.M. Abraham, A comparison of turbulent boundary layer wall pressure spectra. J. Fluids Eng. **114**, 338–347 (1992)
8. M.C. Goody, Empirical spectral model of surface pressure fluctuations. AIAA J. **42**(9), 1788–1794 (2004)
9. S. Finnveden, F. Birgersson, U. Ross, T. Kremer, A model of wall pressure correlation for prediction of turbulence-induced vibration. J. Fluids Struct. **20**(8), 1127–1143 (2005)
10. K. Ciopollo, W. Keith, Effects of pressure gradients on turbulent boundary layer wave number frequency spectra. AIAA J. **38**(10), 1832–1836 (2000)
11. W.K. Blake, Turbulent boundary-layer wall-pressure fluctuations on smooth and rough walls. J. Fluid Mech. **44**(4), 637–660 (1970)
12. B.M. Efimtsov, Characteristics of the field of turbulent wall pressure fluctuations at large reynolds numbers. Sov. Phys. Acous. **28**(4), 289–292 (1982)

13. D.L.L. LeClerq, X. Bohineust, Investigation and modelling of the wall pressure field beneath a turbulent boundary layer at low and medium frequencies. J. Sound Vib. **257**(3), 477–501 (2002)
14. T.S. Miller, M.J. Moeller, Wall pressure phase velocity measurements in a turbulent boundary layer, in *InterNoise 2012,* New York, NY, Aug 2012
15. B.M. Abraham, W.L. Keith, Direct measurements of turbulent boundary layer wall pressure wavenumber-frequency spectra. J. Fluids Eng. **120**, 29–39 (1998)
16. B. Arguillat, D. Ricot, G. Robert, C. Bailly, Measurements of the wavenumber-frequency spectrum of wall pressure fluctuations under turbulent flows, in *AIAA 2005-2855*, May 2005
17. A.V. Smol'yakov, A new model for the cross spectrum and wavenumber-frequency spectrum of turbulent pressure fluctuations in a boundary layer. Acoust. Phys. **52**(3) 331–337 (2006)
18. M.T. Landhal, A waveguide model for turbulent shear flow. J. Fluid Mech. **29**(3), 441–459 (1967)

Wall Pressure Fluctuations Induced by Supersonic Turbulent Boundary Layer

Roberto Camussi and Alessandro Di Marco

Abstract Wall pressure fluctuations induced on a rigid wall by a turbulent boundary layer in supersonic regime are the subject of the present review. The sound and vibration of the structure subjected to the correlated fluctuating forces are modeled and predicted presuming the knowledge of a forcing function related to the wavenumber–frequency spectrum of the boundary layer pressures. In this framework the main results obtained in measurements of equilibrium supersonic turbulent boundary layers and in recent numerical simulations are reviewed evidencing the actual limitations of both methodologies. More emphasis is devoted to the experimental and numerical analysis made by the authors respectively on the pressure field generated on the external surface of a launcher model and on the modelization of the pressure coherence function generated by a supersonic flow in different conditions over a flat plate.

1 Introduction

Aerodynamically induced vibrations have become of great interest with the advent of high performance flight vehicles and aerospace launchers. Vibrations induced in the interior can exceed design requirements and cause costly damages to the Payload while panel vibrations of the external surface must be avoided to prevent fatigue problems and structural damages. One form of significance which has received much attention by vehicle designers is that due to the wall pressure fluctuations induced by the turbulent boundary layer (TBL). This happened because statistical information regarding wall-pressure fluctuations induced by the external

R. Camussi (✉) · A. Di Marco
University Roma TRE, via della Vasca Navale 79, 00146 Rome, Italy
e-mail: roberto.camussi@uniroma3.it

A. Di Marco
e-mail: alessandro.dimarco@uniroma3.it

E. Ciappi et al. (eds.), *Flinovia - Flow Induced Noise and Vibration Issues and Aspects*, DOI 10.1007/978-3-319-09713-8_4

turbulent boundary layer is required in order to determine the vibro-acoustic behavior and predict the structural response of the surface [5].

Experimental investigations at supersonic speeds have primarily included measurements of pressure fluctuations intensities and spectra, whereas limited data on multivariate statistics have been provided. As pointed out in [2] experimental measurements in the high-speed regime pose a considerable challenge associated with several complications: the spatial resolution of the sensors, the contamination induced by noise in the experimental facility, the onset of resonances of the sensor diaphragm and the cavity where the sensor is allocated, and the limited frequency response of the sensor, the latter being probably the dominant issue.

Numerical simulations of equilibrium supersonic TBLs, providing wall pressure statistics, are scarce in literature as well. Only recently, an extensive analysis has been presented in [4] where it is shown that wall pressure autospectra weakly depend on the Mach number (M) even for high supersonic regimes (up to $M = 4$). To the extent of theoretical modeling, the only attempt to model the wall pressure coherence function including the dependence on the flow Mach number was made by Efimtsov [22] who proposed a model that includes a number of additional adjustable coefficients and flow parameters which may be difficult to be measured accurately at high speed, such as the friction velocity.

In the present paper, a review of the state of the art on modeling of wall pressure fluctuations beneath transonic and supersonic TBL is presented. Attention in focused on two recent papers published by the authors research group. The papers concerned both experimental [10] and numerical [20] analyses.

The experimental investigation presented in [10] has been carried out on a scaled instrumented model of the VEGA aerospace launch vehicle that has been installed in a transonic wind tunnel. The measurement campaign was aimed at characterizing the vibro-acoustic behavior induced by the external aerodynamics in particular in correspondence of the Fairing where the payload is expected to be located. An example of a flow visualization is given in Fig. 1, where the formation of a shock-wave is evidenced.

The research activity described in [20] is focused on an extensive investigation of cross-spectral features of the wall pressure fluctuations induced by supersonic turbulent boundary layers at high Mach numbers. This study is based on the analysis of a DNS database [4] providing wall pressure fluctuations at Mach numbers $M = 2, 3, 4$, over a relatively wide range of (moderate) Reynolds numbers. The analysis was mainly targeted towards the accurate characterization of the wall pressure coherence function, being this the most important statistical quantity used by engineers for the estimation of the structural response of panels underneath turbulent boundary layers. The capability of existing simple theoretical models to predict the wall pressure coherence behavior has been investigated and discussed, with particular emphasis on the Efimtzov model [22].

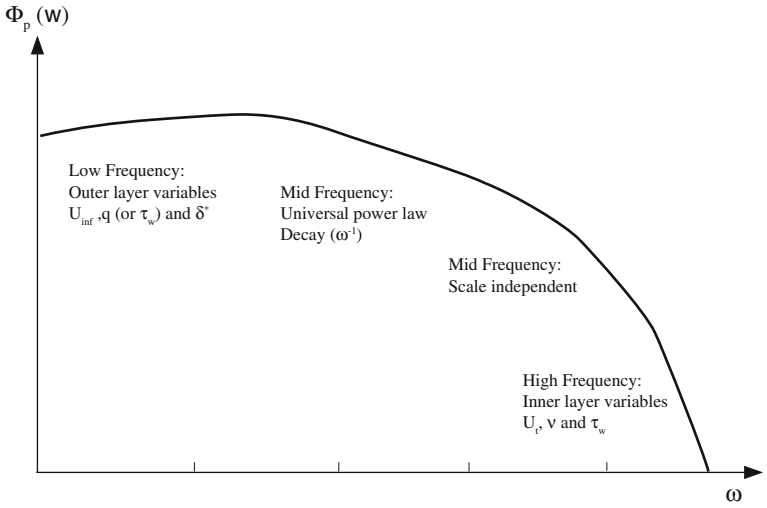

Fig. 1 Sketch clarifying the expected scaling regions of a typical wall pressure auto–spectrum

2 The Wavenumber Frequency Spectrum: Scaling and Modeling

Wavenumber–frequency models of the wall pressure, that are accurately representative of the TBL spectrum, can be reliably used to study vibration and radiated noise from a structure. In this section the main characteristics of the wall pressure spectrum are briefly reviewed. First, the scaling properties of the frequency spectra are discussed taking into account the most relevant experimental investigations conducted in the last 50 years. Then, illustrative examples of statistical models of the wavenumber–frequency spectrum are revised starting from the early Corcos idea up to the most recent developments.

2.1 Scaling of the Frequency Spectra

Due to the complex structure of the turbulent boundary layer, it is not possible to obtain a single scaling that leads to a satisfactory collapse of experimental or numerical frequency spectra $\Phi_P(\omega)$. As will be clarified below, it is possible to normalize the spectra using inner or outer variables, and a universal collapse can be obtained in various regions of the pressure spectra separately (see, among many, the early work by Willmarth [46] and the papers by Farabee and Casarella [24, 29, 33]). This is due to the fact that the wall pressure is influenced by velocity fluctuations from all parts of the boundary layer and because the convection velocity depends

strongly upon the distance from the wall, as a result of the non-uniform mean velocity distribution.

For an incompressible flow, the wall pressure can be written in the form of a Poisson's equation,

$$\nabla^2 p(\mathbf{x}, t) = q(\mathbf{x}, t) \tag{1}$$

where $q(\mathbf{x}, t)$ represents the source terms. As suggested by Farabee and Casarella [24], the analysis of the solution of the above equation in the Fourier domain, shows that the contributions to the high-frequency portion of the spectrum has mainly to be attributed to turbulence activity located in the near wall region while contributions to the lower-frequency portion can originate from activities throughout the boundary layer. Following this physical picture, and the conjectures suggested by Bradshaw [6, 8], it is possible to divide $\Phi_p(\omega)$ into three main regions, depending on the frequency magnitude. At low frequencies, $\Phi_p(\omega)$ scales on outer layer variables; at high frequencies, $\Phi_p(\omega)$ is influenced by the fluid viscosity and thus it scales on inner variables; at intermediate frequencies, the shape of the spectrum is scale independent and an universal power law decay of the type ω^{-1} is expected.

Measurements of the cross-spectral densities (e.g. [7, 24]) confirm that the pressure field can be divided into two distinct families, one associated with the motion in the outer layer and the other with motion in the inner layer. This separation occurs at the frequency where the auto-spectrum exhibit its maximum value. This frequency separates the non-universal from the universal scaling regimes of the frequency spectrum.

More precisely, in the low frequency region, different outer scalings have been identified. Keith et al. [33] suggests to scale the frequency using U (the free stream velocity) and δ^*, whereas the amplitude of the pressure spectrum can be scaled through the free stream based dynamic pressure q. Other authors (including [24]) recommend a more effective scaling using τ_w instead of q. They suggest to scale the frequency upon U/δ and the dimensionless spectrum to be of the form $\Phi_P(\omega)U/\tau_w^2\delta$.

In the high frequency region, there is a more general consensus on the most effective scaling that is achieved through the variables U_τ, ν and τ_w. This implies that the dimensionless frequency is $\omega\nu/U_\tau^2$ and the dimensionless spectrum should be $\Phi_P(\omega)U_\tau^2/\tau_w^2$.

The universal region can be interpreted as an overlap of the two regions described above. In this part of the spectrum it is assumed $\omega\Phi_P(\omega)U/\tau_w^2 = \text{constant}$, thus leading to the ω^{-1} scaling. A precise definition of the amplitude of the frequencies bounding the universal region can be found in [8, 24].

An additional range at very low frequencies has been also identified by some authors. Farabee and Casarella [24] determine this region at $\omega\delta^*/U \leq 0.03$ and they collapsed the spectrum using the normalization $\Phi_P(\omega)U/q^2\delta^*$. In the very low frequency region they observed the spectrum to scale as ω^2. This form of scaling is in agreement with the prediction given by the Kraichnan-Phillips theorem [34, 40]

which suggests that the wavenumber spectrum should scale like k^2 as $k \to 0$. According to the theoretical developments of e.g. [36], this conclusion can be extended to the frequency spectrum under the hypothesis of low Mach number flow conditions.

In Fig. 1 a scheme summarizing the expected scalings is reported.

We refer to the literature (in particular [9, 24]) for further discussions on the above topics and considerations about the scaling of the pressure variance.

2.2 Modeling the Wavenumber-Frequency Spectrum

According to the above discussion, several models have been proposed in the literature to reproduce the shape of the frequency auto-spectrum using suitable fits of experimental data. Here we only cite some of them as illustrative examples of common approaches. We refer to the literature for comprehensive reviews.

An early and widely used model was proposed by Corcos [18]. He gives the following representation of the frequency auto-spectrum:

$$\Phi_p(\omega) = \begin{cases} C & \text{for } \omega \leq \frac{U_e}{\delta^*} \\ C\frac{U_e}{\omega\delta^*} & \text{for } \omega > \frac{U}{\delta^*} \end{cases} \tag{2}$$

The quantity C is a dimensionless constant and U is the external velocity. Note that for $\omega > \frac{U_c}{\delta^*}$ the model correctly predicts the power law decay of the spectrum of the form ω^{-1}.

An example, among many, explaining the way the Corcos' early model has been successively modified, is given by Cousin [19]. This more general approach leads to the following expression:

$$\Phi_p(\omega) = \begin{cases} 2.14 \times 10^{-5} B & \text{for } \omega\delta^*/U_e \leq 0.25 \\ 7.56 \times 10^{-6} B(\omega\delta^*/U)^{-0.75} & \text{for } 0.25 < \omega\delta^*/U_e \leq 3.5 \\ 1.27 \times 10^{-4} B(\omega\delta^*/U)^{-3} & \text{for } \omega\delta^*/U_e > 3.5 \end{cases} \tag{3}$$

where $B = q^2\delta^*/U$.

Other formulations worth mentioning are those by Chase [12, 13, 23]. We refer to the literature for the details.

As pointed out above, the knowledge of the frequency spectrum is not sufficient to determine the modal excitation term of a plate subject to the turbulence induced pressure filed. This quantity is directly related to the shape of the complete wavenumber-frequency spectrum of the wall pressure field. The knowledge of $\Phi_P(k_1, k_2, \omega)$ is therefore fundamental to compute the response of a surface panel subject to the action of the random pressure load. Simplified schemes of the wavenumber–frequency spectrum as a function of the wavenumber and as a function of the frequency are reported in Figs. 2 and 3 respectively.

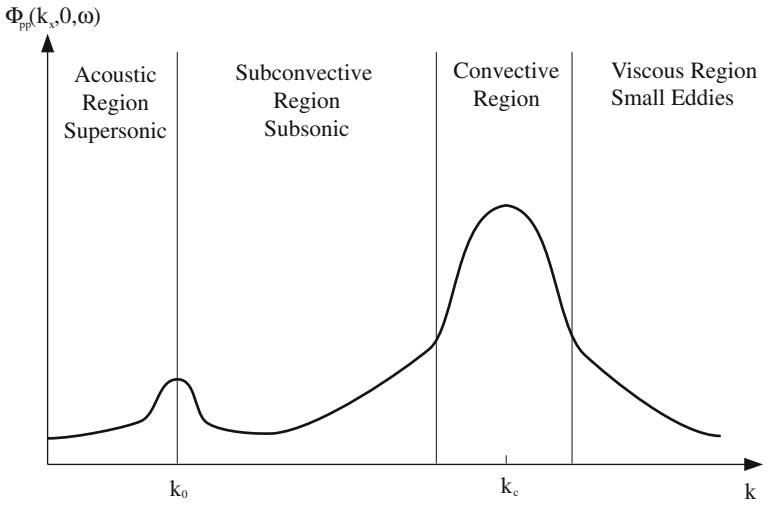

Fig. 2 A scheme representing the wavenumber-frequency spectrum as a function of wavenumber, at constant frequency (scheme adapted from [5])

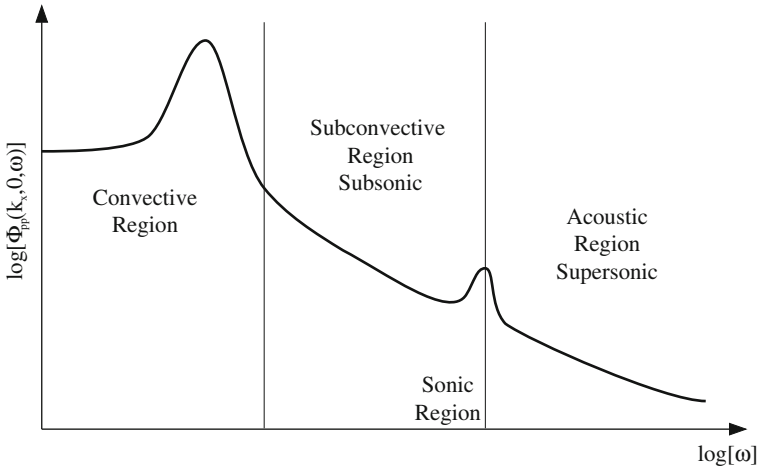

Fig. 3 A scheme representing the wavenumber-frequency spectrum as a function of frequency, at constant wavenumber (scheme adapted from [5])

As pointed out by Bull [9], the highest spectral levels of the pressure fluctuations are associated to the mean flow convection and, in the wavenumber spectrum, are centered on a wavenumber $k_1 = \omega/U_c$, k_1 along the free stream velocity. This part of the spectrum is often referred to as the convective ridge. For $k_1 \ll \omega/U_c$ the spectrum is expected to be independent of the wavenumber. Another important aspect is related to the so–called sonic wavenumber $k_0 = \omega/c$. According to [5], for

$k = k_0$ an apparent singularity is present in the spectrum. However, in real flows, the wavenumber-frequency spectrum is expected to have a local finite peak in the vicinity of k_0. These are among the main features that an analytical model attempting to predict the $\Phi_p(k_1, k_2, \omega)$ shape, have to reproduce correctly.

One of the most reliable model developed in literature is again the early approach proposed by Corcos [18] and based on the Fourier transform of a curve fit of measured narrow band pressure correlations. According to extensive experimental measurements (namely [7, 46]), the cross-spectral density $\Gamma_p(\xi_1, \xi_2, \omega)$ can be represented as:

$$\Gamma_p(\xi_1, \xi_2, \omega) = \Phi_p(\omega) A(\omega\xi_1/U_c) B(\omega\xi_2/U_c) \mathrm{e}^{i\omega\xi_1/U_c} \tag{4}$$

where

$$A(\omega\xi_1/U_c) = \mathrm{e}^{-\alpha_1|\omega\xi_1|/U_c} \quad \text{and} \quad B(\omega\xi_2/U_c) = \mathrm{e}^{-\alpha_2|\omega\xi_2|/U_c}$$

whereas U_c is the convection velocity and α_1 and α_2 are parameters chosen to yield the best agreement with experiments. Various values are given in the literature. The typical range of the values is $\alpha_1 = 0.11 \div 0.12$ and $\alpha_2 = 0.7 \div 1.2$ for smooth rigid walls.

Unfortunately, only few experimental or numerical data concerning direct measurements of the wavenumber–frequency spectrum are available in the literature [1, 14, 25, 32, 37, 39]. However, it appears evident that a big spread is present in the low wavenumber range and that the Corcos model overpredicts levels at wavenumbers below the convective peak. This point is crucial for many applications, in particular in the case of underwater and surface marine vehicles and for aeronautical structures above the aerodynamic coincidence frequency (see also [15]). Later workers used analytical or quasi analytical approaches, or revised versions of the Corcos approach, in attempts to describe this region more accurately (see e.g. [30] for details).

Most of the models proposed continued to follow the philosophy of the Corcos approach that can be generalized as follows. A first common feature of those empirical models is the separation of variables approach to represent the correlation function dependence on the streamwise separation ξ_1 and the crossflow separation ξ_2. This is known as the 'multiplication hypothesis' in which the coherence of the cross-spectral density for an arbitrary separation direction is formed by the product of the cross-spectral densities for streamwise and spanwise separations, respectively. The axisymmetry of the geometry and of the flow is usually not explicit in those formulations but it is accounted for through the adjustable coefficients. According to the Corcos idea given in Eq. 4, most of the models suggest to take exponential decaying form of the functions A and B,

$$A(\omega,\xi_1) = \mathrm{e}^{-\frac{|\xi_1|}{L_1(\omega)}} \text{ and } B(\omega,\xi_2) = \mathrm{e}^{-\frac{|\xi_2|}{L_2(\omega)}} \tag{5}$$

where L_1 and L_2 are the so-called coherence lengths in the streamwise and spanwise direction respectively.

The main advantage of adopting the expression given in Eqs. 4 and 5 is that the auto-spectrum part is decoupled from the cross-spectrum part. That implies that any choice for modeling the function $\Phi_p(\omega)$, as those described above, can be addressed independently of any choice for representing the functions L_1 and L_2.

As for auto-spectra, Cousin modified the Corcos model yielding the following expressions of the coherence lengths:

$$\begin{aligned} L_1 &= \frac{U_c}{\omega\alpha_1}\left\{1+\left(\frac{U_c}{\omega b_M \delta}\right)^2\right\}^{-1/2} \\ L_2 &= \frac{U_c}{\omega\alpha_2}\left\{1+\left(\frac{U_c}{\omega b_T \delta}\right)^2\right\}^{-1/2} \end{aligned} \tag{6}$$

where $U_c = 0.75U$, $b_M = 0.756$, $b_T = 0.378$, $\alpha_1 = 0.115$ for smooth walls and 0.32 for rough walls, whereas $\alpha_2 = 0.32$ in all cases.

A similar model, not reported here for brevity, has been proposed by Cockburn and Robertson [16]. Wu and Maestrello [47] proposed a model where the flow is assumed semi-frozen and decaying in space and time at a constant velocity U_c. After performing a comprehensive set of experimental results of wind tunnel testing, they defined an ensemble average of the cross correlation for the pressure fluctuation due to the turbulent boundary layer in which the effects of the Reynolds number and the boundary layer thickness were included.

Other models proposed by [11, 12, 22, 27, 44] are compared in [30]. It is demonstrated that even at the convective peak, a relevant scattering among the model predictions is evident. Even larger scattering is observed in the estimation of the radiated sound as reported in the same paper.

The best model for high speed aircraft is, according to Graham, the one which provides an accurate description of the convective peak. Efimtsov's model, an extension of Corcos model, is cited as a suitable candidate. For the sake of completeness, we report in the following the Efimtsov idea:

$$\begin{aligned} L_1 &= \delta\left[\left(\frac{a_1 St_\tau}{U_c/U_\tau}\right)^2 + \frac{a_2^2}{St_\tau^2+(a_2/a_3)^2}\right]^{-1/2} && \text{for} \quad 0.41 < M < 2.1 \\ L_2 &= \delta\left[\left(\frac{a_4 St_\tau}{U_c/U_\tau}\right)^2 + \frac{a_3^2}{St_\tau^2+(a_5/a_6)^2}\right]^{-1/2} && \text{for} \quad M < 0.75 \\ L_2 &= \delta\left[\left(\frac{a_4 St_\tau}{U_c/U_\tau}\right)^2 + a_7^2\right]^{-1/2} && \text{for} \quad M > 0.9 \end{aligned} \tag{7}$$

In this model $U_c = 0.75U_e$ and $St_\tau = \omega\delta/U_\tau$ is a Strouhal number defined on the friction velocity. Averaged values of the empirical constants are $a_1 = 0.1$, $a_2 = 72.8$, $a_3 = 1.54$, $a_4 = 0.77$, $a_5 = 548$, $a_6 = 13.5$, $a_7 = 5.66$. It can be shown that at high frequencies, these expressions correspond to a Corcos model with $\alpha_1 = 0.1$ and $\alpha_2 = 0.7$. Even though the number of empirical constants is relevant, the model is extensively used thanks to the introduction of the Mach number as a relevant parameter.

More recently, [42, 43] performed a Large-Eddy Simulation (LES) of a turbulent boundary layer at relatively high Reynolds number and proposed a model that overcomes the 'multiplication hypothesis' that is the basis of all the models based on the Corcos' philosophy. His approach is based on an accurate fit of the two-dimensional coherence and therefore is particularly efficient for the determination of the off-axis coherences.

To the best of our knowledge, the most recent model proposed in literature is the one presented by Finnveden et al. [28]. They suggested a modified version of the Corcos and of the Chase model, thus going back to the 'multiplication hypothesis'. They demonstrated that it is possible to find for both models a complete set of free parameters that provide a fair agreement with experimental data. The key point was to modify the Corcos model by introducing a frequency and flow speed dependence in the parameters and to introduce two new parameters in the Chase model to better fit the spanwise coherence to measurements.

3 Measurements of Wall Pressure Fluctuations in Supersonic TBL

Mapping out the entire TBL wavenumber–frequency wall pressure spectrum experimentally has been difficult because of the effort in accurately measuring low wavenumber surface pressure.

The shape of the wavenumber spectrum near the convective peak has been relatively well established from two–point, cross–spectral density measurements between flush mounted transducers. However, at large transducer separation distances, needed to resolve the low wavenumber spectrum, these measurements are typically overwhelmed by convective pressures and cannot be reliably used. Furthermore, as pointed out by Dolling and Dussauge [21] and reviewed by Beresh et al. [2], the method of measurements of wall pressure fluctuations under zero pressure gradient and perturbed compressible TBL are affected by common sources of error. In the low-frequency region of the pressure spectrum the errors are essentially due to the influence of the facility noise and the limits of the instrumentation. Hence a noise cancellation technique is needed.

The sensor frequency response needs to be adequate for the temporal frequencies of interest to be resolved, but typically in supersonic flow conditions the capability of most pressure sensors are below the requirements. Moreover, in the high frequency range, the measurements are affected by electronic noise, that reduces correlations, and the sensor size is much greater than the smallest fluid structures inducing a cutoff frequency that low–pass filters the signal.

Finally, measurements are contaminated by installation effects. Usually, in order to better utilize their capabilities, pressure transducers are mounted directly on the wetted surface. Two configurations are commonly used: cavity mounting and flush mounting [45]. The first configuration has better spatial resolution independently by the size of the sensor but the dynamic response of the tap–cavity–transducer combination introduces resonance frequencies in the spectrum. The second allows to utilize the full dynamic response of the sensor but the flushness should be carefully checked. The transducer interface with the flow must match closely the shape of the surface in order to avoid local pressure distortion since protrusions of the sensor can cause serious measurements errors [21]. The best recommendation is to recess the transducer slightly.

In a recent paper [2], the authors improved the effort made in 50 years of research by adopting a new solution to measure wall pressure fluctuations beneath a supersonic TBL. Measurement data were compared with an historical database and evident discrepancies where evidenced. Wind tunnel experiments were made on a flat plate and the effect of the Mach and Reynolds numbers was tested. The analyzed Mach ranged from 1.5 to 3 and the Reynolds number based on the momentum thickness (Re_θ) was varied from 15,000 to 51,000 covering most of the supersonic capability of the used wind tunnel.

Data were acquired using two sensors. The sensibility was chosen to accurately resolve an extended pressure spectrum from low frequencies of about 0.1 Hz to very high frequencies of about 400 kHz. Pressure signals were merged to obtain a single spectrum, elaborated using an adaptive filter technique [38] to reduce noise and vibration levels and compensated with the Corcos correction technique [17].

Comparing the spectra, when normalized by outer flow variables, a weak Reynolds dependence was found whereas an increase in Mach number produced a noticeable reduction in the normalized magnitude. Power spectral densities of the wall pressure showed the contribution of the turbulent activity in the logarithmic region leading to a ω^{-1} slope in the high frequency range. In the low frequency range the pressure spectra do not vanish but keep a constant level according to a ω^2 law. However, the very high frequencies that are particularly important for flight applications have not been resolved, as sketched in Fig. 4. The evaluated ω^{-5} region, dotted line in the figure, could be measured with a sensor whose characteristics are beyond the reach of wind tunnel experiment measurement capability. These results suggested that the sensor frequency response still remains the dominant issue for high speed flows.

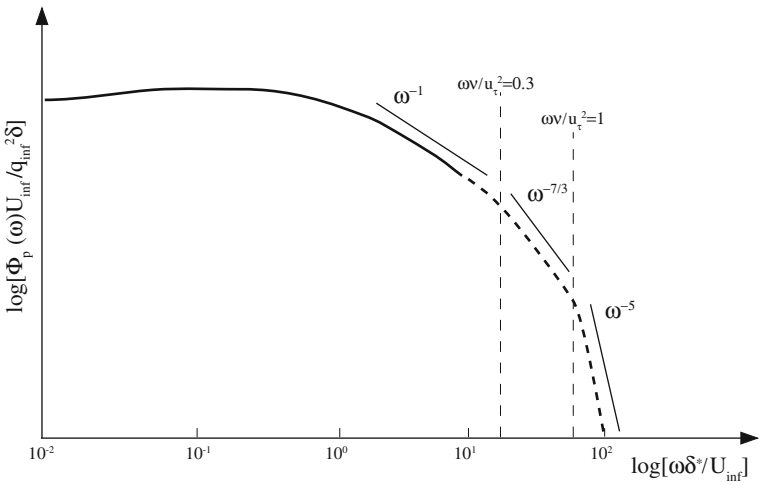

Fig. 4 Sketch of a spectrum extended at the higher frequencies (adapted from [2])

For a more complex geometry than a flat plate the work made by the present authors [10] can be taken into consideration. It deals with the measurements of the wall pressure fluctuations along the surface of a scaled model of the aerospace VEGA launcher. The experimental campaign program was aimed at the characterization of the aerodynamics and aeroacoustics behavior in transonic and supersonic flow conditions. The study was focalized on the transonic range due to the presence of unsteady phenomena that can induce flow instabilities [35] and hence cause vibration of the body which, in turn, may radiate noise. The work was motivated by the need of predicting the structural vibrations responsible for the acoustic radiation, and, as pointed out above, this objective can be pursued by the estimation of the wall pressure statistics. Another important task was the extrapolation at full-scale of the experimental results, this approach baing possible only through a reliable theoretical modelling of the pressure spectra.

The transonic measurements were carried out on a 1:30 scaled model installed within the T1500 wind tunnel of FOI in Stockholm. Miniature pressure transducers were flush mounted on the model surface and accelerometers equipped the ogive and the first stage to exclude vibrational coupling. Schlieren visualizations were used to appreciate the fluid dynamic behaviour and give a physical interpretation of the results. The measurements were made spanning the Mach number from 0.83 to 0.98 and varying the angle of incidence for each flow condition within the range 0–6 with a step of 1.

The effect of the main experimental parameters was evaluated. For what concerns the position along the launcher the influence of the pressure gradients generated by geometry variations modifies the spectra shape as can be inferred examining Fig. 5.

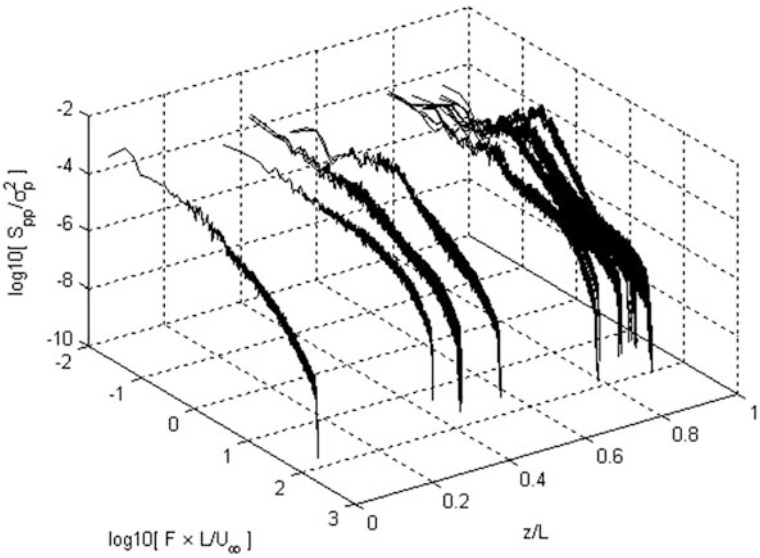

Fig. 5 Normalized auto–spectra evolution along the launcher model for $M = 0.83$ at $\alpha = 0$. U_∞ is the mean velocity upstream the tested model in the wind tunnel conditions. Image courtesy of Aerospace Science and Technology

The Mach number influences the statistical properties of the pressure fluctuations due to the presence of a shock–wave, visible in Fig. 6, moving downstream from the Fairing to the intermediate cylinder as the M was increased.

Depending on the position the effect of M might be relevant. Similar shapes of the pressure spectra with relevant variation of Mach numbers were documented in regions where the shock–wave had less influence, downstream the fairing cylinder. Most critical was the situation at the Fairing cylinder, where a variation of M significantly modified the boundary layer evolution. An example of the spectra shape obtained for the lowest and the highest M analyzed are reported in Fig. 7.

The hydrodynamic effects were negligible at the lowest M as can be qualitatively observed by the typical $-7/3$ power law decay, characteristic of fully developed turbulent flows. At the highest M, vortical structures belonging to the outer region of the boundary layer influenced the spectral frequency decay that exhibited a -1 slope, a common behavior in equilibrium boundary layers.

The lack of universality for the auto–spectra was also found for the cross-–spectra. The coherence functions of Fig. 8 shows that the exponential decay assumption of the Corcos type can be considered to be valid in restricted regions as the M is decreased. The modeling is possible providing a specific model for each M and also for each region since the exponent decay coefficient strongly depends upon the position along the launcher.

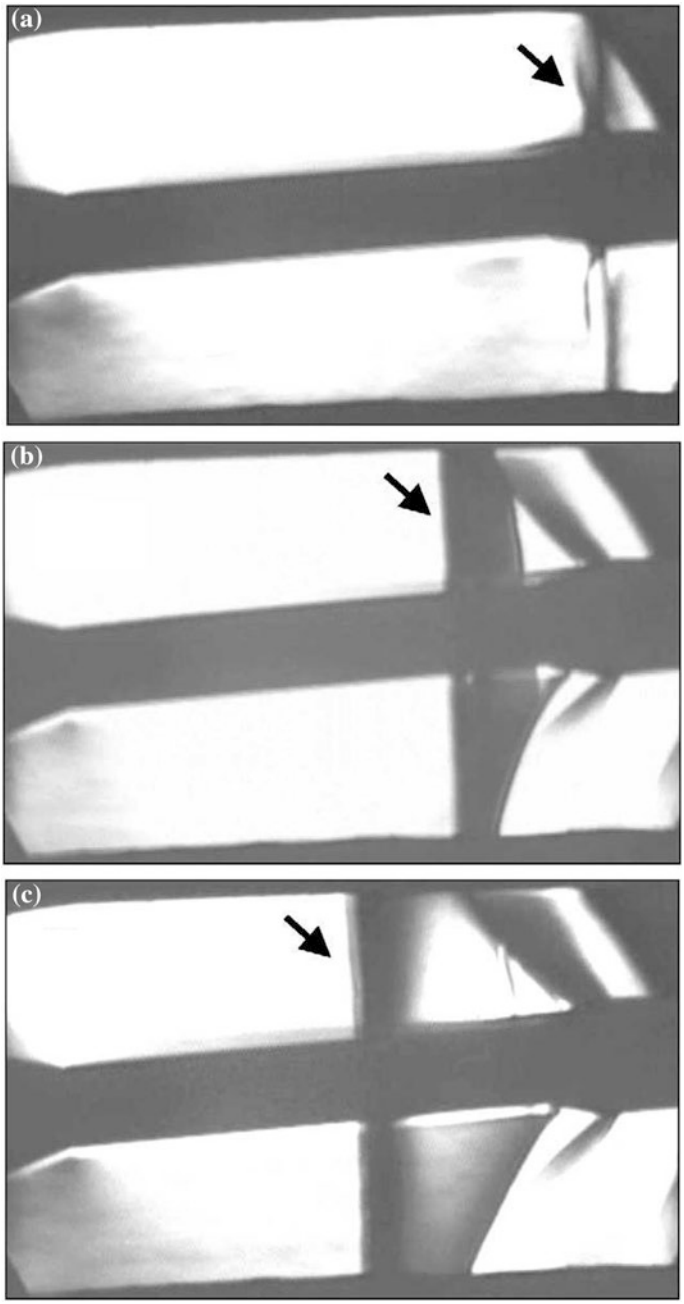

Fig. 6 Schlieren visualizations taken from a video record made during a Mach sweep between 0.7 and 1 at $\alpha = 3$. The three cases reported refer to $M \approx 0.95$ (**a**), $M \approx 0.97$ (**b**) and $M \approx 0.99$ (**c**). The intense shockwave moving downstream is evidenced by the *black arrow*. Image courtesy of Aerospace Science and Technology

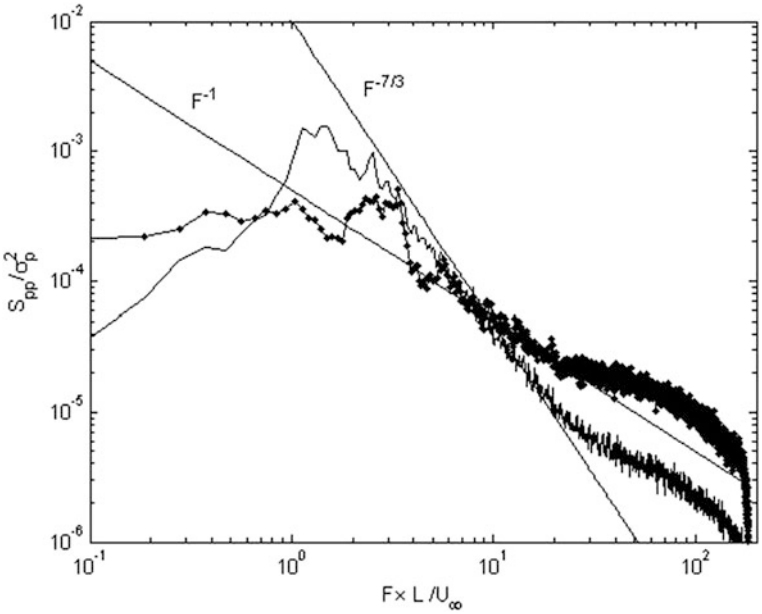

Fig. 7 Auto–spectra determined on the Fairing Cylinder in one position along the launcher model (Payload region in the Fairing Cylinder) showing the effect of M at $\alpha = 0$ (solid line corresponds to $M = 0.83$, solid–dotted to $M = 0.98$). Straight lines represent power law approximations. Image courtesy of Aerospace Science and Technology

4 Wall Pressure Statistics in Supersonic/Compressible TBL Numerical Simulations

The considerable challenge of performing accurate pressure measurements in high–speed flows which draw to the scatter of the available data (Sect. 3) and the difficulty to make definite conclusions on the behavior of the wall pressure field have motivated the numerical research made in [3, 4]. The objectives were to fill in the gap in the existing literature about pressure field statistics in supersonic and transonic boundary layers by means of direct numerical simulation (DNS). The DNS is a invaluable tool which allows to gather information and data difficult or impossible to obtain otherwise. The limitations are due to the maximum possible Reynolds number of the simulation. Higher Reynolds number are desirable to extend the comparison of numerical and measurement results but the simulation would require access to huge computational resources.

The simulation of supersonic TBLs over a flat plate was performed in [4]. Three values of free–stream Mach numbers were considered at different values of the friction Reynolds number (Re_τ). The choice of the Re_τ as appropriate to compare the analyzed flows was motivated by the hypothesis that the wall pressure signature was mainly controlled by the TBL inner variables. As highlighted by the authors, it

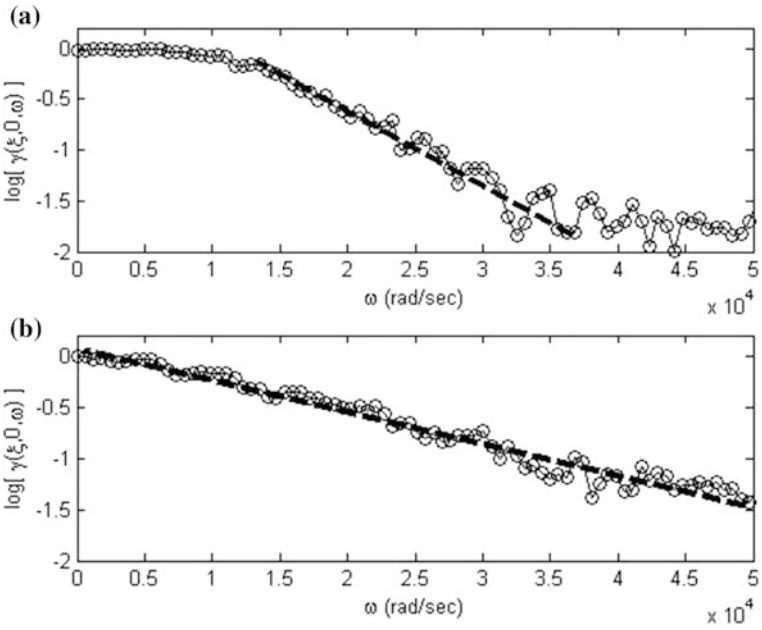

Fig. 8 Semi–log plot of the coherence function computed considering a transducer pair on the Cylinder Fairing at $M = 0.83$ (**a**) and $M = 0.98$ (**b**). The *solid dashed lines* indicates exponential approximations. Image courtesy of Aerospace Science and Technology

is worth to note that the simulation with higher Re_τ significantly extends the range of Reynolds number accessed by DNS of compressible TBLs. The reader is referred to the article for details about the DNS parameters and the assessment of the data.

Data reported in the paper include: wall pressure fluctuations intensities, frequency spectra, space–time correlations and convection velocities. The frequency domain analysis revealed that, as for low–speed TBL [9, 24], the outer layer variables (δ, u_∞) are used to collapse spectra in the low-frequency range (Fig. 9a) whereas a good collapse at high-frequency range (Fig. 9b) is achieved using inner layer variables (δ_ν, u_τ).

At low frequencies the expected ω^2 power law slope characteristic of the incompressible flow was not confirmed. A flat behavior consistent with [26] was found instead. The root mean square value of the wall pressure in the low frequency range was supposed to increase due to the relevant large–scale dynamic.

At high frequencies the contribution of acoustic pressure fluctuations influences the power law decay causing a steeper scaling with respect to the ω^{-5} scaling predicted by Blake [5].

In the overlap region the spectra did not collapse with the $\omega^{-n}\,(n \cong 0.7 - 1)$ behavior [6] except for a narrow spectral range in the higher Reynolds number case.

Another topic of interest in the study of the wall pressure fluctuations concerns with the shock wave/boundary layer interaction. This subject was investigated in [3].

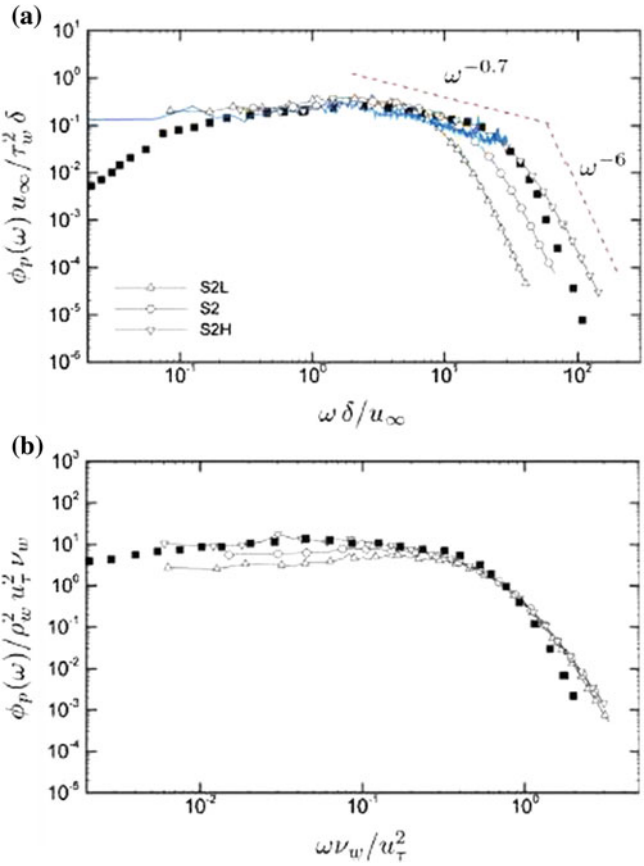

Fig. 9 Frequency spectra of wall pressure fluctuations at station S2L (*triangles*), S2 (*circles*) and S2H (*gradients*). Pressure is scaled by the wall shear stress τ_w and the reference time is δ/u_∞ in (**a**) and ν_w/u_τ^2 in (**b**). Experiments *black squares* ([24] $M_\infty \approx 0, Re_\tau = 1169$); *blue solid line* ([2], $M_\infty = 2, Re_\tau = 3650$). Image courtesy of Phisics of Fluids

The authors analyzed the DNS database [41] of a transonic interaction of moderate strength over a flat plate. The free-stream Mach number was $M_\infty = 1.3$ and the Reynolds number based on the momentum thickness of the incoming boundary layer $Re_\theta = 1{,}200$. The results reported in the article were ideally subdivided with respect to the computational domain in three regions:

1. Zero Pressure Gradient region (ZPG) upstream of the interaction
2. Supersonic Adverse Pressure Gradient region (APG)
3. Subsonic Adverse Pressure Gradient region

The main conclusions regarding the frequency analysis of the wall pressure fluctuations are summarized in the following points:

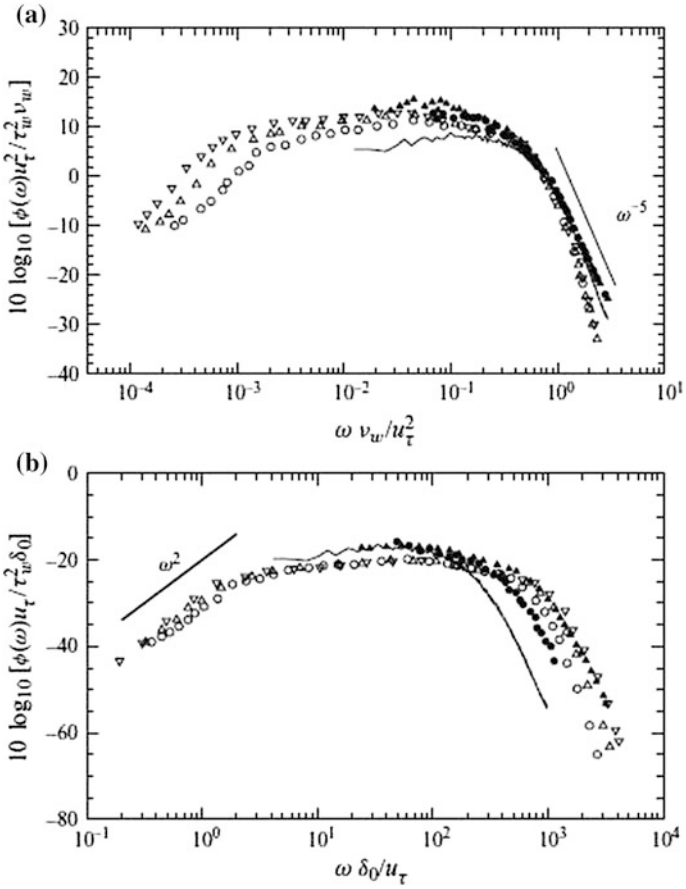

Fig. 10 Wall pressure frequency spectrum in the ZPG region at station 0 (*solid line*), compared with the data of [31] at $Re_\tau = 715$ (*solid circles*), $Re_\tau = 1195$ (*solid triangles*) and [24] at $Re_\tau = 1169$ (*solid circles*), $Re_\tau = 1535$ (*open triangles*) and $Re_\tau = 2010$ (*open gradients*). Pressure is scaled with respect to τ_w^2 and the reference time ν_w/u_τ^2 in (**a**) and δ_0/u_τ in (**b**). Image courtesy of Journal of Fluid Mechanics

- ZPG: Pressure were scaled with τ_w^2. For reference time ν_w/u_τ^2, Fig. 10a, a good collapse and a ω^{-5} decay law were observed at high frequencies. The low-frequency ω^2 and the mid-frequency ω^{-1} were absents even with the use of a mixed time scale (δ_0/u_τ), Fig. 10b.
- Supersonic APG: The reference time was δ^*/u_e, the local boundary layer displacement thickness divided by the local velocity at the edge of the boundary layer. For pressure scaling with the local external dynamic pressure (q_e) the PSD increase as the position of the computational station progress in the streamwise direction. When the pressure is scaled with the maximum value of the turbulent shear stress (τ_m) the spectra collapse.

- Subsonic APG: The reference time was again δ^*/u_e. Pressure scaling with q_e (Fig. 11a) and τ_m (Fig. 11b) gave the same 'universal' distribution confirming the self–similarity behavior already found in [41]. An extended $\omega^{-7/3}$ scaling at intermediate frequencies was found and a ω^{-5} decay law were still observed in the high frequency range.

In a recent work, Di Marco et al. [20] presented an extensive investigation of cross-spectral features of the wall pressure fluctuations induced by supersonic turbulent boundary layers at high Mach numbers. This study was based on the analysis of the DNS database provided by Bernardini and Pirozzoli [4].

The analysis was mainly targeted towards the accurate characterization of the wall pressure coherence function. The capability of existing theoretical models to predict the wall pressure coherence at high speed was investigated and discussed as

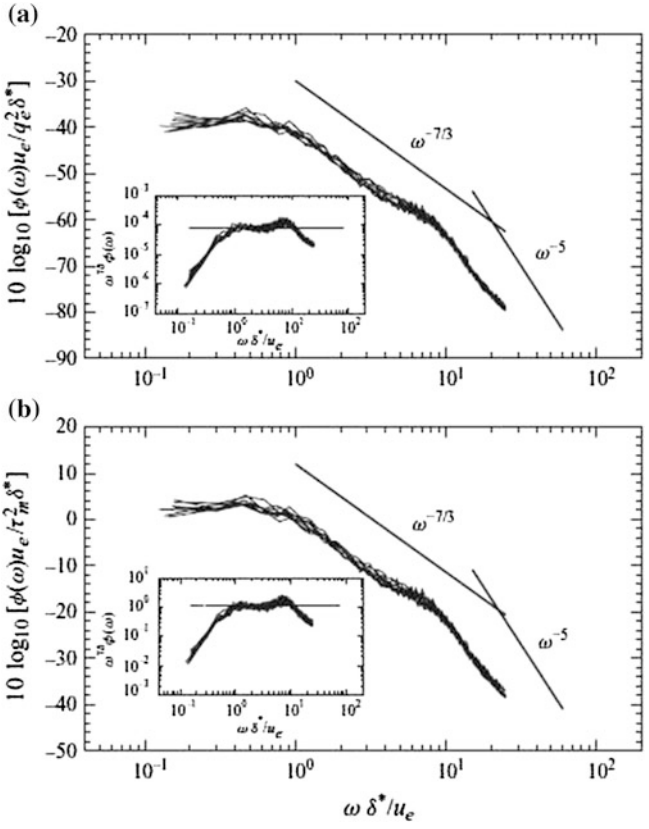

Fig. 11 Frequency spectra of the wall pressure at various stations in the subsonic APG region. Local outer scaling is used and pressure is scaled by either q_e^2 (**a**) or tau_m^2 (**b**). *Insets* in (**a**) and (**b**) show compensated spectra $\omega^{7/3}\phi(\omega)$. Data are taken at $x^* = 1.6, 2.0, 2.3, 2.5, 3.0, 3.5$ and 4.0. Image courtesy of Journal of Fluid Mechanics

well. One of the main results achieved in [20] is that wall pressure coherence functions and cross-correlations induced by supersonic TBLs behaves like those in incompressible flow conditions.

Indeed, it was observed that the Mach and Reynolds numbers does not influence significantly the cross-statistics since the coherence functions evaluated at different separations and different Mach and Reynolds numbers, collapse well when normalized with respect to the convection velocity, estimated from the cross-correlation peaks, and the boundary layer thickness.

It has been also observed that over a sufficiently wide frequency range, the Corcos' model applies well, the extension of the decay coefficients of the model being larger than those measured in incompressible flow conditions, especially for the spanwise coherence.

A more accurate prediction is provided by the Efimtsov's model that applies well but a strong dependency of the adjustable coefficients upon the Mach number, the Reynolds number and the separation distance has been observed. Examples of modelling are presented in Fig. 12. It is undoubtful that the Efimtsov model performs very well since, unlike the Corcos approximation, it is able to yield a reasonable prediction also in the low-frequency range of the coherence functions. However, in this range, the coherence function shape strongly depends on both the separation distance and the flow conditions thus implying that all of the coefficients of the model depend on the flow conditions analyzed. In conclusion, even though the Efimtsov model prediction is satisfactory, the empirical constants have to be determined case by case, this representing a limit for the applicability of the Efimtsov model in practical situations. This result suggests that even for high Mach numbers TBL, the Corcos' model remains the most suited for practical situations. Indeed, despite the development of computational capabilities, structural design

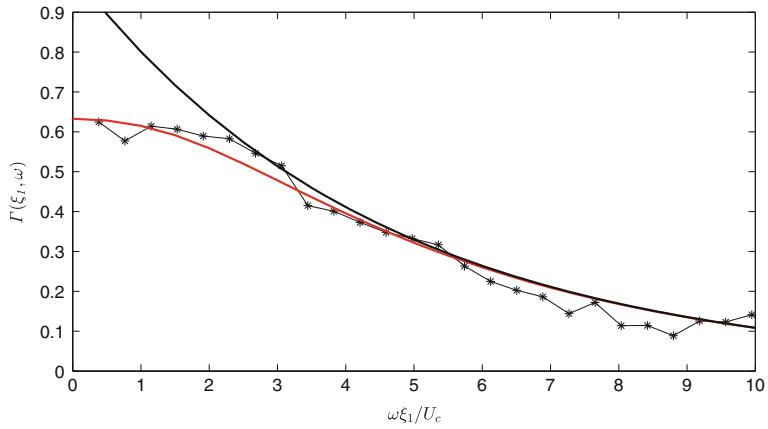

Fig. 12 Examples of Corcos' (*Black Solid Line*) and Efimtzov (*Red Solid Line*) modelling of the wall pressure coherence. The data-base is the same analyzed in [20] and for the case at the highest Mach ($M = 4$)

processes in aerospace applications will still require for simple statistical models allowing for rapid computations to be performed at an early design stage. The applicability of the Corcos' model at high Mach numbers demonstrated by Di Marco et al. [20] therefore represents a relevant contribution in this sense.

5 Concluding Remarks

A brief overview of recent studies made in the field of wall pressure fluctuations generated by supersonic turbulent boundary layer has been presented with particular attention on the actual progression and limitations of experimental techniques and numerical simulations.

The scaling parameters of the frequency spectra have been discussed in connection with the properties of the near wall and the outer layer regions of the turbulent boundary layer. The main properties of the wavenumber-frequency spectra have been also reviewed and discussed along with the main statistical models proposed in literature to predict the auto and cross-spectra trends needed to predict the vibro-acoustic behavior of a fluctuating pressure loaded surface.

The methods and difficulties of making fluctuating wall pressure measurements have been outlined, and some of the results for simple and complex geometries have been presented with particular details about the spectra scaling laws. The main conclusions were that the sensor frequency response is the dominant issue especially for aeroacoustic applications. The refinements and upgrade in experimental techniques will remove existing uncertainties.

Experiments conducted in high speed wind tunnels on a complex geometry have been also briefly reviewed. Pressure fluctuations have been measured at the wall of a scaled model of an aerospace launch vehicle in transonic and supersonic conditions. The wall pressure spectra along the launcher reflected the variable flow physics achieved at the different Mach numbers throughout a variation of the energy distribution in the frequency domain. Indeed, both the position along the launcher and the Mach numbers, have been shown to have relevant influence not only on the overall intensity of the auto and cross-spectra but also on their shape. An exponential decay of the pressure coherence was in any case documented even though it was observed that the decay rate depended strongly on the flow conditions. This outcomes confirmed the impossibility to set up a general spectral model for such complex configurations.

Recent numerical simulations of the wall pressure field beneath supersonic zero-pressure-gradient adiabatic turbulent boundary layer on a flat plate have been reviewed. More practical aspects have been treated by considering the complex behavior arising by the interaction of the boundary layer with shockwaves and the prediction possibilities based on the existing theoretical models. Huge computational resources will allow an extension of the flow conditions and spectral range recently analyzed.

In conclusions, after more than 60 years of research on wall pressure statistics, many answers have been given but there are still many unsolved problems mainly regarding the spectral modelling in realistic situations or the implementation of control system for the pressure fluctuations manipulation. These tasks remain a challenge for future implementations, interpretations and understandings.

References

1. B.M. Abraham, Direct measurements of the turbulent boundary layer wall pressure wavenumber-frequency spectra. J. Fluids Eng. **120**, 29–39 (1998)
2. S.J. Beresh, J.F. Henfling, R.W. Spillers, B.O.M. Pruett, Fluctuating wall pressures measured beneath a supersonic turbulent boundary layer. Phys. Fluids **23**, (2011)
3. M. Bernardini, S. Pirozzoli, F. Grasso, The wall pressure signature of transonic shock/boundary layer interaction. J. Fluid Mech. **671**, 288–312 (2011)
4. M. Bernardini, S. Pirozzoli, Wall pressure fluctuations beneath supersonic turbulent boundary layers. Phys Fluids **23**, (2011)
5. W.K. Blake, Mechanics of flow induced sound and vibrations. Appl. Math. And Mech., Acad. Press Inc., Orlando (1986)
6. P. Bradshaw, 'Inactive' motion and pressure fluctuations in turbulent boundary layers. J. Fluid Mech. **30**, 241–258 (1967)
7. M.K. Bull, Wall pressure fluctuations associated with subsonic turbulent boundary layer flow. J. Fluid Mech. **28**, 719–754 (1967)
8. M.K. Bull On the form of the wall-pressure spectrum in a turbulent boundary layer in relation to noise generation by boundary layer-surface interactions, in *Mechanics of Sound Generation Flows*, *IUTAM Conference* (Springer, Berlin, 1979), pp. 210–216
9. M.K. Bull, Wall-pressure fluctuations beneath turbulent boundary layers: some reflections of forty years of research. J. Sound Vib. **190**(3), 299–315 (1996)
10. R. Camussi, G. Guj, B. Imperatore, A. Pizzicaroli, D. Perigo, Wall pressure fluctuations induced by transonic boundary layers on a launcher model. Aerosp. Sci. Technol. **11**, 349–359 (2007)
11. D. Chase, Modelling the wavevector-frequency spectrum of turbulent boundary layer wall pressure. J. Sound Vib. **70**, 29–67 (1980)
12. D.M. Chase, The character of the turbulent wall pressure spectrum at subconvective wavenumbers and a suggested comprehensive model. J. Sound Vib. **112**, 125–147 (1987)
13. D.M. Chase, Fluctuations in wall-shear stress and pressure at low streamwise wavenumbers in turbulent boundary-layer flow. J. Fluid Mech. **225**, 545–556 (1991)
14. H. Choi, P. Moin, On the space-time characteristics of wall pressure fluctuations. Phys. Fluids A **2**, 1450–1460 (1990)
15. E. Ciappi, F. Mangionesi, S. De Rosa, F. Franco, Hydrodynamic and hydroelastic analyses of a plate excited by the turbulent boundary layer. J. Fluids Struct. **258**, 321–342 (2009)
16. J.A. Cockburn, J.E. Robertson, Vibration response of spacecraft shrouds to in-flight fluctuating pressures. J. Sound Vib. **33**, 399–425 (1974)
17. G.M. Corcos, Resolution of pressure in turbulence. J. Acoust. Soc. Am. **35**(2), 192 (1963)
18. G.M. Corcos, The structure of the turbulent pressure field in boundary-layer flows. J. Fluid Mech. **18**(3), 353–378 (1964)
19. G. Cousin, Sound from TBL induced vibrations. Ph.D. thesis, KTH Marcus Wallenberg Laboratory for Sound and Vibration Research, Stockholm, 1999
20. A. Di Marco, R. Camussi, M. Bernardini, S. Pirozzoli, Wall pressure coherence in supersonic turbulent boundary layers. J. Fluid Mech. **732**, 445–456 (2013)

21. D.S. Dolling, J.P. Dussauge (1989) Fluctuating wall pressure measurements, in *AGARD-AG-315: A Survey of Measurements and Measuring Techniques in Rapidly Distorted Compressible Turbulent Boundary Layers,* pp. 8-1–8-18
22. B.M. Efimtsov, Characteristics of the field of turbulent wall pressure fluctuations at large Reynolds numbers. Sov. Phys. Acoust. **28**, 289–292 (1982)
23. B.M. Efimtsov, Vibrations of a cylindrical panel in a field of turbulent pressure fluctuations. Sov. Phys. Acoust. **32**(4), 336–337 (1986)
24. T.M. Farabee, M.J. Casarella, Spectral features of wall pressure fluctuations beneath turbulent boundary layers. Phys. Fluids A **3**(10), 2410–2420 (1991)
25. T.M. Farabee, F.E. Geib Measurements of boundary layer pressure fluctuations at low wavenumbers on smooth and rough walls, in *ASME Symposium on Flow Noise Modelling, Measurement and Control,* NCA vol. 11, FED-vol. 130, pp. 55–68
26. J.E. Ffowcs Williams, Surface pressure fluctuations induced by boundary layer flow at finite Mach number. J. Fluid Mech. **22**, 507 (1965)
27. J.E. Ffowcs Williams, Boundary-layer pressures and the Corcos model: a development to incorporate low wavenumber constraints. J. Fluid Mech. **125**, 9–25 (1982)
28. S. Finnveden, F. Birgersson, U. Ross, T. Kremer, A model of wall pressure correlation for prediction of turbulence-induced vibration. J. Fluids Struct. **20**, 1127–1143 (2005)
29. M.C. Goody, R.L. Simpson, M. Engel, C.J. Chesnakas, W.J. Devenport (1998) Mean velocity and pressure and velocity spectral measurements within a separated flow around a prolate spheroid at incidence. AIAA paper, 98-0630 (1998)
30. W.R. Graham, A comparison of models for the wavenumber-frequency spectrum of turbolent boundary layer pressures. J. Sound Vib. **206**(4), 541–565 (1997)
31. S.P. Gravante, A.M. Naguib, C.E. Wark, H.M. Nagib, Characterization of the pressure fluctuations under a fully developed turbulent boundary layer. AIAA J 36, 1808–1816 (1998)
32. Y.F. Hwang, G. Maidanik, A wavenumber analysis of the coupling of a structural mode and flow turbulence. J. Sound Vib. **142**, 135–152 (1990)
33. W.L. Keith, D.A. Hurdis, B.M. Abraham, A comparison of turbulent boundary layer wall-pressure spectra. J. Fluids Eng. **114**, 338–347 (1992)
34. R.H. Kraichnan, Pressure fluctuations in turbulent flow over a flat plate. J. Acoust. Soc. Am. **28**, 278–390 (1956)
35. B.H.K. Lee, Self–sustained shock oscillations on airfoils at transonic speed. Prog. Aero. Sci. **37**, 147–196 (2001)
36. G.M. Lilley, T.H. Hodgson, *On Surface Pressure Fluctuations in Turbulent Boundary layers* (AGARD, Report No, 1960). 276
37. E. Manoha, The wavenumber-frequency spectrum of the wall pressure fluctuations beneath a turbulent boundary layer, in *Proceedings of AIAA/CEAS Aeroacoustics Conference*, 6–8 May , State College, PA, AIAA paper, pp. 96–1758
38. A.M. Naguib, S.P. Gravante, C.E. Wark, Extraction of turbulent wall-pressure time-series using an optimal filtering scheme. Exp. Fluids **22**(1), 14–22 (1996)
39. R.L. Panton, G. Robert, The wavenumber-phase velocity representation for the turbulent wall-pressure spectrum. J. Fluid. Eng. **116**, 447 (1994)
40. O.M. Phillips, On the aerodynamic surface sound from a plane turbulent boundary layer. Proc. R. Soc. Lon., Series A. **234**, 327–335 (1956)
41. S. Pirozzoli, M. Bernardini, F. Grasso, Direct numerical simulation of transonic shock/boundary layer interaction under conditions of incipient separation. J. Fluid Mech. **657**, 361–393 (2010)
42. B.A. Singer Turbulent wall-pressure fluctuations: new model for off-axis cross-spectral density. NASA Contractor Report 198297 (1996)
43. B.A. Singer Large-eddy simulation of turbulent wall-pressure fluctuations. NASA Contractor Report 198276 (1996)
44. A.V. Smol'yakov, V.M. Tkachenko, Model of a field of pseudosonic turbulent wall pressures and experimental data. Sov. Phys. Acoust. **37**(6), 627–631 (1991)

45. S. Tavoularis, *Measurements in Fluid Mechanics* (Cambridge University Press, New York, 2005)
46. W.W. Willmarth, Pressure fluctuations beneath turbulent boundary layers. Annu. Rev. Fluid Mech. **7**, 13–38 (1975)
47. S.F. Wu, L. Maestrello, Responses of finite baffled plate to turbulent flow excitations. AIAA. J. **33**, 13–19 (1995)

Turbulent Surface Pressure Field in Low Speed Flow

Stéphane Caro, Vincent Cotoni, Phil Shorter and Fred Mendonça

Abstract The external air low speed flow over a flat plate passed a half cylinder shape is computed using an unsteady CFD technique; the turbulent surface pressure field is analyzed in details; a frequency-wavenumber decomposition is used to identify the convective and acoustic energy concentration. A comparison is then made with results obtained using several standard semi-analytical models of turbulent surface pressure. Finally the wall pressure fluctuations are used as a load on an elastic plate in a vibroacoustic analysis and the transmitted noise inside a trimmed acoustic cavity is computed. Some conclusions are drawn on the pertinence of using a semi-analytical model or unsteady LES-type CFD computations to describe the wall pressure loading for a vibroacoustic analysis.

1 Introduction

The noise induced by wall-pressure fluctuations is of increasing interest for the manufacturers of various types of vehicles (cars, trains, airplanes for comfort reasons, but also space vehicles for fatigue reasons). There is a need for efficient and accurate numerical methods to complement the test facilities, build better prototypes in shorter times and reduce the time-to-product.

A numerical model of interior wind noise requires three ingredients. First, a representation of the interior acoustic cavity together with the noise control treatments, leaks, etc. that impact the cavity dynamics. Second, a model of the transmission path which typically corresponds to a number of elastic structures radiating inside when excited by the exterior wall pressure fluctuation. Third, an outside wall pressure field must be applied as an excitation to the structures. This paper focuses on this last aspect. The study is conducted on a generic car cavity, with an idealized

S. Caro (✉) · V. Cotoni · P. Shorter · F. Mendonça
CD-adapco, Lyon Office, Lyon, France
e-mail: stephane.caro@cd-adapco.com

E. Ciappi et al. (eds.), *Flinovia - Flow Induced Noise and Vibration Issues and Aspects*, DOI 10.1007/978-3-319-09713-8_5

glass window and a pressure excitation induced by the flow downstream of a generic side mirror.

Several previous theoretical, predictive and experimental studies have been devoted to this subject. Chase [1] postulated that for low Mach numbers, flow excitations comprise widely disparate energy levels between the turbulent fluctuations and acoustical pressures. Whereas the acoustical energies are orders of magnitude lower, it is the acoustical wave-numbers rather than the turbulence wave numbers that matches more closely to the structural wave-numbers. These are therefore an potentially significant contributor to noise transmission for car problems, especially around the side-glass coincidence frequency of approximately 3 kHz. This existing expertise serves as a starting point of the present investigations.

This paper is split in three parts. First, a simplified but realistic car side mirror problem is presented. In a second part, the characteristics of the surface pressure field are obtained using two methods: a semi-analytical model and a CFD computation. Finally in a third part this excitation is used in a vibroacoustic computation, and recommendations are given for further work.

2 Description of the ISM

2.1 Idealized Side Mirror

The idealized side mirror (ISM) was first introduced by Siegert et al. [2]. The sketch of the setup is reproduced on Fig. 1. The ISM is made of a half cylinder and a quarter of sphere put on a flat plate, with an upstream homogeneous flow field. The setup dimensions and flow characteristics are as close as possible to a true car side mirror.

Several teams have handled this test case in the past few years, mainly for CFD validation and sometimes for acoustic validation purposes. Amongst the different publications, we can mention Smith et al. [3], who have reproduced the

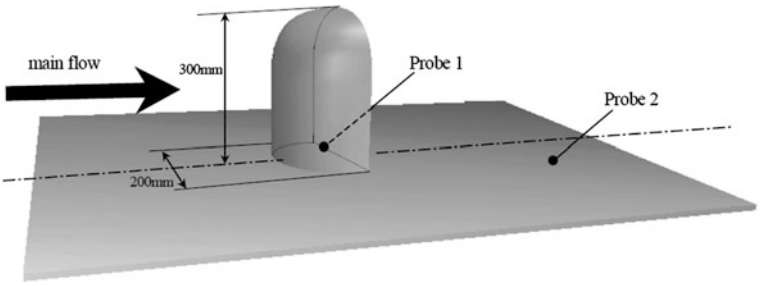

Fig. 1 Idealized side mirror, made of a *half cylinder* and a *quarter of sphere* put on a flat plate

experimental setup in order to get more data that were difficult to acquire in 1999. In [4], a more realistic variant of this setup is handled.

2.2 Flow Characteristics

In [5], the far field noise outside the mirror was computed using a hybrid technique based on a Ffowcs-Williams and Hawkings analogy. The flow characteristics presented hereafter are taken from this document. The CFD computation is consistent with the one of this reference. The parameters of the turbulent boundary layer pressure models are taken from flow characteristics of this CFD result.

3 Flow Characteristics of the Excitation

3.1 Unsteady CFD Analysis

The STAR-CCM+ software package [4], was used for this analysis. The code is validated for large eddy simulation (LES) applications in aeroacoustics across a wide range of industry sectors [5, 6], including the particular case of the generic mirror. The CFD methodology detailed presentation can be found e.g. in [5]. The most important aspects are listed below.

The solver used is a Detached Eddy Simulation (DES), k-ω SST full compressible solver. The flow is solved at the physical Mach and Reynolds numbers. An efficient implicit transient solver is used. The discretization is second order in space and time. The walls are modeled using y+ insensitive boundary conditions (a full boundary layer resolution is possible but not necessary here). A specific Non-Reflecting Boundary Condition is used at the outer domain, which is essential for acoustic computations.

The post-processing is done using STAR-CCM+ tools [4], including Fourier analysis, auto and cross spectra computations, wavenumber analysis, and farfield Ffowcs-Williams Hawkings (FWH) post-processing. All these ingredients have been used here, to increase confidence in the quality of the flow solution obtained, although for the sake of simplicity, only a few of these outputs will be presented here.

The CFD computation gives access simultaneously to the steady part of the flow, the turbulent vortices, and the acoustics (transient compressible simulation). It is possible to visualize the flow patterns at any instant in time, as shown on Fig. 2. The turbulent eddies shed downstream of the mirror have a short characteristic wavelength and are localized only in the wake of the mirror; in contrary, the acoustic waves, which propagate in all directions including upstream (clearly visible on the vertical cut plane), have a larger wavelength and propagate to a larger distance.

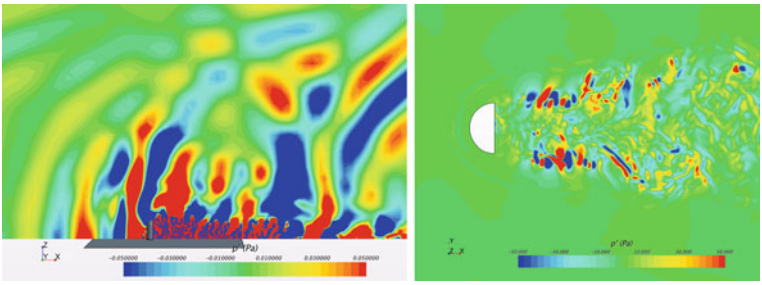

Fig. 2 Instantaneous distribution of the pressure fluctuation at a given time and on a streamwise vertical cut plane (*left*) and on a horizontal cut plane (*right*)

3.2 Wave Number Decomposition

Only a small part of these fluctuations correspond to acoustics. In order to understand what part of the excitation corresponds to acoustics, a specific filtering technique is used.

Figure 3 illustrates how the separate contributions from convecting turbulence and propagating acoustics may be distinguished by means of wave-number analysis. The pressure spectral density variation with frequency may be separated at each frequency into high wave-number convecting turbulence and low wave-number propagating acoustics. This tool is essential to understand the physics of the flow.

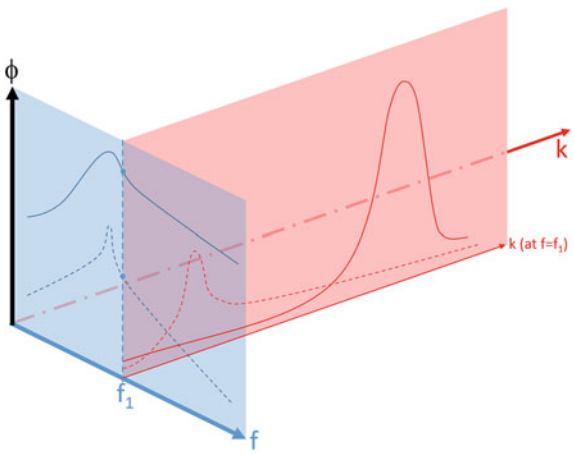

Fig. 3 Wavenumber-frequency (*k–f*) diagram for surface pressure spectrum of a sub-sonic flow. The *blue plane* ($k = 0$) corresponds to the spectrum at wavenumber equals to zero; the classical representations of things look like such spectra, with no distinction between the different wavelengths. In order to highlight the difference between the acoustic (*dotted*) and turbulent (*line*) parts of the information, a possibility is to represent the different wavenumbers k for each frequency, as done on the *red plane* (taken at a certain frequency f_1)

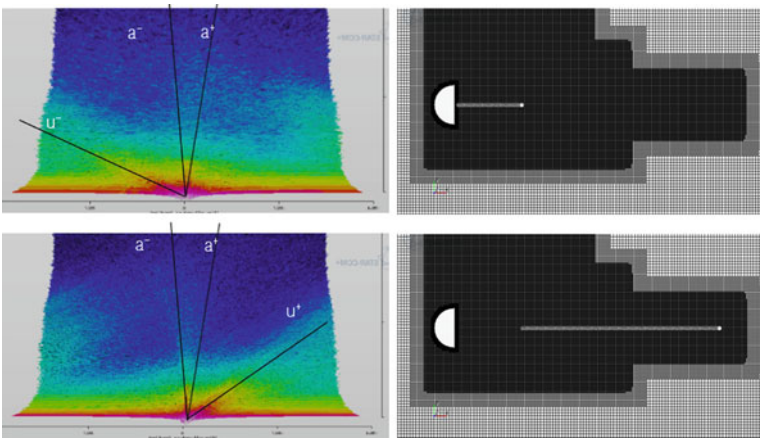

Fig. 4 1D wave number decomposition (*left*) for two different lines (*right*) produced from a CFD result

Such a wavenumber decomposition can be made on various lines on the flat plate (for example). The Fig. 4 shows the wavenumber content of the pressure field along a line as a function of frequency. It highlights that the choice of the line over which the WND is performed has a great influence on the observed wavenumbers. On the left pictures the main directions of the waves are 'recognized': the acoustic forward (+a) and backward (−a) waves are highlighted, as well as the forward (+u) or backward (−u) convected waves.

The same type of wavenumber decomposition can be done on a surface instead of along a line. Examples of resulting wavenumber decompositions at a given frequency are shown on Fig. 5. Again the choice of the control surface on which the decomposition is done has an influence on the result; on the example shown on Fig. 5, the inclination of the convective spot is because the control surface is not centered downstream the mirror.

3.3 Excitation from Turbulent Boundary Layer Pressure Models

A number of models of turbulent boundary layer wall pressure exist [7]. Analyzed in the spectral domain, the models have similar wavenumber content in the convective turbulent region but very different low wavenumber tails. In this section, the spectral content of various models are compared with that of the pressure field simulated by the compressible CFD solution presented above.

Several authors have proposed various semi-analytical models to describe wall pressure fluctuations experienced by a flat structure with a grazing flow. In this section, a few standard models are used: The Corcos model as described in [8], the Mellen model as described in [9], and the Chase model as described in [10].

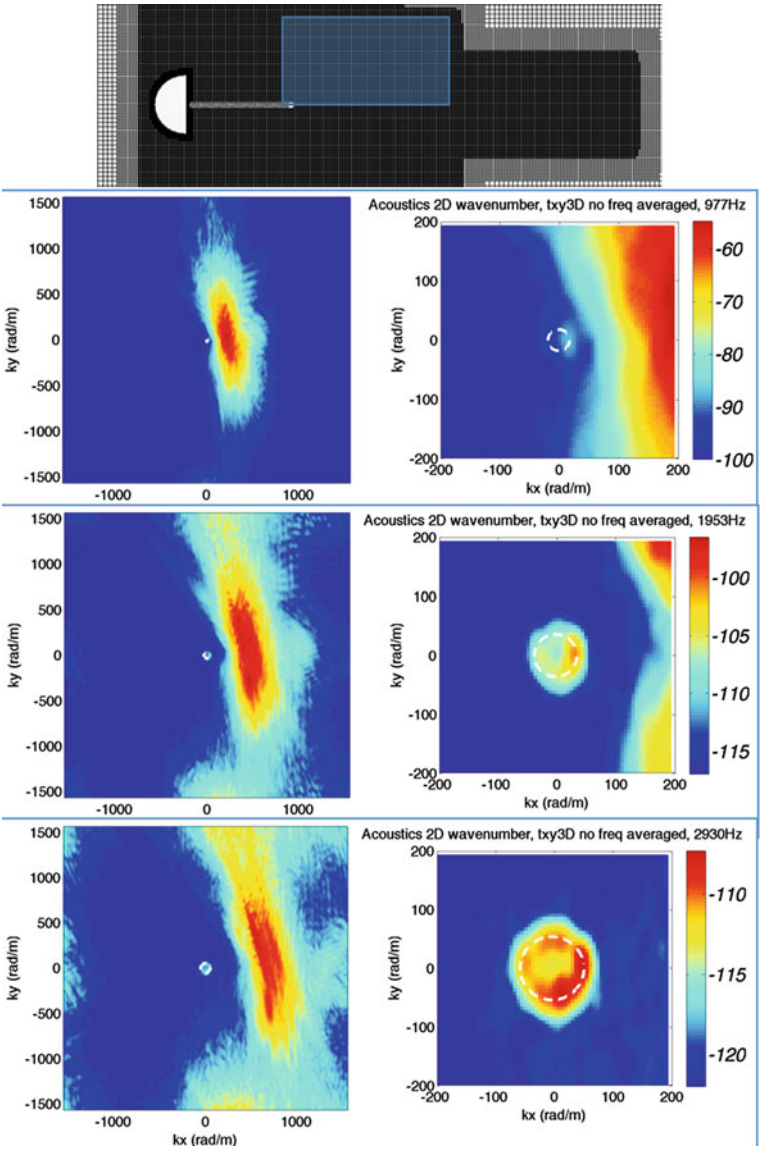

Fig. 5 2D WND result on the spatial window shown on the *top*, for three different frequencies. *Left* convective wavenumbers; *right* zoom on the acoustic wavenumbers

The 1D and 2D wavenumber spectra of these models have been compared with the CFD results. Some examples of the results obtained are shown on Figs. 6 and 7.

The results show lots of similarities, but one important difference is noticeable for the low wavenumbers: none of the models tried shows a correct behavior around the acoustic wavenumbers. This means that the models predict correctly the vortical

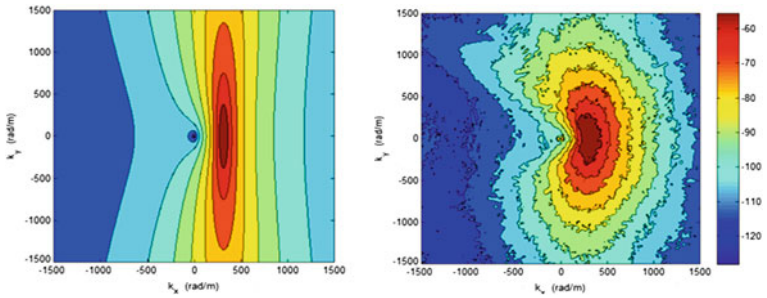

Fig. 6 2D wavenumber decomposition obtained using the Chase model (*left*) and using the CFD result (*right*) at 1,400 Hz

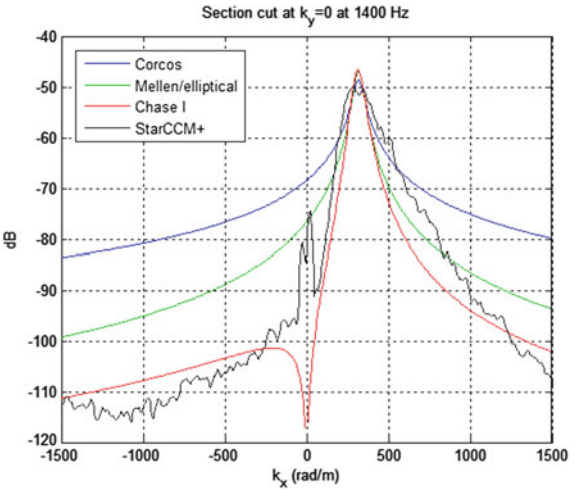

Fig. 7 Axial wavenumber decomposition at 1,400 Hz for $k_y = 0$ obtained using the different models and compared with the CFD result

part of the wall-pressure fluctuations, but not their acoustic part. This observation is consistent with other authors' who have already underlined that these analytical models do not account for the acoustic content in the flow. As demonstrated later, the acoustic content can dominate the vibroacoustic transmission, making the choice of an analytical model a moot point.

Away from the acoustic wavenumbers the Chase model is in reasonable agreement with the CFD model. The other models do not match the observed wavenumber variation. In the remainder of this document, it is considered that the Chase model is the best alternative to the CFD, and the comparisons have been made only with this model.

As a complement to analytical models, CFD therefore provides a way to model the wall-pressure fluctuations in complicated flows where models hardly apply. For example, the near field pressure field around complex geometric details of a vehicle is typically non-uniform, with detached boundary layer. Additionally, CFD

provides a way to model the acoustic component of the pressure field. In the next section, the effects of these differences inside the vehicle are assessed.

4 Vibroacoustics

4.1 Modeling Methods

In the side mirror–side window problem described above, the wall pressure fluctuations experienced by the structure are transmitted inside of the cavity. In this part of the paper, the sensitivity of the sound power transmission (through a simplified window) to the wavenumber components of the pressure field is analyzed. To this aim, the wall pressure fluctuations obtained in the previous section (using either a CFD computation or a semi-analytical model like Chase) are used as loads in a vibroacoustic model.

In a real car application, the sideglass is a curved structure with complex seal damping around the edge; for the frequencies of interest below 4,000 Hz, it has less than 200 structural modes: a Finite Element model of the sideglass is therefore appropriate. On the other hand, the cavity has a complex shape, a very complex sound package distribution (sometimes not perfectly known), and more than a million modes in the same frequency range: a statistical approach is adequate.

The results presented in the next section are obtained using a hybrid FE-SEA model, as would need to be done for a real car. In a first step, the direct field is computed using an FE model of the window excited by the fluctuating pressure coming from the CFD computation (or from the analytical model). In a second step, the reverberant response to this input power is computed to access the total noise in the cavity.

4.2 ISM Results

The Fig. 8 shows the interior sound pressure level at the driver's ear obtained using the STAR-CCM+ input or the Chase analytical model input.

The low frequency results (below 1,000 Hz) show a good agreement, which suggests that at these frequencies the transmission is dominated by the convective component (non-acoustic). At higher frequencies however, the difference increases; near coincidence (2,400 Hz) the acoustic Transmission Loss of the plate is small, and the acoustics contained in the CFD data makes a 10 dB difference.

On this semi-academic test case, the Chase model is applicable for certain locations for convective load. Above 1 kHz however, the Chase model cannot anymore describe the main component that governs interior noise for this application, because the acoustic pressure component is absent from this model. It is

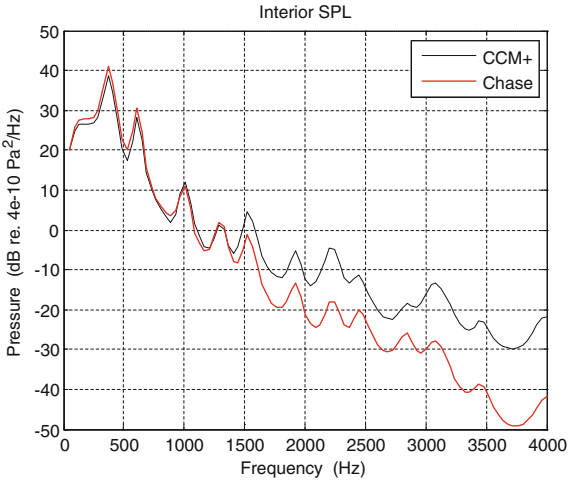

Fig. 8 Interior SPL obtained using either the CFD input or the Chase analytical model input

confirmed that the low wavenumber content, including the acoustic range, can be the dominant contributor to interior noise [11].

On a real car design, the flow will be far more complex with presence of the A-pillar vortex or the rain-gutter sheared flow, to name a few. It is very likely that the difference will be much bigger: the CFD is required for accurately predicting the acoustic and convective components of the exterior surface pressure.

5 Conclusions

In this study, a simplified, Idealized Side Mirror test case has been considered to try understand some of the physical phenomena in flow induced noise and vibration. The unsteady CFD analysis results show a great flow complexity despite the simple shape.

The wavenumber content of the wall pressure compares fairly well with some analytical models, but not perfectly. In particular, the acoustic loads are absent from the analytical models (which model reasonably well the convective wavenumber region). The importance of this difference is not perfectly clear from the sole flow analysis however, as the convective part of the flow contains far more energy than the acoustic.

A vibroacoustic model was then used to compute the noise inside the simplified vehicle and induced by the wall pressure fluctuations computed earlier. The results obtained confirm some limitations of the analytical models even on this simplified problem; the differences have been explained. The analytical models remain complementary to CFD tools, but are now proved to be less appropriate for industrial applications and noise issues, even for academic problems as the one handled in this work.

References

1. D.M. Chase, Modeling the wavevector-frequency spectrum of turbulent boundary layer wall pressure. J. Sound Vib. **70**(l), 29–67 (1980)
2. R. Siegert, V. Schwarz, J. Reichenberger, in *Numerical Simulation of Aeroacoustic Sound Generated by Generic Bodies Placed on a Plate, Part II—Prediction of Radiated Sound Pressure*. Presented at the AIAA Aeroacoustics Conference, AIAA-99-1895, Bellevue, Washington, May 1999
3. M. Smith, E.L. Iglesias, P.G. Bremner, F. Mendonça, in *Validation Tests for Flow Induced Excitation and Noise Radiation from a Car Window*. AIAA 2012–2201 (2012)
4. M. Hartmann, J. Ocker, T. Lemke, V. Schwarz, H. Tokuno, R. Toppinga, P. Unterlechner, G. Wickern in *Wind Noise caused by the A-pillar and the Side Mirror flow of a Generic Vehicle Model*. AIAA 2012–2205
5. M. Caraeni, O. Aybay, S. Holst, in *Tandem Cylinder and Idealized Side Mirror Far-Field Noise Predictions Using DES and an Efficient Implementation of FW-H Equation*. 17th AIAA/CEAS Aeroacoustics Conference, AIAA-2011–2843, Portland, June 2011
6. F. Mendonça, A. Read, F. Imada, V. Girardi, *Efficient CFD Simulation Process for Aeroacoustic Driven Design*. Brazil Noise and Vibration Congress II, SAE-2010-36-0545, Florianopolis, Dec 2010
7. W.R. Graham, A comparison of models for the wavenumber–frequency spectrum of turbulent boundary layer pressures. J. Sound Vib. **206**(4), 541–565 (1997)
8. G.M. Corcos, Resolution of pressure in turbulence. J. Acous. Soc. Am. **35**(2), 192–199 (1963)
9. R.H. Mellen, Wave-vector filter analysis of turbulent flow. J. Acoust. Soc. Am. **95**, 1671 (1994)
10. D.M. Chase, Modeling the wavevector-frequency spectrum of turbulent boundary layer wall pressure. J. Sound Vib. **70**(1), 29–67 (1980)
11. S.A. Hambric, Y.F. Hwang, W.K. Bonness, Vibrations of plates with clamped and free edges excited by low-speed turbulent boundary layer flow. J. Fluids Struct. **19**, 93–110 (2004)

Characterization of Synthetic Jet Resonant Cavities

Luigi de Luca, Michele Girfoglio, Matteo Chiatto and Gennaro Coppola

Abstract The acoustic properties of piezo-electric driven resonant cavities usually employed to generate the so-called synthetic jets are analytically and numerically investigated in order to characterize the performances of such devices. It is shown that the actuator behaves as a two-coupled oscillators system and the dimensionless form of the governing equations allows one to identify various particular operating conditions. The theoretical predictions are validated through experimental tests carried out on devices having different mechanical and geometrical characteristics, designed in order to achieve an increasing coupling strength. Practical design implementations are discussed as well.

1 Introduction

The literature concerned with the synthetic jet actuators is huge and includes a wide field of applications such as flow control (perhaps the original one), heat transfer from small size surfaces, overall enhancement of mixing between fluid currents, generation of micro-thrust for propulsion or attitude control of Micro Aerial Vehicle (MAV). We limit to cite here the review papers of Glezer and Amitay [1] and Cattafesta and Sheplak [2]. Regarding present authors, previous contributions dealt with the direct numerical simulation of jet vectoring, as described by Mongibello et al. [3], a design procedure of synthetic jet actuator to be employed as heat transfer device, as reported by Monaco et al. [4], and the formulation and the experimental validation of a lumped element physical model of the operation of the actuator devoted to the prediction of its frequency response, by de Luca et al. [5].

L. de Luca (✉) · M. Girfoglio · G. Coppola
Department of Industrial Engineering, Aerospace Section, Universita' degli Studi di Napoli, P.le Tecchio 80, 80125 Naples, Italy
e-mail: luigi.deluca@unina.it

M. Chiatto
Von Karman Institute, 1640 Rhode-St-Genese, Belgium

E. Ciappi et al. (eds.), *Flinovia - Flow Induced Noise and Vibration Issues and Aspects*, DOI 10.1007/978-3-319-09713-8_6

The overall design of the actuator needs practical modeling tools, which are generally based on reduced order, lumped element physical models. A significant lumped element model of a piezoelectric-driven synthetic jet device is described by Prasad [6] and Prasad et al. [7], who gave detailed relationships for the transverse deflection of the inner and outer regions of the composite membrane in the simultaneous presence of applied voltage and pressure load. They resorted to the approach based on the equivalent electric circuit. Following the same approach, Gallas et al. [8] noted that in a lumped model one may use the acoustic compliance of the shim only reduced by a proper factor depending on the ratio of the radius, thickness and Young's modulus of the piezoceramic and shim materials. Later on, Sharma [9] proposed a different model directly based on the equations of fluid dynamics, where the oscillating membrane is considered as a single-degree-of-freedom mechanical system, while the cavity and the orifice are described by means of proper forms of the continuity and Bernoulli's unsteady equations, respectively. Sharma [9] validated his model on the very same experimental data of Gallas et al. [8].

Chaudhari et al. [10] carried out systematic measurements about the effects of the excitation frequency on the ejection and suction velocities, by varying the geometrical parameters of the cavity. Krishnan and Mohseni [11] studied the characteristics of the flow field produced by a round synthetic jet by using detailed numerical simulations of the turbulent Navier-Stokes equations. Seeley et al. [12] described a simplified fluid-structure interaction model based on the implementation of commercial Finite Elements codes, and proved its validity at relatively low frequency, namely well below the Helmholtz frequency. Persoons [13] proposed a low-order model of prediction of the frequency response of synthetic jet actuators driven by electromagnetic or piezoelectric supply. Based on the equivalent circuit approach, its model yields analytical expressions for the two resonance frequencies, as a function of the structural and Helmholtz resonance frequencies.

Recently de Luca et al. [5] presented a fluidic type lumped element modeling, that has been inspired by the Sharma's work [9], yielding the frequency response of the resonant cavity in terms of pressure disturbances, membrane displacement and external jet velocity. The model, validated against systematic experimental measurements, gave also simple but accurate analytical relationships for the two resonance frequencies characterizing the overall system response. The present contribution is a follow-up inspection of the previous investigation and is devoted to gain new insights on the fluid-structure interaction occurring during the operation of a typical piezoelectric-driven resonant cavity. The analysis hereafter presented is based on the dimensionless form of the equations governing the behavior of the two-coupled oscillators, the membrane and the Helmholtz one.

2 Model Formulation

The model described hereafter is essentially the same as the one presented by de Luca et al. [5], in turn inspired by the Sharma's work [9]. It refers to the three basic elements of the actuator: the oscillating membrane (diaphragm or wall, constituted

by a thin round metal shim on which a smaller diameter piezoceramic disk is bonded), the cavity, the orifice.

For the sake of convenience, the three differential equations which describe the dynamics of the actuator are summarized below

$$\ddot{x}_w + 2\zeta_w \omega_w \dot{x}_w + \omega_w^2 x_w = \omega_w^2 \Delta x_w \sin \omega t - \frac{p_i A_w}{m_{wt}} \tag{1}$$

$$\frac{V_c}{\gamma p_o} \frac{\mathrm{d}p_i}{\mathrm{d}t} - A_w \dot{x}_w = -A_o U \tag{2}$$

$$\ddot{U} + \frac{K}{l_e} |U| \dot{U} + \omega_h^2 U = \frac{A_w}{A_o} \omega_h^2 \dot{x}_w \tag{3}$$

The dynamics of the membrane is described through the motion equation of a one-degree of freedom forced-damped spring-mass system, Eq. (1), where x_w is the (average) membrane displacement, t is time, p_i is the cavity (internal) differential pressure, m_{wt} is the diaphragm total mass, including shim, piezo-element and air added mass, ω_w is the natural frequency of membrane, ω is the operating frequency, Δx_w is the average linear membrane displacement due to the application of a certain voltage to the piezo-element, A_w is the membrane surface area, ζ_w is the diaphragm damping ratio, dot denotes time derivative; the second equation of the model is the conservation of mass in the cavity under the assumption of zero-dimensional (lumped) system, Eq. (2). By relating the density and pressure variations by means of an isentropic compression/expansion transformation, the continuity equation can be formulated as above written, where V_c is the cavity volume, p_o is the ambient pressure, γ is the specific heat ratio, U is the instantaneous orifice jet-flow velocity, A_o is the orifice area; the application of the unsteady Bernoulli's equation between a point inside the cavity where the flow velocity is practically null and a point, just outside the cavity, representing the location where the pressure matches the unperturbed external ambient value, yields the third equation of the model, Eq. (3), where ω_h is the natural Helmholtz frequency, K is the head loss coefficient.

In particular, the (first mode) structural circular frequency of the membrane is given by

$$\omega_w = \sqrt{\frac{k_w}{m_{wt}}} \tag{4}$$

and represents the uncoupled natural frequency of the membrane oscillator, where k_w is the equivalent spring stiffness of the membrane. This last can be obtained as

$$k_w = m_w (2\pi \widetilde{f}_w)^2 \tag{5}$$

where $\widetilde{f}_w$ is the frequency of the principal mode of vibration of a rigidly clamped disk. Although the presence of the piezoceramic element bonded to the metal shim

enhances the flexural rigidity of the membrane (and in principle the very thin layer of glue should be taken into account as well), for standard operating conditions $\widetilde{f}_w$ can be referred to the first fundamental mode of the shim only (that is the membrane structural element actually clamped) and calculated by using the standard formula reported in many textbooks (de Luca et al. [5]). Here m_w is the diaphragm mass taking into account both shim and piezoceramic disk, but not including the dynamic contribution of the air added mass.

The uncoupled natural frequency of the acoustic oscillator is the so called Helmholtz frequency ω_h, which is usually recognized to be:

$$\omega_h = \sqrt{\frac{\gamma A_o^2 p_o / V_c}{\rho_a l_e A_o}} = \sqrt{\frac{k_a}{M_a}} \tag{6}$$

where k_a and M_a are, respectively, the equivalent stiffness of the air inside the cavity, $k_a = \gamma A_o^2 p_o / V_c$, and the effective mass of the air at the orifice, $M_a = \rho_a l_e A_o$.

It is worth to stress that the membrane dynamics is forced by the acoustic oscillator via the cavity pressure term as well as by the piezoelectric effect due to the applied sine voltage. The amplitude of this forcing, F_o, is expressed conveniently as

$$F_o = \frac{\omega_w^2 d_A V_a}{A_w} = \omega_w^2 \Delta x_w \tag{7}$$

where d_A is the effective acoustic piezoelectric coefficient that represents the ratio between the cavity volume variation ΔV and the applied voltage V_a, when the driving differential pressure is equal to zero [7]. Note that in the previous Eq. (7) the cavity volume variation $\Delta V = d_A V_a$ is divided by the membrane area A_w in order to obtain the average linear membrane displacement Δx_w (to be multiplied by k_w in order to obtain the driving force).

$$\Delta x_w = \frac{d_A V_a}{A_w} \tag{8}$$

The coefficient d_A could be evaluated analytically by means the distribution of the transverse displacement of the composite diaphragm, as made by Prasad [6] and Prasad et al. [7]. This procedure is not practical due to the difficulty of determining the required coefficients. An alternative way consists in determining the acoustic compliance of the membrane C_{ac} which, through a dual definition of d_A, is given by the ratio of the volume variation ΔV to a uniformly distributed pressure load p, in condition of electrical short-circuit [7]. Of course the evaluation of C_{ac} would require the same difficulties. However, one can refer to the acoustic compliance of a homogeneous circular plate (namely, having the properties of the piezoceramic disk) that yields insight into the scaling behavior of the diaphragm, and ultimately obtain d_A by means of the relationship

$$d_A = C_{ac}\phi_a \tag{9}$$

in which ϕ_a is the electroacoustic transduction coefficient [7]. As introduced by de Luca et al. [5], the electroacoustic transduction coefficient is assumed to be a fitting parameter of the computer code.

In summary, the behavior of the synthetic jet actuator can be described by the dynamics of two mutually coupled oscillators: the first one, describing the membrane displacement x_w, is characterized by its uncoupled natural frequency ω_w, while the second one, acoustic oscillator, describing the dynamics of the mass of air at the orifice, M_a, through its velocity U, is characterized by the its natural frequency ω_h. The system of Eqs. (1–3) shows that both the dynamics of the membrane and of the orifice air mass are forced by the cavity pressure which couples them by means of the continuity Eq. (2). An external forcing due to the supply power also acts on the membrane dynamics. In order to investigate in more detail the coupling of the two oscillators, it is convenient to reformulate the equations.

By taking the time derivative of Eq. (1), and by eliminating the pressure derivative by means of Eq. (2), one obtains:

$$\ddot{V}_w + 2\zeta_w\omega_w\dot{V}_w + (\omega_w^2 + \omega_{wc}^2)V_w - \frac{A_o}{A_w}\omega_{wc}^2 U = (\omega\Delta x_w)\omega_w^2\cos\omega t \tag{10}$$

which is coupled with the Eq. (3). Note that another characteristic frequency ω_{wc} is introduced in Eq. (10), defined as

$$\omega_{wc} = \sqrt{\frac{\gamma A_w^2 p_o/V_c}{m_w}} = \sqrt{\frac{\gamma A_w p_o}{m_w H}} \tag{11}$$

which, according to Sharma [9], may be interpreted as the natural frequency of the pneumatic spring made of the air enclosed within the cavity of volume V_c and of the diaphragm mass m_w. Note that the height of the cavity, H, is explicitly introduced.

3 Dimensionless Form of the Equations

In order to give more insight to the problem physics, it is worth recasting the governing equations into a convenient dimensionless form. As far as the acoustic oscillator is concerned, proper choices of the reference quantities for time, length and velocity are the reciprocal of the operating frequency $1/\omega$, the cavity height H and the speed of sound of air c, respectively. The dimensionless form of the dynamics of the acoustic oscillator accordingly is:

$$St^2 \frac{\mathrm{d}^2 U^*}{\mathrm{d}t^{*2}} + St\left(K\sqrt{\frac{H}{l_e}}|U^*|\right)\frac{\mathrm{d}U^*}{\mathrm{d}t^*} = V_w^* - \frac{A_o}{A_w}U^* \tag{12}$$

where the Strouhal number is defined as

$$St = \frac{\omega H}{c}\sqrt{\frac{l_e}{H}} \tag{13}$$

The condition corresponding to $St \ll 1$ is physically relevant. Apart from the scaling factor represented by the factor $\sqrt{l_e/H}$, this situation represents the case of acoustically thin cavity, the traveling time of a small pressure disturbance over the distance H being much smaller than the reference time $1/\omega$; in other terms, the air inside the cavity behaves as an incompressible medium (i.e., the air stiffness is infinite). By inspecting Eq. (12), it is evident that this equation reduces to the dimensional relationship:

$$A_w V_w = A_o U \tag{14}$$

namely, the volume rate entering the cavity as a consequence of the membrane displacement equals the volume rate of air expelled through the orifice. On the other hand, the Eq. (1) of the membrane dynamics shows that this last is decoupled from that of the acoustic oscillator. When $St \ll 1$, once the air velocity at the orifice has been obtained from Eq. (14), the cavity pressure may be evaluated by using the unsteady form of the Bernoulli's equation.

The physical situation of $St \gg 1$ also corresponds to decoupled membrane dynamics. In this case, however, the air stiffness is vanishing (the pressure field inside the cavity is practically unperturbed), so that the air jet velocity U is vanishing too.

The equation of motion of the membrane is made dimensionless with the aid of different time and velocity scales, a convenient choice being $1/\omega_w$ and $\omega \Delta x_w$, respectively. The non-dimensional form of such an equations is

$$\ddot{V}_w^* + 2\zeta_w \dot{V}_w^* + V_w^* + CF\left(V_w^* - \frac{A_o}{A_w}U^*\right) = \cos \omega t \tag{15}$$

where the coupling factor is defined as

$$CF = \frac{\omega_{wc}^2}{\omega_w^2} \tag{16}$$

It is straightforward to observe that under the condition for which $CF \ll 1$ (which means that the air stiffness is negligible in comparison with the membrane stiffness) the membrane dynamics is decoupled from the acoustic oscillator one. In this case the jet velocity and the cavity pressure are determined via the continuity and the

unsteady Bernoulli's equations. Another aspect of this decoupling is that the modified structural and Helmholtz's frequencies tend to coincide with the corresponding uncoupled frequencies, as one may verify by inspecting the relationship yielding the eigenvalues of governing system under the assumption that any damping effects is negligible (de Luca et al. [5]):

$$\frac{\omega_{1,2}^2}{\omega_w^2} = \frac{-(1+\frac{\omega_{wc}^2}{\omega_w^2}+\frac{\omega_h^2}{\omega_w^2}) \pm \sqrt{(1+\frac{\omega_{wc}^2}{\omega_w^2}+\frac{\omega_h^2}{\omega_w^2})^2 - 4\frac{\omega_h^2}{\omega_w^2}}}{2} \tag{17}$$

Following de Luca et al. [5], the modified (i.e. coupled) natural frequencies are

$$f_{1,2} = \omega_{i1,2}/(2\pi), \tag{18}$$

$\omega_{i1,2}$ being the imaginary coefficients of the eigenvalues.

4 Validation of the Theory Against Experimental and Numerical Data

The theoretical issues developed before have been verified by means of both experimental measurements as well as numerical simulations of the governing Eqs. (1–3). The basic experimental validation of the physical model as well as of the related computer code has been already presented in a previous paper by de Luca et al. [5]. Hereafter we will refer to the coupling effects of the two oscillators and to the conditions governing them. Moreover, it has to be stressed that, in general, the coupling effects represented by the CF parameter refer to a certain device and may be neglected on the basis of design characteristics of the actuator, whatever is the operating condition. On the contrary, the conditions of decoupling occurring for $St \ll 1$ and $St \gg 1$ depend essentially on the operating condition and they may occur for any device.

4.1 Effect of CF

Experimental tests have been carried out on three different synthetic jet actuators (one with the membrane in brass and the other two in aluminum) designed to the purpose. The basic characteristics of such actuators are summarized in Table 1. They have been designed essentially in order to obtain different values of the coupling factor, ranging from about 0 to 1.88. The schematic of the devices is shown in Fig. 1 highlighting their modular structure, which permits independent variations of cavity diameter and height, orifice diameter, and piezoelectric diaphragm.

Table 1 Features of the tested devices predicted analytically

	Property	Brass	Aluminum 1	Aluminum 2
Geometry	Shim diameter (mm)	35	42	80
	Shim thickness (mm)	0.4	0.24	0.25
	Piezoelectric diameter (mm)	23	31.8	63.5
	Piezoelectric thickness (mm)	0.23	0.191	0.191
	Cavity diameter (mm)	35	42	80
	Cavity height (mm)	3–5	3–8	4–7–11
	Orifice diameter (mm)	2	2	5
	Orifice length (mm)	2	2	2
	H/d_o	1.5–2.5	1.5–4	0.8–1.4–2.2
	l_e/d_o	1	1	0.4
Shim	Young's module (Pa)	9.7×10^{10}	7.31×10^{10}	7.31×10^{10}
	Poisson's module	0.36	0.31	0.31
	Density (kg/m^3)	8,490	2,780	2,780
Piezoelectric	Young's module (Pa)	6.7×10^{10}	6.6×10^{10}	6.6×10^{10}
	Poisson's module	0.31	0.31	0.31
	Density (kg/m^3)	8,000	7,800	7,800
Frequency response	f_w (Hz)	2,176	1,376	401
	f_1 (Hz)	2,256–2,221	1,632–1,462	307–297–283
	f_h (Hz)	1,000–775	833–510	723–547–436
	f_2 (Hz)	964–759	702–480	944–737–617
	CF	0.06–0.04	0.30–0.11	1.88–1.08–0.68

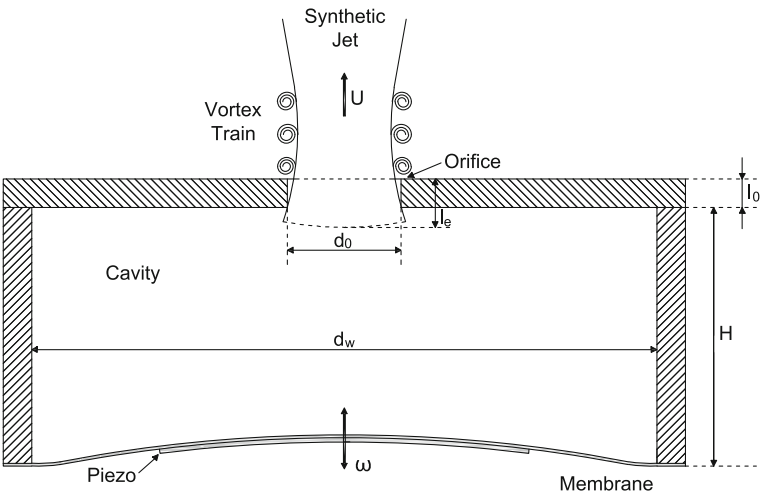

Fig. 1 Sketch of a typical device

The brass actuator is a commercially available piezoelectric ceramic disk bonded to a thin brass metal plate fabricated by Murata Manufacturing Co. The aluminum membranes were built in-house by gluing a LZT piezoceramic disk (manufactured by PIEZO Inc.) on a thin aluminum foil.

In Table 1 geometrical and mechanical properties, as well as nominal characteristic frequencies of the tested devices, listed on the basis of the shim material, are summarized. The frequencies reported in Table 1 have been calculated by means of the analytical model illustrated before. f_w and f_h denote the (uncoupled) first-mode structural and Helmholtz natural frequencies, respectively, defined through Eqs. (4) and (6), respectively; f_1 and f_2 are the frequencies of the two coupled oscillators, i.e. the modified first-mode structural and Helmholtz resonance frequencies, defined by Eq. (18); the coupling factor CF introduced by Eq. (16) is reported in the last line.

As a general trend, on the grounds of Eq. (17) the coupling effect increases the structural resonance frequency and lowers the Helmholtz resonance frequency. Furthermore, the coupling factor CF is higher as the cavity height decreases. However, since for the aluminum 2 device the nominal structural frequency is less than the Helmholtz one, the situation is reversed in the sense that the coupling of the oscillators lowers f_1 and raises f_2.

As shown in Table 1, the nominal structural frequency of the brass devices is very close to the value predicted by the model of the coupled oscillators. For the brass device it results that also the Helmholtz frequency (i.e., the natural frequency of the acoustic oscillator) is almost coincident with the value predicted by means of the coupling model. The quasi-coincidence between the uncoupled natural structural and Helmholtz frequencies and the corresponding values of $\omega_{1,2}$, observed for the brass actuator, is much more weak for the aluminum 1 and totally disappears for the aluminum 2 actuator which exhibits the strongest coupling effect.

As already pointed out before, the model has been validated against systematic experimental tests whose findings have been already published in a previous paper by de Luca et al. [5]. Here we limit to remember that we made measurements of pressure disturbances produced by the motion of the membrane into the external ambient, deflection of the (composite) membrane by means of a laser scanning vibrometer, and jet exit velocity (by using a standard Pitot tube) in the external ambient at a station located on the jet axis just downstream of the stagnation point (the so called saddle point) separating near and far fields.

Plots showing the frequency response of the actuators in terms of the downstream-directed velocity U_e measured by means of the Pitot tube just downstream of the saddle point (i.e. at a point one orifice diameter downstream of the orifice exit), are reported in Figs. 2, 3 and 4. Following the basic definitions and findings of literature (e.g., [14, 15]), the saddle point velocity is roughly 1.1 times the stroke length velocity, U_o, namely the time-average of the orifice blowing velocity over the entire period. Thus, in order to compare experimental measurements of U_e to numerical computations of the peak value $U_{\max}$ of the exit velocity U, the relationship is used $U_e \cong (1.1/\pi)U_{\max} = U_{\max}/2.85$.

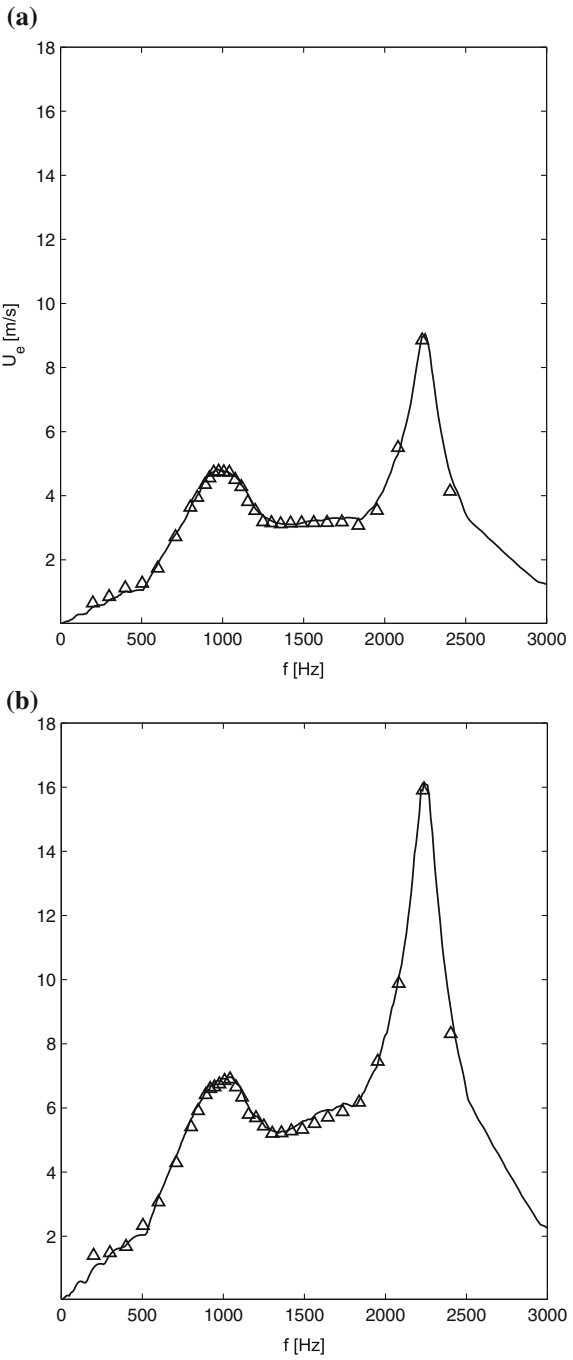

Fig. 2 Numerical-experimental comparison of average exit flow velocity frequency response for the brass actuator ($\boldsymbol{H} = \mathbf{3}$ mm); *triangles* represent the experimental measurements, *black curves* represent the numerical solution; **a** $\boldsymbol{V_a} = \mathbf{35}$ V, **b** $\boldsymbol{V_a} = \mathbf{70}$ V

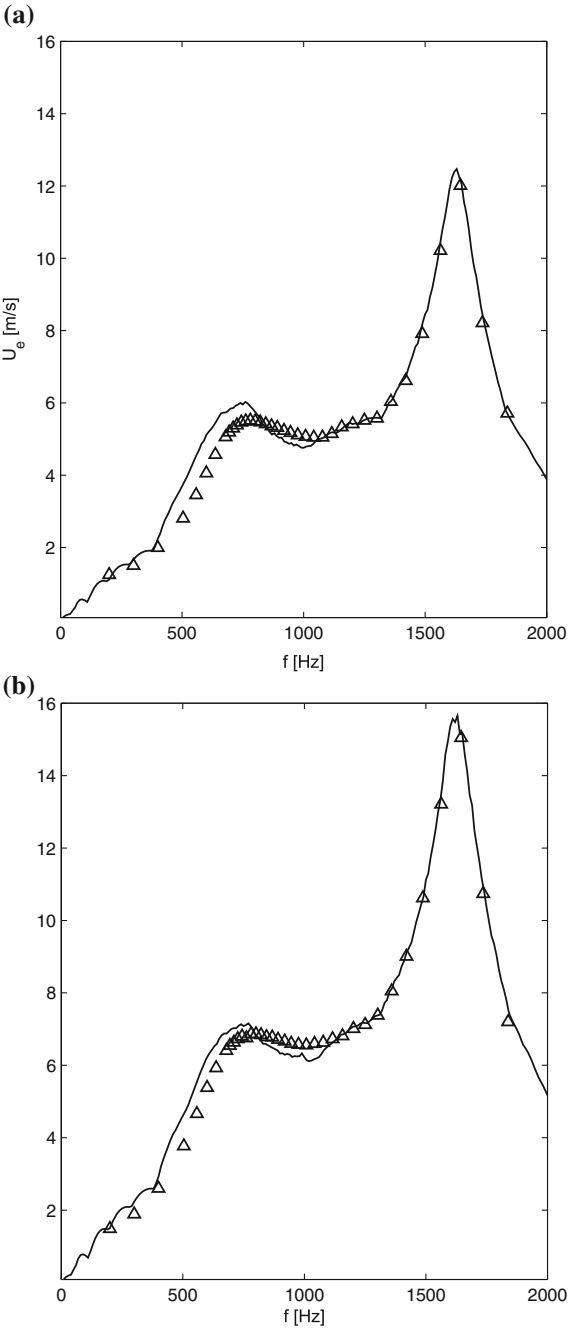

Fig. 3 Numerical-experimental comparison of average exit flow velocity frequency response for the aluminum 1 actuator ($\boldsymbol{H} = \mathbf{3}$ mm); *black curves* represent the numerical solution, *triangles* represent the experimental measures; **a** $\boldsymbol{V_a} = \mathbf{25}$ V, **b** $\boldsymbol{V_a} = \mathbf{35}$ V

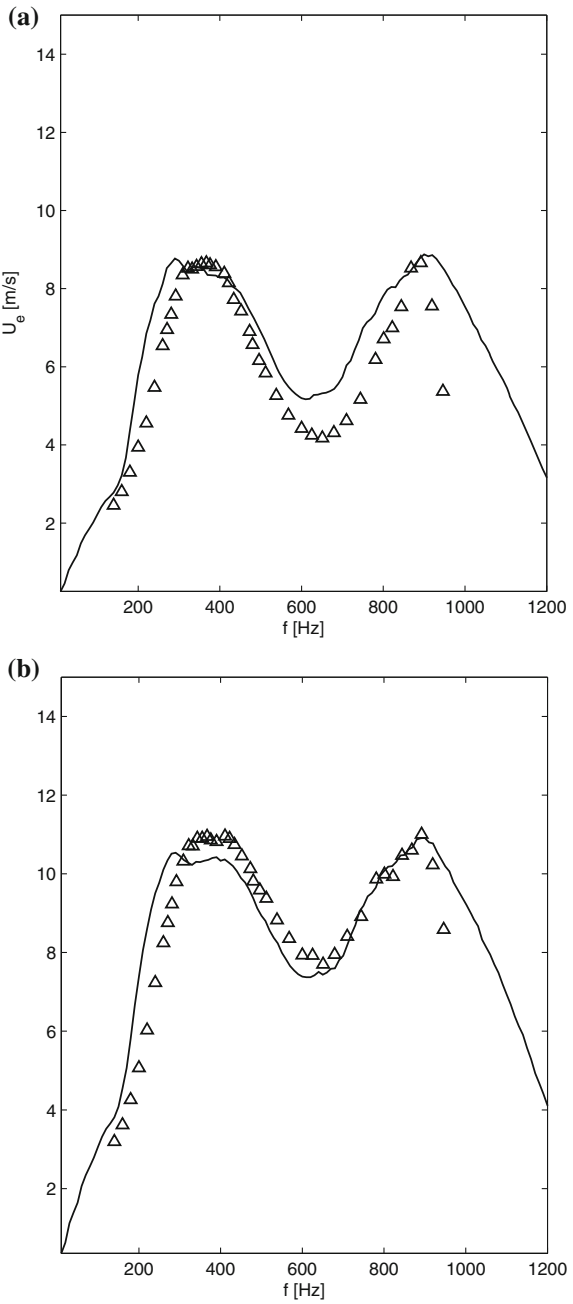

Fig. 4 Numerical-experimental comparison of average exit flow velocity frequency response for the aluminum 2 actuator ($\boldsymbol{H} = \mathbf{4}$ mm); *triangles* represent the experimental measures; *black curves* represent the numerical solution; **a** $\boldsymbol{V_a} = \mathbf{35}$ V, **b** $\boldsymbol{V_a} = \mathbf{50}$ V

Data points of Figs. 2, 3 and 4 are compared to the corresponding numerical values obtained by integrating numerically the complete governing Eqs. (1–3). The numerical simulations have been carried out by means of a standard fourth order Runge-Kutta method in MATLAB environment with *ode45* routine. Initial conditions of $x_w = 0$, $\dot{x}_w = 0$, $p_i = 0$, and $U = 0$ have been assumed for all the computations; it has been observed that the quasi-steady oscillatory solution is generally reached in about 20–30 cycles. Typical values of the electroacoustic transduction coefficient ϕ_a that best fit the continuous numerical curves to the velocity measurements are 105, 133, 47.7 for brass, aluminum 1, aluminum 2 actuators, respectively.

Table 2 reports the resonance frequencies calculated numerically for each device at $V_a = 35\,\text{V}$. This table should be compared to Table 3 showing analogous experimental findings in order to appreciate the data agreement. For the sake of convenience, data to be compared are reported in bold type in both tables. Data spread is generally less than 4 % except for the value of the modified structural frequency of aluminum 2 actuator, for which it appears to be about 26 %. However, it should be noted that computer simulations of Fig. 4 show a rather wide plateau around this peak frequency, whereas the the data spread of 26 % refers exactly to the peak value. For a more general comparison including analytical, numerical and experimental velocity results, one should glance at Tables 1, 2 and 3 simultaneously.

Table 2 Numerical resonance frequencies at $V_a = 35\,\text{V}$

	H (mm)	Modified Helmholtz frequency (Hz)	Modified structural frequency (Hz)
Brass	3	**960**	**2,260**
	5	760	2,210
Aluminum 1	3	**770**	**1,630**
	8	490	1,480
Aluminum 2	4	**900**	**290**
	7	690	320
	11	570	330

Table 3 Experimental resonance frequencies from Pitot tube

	V_a (V)	Modified Helmholtz frequency (Hz)	Modified structural frequency (Hz)
Brass (H = 3 mm)	35	**976**	**2,232**
	70	1,042	2,232
Aluminum 1 (H = 3 mm)	25	781	1,645
	35	**801**	**1,645**
Aluminum 2 (H = 4 mm)	35	**892**	**367**
	50	892	367

4.2 Effect of Strouhal Number

The effect of the Strouhal number can be appreciated by focusing the attention on particular operating conditions; for a given device, in particular, the conditions of $St \ll 1$ and $St \gg 1$, that are achieved for relatively low and high values of operation frequency, respectively, will be analyzed hereafter. Of course, one has to keep in mind that more in general the conditions of $St \ll 1$ and $St \gg 1$ correspond to situations of acoustically thin and thick resonant cavity, respectively, as before observed. This effect will be analyzed numerically with particular reference to the frequency response in terms of exit velocity of the three devices mentioned in the previous sections.

The maximum jet-flow exit velocity trends as functions of the operation frequency are depicted in Figs. 5, 6 and 7 for the three tested devices and for various dimensionless cavity heights H/d_o. The supply voltage V_a is equal to 35 V in all these simulations.

For all the devices two velocity peaks corresponding to the two resonance frequencies are clearly evident. For the brass device both the velocity peaks increase with decreasing the cavity height, whilst for the aluminum 1 one the trend is that the velocity peak of the structural resonance reaches a plateau for intermediate values of H/d_o and then it decreases at the largest height. For the brass actuator the distance between the two resonance frequencies slightly increases with increasing H/d_o, in agreement with experimental results of Gomes et al. [16] obtained for $l_o/d_o > 1$, while for the aluminum 1 such a distance slightly decreases.

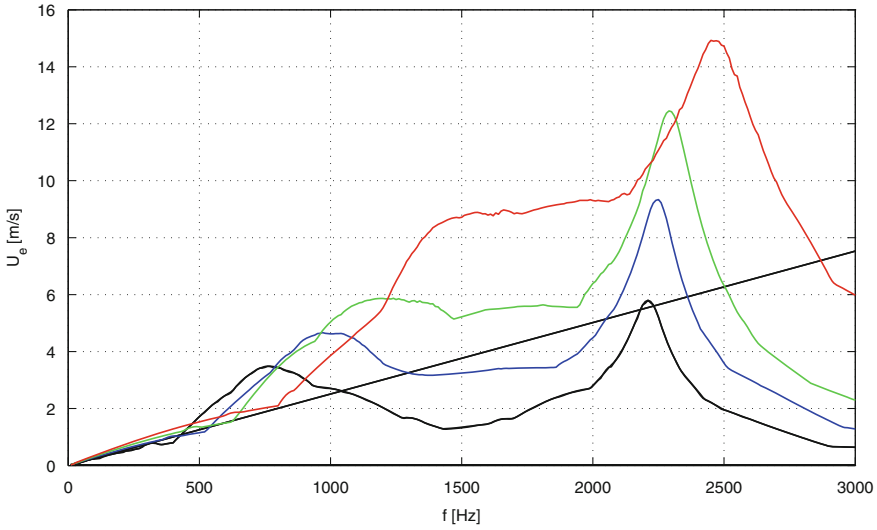

Fig. 5 Frequency response of average exit flow velocity for the brass actuator at $V_a = 35$ V; *red line* is for $H/d_o = 0.5$, *green* $H/d_o = 1$, *blue* $H/d_o = 1.5$, *black* $H/d_o = 2.5$. The *straight line* refers to Eq. (14)

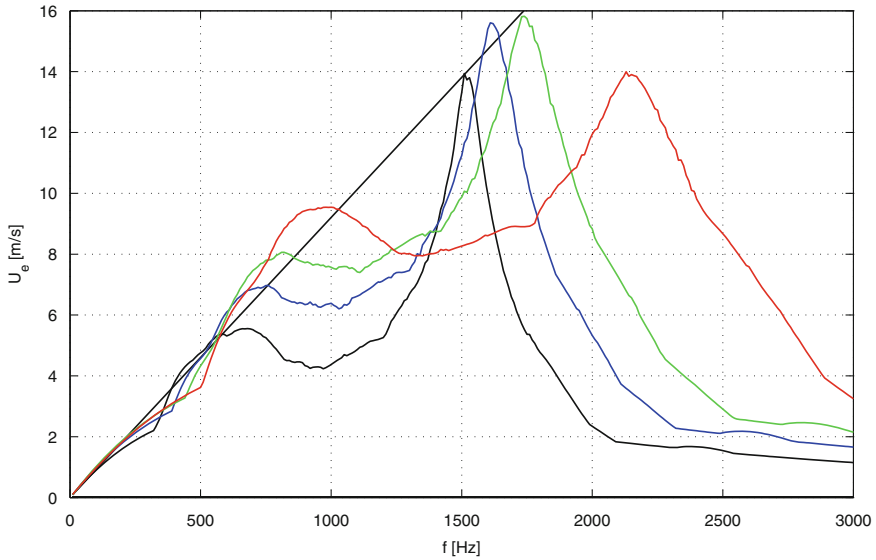

Fig. 6 Frequency response of average exit flow velocity for the aluminum 1 actuator at $V_a = \mathbf{35}$ V; *red line* is for $H/d_o = 0.5$, *green* $H/d_o = 1$, *blue* $H/d_o = 1.5$, *black* $H/d_o = 2.5$. The *straight line* refers to Eq. (14)

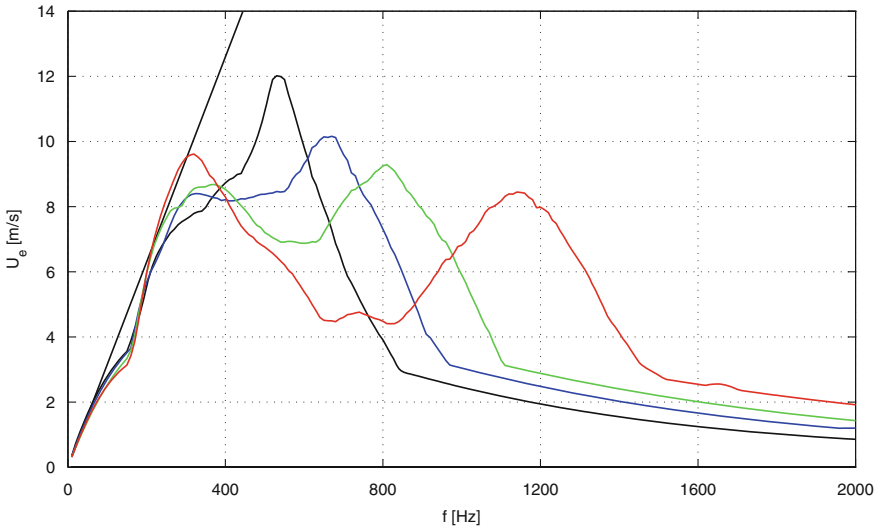

Fig. 7 Frequency response of average exit flow velocity for the aluminum 2 actuator at $V_a = \mathbf{35}$ V; *red line* is for $H/d_o = 0.5$, *green* $H/d_o = 1$, *blue* $H/d_o = 1.5$, *black* $H/d_o = 2.5$. The *straight line* refers to Eq. (14)

Note that the experimental findings of Gomes et al. [16] show also that the resonance frequencies distance becomes practically constant as H/d_o further increases, in agreement with the analytical prediction of de Luca et al. [5] valid in the case of $\omega_w \gg \omega_h$.

The straight lines present in the plots of Figs. 5, 6 and 7 refer to the linear dependance of the jet velocity upon the operating frequency given by the incompressible model described by the Eq. (14). For the brass and the aluminum 1 and 2 actuators it is clearly evident that such a simplified model closely agrees with the simulations of the complete model at low frequencies, the frequencies range of such an agreement widening for the smaller cavity heights, as predicted by the theory for $St \ll 1$. Note also that for this range of frequencies the response in terms of jet velocity is the same whatever is the cavity height, thus confirming that the membrane dynamics is decoupled from the acoustic oscillator one. These figures show that the uncoupled behavior is recovered also for relatively high frequencies, i.e. $St \gg 1$, where the expected response is of vanishing U_e, anticipated at lower frequencies for the highest cavity heights.

In order to complete the discussion about the behavior of the aluminum 2 device, note that the two nominal Helmholtz and structural frequencies, which for this actuator are reversed, are remarkably modified by the high coupling ratio. The jet velocity decreases with increasing the cavity height at the structural resonance frequency, whereas it increases with increasing H/d_o at the Helmholtz resonance frequency, with the result that the maximum peak is reached at the Helmholtz frequency for the highest simulated cavity height. This particular finding agrees with the theoretical prediction of de Luca et al. [5] that if $\omega_w \ll \omega_h$ then the distance between the two eigenvalues $|\omega_1^2 - \omega_2^2|/\omega_h^2$ does not depends on the cavity height H/d_o and therefore $|\omega_1^2 - \omega_2^2| \simeq 1/(H/d_o)$. The quasi-coincidence of the two resonance frequencies justifies that the maximum peak is reached for the highest cavity height.

5 Conclusions

Basic properties of resonant cavities driven by piezo-electric thin elements, typically employed in order to produce the so-called synthetic jets, have been analyzed by means of a lumped-element physical model. The model is fluid-dynamics based and, although his genesis is inspired by an analogous model of previous literature, it is innovative because it needs in input just electro-mechanical properties easily available from commercial data sheet of the materials. The synthetic jet devices are usually employed to control fluid flows. They are also used to cool locally reduced-size surfaces, as well as to enhance the mixing between fluid currents.

In these frameworks, the proposed model represents a practical tool for the overall design of the actuator. This has been idealized as an acoustic-mechanical system of two-coupled oscillators, the membrane one (i.e., the structural element)

and the Helmholtz's one (i.e., the acoustic one). Simplified, but rather accurate relationships have been given in order to predict the two modified (coupled) resonance frequencies, as a function of the decoupled natural frequencies of the two basic oscillators. The analytical investigation has been completed through an inspection of the dimensionless form of the governing equations, which introduce two characteristic parameters: the frequencies coupling factor and the Strouhal number. The study showed that the acoustic oscillator is always driven by the membrane dynamics, while there are conditions under which the membrane behavior is decoupled from the Helmholtz oscillator.

The fully nonlinear governing equations have been integrated numerically in MATLAB environment. In order to validate the computer code, various experimental campaigns have been carried out on three different actuators especially designed and manufactured to the purpose of obtaining an increasing coupling factor. In this paper, the comparison of the frequency response predicted numerically against experimental findings has been presented with reference in particular to the external jet velocity.

The theoretical and experimental results show that when the coupling factor is very small the two oscillators are decoupled, in the sense that the two modified resonance frequencies tend to the corresponding nominal values, yielded by simplified but accurate relationships.

The case of $St \ll 1$ is very interesting too. It physically corresponds to acoustically thin cavity and, for a given device, occurs at relatively low operating frequencies. In this decoupled regime it has also been found that the behavior of the actuator is well described by the so called incompressible model, where the air volume rate entering the cavity as a consequence of the membrane displacement equals the air volume rate leaving the cavity through the orifice.

A detailed numerical investigation about the influence of the cavity height has been also carried out. An interesting but perhaps not expected result is that for the device exhibiting the strongest coupling the jet velocity peak occurs for the highest investigated cavity.

Acknowledgments This work has been funded by Compagnia di S. Paolo and Polo delle Scienze e delle Tecnologie of Universita' degli Studi di Napoli Federico II, within the F.A.R.O. projects 2009 and 2012.

References

1. A. Glezer, M. Amitay, Synthetic jets. Annu. Rev. Fluid Mech. **34**, 503–529 (2002). doi:10.1146/annurev.fluid.34.090501.094913
2. L.N. Cattafesta III, M. Sheplak, Actuators for active flow control. Annu. Rev. Fluid Mech. **43**, 247–272 (2011). doi:10.1146/annurev-fluid-122109-160634
3. L. Mongibello, G. Rocco, G. Coppola, L. de Luca, Numerical investigation of two adjacent synthetic jets for flow control, in *2nd European Conference for Aero-Space Sciences (EUCASS),* Brussels, CD proceedings, paper 02-06-08

4. G. Monaco, L. Mongibello, L. de Luca, Impingement heat transfer by means of synthetic jets, in *Proceedings of ASME-ATI-UIT 2010 Conference on Thermal and Environmental Issues in Energy Systems, Edizioni ETS, PISA*, vol. II, Sorrento, 16–19 May 2010, pp. 1413–1417. ISBN 978-884672659-9
5. L. de Luca, M. Girfoglio, G. Coppola, Modeling and experimental validation of the frequency response of synthetic jet actuators. AIAA J. **52**(8), 1733–1748 (2014). doi:10.2514/1.J052674
6. S.A.N. Prasad, Two-port electroacoustic model of piezoelectric composite circular plate, M.S. thesis, Department of Aerospace Engineering, Mechanics, and Engineering Sciences, University of Florida, Gainesville, 2002, pp. 1–166
7. S.A.N. Prasad, Q. Gallas, S. Horowitz, B. Homeijer, B.V. Sankar, L.N. Cattafesta, M. Sheplak, Analytical electroacoustic model of a piezoelectric composite circular plate. AIAA J. **44**(10), 2311–2318 (2006). doi:10.2514/1.19855
8. Q. Gallas, R. Holman, T. Nishida, B. Carroll, M. Sheplak, L. Cattafesta, Lumped element modeling of piezoelectric-driven synthetic jet actuators. AIAA J. **41**(2), 240–247 (2003). doi:10.2514/2.1936
9. R.N. Sharma, Fluid dynamics based analytical model for synthetic jet actuation. AIAA J. **45** (8), 1841–1847 (2007). doi:10.2514/1.25427
10. M. Chaudhari, G. Verma, B. Puranik, A. Agrawal, Frequency response of a synthetic jet cavity. Exp. Thermal Fluid Sci. **33**, 439–448 (2009). doi:10.1016/j.expthermflusci.2008.10.008
11. G. Krishnan, K. Mohseni, Axisymmetric synthetic jets: an experimental and theoretical examination. AIAA J. **47**(10), 2273–2283 (2009). doi:10.2514/1.42967
12. C. Seeley, Y. Utturkar, M. Arik, T. Icoz, Fluid-structure interaction model for low-frequency synthetic jets. AIAA J. **49**(2), 316–323 (2011). doi:10.2514/1.53408
13. T. Persoons, General reduced-order model to design and operate synthetic jet Actuators. AIAA J. **50**(4), 916–927 (2012). doi:10.2514/1.J051381
14. B.L. Smith, A. Glezer, The formation and evolution of synthetic jets. Phys. Fluids **10**(9), 2281–2297 (1998)
15. B.L. Smith, G.W. Swift, A comparison between synthetic jets and continuous jets. Exp. Fluids **34**(4), 467–472 (2003). doi:10.1007/800348-002-0577-6
16. L.D. Gomes, W.J. Crowther, N.J. Wood, Towards a practical piezoceramic diaphragm based synthetic jet actuator for high subsonic applications—effect of chamber and orifice depth on actuator peak velocity, in *3rd AIAA Flow Control Conference,* 5–8 June 2006, San Francisco, AIAA paper 2006–2859

Part II
Direct and Inverse Methods

Since the beginning of routine flight tests, measurements of the vibro-acoustic response of structures excited by turbulent boundary layer (TBL) pressure fluctuations have remained a challenging and time-consuming activity. In operating conditions, such as in-flight and underwater tests, these measurements are extremely expensive and difficult to manage. In-situ measurements, such as in wind tunnels and water tanks, require expensive facilities and cannot span the whole range of interest. In fact, each facility has some limits in terms of speed, flow quality, Reynolds number, etc. In addition, both measurement approaches, in situ and in operating conditions, usually face a difficult problem related to background noise levels.

Therefore, along with direct measurement and simulation methods, some authors are pursuing inverse methods to either infer or synthesize TBL wall pressure fluctuations using traversing microphones and panel vibrations. The goal is to synthesize effective TBL wall pressures in a test facility without a moving fluid, usually using a wavenumber filtering and an assumed field of partially correlated plane wave sources. The different techniques in these papers show that simulating TBL wall excitation this way is quite challenging, mainly due to the requirement of a very large array of sensors.

This part describes approaches for simulating TBL wall pressures using a single traversing source and an acoustic holography technique or a surface plane wave decomposition. The proposed methods benefit from a synthetic antenna concept because one moving sensor is used instead of a full array. Finally, the last paper describes some attempts to use vibration measurements to identify the wall pressure fluctuations responsible for a panel vibration.

Source Scanning Technique for Simulating TBL-Induced Vibrations Measurements

Mathieu Aucejo, Laurent Maxit and Jean-Louis Guyader

Abstract Measuring the vibro-acoustic response of structures subjected to a turbulent boundary layer (TBL) excitation in operating conditions remains an open issue for experimenters. Generally, in situ measurements, e.g. flight tests, underwater measurements and wind tunnel measurements are carried out, although they require expensive facilities. As an alternative to in situ measurements, experimental simulations in a laboratory environment have been developed. The main issue of these substitute experiments is the synthesis of an excitation field equivalent to TBL wall-pressure fluctuations with the help of standard transducers (shakers, loudspeakers, etc.). In the present paper, we propose an alternate off-line methodology to deal with the experimental simulation of vibrations induced by a spatially correlated random pressure field, such as TBL excitation. The proposed methodology is called source scanning technique (SST) and relies on two main features: a wall-pressure plane wave expansion of the target random wall-pressure field and two identification steps based on the concept of synthetic array to simulate TBL-induced vibrations from a set of transfer functions. In the present paper, the theoretical description of the SST and its experimental implementation are detailed.

M. Aucejo (✉)
Structural Mechanics and Coupled Systems Laboratory,
Cnam Paris, 2 rue Conté, 75003 Paris, France
e-mail: mathieu.aucejo@cnam.fr

L. Maxit · J.-L. Guyader
Laboratoire Vibrations Acoustique, INSA-Lyon,
25 bis Avenue Capelle, 69621 Villeurbanne Cedex, France
e-mail: laurent.maxit@insa-lyon.fr

J.-L. Guyader
e-mail: jean-louis.guyader@insa-lyon.fr

E. Ciappi et al. (eds.), *Flinovia - Flow Induced Noise and Vibration Issues and Aspects*, DOI 10.1007/978-3-319-09713-8_7

1 Introduction

Measuring turbulent boundary layer (TBL) induced vibrations is of particular interest in numerous transportation applications. From a practical point of view, in situ measurements, e.g. flight tests [1], underwater measurements [2] and wind tunnel measurements [3] are generally carried out. However, these experimental set-ups are expensive due to the equipment and resources needed. Furthermore, measurements are difficult to perform because of background noise levels. It is thus of considerable interest to develop substitute experiments to assess TBL-induced vibrations under laboratory conditions. Nevertheless, very few studies have been carried out in the last few decades. One of the first studies on this topic was proposed by Fahy [4], in which several ways of simulating TBL wall-pressure fluctuations such as arrays of shakers or loudspeakers have been mentioned. Unfortunately, these approaches had not been assessed experimentally because of the practical difficulties of implementing these solutions at that time.

The practical feasibility of using an array of suitably driven shakers has been studied by Robert [5], while the real-time synthesis of spatially correlated random pressure fields with a near-field array of appropriately-driven loudspeakers was studied by Elliot et al. [6], Maury and Bravo [7] and Bravo and Maury [8]. Apart from these works, other semi-experimental techniques have been proposed. For instance, it is worth citing the work of Audet et al. [9] based on the standard formulation of random vibration theory and the measurement of the required transfer functions and the work proposed by Robin et al. [10] based on the planar NAH.

In the present paper, we propose an alternate off-line methodology called Source Scanning Technique (SST) to investigate structural vibrations induced by random pressure fields such as TBL excitation [11, 12]. The aim is to overcome the difficulty of generating TBL excitation experimentally and gain the practical advantage of performing a substitute experiment based on acoustic excitation. For this purpose, the methodology developed in this paper relies on two main features: a wall-pressure plane wave expansion of the target random wall-pressure field and two identification steps based on the concept of synthetic array to simulate TBL-induced vibrations from a set of transfer functions. Practically, SST requires the generation of a set of uncorrelated wall-pressure fields corresponding to those of propagating and evanescent acoustic plane waves. For this purpose, a single moving monopole-like source simulating a full array of acoustic monopoles is used.

In the next of the paper, the theoretical description of SST and its experimental implementation are presented. A particular attention is paid to the definition of the grid covered by the monopole source (number of nodes, dimension and distance from the observation area) as well as the design of the test bench used to assess the validity of SST. This test bench being developed for validation purposes only, it can not be used as it is in an industrial context. That is why, a test bench is proposed for industrial applications in the last part of the paper.

2 Basic Principles of SST

In room acoustics, it is well-known that a diffuse sound field can be thought as an uncorrelated isotropic superposition of acoustic plane waves [13]. As the diffuse sound field, the TBL excitation is a partially space-correlated random pressure field. Consequently, it can also be modelled as a superposition of uncorrelated wall-pressure plane waves.

2.1 Modelling of TBL Excitation as a Superposition of Uncorrelated Wall Plane Waves

As a random process, the TBL excitation classically is modelled from the cross-spectral density (CSD) function of the wall-pressure fluctuations. Here, the basic idea is to represent the TBL CSD function as a superposition of uncorrelated wall-pressure plane waves.

By definition, the pressure of a wall-pressure plane wave P_{rs} of wavenumbers (k_r, k_s) is:

$$P_{rs}(x, y, t) = A_{rs}(t)\mathrm{e}^{jk_r x + jk_s y} \tag{1}$$

where $A_{rs}(t)$ is a random variable corresponding to the amplitude of a wall-pressure plane wave of wavenumbers (k_r, k_s).

The corresponding CSD function $S_{P_{rs}P_{rs}}$ between 2 points is therefore:

$$S_{P_{rs}P_{rs}}(\xi_x, \xi_y, \omega) = S_{A_{rs}A_{rs}}(\omega)\mathrm{e}^{jk_r\xi_x + jk_s\xi_y} \tag{2}$$

where ξ_x and ξ_y are the spatial shifts between 2 points along x-axis and y-axis respectively, $S_{A_{rs}A_{rs}}(\omega)$ is the auto-spectral density (ASD) function of the wall-pressure plane wave amplitude and ω is the angular frequency.

Let us suppose now a rigid surface impacted by a set of uncorrelated wall-pressure plane waves. The total pressure $p(x, y, t)$ at point (x, y) of the rigid surface is thus given by:

$$p(x, y, t) = \sum_{r,s} P_{rs}(x, y, t) \tag{3}$$

As the wall-pressure plane waves are supposed uncorrelated, $S_{A_{rs}A_{r's'}}(\omega) = 0$ if $r \neq r'$ and $s \neq s'$. Consequently, the CSD function of the total pressure is:

$$S_{pp}(\xi_x, \xi_y, \omega) = \sum_{r,s} S_{A_{rs}A_{rs}}(\omega)\mathrm{e}^{jk_r\xi_x + jk_s\xi_y} \tag{4}$$

To obtain a pressure field compatible with the TBL excitation, the CSD function of the total pressure has to be scaled on the TBL CSD function.

In [12], it has been shown that TBL excitation can be represented as a superposition of uncorrelated wall-pressure plane waves, if the ASD function $S_{A_{rs}A_{rs}}(\omega)$ of each wall-pressure plane wave satisfies:

$$S_{A_{rs}A_{rs}}(\omega) = \frac{\Gamma_{pp}(k_r, k_s, \omega)\Delta k_r \Delta k_s}{4\pi^2} \tag{5}$$

2.2 Vibration Response to a TBL Excitation

Let us consider a structure subjected to a homogeneous stationary TBL excitation. It has been shown in [12] that the ASD function of the velocity $S_{vv}(Q, \omega)$ at point Q of the structure can be obtained from the uncorrelated wall-pressure plane waves expansion described previously. After some calculations based on the classical random vibration theory [14] and the wall-pressure plane waves expansion, it readily comes:

$$S_{vv}(Q, \omega) = \sum_{r,s} S_{A_{rs}A_{rs}}(\omega)\left|H_v(Q, k_r, k_s, \omega)\right|^2 \tag{6}$$

where the transfer function $H_v(Q, k_x, k_y, \omega)$ is the structural response at point Q excited by a wall-pressure plane wave of unit amplitude.

Consequently, the experimental process has to be divided in two main steps to compute the response $S_{vv}(Q, \omega)$, namely the measurement of the transfer function $H_v(Q, k_r, k_s, \omega)$ and their post-processing according to Eq. (6). However, since $H_v(Q, k_r, k_s, \omega)$ is the response of the structure at point Q to a wall-pressure plane wave of unit amplitude, the main question that arises here is: How to generate a wall-pressure plane wave of unit amplitude?

2.3 Generation of Wall-Pressure Plane Waves

A natural approach to obtain a wall-pressure field of plane wave type is to generate an acoustic plane wave. However, as illustrated in Fig. 1, it is necessary for a TBL excitation to generate wall-pressure fields corresponding to those of propagating and evanescent acoustic plane waves. Actually, the nature of the wall-pressure field to reproduce only depends on the values of the wavenumbers k_r and k_s with respect to the acoustic wavenumber k_0.

Unfortunately, evanescent acoustic plane waves are difficult to generate in practice. That is why, an array of acoustic monopoles is used instead to simulate the required near-field interferential conditions. A schematic representation of such a device is proposed in Fig. 2.

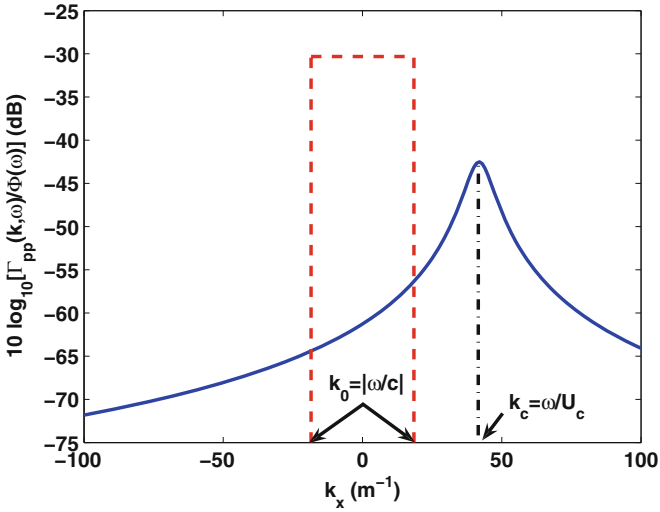

Fig. 1 Comparison of cross-spectral density function of (*blue line*) a TBL and (*red lines*) a diffuse field—k_c convective wavenumber, k_0 acoustic wavenumber

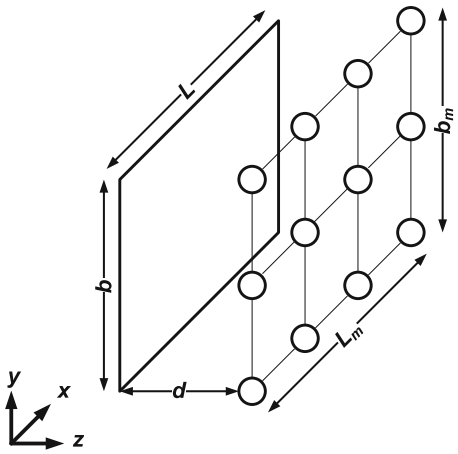

Fig. 2 Definition of the array of acoustic monopoles

To properly describe these interference conditions, one has to estimate, for each wall-pressure plane wave, the complex amplitude $B_m^{rs}(\omega)$ of each monopole m of the array. Actually, this amplitude is obtained by writing the equality of a wall-pressure plane wave of unit amplitude and the wall-pressure field generated by the monopole array over a grid of p observation points located on a rigid plane:

$$\sum_m B_m^{rs}(\omega) H_{mp}(\omega) = \mathrm{e}^{jk_r x_p + jk_s y_p} \tag{7}$$

where $H_{mp}(\omega)$ is the transfer function between a monopole m of coordinates (x_m, y_m, z_m) and an observation point p of coordinates $(x_p, y_p, 0)$ belonging to a rigid wall.

However, it can be inferred from Eq. (7) that the more the values of the wavenumbers k_r and k_s are important, the more the number of monopoles necessary to properly reproduce a wall-pressure plane wave of unit amplitude is high. Consequently, using a monopole array can be intractable in practice. To bypass this experimental limitation, a Source Scanning Technique has be developed.

2.4 Source Scanning Technique

The Source Scanning Technique relies on the linearity of the problem and consists in using a single moving monopole-like source to reconstruct a target wall-pressure plane wave from sequential measurements. It could be stressed that it is closely related to the concept of synthetic antenna [15], which consists in post-processing the signals of a moving receiving array to reconstruct an unknown target image with a finer spatial resolution than that obtained with a fixed array. Actually, the reciprocal mechanism is used in this paper.

To properly implement this technique in the proposed experimental framework, one has to notice that the evaluation of the transfer function $H_v(Q, k_r, k_s, \omega)$ requires two measurements, the first one to characterize the acoustic medium and the second one to characterize the dynamic behaviour of the structure excited by an acoustic monopole. By combining both information, one can obtain an evaluation of the target transfer function, that can be used to compute the response of the structure to a TBL excitation. Consequently, the Source Scanning Technique is carried out in 3 steps.

2.4.1 Step 1: Characterization of the Source Radiation in a Real Acoustic Medium

The characterization of the source radiation in a real acoustic medium is performed by the measurement of the transfer functions $H_{mp}(\omega)$, corresponding to the blocked pressure on a rigid wall at position p due to the monopole-like source at position m as illustrated in Fig. 3.

From this set of transfer functions, it is possible to compute the amplitude $B_m^{rs}(\omega)$ for each position of the monopole-like source and each couple of wavenumbers (k_r, k_s) [see Eq. (7)].

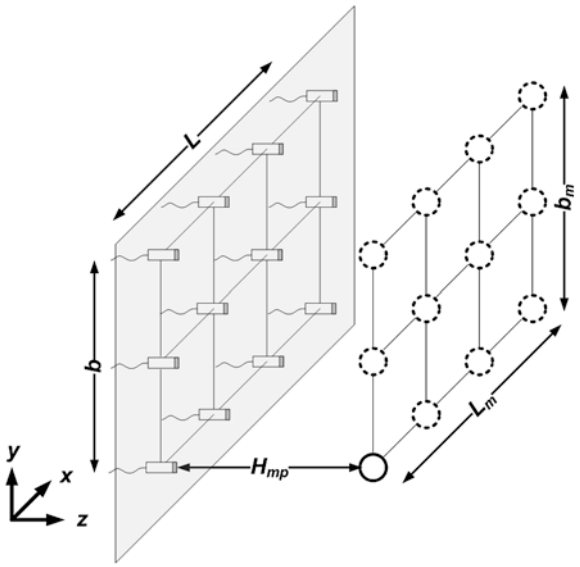

Fig. 3 Example of measurement of the transfer functions $H_{mp}(\omega)$

It should be noted that this step is compulsory if the acoustic medium can not be considered as semi-anechoic and the source as a monopole. However, it can be emphasized that the measurement have to be performed only once and are independent of the structure under test. On the contrary, if the acoustic medium is semi-anechoic and the source is a monopole, a theoretical expression of $H_{mp}(\omega)$ can be used to avoid these measurements. This expression writes:

$$H_{mp}(\omega) = \frac{\mathrm{e}^{-jk_0\sqrt{(x_m-x_p)^2+(y_m-y_p)^2+z_m^2}}}{2\pi\sqrt{(x_m-x_p)^2+(y_m-y_p)^2+z_m^2}}. \tag{8}$$

2.4.2 Step 2: Characterization of Dynamic Behaviour of the Structure

The characterization of the dynamic behaviour of the structure excited by an acoustic monopole is performed by the measurement of the transfer functions H_{Qm}, corresponding to the velocity at point Q due to the monopole-like source at position m (see Fig. 4).

From this set of transfer functions and the amplitude $B_m^{rs}(\omega)$ computed in the first step, the transfer function $H_v(Q, k_r, k_s, \omega)$ can be calculated off-line from the following relation:

$$H_v(Q, k_r, k_s, \omega) = \sum_m H_{Qm}(\omega) B_m^{rs}(\omega). \tag{9}$$

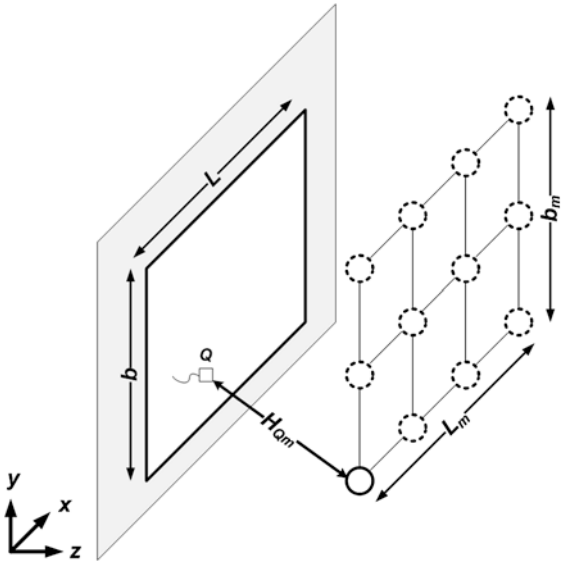

Fig. 4 Example of measurement of the transfer functions $H_{Qm}(\omega)$

2.4.3 Step 3: Reconstruction of TBL-Induced Vibrations

At this stage, the contribution of each wall-pressure plane wave are combined, by linear processing, to obtain the structural velocity ASD function from Eq. (6).

2.4.4 Summary of SST

In this section, SST is presented under a block diagram form to clearly distinguish measurement stages from numerical processing stages based on measured data (see Fig. 5).

The proposed block diagram shows that the use of a synthetic array requires two transfer functions measurements and numerical processings. Such a process

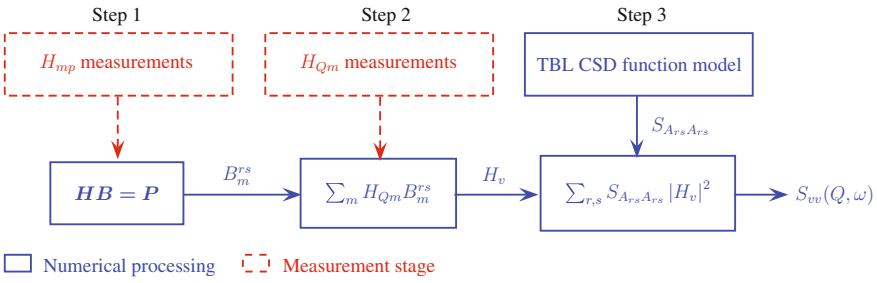

Fig. 5 Block diagram of the proposed experimental procedure

presents several advantages to assess TBL-induced vibrations. Firstly, a synthetic array allows not only a greater flexibility with respect to the number of monopoles, but also to avoid the scattering of the sound field on a dense set of sources involved into a physical array. Furthermore, only transfer function measurements are required. These two latter points are very interesting, since it is not necessary to control the amplitude and phase of several sources simultaneously. Furthermore, dispersions of sensor characteristics are avoided as are all the reference problems occurring when an array of sources is used.

Nevertheless, the sequential nature of the experimental process requires measurements to be made with care. Indeed, inaccuracies of source positioning can generate phase shift dispersions between two successive positions of the source. This problem can be easily managed by using a two-axis robot. Another issue is related to the variations of the set-up with time, since sequential measurements are quite lengthy. Consequently, the behaviour of the structure may change during the experiment, because of environmental variations for instance. To insure the consistency of measurements throughout the experiment, measurements have to be made in a stable environment to keep the linearity assumption valid.

3 Experimental Aspects

When analysing Eq. (6), it is obvious that the accuracy of the reconstruction of the structural velocity ASD function depends on two main criteria, namely the number of wall-pressure plane waves and the definition of the scanning grid.

3.1 Number of Wall-Pressure Plane Waves

3.1.1 Basic Principle

The numerical evaluation of the series given by Eq. (6) theoretically requires an infinite number of wavenumber couples (k_r, k_s). However, the structure acts as a wave-vector filter characterized by the transfer function H_v. This enables limiting the wavenumber couples to those mainly contributing to the structural response. Consequently, the structural velocity ASD function can be approximated from a finite number of uncorrelated wall-pressure plane waves. This, however, requires some knowledge about the structure under test to determine an optimal cut-off wavenumber allowing properly truncating the series given by Eq. (6).

A simple indicator for the practical choice of $\overline{k}$ can be derived from the analysis of the physical mechanisms governing the response of a plate excited by a TBL, such as the aerodynamic coincidence and the filtering effect of the structure.

For a flat plate with natural bending wavenumber k_f, immersed in a light fluid such as air, the aerodynamic coincidence associated with the filtering effect of the

structure on the TBL excitation allows explaining the physical mechanisms of the TBL-induced vibrations in a straightforward manner. In general, three configurations are observed. Indeed, for $k_c < k_f$, the resonant and non-resonant modes in aerodynamic coincidence of the plate are the main contributors to vibration response. For $k_c \approx k_f$, the number of resonant modes in aerodynamic coincidence is maximal [5]. In this case, these modes mainly contribute to the vibration response. Finally, for $k_c > k_f$, only the resonant modes have a significant contribution to the vibration response due to the filtering effect of the plate.

As a result, the wavenumbers (k_r, k_s) defining the wall-pressure plane waves can be restrained to those matching with the modes, that mainly contribute to the vibration response. Furthermore, this analysis implies a substantial reduction in the number of positions of the monopole-like source, since only the plane waves matching with the most important modes have to be reconstructed. However, the a priori determination of structural modes as well as natural wavenumber k_f can be a challenging task for industrial structures. For all these reasons, it is preferable to defined a simple but robust indicator to take into account all the physical mechanisms above-cited. Here, a practical choice of the cut-off wavenumber $\bar{k}$ is such that $\bar{k} > k_f$, where k_f is the natural wavenumber of the plate equivalent to the real structure. Based on this indicator, the set of wall-pressure plane waves is thus defined to satisfy $(k_r, k_s) \in \left[-\bar{k}, \bar{k}\right]^2$ with a prescribed wavenumber resolution $(\Delta k_r, \Delta k_s)$. Of course, to take advantage of the filtering effect of the structure on the excitation, it is necessary to have a good knowledge of the structure under test. In particular, this means that for industrial structures, such as multilayer or ribbed structures, the dynamic behaviour has to be studied carefully to properly identify the cut-off wavenumber.

3.1.2 Numerical Validation

To validate the reasoning presented in Sect. 3.1.1, the response of a simply supported steel plate immersed in air and subjected to a TBL excitation model by a Corcos model [16] is calculated using either the classical random vibration theory or the wall-plane wave expansion.

For the sake of completeness, it should be noted that the reference calculation was carried out using the discretized version of the velocity ASD function given by the random vibration theory, that is:

$$S_{vv}(Q,\omega) = \sum_{i,j} H_v^*(Q, M_i, \omega) S_{pp}(M_i, M_j, \omega) H_v(Q, M_j, \omega) \Delta M_i \Delta M_j, \tag{10}$$

where $S_{pp}(M_i, M_j, \omega)$ is the TBL CSD function, ΔM_i is the spatial resolution and $H_v(Q, M_i, \omega)$ is the transfer function corresponding to the structural velocity at point Q when the plate is excited by a point force at point M_i.

In the present case, the transfer function $H_v(Q, M_i, \omega)$ is computed analytically using the following mode expansion:

$$H_v(Q, M_i, \omega) = j\omega \sum_n \frac{\phi_n(Q)\phi_n(M_i)}{M_n\left(\omega_n^2 - \omega^2 + j\eta_n\omega\omega_n\right)}, \tag{11}$$

where M_n is the generalized mass, ω_n the natural frequency of the plate, ϕ_n the mode shape, η_n the modal damping.

Regarding the wall-plane wave expansion, the calculation of the velocity ASD function is derived from Eq. (6), in which the transfer function $H_v(Q, k_r, k_s, \omega)$ is written:

$$H_v(Q, k_r, k_s, \omega) = j\omega \sum_n \frac{P_n\phi_n(Q)}{M_n\left(\omega_n^2 - \omega^2 + j\eta_n\omega\omega_n\right)}, \tag{12}$$

where the generalized force P_n is given by the following equation:

$$P_n = \int_{S_p} \mathrm{e}^{jk_r x + jk_s y}\phi_n(P)\mathrm{d}S_p \approx \sum_p \mathrm{e}^{jk_r x_p + jk_s y_p}\phi_n^p \Delta S_p, \tag{13}$$

where ϕ_n^p is the mode shapes of the plate discretized over the p points and ΔS_p is a surface element.

The simulation parameters of the proposed numerical validation are given in Table 1.

The result presented in Fig. 6 shows a good agreement between the classical random vibration formulation and the wall-plane wave expansion and allows validating the selection process of the wall-plane waves explained in Sect. 3.1.1.

Table 1 Simulation parameters of the numerical validation

Parameters	Values
Length of the plate	0.6 m
Width of the plate	0.3 m
Thickness of the plate	5.10^{-3} m
Modal damping	$\eta_n = \eta = 1$ %
Number of grid points	231 (21 × 11)
Observation point	Q (0.2, 0.1 m)
Free stream velocity	$U_\infty = 50$ ms^{-1}
Longitudinal and lateral decay rates	$(\alpha_x, \alpha_y) = (0.116, 0.7)$
Maximal frequency studied	$f_{\max} = 250$ Hz
Cut-off wavenumber	$\overline{k} = 50$ ms^{-1}
Wavenumber resolution	$\Delta k_r = \Delta k_s = 1$ m^{-1}

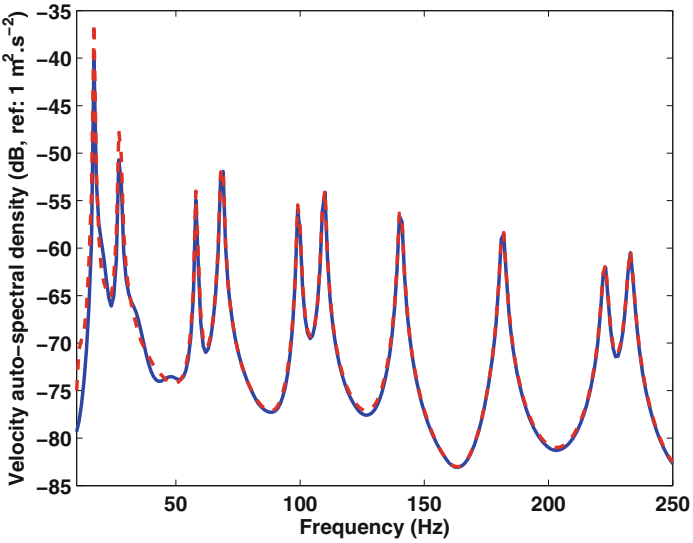

Fig. 6 Comparison of the structural velocity ASD function $S_{vv}(Q,\omega)$ at point Q (0.2, 0.1 m) computed by (*blue line*) the classical random vibration formulation (reference) and (*red line*) the wall plane-wave expansion

3.2 Definition of the Scanning Grid

Three main parameters are involved in the design of the scanning grid, namely the number of grid points, its dimension and its distance from the observation area.

From a numerical parametric study using parameters defined in Table 1 (see Ref. [12] for further details), it has been shown that the grid covered by the monopole source has to satisfy the following criteria:

- a minimum of 4 monopoles per wavelength $\overline{\lambda} = \frac{2\pi}{\overline{k}}$ is required to properly reconstruct a wall-pressure plane wave;
- the grid size has to be equal to or greater than the size of the observation area to ensure a good acoustic coverage of the observation area;
- the distance of the grid from the observation plane can be arbitrarily chosen in the interval $\left[\frac{\overline{\lambda}}{4}, 3\overline{\lambda}\right]$ to limit the condition number of the propagation operator H_{mp}.

When applying all the rules cited above, the reconstruction of a wall-pressure plane wave as well as that of the TBL CSD function modelled by the Corcos model are very satisfactory as illustrated in Figs. 7 and 8.

It should be noted that this pre-design parametric study has been performed by considering theoretical acoustic monopoles. In practice, monopole-like sources differ from theoretical ones, since the acoustic pressure field is not singular in the very near-field of the source. However, it has been pointed out that the source array

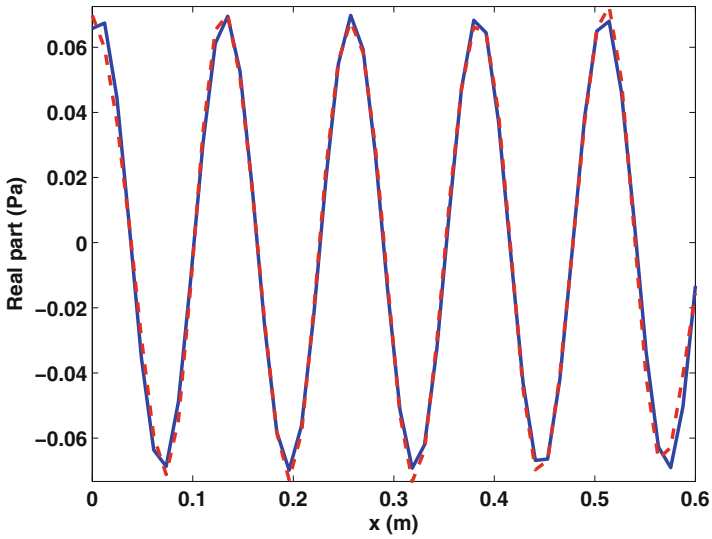

Fig. 7 Comparison between (*blue line*) the target wall-plane wave and (*red line*) the reconstructed wall-pressure plane using the design rules of the scanning grid for $(k_r, k_s) = (\overline{k}, \overline{k})$ at 250 Hz

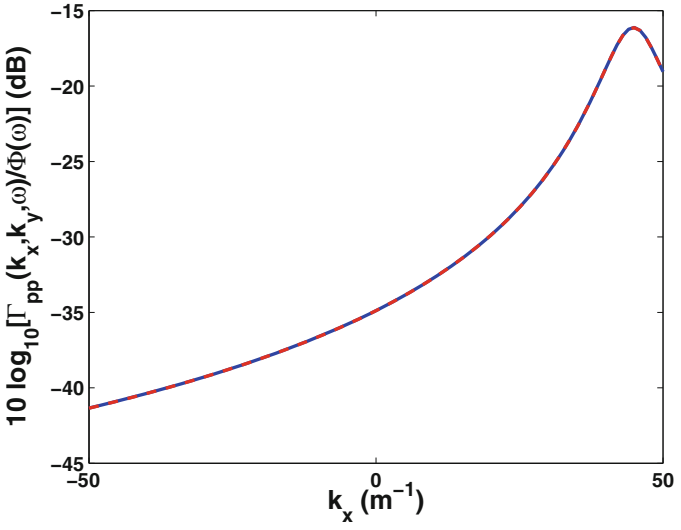

Fig. 8 Comparison between (*blue line*) the target TBL CSD function and (*red line*) the reconstructed TBL CSD using the design rules of the scanning grid in the plane $(k_x, 0)$ at 250 Hz

should not be too close to ensure a good acoustic coverage of the observation area. Consequently, one can reasonably expect that above results remain acceptable for real acoustic monopole-like sources, as will be shown in Sect. 4.

4 Experimental Validation

The aim of this experimental validation is to reproduce a wind measurement with the Source Scanning Technique. The wind tunnel measurement has been carried out by Totaro et al. [17] on a steel plate with dimensions $0.6 \times 0.3 \times 0.0005$ m^3 glued on its edges to a rigid baffle (see Fig. 9).

For this experiment, three quantities have been measured for a free stream velocity $U_\infty = 50$ ms^{-1}, namely:

- the correlation parameters $\alpha_1 = \frac{1}{\alpha_x}$ and $\alpha_2 = \frac{1}{\alpha_y}$ of the Corcos model (see Fig. 10):
- the TBL wall-pressure frequency spectrum $S_{pp}(\omega)$ required to scale the Corcos model (see Fig. 11):
- the structural velocity ASD function at 72 points (see Fig. 12):

Fig. 9 Wind tunnel measurement

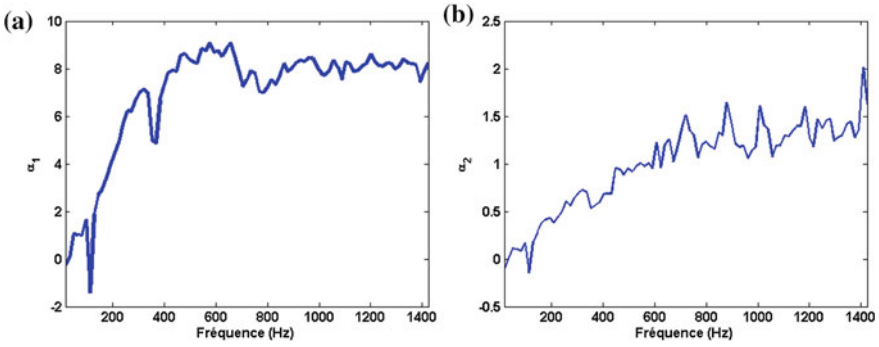

Fig. 10 Measurements of the the correlation parameters α_x and α_y of the Corcos model for $U_\infty = 50$ ms^{-1} **a** α_1 and **b** α_2, after Totaro et al. [17]

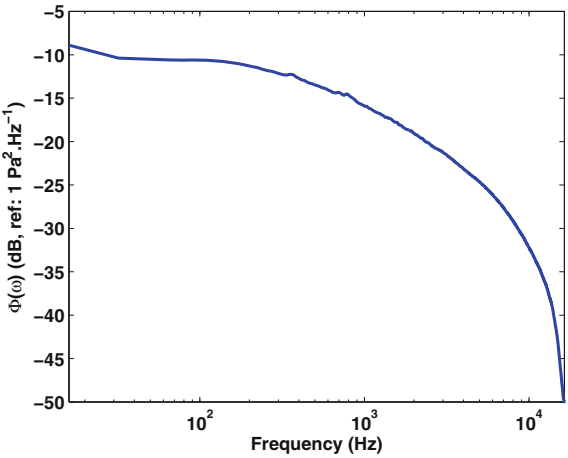

Fig. 11 TBL wall-pressure frequency spectrum measured in wind-tunnel for $U_\infty = 50\ \mathrm{ms}^{-1}$, after Totaro et al. [17]

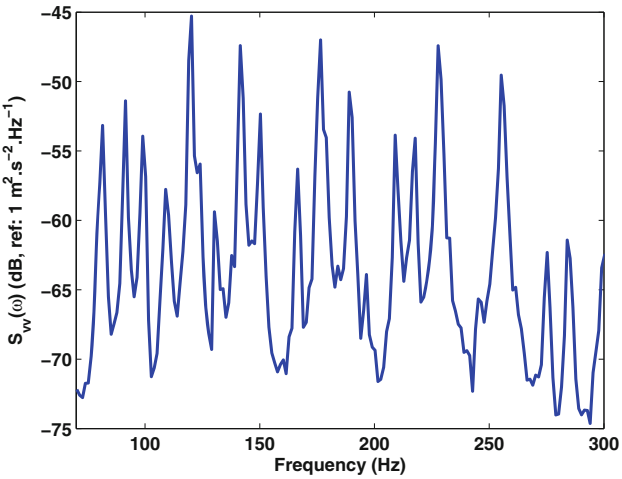

Fig. 12 Structural velocity ASD function at point $(x, y) = (0.22, 0.23\ \mathrm{m})$, after Totaro et al. [17]

4.1 Description of the Test Bench

As highlighted in Sect. 2.4, SST requires the measurement of two sets of transfer functions, namely H_{mp} and H_{Qm}, to derive the transfer function $H_v(Q, k_r, k_s, \omega)$ from Eq. (9). A schematic representation of the measurement process of H_{mp} and H_{Qm} has been proposed in Figs. 3 and 4.

From the practical point of view, the aim is to develop a test bench able to reproduce the measurement process of H_{mp} and H_{Qm} explained in Sect. 2.4.

4.1.1 Experimental Set-up for H_{mp} Measurements

The measurements of the transfer functions H_{mp} between the particle velocity of the monopole-like source at positions m and the pressure at positions p have been carried out in a sound-treated room by using a white-noise excitation and measuring the blocked pressure on a rigid wall, consisting of a thick wooden plate $1.02 \times 1.25 \times 0.036\,\mathrm{m}^3$, as presented in Fig. 13.

In this study, the excitation system consists in a monopole-like source, made with the help of a loudspeaker emitting noise through a tube, fixed to a two-axis robot, while the reception system is a near-field linear microphone array used to measure the blocked pressure over the rigid surface.

4.1.2 Experimental Set-up for H_{Qm} Measurements

The measurements of the transfer functions H_{Qm} have consisted in measuring the transfer function between the particle velocity of the monopole-like source and the structural velocity at an observation point Q located on the plate. To this end, an aperture of dimensions $0.6 \times 0.3\ \mathrm{m}^2$ has been made in the thick wooden plate used for H_{mp} measurements, above which the studied plate was glued to allow bending motions. Then, the measurements of the structural velocity of the plate excited by the monopole source at positions m have been performed with a lightweight 4 g accelerometer to limit the effect of the added mass of the sensor on the plate.

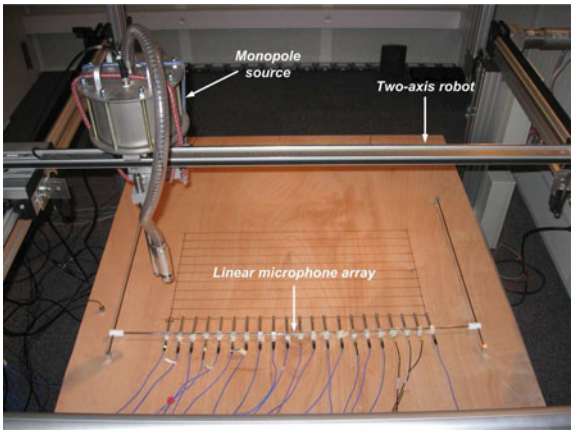

Fig. 13 Experimental set-up for measuring the transfer functions H_{mp}

4.2 Description of the Monopole-Like Source

As explained in Sect. 4.1.2, the monopole-like source is obtained from a loudspeaker emitting a white noise excitation through a tube, whose diameter is smaller than a third of the acoustic wavelength (see Fig. 14). The reference signal is measured by a velocity sensor fitted in a small nozzle mounted at the end of the tube, in order to take into account the standing waves existing in the tube. The inner diameter of the nozzle is 15 mm. Consequently, the upper frequency for a monopole-like behaviour of the source is much lower than 7.5 kHz.

To be considered as a monopole source, the physical source should have, in particular, an omnidirectional directivity pattern. This property of the source has been experimentally verified by measuring the acoustic pressure along two circumferences delimiting two orthogonal planes of a sphere of radius 30.5 cm. These measurements are presented in Fig. 15.

Finally, the monopole source being not an efficient radiator at low frequency, the lower bound of the measurement frequency range is related to the signal-to-noise ratio. Preliminary measurements showed that SNR was acceptable for frequencies above 70 Hz.

Fig. 14 Monopole-like source

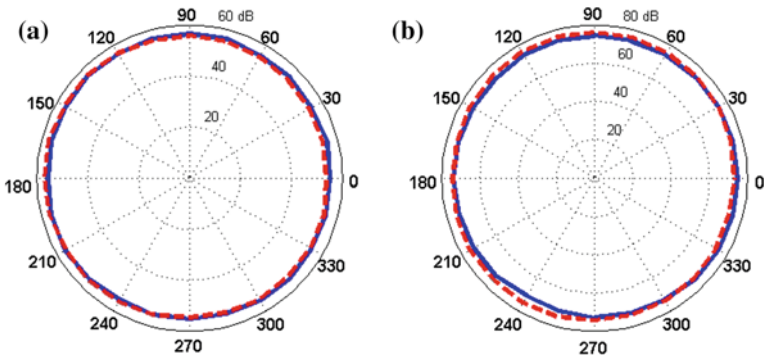

Fig. 15 Directivity pattern of the monopole-like source at **a** 125 Hz and **b** 2,000 Hz—(*blue line*) First plane and (*red line*) Second plane (perpendicular to the first plane)

4.3 Study of Measurement Biases

To properly analyse the experimental results presented in Sects. 4.4 and 4.6, it is important to study the possible measurement biases beforehand.

4.3.1 Screen Effect of the Baffle

As shown in Figs. 13 and 16, the dimensions of the baffle are finite. As a result, a part of the pressure emitted by the source on the upper face of the plate can be indirectly transmitted to the other face due to the diffraction of the pressure field on the edges of the baffle. That is why, it is worth ensuring that the pressure field measured on the hidden face of the plate is weak compared to the the one measured on the upper face in order to reproduce as accurately as possible the wind tunnel

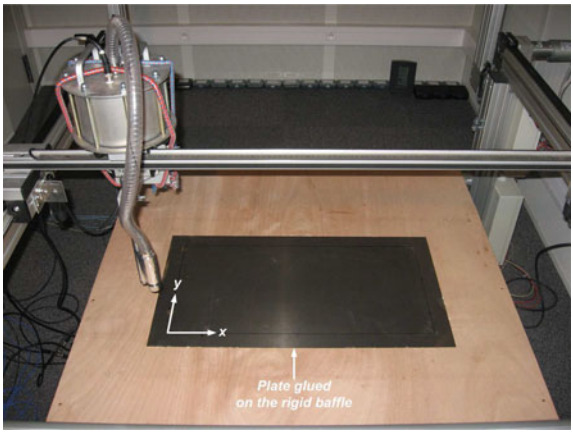

Fig. 16 Experimental set-up for measuring the transfer functions H_{Qm}

measurement. For this purpose, the pressure is measured on both sides of the baffle as illustrated in Fig. 17.

From there, an indicator E is defined as the difference of the pressure levels measured on both sides of the baffle, namely:

$$E = 20\log_{10}\left(\frac{|p_u|}{|p_h|}\right), \tag{14}$$

where p_u and p_h are respectively the acoustic pressure measured on the upper and hidden faces of the baffle.

Figure 18 presents the value of the indicator E with respect to frequency. It shows that the pressure on the hidden face of the baffle is at least 10 dB lower than the pressure measured on the upper face of the baffle. Consequently, the bias introduced by the finite dimensions of the baffle is negligible.

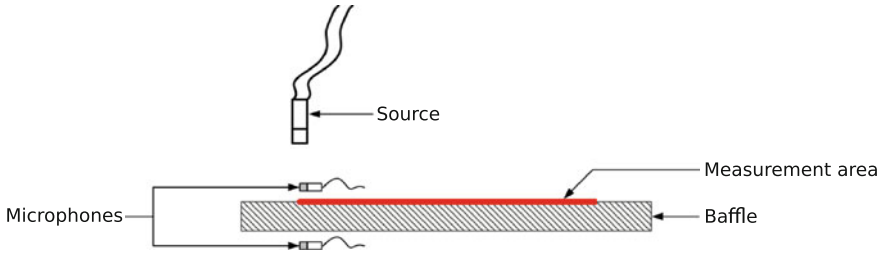

Fig. 17 Measurement of the screen effect of the baffle

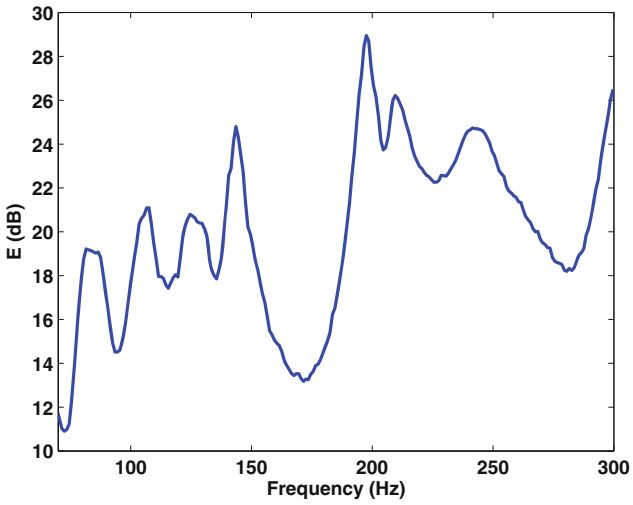

Fig. 18 Screen effect of the baffle

4.3.2 Baffle Rigidity

The rigidity of the baffle is an important parameter to ensure the validity of H_{Qm} measurements. Indeed, if the baffle and plate vibration levels are of the same order, then the boundary conditions of the plate will be altered. In the present paper, the baffle rigidity is evaluated by measuring the difference of the vibration levels at a point $A_1(0.22, 0.23\ \text{m})$ of the plate and a point $B_1(-0.08, 0.675\ \text{m})$ of the baffle (The coordinates of each point are defined in the frame of the plate presented in Fig. 4). Practically, vibration levels are measured using accelerometers. From there, an indicator E_v, defining the difference of the vibration levels, is derived as in Eq. (14).

Figure 19 presents the value of the indicator E_v with respect to frequency. This figure shows that the difference of the vibration levels ranges from 5 to 10 dB in average. Consequently, baffle vibrations are larger than expected. The direct consequence is an alteration of the boundary conditions of the plate since vibration energy is injected to the structure through the baffle. This can be a major bias when comparing SST with wind tunnel measurements.

4.3.3 Influence of the Accelerometers

The thickness of the plate under test being relatively low, the accelerometers used to measure the vibration field can modify its dynamic behaviour. Practically, only one accelerometer has been used. To assess the influence of this accelerometer on the dynamic behaviour of the plate, the input mobility Y_p of the studied plate equipped

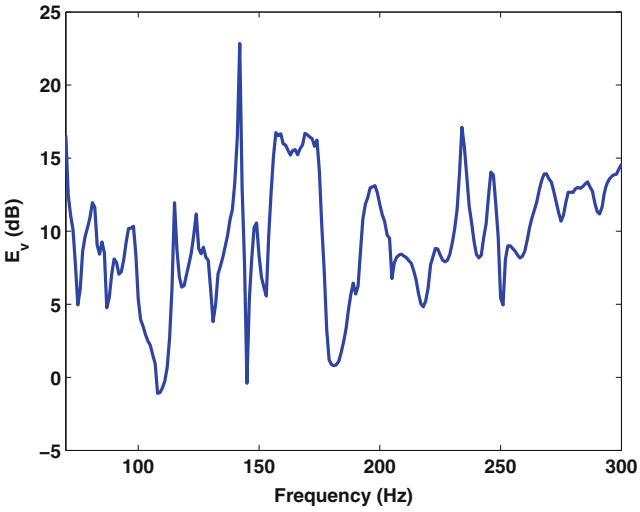

Fig. 19 Influence of the baffle rigidity

with a lightweight accelerometer (4 g) has been numerically computed from the following formula [18]:

$$Y_p = \widetilde{Y_p} \frac{Y_a}{Y_a + \widetilde{Y_p}}, \tag{15}$$

where $\widetilde{Y_p}$ is the input mobility of the plate alone and Y_m is the mobility of the accelerometer of mass m.

Equation (15) indicates that the eigen frequencies of the plate are modified by the presence of the accelerometer. The modified eigen frequencies can be obtained from the following equation:

$$\mathrm{Im}\left(\widetilde{Y_p}\right) = \mathrm{Im}(Y_a) = \frac{1}{m\omega}, \tag{16}$$

where $\mathrm{Im}(\widetilde{Y_p})$ is the imaginary part of $\widetilde{Y_p}$.

A graphical representation of the previous equation is proposed in Fig. 20. In particular, it shows that if the structure is lightly damped (which is the case here), then the presence of a sole accelerometer on the structure has almost no influence on the dynamic behaviour of the plate. As a consequence, the use of an unique accelerometer glued on the plate does not disturb the measurement of the transfer functions H_{Qm}.

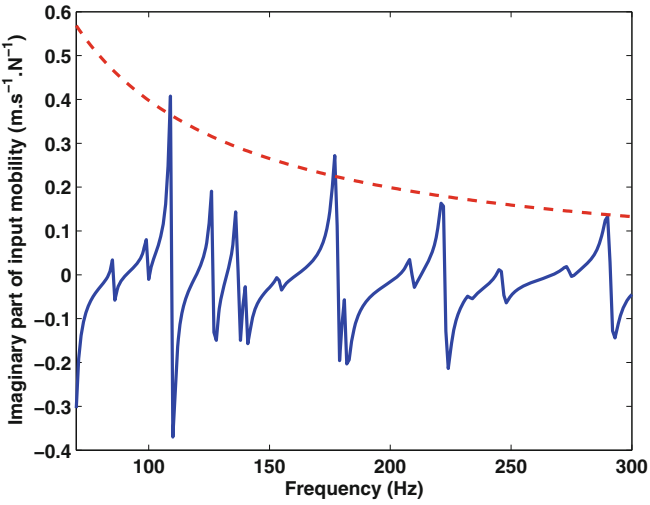

Fig. 20 Influence of the accelerometer mass on the eigen frequencies of the plate—(*blue line*) imaginary part of the input mobility $\widetilde{Y_p}$ of the plate alone and (*red line*) imaginary part of the accelerator's mobility Y_a

4.4 Reconstruction of Wall-Pressure Plane Waves

In this section, a wall-pressure plane wave of unit amplitude is compared to that reconstructed by using SST for two couples of wavenumbers $(k_r, k_s) = (4.5\ \mathrm{m}^{-1}, 4.5\ \ \mathrm{m}^{-1})$ and $(k_r, k_s) = (20\ \mathrm{m}^{-1}, 20\ \mathrm{m}^{-1})$.

Figure 21 presents, for both couples of wavenumbers, the comparison of the wall-pressure plane waves to be reconstructed and those reconstructed from SST at 250 Hz. This figure shows clearly that the amplitudes as well as the spatial variations of the wall-pressure plane waves are well reproduced. Consequently, this validates the experimental technique proposed for reconstructing wall-pressure plane waves.

4.5 Semi-analytical Validation of SST

In this section, a semi-analytical validation of SST is proposed. It consists in comparing the structural velocity ASD function at one point of simply supported plate calculated on the basis of the classical random vibration formulation given by Eq. (10) with that obtained from SST. The proposed validation is semi-analytical since the transfer functions H_{mp} are measured while the transfer functions H_{Qm} are computed using the following relation:

$$H_{Qm}(\omega) = j\omega \sum_n \frac{P_n^m \phi_n(Q)}{M_n\left(\omega_n^2 - \omega^2 + j\eta_n \omega \omega_n\right)}, \tag{17}$$

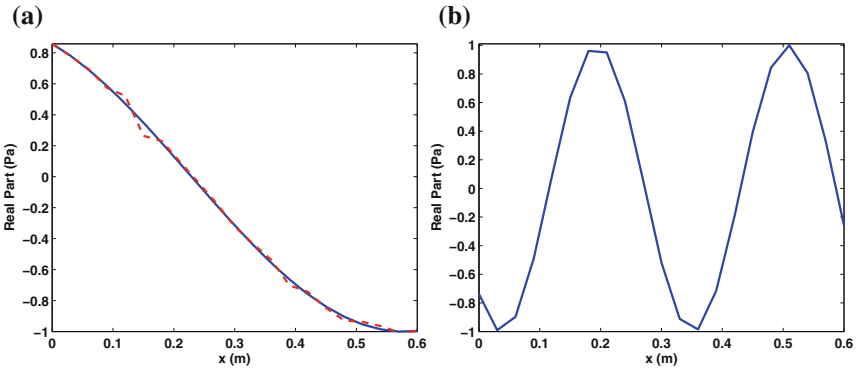

Fig. 21 Reconstruction of wall-pressure plane waves **a** for $(k_r, k_s) = (4.5\ \mathrm{m}^{-1}, 4.5\ \mathrm{m}^{-1})$ and **b** for $(k_r, k_s) = (20\ \mathrm{m}^{-1}, 20\ \mathrm{m}^{-1})$ in the plane $(x, 0.12\ \mathrm{m})$ at 250 Hz—(*blue line*) wall-pressure plane wave to be reconstructed (reference) and (*red line*) wall-pressure plane wave reconstructed by SST

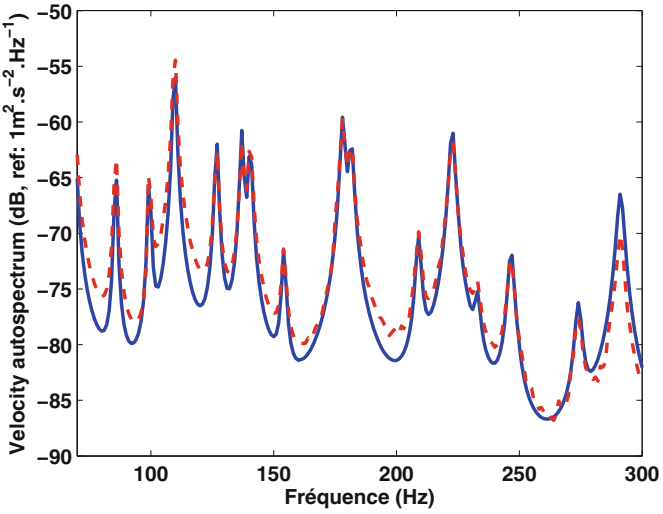

Fig. 22 Comparison of the structural velocity auto-spectral density function $S_{vv}(Q, \omega)$ at point Q (0.22, 0.23 m) computed by (*blue line*) the classical random vibration formulation (reference) and (*red line*) SST by using the measurements of H_{mp} and a semi-analytical calculation of H_{Qm}

where the generalized force P_n^m is written:

$$P_n^m \approx \sum_p H_{mp}(\omega)\phi_n^p \Delta S_p. \tag{18}$$

Figure 22 presents a comparison of the structural velocity ASD function at point Q (0.22, 0.23 m) of a $0.6 \times 0.3 \times 0.0005$ m^3 simply supported steel plate, obtained either from the classical random vibration formulation given by Eq. (10) or assessed by SST from Eqs. (6) and (9). As expected, good agreement between both results is observed, despite discrepancies of 3 dB in some frequency bands of low level, which is not crucial, since the vibration levels at the resonance frequencies are well estimated. Thus this result allows validating the experimental technique developed in this paper to characterize the vibrations induced by TBL.

4.6 Complete Experimental Validation

In the present section a complete experimental validation is proposed. This means that the measured transfer functions H_{mp} and H_{Qm} have been used to simulate the vibration response at one point of the plate from Eqs. (6)–(9). Considering the measurement biases detailed in Sect. 4.3, discrepancies between SST results and wind tunnel measurements are expected.

This is confirmed by Fig. 23 presenting a comparison of structural velocity ASD function at point A_1 measured in wind tunnel or reconstructed from SST. This

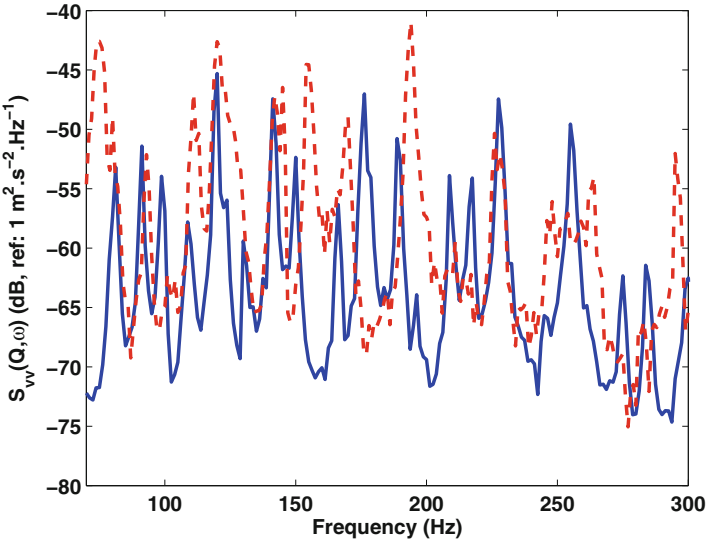

Fig. 23 Comparison of the structural velocity auto-spectral density function $S_{vv}(Q, \omega)$ at point Q (0.22, 0.23 m) (*blue line*) measured in wind tunnel and (*red line*) reconstructed using SST

comparison shows that the frequency content of the reconstructed ASD function differs from the measured one, while the range of variation of the ASD function is well described. The observed frequency discrepancy is mainly explained by the rigidity of the baffle which leads to an alteration of the boundary conditions as underlined in Sect. 4.3.2.

4.7 Versatility of SST

Numerous models are available in the literature to represent TBL wall-pressure fluctuations on a rigid plane. These models link wall-pressure fluctuations to the main features of the flow (convection velocity, boundary layer thickness). One of the main features of SST is its versatility with respect to the TBL excitation model $\Gamma_{pp}(k_r, k_s, \omega)$, since the technique proposed is based on discrete wave-vector integration models. Consequently, all the TBL models expressed in the wave-number-frequency space can be used. Furthermore, the comparison of these models can be carried out in a straightforward manner, since the introduction of TBL excitation is performed in the numerical stages by using Eqs. (6) and (9).

To demonstrate the ability of our experimental technique to deal with different TBL excitation models, the full implementation of SST is adopted, that is to say that measurements of H_{mp} and H_{Qm} are used to evaluate the TBL-induced vibrations of the steel plate defined previously.

Table 2 Turbulent flow parameters after Totaro et al. [17]

Parameters	Values
Convection velocity	$U_c = 35$ ms^{-1}
Friction velocity	$u_\tau = 1.96$ ms^{-1}
Boundary layer thickness	$\delta = 85$ mm
Displacement thickness	$\delta^* = 8.8$ mm
Momentum thickness	$\theta = 6.7$ mm
Wall shear stress	$\tau_w = 4.58$ Pa

In the following discussion, TBL models proposed by Corcos [16], Efimtsov [19], Chase [20] and Smol'yakov and Tkachenko [21] are compared for a fully developed turbulent flow whose parameters were measured in a wind tunnel by Totaro et al. [17] (see Table 2). Figure 24 presents the wavenumber-frequency spectrum predicted by the 4 models. For the sake of brevity, these models are not presented here, but detailed reviews and discussions about TBL models can be found in Refs. [22–24]. Finally, the parameters of the TBL models used in this article are those proposed by their authors, except for the Corcos model, whose parameters are defined from measurements presented in Fig. 10.

The comparison of the structural velocity ASD function $S_{vv}(Q, \omega)$ at point Q (0.22, 0.23 m) of the plate, evaluated from SST for the four TBL excitation models mentioned above, is presented in Fig. 25. Observation of these results brings to light the fact that they are clustered together within 6 dB at most throughout the frequency range, despite large differences of TBL wall-pressure spectra in the low-wavenumber region. These results are consistent with previous investigations into TBL-induced vibrations [24–26]. Indeed, plate bending waves are only excited by the TBL pressure components of the matching scales and, in the present case, the bending waves are predominantly excited by convective components, since the frequency range of interest is below the aerodynamic coincidence frequency (≈250 Hz) for the plate under consideration. Consequently, the differences observed in Fig. 25 can be explained for the most part by the modelling of the convective components in the four TBL models, as shown in Fig. 24.

5 Possible Implementation of SST in an Industrial Context

The test bench presented in Sect. 4 has been developed for validation purposes only and can not be used as it is in an industrial context. For industrial applications, a test bench could be developed for simulating the vibro-acoustic behaviour of multilayer structures submitted to a random excitation in a controlled environment.

As illustrated in Fig. 26, the proposed test bench is made up of two rooms separated by a concrete wall, in which an aperture is made for inserting the structure under test. The relatively small size of the synthetic array allows installing in

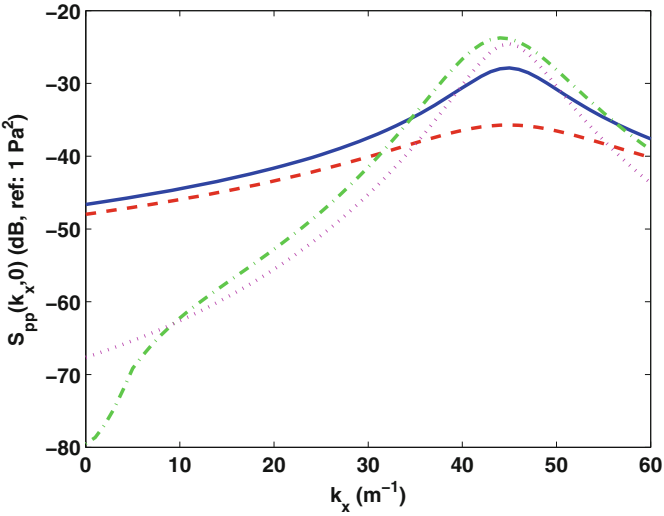

Fig. 24 Comparison of TBL wavenumber-frequency spectra at 250 Hz—(*blue line*) Corcos model, (*red line*) Efimtsov model, (*green line*) Chase model and (*red dots*) Smol'yakov and Tkachenko model

receiving and emission rooms climatic chambers for controlling temperature (typically in the range of −30 to +70 °C) and humidity (standard conditions). In this context, the size of the excitation device is one of the advantage of SST compared

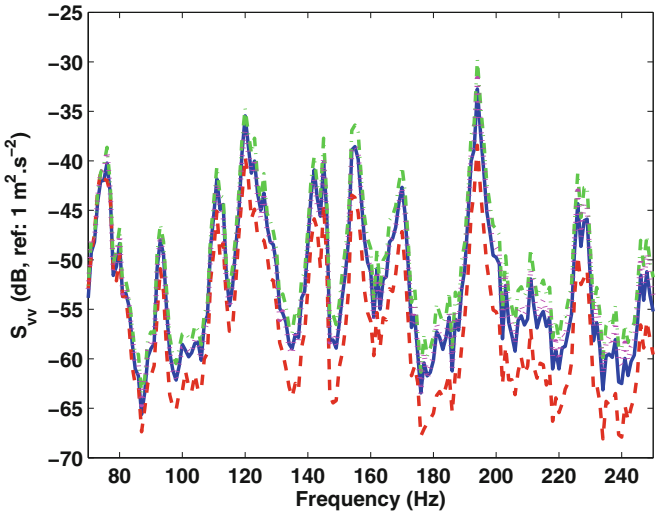

Fig. 25 Comparison of structural velocity auto-spectral density function $S_{vv}(Q,\omega)$ at point Q (0.22, 0.23 m) for various TBL excitation models—(*blue line*) Corcos model, (*red line*) Efimtsov model, (*green line*) Chase model and (*red dots*) Smol'yakov and Tkachenko model

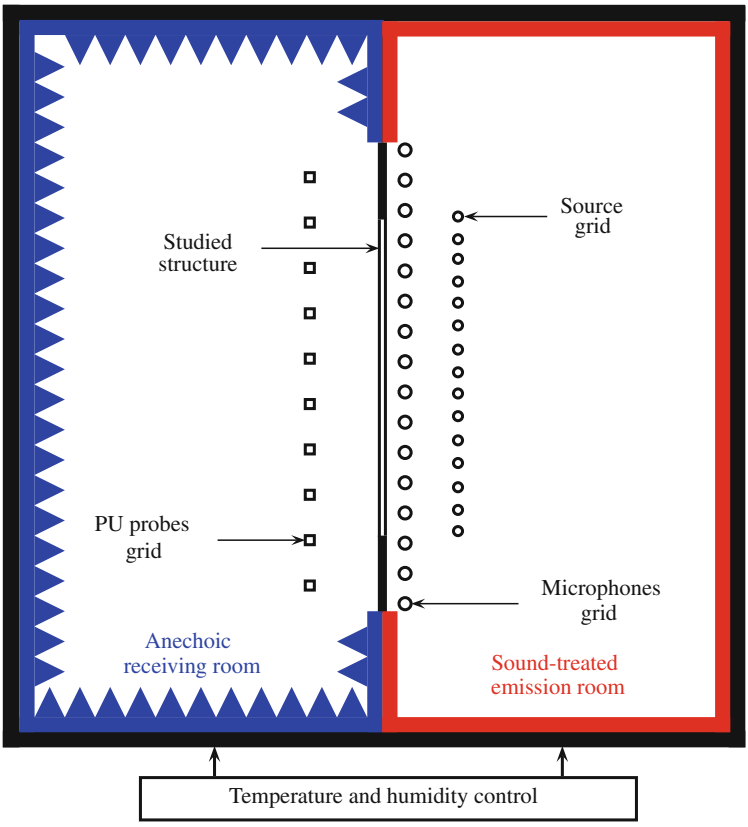

Fig. 26 Schematic representation of the proposed test bench

to reverberant rooms or wind tunnel for which temperature and humidity control can not be performed at low cost.

To properly perform acoustic transparency measurements, the receiving room should be anechoic, while the emission room should be sound-treated. This experimental facility allows performing two types of research:

- Studying the filtering effect of multilayer structures on the TBL excitation. Indeed, for industrial multilayer structures, the filtering effect is not well controlled, while it could be a means of designing such a structure to noise annoyance due TBL excitation. In this context, the test bench described above would help in analysing experimentally the filtering effect of the structure by studying the vibro-acoustic response of the structure to wall-pressure plane waves generated by the synthetic array;
- Studying the influence of climatic conditions on the transmission loss of structures subjected to random excitations. Such studies are relevant in an industrial context, since mechanical properties of numerous materials used in

industry (visco-elastic materials, rubber, etc.) depend on the temperature and hygrometric parameters. The variations of mechanical parameters with respect to environmental conditions play a central role in the vibro-acoustic behaviour of structures. However, because of the practical difficulty of maintaining temperature and humidity levels in a reverberant room or in a wind tunnel, the influence of environmental parameters is often neglected. From this particular standpoint, the proposed test bench would be an original experimental facility.

6 Conclusion

The Source Scanning Technique aims at simulating experimentally the response of structures excited by stationary random pressure fields, such as TBL excitation. It relies on the experimental simulation of a set of uncorrelated wall-pressure plane waves, whose amplitudes are scaled on the TBL CSD function expressed in the wavenumber space. From the practical point of view, the set of wall-pressure plane waves can be reconstructed using an array of acoustic monopoles. Nevertheless, such an approach can be intractable in practice because of the increase in the sources density with frequency. The key point of the proposed technique is the use of a synthetic array made up of a single acoustic monopole moved in space to replace the monopole array. By virtue of its sequential nature, SST allows a higher flexibility of the experimental set-up regarding the total number of monopoles required to suitably reconstruct wall-pressure plane waves. The counterpart of this sequential nature is the need of a precise source positioning to avoid phase shifts, as well as the need of a stable environment to avoid variations of the experimental set-up with time.

From these technical requirements, an experimental set-up was designed to validate the approach proposed under laboratory conditions. The results obtained on an academic structure show the method is capable of reconstructing wall-pressure plane waves and the structural velocity ASD function of a plate subjected to TBL excitation. Finally, the versatility of SST with respect to TBL excitation models has been highlighted.

In the future, SST could be used to develop a test bench for simulating the vibro-acoustic behaviour of multilayer structures submitted to a random excitation (e.g. diffuse sound field or TBL excitations) in a controlled environment (i.e. humidity and temperature).

References

1. W.V. Bhat, Flight test measurement of exterior turbulent boundary pressure fluctuations on Boeing 737 Airplane. J. Sound Vib. **14**(4), 439–457 (1971)
2. T.A. Galib, R.A. Katz, S.H. Ko, B. Sandman, Measurements of turbulent pressure fluctuations using a buoyant vehicle coated with a thin elastomer layer. J. Acoust. Soc. Am. **96**(6), 3800–3803 (1994)

3. S. Finnveden, F. Birgersson, U. Ross, T. Kremer, A model of wall pressure correlation for prediction of turbulence-induced vibration. J. Fluids Struct. **20**, 1127–1143 (2005)
4. F. Fahy, On simulating the transmission through structures of noise from turbulent boundary layer pressure fluctuations. J. Sound Vib. **3**(1), 57–81 (1966)
5. G. Robert, Modélisation et simulation du champ excitateur induit sur une structure par une couche limite turbulente (modelling and simulation of the induced exciting field on a structure by a turbulent boundary layer). Ph.D. thesis, Ecole Centrale de Lyon (1984)
6. S.J. Elliot, C. Maury, P. Gardonio, The synthesis of spatially correlated random pressure fields. J. Acoust. Soc. Am. **117**(3), 1186–1201 (2005)
7. T. Bravo, C. Maury, The experimental synthesis of random pressure fields: methodology. J. Acoust. Soc. Am. **120**(5), 2702–2711 (2006)
8. C. Maury, T. Bravo, The experimental synthesis of random pressure fields: practical feasibility. J. Acoust. Soc. Am. **120**(5), 2712–2723 (2006)
9. J. Audet, M. Lagier, P. Marin-Curtoud, T. Rohan, Turbulent boundary layer simulation setup on a sonar dome. J. Acoust. Soc. Am. **84**(S1), S118–S119 (1988)
10. O. Robin, A. Berry, S. Moreau, Reproduction of random pressure fields based on planar nearfield acoustic holography. J. Acoust. Soc. Am. **133**(6), 3885–3899 (2013)
11. M. Aucejo, Vibro-acoustique des stuctures immergées sour écoulement turbulent (vibro-acoustics of immersed structures subjected to turbulent flow). Ph.D. thesis, INSA de Lyon, France (2010)
12. M. Aucejo, L. Maxit, J.-L. Guyader, Experimental simulation of turbulent boundary layer induced vibrations by using a synthetic array. J. Sound Vib. **331**(16), 3824–3843 (2012)
13. A.D. Pierce, *Acoustics: An Introduction to Its Physical Principles and Applications* (Acoustical Society of America, New York, 1981)
14. A. Powell, *On the Response of Structures to Random Pressures an to Jet Noise In Particular,* ed. S.H. Crandall Random Vibration, vol. 1 (MIT Press, 1959), pp. 187–229
15. L.J. Cutrona, *Synthetic Aperture Radar*, ed. M.I. Skolnik, *Radar Handbook*, 2nd edn. (McGraw-Hill, 1990), pp. 21.1–21.23
16. G.M. Corcos, Resolution of pressure in turbulence. J. Acoust. Soc. Am. **35**(2), 192–199 (1963)
17. N. Totaro, G. Robert, J.-L. Guyader, Frequency averaged injected power under boundary layer excitation: an experimental validation. Acta Acustica United Acustica **94**(4), 534–547 (2008)
18. L. Cremer, M. Heckl, B.A.T. Petersson, *Structure Borne Sound: Structural Vibrations and Sound Radiation at Audio Frequencies*, 3rd edn. (Springer, Berlin, 2005)
19. B.M. Efimtsov, Characteristics of the field of turbulent wall pressure fluctuations at large Reynolds numbers. Sov. Phys. Acoustics **28**(4), 289–292 (1982)
20. D.M. Chase, The character of turbulent wall pressure spectrum at subconvective wavenumbers and a suggested comprehensive model. J. Sound Vib. **112**(1), 127–147 (1987)
21. A.V. Smol'yakov, V.M. Tkachenko, Model of a field of pseudosonic turbulent wall pressures and experimental data. Sov. Phys. Acoustics **37**(6), 627–631 (1991)
22. Y.F. Hwang, W.K. Bonness, S.A. Hambric, On modeling structural excitations by low speed turbulent boundary layer flows. Technical Report, Applied Research Laboratory, Pennstate University (2003)
23. M.K. Bull, Wall-pressure fluctuations beneath turbulent boundary layer: some reflections on forty years of research. J. Sound Vib. **190**(3), 299–315 (1996)
24. W.R. Graham, A comparison of models for the wavenumber-frequency spectrum of turbulent boundary layer pressures. J. Sound Vib. **206**(4), 541–565 (1997)
25. A.O. Borisyuk, V.T. Grinchenko, Vibration and noise generation by elastic elements excited by turbulent flow. J. Sound Vib. **204**(2), 213–237 (1997)
26. C. Maury, P. Gardonio, S.J. Elliott, A wavenumber approach to modelling the response of a randomly excited panel Part II: Application to aircraft panels excited by a turbulent boundary layer. J. Sound. Vib. **252**(1), 115–139 (2002)

Experimental Synthesis of Spatially-Correlated Pressure Fields for the Vibroacoustic Testing of Panels

Olivier Robin, Alain Berry and Stéphane Moreau

Abstract The problem of reproducing random pressure fiels on plane structures for the measurement of their vibroacoustic properties is investigated using different reproduction approaches and a synthetic array. The main application is the simulation of a Turbulent Boundary Layer excitation in a laboratory environment, as an alternative to in-flight or wind tunnel experiments. The reproduction of a repeatable and accurate Diffuse Acoustic Field which is of great practical importance is also studied. Most of the experimental results obtained with synthesized random pressure fields and compared with numerical and experimental reference data confirm the potential of the proposed strategies.

1 Introduction

A Turbulent Boundary Layer (TBL) can be produced by a fluid flow on the external structure of a vehicle moving at a sufficient speed, such as an aircraft fuselage or a ship hull. Corresponding wall pressure fluctuations will result in flow-induced loads that can generate vibration and also noise. These vibroacoustic excitations induced by the TBL are important or even main contributors to the interior noise of vehicles, and are of great importance for the aeronautical, automotive or naval industries (Fig. 1). More specifically, the experimental measurement or characterization of fuselage panels can be conducted in situ or in wind-tunnels, but such tests are highly complex and require expensive facilities. Therefore the vibroacoustic testing of such structures is usually done in Transmission Loss (TL) facilities under a Diffuse

O. Robin (✉) · A. Berry · S. Moreau
Université de Sherbrooke, Sherbrooke J1K2R1, Canada
e-mail: olivier.robin@usherbrooke.ca

A. Berry
e-mail: alain.berry@usherbrooke.ca

S. Moreau
e-mail: stephane.moreau@usherbrooke.ca

E. Ciappi et al. (eds.), *Flinovia - Flow Induced Noise and Vibration Issues and Aspects*, DOI 10.1007/978-3-319-09713-8_8

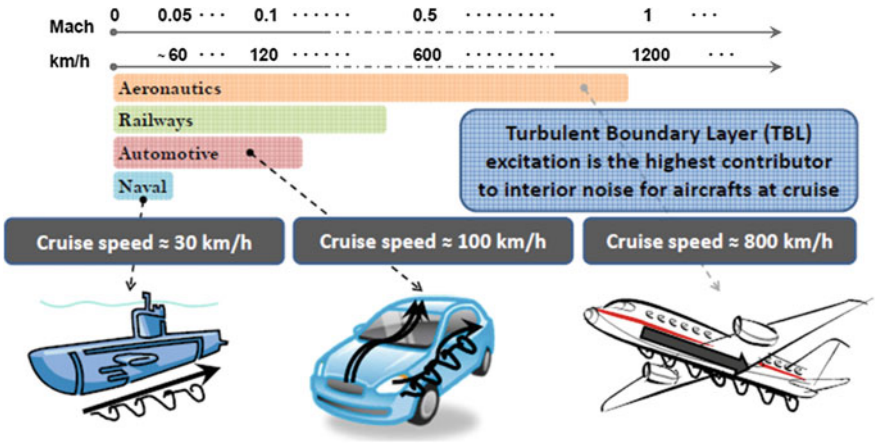

Fig. 1 Usual speed ranges and cruise speeds in aeronautical, railroad, automotive and naval transportation means

Acoustic Field (DAF) excitation (see Fig. 2), associated with lower cost and time but at the expense of using a non-representative pressure field. It is well documented that panels under a TBL excitation radiate less sound than under a DAF excitation for example [1–4]. The DAF produced in reverberant rooms is also rarely close to its theoretical definition and high variability can be seen between different test facilities [5, 6].

The first objective in this research project is to achieve accurate and repeatable reproduction of spatially correlated pressure fields, corresponding to either a DAF or a TBL, in a laboratory-like environment and using an antenna of acoustic sources. The question is then the following: 'how to drive an array of sources to achieve specific target spatial correlations on a parallel plane surface?' Three different approaches are used to deduce the Cross-Spectral Density (CSD) of particle

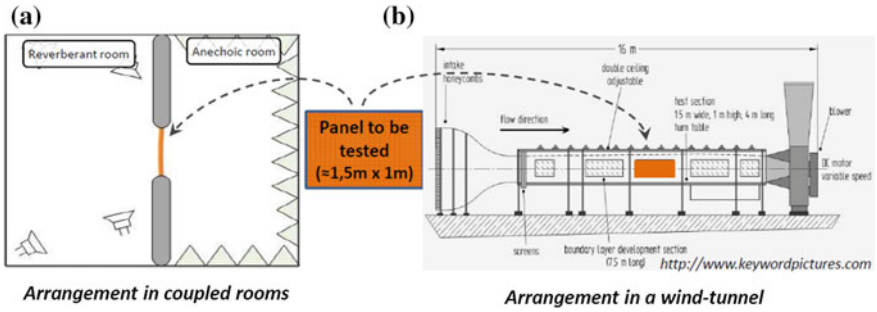

Fig. 2 **a** Usual arrangement of a panel in coupled rooms for Transmission Loss measurement under a diffuse acoustic field excitation. **b** Usual arrangement of a panel in a wind-tunnel for vibroacoustic measurements under a turbulent boundary layer excitation

velocity to be imposed to the reproduction sources distributed on a surface facing the reproduction plane (i.e. a panel to be tested), so that a target pressure CSD would be reproduced on this plane. A Least Squares approach is proposed as the first method, while the two others are based on sound field reproduction techniques, namely Wave Field Synthesis [7, 8] (WFS) and Planar Nearfield Acoustic Holography [9, 10] (P-NAH). Numerical simulations help defining adequate source spatial sampling and plane separations to reproduce the target correlation scales of a DAF or a TBL.

The second objective is to apply these reproduction strategies to vibroacoustic testing of panels, and verify their experimental feasibility using the synthetic array concept [11]. To test the three proposed methods, a series of experiments have been performed in hemi-anechoic conditions. The synthesis of a DAF and a TBL, either subsonic or supersonic, has been first tested on a small aluminum panel. Experimental synthetic TL results are compared with numerical calculations, because practical measurements are highly difficult to obtain for both excitations. The reproduction of a DAF has also been tested on a composite panel, representative of fuselage structures, and compared with the experimental TL results obtained with a coupled rooms facility.

This paper is organized as follows: The theoretical CSD functions used for the description of the DAF and TBL pressure fields are given in Sect. 2. The three reproduction approaches are described in Sect. 3, and results of numerical simulations for the P-NAH case are reported in Sect. 4. Validation of experimental conditions and the reconstruction approach using a synthetic array are thoroughly described in Sect. 5, and results of experiments conducted on a small aluminum panel and a large composite panel are given in Sects. 6 and 7, respectively. The main results of the paper are summarized in the conclusion.

2 Cross-Spectral Density Functions of Target Pressure Fields

Figure 3 describes the general problem to be solved here. Starting with a target pressure Cross-Spectral Density (CSD) function that is defined in plane S_1 (the reproduction plane), the goal is to calculate the source volume accelerations CSD function in plane S_2 (the source plane) so that the target CSD would be reproduced on the reproduction plane. Finally, $\mathbf{r_1}$ and $\mathbf{r_1'}$ are the position vectors of two different points belonging to plane S_1 (subscript 2 is used for points on plane S_2). The symbols S_1 and S_2 will equally denote the considered plane and its area.

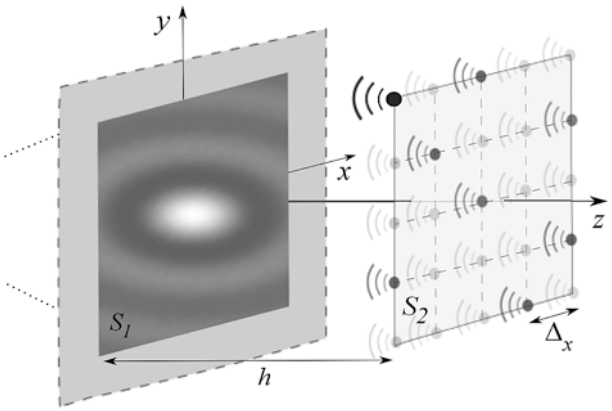

Fig. 3 Description of the coordinate system, with the reproduction plane S_1 and source plane S_2 (plane separation distance h and source separation in the x-direction Δ_x are indicated)

2.1 Diffuse Acoustic Field

The CSD of a DAF can be written [12, 13]

$$S_{pp}(\mathbf{r_1}, \mathbf{r'_1}; \omega) = S_{pp}(\omega) \frac{\sin k_0 |\mathbf{r_1} - \mathbf{r'_1}|}{k_0 |\mathbf{r_1} - \mathbf{r'_1}|}. \tag{1}$$

The corresponding wavenumber-frequency spectrum is expressed as [13]

$$S_{pp}(\mathbf{k}; \omega) = \begin{cases} \frac{S_{pp}(\omega)}{2\pi k_0^2} \frac{1}{\sqrt{1-(|\mathbf{k}|/k_0)^2}} & \text{if} \quad |\mathbf{k}| < k_0, \\ 0 & \text{if} \quad |\mathbf{k}| > k_0, \end{cases} \tag{2}$$

where $|\mathbf{k}| = \sqrt{k_x^2 + k_y^2}$, k_0 is the acoustic wavenumber ($= \omega/c_0$) and the auto-spectrum $S_{pp}(\omega)$ is considered here unitary. Theoretically, DAF corresponds to the summation of uncorrelated acoustic plane waves propagating at the speed of sound c_0 and equally distributed in space at a given frequency.

2.2 Turbulent Boundary Layer

As for a DAF, the wall pressure fluctuations related to TBL excitation can be theoretically described by a summation of uncorrelated plane waves [11]. The simple empirical model of Corcos [14] corresponding to a fully developed TBL without pressure gradient is used here, and its CSD is given by the relation

$$S_{pp}(\mathbf{r_1}, \mathbf{r'_1}; \omega) = S_{pp}(\omega) \mathrm{e}^{-\frac{\omega|\xi_{x_1}|}{\alpha U_c}} \mathrm{e}^{-\frac{\omega|\xi_{y_1}|}{\beta U_c}} \mathrm{e}^{j\frac{\omega(\xi_{x_1})}{U_c}}, \tag{3}$$

where $S_{pp}(\omega)$ is the autospectrum of the pressure field (supposed unitary as for DAF), U_c the convection speed, $\xi_{x_1} = x_1 - x'_1$ and $\xi_{y_1} = y_1 - y'_1$ are longitudinal and transverse separations respectively. The coefficients α et β describe spatial correlation decays in the streamwise and crosswise directions respectively (here, $\alpha = 8$ and $\beta = 1.2$). The convection speed U_c will be assumed to be constant with respect to frequency and is given by $U_c = 0.7U_\infty$ (with U_∞ the free stream velocity), and the convective wavenumer k_c equals ω/U_c. The wavenumber-frequency spectrum of the Corcos model is

$$S_{pp}(k_x, k_y, \omega) = S_{pp}(\omega) \frac{\alpha\beta}{\left[1 + \alpha^2\left(1 - \frac{k_x}{k_c}\right)^2\right]\left[1 + \beta^2\left(\frac{k_y}{k_c}\right)^2\right]}. \tag{4}$$

Figure 4 compares the CSD of a DAF and a subsonic TBL (with $U_\infty = 300$ m/s) in the spatial and in the wavenumber domain. The two pressure fields to be reproduced have spatial scales and wavenumber contents that differ significantly,

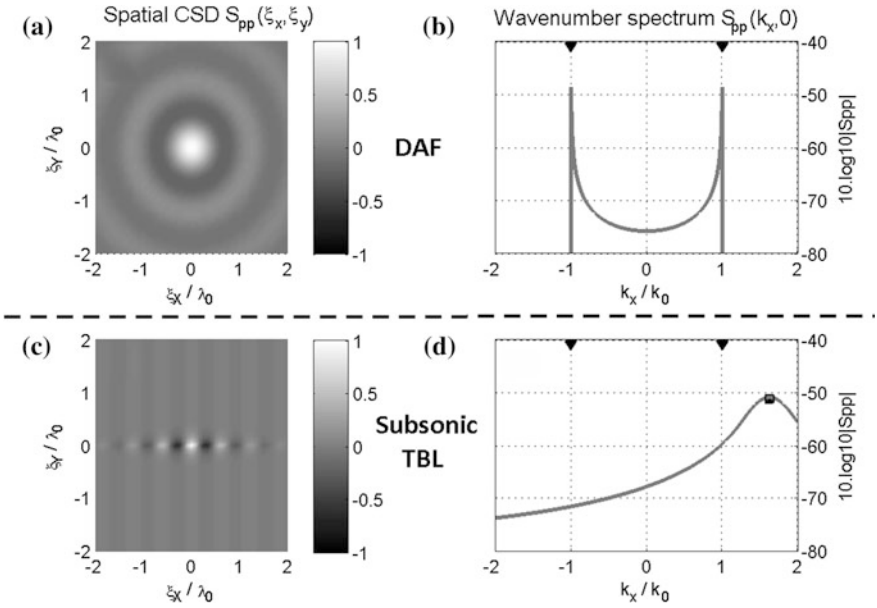

Fig. 4 **a**, **c** Real part of the spatial CSD for DAF (Eq. 1) and subsonic TBL (Eq. 3) respectively, with separations normalized by the acoustic wavelength λ_0. **b**, **d** Absolute value of the wavenumber spectrum $|S_{pp}(k_x, 0)|$ for DAF (Eq. 2) and subsonic TBL (Eq. 4) respectively, with wavenumbers normalized by the acoustic wavenumber k_0. *Down triangles* indicate the limit of the dimensionless acoustic domain, and the *black square* gives the dimensionless convective wavenumber k_c/k_0

since the subsonic TBL includes subwavelength components (mainly corresponding to the convective wavelength, which is significantly smaller than the acoustic wavelength) and evanescent or non-acoustic wavenumbers (higher than the acoustic wavenumber, typically the convective wavenumber k_c). In the case of a supersonic TBL (not illustrated), the spatial scales are comparable to those of a DAF.

3 Calculating the Reproduction Sources Complex Amplitudes

3.1 Least Squares Approach

The Least Squares (LS) method has been widely used for the reconstruction of acoustic sources strengths using a set of acoustic pressure measurements on an array of sensors [15], or for the calculation of reproduction source strengths (or source acceleration, the derivative of the source strength) for the reproduction of an acoustic plane wave [16]. In the case of the reproduction of random pressure fields, LS method has been used by Bravo and Maury [17] and Aucejo et al. [11], to derive an optimum matrix of control filters or to calculate the vector of reproduction monopoles amplitudes, respectively. The complex vector of the target sound pressure field $\mathbf{p}$ at N points of the panel is written $\mathbf{p} = [p_1 \ldots p_N]^T$, and the vector $\dot{\mathbf{q}}$ of the complex volume accelerations to be applied to the M reproduction sources is $\dot{\mathbf{q}} = [\dot{q}_1 \ldots \dot{q}_M]^T$. The matrix G is the matrix of the theoretical Green's functions in semi-infinite space between each of the N reproduction points on the reproduction surface and the M reproduction sources. The relation between the vector of wall pressures and the vector of complex source amplitudes can be written [16]

$$\mathbf{p}(\omega) = \rho_0 \mathbf{G}(\omega)\dot{\mathbf{q}}(\omega), \tag{5}$$

where ρ_0 is the air mass density. The optimal vector of source accelerations for the reproduction of the sound pressure field $\mathbf{p}$, the solution of the LS problem, is

$$\dot{\mathbf{q}}(\omega) = \frac{1}{\rho_0}\mathbf{G}^{+}(\omega)\mathbf{p}(\omega), \tag{6}$$

where $^+$ denotes the pseudoinverse of a matrix. The extension of the least squares approach to random pressure fields leads to the relationship

$$\mathbf{S}_{\dot{q}\dot{q}}^{\mathrm{LS}}(\omega) = \frac{1}{\rho_0^2}\mathbf{G}^{+}(\omega)\mathbf{S}_{pp}(\omega)\mathbf{G}^{+H}(\omega), \tag{7}$$

with ^{H} denoting the conjugate transpose (see Robin et al. [18] for details). The accuracy of the source strengths calculation is highly dependent on the conditioning

of the matrix **G** to be inverted [15] (this conditioning depends on the separation distance between the source and the reproduction plane, of their relative sizes and geometries), and on the chosen target pressure field. A regularization of this inverse problem will be needed in some cases, and the Singular Value Decomposition (SVD) of the matrix **G** is thus introduced, and given by

$$\mathbf{G} = \mathbf{U}\Sigma\mathbf{V}^H, \tag{8}$$

where **U** and **V** are unitary matrices ($\mathbf{U}^H\mathbf{U} = \mathbf{V}^H\mathbf{V} = \mathbf{I}$), and Σ is a diagonal matrix which contains the singular values σ_i (ordered in decreasing order). The solution given by Eq. (7) can be written in terms of the SVD of the matrix **G**

$$\mathbf{S}_{\dot{q}\dot{q}}^{\mathrm{LS}}(\omega) = \frac{1}{\rho_0^2}\{\mathbf{V}\Sigma^{+}\mathbf{U}^H\}(\omega)\mathbf{S}_{pp}(\omega)\{\mathbf{U}\Sigma^{+H}\mathbf{V}^H\}(\omega). \tag{9}$$

Even though the matrix **G** is not rank deficient, the chosen direct regularization method is the truncated SVD because of its simplicity [19]. This method involves the cancellation of the singular values σ_i below a threshold value, calculated at each frequency and defined as a percentage $\%_{\mathrm{reg}}$ of the maximum (or first) singular value (i.e. $\sigma_i = 0$ for $\sigma_i < \sigma_{\max} \times \%_{\mathrm{reg}}$).

3.2 Wave Field Synthesis Approach

The Wave Field Synthesis (WFS), a sound field reproduction technique based on Huygens' principle, has been developed in the 1990s by Berkhout et al. [7]. The WFS formulation has been recently extended to the reproduction of spatially correlated sound fields [8]. Equation (10) below is the fundamental relation providing the auto and cross-spectral density of particle velocity of reproduction sources (see [8] for details)

$$\mathbf{S}_{vv}^{\mathrm{WFS}}(\omega) = \frac{1}{\rho_0^2\omega^2}\left(\frac{S_1}{N}\right)^2\mathbf{A}^H\mathbf{S}_{pp}(\omega)\mathbf{A}, \tag{10}$$

where $\mathbf{S}_{vv}(\omega)$ is the CSD matrix of the reproduction source velocities, **A** is a propagation matrix and S_1 and S_2 are the reproduction and source areas, respectively (see Fig. 3).

Using Eq. (10) and writing $\dot{q} = -j\omega q = -j\omega(S_2/M)v$, the corresponding CSD matrix of source volume accelerations is simply obtained using the relation

$$\mathbf{S}_{\dot{q}\dot{q}}^{\mathrm{WFS}}(\omega) = \frac{1}{\rho_0^2}\left(\frac{S_2}{M}\right)^2\left(\frac{S_1}{N}\right)^2\mathbf{A}^H\mathbf{S}_{pp}(\omega)\mathbf{A}. \tag{11}$$

Numerical simulations have shown than even if this method can not reconstruct the small wavelengths corresponding to a subsonic TBL wall pressure excitation (the convective part of this excitation), it is well adapted to the reproduction of the acoustic part of any target pressure CSD [8]. Berry et al. have also shown that the size of the reproduction plane is an important parameter for the minimization of the reproduction error when propagating the target pressure field from the reproduction plane S_1 to the source plane S_2. The reproduction error is greatly reduced when S_1 is increased (for the same size of the source plane S_2). A virtual reproduction surface of n_{WFS} times the (x, y) dimensions of the real reproduction plane (the panel) is used for the calculation of the sources CSD with this approach (with $n_{\mathrm{WFS}} = 3$ for the 25 sources array and $n_{\mathrm{WFS}} = 5$ for the 110 sources array).

3.3 Holographic Approach

Nearfield Acoustical Holography (NAH) is widely used as a measurement technique for the prediction of acoustical quantities on a surface, using acoustical quantities generally measured on a parallel surface [9], but rarely used as a sound field reproduction technique. The fundamental relations of Planar-NAH are used here to propagate a target pressure distribution from the reproduction plane S_1 to the source plane S_2, and to derive the particle velocity to be imposed to acoustic sources distributed on S_2. For given discrete separations ξ_x and ξ_y between any arbitrary two points in the source plane, the CSD of particle velocity to be imposed to acoustic sources is given by the relation [10]

$$S_{vv}(\xi_x, \xi_y; \omega) = \sum_m \sum_n (S_{pp}(k_m, k_n; \omega) \left(\frac{|k_{z_{mn}}|}{\rho_0 \omega}\right)^2 |\mathrm{e}^{jk_{z_{mn}}h}|^2) \times \mathrm{e}^{jk_m\xi_x}\mathrm{e}^{jk_n\xi_y} \frac{\Delta k_m \Delta k_n}{4\pi^2}, \tag{12}$$

with h the planes separation distance, k_m and k_n the discrete wavenumbers in the x and y directions, and $k_{z_{mn}}$ the discrete wavenumber in the z direction, estimated using $k_{z_{mn}} = \sqrt{k_0^2 - k_m^2 - k_n^2}$. The CSD matrix of the source volume accelerations is obtained using the relation

$$S_{\dot{q}\dot{q}}^{\mathrm{Holo}}(\omega) = \omega^2 \left(\frac{S_2}{M}\right)^2 \sum_m \sum_n (S_{pp}(k_m, k_n; \omega) \left(\frac{|k_{z_{mn}}|}{\rho_0 \omega}\right)^2 |\mathrm{e}^{jk_{z_{mn}}h}|^2) \times \mathrm{e}^{jk_m\xi_x}\mathrm{e}^{jk_n\xi_y} \frac{\Delta k_m \Delta k_n}{4\pi^2}. \tag{13}$$

Similarly to the WFS approach, the acoustic component of a target wall pressure distribution can be well reproduced with the P-NAH approach, which leads to adequate reproduction of DAF and supersonic TBL. This wavenumber-based

formulation seems also suitable for the reproduction of the convective components of a subsonic TBL, as was shown from simulations using a nearfield and dense array of reproduction sources [10]. The use of a backpropagation scheme was also suggested to improve the reproduction of sub-wavelength, i.e. convective components. This backpropagation operation simply involves the inversion of the propagation direction, i.e. a sign change in the complex exponential of Eq. (13). In order to avoid an uncontrolled amplification of the non-acoustic components, a wavenumber filtering operation is needed, similar to the truncated SVD operation in the LS problem, both consisting in the limitation or elimination of contributions to the solution that lead to non-physical solutions [15].

The regularization window, a low pass wavenumber filter defined by a cut-off wavenumber $k_{\text{cut-off}}$ and a parameter α_{reg} which controls the decay rate past $k_{\text{cut-off}}$, is directly inspired from those widely used in classical NAH problems [9]. As an example, when dealing with a set of noisy pressure measurements on a plane to reconstruct source amplitudes and distribution on a parallel plane, those two regularization parameters are usually defined by trial and error [20]. The main difference in the present situation is that we have an a priori knowledge of the cut-off wavenumber and the decay, which are simply defined by the convective wavenumber k_c and the decreasing slope of the convective peak above the convective wavenumber, both defined by the chosen TBL model. Note also that we rely on theoretical target CSDs, which means that we are only concerned with potential numerical noise.

As in Williams [9], the window is defined by (see Robin et al. [18])

$$\text{Reg}_{\text{window}}(\mathbf{k};\omega) = \begin{cases} 1 - \frac{1}{2}\exp^{-(1-|\mathbf{k}|/k_c)/\alpha_{\text{reg}}} & \text{if} \quad |\mathbf{k}| \leq k_c, \\ \frac{1}{2}\exp^{(1-|\mathbf{k}|/k_c)/\alpha_{\text{reg}}} & \text{if} \quad |\mathbf{k}| > k_c. \end{cases} \tag{14}$$

Equation (13) can now be rewritten using this window and under a backpropagation assumption

$$\begin{aligned} \mathbf{S}^{\text{Holo}}_{\dot{q}\dot{q}}(\omega) = \omega^2 \left(\frac{S_2}{M}\right)^2 \sum_m \sum_n (S_{pp}(k_m, k_n; \omega) \left(\frac{|k_{z_{mn}}|}{\rho_0 \omega}\right)^2 |\mathrm{e}^{-jk_{z_{mn}}h}|^2 \\ \times |\text{Reg}_{\text{window}}(k_m, k_n; \omega)|^2) \mathrm{e}^{jk_m\xi_x} \mathrm{e}^{jk_n\xi_y} \frac{\Delta k_m \Delta k_n}{4\pi^2}. \end{aligned} \tag{15}$$

4 Numerical Simulations for the P-NAH Case

The simulations results presented in this section are obtained with reproduction and sources planes of identical dimensions ($[-3\lambda_0 : 3\lambda_0] \times [-3\lambda_0 : 3\lambda_0]$), separated by a distance $h = \lambda_0$ (other plane separations are presented for the DAF case). The spatial sampling for the source plane is $\lambda_0/2$, this value of two acoustic sources per acoustic wavelength normally preventing spatial aliasing in the acoustic domain [7].

In the following figures, the target pressure field is always indicated with a bold grey line, whereas the reproduced pressure field is illustrated with a thin black line. For a better visualization of spatial results, scales are adjusted and given on the left y-axis for the target CSD, and on the right y-axis for the reproduced CSD. The presented results are all obtained with the P-NAH approach. Specific results for the WFS approach can be found in [8].

4.1 Diffuse Acoustic Field Reproduction

Figure 5a compares the real part of the DAF target CSD and reproduced CSD, with a spatial structure clearly well reproduced compared to the target, but with slightly smaller amplitudes. The results in Fig. 5b show that the reproduction of grazing plane waves (i.e. waves with wavenumber close to $\pm k_0$) requires that source and reproduction planes are not too much spaced compared to their respective sizes. As the planes separation h increases (keeping planes dimensions unchanged), the reproduced wavenumber content narrows because it becomes physically impossible to reproduce waves with grazing incidences and thus wavenumber values close to k_0 (with the consequence that reproduced field amplitudes become smaller). Obviously, a source plane smaller than the reproduction plane will also prevent the reproduction of grazing plane waves.

4.2 Supersonic and Subsonic TBL Reproduction

Results for the reproduction of a supersonic TBL are given in Fig. 6. In the streamwise direction, correlation scales are correctly reproduced (with a maximal

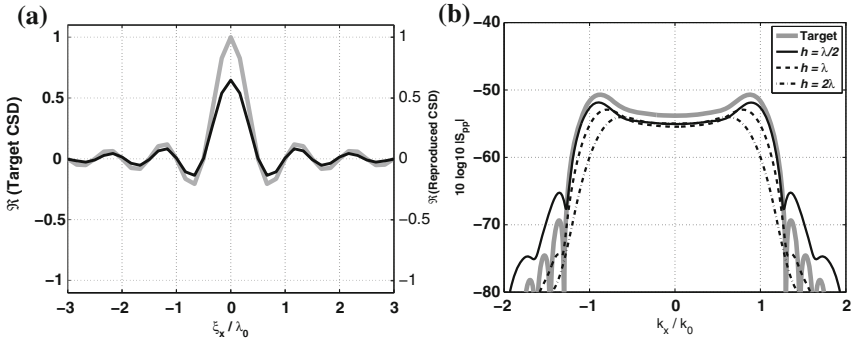

Fig. 5 Reproduction of DAF. **a** Target CSD and reproduced CSD in the $(\xi_x, 0)$ plane. **b** Target CSD wavenumber-spectrum and reproduced CSD wavenumber spectrum in the $(k_x, 0)$ plane for various plane separations

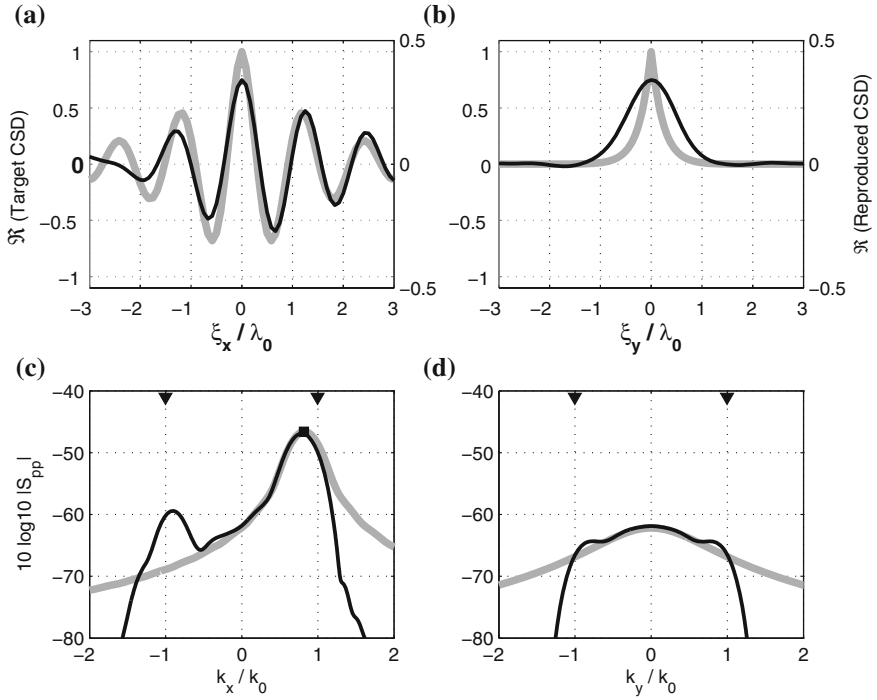

Fig. 6 Supersonic TBL ($U_\infty = 600$ m/s). Target CSD (*bold gray line*) and reproduced CSD in the $(\xi_x, 0)$ plane (**a**) and $(0, \xi_y)$ plane (**b**). Target CSD wavenumber spectrum and reproduced CSD wavenumber spectrum in the $(k_x, 0)$ plane (**c**) and $(0, k_y)$ plane (**d**)

reproduced amplitude which is nearly half the target one), but those in the crosswise direction are coarsely reproduced. Corresponding results in the wavenumber domain are also given in Fig. 6c, d showing that the target spectrum is clearly well reproduced inside the acoustic domain ($|\mathbf{k}|/k_0 \leq 1$). Note also in Fig. 6c that a propagating phenomenon is clearly reproduced, with a highly asymmetric spectrum in k_x (the peak visible for $k_x/k_0 \approx -1$ is attributed to aliasing in the wavenumber domain, due to the extension of the wavenumber content above k_0 [7]).

Figure 7 shows simulation results for a subsonic TBL. Compared with results in Fig. 6, two important observations can be made. First, the reproduced magnitudes in Fig. 7a, b are significantly smaller than the target values, more than 25 times less. Second, target correlation scales are clearly not reproduced and have now the shape of those obtained in the case of DAF (see Fig. 5a). Explanations are found in Fig. 7c, d. As for the supersonic TBL, the target CSD wavenumber spectrum is clearly well reproduced inside the acoustic domain ($|\mathbf{k}|/k_0 \leq 1$) but the convective peak is now located outside this domain. Energy and correlation scales being driven by the convective peak, this explains small reproduced magnitudes and large

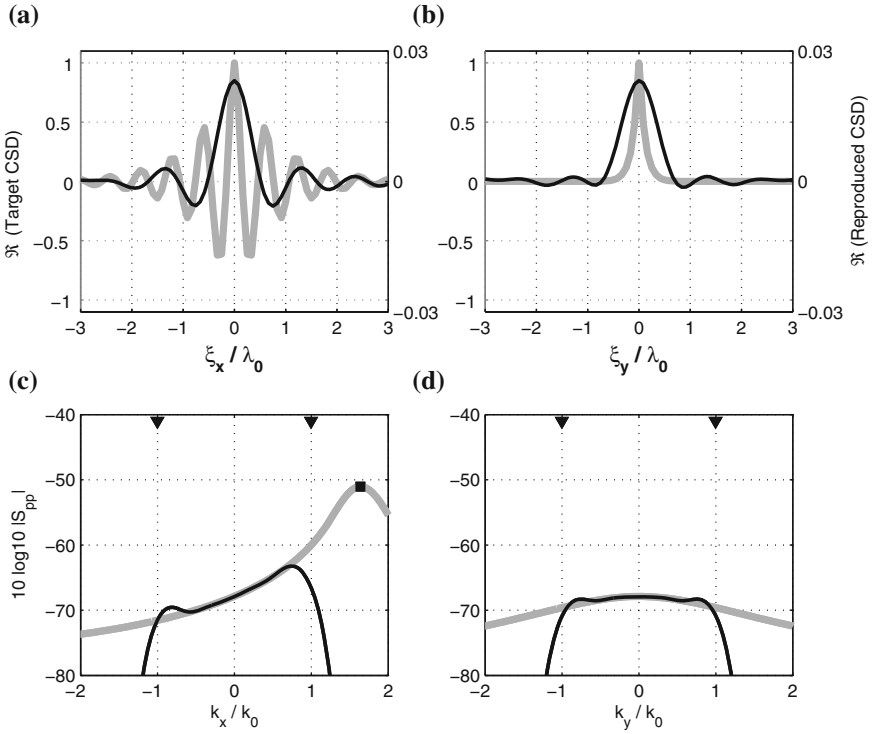

Fig. 7 Subsonic TBL ($U_\infty = 300$ m/s). Target CSD (*bold gray line*) and reproduced CSD in the $(\xi_x, 0)$ plane (**a**) and $(0, \xi_y)$ plane (**b**). Target CSD wavenumber spectrum and reproduced CSD wavenumber spectrum in the $(k_x, 0)$ plane (**c**) and $(0, k_y)$ plane (**d**)

reproduced correlations scales. The reproduced spectrum is slightly asymmetric in k_x (compared with the supersonic case) and symmetric along k_y (which partially explains the shape of the reproduced CSD in Fig. 7a, b).

Figure 8a–d show the results obtained in terms of spatial CSD and CSD wavenumber spectrum, using parameters defined following a parametric study (see Robin et al. [10]) and indicating that smaller plane and source separation are needed to reproduce the convective scales (a normalized source separation $\Delta_x/\lambda_0 \approx 0.14$ and a normalized plane separation $h/\lambda_0 = 0.05$ are used here, as in Robin et al. [10]). In Fig. 8a, b (and compared with Fig. 7a, b), correlation scales are now better reproduced in both streamwise and crosswise directions, even though reproduced amplitudes are nearly a quarter of the targeted amplitude. In the wavenumber domain (Fig. 8c), a peak is reproduced for $k_x/k_0 \approx 1.6$, but with a lower magnitude than the targeted one. The level of the corresponding convective peak is nevertheless higher than the maximum of the reproduced acoustic part.

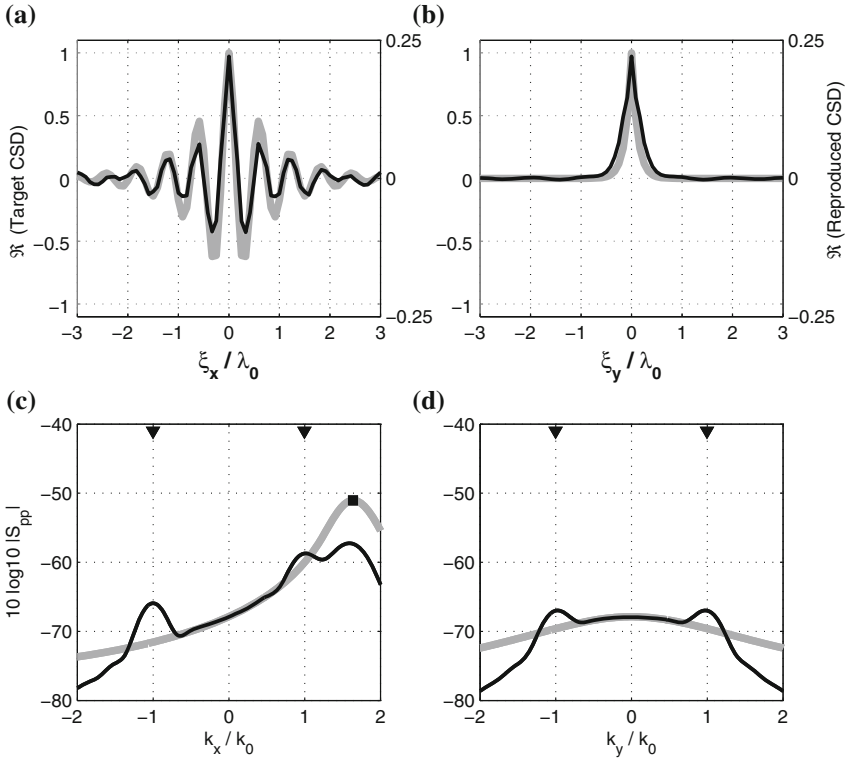

Fig. 8 Subsonic TBL with $\Delta_x = 0.14\,\lambda_0$ and $h = \lambda_0/20$. Target CSD and reproduced CSD in the $(\xi_x, 0)$ plane (**a**) and $(0, \xi_y)$ plane (**b**). Target wavenumber-spectrum and reproduced wavenumber-frequency spectrum in the $(k_x, 0)$ plane (**c**) and $(0, k_y)$ plane (**d**)

For the reproduction of subsonic TBL, Bravo and Maury [17] found that at least 3.7 monopoles per correlation length were needed, and Aucejo et al. [11] obtained a value of at least 4 monopoles per smallest wavelength (even if they are not referred to the same quantity, their two results are quite equivalent as explained in [8]). In the presented results, the value of $\Delta_x/\lambda_0 \approx 0.14$ corresponds to 7 monopoles per acoustic wavelength. The corresponding number of acoustic sources per corresponding convective wavelength λ_c (i.e. to reproduce wavenumber up to λ_c) can be obtained by simply multiplying this value by the ratio $k_0/k_c(= 0.6)$, which leads to a value of 4.3 monopoles per convective wavelength. This value is coherent with the results previously cited.

5 Description of Experiments and Reconstruction Approach

5.1 Validation of Experimental Conditions

A volume source (LMS Mid High Frequency Volume Source) was used for all our experiments. The $1/R$ spherical wave spreading (6 dB amplitude decay per distance doubling) and the constant directivity of this source have been experimentally verified using microphones positioned at different locations and distances from the source. The source volume acceleration $\dot{q}(\omega)$ is directly derived from an internal sensor. If the acoustic space is hemi-infinite as expected, using a monopole and following Eq. (5), the acoustic pressure $p(\mathbf{r}, \omega)$ measured at any point on the panel's surface should verify the relation

$$p(\mathbf{r}, \omega) = \rho_0 \frac{e^{jk_0 R}}{2\pi R} \dot{q}(\mathbf{r}', \omega), \tag{16}$$

where $\frac{e^{jk_0 R}}{2\pi R}$ is the Green's function in hemi-infinite space and $R = |\mathbf{r} - \mathbf{r}'|$.

The measurement of the experimental Green's function has been performed for several source-microphone separation distances (see an example in Fig. 10b), and one of the obtained results is shown in Fig. 9a, b. The agreement between the theoretical Green's function and the experimental measurement is clearly acceptable between 200 and 1,000 Hz (other results at other separation distances show also good agreement), and this allows relying on a theoretical matrix of Green's functions $\mathbf{G}(\omega)$ for the calculation of reproduced pressures on the panel surface and the calculation of reproduction source amplitudes.

The vibration behavior of the test panel has also been experimentally verified. A simply-supported aluminum panel is chosen for the experiments because its theoretical response can be exactly computed (the geometry and properties of the panel are given in Table 1). The aluminum panel is mounted on a rigid steel support to ensure mechanical decoupling. It is also baffled with a plywood panel (4 by 4 ft, 1 in. thick), which is only linked to the rigid steel support. Mechanical decoupling around the edges of the panel is ensured by a silicone seal. The natural frequencies f_{mn} of the simply supported aluminum panel, considered thin, homogeneous and isotropic, are calculated using the relation [21]

$$f_{mn} = \frac{1}{2\pi} \left(\frac{D}{m_s} \right)^{1/2} \left[\left(\frac{m\pi}{a} \right)^2 + \left(\frac{n\pi}{b} \right)^2 \right], \tag{17}$$

with D the bending stiffness of the panel, m_s the mass per unit area of the panel, a, b the dimensions of the panel (see Table 1) and m, n integers. Figure 8c shows a good agreement between the measured and calculated eigenfrequencies, which is within 2 % error, except for mode (2, 3) with a 4 % error. An average structural loss factor of $\eta = 4 \times 10^{-3}$ was estimated using the −3 dB bandwidth method on the first few resonances of the panel, and was set as a constant damping coefficient in simulations.

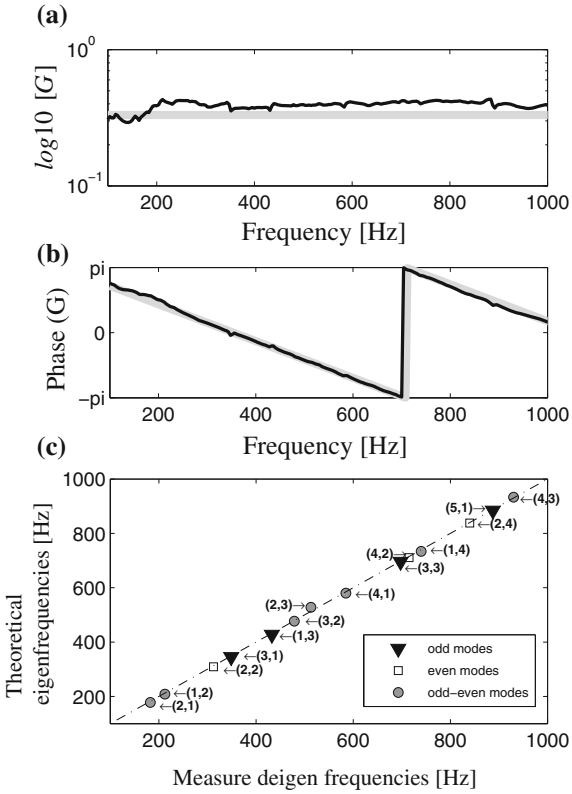

Fig. 9 Validation of experimental conditions. Comparison between the theoretical Green's function (*thick line*) and the measurement (*thin line*). **a** Logarithm of the absolute value and **b** Phase. **c** Theoretical versus measured eigenfrequencies. The type of vibration mode of the aluminum panel is given by the legend, with corresponding (m, n) indices of the mode near *left arrows*

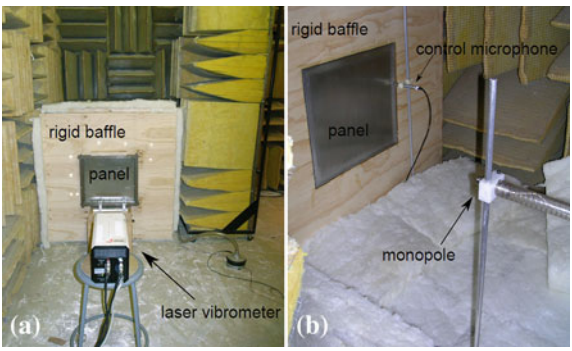

Fig. 10 Pictures of the experiments. **a** *Front view* The baffled panel stands in front of the laser vibrometer, and is surrounded by anechoic panels. **b** *Rear view* The monopole source is on its stand, the microphone used for the measurement of the experimental transfer function between the wall pressure and the monopole can be seen (5 in. of glass wool are added on the floor to improve anechoicity)

Table 1 Properties of the simply supported aluminium panel

Parameter (*symbol*), unit	Value
Length (a), m	0.48
Width (b), m	0.42
Thickness (h), mm	3.2
Mass density (ρ), kg/m^3	2700
Bending stiffness (D), N/m	270.5
Poisson's ratio (ν)	0.3
Loss factor (η)	4.10^{-3}

5.2 The Synthetic Array

To create the synthetic source array, the acoustic monopole is moved in a plane parallel to the panel. For each position of the monopole, a white noise excitation is sent to the source, and the transverse velocity of the panel $v(\omega)$ is measured on a mesh of 13×11 points using a Polytec Scanning Laser Vibrometer. For each source position, 143 $H_{v/\dot{q}}$ Frequency Response Functions (FRFs) are thus measured from 170 to 2,000 Hz. The lower frequency limit of 170 Hz is caused by low frequency limitations of the source, and implies that the (1,1) mode of the panel was never excited during our experiments ($f_{11} = 77.3$ Hz). Two synthetic arrays are created, with different parameters that are detailed in Table 2.

The array, although virtual, has a finite size which implies possible truncation effects, and is composed of discrete virtual reproduction sources causing possible aliasing effects (Fig. 11b illustrates the reproduction of a single acoustic plane wave in a 2D plane). The maximum incidence angle $\theta_{\max}$ of the plane wave that can be reproduced at the center of the reproduction plane is defined by the source to reproduction plane separation h and the half-width of the source plane

Table 2 Summary of the experimental parameters, with the reference frequency $f_0^{\text{ref}} = 958$ Hz, and the reference wavelength $\lambda_0^{\text{ref}} = 0.36$ m

Parameter (symbol), unit	Value
Array 1	
Number of sources (M)	25
Source separation ($\lambda_0^{\text{ref}}/2$), m	0.18
Plane separation (λ_0^{ref}), m	0.36
Physical size ($L_x \times L_y$), m	0.72 × 0.72
Maximum incidence angle (θ), degrees	45
Array 2	
Number of sources (M)	110
Source separation ($\lambda_0^{\text{ref}}/6$), m	0.06
Plane separation ($\lambda_0^{\text{ref}}/4$), m	0.1
Physical size ($L_x \times L_y$), m	0.6 × 0.54
Maximum incidence angle (θ), degrees	73

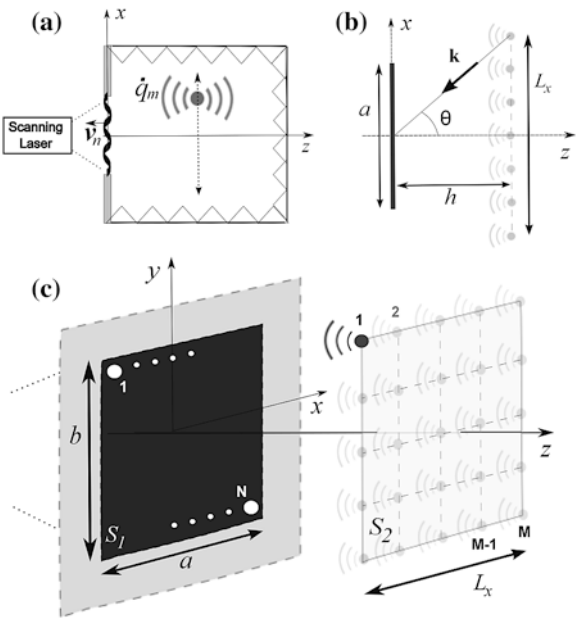

Fig. 11 Principle of the method. **a** The panel to be tested is placed in a rigid baffle, a monopole is moved in a hemi-anechoic room and the panel response is measured using a scanning laser vibrometer. **b** Illustration of the reproduction of a single plane wave component of wavevector **k** in the (x, z) plane. **c** Measurement mesh of N points on the panel, and a M elements synthetic antenna created by moving successively the monopole from position 1 to position M

$$\theta_{\max} = \tan^{-1}(L_x/2h). \tag{18}$$

For a DAF excitation, the higher the incidence angle is, the lower the TL is. This is a well-known result concerning the transmission of sound through such simple partitions and the related effect of the highest angle of incidence of the considered DAF [21, 22].

If the individual reproduction sources are (virtually) positioned along the x axis with a source separation Δ_x, spatial aliasing occurs for plane wave components of incidence θ at frequencies above a maximum frequency $f_{\max}$ defined by [7]

$$f_{\max} = \frac{c_0}{2\Delta_x \sin\theta}, \tag{19}$$

which simplifies to $f_{\max} = c_0/2\Delta_x$ for angles up to 90°. The two virtual arrays studied being both centered on the reproduction plane with nearly identical length and width, the same angle of incidence in the x and the y directions will be considered and the same $f_{\max}$ will thus apply for the reproduction of plane wave components.

5.3 Reconstructing Vibroacoustic Behavior of the Panel and Obtaining Vibroacoustic Indicators

The Transmission Loss (TL) will be used as a main vibroacoustic indicator and is defined as

$$\mathrm{TL}(\omega) = 10\log_{10}\frac{\Pi_{\mathrm{inc}}(\omega)}{\Pi_{\mathrm{rad}}(\omega)}, \tag{20}$$

where $\Pi_{\mathrm{inc}}(\omega)$ and $\Pi_{\mathrm{rad}}(\omega)$ are the incident and the radiated acoustic power, respectively.

In the case of a DAF generated in a reverberant room, the incident acoustic power is usually calculated using the relationship [21]

$$\Pi_{\mathrm{inc}}^{\mathrm{DAF}}(\omega) = \frac{\langle p_{\mathrm{RMS}}^2\rangle ab}{4\rho_0 c_0}, \tag{21}$$

where $\langle p_{\mathrm{RMS}}^2\rangle$ is the mean quadratic pressure of the DAF at large distance from the panel. In the case of a TBL, for which no far field pressure is defined but only a power spectral density on the plate surface, the incident power is calculated using the relationship

$$\Pi_{\mathrm{inc}}^{\mathrm{TBL}}(\omega) = \frac{\langle p_{\mathrm{RMS}}^2\rangle ab}{8\rho_0 c_0}, \tag{22}$$

where $\langle p_{\mathrm{RMS}}^2\rangle$ is now the mean quadratic pressure of the TBL pressure fluctuations on the surface of the panel, and the factor 8 accounts for the doubling of pressure on the surface (blocked pressure hypothesis [3]). The CSD matrix $\mathbf{S}_{\hat{p}\hat{p}}^{\mathrm{panel}}(\omega)$ of reconstructed surface pressure on the panel is calculated using the matrix of theoretical Green's functions $\mathbf{G}(\omega)$ and the reproduction source accelerations CSD $\mathbf{S}_{\dot{\mathbf{q}}\dot{\mathbf{q}}}(\omega)$

$$\mathbf{S}_{\hat{p}\hat{p}}^{\mathrm{panel}}(\omega) = \rho_0^2\mathbf{G}(\omega)\mathbf{S}_{\dot{\mathbf{q}}\dot{\mathbf{q}}}(\omega)\mathbf{G}^{\mathbf{H}}(\omega), \tag{23}$$

and finally $\langle p_{\mathrm{RMS}}^2\rangle(\omega) = \frac{1}{N}Tr(\mathbf{S}_{\hat{p}\hat{p}}^{\mathrm{panel}}(\omega))$ where Tr denotes the trace of a matrix (for convenience, the reproduced pressure is calculated at the panel positions where the transverse vibration is measured). Since only wall pressure fluctuations are considered, the incident power for a DAF or a TBL will be both calculated using Eq. (22).

The matrix of the $N \times M$ measured FRFs between the M source volume accelerations and the N panel velocity responses is noted $\mathbf{H}(\omega)$ (see Fig. 11c). Using this matrix, the calculation of the vibration velocity CSD of the panel with a

CSD of the source volume accelerations [calculated with either Eqs. (7), (9), (11), (13) or (15)] is straightforward and given by the equation

$$\mathbf{S}_{vv}^{\text{panel}}(\omega) = \mathbf{H}(\omega)\mathbf{S}_{\dot{\mathbf{q}}\dot{\mathbf{q}}}(\omega)\mathbf{H}^{\mathbf{H}}(\omega). \tag{24}$$

The corresponding radiated acoustic power is calculated using [21, 23]

$$\Pi_{\text{rad}}(\omega) = Tr\left(\mathbf{S}_{vv}^{\text{panel}}(\omega)\mathbf{R}_{\text{rad}}(\omega)\right), \tag{25}$$

where $\mathbf{R}_{\text{rad}}$ is the element radiation matrix [3, 21] of dimension $[N \times N]$.

Using Eqs. (20)–(25), synthetic TL values can be calculated and compared with simulated TL obtained with a commercial software, NovaFEM [24]. Such a comparison is made for two reasons. The first is that the case of a simply supported panel makes the exact calculation of its response possible. The second reason is more practical, since obtaining measured data to compare our results with can be difficult, especially in the TBL case.

To complement this frequency domain indicator that indiscriminately combine acoustic and convective excitations effects, a wavenumber analysis can be achieved to separate both excitations and their respective contributions in this problem. The availability of measured spatial vibratory information on the panel and calculated spatial information for the incident pressure field allows calculating the two-dimensional Fourier transform upon the spatial separations ξ_x and ξ_y, for example for the vibration velocity CSD of the panel

$$S_{vv}^{\text{panel}}(k_x, k_y; \omega) = \int_{-\infty}^{+\infty}\int_{-\infty}^{+\infty} S_{vv}^{\text{panel}}(\xi_x, \xi_y; \omega) \times \mathrm{e}^{-jk_x\xi_x}\mathrm{e}^{-jk_y\xi_y}\mathrm{d}\xi_x\mathrm{d}\xi_y. \tag{26}$$

The vibratory behavior of the panel can be studied using the magnitude of this function, often called the wavenumber sensitivity function, which yields physical insight into the structural acoustic response [13, 25]. Another possibility for analyzing the vibratory behavior of the plate under different pressure fields is to normalize the incident pressure field by the radiated power, both calculated in the wavenumber domain. The ratio

$$\text{TL}(k_x, k_y; \omega) = 10\log_{10}\left(\frac{|S_{\hat{p}\hat{p}}^{\text{panel}}(k_x, k_y; \omega)|^2}{\Re(\rho_0\omega/k_z)^2|S_{vv}^{\text{panel}}(k_x, k_y; \omega)|^2}\right), \tag{27}$$

is used, which to a multiplicative constant is proportional to the ratio of the incident acoustic power to the radiated acoustic power, and thought to be a simple basis for the comparison of the wavenumber filtering effect of the panel.

6 Experimental Results for a Simply Supported Aluminum Panel

6.1 Reproduction of a DAF

6.1.1 25 Source Array

Figure 12a shows the TL results for the three reproduction approaches. For the LS approach, Eq. (9) is used for the calculation of the source CSD, with a regularization parameter $\%_{\text{reg}}$ set to 10 % for all frequencies. This parameter has been chosen mainly by trial and error; the discontinuities observed in the LS solution in Fig. 12a are directly related to the truncation of the singular values. It should be pointed that if no regularization is used, the LS solution provides a perfect reconstruction of the target pressure field but with source amplitudes that are much larger than those obtained for the two other approaches. Excessively large calculated source inputs coupled with the measured FRFs lead to an overestimated radiated power and a perfectly reproduced incident power (compared with the target

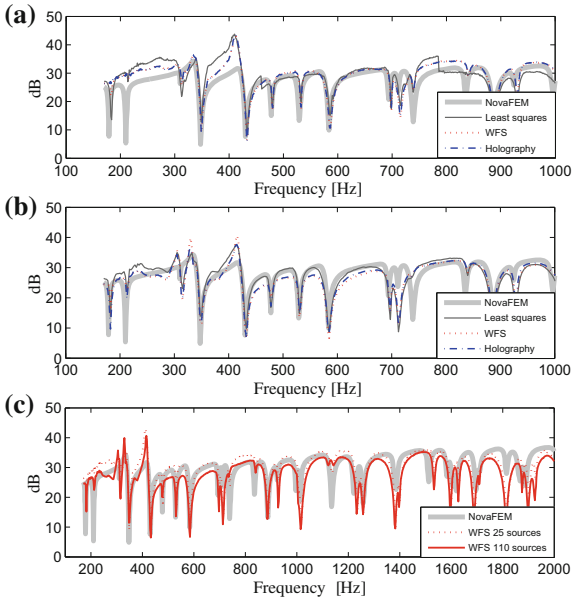

Fig. 12 **a** TL results using array 1 (25 sources) and the three reproduction approaches (*thin lines*), and the NovaFEM calculation (*thick gray line*). LS results are obtained using a regularization percentage set to 10 %. **b** TL results using array 2 (110 sources) and the three reproduction approaches (*thin lines*), and the NovaFEM calculation (*thick line*). LS results are not regularized. **c** TL results up to 2 kHz using the WFS approach for the 25 sources (*thin dotted line*) and 110 sources array (*thin solid line*), and the NovaFEM calculation (*thick line*). *Note* For all cases, the target pressure field (NovaFEM calculation) is a perfect DAF (angles of incidence up to 90°)

value), and consequently to a TL that is highly underestimated. Compared with the unregularized LS solution, the WFS and Holographic approaches provide a physical solution in terms of source amplitude to the reproduction problem. Even if the incident powers are slightly different for the two approaches (and are consistent with the results presented in Berry et al. [8] and Robin et al. [10]) this difference of incident powers is translated into a similar difference of corresponding radiated powers and leads to almost identical TL over the frequency range considered. In comparison to NovaFEM result in Fig. 12a, the values of reproduced TL are slightly overestimated, but the NovaFEM calculation assumes that the DAF contains all the incidence angles up to 90°. In the case of the 25 sources array, the maximum angle of incidence that can be reproduced is $\theta_{\max} = 45°$ (see Eq. 18). The reproduced TL values are thus above those obtained for an ideal DAF. The regularized Least Squares approach is in good agreement with the target TL and the other two approaches.

6.1.2 110 Source Array

The influence of using a denser and closer virtual array on the reproduction of a DAF excitation and on the corresponding TL estimation is now studied. Figure 12b shows the corresponding TL results using the three approaches, which are still compared with a TL calculated under the assumption of a perfect DAF excitation. Note that no regularization of the LS problem is used here. As stated by Nelson and Yoon [15] with closer source and reproduction planes and with (x, y) source positions that have a similar distribution compared with the calculation positions on the panel, the conditioning of the problem is improved. Aucejo et al. [11] also noticed that a large source to reproduction plane separation leads to poor reconstructions and conditioning problems. The three methods now give lower (and close) TL values over the whole frequency range compared with the 25 sources case. The WFS and Holography approaches give comparable TL values, while the LS approach leads to the highest TL estimation.

The comparison of the results presented in Fig. 12a, b confirms that when plane waves with higher incidence angles can be reproduced ($\theta_{\max} = 73°$ for the 110 sources array), the reproduced TL values decrease (between 2 and 6 dB depending on the considered method and frequency). Finally and regarding spatial aliasing effects, the TL results up to 2 kHz are shown in Fig. 12c as an example for the WFS approach. For the 25 sources array and $\theta_{\max} = 45°$, Eq. (19) indicates a spatial aliasing frequency of 1,355 Hz. For the 110 sources array, this frequency becomes 5,800 Hz. The TL results of Fig. 12c do not significantly vary above 1,355 Hz. Even if aliasing occurs on reproduced CSDs, the TL estimation seems to filter out this adverse reproduction effect.

6.2 Reproduction of a TBL

6.2.1 Supersonic TBL and 25 Source Array

In this section, the reproduction of a supersonic TBL ($U_\infty = 600$ m/s) is investigated with the 25 source array. When the TBL is supersonic, the major part of its energy (the convective peak) is contained in the acoustic domain and the main correlation scales of the TBL in the flow direction are larger than the acoustic wavelength. It was shown that the WFS [8] and Holographic [10] approaches are able to reproduce these spatial scales with a source separation of half an acoustic wavelength, and a plane separation of an acoustic wavelength. The 25 sources array (see Table 2) should be thus adapted to this application, but not to a subsonic TBL reproduction.

Similarly to the previous section, Fig. 13a shows the TL results obtained for the three reproduction methods and for a supersonic TBL. No filtered backpropagation is applied for the holographic approach. As for the DAF case, the LS solution is regularized using a regularization parameter set to 10 %. If no regularization is used, the target S_{pp} is nearly perfectly reproduced on the panel, but with source amplitudes that lead to an overestimated radiated power and dramatically underestimated TL values.

For the three approaches, the reproduced TL values slightly underestimate the NovaFEM result, and are close to a TL calculated under a DAF excitation

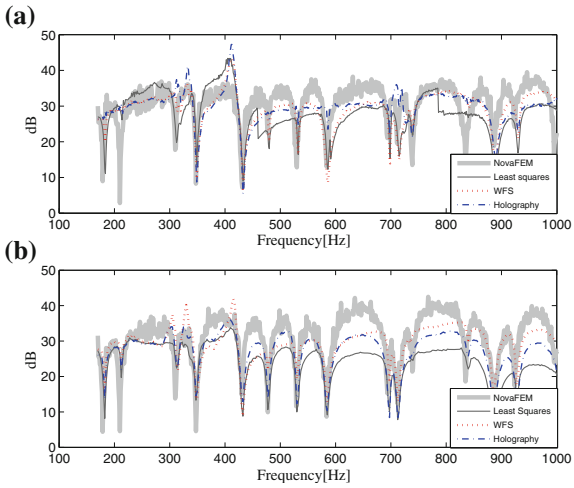

Fig. 13 **a** TL results using the three reproduction approaches (*thin lines*), and the NovaFEM calculation (*thick line*). The target pressure field is a supersonic TBL ($U_\infty = 600$ m/s) and the synthetic array has 25 sources. LS results are regularized using $\%_{\text{reg}} = 10\,\%$. **b** TL results using the three reproduction approaches (*thin lines*), and the NovaFEM calculation (*thick line*). The target pressure field is a subsonic TBL ($U_\infty = 300$ m/s) and the synthetic array has 110 sources. LS results are regularized using $\%_{\text{reg}} = 10\,\%$

especially for the WFS and Holographic approaches. This is attributed to the fact that only the acoustic part of the target TBL pressure field is effectively reproduced, as was previously observed in simulations [8, 10]. The large source to reproduction plane separation with a source separation that is based on an 'acoustic reproduction' criterion (two sources per acoustic wavelength at a reference frequency of 958 Hz) thus leads to the reproduction of acoustic wavenumbers only. Note that at each calculation frequency and for the TBL case, NovaFEM calculation uses several realizations with the final TL result at this frequency being the mean obtained value, which explains its irregular and noisy behavior.

6.2.2 Subsonic TBL and 110 Source Array

The reproduction of a subsonic TBL ($U_\infty = 300$ m/s) with the 110 source array is finally investigated. As stated in the introduction, the reproduction of a subsonic TBL implies a number of reproduction sources that is not referred to the acoustic wavelength, but to the smallest wavelength or correlation length to be reproduced that should be at least equal to the convective wavelength. Bravo and Maury [17] and Aucejo et al. [11] concluded that three to four reproduction monopoles per smallest correlation length or smallest wavelength were needed, respectively. Robin et al. [10] share a similar conclusion, with acceptable reproduction results using 4.2 monopoles per convective wavelength. For a subsonic TBL and $U_\infty = 300$ m/s, the convective wavelength at the reference frequency of 958 Hz is $\lambda_c = 22$ cm, which implies a source separation of 5.5 cm if we consider four monopoles per convective wavelength. All these authors also agree on the fact that the source to reproduction plane separation should be at least equal to the source separation. For these reasons, the 110 sources array should be adapted to the reproduction of a subsonic TBL.

As in the previous case, the regularization of the LS problem is needed to avoid the possible overestimation of the radiated power, and also because the target pressure CSD now mainly includes large wavenumber components (or evanescent components) that can be exponentially amplified (the regularization filters out the smallest singular values that usually correspond to the smallest spatial variations, that is the convective wavelengths). The LS approach is regularized using a regularization parameter set to 10 %. For the Holography approach, the filtered backpropagation is used, with parameters $\alpha_{\text{reg}}^{\text{holo}} = 0.25$ and $k_{\text{cut-off}} = k_c$.

The corresponding TL results are given in Fig. 13b for the three approaches, respectively. The target CSD S_{pp} and reproduced CSDs $S_{\hat{p}\hat{p}}$ are shown in Fig. 14a–d. From Fig. 14d, it is clear that the filtered backpropagation operation for the holographic approach behaves as expected. It provides a good reproduction of correlation scales in the streamwise direction, but a coarse reproduction in the spanwise direction (which is the case for the three approaches). Even with a plane separation that is a quarter of the reference acoustic wavelength, the maximum reproduced magnitude is higher compared with simulation results obtained in Robin et al. [10] when no backpropagation was used and with a plane separation of one twentieth of the

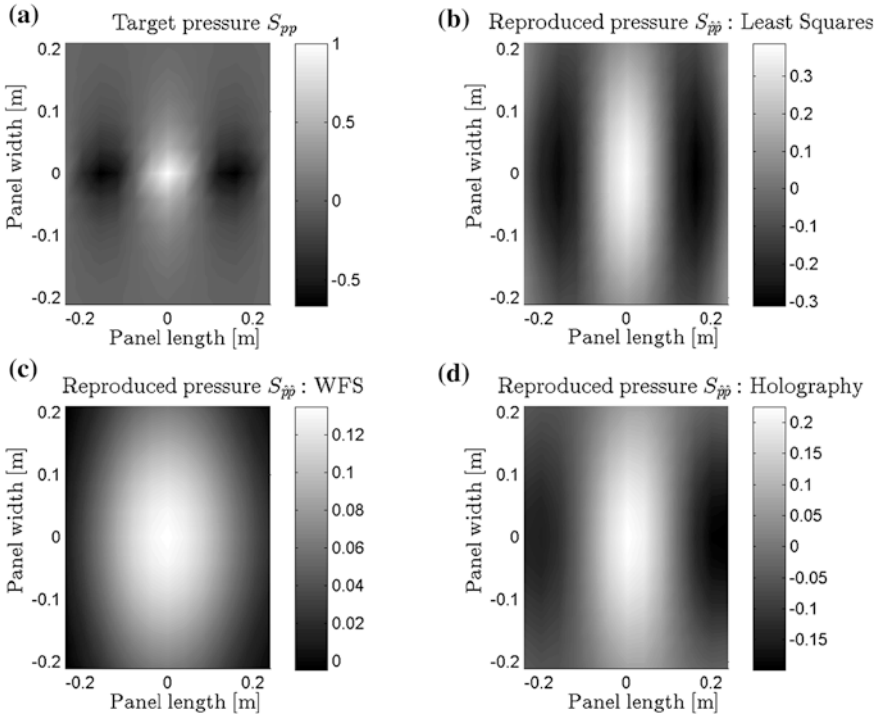

Fig. 14 **a** Real part of target CSD $\Re(S_{pp})$ (subsonic TBL with $U_\infty = 300$ m/s). **b** Real part of reproduced pressure $\Re(S_{\hat{p}\hat{p}})$ for the LS approach. **c** Real part of reproduced pressure $\Re(S_{\hat{p}\hat{p}})$ for the WFS approach. **d** Real part of reproduced pressure $\Re(S_{\hat{p}\hat{p}})$ for the Holographic approach. The source array is composed of 110 sources. All the CSDs are calculated between the center of the reproduction plane and a variable point, and at 750 Hz

reference acoustic wavelength. Note that the WFS solution does not reproduce the spanwise correlation scales of the subsonic TBL as well as LS and holography.

The TL result is almost identical for the three approaches below 400 Hz (see Fig. 13b). Above this frequency, WFS and holographic approaches lead to comparable values, with systematically smaller TL values for the LS approach. Compared with the NovaFEM simulation, all the experimental TL values are underestimated in most of the studied frequency range.

6.3 Comparison Between DAF and TBL Results for the 110 Source Array

Figure 15 illustrates the results obtained with the NovaFEM software, the WFS and Holographic approaches in terms of Transmission Loss difference between a TBL

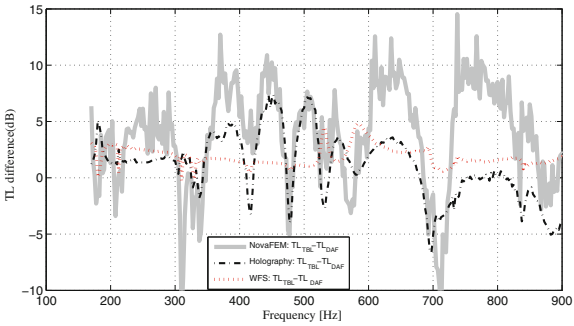

Fig. 15 TL differences between TBL excitation and DAF excitation for the NovaFEM simulation (*thick line*), the WFS approach (*thin dotted line*) and the holographic approach (*thin dash-dotted line*)

excitation and a DAF excitation. Except at structural resonance frequencies and below a frequency of roughly 700 Hz, the TL difference is nearly systematically positive (between +1.5 and +7 dB, depending on the method and the frequency), which indicates a higher TL value for the TBL excitation, and a TBL mainly transmitted at structural resonances. The best agreement is obtained between the Holographic result and the NovaFEM calculation, and confirm the suitability of the P-NAH approach for reproducing the small scales linked to the subsonic TBL excitation, with TL differences between DAF and TBL inputs that are partially but nevertheless captured in reproduction results. These results also confirm the fact that WFS is better adapted for reproducing acoustic pressure fields, even if the use of this approach also shows higher TL in the TBL case, but with a nearly constant difference. Note that the upper frequency limit (above 700 Hz) is attributed to the source separation and the inherent impossibility of reproducing the smallest correlation length (the spanwise correlation length L_y, defined as $L_y = \beta U_c/\omega$, becomes smaller than the source separation above 668 Hz).

We now illustrate the possibility of analyzing the vibroacoustic behavior of the panel in the wavenumber domain using the ratio suggested in Eq. (27). Figure 16a, b shows corresponding results for the $(3, 1)$ resonant mode and for the DAF and TBL excitations, respectively. The maps in the wavenumber domain are nearly identical. In an off-resonance case ($f = 505$ Hz), a very different situation occurs as illustrated in Fig. 16c, d, respectively. For both excitations, the ratios are significantly higher compared with those obtained on resonance of the (3,1) mode, which translates into a higher transmission loss. The ratio for a DAF is now nearly the same for all the acoustic wavenumbers, but the one obtained for the TBL has a minimum in the convective peak direction and is slightly higher than for the DAF in the opposite wavenumber direction. This results in a larger global transmission efficiency for the DAF case, and explains the smaller TL values for this case.

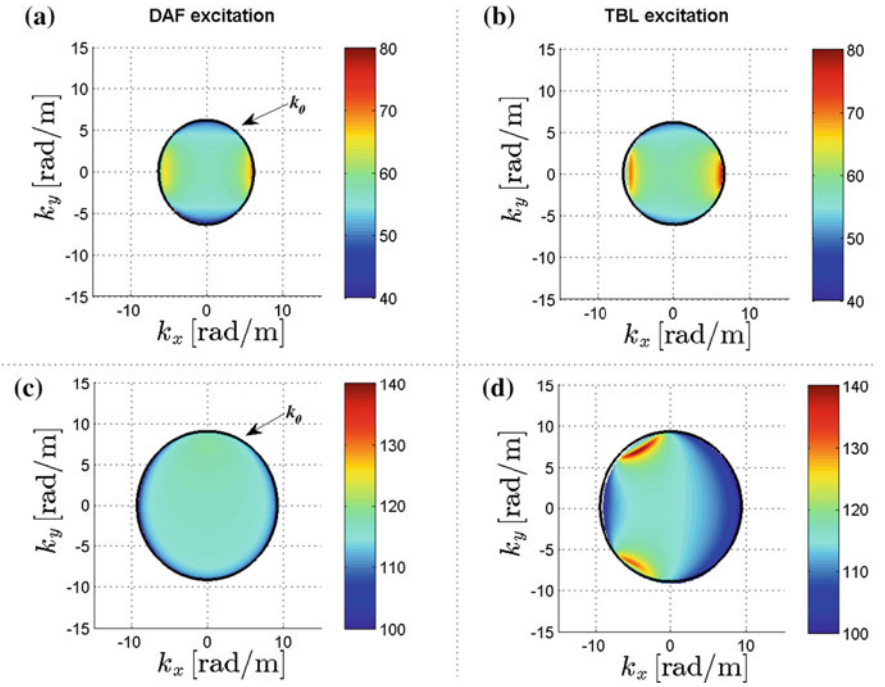

Fig. 16 Ratio of the incident acoustic power to the radiated acoustic power in the wavenumber domain using Eq. (27) (P-NAH case). The acoustic circle of radius k_0 in the wavenumber domain is indicated. **a** Wavenumber filtering of the panel for a DAF excitation on resonance of the (3, 1) mode. **b** Wavenumber filtering of the panel for a TBL excitation on resonance of the (3, 1) mode. **c** Wavenumber filtering of the panel for a DAF excitation at 505 Hz. **d** Wavenumber filtering of the panel for a TBL excitation at 505 Hz

7 Measuring Transmission Loss of Panels Under Synthesized DAF Excitation: A Comparison with Coupled Rooms Measurement

In the previous section, an experimental procedure for the TL estimation of a plane panel under synthesized random pressure fields was presented, and experimental results were compared with numerical simulations. In this section, an experimental validation is proposed by a comparison between the usual coupled rooms method and a synthesized DAF excitation. A composite panel was tested, which is representative of fuselage panels usually tested in coupled rooms. Since this part of the work is a purely experimental validation, no calculation for the TBL excitation is made.

7.1 Description of the Two Measurements

Figure 17 schematically illustrates the two measurements techniques that are to be compared. The first measurement method is the coupled rooms method, where a reverberant room is used to produce the DAF excitation (see Fig. 17a). The panel is mounted between this reverberant room and an anechoic room, where the radiated acoustic power is estimated using an intensity probe. The second method uses a synthetic antenna, the calculation of CSD reproduction source amplitudes and the measurement of the panel's vibration response to calculate the TL of the panel at a post-processing step (see Sect. 5.3 and Fig. 17b).

The coupled rooms measurement is first conducted as follows:

- A DAF excitation is generated in the reverberant room using three low and mid frequencies speakers positioned in the corners of the room, and four compression chambers at the center of the ceiling that generate the high frequency content. Acoustic diffusers are also positioned in the room to improve the diffuseness of the acoustic field (see Fig. 18b).
- The mean quadratic acoustic pressure in the reverberant room $\langle p^2_{\mathrm{RMS}} \rangle$ is obtained by rotating a microphone during measurements, with at least a complete rotation of the microphone. This measurement allows calculating the incident acoustic power Π_{inc} on the panel of area S ($\Pi_{\mathrm{inc}} = \langle p^2_{\mathrm{RMS}} \rangle S/(4\rho_0 c_0)$).
- The radiated acoustic pressure Π_{rad} by the panel of area S is estimated using the measured active acoustic normal intensity I_{rad}, integrated over S. A Bruel and Kjaer intensity probe was used, composed of two half-inch microphones and a 12 mm spacer. The panel was manually scanned during the measurement, of 1 min duration approximately, so that a temporal and a spatial averaging are achieved. The acoustic intensity was measured at 20 cm from the surface of the panel, and the edges of the panel were excluded from the scan to avoid measuring potential acoustic leaks. The δ_{pi} indicator was used to check the measurement quality, and a repeatability study was also performed.
- The Transmission Loss is finally obtained using Eq. (20).

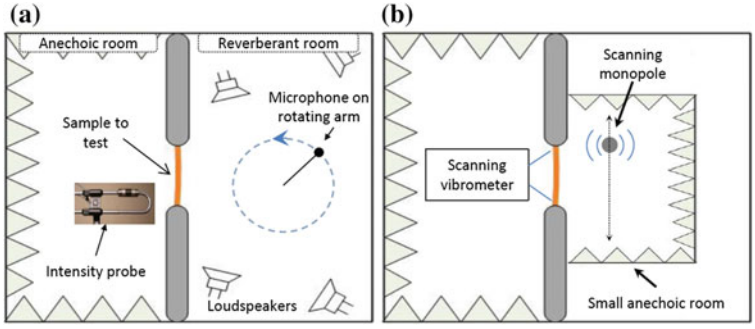

Fig. 17 Schematic description of the experimental comparison. **a** Typical panel mounting for a TL measurement using coupled rooms. **b** Measurement setup for the panel testing under a synthesized DAF excitation (on the same panel and under same mounting conditions)

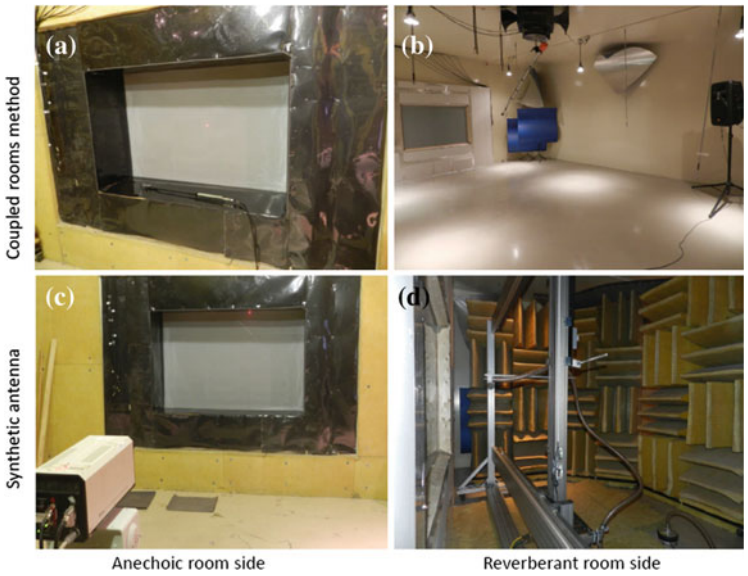

Fig. 18 Pictures of the two experimental setups. **a** Panel seen from the anechoic room with the sound intensity probe. **b** Panel seen from the reverberant room with one of the acoustic sources and the microphone on its rotating arm. **c** Panel seen from the anechoic room with the scanning laser measurement. **d** Motorized monopole source on the reverberant room side, with dihedrons positionned in the room to create a hemi-anechoic space in the reverberant room

Regarding the measurement under synthetic DAF, the procedure described in Sect. 5.3 was applied to obtain the incident and radiated acoustic powers, and summarized in Fig. 19. Note that for this measurement, a hemi-anechoic space was created in the reverberant room using rockwool dihedrons and rockwool panels on floor and ceiling. This small hemi-anechoic space is needed to obtain experimental conditions that allow calculating the reproduced pressure or reproduction source amplitudes using theoretical Green's functions. The choice of transforming the reverberant room into a small anechoic room, which is not the simplest to realize in practice, was dictated by the choice of avoiding possible niche effects (the panel was nearly flush-mounted in the reverberant room) or dismounting the panel between the two measurements. The monopolar source was translated using a motorized robot.

7.2 Description of the Panel and Setup

The tested panel is a composite multilayer of 1.5 m^2 area (1.5 × 1 m), composed of an orthotropic honeycomb core, surrounded by two carbon faces (considered isotropic). The thickest carbon face was positioned on the reverberant room side. The

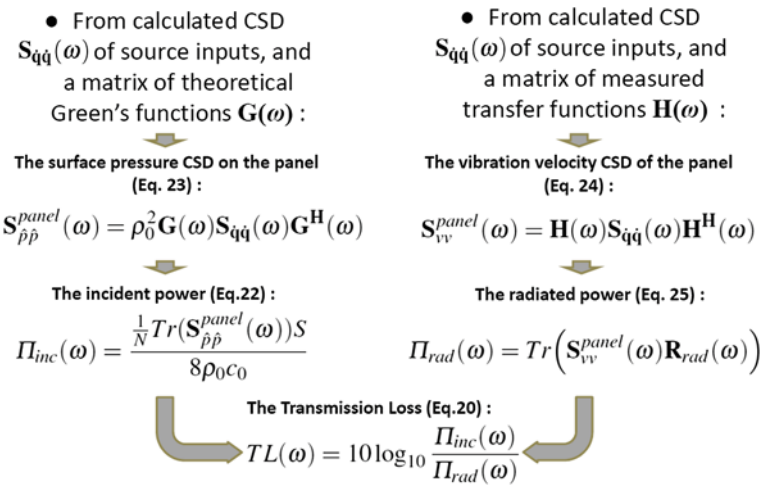

Fig. 19 TL calculation procedure using CSD of calculated source volumic accelerations $S_{\dot{q}\dot{q}}(\omega)$, theoretical Green's functions matrix $\mathbf{G}(\omega)$ and measured transfer functions matrix $\mathbf{H}(\omega)$

dimensions and properties of the panel are given in Table 3. In the honeycomb case, direction 1 is defined with respect to the width of the panel, direction 2 with respect to the length of the panel and direction 3 with respect to the panel thickness.

Regarding the panel boundary conditions, a wood frame was first set around the panel so that a small gap of 1 mm was present along all the edges of the panel. The panel was then maintained centered on this frame using small wedges, and a

Table 3 Dimensions and properties of the tested composite panel

Carbon faces	
Young's modulus E (GPa)	46
Shear modulus G (GPa)	17.7
Poisson's ratio v (-)	0.3
Mass density ρ_c (kg/m^3)	1581
External face thickness (internal) (mm)	2.2 (1.2)
Honeycomb core	
Young's modulus $E1, E2$ (MPa)	1
Young's modulus $E3$ (MPa)	176
Shear modulus $G12$ (MPa)	1
Shear modulus $G13$ (MPa)	26.2
Shear modulus $G23$ (MPa)	55.9
Poisson's ratio v_{12} (-)	0.45
Poisson's ratio v_{13}, v_{23} (-)	0.01
Mass density ρ_n (kg/m^3)	64
Thickness (mm)	19

silicone seal is finally applied around the edges. This setup leads to boundary conditions close to free-free conditions. On the reverberant room side, the panel was nearly flush mounted as previously stated. On the anechoic room side, the niche partitions and the edges of the panel were covered with an acoustic insulating material, composed of a polyurethane foam and a viscoelastic layer.

7.3 Measurement Results

7.3.1 Coupled Room Measurement

The coupled rooms measurement was performed as described in the previous section. The corresponding TL results in terms of linear and third octave band spectra are given in Fig. 20. The acoustic coincidence frequency is approximately located at a frequency of 1,000 Hz. Below (respectively above) this frequency, the slope is a 5 dB per octave slope (3 dB/octave slope).

7.3.2 35 Source Synthetic Antenna Measurement

In order to realize a first comparison between the two methods, a 35 sources synthetic antenna was created (7 by 5 source positions, spaced by 25 cm). The vibratory response of the panel was measured on a 221 points mesh (17 by 13

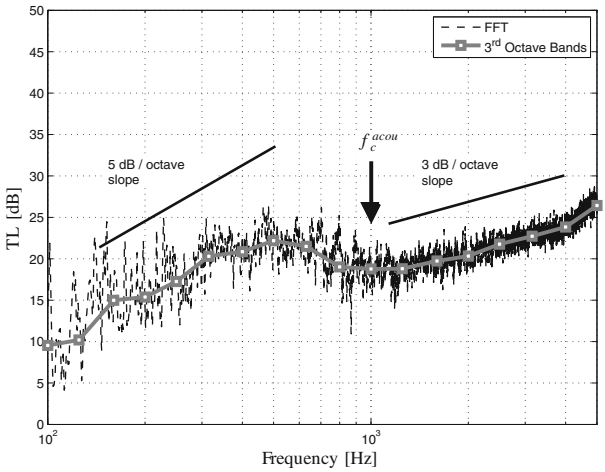

Fig. 20 TL measurements using coupled rooms arrangement. The narrow band spectrum is the *thin dotted black line*, while the third octave spectrum is the *thick gray line* with markers at the center frequencies. The acoustic coincidence frequency is indicated by a vertical arrow, and the TL slopes are recalled

points, spaced by 8 cm). The source plane and reproduction plane were spaced by $h = 30$ cm. This first test is mainly intended to check that reproduction results are consistent even with a coarse array, with limited incidence angle [$\theta_{\max} = 68°$ (see Eq. 18)] and a maximum frequency without potential spatial aliasing of 733 Hz (see Eq. 19).

Figure 21 compares the obtained results for the coupled rooms measurement and the 35-source synthetic antenna, in terms of linear and third octave spectra. The TL estimated using the synthetic antenna approach is systematically lower than the one obtained by the coupled rooms method, and is contaminated with larger measurement noise. Given the maximum incidence angle and the related effect of this angle on the TL, a higher TL estimation would be expected with the synthetic antenna measurement (the highest incidence angle obtained with the reverberant room is supposed to be equal to 78°). The lower TL values obtained with the synthetic antenna are attributed to the presence of important gaps in the synthetic TL, and their related contribution in the calculation of the TL in third octave bands. The global trends are nevertheless well captured with this first measurement, and also helps validating the experimental conditions (i.e. a creation of an anechoic room in the reverberant room).

Figure 22 illustrates the effect of the synthesis procedure on the estimated TL. If only one source position is used to synthesize the panel's TL (a corner source is used, that includes the highest possible incidence angle), the obtained values are highly overestimated compared to the coupled rooms measurement, and do not reflect the same trends as a function of frequency.

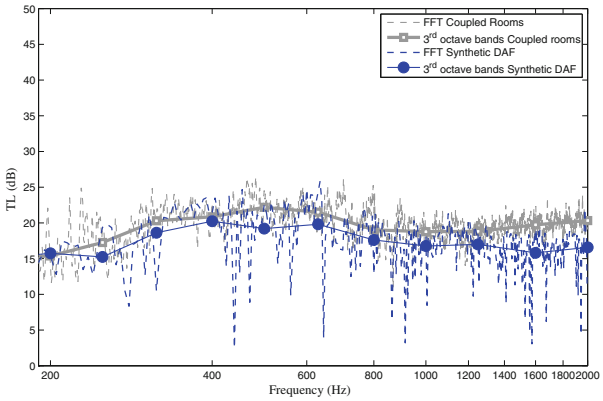

Fig. 21 Comparison of TL estimation using a 35 sources antenna with the coupled rooms measurement. The linear spectrum for the coupled rooms is given by a *thin gray dotted line* (*blue thick dotted line*). The third octave result for the coupled rooms is indicated by the *thick gray line with square markers* at the center frequencies, while the synthetic antenna result is indicated by a *thin blue line* and *circle markers*

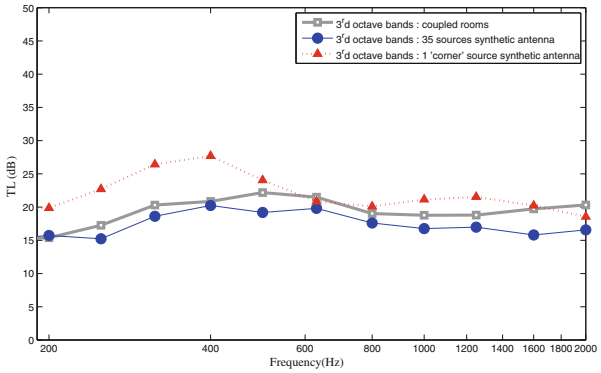

Fig. 22 Comparison of results in third octave bands. The coupled rooms measurement is indicated by a *gray thick line* and *square markers*. The 35 sources synthetic antenna is indicated by a *blue line with circle markers* (one source antenna with a *red dotted line* and *triangle markers*)

7.3.3 345 Source Synthetic Antenna Measurement

A denser synthetic antenna composed of 345 sources was then realized. The virtual sources were now spaced by 7 cm, on a mesh of 23 × 15 points. The separation distance of the source plane and the panel equaled 10 cm (with a corresponding maximum incidence angle of 83°). The vibratory response of the panel is still measured on a 221 point grid. Even if more measurement points could be desirable, this mesh is used to limit the testing time (the measurement of the vibratory response of the panel for one excitation point and 221 response point takes approximately 5 min, but can be automated).

As in the previous section, Fig. 23 compares the obtained results in terms of linear (Fig. 23a), and third octave bands spectra (Fig. 23b). In Table 4 are reported third octave band results for each method and corresponding differences.

Compared with the 35 source synthetic antenna, notable differences are highlighted:

- The results are now much less contaminated by measurement noise, and obtained results with the synthetic antenna are close to the mean value of coupled rooms results.
- Differences between the two measurements are now distributed, and not systematically lower as it was the case with the previous antenna, with a maximum difference of 2.1 dB for the 1,000 Hz third octave band.
- Compared with TL estimation discrepancies that can be obtained for different laboratories using the coupled rooms arrangement (see Kihlman and Nillson [5] for example), the differences obtained in the present case between the two measurement methods are generally lower or comparable. This allows validating the synthetic antenna approach for measuring the TL of panels under a synthesized DAF excitation, and opens interesting perspectives for such measurements.

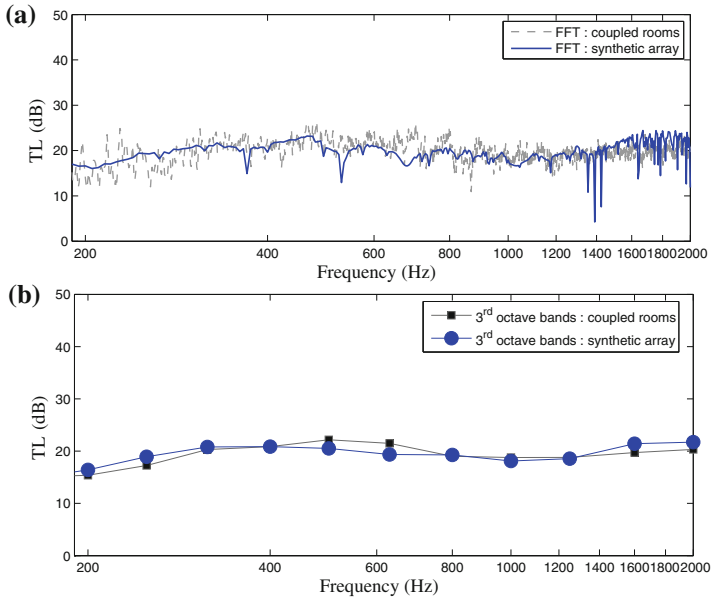

Fig. 23 TL measurement results using a 345 source synthetic antenna and a coupled rooms arrangement. **a** Narrow band result for the coupled rooms measurement is indicated by a *thin dotted black line* (continuous *blue line* for the synthetic antenna measurement). **b** Third octave band results for the coupled rooms measurement are indicated by a *thick gray line*, with *square markers* (*blue line and circle markers* for the synthetic antenna measurement)

Table 4 Third octave bands results for the two methods

	Third octave band center frequencies (Hz)										
	200	250	315	400	500	630	800	1,000	1,250	1,600	2,000
1. C.R. (dB)	15.4	17.2	20.3	20.8	22.2	21.5	19	18.7	18.8	19.7	20.3
2. S.A. (dB)	16.4	18.9	20.8	20.9	20.5	19.4	19.3	18.1	18.5	21.4	21.7
Delta (1–2) (dB)	−1	−1.7	−0.5	−0.1	1.7	2.1	−0.3	0.6	0.3	−1.7	−1.4

C.R. Coupled Rooms; *S.A.* 345 source synthetic antenna

8 Conclusion

A method has been presented for the experimental vibroacoustic testing of panels under DAF or TBL excitation, either subsonic or supersonic. Three possible reproduction approaches have been described and implemented in hemi-anechoic conditions, using a synthetic array and a calibrated monopole source. One of the major interest of the method is that it does not require wall pressure measurements. Random pressure field excitations and related vibroacoustic metrics are synthesized at a post-processing phase.

The experimental results have confirmed the potential of two approaches for the reproduction of random pressure fields, based on WFS and P-NAH, which lead to physical solutions of this problem. The LS solution also provides good results, but requires a regularization procedure for which the proper choice of the regularization parameter can be difficult without an a priori knowledge of the possible reproduction source amplitudes or possible radiated power from the excited panel.

Regarding TBL reproduction, results of previous simulations are confirmed in the sense that a plane separation smaller than half the acoustic wavelength and a source separation referred to the smallest wavelength to be reproduced (i.e. the convective wavelength) are needed to allow reproduction of the target subsonic TBL pressure field. The comparison of the TL values obtained under a subsonic TBL excitation and a DAF excitation with the 110 source array agrees well with the trends observed in simulations. Except at the structural resonances and on a frequency range from 170 to 700 Hz, the results indicate higher TL values under a TBL excitation than those obtained under a DAF excitation. A Transmission Loss analysis in the wavenumber domain can help studying the transmission mechanisms.

In the case of DAF reproduction, it was shown that the method leads to a very good estimation of the TL of the tested panel. It can also reproduce the effect of grazing incidences on the vibroacoustic indicators. It thus provides an alternative to coupled rooms for the measurement of TL under accurate and repeatable DAF, as was shown by an experimental validation.

References

1. M.J. Crocker, The response of a supersonic transport fuselage to boundary layer and to reverberant noise. J. Sound Vib. **9**(1), 6–20 (1969)
2. C. Lesueur, G. Poumerol, A. Blaise, Vibroacoustic response of a composite multilayered plate coupled to a rectangular cavity and excited by white noise and a turbulent boundary layer. Acta Acoustica **3**, 153–167 (1995)
3. J. Rohlfing, P. Gardonio, Homogeneous and sandwich active panels under deterministic and stochastic excitation. J. Acoust. Soc. Am. **125**, 3696–3706 (2009)
4. U. Orrenius, V. Cotoni, A. Wareing, Analysis of sound transmission through aircraft fuselages excited by turbulent boundary layer or diffuse acoustic pressure fields, in *Proceedings of the 38th InterNoise Congress*, Ottawa, Canada, 23–26 Aug 2009, pp. 1–9
5. T. Kihlman, A.C. Nilsson, The effects of some laboratory designs and mounting conditions on reduction index measurements. J. Sound Vib. **24**(3), 349–364 (1972)
6. T. Bravo, S.J. Elliott, Variability of low frequency sound transmission measurements. J. Acoust. Soc. Am. **115**(6), 2986–2997 (2004)
7. A.J. Berkhout, D. De Vries, P. Vogel, Acoustic control by wave field synthesis. J. Acoust. Soc. Am. **36**(12), 2764–2778 (1993)
8. A. Berry, R. Dia, O. Robin, A wave field synthesis approach to reproduction of spatially-correlated sound fields. J. Acoust. Soc. Am. **131**(2), 1226–1239 (2012)
9. E.G. Williams, *Fourier Acoustics: Sound radiation and Nearfield Acoustical Holography* (Academic Press, San Diego, 1999), pp. 15–114. (Chaps. 2 and 3)

10. O. Robin, A. Berry, S. Moreau, Reproduction of random pressure fields based on planar nearfield acoustic holography. J. Acoust. Soc. Am. **133**(6), 3885–3899 (2013)
11. M. Aucejo, L. Maxit, J.-L. Guyader, Experimental simulation of turbulent boundary layer induced vibrations by using a synthetic array. J. Sound Vib. **331**, 3824–3843 (2012)
12. B. Rafaely, Spatial-temporal correlation of a diffuse sound field. J. Acoust. Soc. Am. **107**(6), 3254–3258 (2000)
13. W.K. Blake, *Mechanics of Flow-Induced Sound and Vibration*, vol. II (Academic Press, New York, 1986), pp. 595–657. (Chap. 9)
14. G.M. Corcos, Resolution of pressure in turbulence. J. Acoust. Soc. Am. **35**, 192–199 (1963)
15. P.A. Nelson, S.H. Yoon, Estimation of acoustic source strength by inverse methods : Part I, conditioning of the inverse problem. J. Sound Vib. **233**(4), 643–668 (2000)
16. O. Kirkeby, P.A. Nelson, Reproduction of plane wave sound fields. J. Acoust. Soc. Am. **94**(5), 2992–3000 (1993)
17. T. Bravo, C. Maury, A synthesis approach for reproducing the response of aircraft panels to a turbulent boundary layer excitation. J. Acoust. Soc. Am. **129**(1), 143–153 (2011)
18. O. Robin, A. Berry, S. Moreau and S. Campeau, Experimental reproduction of random pressure fields for vibroacoustic testing of plane panels, in *Proceedings of the 19th AIAA/CEAS Aeroacoustics Conference*, Berlin, Germany, Paper No. 2013–2027, 27–29 May 2013, pp. 1–23
19. P.C. Hansen, *Rank-Deficient and Discrete Ill-Posed Problems* (SIAM, Philadelphia, 1998), pp. 99–134. (Chap. 5)
20. E.G. Williams, Regularization methods for near-field acoustical holography. J. Acoust. Soc. Am. **110**(4), 1976–1988 (2001)
21. F. Fahy, P. Gardonio, *Sound and Structural Vibration: Radiation, Transmission and Response*, 2nd edn (Academic Press, Oxford, 2007), pp. 135–242 and pp. 277–374 (Chaps. 3 and 5)
22. A. De Bruijn, Influence of diffusivity on the transmission loss of a single-leaf wall. J. Acoust. Soc. Am. **47**(3), 667–675 (1970)
23. C. Maury, S.J. Elliott, P. Gardonio, Turbulent boundary layer simulation with an array of loudspeakers. AIAA J. **42**, 706–713 (2004)
24. Finite Element Modeling of Nova software, developed by Mecanum Inc and distributed by ESI group. http://www.esi-group.com/products/vibro-acoustics/VA%20One%20Modules/nova (date last viewed 11/09/12)
25. M.R. Shepherd, S.A. Hambric, Comment on plate modal wavenumber transforms in Sound and structural vibration. J. Acoust. Soc. Am. **132**(4), 2155–2157 (2012). [Academic Press (1987, 2007)]

Identification of Boundary Pressure Field Exciting a Plate Under Turbulent Flow

Nicolas Totaro, Charles Pézerat, Quentin Leclère, Damien Lecoq and Fabien Chevillotte

Abstract The characterisation of the aeroacoustic wall pressure field generated by turbulent flow is a difficult task that often requires instrumented panels and huge facilities like wind tunnels. In situ and non-intrusive experiments are rather not possible. In addition, the pressure field is dominated by the aerodynamic component and the experimental dynamics are not sufficient to measure correctly spectra in low wavenumbers by microphones. The present chapter deals with such a separation method by using the Force Analysis Technique (FAT). FAT is based on the use of the equation of motion of the structure (here a plate) and on the approximation of the fourth derivatives by a finite difference scheme. In the case of turbulent flow, the force auto-spectrum can be deduced at one point of the structure by measuring the velocity at 13 points synchronously. To this purpose, an array of 13 pU (acoustic pressure/particle velocity) probes has been made up. This array is moved in the near-field of the plate to identify map of the wall pressure level applied on the surface of the plate. In the present application, it is shown that FAT only identifies the component of the excitation with wavenumber lower than the natural flexural wavenumber of the plate, due to filtering effect of the plate and of the finite difference scheme. In most cases, the convective peak is then canceled and

N. Totaro (✉) · Q. Leclère
Laboratoire Vibrations Acoustique, INSA-Lyon, 25 bis Avenue Jean Capelle,
F-69621 Villeurbanne Cedex, France
e-mail: nicolas.totaro@insa-lyon.fr

Q. Leclère
e-mail: quentin.leclere@insa-lyon.fr

C. Pézerat · D. Lecoq
LUNAM université, Université du Maine, CNRS UMR 6613, LAUM-ENSIM,
Avenue O. Messiaen, 72085 Le Mans Cedex 9, France
e-mail: charles.pezerat@univ-lemans.fr

D. Lecoq
e-mail: lecoq.damien@gmail.com

F. Chevillotte
Matelys, 1 rue Baumer, 69120 Vaulx-en-Velin, France
e-mail: fabien.chevillotte@matelys.com

E. Ciappi et al. (eds.), *Flinovia - Flow Induced Noise and Vibration Issues and Aspects*, DOI 10.1007/978-3-319-09713-8_9

only the acoustic part of the turbulent flow is identified. This property can be of great interest for vehicle manufacturers to quantify the part of the wall pressure that is responsible of the radiated noise or to use FAT as a source separation technique.

1 Introduction

The direct measurement of the wall pressure induced by a turbulent flow on a structure needs the use of flush-mounted microphones or the use of specific instrumented panels [1, 2]. For example, the estimation of the wall pressure, due to an aerodynamic flow exciting an automotive glass is a particularly difficult task.

Classically, the turbulent flow are not characterized by an explicit description in time and space but by a statistical description only. For excitations due to Turbulent Boundary Layers (TBL), this statistical description relies on semi-empirical spectral models usually expressed in wavenumber domain [3, 4]. The parameters of TBL models can be deduced from measurements in a wind tunnel [5, 6]. This spectral formulation is extensively used in the literature, for example in modal models [7–9], Finite Element models [10] and energy methods [11].

The objective of the proposed approach is to identify the pressure field by measuring the vibration field of the excited structure (the glass downstream the rearview mirror for example).

The Force Analysis Technique (FAT) [12, 13] is a method identifying the force distribution acting on a structure by measuring its velocity field. As Martin and Leehey [14] have done it on a membrane, FAT uses the plate as a sensor by taking advantage of filtering effects of the structure. In FAT, the spatial derivatives of the equation of motion of the structure must be approximated and are estimated by finite different schemes. This method has been successfully applied to different kinds of excitations or structures [15–17].

In the present chapter, after a description of FAT and its newer version CFAT, the method is studied thanks to a simulation with a TBL excitation and to an experimentation with a detached flow excitation. The goal of the simulation is to show how the FAT extracts the information of the excitation in the low wavenumber domain. The advantage of this simulation is the possibility to control the aerodynamic and the acoustic components. It is then shown in what circumstances the FAT can isolate and can quantify the acoustic component exciting the plate. The experimentation was made in a wind tunnel where the turbulences exciting the plate are due to the presence of a cube in the flow. In practice, the velocity field of the plate is measured by an array of 13 pU probes [18] placed in the near-field of the plate at the opposite side of the excitation. The reconstructed wall pressures are then compared to pressures measured on a rigid panel equipped by flush-mounted microphones. The results show clearly that FAT identifies levels in the low wavenumber domain 20 dB lower than the total pressure level. It is in particular shown that acoustic phenomena of the wind tunnel are observed thanks to the

filtering aspect of the plate and to the post-process used. Of course, limitations of the use of FAT for the acoustic component identification for car applications is discussed and the conclusion attempts to highlight other potential applications in other industry sectors.

2 Principle of the Force Analysis Technique

The Force Analysis Technique [12, 13] uses the equation of motion of a structure to identify the load distribution applied to the structure. In the case of flexural plate in harmonic regime, the equation of motion writes

$$D\left(\frac{\partial^4 w(x,y,\omega)}{\partial x^4}+2\frac{\partial^4 w(x,y,\omega)}{\partial x^2 y^2}+\frac{\partial^4 w(x,y,\omega)}{\partial y^4}\right)-\rho h\omega^2 w(x,y,\omega)=p(x,y,\omega), \tag{1}$$

where $D=Eh^3/(12(1-\nu^2))$ is the flexural rigidity of the plate. The plate is characterized by the Young's modulus E (Pa), the density ρ (kg/m^3), the Poisson's coefficient ν and the thickness h (m). $p(x,y,\omega)$ is the load distribution (N/m^2) applied on the surface of the plate. $w(x,y,\omega)$ is the out-of-plane displacement of the plate at the position (x, y) at angular frequency ω.

The load distribution at point (x, y) can then be deduced if the displacement and the fourth derivatives of the displacement are known at the same point. A finite difference approximation is used to estimate the fourth derivatives of the displacement at point (x, y) by measuring the response of the plate at 13 points located in a finite difference scheme centered on point (x, y) as presented in Fig. 1. As the equation of motion describes a local equilibrium of forces, the identification does not depend on boundary conditions of the plate.

The equation of motion, and so the load distribution, can be approximated by:

$$p_{\mathrm{FAT}}(x,y,\omega)=D\left(\delta_{\Delta}^{4x}+2\delta_{\Delta}^{2x2y}+\delta_{\Delta}^{4y}\right)-\rho h\omega^2 w(x,y,\omega), \tag{2}$$

where

$$\delta_{\Delta}^{4x}=\frac{1}{\Delta^4}\sum_{p=-2}^{2}\Psi_p w(x-p\Delta,y,\omega), \tag{3}$$

$$\delta_{\Delta}^{4y}=\frac{1}{\Delta^4}\sum_{p=-2}^{2}\Psi_p w(x,y-p\Delta,\omega), \tag{4}$$

where $\Psi_{-2}=\Psi_2=1$, $\Psi_{-1}=\Psi_1=-4$ and $\Psi_0=6$ and:

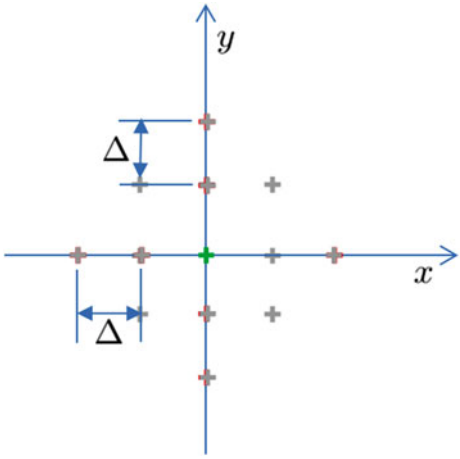

Fig. 1 Finite difference scheme used to approximate the fourth derivatives of the equation of motion of a flexural plate. Δ is the spacing between points of the finite difference scheme

$$\delta_{\Delta}^{2x2y} = \frac{1}{\Delta^4} \sum_{p=-1}^{1} \sum_{q=-1}^{1} \Phi_{pq} w(x + p\Delta, y + q\Delta, \omega), \tag{5}$$

where $\Phi_{00} = 4$, $\Phi_{-10} = \Phi_{10} = \Phi_{0-1} = \Phi_{01} = -2$ and $\Phi_{-1-1} = \Phi_{11} = \Phi_{1-1} = \Phi_{-11} = 1$.

Due to the spacings between sensors, FAT is only valid on a limited frequency band. The low frequency limit depends on the size of the finite difference scheme. It has been defined empirically that at least one bending wavelength is required along the length of the scheme. Thus, the low frequency limit of FAT is given by:

$$f_{\min} = \frac{2\pi}{\sqrt{\frac{\rho h}{D}}(4\Delta)^2}. \tag{6}$$

The high frequency limit of FAT is given by the Nyquist-Shannon sampling theorem. The maximal wavenumber is defined as π/Δ and the high frequency limit is:

$$f_{\max} = \frac{\pi}{2\sqrt{\frac{\rho h}{D}}\Delta^2} = 4 f_{\min}. \tag{7}$$

Recently, a revised version of FAT was also proposed by Leclère and Pézerat [21]. The proposed approach is called "Corrected Force Analysis Technique" and is noted CFAT in the following. CFAT consists in adapting the finite difference scheme in order to be a low-pass wavenumber filter in addition to the derivation approximation. By observing the effects of the approximation of the finite

difference scheme in the wavenumber domain, authors showed that the operation filters high wavenumbers but amplify information around the natural wavenumber of the plate. A new scheme is then proposed:

$$p_{\mathrm{CFAT}}(x,y,\omega) = D\left(\mu^4\delta_{\Delta}^{4x} + 2\upsilon^4\delta_{\Delta}^{2x}\delta_{\Delta}^{2y} + \mu^4\delta_{\Delta}^{4y}\right) - \rho h\omega^2 w(x,y,\omega), \tag{8}$$

where the two constants μ and υ are defined as follows:

$$\mu^4 = \frac{\Delta^4 k_f^4}{4\left[1-\cos\left(k_f\Delta\right)\right]^2}, \tag{9}$$

and

$$\upsilon^4 = \frac{\Delta^4 k_f^4}{8\left[1-\cos\left(\frac{k_f\Delta}{\sqrt{2}}\right)\right]^2} - \mu^4. \tag{10}$$

The wavenumber responses of FAT and CFAT are shown in Fig. 2.

The low-pass filtering effect of FAT is clear but a drastic amplification exists on a circle having a radius k_f. Of course, the filtering is more intensified when the frequency increases because the effects of the discretisation are more important. Concerning the CFAT filtering, the effects are close to the FAT filtering, except that the discontinuity at k_f is soften.

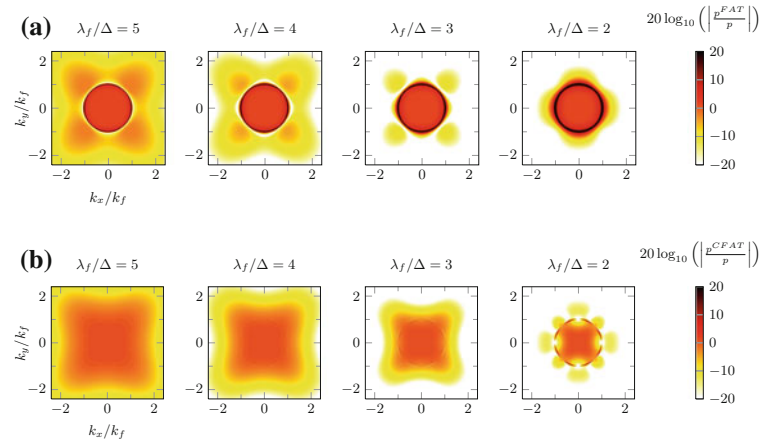

Fig. 2 Wavenumber responses of **a** FAT and **b** CFAT for different number of points n per wavelength

3 Numerical Study of the Filtering Effects of Force Analysis Technique

Due to the filtering effect of the finite difference scheme, the Force Analysis Technique cannot identify the entire wall pressure because it is limited to a wavenumber region. The question is to know if it is able to separate correctly a physical acoustic excitation as it is located in the low wavenumber domain, even if it is a very small component. The following part of this chapter comes from the work of the Lecoq's PhD thesis [20, 22]. It is based on a pure numerical simulation where the excitation can be entirely controlled. The principle of the simulation is first described. Then the effects of filtering are discussed.

3.1 Numerical Synthesis of Wall Pressure Field Using Cholesky Decomposition

3.1.1 Synthesis of the Excitation

The numerical experiment consists in calculating the wall pressure exciting the plate from given auto and cross-spectrum templates, calculating the displacement field of a plate, adding a noise in order to simulating measurements and simulating the Force Analysis Technique. Signals of wall pressures are obtained on a given mesh grid from a signal processing technique synthesizing time signals. This technique [23] provides the simulation of multicorrelated random processes. Recently, Hekmati et al. [24] used this method for turbulent wall pressures. A simplified explanation of this method is proposed here:

First Step

Write the cross-spectrum matrix $\mathbf{S}(\omega)$ where each term is the desired cross-spectrum $S_{pp'}(r_x, r_y, \omega)$ between two points. With M points in the space domain, $\mathbf{S}(\omega)$ is a $(M \times M)$ matrix.

Second Step

Factorize the matrix $\mathbf{S}(\omega)$ by the Cholesky decomposition:

$$\mathbf{S}(\omega) = \mathbf{H}(\omega)\mathbf{H}^H(\omega), \tag{11}$$

where $\mathbf{H}(\omega)$ is a lower triangular matrix and $\mathbf{H}^H(\omega)$ its conjugate transpose.

Third Step

Generate a vector Γ of random phases with M elements:

$$\Gamma_i = e^{j2\pi\gamma_i}, \tag{12}$$

where γ_i is a uniformly distributed random number between 0 and 1. We note that the expected value of each element is:

$$E[\Gamma_i] = 0. \tag{13}$$

Fourth Step

Create a vector $\mathbf{P}(\omega)$ for a given angular frequency ω:

$$\mathbf{P}(\omega) = \mathbf{H}(\omega)\Gamma. \tag{14}$$

Each element of the vector $\mathbf{P}(\omega)$ represents the Fourier transform at the angular frequency ω of the time signals $p(x, y, t)$.

Fifth Step

Finally, steps 1 through 4 are performed for each angular frequency ω up to the Nyquist frequency $f_e/2$. An inverse Fourier transform provides the time signals $p(x, y, t)$.

We can prove easily that the cross-spectrum matrix $\mathbf{S}_P(\omega)$ of the field $\mathbf{P}(\omega)$ in Eq. (14) corresponds to the desired $\mathbf{S}(\omega)$. Indeed, $\mathbf{S}_P(\omega)$ yields

$$\mathbf{S}_P(\omega) = E[\mathbf{P}(\omega)\mathbf{P}^H(\omega)]. \tag{15}$$

By replacing $\mathbf{P}(\omega)$ by its expression in Eq. (14), it becomes:

$$\mathbf{S}_P(\omega) = E[\mathbf{H}(\omega)\Gamma[\mathbf{H}(\omega)\Gamma]^H] = \mathbf{H}(\omega)E[\Gamma \cdot \Gamma^H]\mathbf{H}^H. \tag{16}$$

According to Eq. (13) and since the random numbers γ_i are independent, the expected value $E[\Gamma \cdot \Gamma^H]$ is the identity matrix. Finally, according to Eq. (11),

$$\mathbf{S}_P(\omega) = \mathbf{S}(\omega). \tag{17}$$

The pressure field $\mathbf{P}(\omega)$ complies with the desired cross-spectrum.

In order to understand how the inverse method FAT identifies the excitations with a cross-spectrum similar to that of the turbulent wall pressures the following desired cross spectrum were defined:

$$S_{pp'}(r_x, r_y, \omega) = S_{pp}(\omega)\left(\mathrm{e}^{-\omega\frac{|r_x|}{\alpha_x U_c}} e^{-\omega\frac{|r_y|}{\alpha_y U_c}} e^{j\omega\frac{r_x}{U_c}} + A\ \mathrm{sinc}\left(k_{ac}\sqrt{r_x^2 + r_y^2}\right)\right), \quad (18)$$

where $S_{pp}(\omega)$ is obtained from the semi-empirical model of Goody [25]. In Eq. (18), the first term in parenthesis corresponds to the model of Corcos and corresponds to the aerodynamic component. The second term corresponds to the cross-spectrum of an acoustic diffuse field. The term A reflects the relationship between the aerodynamic and the acoustic energies. In the following, A is set to 0.05 in order to have a small acoustic energy (5 % of the aerodynamic energy). Figure 3 shows, for different frequencies, the cross-spectra of the wall pressure analysed after obtaining all time signals by the described synthesis above. The acoustic and the aerodynamic component are visible; the acoustic component corresponds to a small disc centred at the origin, the aerodynamic energy is located on the right around the convective wavenumber.

3.1.2 Calculation of the Vibration

For the calculation of the vibration field in the time domain, the modal decomposition method, explained by Guyader [26], is used. The plate is supposed to be rectangular and simply supported at its boundaries. Its dimensions are noted L_x and L_y along x and y axes. The plate is also excited by the pressure field $p(x, y, t)$ calculated above (we consider a weak fluid-structure coupling). The equation of motion and the boundary conditions are:

$$\rho h \frac{\partial^2 w}{\partial t^2} + D\left(\frac{\partial^4 w}{\partial x^4} + 2\frac{\partial^4 w}{\partial x^2 y^2} + \frac{\partial^4 w}{\partial y^4}\right) = p(x, y, t), \quad (19)$$

$$w(x, y, t) = \frac{\partial^2 w}{\partial x^2} = 0 \quad \text{for } x = 0 \text{ and } x = L_x, \quad (20)$$

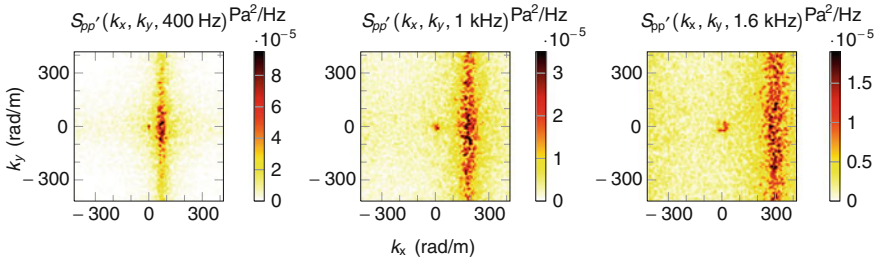

Fig. 3 Representation of the synthetised wall pressure field in the wavenumber domain at frequencies 400 Hz, 1 and 1.6 kHz

$$w(x,y,t) = \frac{\partial^2 w}{\partial y^2} = 0 \quad \text{for } y = 0 \text{ and } y = L_y. \tag{21}$$

The displacement is decomposed on the basis of the normalized eigenfunctions $\phi_{mn}(x,y)$

$$w(x,y,t) = \sum_{m=1}^{\infty}\sum_{n=1}^{\infty} a_{mn}(t)\phi_{mn}(x,y), \tag{22}$$

where $\phi_{mn}(x,y) = \frac{2}{\sqrt{L_x L_y}}\sin\left(\frac{m\pi}{L_x}x\right)\sin\left(\frac{n\pi}{L_y}y\right)$. After projection of Eq. (19) on eigenfunctions $\phi_{mn}(x,y)$ and the heuristic introduction of a modal damping term [26], the coefficients $a_{mn}(t)$ of Eq. (22) verify

$$\ddot{a}_{mn}(t) + 2\zeta_{mn}\omega_{mn}\dot{a}_{mn}(t) + \omega_{mn}^2 a_{mn}(t) = \frac{p_{mn}(t)}{\rho h}, \tag{23}$$

where $p_{mn}(t)$ refers to the projection of $p(x,y,t)$ on eigenfunctions $\phi_{mn}(x,y)$, $\omega_{mn} = \sqrt{\frac{K_{mn}}{\rho h}}$ is the natural angular frequency of the plate with K_{mn} the generalized stiffness of modes (m, n) defined by:

$$K_{mn} = D\left(\left(\frac{m\pi}{L_x}\right)^4 + \left(\frac{n\pi}{L_y}\right)^4 + 2\left(\frac{m\pi}{L_x}\right)^2\left(\frac{n\pi}{L_y}\right)^2\right). \tag{24}$$

$\zeta_{mn} = \frac{\lambda_{mn}}{2\rho h\omega_{mn}}$ is the damping ratio and λ_{mn} the generalized damping. Without loss of generality the damping is artificially constant with the order of the eigenmode to simplify the problem. Then impulse response of the system defined by Eq. (23) is:

$$h_{mn}(t) = \frac{\mathrm{e}^{-\zeta\omega_{mn}t}}{\sqrt{1-\zeta^2}\omega_{mn}}\sin\left(\sqrt{1-\zeta^2}\omega_{mn}t\right). \tag{25}$$

Finally, coefficients $a_{mn}(t)$ are obtained by a convolution such as:

$$a_{mn}(t) = \int_{-\infty}^{+\infty} h_{mn}(t-\tau)\frac{p_{mn}(\tau)}{\rho h}\mathrm{d}\tau \tag{26}$$

and provide the displacement of Eq. (22).

The inverse problem tested here to identify the turbulent wall pressure is an experimental technique that requires a regularization in the presence of noise. To simulate experimental conditions, some noise is added to the displacement:

$$w_b(x, y, t) = w(x, y, t) + b(x, y, t), \tag{27}$$

where $b(x, y, t)$ is a normally distributed random signal with zero mean and a standard deviation σ. The latter is adjusted to have a given Signal to Noise Ratio (SNR), defined as the ratio at each point between the power of the signal $w(x, y, t)$ and that of the noise $b(x, y, t)$.

3.1.3 System Under Study

The structure excited by this TBL is a glass plate with a thickness equal to 3.85 mm. This is the typical case of a windscreen and its parameters are given in Table 1.

The number of modes N_{mn} used in the calculation of the plate response is chosen such that the last modal wavenumber must be much higher than the convection wavenumber.

The parameters used in the Corcos model are given in Table 2.

The aerodynamic coincidence occurs at very low frequencies (f_{conv} = 34 Hz) while the acoustic coincidence occurs at the frequency f_{ac} = 3.2 kHz. In this case, the aerodynamic component moves very quickly towards the high wavenumbers as the frequency increases and the acoustic part has the strongest influence on the vibration and radiation of the wall since the acoustic and flexural wavenumbers are of the same order of magnitude over a wide frequency range.

Table 1 Plate parameters

Young's modulus	$E = 70 \times 10^9$ Pa
Density	ρ = 2,700 kg/m^3
Thickness	h = 3.85 mm
Length	L_x = 0.6 m
Width	L_y = 0.6 m
Poisson's ratio	$\nu = 0.22$
Damping	$\zeta = 0.05$
Number of modes	$N_{mn} = 125 \times 125$

Table 2 Numerical values of the TBL parameters

Fluid velocity	$U_\infty = 50$ m/s
Convection velocity	$U_c = 35$ m/s
Friction velocity	$u_* = 1.58$ m/s
Boundary layer thickness	$\delta = 11.4$ cm
Kinematic viscosity	$\nu' = 1.54 \times 10^{-5}$ m^2/s
Wall shear stress	$\tau_w = 3$ N/m^2
Corcos coefficients	$\alpha_x = 8$; $\alpha_y = 1$

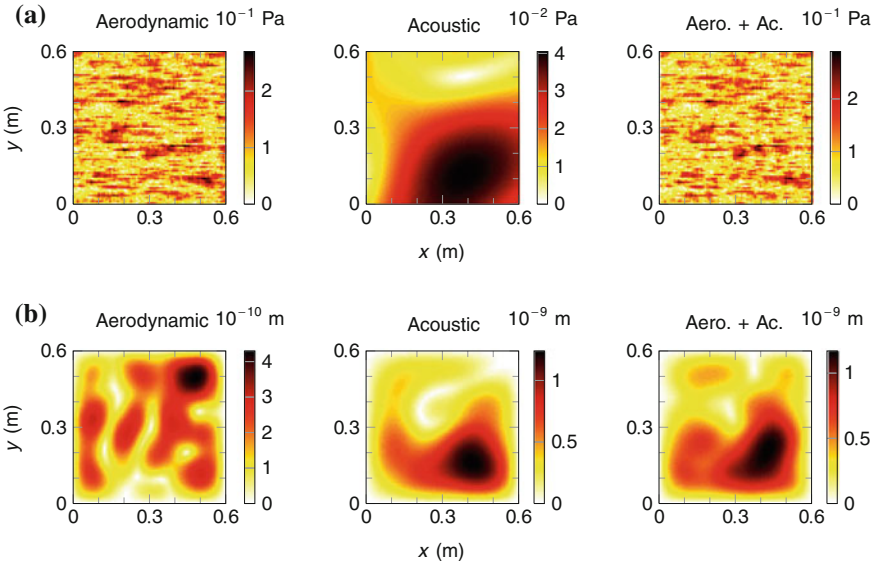

Fig. 4 Representation of the aerodynamic component, the acoustic component and the combinaison of both components on the **a** the pressure field and **b** the displacement field of the plate in the space domain

3.2 Natural Filtering Effect of the Plate

The wall pressures and displacement fields obtained at 200 Hz from excitations containing both components, diffuse field only and aerodynamic field (Corcos) only are shown in Fig. 4. In this example, the acoustic component is very weak (ratio between both components is 5 %), so that it is not observable in the pressure field corresponding to the excitation with both components. However, the contribution of the acoustic component on vibration is clearly visible because the displacement fields obtained from the diffuse field with and without the aerodynamic component are very close. In fact, this phenomenon is accentuated when the frequency increases as the plate becomes to be less sensitive to the aerodynamic energy which moves quickly in the high wavenumber domain. Thus, we can say that the plate provides an interesting filter since it is very sensitive to low wavenumbers where the acoustic component is located.

3.3 Filtering Effect of the Finite Difference Scheme

In this section, it is proposed to evaluate FAT identification. More exactly, the CFAT version will be used as it has the advantage to be more accurate since it avoids amplification of information around the natural wavenumber of the plate.

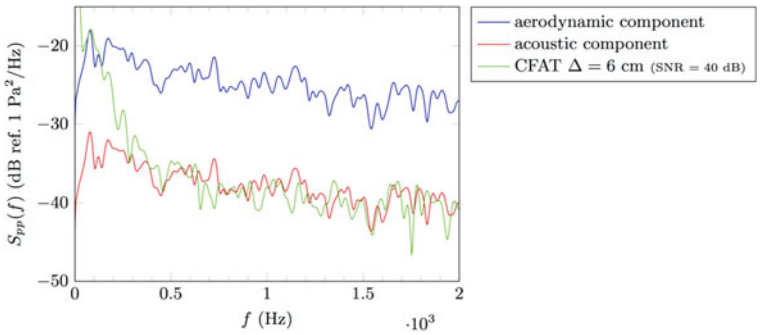

Fig. 5 Frequency spectra of identified pressures where a noise is added to the displacement field (SNR = 40 dB)

The spacing between displacement points is Δ = 60 mm. In order to apply the method in experimental conditions, a noise was added to vibration signals to have a Signal-to-Noise ratio (SNR) equal to 40 dB.

Results in term of frequency autospectra are shown in Fig. 5.

Spectra of the aerodynamic and the acoustic parts (obtained by the synthesis of signals presented above) are also plotted. From 400 Hz to 2 kHz, CFAT identifies exclusively the acoustic component. Indeed, for these frequencies, the filtering of the method has a cutoff wavenumber k_f much smaller than the convection wavenumber k_{conv}. In other words, the convective energy is too far from the circle of radius k_f. For the acoustic component, located inside this circle up to the acoustic coincidence (f_{ac} = 3.2 kHz), the method can reconstruct it precisely. Between 200 and 400 Hz, CFAT reconstructs a small part of the aerodynamic component which is close to the flexural wavenumber k_f in low frequencies. Finally, below 200 Hz, the method can measure the total energy of the aerodynamic component. However, for frequencies below 100 Hz, filtering is not selective enough and the impact of noise located in the high wavenumbers makes the inverse problem unstable.

4 Experimental Illustration of FAT Filtering Effects

The experimental setup was made in a wind tunnel of 50 × 50 cm^2 section in an anechoic chamber. An obstacle (a rigid cube) is placed in the wind tunnel and generates turbulences as presented in Fig. 6. The cube is 10 cm high and is located in the first element of the wind tunnel (the tunnel is composed by three 2 m long elements).

The measurements presented in the following have been done for 3 different flow speeds (U_∞ = 18.5; U_∞ = 25; U_∞ = 30 m/s) with and without the obstacle.

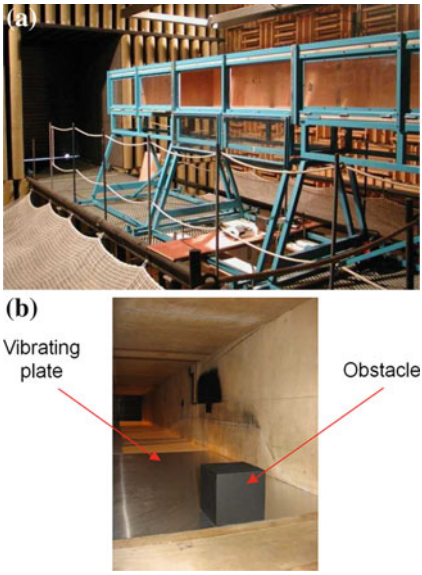

Fig. 6 Experimental setup. **a** Wind tunnel in anechoic chamber. **b** Obstacle in the wind tunnel

4.1 Direct Measurement of the Pressure Field

To directly measure the pressure field downstream the cube, a rigid panel with 45 pinholes equipped with deported microphones is used. This rigid panel is moved sequentially from the cube to obtain a map of 405 points (9 positions of the rigid panel, see Fig. 7). This measurement of the pressure field will be considered as the reference assuming that the pressure field is not affected by the vibration of the plate.

The measured mean square pressures are plotted in Fig. 8 for the three flow speeds, with or without the obstacle.

As can be seen in Fig. 8, the obstacle has a significant influence on the mean wall pressure level whatever the flow speed below 2 kHz. Above this frequency, the obstacle has rather no influence on mean pressure levels that tend to the ones measured without obstacle. In addition, the difference due to the flow speed is clearly shown in Fig. 8. An increase of the flow speed produces an increase of the mean wall pressure level with and without obstacle. The maps of wall pressure level shown in Fig. 9 are also characteristic of the turbulent flow generated by a cube. High level of wall pressure are observed close to the cube in the extension of its lateral faces. The wall pressure level then decreases with the distance to the cube.

The objective of FAT is here to identify the wall pressure distributions by measuring the acoustic pressures radiated to the opposite side of the plate.

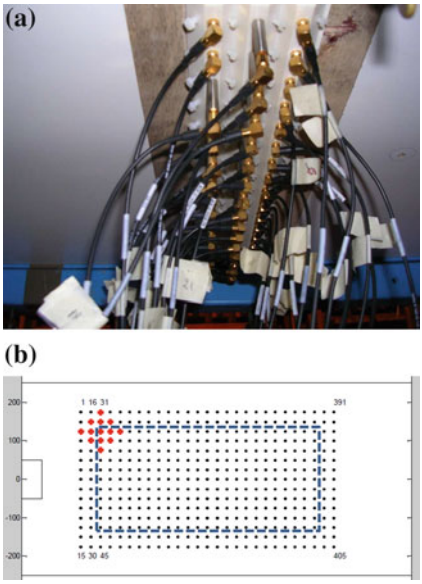

Fig. 7 **a** Direct measurements of the wall pressure field with a rigid panel with 45 pinholes equipped with deported microphones. **b** Mesh of the 405 measurement points (9 positions of the rigid panel). The *red dots* represent the position of the 13 pU probes array. The *rectangle* with *dashed lines* represents the surface of FAT identification

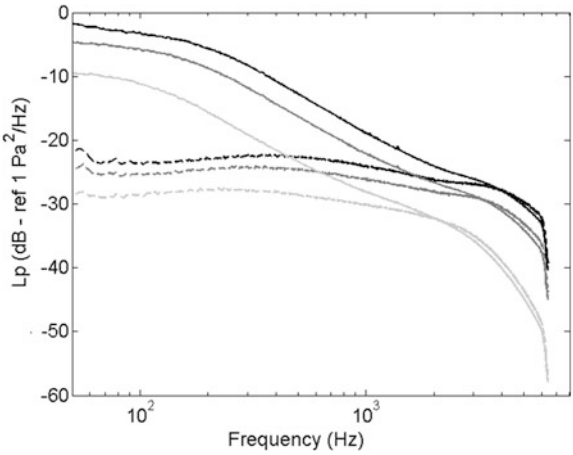

Fig. 8 Mean wall pressure level of the reference measurements with (*solid lines*) or without (*dashed lines*) obstacle for three different flow speeds: 18.5 m/s (*light gray lines*), 25 m/s (*gray lines*) and 30 m/s (*black lines*)

4.2 FAT Identification of the Pressure Field

4.2.1 Practical Application of FAT to Turbulent Flow Excitation

Turbulent flow are random, non stationary and highly uncorrelated excitations and this raises some fundamental issues for the application of FAT or CFAT to this kind of excitations. Usually, measurements of the velocity field of the structures are easily done by using a scanning laser vibrometer. In that case, the measurements are

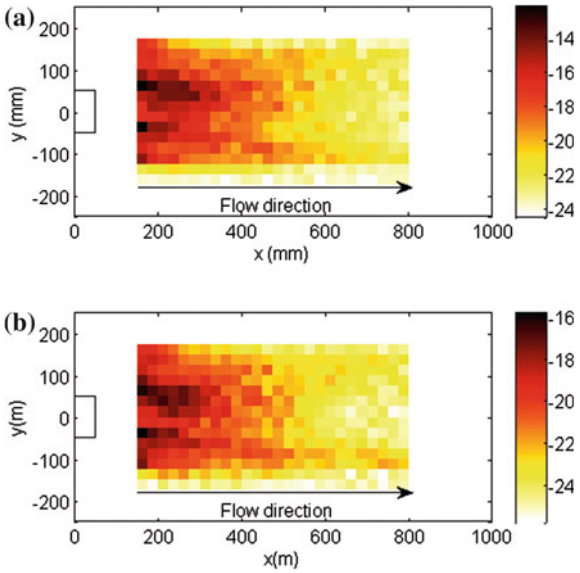

Fig. 9 Maps of wall pressure level downstream the cube obtained with direct reference measurements, U_∞ = 30 m/s. **a** 1,085 Hz; **b** 1,414 Hz

obtained point by point and are unsynchronized and the use of a phase reference is also not possible because the vibration field is spatially uncorrelated.

To overcome this issue, an array of 13 pU probes has been used to measure synchronously the velocity of the plate at the 13 positions of the finite difference scheme. This antenna, presented in Fig. 10, allows one to compute the load only at the center of the array. To obtain a map of load distribution, the array has to be moved sequentially. Obviously, only the force autospectra can be compared since phase reference cannot be used between each load identification.

As pU probes are acoustic sensors used to measure the acoustic pressure and the particle velocity of the noise radiated by the plate, the array has to be placed in the near-field of the plate. By using a very small distance between the antenna and

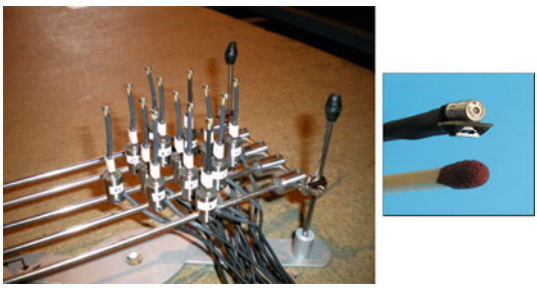

Fig. 10 Array of 13 pU probes to make synchronous measurements on the 13 positions of the finite difference scheme

the plate with respect to the acoustic wavelength, it is assumed, in the following, that the measured acoustic velocity is equal to the plate velocity.

To improve the estimation of vibratory velocity of the plate taking into account the distance between the antenna and the plate, a way is to use the velocity-velocity near-field acoustic holography as shown in [27].

In the following, the acoustic measurements is done at 1 cm from the plate to avoid any need of back-propagation technique.

The studied vibrating structure is here a plate glued on a rigid frame (visible in Figs. 6 and 11) and is placed downstream the cube. This 0.8 mm thick plate is made of aluminum (Young's Modulus 69 GPa, density 2,700 kg/m^3, Poisson's coefficient 0.3). The vibrating surface of the plate has dimensions 0.8 × 0.48 m^2. Due to the turbulence generated by the presence of the cube in the flow, the plate vibrates and radiates in the opposite side of the flow in the anechoic chamber.

In the following, the spacings between sensors are chosen to be $\Delta = 22$ mm and the distance between the antenna and the plate is 1 cm.

4.2.2 FAT Identification Results

The identified mean wall pressure level are presented in Fig. 12. The mean wall pressure level obtained with the rigid panel equipped with pinholes (Fig. 11) are also plotted in Fig. 12.

In the validity domain of FAT (defined by $f_{\min} = 993$ and $f_{\max} = 3{,}972$ Hz), the comparison between direct measurements and identified mean wall pressure level clearly shows a big difference in the whole frequency band. This difference is about 20 dB whatever the flow speed. Based on these results, FAT seems not to assess correctly the wall pressure. This is because a large part of the aerodynamic pressure is filtered by the method. However, the FAT results present interesting information:

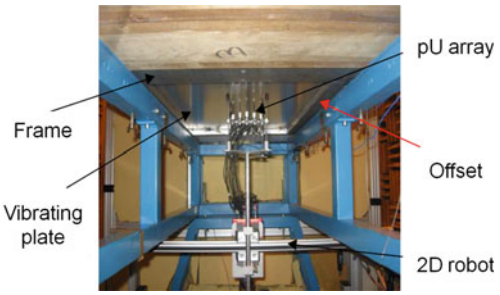

Fig. 11 Measurements of the plate velocity at 13 synchronous points using the 13 pU probes array. The pU array is moved by a 2D robot to scan the whole surface of the plate

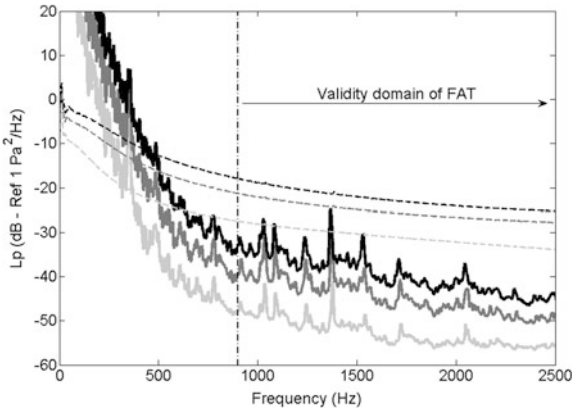

Fig. 12 Mean wall pressure level of the FAT identification (*solid lines*) compared to reference measurements (*dashed lines*) for three different flow speeds: 18.5 m/s (*light gray lines*), 25 m/s (*gray lines*) and 30 m/s (*black lines*). The *vertical dashed-dotted line* represents the low frequency limit of validity of FAT

1. the identified mean wall pressure level increases with flow speed in the same manner as direct measurements;
2. on each curve, one can notice the presence of peaks. As the frequencies of these peaks do not vary with flow speed, they are not due to an aerodynamic phenomenon.

To identify the phenomenon causing these peaks, it is interesting to plot pressure maps obtained by FAT at the corresponding frequencies. Figure 13 presents wall pressure maps at two different frequencies: 1,085 and 1,414 Hz.

This figure reveals completely different pressure distributions than those directly measured and presented in Fig. 9. Contrary to what was expected, the identified pressure level doesn't decrease with the distance to the obstacle and a clear transversal variation is visible. These peaks and pressure distributions reflect the presence of the acoustic modes in the wind tunnel. Indeed, the wind tunnel is a long acoustic volume with rigid lateral walls. Acoustic modes, excited by the air flow, inevitably appear and FAT extracts this phenomenon from vibration of the plate.

Considering the wind tunnel having rigid side panels and an infinite length in the direction of the flow, the eigen-frequencies of the acoustic modes in the cross section are given by:

$$f_{mn} = \frac{c_0}{2\pi}\sqrt{\left(\frac{m\pi}{L_x^{wt}}\right)^2 + \left(\frac{n\pi}{L_y^{wt}}\right)^2}, \tag{28}$$

where $c_0 = 343$ m/s is the sound speed, $L_x^{wt} = 0.5$ and $L_y^{wt} = 0.5$ m are the dimensions of the section of the wind tunnel and m and n are the indices of the mode. The corresponding mode shapes are given by:

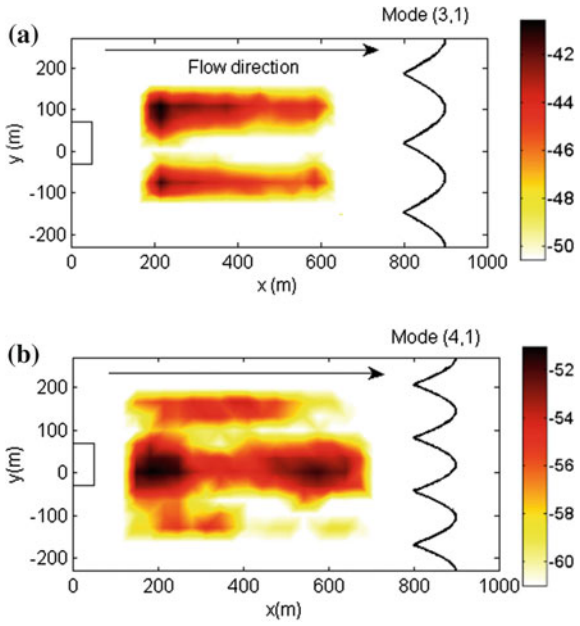

Fig. 13 Maps of wall pressure level downstream the cube obtained with FAT identification, U_∞ = 30 m/s. **a** 1,085 Hz; **b** 1,414 Hz

$$\phi_{mn}(x,y) = \cos\left(\frac{m\pi}{L_x^{wt}}x\right)\cos\left(\frac{n\pi}{L_y^{wt}}y\right). \tag{29}$$

The eigen-frequencies of the wind tunnel are marked in Fig. 14 where the correspondence with the observed peaks is obvious. This good correlation demonstrates that peaks are effectively due to the presence of eigen-modes in the wind tunnel. Figure 13 also shows the identified pressure maps at two frequencies: 1,085 Hz [that corresponds to modes (1,3)] and 1,414 Hz [that corresponds to mode (1,4)]. The identified wall pressure is comparable to the shape of modes (1,3) and (1,4) in the transverse direction.

It is interesting to notice that the acoustic resonances were observed only in the results of the FAT. Because the energy level of the aerodynmic component is very important, these acoustic resonances cannot be seen by a direct measurement of the wall pressure by microphones. This observation could be carried out, because the FAT extracts the information in the low wavenumber domain.

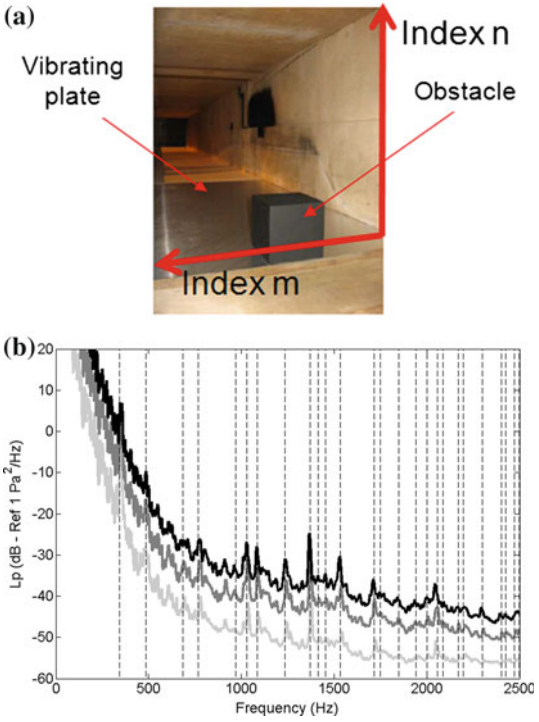

Fig. 14 **a** Representation of modes indices (*m*,*n*) directions. **b** Comparison of identified mean wall pressure level to acoustic natural frequencies in the cross-section of the wind tunnel

5 Conclusion

The knowledge of aeroacoustic excitation is very difficult to assess in the low wavenumber domain. This is due to the fact that aerodynamic component contains a very high energy, so that experimental dynamics are not sufficient to measure correctly spectra in low wavenumbers by microphones. A lot of empirical models exist, like Corcos, Chase, Fowcs-Williams, etc. They are based on a wavenumber description of auto and cross-spectra. They all give good estimations of the energy level around the convective wavenumber but, because of the bad knowledge in the low wavenumber domain, the proposed levels in the acoustic region are not corresponding. Nevertheless, the knowledge of the acoustic component is very important, because thin structures have a high sensitivity to excitation in the low wavenumber domain. Reciprocally, they have also high acoustic radiation efficiency in the low wavenumber domain, so that we can suspect that the acoustic component is particularly responsible to aeroacoustic noise inside automotive cabins.

The use of the Force Analysis Technique is based on the possibility to assess the wall pressure by using the structure as a sensor. The first advantage is that the structure has not to be replaced by another and that it does not require to be drilled. The handling of accelerometer is also an advantage since they are robust sensors

and have excellent sensitivities. As shown in this study, the structure improves the signal to noise ratio thanks to its sensitivity in low wavenumbers, the experimental conditions becomes then more adapted to assessment in this domain. All these conditions are finally linked to a better sensitivity when using vibration measurements rather than pressure measurements.

Because FAT uses displacements measured on a mesh grid and a discrete equation of motion, it filters information contained in the high wavenumber domain. The method comprises then a low-pass wavenumber filter, which brings two important things:

1. it regularizes the inverse problem, so that noise amplification is reduced;
2. it can filter the effects of the aerodynamic component on the vibration.

Even if the plate has finite dimensions, it is very interesting to notice also that the FAT operations do not introduce wavenumber conversion, since it corresponds to a linear shift-invariant system in the space domain while the usual direct problem (displacement obtained from force distribution) is not, due to the boundaries of the structure. In fact, the wavenumber components of the vibration field due to other wavenumber components in the excitation are due to reacting forces at boundaries introducing forced wave field corresponding to a null force distribution at any locations inside the studied area. Of course, the finite dimensions of the plate still restrict the calculation of the wavenumber spectrum of the excitation because the parietal pressure cannot be identified outside the studied area. Computed wavenumber spectra correspond nevertheless to those of the truncated wall pressure exciting the plate in the studied area.

Until now, the use of FAT was studied for car applications, where the fluid is air and the fluid velocity (relative to the structure) is also smaller than the speed of sound. In this case, weak fluid-structure coupling and separation of acoustic and aerodynamic components can be considered. Contrariwise, for other industrial sectors, these assumptions cannot be stated. In naval applications, the velocity of the fluid is smaller and the speed of sound is greater, so that the separation should be more accentuated, but the fluid-structure coupling should be taken into account if one is interested in identifying the acoustic component of the excitation. In aeronautic applications, the fluid velocity is much higher and can even be greater than the speed of sound. In this case, FAT should not be able to separate components, but it could be used to measure the complete wall pressure, so that it can be seen as an alternative to microphones, with the advantage of being usable in situ on real structures.

In term of immediate perspectives, the application of FAT to more complex structures should be done. The complexities can come from the dynamic comportment of the structure. This is for example the case of windscreens which are not made with a monolithic glass. In this case of composite materials, the use of a homogenised equation of motion should then be made. In case of geometry complexities, the excitation should be more controlled by a detached flow and the dynamic comportment must be modelled numerically by a Finite Element approach. The development of FAT using Finite Element operator instead of an analytic

equation of motion was already made by Cédric Renzi in his PhD thesis [28], but the principal difficulty should be here the conversion of nodal forces to wall pressure.

Acknowledgments The authors are indebted to the institut Carnot Ingénierie@Lyon for its support and funding.

The authors want to thank the Laboratoire de Mécanique des Fluides et d'Acoustique and more particularly P. Souchotte and G. Robert for their help and support.

This research project was funded by the Ministry of National Education Research and Technology of France.

This work was performed within the framework of the Labex CeLyA of Université de Lyon, operated by the French National Research Agency (ANR-10-LABX-0060/ANR-11-IDEX-0007).

References

1. W.K. Blake, Mechanics of flow induced sound and vibration (Academic Press, Waltham 1986)
2. C. Durant, G. Robert, P.J.T. Filippi, P.-O. Mattei, Vibroacoustic response of a thin cylindrical shell excited by a turbulent internal flow: comparison between numerical prediction and experimentation. J. Sound Vib. **229**(5), 1115–1155 (2000)
3. M.K. Bull, Wall-pressure fluctuations beneath turbulent boundary layers: some reflections on forty years of research. J. Sound Vib. **190**, 299–315 (1996)
4. W. Graham, A comparison of models for the wavenumber-frequency spectrum of turbulent boundary layer pressures. J. Sound Vib. **206**, 541–565 (1997)
5. G.M. Corcos, Resolution of pressure in turbulence. J. Acoust. Soc. Am. **49**(3), 192–199 (1963)
6. B.M. Efimtsov, Characteristics of the field of turbulent wall pressure fluctuations at large Reynolds numbers. Sov. Phys. Acoust. **28**(4), 289–292 (1982)
7. C. Maury, P. Gardonio, S.J. Elliot, A wavenumber approach to modelling the response of a randomly excited panel, part I: general theory. J. Sound Vib. **252**, 83–113 (2002)
8. S. De Rosa, F. Franco, Exact and numerical responses of a plate under turbulent boundary layer excitation. J. Fluids Struct. **24**, 212–230 (2008)
9. O. Collery, J.L. Guyader, Solving the vibroacoustic equations of plates by minimization of error on a sample of observation points. J. Acoust. Soc. Am. **127**, 1347–1356 (2010)
10. S. Finnveden, F. Birgersson, U. Ross, T. Kremer, A model of wall pressure correlation for prediction of turbulence-induced vibration. J. Fluids Strcut. **20**, 1127–1143 (2005)
11. N. Totaro, G. Robert, J.L. Guyader, Frequency averaged injected power under boundary layer excitation: an experimental validation. Acta Acust. **94**, 534–547 (2008)
12. C. Pézerat, J.L. Guyader, Two inverse methods for localization of external sources exciting a beam. Acta Acust. **3**, 1–10 (1995)
13. C. Pézerat, J.L. Guyader, Force analysis technique: reconstruction of force distribution on plates. Acust. United Acta Acust. **86**, 322–332 (2000)
14. N. Martin, P. Leehey, Low wavenumber wall pressure measurements using a rectangular membrane as a spatial filter. J. Sound Vib. **52**, 95–120 (1977)
15. C. Pézerat, J.L. Guyader, Identification of vibration sources. Appl. Acoust. **61**, 309–324 (2000)
16. M.C. Djamaa, N. Ouella, C. Pézerat, J.L. Guyader, Reconstruction of a distributed force applied on a thin cylindrical sheel by an inverse method and spatial filtering. J. Sound Vib. **301**, 560–575 (2007)

17. C. Renzi, C. Pézerat, J.L. Guyader, Vibratory source identification by using the finite element model of a subdomain of a flexural beam. J. Sound Vib. **332**(3), 545–562 (2013)
18. H.E. de Bree, P. Leussink, T. Korthorst, H. Jansen, T. Lammerink, M. Elwenspoek, The microflown: a novel device measuring the acoustical flows. Sens. Actuators A, Phys **SNA054/1-3**, 552–557 (1996)
19. B. Arguillat, D. Ricot, C. Bailly, G. Robert, Measured wavenumber-frequency spectrum associated with acoustic and aerodynamic wall pressure fluctuations. J. Acoust. Soc. Am. **128** (4), 1647–1655 (2010).
20. D. Lecoq, C. Pézerat, J.-H. Thomas, W. Bi, in *How an inverse vibration method can be used for the extraction of the acoustic component of a turbulent boundary layer*? Proceedings of Internoise 2012, New York (2012)
21. Q. Leclère, C. Pézerat, Vibration source identification using corrected finite difference schemes. J. Sound Vib. **331**(6), 1366–1377 (2012)
22. D. Lecoq, Identification par problème inverse vibratoire des bas nombres d'onde de pressions pariétales turbulentes, PhD thesis, 2013
23. L.E. Wittig, A. Sinha, Simulation of multicorrelated random processes using the FFT algorithm. J. Acoust. Soc. Am. **58**, 630–634 (1975)
24. A. Hekmati, D. Ricot, P. Druault, Numerical synthesis of aeroacoustic wall pressure fields over a flat plate: Generation, transmission and radiation analyses. J. Sound Vib. **332**(13), 3163–3176 (2013)
25. M. Goody, in *An empirical spectral model of surface-pressure fluctuations that includes Reynolds number effects*. Proceedings of 8th AIAA/CEAS Aeroacoustics Conference and Exhibit, Brenckenridge (2002), pp. 2002–2565
26. J.L. Guyader, Vibration of continuous media. ISTE Ltd (2006)
27. C. Pézerat, Q. Leclère, N. Totaro, M. Pachebat, Identification of vibration excitations from acoustic measurements using near-field acoustic holography and the force analysis technique. J. Sound Vib. **326**, 540–556 (2009)
28. C. Renzi, Identification expérimentale de sources vibratoires par résolution du problème inverse modélisé par un opérateur éléments finis local, PhD thesis, 2011

Part III
Structural Vibration and Noise

In this section, the turbulent boundary layer (TBL) pressure field is considered as a known input load, which is applied to models of underlying structures so that vibration, stresses, and radiated noise may be simulated.

Initially, we outline the importance of flow-induced noise for underwater and aerospace structures. Then, different approaches for modelling flow-induced vibrations are presented. These approaches belong to two main groups: frequency- and time-domain approaches.

Most of the methods in the frequency-domain are based on the Finite Element Method, which becomes computationally infeasible for large structures excited by slowly moving fluid due to the exorbitant mesh sizes required.

For these reasons, energy methods are discussed which allow for coarser meshes. These methods still provide sufficient spatial resolution of results to visualize structural vibrations and the related energy distribution. Attention is also paid to the possibility of inferring equivalent distributed source forcing functions. Similar in some extent to the synthetic array methods described in Part II, the proposed approach pursues reconstructing the effective structural forcing functions based on structural vibrations. The mathematical development leads to an equivalent pseudo deterministic excitation.

Again with the aim of reducing the computational cost, a dimensional analysis, with flow and structural variables, is proposed. It is based on the collapse of a large series of disparate structural vibration measurements into a somewhat universal curve.This part includes also some time-domain analyses, which are required, particularly, for two specific cases: (i) non-statistically stationary or ergodic flows; (ii) acoustic and/or structural waves well coupled with the flow. Finally, we present some time-domain calculations of fluctuating stress, for assessing fatigue damage of structural materials.

Turbulent Flow-Induced Self Noise and Radiated Noise in Naval Systems—An Industry Point of View

Frédérique Chevalier and Christian Audoly

Abstract In naval warfare strategy, different scenarios are considered according to vessels involved and most of the time their acoustic performances determine the advantage of one over the other. To succeed, the vessel needs to be the most silent while being the most efficient in detecting the others. That is why naval reducing both the ship far field radiated noise and the self noise affecting sonar array efficiency is a permanent matter of concern for the naval industry. Several phenomena have to be considered to describe far field radiated noise and self noise. This study focuses on contributions generated by flow noise phenomena induced by Turbulent Boundary Layer (TBL) along the hull. In order to fulfil contractual commitments and design requirements, naval industry has to know how to model these phenomena to predict acoustic performances as accurately as possible. Nowadays, several models enable to describe TBL excitation from which it is possible to calculate vibro-acoustic response by different ways according to the phenomenon and the frequency range considered. In this study, flow noise phenomena induced by TBL in the hydro-acoustic studies of naval vessels and Chase model [3] are first described in general. Then, different modelling techniques of noise prediction are especially introduced for TBL excitation generating self noise on the sonar array located inside a cavity [1, 7] and far field radiated noise through external structure response. To illustrate the problems the naval industry has to deal with, some practical examples are discussed.

F. Chevalier (✉)
DCNS Lorient, Rue Choiseul, CS 800001, 56311 Cedex Lorient, France
e-mail: frederique.chevalier@dcnsgroup.com

C. Audoly
DCNS Research, Le Mourillon, BP404, 83055 Cedex Toulon, France
e-mail: christian.audoly@dcnsgroup.com

E. Ciappi et al. (eds.), *Flinovia - Flow Induced Noise and Vibration Issues and Aspects*, DOI 10.1007/978-3-319-09713-8_10

1 Introduction

In underwater warfare strategy, different scenarios are considered according to vessels involved and most of the time their acoustic performances determine the advantage of one over the other.

A first scenario can be "a submarine against an adverse submarine" and the strategy here is based on the acoustic advantage. In fact, the challenge for submarine SM1 (see Fig. 1) is to detect submarine SM2 before being detected and for that, the following passive sonar equation has to be verified:

$$\mathrm{Ga1} - \mathrm{SN1} - \mathrm{RN1} > \mathrm{Ga2} - \mathrm{SN2} - \mathrm{RN2} \tag{1}$$

where Ga is the sonar gain, SN the self noise on the sonar array and RN the radiated noise.

Another relevant scenario involving a surface ship and a submarine can also be defined, and the strategy here is based on the passive detection of an ASW (Anti Submarine Warfare) frigate by the submarine at a large distance before the surface ship uses its active sonar. In fact, the success of the submarine on the ASW frigate is guaranteed by its sonar array efficiency depending on its self noise.

Finally, to succeed, the vessel needs to be the most silent possible while being the most efficient in detecting the others. That is why reducing both the ship far field radiated noise and the self noise affecting sonar array efficiency is a permanent matter of concern for the naval industry.

Several phenomena have to be considered to describe far field radiated noise and self noise. Concerning far field radiated noise, it can be decomposed into 3 components:

- Internal noise sources radiating through the hull, using three different transmission paths: airborne, structure-borne and fluid transmission
- Flow noise: Turbulent Boundary Layer (TBL) excitation, cavity noise…
- Propeller noise: Blade Rate, blade modes, cavitation…

Regarding sonar array self noise in cavity, it can also be decomposed into the same 3 components, in addition to sea ambient noise. By analysing experiments at sea, it is

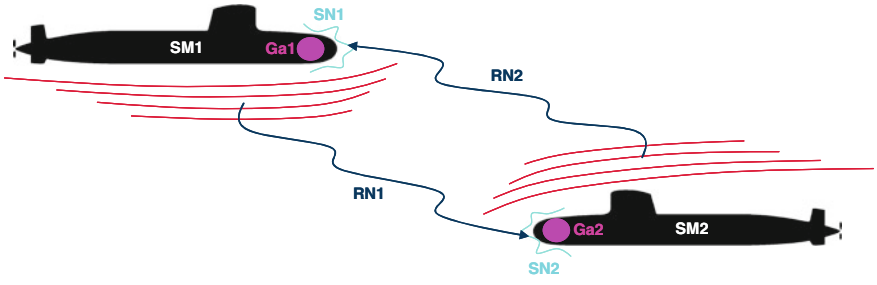

Fig. 1 Scenario where submarines SM1 and SM2 chasing each other

possible to estimate which noise component is dominant. As shown on (Fig. 2) the dominant component depends on frequency and on the speed of the vessel.

Generally, above a certain speed, propeller and flow noise components are predominating for the both kinds of noise considered here.

Industry has to deal with these different kinds of noise to design an efficientship. The industrial process leads to design requirements on noise and vibration levels of machinery equipment items, transfer functions of supporting structures and mounting devices, and on the propeller itself. The final verification of the requirements relies on scale one measurements:

- Machinery noise and vibrations: near field measurements…
- Radiated noise: for vessel acceptance, far field radiated noise measurements are compared to a contractual noise spectrum limit.

Regarding measurement of radiated noise, difficulties are still encountered in identifying each noise component and which one is predominating (internal sources, propeller or flow noise). This is why, for example, extrapolations are done from scale models in tank facilities or water tunnels to estimate propeller noise contribution.

In order to fulfil contractual commitments and design requirements, naval industry has to know how to model them, in order to predict acoustic performances as accurately as possible, and to optimize the systems.

The present paper will focus on contributions generated by flow noise phenomena induced by TBL along the hull because of its important contribution to both radiated noise and self noise at sufficiently high vessel speed.

First, the TBL excitation will be characterized and the different ways to calculate vibro-acoustic response will be recalled according to the phenomena and the frequency range considered.

Then, different modelling techniques of noise predicting are especially introduced for TBL excitation generating flow self noise on sonar array inside cavity [1, 7] and far field radiated noise through external structure response. To illustrate the problems the naval industry has to deal with, some practical examples are discussed.

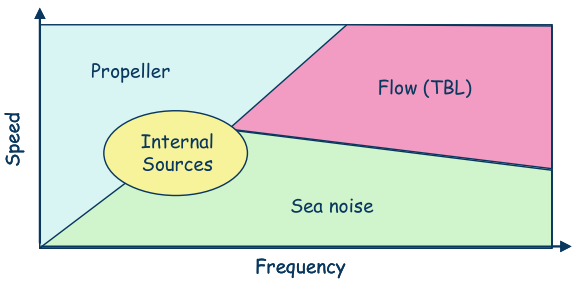

Fig. 2 Result of an analysis allowing to identify the dominant noise component on a sonar array with respects to vessel speed and frequency

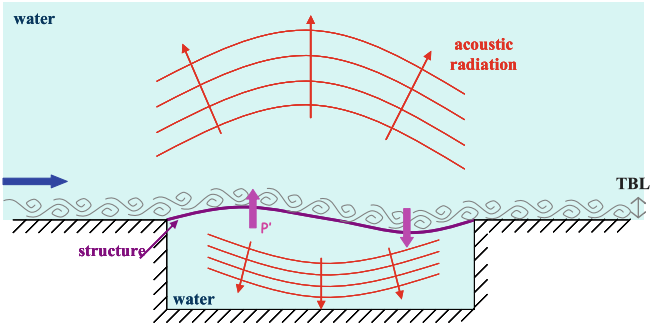

Fig. 3 Schematization of a radiated structure excited by TBL

2 Flow Noise Phenomena Induced by TBL in the Hydro-Acoustic Studies of Naval Vessels

2.1 Turbulent Boundary Layer Excitation

The first difficulty in calculating flow noise phenomena induced by TBL is to extract the wall pressure fluctuation created by the TBL which excites the radiating structure (Fig. 3).

Usually, DNS (Direct Numerical Simulation) or LES (Large Eddy Simulation) CFD (Computational Fluid Dynamics) calculations are necessary to well describe the turbulent structures appearing in the boundary layer but these methods are very time consuming because of the required accuracy of spatial and temporal discretizations. As a consequence, these methods can not be used for industrial applications, but intermediate modelling techniques described afterward can be implemented. Indeed, the wall pressure fluctuation excitations can be directly calculated from local TBL mean parameters through a statistical approach.

2.1.1 Wall Pressure Fluctuation

The wall pressure characterizes the excitation source to be applied into the vibro-acoustic model (Sect. 2.2). Fluctuations appear only when the boundary layer is no more laminar because they come from the TBL vortex formation.

The flow can be split into mean and fluctuant parts and especially for the parietal pressure:

$$p(\vec{x},t) = p_0(\vec{x}) + p'(\vec{x},t) \tag{2}$$

where p_0 is the mean wall pressure and p' its fluctuating part.

In fact, this wall pressure has a random behaviour, so its determination requires a spectral analysis. It is characterized in the frequency domain by a cross-spectrum

density which can be written in the physical space as well as in the wave numbers space. By assuming that the turbulence is homogenous and steady, the wall pressure field can be described by the spatiotemporal correlation function, R_{pp}, defined by:

$$R_{pp}(\vec{x}, \vec{r}, t') = \langle p'(\vec{x}, t), p'(\vec{x} + \vec{r}, t + t') \rangle \tag{3}$$

where $\langle\rangle$ represents the time average. Assuming turbulence is homogenous, this function only depends on the spatial separation r between two points.

The Time Fourier Transform applied on this spatiotemporal function of correlation gives the Power Spectral Density (PSD):

$$S_{pp}(\vec{r}, \omega) = \frac{1}{2\pi} \int_{-\infty}^{+\infty} R_{pp}(\vec{r}, t') \mathrm{e}^{-i\omega t'} \mathrm{d}t' \tag{4}$$

where ω is circular frequency. When the PSD is translated in the wave numbers space, it gives the cross-spectrum in the wave numbers space, Φ_{pp}:

$$\Phi_{pp}(\vec{k}, \omega) = \frac{1}{(2\pi)^3} \int_{-\infty}^{+\infty} \int_{-\infty}^{+\infty} R_{pp}(\vec{r}, t') \mathrm{e}^{i(\vec{k}\vec{r} - \omega t')} \mathrm{d}\vec{r} dt' \tag{5}$$

where $|k| = (k_1 + k_2 + k_3)^{1/2}$ is the wave number, (k_1, k_2) are respectively the longitudinal (same direction as the flow) and transversal wave numbers and k_3 is normal to the structure.

2.1.2 Characterization of TBL Excitation

In literature, cross-spectrum models consider that the boundary layer develops itself on a flat plate or on any surface which has a large enough curvature radius and very small pressure gradients. When the pressure fluctuations spectrum is drawn in the longitudinal and transversal wave numbers plan, two excitation peaks are highlighted in Fig. 4.

The smaller peak, denoted acoustic peak, appears when the excitation has the same wave number as the acoustic one, $k_0 = \omega/c_0$ (where c_0 is the acoustic propagation field). In the wave numbers plane, this region corresponds to the circle of radius k_0. In this acoustic region, the energy can theoretically propagate at large distance but the spectral levels are very low.

Concerning the stronger peak, it corresponds to the convective peak associated to the excitation of the vortex moving in the boundary layer with the convective velocity U_c. In the wave numbers plane, this peak evolves around with $k_c = \omega/U_c$ and its width on the transversal wave number axis is higher than on the longitudinal wave number axis. This convective region corresponds to largest part of the TBL energy, but the corresponding waves are evanescent, so they cannot propagate

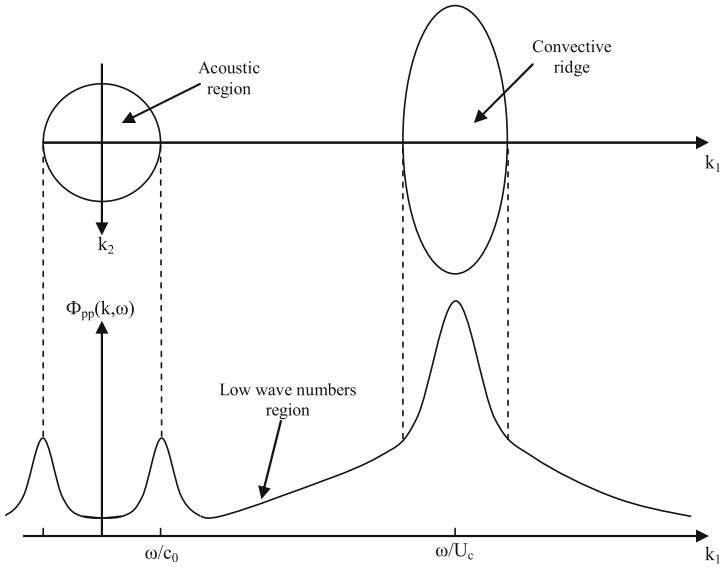

Fig. 4 Regions of the Φ_{pp} spectrum with k_1 and k_2

directly at large distances. Between these two peaks, there is an other region named the low wave numbers region.

The convective velocity is a key parameter in the wall pressure model because it determines the position of the convective peak in the spectrum. At low frequencies, still in the scope of the flat plate assumption, this velocity can be defined with the exterior boundary layer velocity and the boundary layer displacement thickness:

$$U_c = U_e\left(0.6 + 0.4\,\mathrm{e}^{-2.2\frac{\omega\delta_1}{U_e}}\right) \tag{6}$$

In literature, several models exist, under the flat plate assumption, to represent the wall pressure generated by TBL excitation like Corcos 1963, Chase 1987, Flowcs Williams, Smol'yakov-Tkachenko, Efimtsov, etc. Usually, the two first models are mainly used but even if Corcos model describes well the convective peak, many studies have shown that it overestimates the excitation in the low wave-number region. However, structures Naval industry have to deal with generally respond to low wave-number region excitations, that is why Chase model (1987) [2] will be studied afterward because it is more accurate in this region, especially for hydroacoustic phenomenon [1].

2.1.3 Chase Model (1987)

Chase's model is a quasi-analytic model which comes from the Poisson equation for a TBL assumed being parallel (here, $k = (k_1 + k_2)^{1/2}$).

In Chase theory, the cross-spectrum in the wave numbers space can be decomposed into one term associated to the mean shear/turbulence interaction, Φ_{pp}^{M}, and an other term associated to the turbulence/turbulence interaction, Φ_{pp}^{T}.

$$\phi_{pp}(k_1, k_2, \omega) = \phi_{pp}^{M}(k_1, k_2, \omega) + \phi_{pp}^{T}(k_1, k_2, \omega) \tag{7}$$

These two terms can be calculated thanks to the local TBL mean parameters. Chase model defines them as follows:

$$\phi_{pp}^{M}(k_1, k_2, \omega) = \frac{\rho_0^2 U_\tau^3 C_M k_1^2}{\left(\left(\frac{\omega - U_c k_1}{h U_\tau}\right)^2 + k^2 + (b\delta)^{-2}\right)^{\frac{5}{2}}} \tag{8}$$

$$\phi_{pp}^{T}(k_1, k_2, \omega) = \frac{\rho_0^2 U_\tau^3 C_T k^2}{\left(k^2 + (b\delta)^{-2}\right)\left(\left(\frac{\omega - U_c k_1}{h U_\tau}\right)^2 + k^2 + (b\delta)^{-2}\right)^{\frac{3}{2}}} \tag{9}$$

where $U_\tau = (\tau/\rho_0)^{1/2}$ is the friction velocity.

Regarding the constants, C_M enforces the convective peak level, C_T adjusts the low wave numbers level, h characterizes the energy dispersion around the convective peak and b comes from the determination of the maximum spectral frequency. These Chase model constant values were regularly improved by experimental data, such as values suggested by Iddir [5] which are:

$$h = 3.9, \quad C_T = 3.589 \times 10^{-3}, \quad C_M = 0.119, \quad b = 0.75 \tag{10}$$

2.2 Vibro-Acoustic Response and Radiation into Water

2.2.1 Low Frequencies

Different commonly used methods exist to solve vibro-acoustic problem at low frequencies like FEM (Finite Element Method), BEM (Boundary Element Method), and the combination of both, but they have some well known limitations.

Regarding FEM, fluid volume needs to be meshed and in each element, physical quantities are approximated by element interpolation functions. The advantage is that the FEM can also represent the vibrations of the structure excited by the flow. However, the structure modal base has to be truncated and the maximal frequency chosen has to be high enough to solve properly the problem considered. In addition, a difficulty arises for unbounded fluid domains involved in far field radiation problems. In that case, it is necessary to limit the finite element mesh to a bounded domain and to apply non-reflecting impedance boundary conditions to prevent reflection of radiating acoustic waves.

Regarding BEM, even if it only needs to mesh the radiating surface (no fluid volume meshing needed) and physical quantities are just calculated from radiated surface ones (Green function), the method is limited with a cavity problem and requires coupling with finite elements code to get the structure modal base as an input.

In the present case, the structures considered can be very large. In practice, these methods can only be used at low frequencies.

2.2.2 High Frequencies

As a complement of previous introduced methods, a classic approach exists to solve vibro-acoustic problem in high frequencies: the Statistical Energy Analysis (SEA). In this method, the system is divided into subsystems and energy exchanges are calculated between each subsystem. The method assumes that resonance frequencies are uniformly distributed in each frequency band that is to say that energy is distributed over all modes.

To solve the vibro-acoustic problem, each SEA subsystem needs internal loss factors, coupling loss factors and injected power as an input data. To calculate injected power extracted from TBL pressure fluctuation spectrum [7], the following formula can be used in the case where the structure can be modelled as a thin plate vibrating in bending modes:

$$\langle \pi_{inj} \rangle_{\Delta f} = \frac{2\pi^3}{\sqrt{MD}} \phi_{pp}(k_f, 0, \omega) \tag{11}$$

with k_f the structure bending wave number and assuming that k_f is close to plate resonant modes in high frequencies.

Finally, energy balance provides pressure and vibration mean levels for each subsystem as SEA output data.

Note that as this approach requires high modal density, SEA should not be used at low frequencies. In addition, it gives frequency band-averaged and spatially-averaged on each subsystem.

2.2.3 Medium Frequencies

Intermediate approaches also exist to solve medium frequencies vibro-acoustic problems. For example, the Patch Transfer Function (PTF−INSA Lyon) is based on low frequencies FEM method extended to medium frequencies by using system divided into sub-problem and the interface between these subsystems is discretized into patch. Then, the transfer function is calculated between each excited patch and the global system response is reconstituted from each patch transfer functions.

An other method called Virtual SEA (InterAC) is based on high frequencies SEA method extended to medium frequencies. The principle is that improved SEA subsystems are created from extrapolation of FE calculations.

It can be noticed that for these two specific approaches, TBL excitation can be taken into account.

3 Prediction of TBL Flow Self Noise on a Sonar Array Inside a Cavity

In naval industry, self noise phenomena generated by TBL excitation can be encountered on different systems of interest like echo sounder cavities on research vessels or bow sonar cavity of a submarine.

As near field noise impacts the efficiency of the systems especially in medium and high frequencies, that is why a calculation methodology was developed to predict TBL flow self noise.

3.1 Modelling Technique for Medium and High Frequencies

By using the different approaches described previously to predict wall pressure fluctuations and the associated vibro-acoustic response of the structure, a first calculation methodology, shown on Fig. 5, consists in:

- First, a potential flow calculation is performed around the structure with a potential flow code like REVA (Ecole Centrale de Nantes). From this first step, the velocity field around the structure, required as input data for the next step, is computed,
- Then, TBL is calculated using a boundary layer code such as 3C3D (ONERA software). The parameters of the TBL are then used as an input of a Matlab routine to model the wall pressure cross-spectrum and to convert it in a format compatible with the vibro-acoustic code used for the last step (for example the injected power in different frequency bands for the SEA approach),
- In the last step, the structure is excited and the self noise is extracted from its vibro-acoustic response calculated by the adapted code according the frequency range considered.

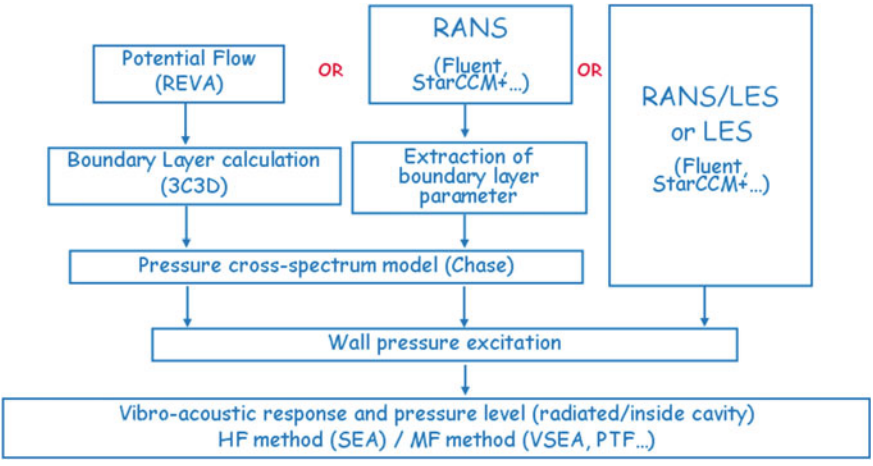

Fig. 5 Vibro-acoustic calculation methodologies to estimate self noise

In this calculation methodology, it is assumed that the interaction between the structure and the fluid is weak because it is considered that the flow is not modified by the structure motion as shown by experiments. In addition, it is assumed that the direct acoustic radiation from the TBL is negligible by comparison to the vibro-acoustic radiation of the structure excited by the flow. So the problem can be separated in two parts:

- Identifying excitation sources independent from the structural response,
- Calculating the structural vibro-acoustic response to this excitation.

In fact, we can expect that the more the methodology is decomposed into several steps (from the right to the left on Fig. 5), the less accurate is are the final results. Moreover, even if cross-spectrum model can be adapted to take into account pressure gradient, detachment zone can not be calculated (3C3D limitations). According to the accuracy expected, a better wall pressure excitation can be found by using an intermediate methodology, with less limitation, proposed by Peltier and Hambric [8] and based on CFD results calculated directly with RANS (Reynolds Averaged Navier Stokes) approach.

3.2 Application to a Submarine Bow Sonar Cavity

By assuming that the sonar dome has a large enough curvature radius (flat plate assumption), the previous approach can be used with Chase model (Fig. 6).

Here the Matlab functions calculated injected power necessary for SEA calculations from the cross-spectrum [7] (Fig. 7).

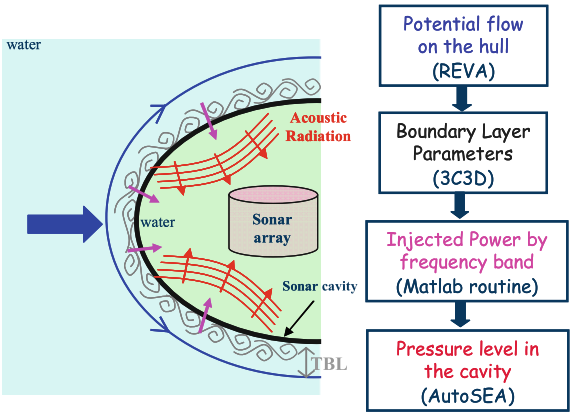

Fig. 6 Vibro-acoustic calculation methodologies adapted to estimate self noise of a bow sonar cavity

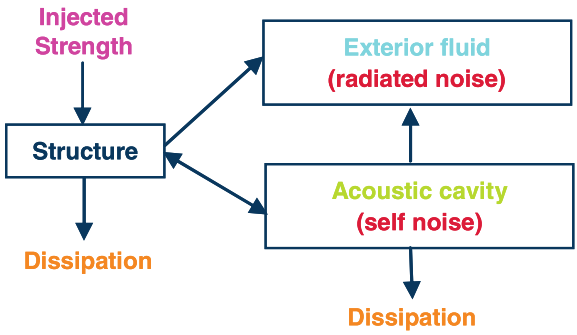

Fig. 7 SEA sub-systems to calculated self noise of a bow sonar cavity

3.3 Feedback from Industrial Use

After calculations, comparisons have to be done to measurement on real systems and these step by step comparisons enable to validate the methodology and final results. Then, numerical parametric studies enable to establish laws on self noise evolution, according frequency and velocity considered.

These studies enable also to choose the best vessel design reducing self noise. First optimizations can be done on the flow excitation by delaying the transition (vessel shape, shape continuity, coating roughness…) or controlling the TBL (TBL manipulation, specific coating…). An other optimization can be done on the structure response by using damping material (filter flow excitation…) and specific structure fixations like passive system (decoupled or damping mounting…) or active system (vibrations filter…).

4 Far Field Radiated Noise Due to TBL Excitation on External Structures

In naval industry, significant far field noise phenomena can appear for example when a TBL excites light external structures. A far field noise can also appear on optimized structure when this one has a geometrical or fixation default. In the latter case, it was observed that few noise contribution is due to the default itself, but an indirect effect can appear because the structural vibro-acoustic response can be modified.

For example, the case of a downward step default experimented by Lee et al. [6] find that the pressure excitation spectrum increases in low frequencies near the detachment zone or downstream, whereas in the far field of the step, spectrum increases in high frequencies because of small structure presence. As the excitation is modified, indirectly the vibro-acoustic response of the structure is impacted.

Concerning fixation default, in addition to the direct modification of the structure modes, Hambric et al. [4] found that the boundary conditions have also an impact on the excitation contribution. Experiments show that a plate with one free edge (perpendicular to the flow) is more impacted by the convective peak than a clamped plate which is more impacted by low wave number. Finally, a fixation default can indirectly have an impact on the structure vibro-acoustic response.

Generally, all these kinds of phenomena impact especially the low and medium frequencies of the vessel acoustic signature.

4.1 Modelling Technique for Low and Medium Frequencies

As already discussed in Sect. 3.1, TBL pressure excitation can be found more or less accurately, and then the vibro-acoustic response of the structure can be calculated directly with FEM approach (see right side of Fig. 8). Even if this approach is more accurate, it can be too expensive in computation time. An alternative approach is to solve the vibro-acoustic problem which consists in:

- First performing structural modes in vacuum (FEM)
- Then importing them with the pressure excitation in entrance of the BEM vibro-acoustic software, which first calculates the structure coupled modes in sea water and then computes the radiated noise in the far field.

This weak fluid structure interaction methodology can be adapted to the specific case of a geometrical default when the TBL pressure excitation has to be calculated (LES approach, no empirical model available).

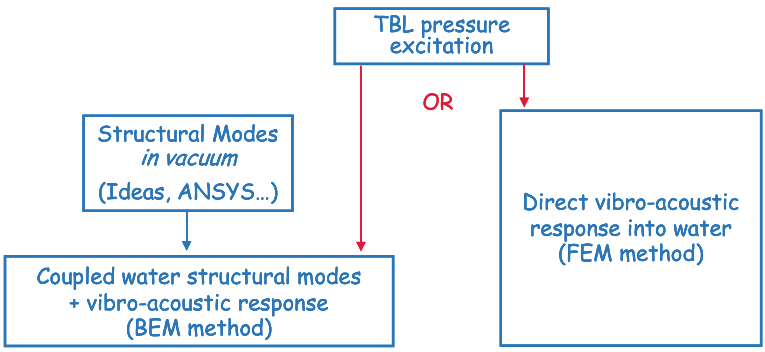

Fig. 8 Vibro-acoustic calculation methodology to estimate far field radiated noise

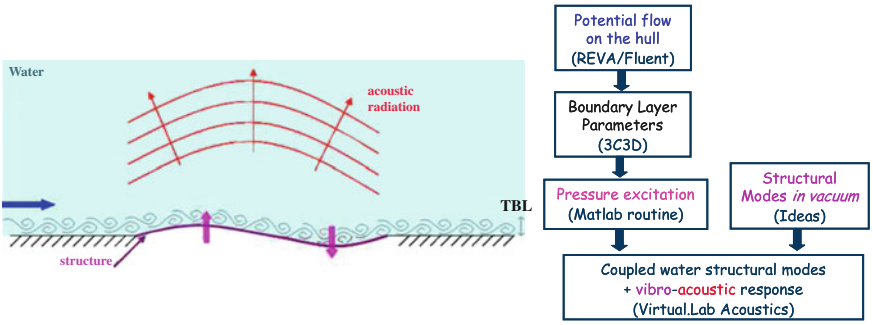

Fig. 9 Vibro-acoustic calculation methodologies adapted to estimate radiated noise of a baffled flat plate

4.2 Application to Baffled Flat Plate Case

Here Matlab functions calculate Chase cross-spectrum and use an accumulated uncorrelated plane waves approach [1] to have an input compatible in entrance of vibro-acoustic code (Fig. 9).

4.3 Feedback from Industrial Use

After calculations, comparisons have to be done to measurement on real systems but there are difficulties in identifying the specific flow noise contribution in measurements from the vessel global radiated noise. Presently, noise levels are well predicted qualitatively, but it is difficult to obtain the actual pressure levels only from simulation. For quantitative prediction, it is necessary in most cases to adjust the model parameters in order to fit with experimental results. Even if several local measurements exist from tank tests, it remains to solve the scaling problem… However, as for the self noise case, it is possible to validate the methodology with comparisons step by step.

These studies enable also to choose the best vessel design reducing far field hydrodynamic noise. First optimizations can be done on the flow excitation by designing a hull shape which does not generate detachment (e.g. no circular cylinder…) or a shape without discontinuities: upward or downward step, hull apertures shape or size… Another optimization can be done on the structure response by increasing mass and/or rigidity, or modifying external structure extremities: well fixed or with rigid trailing edge.

5 Conclusions–Needs

In order to provide high value naval vessels, industry has to design vessel with the best acoustic performances possible:

- Low self noise to have the most efficient sonar array,
- Low radiated noise to remain undetectable.

For sufficiently high vessel speed, flow noise induced by TBL contributed greatly to both noises studied here, and that is why the naval industry has to know how to model this kind of noise:

- To predict the vessel acoustic performance,
- To design vessel and optimize acoustic performance.

Modelling techniques has to be adapted to phenomena and frequency ranges considered and it is necessary to validate each step of the modelling method and final results with comparison to measurements. At the present stage, direct flow computations and FEM type modelling are usable in practice only at low frequencies. At higher frequencies, because of the large size of structures considered, semi-empirical models for the excitation and statistical models for the structural responses are best suited, despite of their limitations.

In the overall, our experience shows that the present models allow understanding the main mechanisms of noise generation, and allow determining qualitatively the evolution of noise along speed and frequency.

On the other hand, accurate quantitative determination of noise levels only with simulation is difficult, so it is still necessary to fit with experimental data. This is due to the complexity of systems considered, and more studies are necessary, both numerical and experimental to enable the Naval industry to improve its prediction and vessel performance design.

Some current research topics are for instance the influence of pressure gradients on TBL excitation, vibro-acoustic response of complex structures, prediction of noise from transition region…

Moreover, methods can be adapted to other components of flow noise like cavity excitation (ballast grid, torpedo tube…) or strong fluid-structure interaction as VIV (Vortex Induced Vibration) phenomenon which can generate tonal noise generally easy to identify on vessel noise spectrum (vortex shedding on submarine fin or sail trailing edge…).

Methods can be also adapted to other components of far field noise like propeller noise (Blade modes, blade singing, wide band spectrum…).

Finally, these topics are also of interest for civilian applications like flow noise on acoustic sensors integrated on the hull of research vessels. Presently, there is also an increasing concern about protection of marine life against underwater noise produced by man activity at sea (ship traffic, oil industry, marine renewable energy systems…).

References

1. M. Aucejo. 'Vibro-acoustique des structures immergées sous écoulement turbulent', PhD thesis, INSA Lyon, 2010
2. M. Aucejo, L. Maxit, J.L. Guyader, Improving the Patch Transfer Functions approach for fluid-structure modelling in heavy fluid. ASME **134**, 051011 (2012)
3. D.M. Chase, The character of the turbulent wall pressure spectrum at subconvective wave numbers and a suggested comprehensive model. J. Sound Vib. **112**(1), 125–147 (1987)
4. S.A. Hambric, Y.F. Hwang, W.K. Bonness, Vibrations of plates with clamped and free edges excited by low-speed turbulent boundary layer flow. J. Fluids Struct. **19**(2004), 93–110 (2004)
5. A. Iddir. 'Effets d'une couche limite turbulente hydrodynamique sur le comportement vibro-acoustique d'une plaque bafflée couplée à une cavité rectangulaire', PhD thesis, Aix-Marseilles II University, 1997
6. Y.-T. Lee, W.K. Blake, T.M. Farabee, Modeling of wall pressure fluctuations based on time mean flow field. J Fluids Eng. **127**(2), 233–240 (2005)
7. L. Maxit and C. Audoly. 'Hydrodynamic noise prediction in a Sonar cavity : injected power estimation from the wavevector—frequency spectrum of turbulent wall pressure', Proceedings of Novem 2005 (Saint Raphael)
8. L.J. Peltier, S.A. Hambric, Estimating turbulent-boundary-layer wall-pressure spectra from CFD RANS solutions. J. Fluids Struct. **23**, 920–937 (2007)

Vibroacoustics Under Aerodynamic Excitations

Mohamed N. Ichchou, Olivier Bareille, Bernard Troclet, Bastien Hiverniau, Marie De Rochambeau and Dimitrios Chronopoulos

Abstract This paper gives a number of energy considerations related to the flow induced vibration and noise predictions. In this context, reduced modeling of structural-acoustic issues are the main red line of the work. The present paper deals thus with equivalent "rain on the roof" (ROF) excitations, which allow the modeling of spatially correlated broadband sources by statistically independent point forces. ROF excitation largely simplifies the expressions of the joint acceptance functions and can be easily modeled using finite element method (FEM). Two approaches are presented here and an equivalent model of excitation is developed and validated on acoustic and aerodynamic excitations, such as diffuse field or turbulent boundary layer (TBL) excitations. The first idea, considers the equivalence over the extended physical domain. It allows equivalent ROF excitation only for frequencies over the acoustic coincidence effect. The second method is based on the wavenumber space equivalence. Validation of this approach has been carried out for different acoustic and aerodynamic excitations, and for different structural boundary conditions. Numerical experiments show that this approach gives acceptable results for a wide frequency range specifically for TBL excitations. Then, the problem of the structural–acoustic response under aerodynamic sources is considered further. The structure is a composite structure of arbitrary thickness and anisotropy. The fully coupled system is modeled using a Statistical Energy Analysis like (SEA-like) approach, and the energetic characteristics for each subsystem are computed and compared to the direct FEM solution. The error of the reduced model calculations for each frequency band is presented and the limits of the reliability of the reduction are explored. Different strategies concerning the reduction process

M.N. Ichchou (✉) · O. Bareille · B. Hiverniau · M. De Rochambeau
LTDS, Ecole Centrale de Lyon, UMR CNRS 5513, Ecully Cedex, France
e-mail: mohamed.ichchou@ec-lyon.fr

B. Troclet
LMT Cachan, Ecole Normale Supérieur de Cachan and EADS Defense and Space, Cachan Cedex, France

D. Chronopoulos
Nottingham University, Nottingham, UK

E. Ciappi et al. (eds.), *Flinovia - Flow Induced Noise and Vibration Issues and Aspects*, DOI 10.1007/978-3-319-09713-8_11

parameters are investigated in order to optimize the accuracy with respect to time efficiency. The loading applied to the model comprises typical random distributed excitations, such as a 'rain-on-the-roof' excitation, a diffused sound field and a Turbulent Boundary Layer (TBL) excitation.

1 Introduction

During lift-off and flight ascent, spatial vehicles are excited by aerodynamic loads. Those excitations are broadband and random. The satellites inside the spatial vehicles are thus excited, which leads to the necessity of modeling the vibration field inside the vehicle throughout the atmospheric flight. Electronic equipments and satellites are consequently excited and the random vibration levels induced by the acoustic environment must be predicted before flights. These random excitations are mainly described by the spatial coherence function. The spatial coherence function of turbulent boundary layer has been widely studied in the literature. Corcos [1] presented one of the early modeling for TBL excitation. Other models derived from Corcos expression were then proposed in order to fit better the turbulent boundary layer behavior in the low-wavenumber region: among others Chase [2] and Efimstov [3]. Graham analyzed the accuracy of those TBL modeling in Ref. [4].

The response of fluid loaded structures can be estimated from data on the unsteady pressure field and their correlation functions. In the high-mid frequency range Statistical Energy Analysis (SEA) [5], hybrid FEM/SEA techniques [6] or SEA-like (SEAL) [7, 8] are the most considered energy methods in the literature. Joint acceptance functions (expressing to some extent the part of unsteady pressure field energy, which is converted into vibrations) are then the key concern. Closed formulations of theses acceptances functions in the case of standard structures (such as plates and cylinders), can be obtained for use in SEA. However, the computations of these functions are time consuming in the mid-high frequency range, when FEM of the given structure is used. SEAL [7] can be considered to bridge the gap between low frequency and high frequency analyses. Reference [7] offers also some theoretical and applicative definition of the energy methods, and through the concept of Energy Distribution Approach justifies also some 'inconsistencies' of the standard SEA approach. A key concept in SEAL formulation [7, 8] is the Energy Influence Coefficients (EIC). To compute such EIC the FEM of the structure is excited by ROF excitations. One of the main difficulties lies then in the modeling of **real excitations** encountered such as aerodynamic and diffuse noises.

The aim of the present paper is to define equivalent ROF excitations for spatially correlated sources to be used in mid-high frequency vibroacoustic predictions [9]. Many studies [1, 2, 10–15] have considered spatially correlated acoustic and aerodynamic excitations. Most of them were carried out in order to estimate the spatial correlation function for specific excitations. Aerodynamic loads are often

represented by empirical models of correlation functions provided by experimental measurements [1, 2, 11, 14, 15]. Most recent studies about spatially correlated excitations focus on the representation of the power spectral density of response in the wavenumber space [16–18]. The method expresses all modal expansion terms in the wavenumber space and has two main advantages. The expressions in the wavenumber space allow a better understanding of different modes contributions to the total response of the structure to an incident pressure field. The second aspect is connected to time-consumption, since correlation functions have lower variations in the wavenumber space, joint acceptance computation time is reasonable when compared to the space-frequency representation. It should be noted that some numerical advances in the derivation of random vibration was recently presented [19]. Specific approximations referring to the meshing condition and to the transformation of the distributed excitation, as well as a numerical scheme named Asymptotic Scaled Modal Analysis was introduced. The work [19] demonstrates that FEM can be used in the random vibration predictions without increasing the computational costs.

The present study is performed assuming that the correlation function of the excitation sound field under interest is known and well described. ROF excitations, equivalent to the acoustic and aerodynamic excitation of interest, are developed. An existing equivalent model was presented in the literature by Maidanik [12]. This model has been validated on aerodynamic excitations encountered in the aerospace industry. This model is called spatial extent equivalence and has been studied more deeply in the Ref. [13]. The present paper demonstrates that this approach is not sufficient, and a second model, called **wavenumber space equivalence,** is then developed. Different random broadband noises are then investigated, and a wavenumber space equivalence model is validated for different excitations cases. The generality of the proposed equivalence is also considered. Indeed, different structural boundary conditions are used in order to check the feasibility. The paper is then structured as follows. Section 2 provides basic concepts concerning random vibration characterization and describes random excitations under interest. Section 3 is devoted to the equivalent ROF excitations analysis. Section 3 gives also some numerical interrogations to evaluate the proposed approach accuracy.

2 Characterization of Random Broadband Excitations

Standard approaches used to predict vibration levels under random pressure fields are often based on modal decomposition. The response to a broadband random noise is expressed in terms of power spectral density. Statistical considerations are then introduced, and power spectral density is deduced from the correlation function which is defined in what follows as:

$$R_{\mathrm{pp}}(\xi,\tau) = E[p(\mathbf{x};t)p(\mathbf{x}+\xi;t+\tau)] \tag{1}$$

with $\xi = \mathbf{x}' - \mathbf{x}$ the spatial separation vector, τ the time shift and E the mathematical expectation. In this paper, the stochastic field $p(\mathbf{x};\ t)$ is assumed to be homogenous. The space-frequency spectrum can then be written as follows:

$$S_{\mathrm{pp}}(\xi;\ \omega) = \int_{-\infty}^{\infty} R_{\mathrm{pp}}(\xi;\ t)\mathrm{e}^{-j\omega t}\mathrm{d}t \tag{2}$$

The power spectral density of structural motion is estimated from the pressure field considered in terms of blocked pressure. This corresponds to the fact that the wall-pressure fluctuations are not affected by the structural vibration. The pressure field is then the same as observed on a rigid wall. The power spectral density of velocity of a structure submitted to random excitations can be expressed as follows from the generalized Green functions:

$$\begin{aligned} S_{\mathrm{vv}}(x,y;\omega) = \omega^2 \sum_r \sum_s \mathrm{Re}\left(\alpha_r(\omega)\alpha_s^*(\omega)\right)\Phi_r(x,y)\Phi_s(x,y) \\ \times \int_A \int_A \Phi_r(x,y)\Phi_s(x',y')S_{\mathrm{pp}'}(\omega)\mathrm{d}A\mathrm{d}A' \end{aligned} \tag{3}$$

Φ_r is the mode shape of the excited structure, Re the real part of the complex number, $S_{\mathrm{pp}'}$ the cross-spectral density of the wall pressure, A the area excited by the pressure field and α_r the modal receptance of the structure,

$$\alpha_r(\omega) = \frac{1}{\omega_r^2(1+i\eta_r) - \omega^2} \tag{4}$$

ω_r is the pulsation of the mode r and η_r the associated damping loss factor. The cross-spectral density of the wall pressure between two excitation points of the structure can be expressed as follows:

$$S_{\mathrm{pp}'}(\omega) = C(P,Q;\ \omega)S_{\mathrm{pp}}(\omega) \tag{5}$$

where C is the correlation function of the pressure field and S_{pp} the point power spectral density of the pressure field, assumed to be constant over the surface of the structure. We notice here that the correlation function is only dependent on the frequency and the distance between the given points P and Q. This correlation function is generally expressed by analytical formulations with coefficients derived from experimental data for a given excitation. Consequently, the power spectral density of velocity averaged over space domain (D) and frequency ($\Delta\omega$) is:

$$\langle S_{\mathrm{vv}} \rangle_{\Omega,\Delta\omega} = \frac{1}{\Delta\omega} \int_{\Delta\omega} \int_{D} \omega^2 \sum_r \sum_s \mathrm{Re}\left(\alpha_r(\omega)\alpha_s^*(\omega)\right) \Phi_r(x,y)\Phi_s(x,y) A^2 S_{\mathrm{pp}}(\omega) j_{\mathrm{rs}}(\omega) \mathrm{d}S \mathrm{d}\omega \tag{6}$$

The joint acceptance function j_{rs} has been introduced above, and is computed performing a double integration of the product of the correlation function and the mode shapes of the structure over the surface of the structure.

$$j_{\mathrm{rs}}(\omega) = \frac{1}{A^2} \int_A \int_A \Phi_r(x,y)\Phi_s(x',y') C(x-x', y-y'; \omega) \mathrm{d}x \mathrm{d}x' \mathrm{d}y \mathrm{d}y' \tag{7}$$

Different excitation models can be compared in terms of mean joint acceptance function over resonant modes, as done in the high frequency approach [20]. Indeed, total mean energy of an SEA subsystem excited by a spatially correlated excitation is expressed as follows:

$$\langle S_E \rangle = \langle j_{\mathrm{mm}}(\omega) \rangle \sum_m \frac{1}{\Delta\omega} \int_{\Delta\omega} \omega^2 |\alpha_m(\omega)|^2 A^2 S_{\mathrm{pp}}(\omega) \mathrm{d}\omega \tag{8}$$

$\langle j_{\mathrm{mm}}(\omega) \rangle$ is the average of the joint acceptance functions over the resonant modes in the considered frequency band. In order to simplify the expression and the post processing, simply supported plates are considered here, as often in the literature. The joint acceptance functions can then be written in an analytical way for comparisons issue mainly. Three types of excitations are investigated in this paper: the purely random noise, the incident diffuse field, the turbulent fluctuations of wall pressure. ROF excitation is then considered as a reference and all other types of excitations are then derived.

2.1 Purely Random Excitation

Purely random excitation corresponds to a white noise in the wavenumber space. It can be defined from a spatially delta-correlated function from one point to another:

$$C(x-x', y-y'; \omega) = \delta(x-x')\delta(y-y') \tag{9}$$

where δ is the delta function. The use of this type of correlation function allows us to simplify the modal expression of the power spectral density of the response. Indeed, for local mode shapes over the area A, and considering the normalization to 1 of the orthogonal basis of the mode shapes,

$$\int_A \Phi_r(x,y)\Phi_s(x,y)\mathrm{d}x\mathrm{d}y = \delta_{\mathrm{rs}} \tag{10}$$

The joint acceptance functions can be expressed explicitly as follows:

$$j_{\mathrm{rs}}(\omega) = \frac{1}{A^2}\int_A \int_A \Phi_r(x,y)\Phi_s(x',y')\delta(x-x')\delta(y-y')\mathrm{d}x\mathrm{d}x'\mathrm{d}y\mathrm{d}y' \tag{11}$$

$$j_{\mathrm{rs}}^{\mathrm{rain}}(\omega) = \frac{\delta_{\mathrm{rs}}}{A^2} \tag{12}$$

This relation simplifies the modal summation and leads to the following expression of the power spectral density:

$$S_{\mathrm{vv}}^{\mathrm{PR}}(x,y;\omega) = \omega^2 \sum_r |\alpha_r(\omega)|^2 \Phi_r^2(x,y) S_{\mathrm{pp}}(\omega) \tag{13}$$

According to previous simplifications, standard vibroacoustic methods are validated under the hypothesis of a ROF excitation. In order to use such methods, equivalent ROF excitations for every spatially correlated loading case are developed in the next section. This equivalent model enables us to represent aerodynamic loading from a spatially delta-correlated excitation, and to use all developments obtained under the hypothesis of ROF excitation. The correlation functions can be defined in the wavenumber-frequency spectrum from the space-frequency spectrum as follows:

$$C\left(k_x,k_y;\omega\right) = \frac{1}{(2\pi)^2}\iint_\infty C(\zeta,\chi;\omega)\mathrm{e}^{-ik_x\zeta - ik_y\chi}\mathrm{d}\zeta\mathrm{d}\chi \tag{14}$$

k_x and k_y are the wavenumbers in the two directions, $\zeta = x - x'$ and $\chi = y - y'$. In most cases, this formulation gives relatively simple expressions of the correlation functions. The expression of the ROF correlation function in the wavenumber space requires that the energy be uniformly distributed over the entire wavenumber-frequency range, given that the density is uniform over the entire area:

$$C(k_x,k_y;\omega) = \frac{1}{4\pi^2} \tag{15}$$

The energy of the pressure field is uniformly distributed over the entire wavenumber-frequency range, which implies that the mean-square pressure is infinite. In practice, to overcome this difficulty, the ROF excitation is approximated by an ideal low-pass process described by a uniform spectral density defined over a limited wavenumber band [16].

2.2 Incident Diffuse Field

The incident diffuse field is represented by an infinite sum of uncorrelated plane waves whose incidence angles are uniformly distributed over a half-space. The correlation function is given in the space-frequency domain by:

$$C(x-x', y-y'; \omega) = \frac{\sin(k_0(x-x'))}{k_0(x-x')} \frac{\sin(k_0(y-y'))}{k_0(y-y')} \tag{16}$$

k_0 is the acoustical wavenumber given by $k_0 = \omega/c_0$, with c_0 the speed of sound, and $x - x'$ and $y - y'$ the distances between the two excitation points. For an incident diffuse field, representation of the correlation function in the wavenumber space is,

$$\begin{array}{ll} C(k_x, k_y) = \frac{1}{4k_0^2} & \text{if} \quad |k_x| < k_0 \quad \text{and} \quad |k_y| < k_0 \\ C(k_x, k_y) = 0 & \text{else} \end{array} \tag{17}$$

This expression implies that acoustically slow modes $\left(|k_x| > k_0 \text{ and } |k_y| > k_0\right)$ do not respond to an incident diffuse field. In practice, these modes respond in the form of corner modes [10]. The last excitation type studied in this paper is the TBL.

2.3 Turbulent Boundary Layer Excitation

Many authors have developed analytical formulations of the spatial correlation function of TBL excitations from experimental results [1, 2]. The model of a correlation function used in this paper was introduced by Corcos:

$$C(x-x', y-y'; \omega) = \mathrm{e}^{-\delta_x |x-x'|} \cos(\gamma_x (x-x')) \mathrm{e}^{-\delta_y |y-y'|} \tag{18}$$

In this model, x-axis is the direction of the flow. The parameters of the model are derived from measurements and are expressed as follows:

$$\begin{cases} \gamma_{x,y} = \omega / U_c \\ \delta_{x,y} = a_{x,y} \gamma_x + b_{x,y} / \delta \end{cases} \tag{19}$$

U_c is the convection velocity and δ the thickness of the TBL (see Fig. 1). $a_{x,y}$ and $b_{x,y}$ are empirical coefficients. The expression in the wavenumber-frequency domain obtained for TBL excitation is analytically formulated as follows:

$$C(k_x, k_y; \omega) = \frac{\delta_x \delta_y}{\pi^2 (\delta_x^2 + (\gamma_x - k_x)^2)(\delta_y^2 - k_y^2)} \tag{20}$$

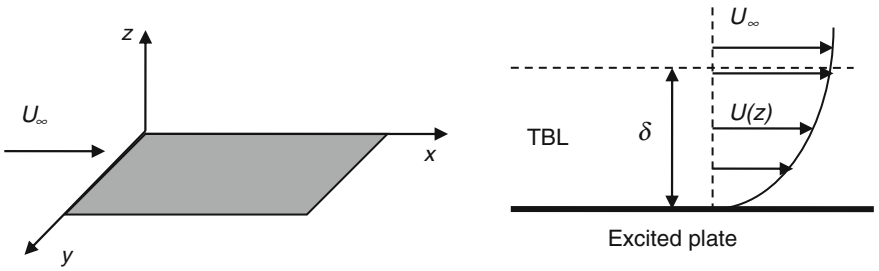

Fig. 1 Turbulent boundary layer excitation

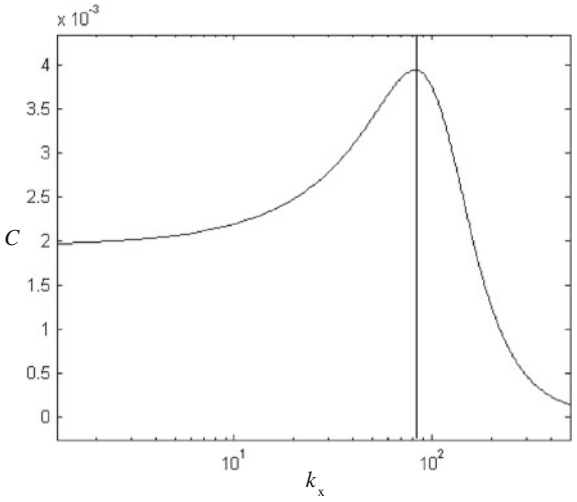

Fig. 2 Spatial correlation in the direction of the flow for TBL versus wavenumber k_x

TBL excitation is characterized by an acoustic coincidence effect considering wavenumbers in the direction of the flow. The representation of the spatial correlation function in the wavenumber space highlights the coincidence effect when equality occurs between the structural wavenumber and the acoustical wavenumber (Fig. 2). The coincidence effect in the flow direction corresponds to the maximum and is obtained in the case of $k_x = \gamma_x$.

3 Equivalent ROF Excitation

In order to use simplified modal summation expressions, an equivalent spatially de-correlated excitation is introduced here. ROF excitations can be described from general closed formulations of spatially de-correlated functions. For the present

applications, the correlation functions are defined in order to use modal basis normalization property:

$$\int_A \Phi_r(x,y)\Phi_s(x,y)\mathrm{d}x\mathrm{d}y = \delta_{\mathrm{rs}} \tag{21}$$

The spatial correlation function is then mass proportional and can be written as:

$$C(x-x',y-y';\omega) = C^{\mathrm{eq}}(\omega)\delta(x-x')\delta(y-y') \tag{22}$$

The present approach consists in finding the frequency function $C^{\mathrm{eq}}(\omega)$ that induces the same amount of vibration levels on the structure as a spatially correlated excitation. The function C^{eq} is only dependent on frequency, which implies that the power spectral density obtained for any excitation type is as follows:

$$S_{\mathrm{vv}}(x,y;\omega) = \omega^2 \sum_r |\alpha_r(\omega)|^2 \Phi_r^2(x,y) C^{\mathrm{eq}}(\omega) S_{\mathrm{pp}}(\omega) \tag{23}$$

From Eq. (13), any spatially correlated excitations can be characterized considering the equivalent point power spectral density:

$$S_{\mathrm{pp}}^{\mathrm{eq}}(\omega) = C^{\mathrm{eq}}(\omega) S_{\mathrm{pp}}^{\mathrm{rain}}(\omega) \tag{24}$$

Thanks to the previous equation, the vibroacoustic analysis of any structure subjected to acoustic or aerodynamic loads can be performed by exciting the structure with an equivalent ROF load. The developed equivalent model needs to be suited principally in the mid and high frequency ranges. Two approaches are investigated in this paper by expressing the equivalence over the extended physical domain and by expressing the equivalence in the wavenumber space.

3.1 Spatial Extent Equivalence

The spatial extent equivalence is based on previously published work on estimating vibrations induced by turbulent fluctuations of wall pressure. This work has been presented in [12, 13]. The equivalence is made from spatial extent integration of the spatial correlation functions for two different excitations named exc1 and exc2 respectively,

$$\int_\infty \int_\infty \int_\infty C_{\mathrm{exc1}}(\zeta,\chi;\omega)\mathrm{d}\zeta\mathrm{d}\chi\mathrm{d}\omega = \int_\infty \int_\infty \int_\infty C_{\mathrm{exc2}}(\zeta,\chi;\omega)\mathrm{d}\zeta\mathrm{d}\chi\mathrm{d}\omega \tag{25}$$

This relation enables the explicit expression of the equivalent correlation function of the frequency in the form of:

$$\int_{\infty}\int_{\infty}\int_{\infty} C^{\mathrm{eq}}(\omega)\delta(\zeta)\delta(\chi)\mathrm{d}\zeta\mathrm{d}\chi\mathrm{d}\omega = \int_{\infty}\int_{\infty}\int_{\infty} C_{\mathrm{exc2}}(\zeta,\chi;\omega)\mathrm{d}\zeta\mathrm{d}\chi\mathrm{d}\omega \tag{26}$$

$$C^{\mathrm{eq}}(\omega) = \int_{\infty}\int_{\infty} C_{\mathrm{exc1}}(\zeta,\chi;\omega)\mathrm{d}\zeta\mathrm{d}\chi \tag{27}$$

As a first analysis of the previous relation, the method will produce relatively low errors for short correlation lengths corresponding to acoustically fast modes. Indeed, space integration being extended to infinity, implicitly implies that the correlation lengths are much smaller than the length of the excited structure. In Refs. [12, 13], the authors justify this approximation when the decay rates of the correlation function are sufficiently high. In other words, results will be accurate in the high frequency limit, as the correlation length decreases with frequency.

3.1.1 Application to an Incident Reverberant Pressure Field

For an incident diffuse wall pressure, the spatial extent equivalence leads to the following function:

$$C^{\mathrm{eq}}(\omega) = \int_{\infty}\int_{\infty} \frac{\sin(k_0\zeta)}{k_0\zeta}\frac{\sin(k_0\chi)}{k_0\chi}\mathrm{d}\zeta\mathrm{d}\chi \tag{28}$$

According to the result,

$$\int_{0}^{\infty} \frac{\sin(t)}{t}\mathrm{d}t = \frac{\pi}{2} \tag{29}$$

The equivalent excitation function C^{eq} is expressed by,

$$C^{\mathrm{eq}}(\omega) = \frac{\pi^2}{k_0^2} \tag{30}$$

The equivalent ROF excitation to a diffuse incident field involves a simple equivalent function. The previous formulation is applied here to a simply supported aluminum plate excited by an incident diffuse field. The length and width of the plate are $l_x = 2$ m and $l_y = 1.5$ m respectively and 1.5×10^{-2} m thickness. Validation is made here in terms of the mean joint acceptance functions over resonant modes.

The boundary conditions of the simply supported plate lead to analytical formulation of the mode shapes and the joint acceptance functions are:

$$j_{\mathrm{mm,rs}}(\omega) = \int_A \int_A \sin\left(\frac{m\pi z}{l_x}\right) \sin\left(\frac{r\pi z'}{l_x}\right) \sin\left(\frac{n\pi y}{l_y}\right) \sin\left(\frac{s\pi y'}{l_y}\right) \times \frac{\sin(k_0(z-z'))}{k_0(z-z')} \frac{\sin(k_0(y-y'))}{k_0(y-y')} \mathrm{d}y\mathrm{d}y'\mathrm{d}z'\mathrm{d}z' \tag{31}$$

Considering the equivalent ROF excitation, joint acceptance functions are expressed as follows,

$$j_{\mathrm{mn,rs}}(\omega) = \frac{\pi^2}{k_0^2} \int_A \int_A \sin\left(\frac{m\pi z}{l_x}\right) \sin\left(\frac{r\pi z'}{l_x}\right) \sin\left(\frac{n\pi y}{l_y}\right) \sin\left(\frac{s\pi y'}{l_y}\right) \delta(z-z')\delta(y-y')\mathrm{d}y\mathrm{d}y'\mathrm{d}z\mathrm{d}z' \tag{32}$$

$$j_{\mathrm{mm,rs}}(\omega) = \frac{\pi^2}{k_0^2} \cdot \frac{A}{4} \delta_{\mathrm{mr}} \delta_{\mathrm{ns}} \tag{33}$$

Results are plotted from the third octave frequency band 200 Hz, up to 2,500 Hz (Fig. 3). It can be noticed that the acoustic coincidence frequency, defined as follows, is f_c = 830 Hz

$$f_c = \frac{c_0^2}{2\pi} \sqrt{\frac{\rho_S}{D}} \tag{34}$$

The mean joint acceptance functions over resonant modes is then well-described based on the ROF excitation equivalent to the incident diffuse field for frequencies higher than the acoustic coincidence frequency. Figure 3 shows a relatively large error factor below the acoustic coincidence (up to 8 dB for the first frequency band).

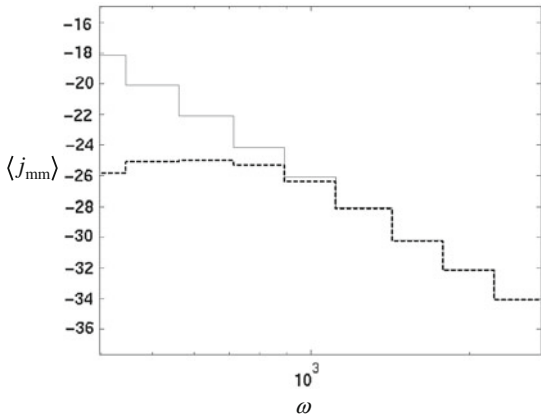

Fig. 3 Mean 'joint acceptance' function over resonant modes $\langle j_{\mathrm{mm}} \rangle$ versus frequency: *dashed line* analytical, *line* spatial extent equivalence

The obtained results imply that only acoustically fast modes are well-described using the equivalent ROF excitation obtained from the spatial extent equivalence idea. According to the wavenumber description of an incident diffuse field (17), previous results show that acoustically slow modes have to be taken into account in the entire response of the structure. These considerations are used by Maidanik [10] to developed analytical formulations of radiation efficiency.

3.1.2 Application to TBL Excitation

The spatial extent equivalence is here applied to a TBL excitation. TBL excitation is an important source of vibration and noise in the space and aeronautical industry. Most research concerns the definition of the spatial correlation function. The present approach can be applied to any analytical definition of the correlation function. The Corcos analytical model is used here. The spatial extent equivalent ROF excitation can then be expressed by:

$$C^{\mathrm{eq}}(\omega) = \int_{\infty}\int_{\infty} \mathrm{e}^{-\delta_x|\zeta|}\cos(\gamma_x\zeta)\mathrm{e}^{-\delta_y|\chi|}\cdot \mathrm{d}\zeta\cdot \mathrm{d}\chi \tag{35}$$

$$C^{\mathrm{eq}}(\omega) = \frac{4\delta_x}{\delta_y(\delta_x^2+\gamma_x^2)} \tag{36}$$

The numerical application consists of an aluminum plate of 2.8 m length and 1.9 m width, and 5×10^{-3} m thickness. The acoustical coincidence effect is related to the convection speed and to the structural properties. Regarding the response of the structure to a TBL excitation, and considering out-of-plane motion, this coincidence occurs at the critical frequency:

$$f_c = \frac{U_c^2}{2\pi}\cdot\sqrt{\frac{\rho_s}{D}} \tag{37}$$

where U_c is the convection speed, ρ_s the plate density and D the plate bending stiffness. The present analysis is performed for frequency ranges over the coincidence effect. The convection speed is 75 m/s, and the corresponding coincidence frequency is f_c = 120 Hz. Levels are observed in terms of mean square velocity (6) and are averaged over third octave bands in the frequency range 200–5,000 Hz.

Figure 4 shows good agreement between the equivalent ROF mean square velocity levels and the "exact" solution. It can be observed that the discrepancy between the spatial extent equivalence results and the "exact" solution are less than 2 dB for all third octave frequency bands. TBL excitations encountered in the aerospace industry can present convection speeds up to 650 m/s. For such high convection speed, structures are studied either near or far the coincidence effect. The equivalent excitation needs to accurately describe these frequency bands to

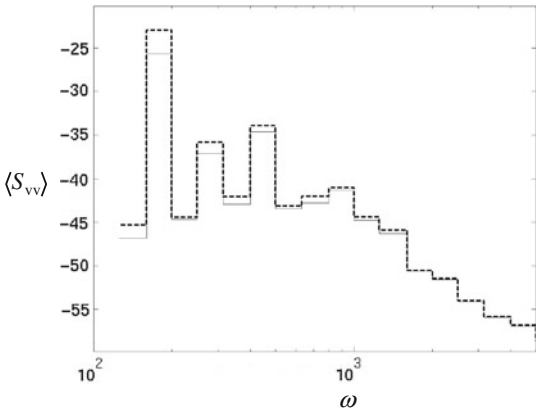

Fig. 4 Mean square velocity in third octave band $\langle S_{vv} \rangle$ versus frequency for U_c = 75 m/s. *Line* analytical, *dashed line* spatial extent equivalence

meet industrial requirements. For the following computation, a convection speed of 270 m/s has been chosen and corresponds to real aerodynamic loading measurements concerning ARIANE 5 wind tunnel testing (Mach 1.2). The coincidence effect occurs at a frequency f_c = 1,540 Hz. The frequency bands being studied can then correspond to a wide frequency range. Vibration levels observed for third octave frequency bands over the coincidence effect are in agreement with the "exact" solution (Fig. 5). From a physical point of view, the results obtained from this model were foreseeable, since the correlation lengths decrease when the frequency increases. The correlated excitation tends to become spatially delta-correlated in the high frequency limit. This is especially true for the TBL as the correlation lengths have exponential terms, which depend on the distance between the application points and the frequency. Previous comments concerning the validity of such approach are then verified in this application.

Large errors can be observed for third octave frequency bands below the coincidence effect. Correlation lengths are large here, and the spatial extent equivalence

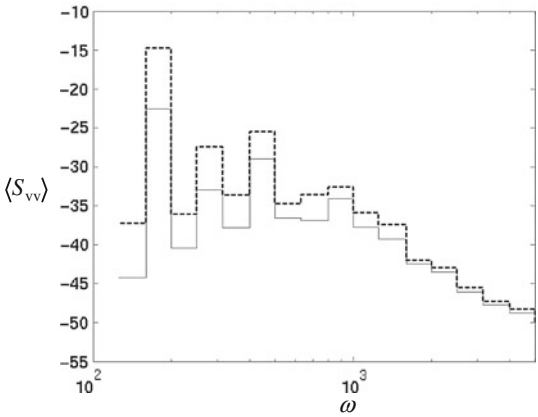

Fig. 5 Mean square velocity $\langle S_{vv} \rangle$ in third octave band versus frequency for U_c = 270 m/s. *Line* analytical, *dashed line* spatial extent equivalence

does not represent the real excitation around or below the coincidence effect. Induced discrepancies are over 5 dB around the acoustical coincidence frequency.

The coincidence and high wavenumber regions must then be accurately described from the equivalent spatially de-correlated approach. The interaction between the pressure field and the mode shapes can be observed in the physical domain or in the wavenumber space. The second case gives a convenient representation of the coupling between the modes and the acoustic environment, and leads to relatively simple expressions for correlation functions. In order to highlight the coincidence effect, the equivalent excitations are described hereafter in the wavenumber space.

3.2 Wavenumber Space Equivalence

The approach proposes an equivalent ROF excitation from a wavenumber-frequency spectrum equivalence. The equivalence can be written in the wavenumber space considering a given wavenumber band. Each wavenumber band can be connected to a given frequency band. The equivalent correlation function can be expressed in the wavenumber space as:

$$C^{\mathrm{eq}}(k_x, k_y; \omega) = \frac{C^{\mathrm{eq}}(\omega)}{4\pi^2} \tag{38}$$

Using the wavenumber-frequency spectrum of the excitation under study, and the one of the equivalent ROF excitation, the frequency function C^{eq} can be explicitly as:

$$\begin{aligned} &\int_{k=k_1}^{k_2} \int_{\theta=0}^{2\pi} C^{\mathrm{eq}}(k\cos(\theta), k\sin(\theta), \omega) k \mathrm{d}k\mathrm{d}\theta \\ &= \int_{k=k_1}^{k_2} \int_{\theta=0}^{2\pi} C(k\cos(\theta), k\sin(\theta), \omega) k \mathrm{d}k\mathrm{d}\theta \end{aligned} \tag{39}$$

Injecting expression (38) in Eq. (39) leads to:

$$C^{\mathrm{eq}}(\omega) = \frac{4\pi}{\left(k_2^2 - k_1^2\right)} \int_{k=k_1}^{k_2} \int_{\theta=0}^{2\pi} C(k\cos(\theta), k\sin(\theta), \omega) k \mathrm{d}k\mathrm{d}\theta \tag{40}$$

k is the structural wavenumber for the out-of-plane motion, k_1 and k_2 the limit of the given wavenumber band. The equivalent model can be applied to any analytical correlation function in the same way.

3.2.1 Application to an Incident Reverberant Pressure Field

According to the expression of the correlation function of an incident diffuse field (17) in the wavenumber space, the equivalence in the wavenumber space can be written as follows:

$$C^{\mathrm{eq}}(\omega) = \frac{\pi^2}{k_0^2}, \quad \begin{array}{l} \text{if resonant modes are acoustically fast} \\ \text{otherwise} \quad C^{\mathrm{eq}}(\omega) = 0 \end{array} \tag{41}$$

The previous relation and comments in Sect. 3.1.1 imply that the response of the structure excited by a reverberant diffuse field is well described only for frequency bands over the acoustic coincidence. For frequency bands below the acoustic coincidence, both approaches, spatial extent equivalence and wavenumber equivalence, need to include considerations of the reciprocity between the power radiated in a reverberant field and power injected into a structure from an incident diffuse field.

3.2.2 Application to TBL Excitation

It has been shown that the space equivalence approach allows an estimation of the vibration levels of the structure excited by a TBL for a relatively low convection speed. The present equivalence must be able to predict vibration levels above or around the acoustic coincidence effect. The application of the wavenumber space equivalence for the TBL source gives the equivalent excitation profile:

$$C^{\mathrm{eq}}(\omega) = \frac{4\pi}{\left(k_2^2 - k_1^2\right)} \int_{k=k_1}^{k_2} \int_{\theta=0}^{2\pi} \frac{\delta_x \delta_y}{\pi^2 (\delta_x^2 + (\gamma_x - k\cos(\theta))^2)(\delta_y^2 - k^2 \sin(\theta)^2)} k \mathrm{d}k \mathrm{d}\theta \tag{42}$$

Analytical expression of the equivalent function is not of practical interest here and a numerical integration can be performed. A convective speed of 270 m/s, representative of a convective speed appearing at Mach 1.2 in an ARIANE 5 flight was investigated. The numerical application consists of an aluminum plate of 2.8 m length and 1.9 m width, and 5×10^{-3} m thickness. The coincidence frequency is then f_c = 1,540 Hz, and the frequency range of interest allows us to describe three interesting wavenumber regions (i.e. the low, mid and high wavenumber bands). A first validation was carried out through the comparison of the mean joint acceptance functions of the resonant modes for each third octave frequency band (Fig. 6). The reference value is obtained using an SEA software.[1]

[1] SEALASCAR is an SEA based code developed and employed by EADS Space Transportation [15, 19] for ARIANE vibroacoustic design.

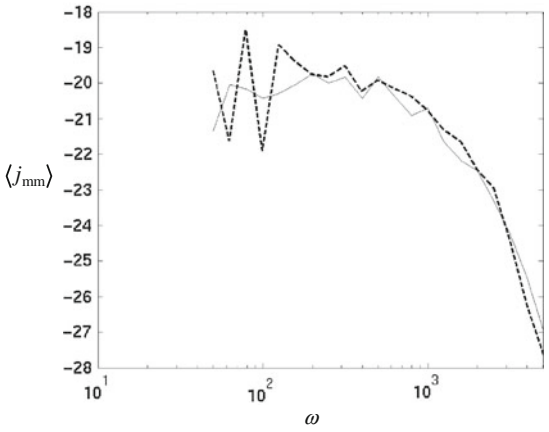

Fig. 6 Mean joint acceptance $\langle j_{mm} \rangle$ in third octave band versus frequency for U_c = 270 m/s, *line* SEALASCAR, *dashed line* wavenumber space equivalence

Results show that the equivalent model gives satisfactory results for the joint acceptance averaged over third octave bands in the frequency range 40 Hz–10 kHz. Errors are lower than 2 dB over the entire frequency range of concern and a good estimate is achieved before and after the coincidence frequency of 1,540 Hz. In the first frequency bands, below 200 Hz, the number of modes per third octave band is lower than 10, and the modal overlap is sufficiently low to consider that these frequency bands are the first mid frequency ones.

The equivalent model obtained in the wavenumber space is accurate for mid and high frequency ranges. Vibration levels are estimated here without computing the joint acceptance functions, which can lead to a high cost of CPU time for the mid frequency range.

The comparison of averaged joint acceptances might not be sufficient to prove the validity of the methodology in the mid frequency regime. In order to be more general, the equivalent ROF excitation is validated in terms of power spectral density of velocity (6) without averaging the joint acceptance functions over the resonant modes of the structure (see Fig. 6). Mean square velocity predictions using the wavenumber equivalence seems better than those obtained using the spatial extent ROF equivalent model (see Fig. 7), without any consideration of the acoustic coincidence effect. The deviations observed on averaged values per third octave bands are lower than 2 dB over the entire frequency range studied when the wavenumber equivalence is employed.

This Equivalent TBL (ETBL) can then be used over all frequency bands regardless of the acoustic coincidence effect. Figure 7 shows also that errors in the vibration prediction increase as the frequency decreases. Figure 8 provides narrow bands mean velocity comparisons.

The previous figure shows that the vibration level is well described in narrow bands as well. Errors on the modal peaks are lower than 2 dB over the entire given frequency range. As mentioned before, convection speed can reach 650 m/s for aerospace applications, appearing at Mach 3 in an ARIANE 5 flight. For the present

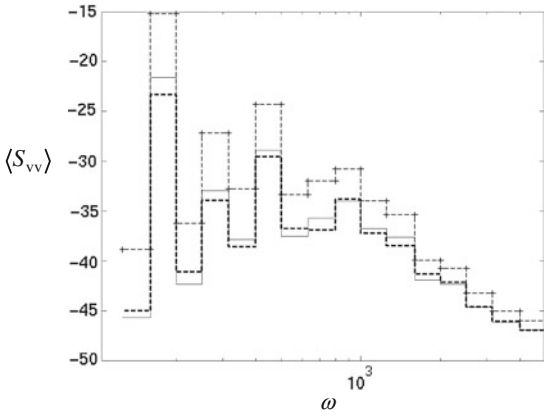

Fig. 7 Mean velocity $\langle S_{vv} \rangle$ in third octave band versus frequency for U_c = 270 m/s, *dashed line* analytical, *line* wavenumber equivalence, *dashed line along with plus symbol* spatial extent equivalence

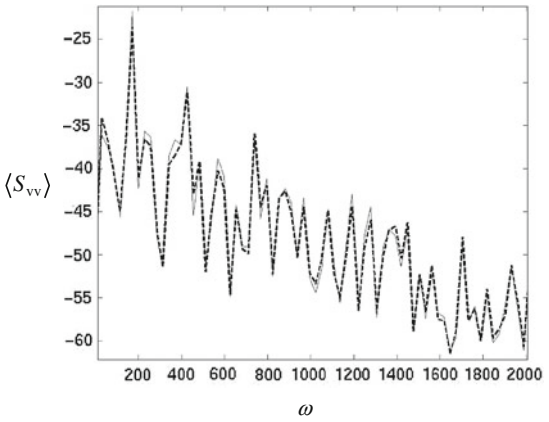

Fig. 8 Mean velocity $\langle S_{vv} \rangle$ in narrow band for U_c = 270 m/s, *dashed line* analytical, *line* wavenumber space equivalence

structure and frequency range, this convection speed means that all third octave frequency bands are far above the acoustic coincidence effect. Indeed a convection speed of U_c = 650 m/s corresponds, for the given structure, to a coincidence frequency f_c = 9,000 Hz. The previous results in the wavenumber equivalent model showed that the errors introduced in the vibration level estimate become larger as the given frequency decreases or, in other words, as the frequency range moves far from the acoustic coincidence effect. This approach is applied to the Mach 3 TBL loading case (see Fig. 9). Even though the given frequency bands are far below the coincidence effect, results from the ETBL are still relevant. Indeed, the deviation observed is lower than 3 dB for the first third octave frequency bands and convergence to the exact value occurs in the mid frequency range.

This method is promising because it enables the use of FEM approaches for any correlated excitation case in the mid and high frequency ranges with a relatively low calculation cost. Once the equivalent model is found, the induced vibration levels can be computed without estimating the joint acceptance functions. It can be observed

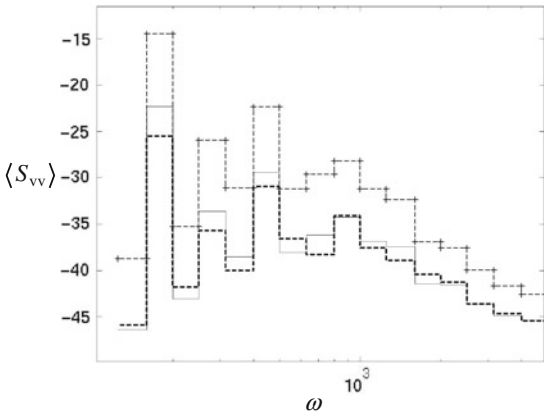

Fig. 9 Mean velocity $\langle S_{vv} \rangle$ in third octave band versus frequency for U_c = 650 m/s, *dashed line* analytical, *line* wavenumber equivalence, *dashed line along with plus symbol* spatial extent equivalence

from the previous model that the ROF equivalent excitation does not take into account the structure boundary conditions. Indeed, these boundary conditions are expressed in the integration of the mode shapes over the surfaces of the subsystems.

4 Application to a Structural-Acoustic Case

The aeroacoustic excitation is applied to a simply supported panel coupled with a cavity, already modeled with SEA-like method (see Fig. 10).

The SEA-like matrix of the coupled system was calculated by applying a ROF excitation on the panel and the cavity and by calculating the averaged energies and injected powers in each subsystem. If the same approach were to be used to model the aeroacoustic excitation on the coupled system, one would have to calculate a new SEA-like matrix, corresponding to the excitation. The method presented in this paper enables the use of the ROF, SEA-like matrix for aerocoustic excitation modeling with SEA-like, by calculating an equivalent injected power vector corresponding to the aeroacoustic excitation.

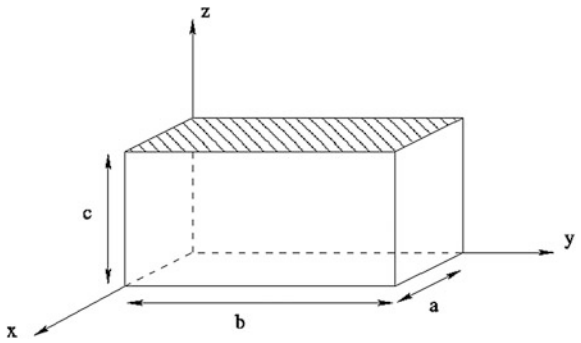

Fig. 10 Panel-cavity coupled system with aerodynamic loadings

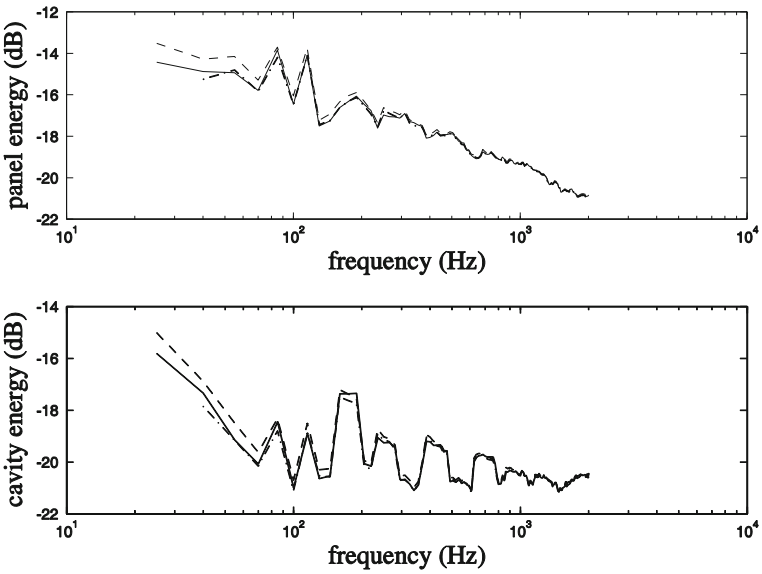

Fig. 11 Energetic behavior of the coupled system excited with TBL where the convective velocity is 75 ms^{-1}: *line* analytical, *dashed line* spatial extend equivalence

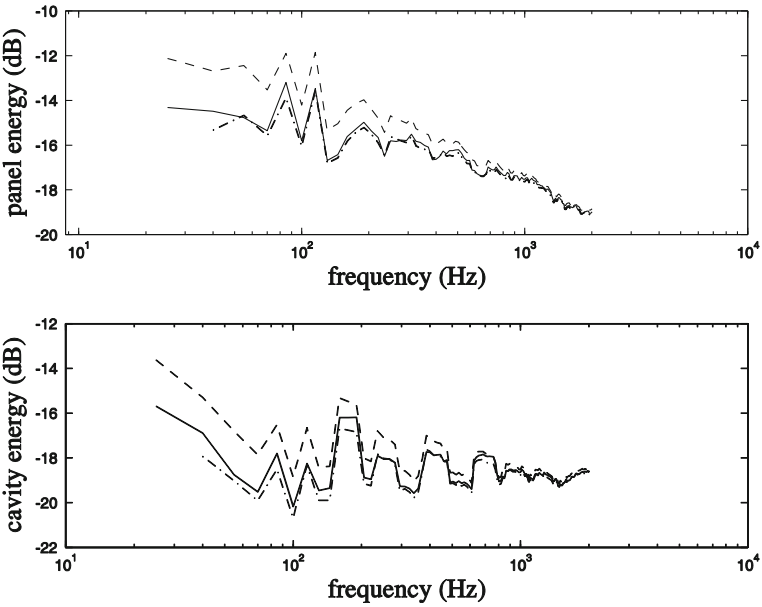

Fig. 12 Energetic behavior of the coupled system excited with TBL where the convective velocity is 200 ms^{-1}: *line* analytical, *dashed line* spatial extend equivalence

Figures 11 and 12 present the energetic behavior of the coupled system for two TBL excitation of the panel and two modeling: an analytical model based on modal coupling and the SEA-like model based on spatial extend equivalence. For low convective velocity, the spatial extend equivalence leads to accurate results for low convective velocity. However, for higher convective velocity, there is a discrepancy below the coincidence frequency. Indeed, effects of TBL excitation on the panel modes below and above coincidence frequency are different.

5 Conclusion

A ROF excitation equivalent to acoustic and aerodynamic excitations has been developed and validated in this paper. This approach allows the description of a broadband random spatially correlated excitation from a de-correlated pressure field. Two methods have been presented here. The first, considers the equivalence over the extended physical domain. It does not meet industrial needs, as it allows equivalent ROF excitation only for frequencies over the acoustic coincidence effect. A second method has been proposed and validated. It is based on the equivalence definition in the wavenumber space. Validation of the approach has been carried out for different acoustic and aerodynamic excitations, and for different structural boundary conditions. This approach gives acceptable results for a wide frequency range specifically for turbulent boundary layer excitations. The deviations observed between the equivalent ROF approach and the standard modal analysis using the joint acceptance functions are convenient (for a large scale of convective speed in the case of TBL). In addition, narrow bands results predicting the power spectral density of velocity are very promising. The equivalent ROF excitation has been validated for TBL excitation based on the Corcos model but the present approach can be applied to any analytical correlation function and work on this subject will be pursued. Full scale validation (for a simplified ARIANE 5 vehicle) of what was offered in this paper was already achieved and confirmed the main finding.

References

1. G.M. Corcos, Resolution of pressure in turbulence. J. Acoust. Soc. Am. **35**(2) (1963)
2. D.M. Chase, Modelling the wavevector-frequency spectrum of turbulent boundary layer wall-pressure. J. Sound Vib. **70**, 29–67 (1980)
3. B.M. Efimstov, Characteristics of the field of turbulent wall pressure fluctuations at large Reynolds numbers. Sov. Pysics—Acoust. **28**(4), 289–292 (1992)
4. W.R. Graham, A comparison of models for the wavenumber-frequency spectrum of turbulent boundary layer pressures. J. Sound Vib. **206**(4), 541–565 (1997)
5. R.H. Lyon, R. Dejong, *Theory and Application of Statistical Energy Analysis*, 2nd edn. (Butterworth Heinemann, Newton, 1995)

6. R.S. Langley, P.G. Bremner, A hybrid method for the vibration analysis of complex structural-acoustic systems. J. Acoust. Soc. Am. **105**, 1657–1671 (1999)
7. B. Mace, Statistical energy analysis: coupling loss factors, indirect coupling and system modes. J. Sound Vib. **279**(1–2), 141–170 (2005)
8. C.R. Fredö, *Statistical energy analysis and the individual case.* PhD thesis, Chalmers University of Technology, 1995
9. B. Hiverniau, Transmissions solidiennes: méthodologie de prévision vibroacoustique moyennes et hautes fréquences sous excitations aéroacoustiques, (Structural vibration transmission: mid-high frequency approaches under aerodynamic excitations). PhD thesis, Ecole Centrale de Lyon, 2007
10. G. Maidanik, Response of ribbed panels to reverberant acoustic fields. J. Acoust. Soc. Am. **34** (6) (1962)
11. S. Finnveden, F. Birgersson, U. Ross, T. Kremer, A model of wall pressure correlation for prediction of turbulence-induced vibration. J. Fluids Struct. **20**, 1127–1143 (2005)
12. G. Maidanik, Use of delta function for the correlations of pressure fields. J. Acoust. Soc. Am. **33**(11), 1598–1606 (1961)
13. J. Park, T. Siegmund, L. Mongeau, Analysis of the flow-induced vibrations of viscoelastically supported rectangular plates. J. Sound Vib. **261**, 225–245 (2003)
14. S.J. Elliot, P. Gardonio, C. Maury, A feasibility study for the laboratory simulation of turbulent boundary layer pressure fields, in *7th AIAA/CEAS Aeronautics Conference*, Maastricht, Netherlands, 28–30 May 2001
15. B. Troclet, *Manuel théorique LASCAR.* EADS Launch Vehicles (1987)
16. C. Maury, P. Gardonio, S.J. Elliot, A wavenumber approach to modeling the response of a randomly excited panel, part I: general theory. J. Sound Vib. **252**(1), 83–113 (2002)
17. F. Birgersson, S. Finnveden, A spectral element for modeling of plate vibration. Part 2: turbulence excitation. J. Sound Vib. **287**, 315–328 (2005)
18. S.A. Hambric, Y.F. Hwang, W.K. Bonness, Vibrations of plates with clamped and free edges excited by low-speed turbulent boundary layer. J. Fluid Sand Struct. **19**, 93–110 (2004)
19. S. De Rosa, F. Franco, Exact and numerical responses of a plate under a turbulent boundary layer excitation. J. Fluids Struct. **24**, 212–230 (2008)
20. B. Troclet, M. Depuydt, P. Gonzalez, Experimental analysis of the aerodynamic noise on the Ariane 5 Launch Vehicle Upper Part, in *Ariane 5 Structures et Technologies*, Cépaduès–Editions (1993), pp. 515–526

Discussion About Different Methods for Introducing the Turbulent Boundary Layer Excitation in Vibroacoustic Models

Laurent Maxit, Marion Berton, Christian Audoly and Daniel Juvé

Abstract For controlling the noise radiated from vibrating structures excited by turbulent boundary layer (TBL) it is relevant to develop numerical tools for understanding how the structure reacts to TBL excitation. Usually, the wall pressure fluctuations of the TBL are described through statistical quantities (i.e. space-frequency or wavenumber-frequency spectra) which depend on the TBL parameters. On the other hand, the vibro-acoustic models (i.e. Finite Elements, Boundary Elements, Transfer Matrix Methods, Analytical models, etc.) evaluate deterministic transfer functions which characterise the response of the considered structures. The first part of this paper focuses on the coupling between the stochastic TBL and the deterministic vibro-acoustic models. Five techniques are presented. Numerical applications on an academic marine test case are proposed in order to discuss the calculation parameters and the interests/drawbacks of each technique. In the second part of the paper, the high frequency modelling with the Statistical Energy Analysis (SEA) method is considered. The focus is placed on the estimation of an important input of this method: the injected power by the TBL into the structure for each third octave band.

L. Maxit (✉)
Laboratoire Vibrations Acoustique, INSA-Lyon, 25 bis Avenue Capelle,
69621 Villeurbanne Cedex, France
e-mail: laurent.maxit@insa-lyon.fr

M. Berton · D. Juvé
Centre Acoustique, LMFA UMR 5509, Ecole Centrale de Lyon,
36 av. Guy de Collongue, 69134 Ecully Cedex, France
e-mail: marion.berton@ec-lyon.fr

D. Juvé
e-mail: daniel.juve@ec-lyon.fr

C. Audoly
DCNS Research, Rond-point de l'Artillerie de la Marine, 83000 Toulon, France
e-mail: christian.audoly@dcnsgroup.com

E. Ciappi et al. (eds.), *Flinovia - Flow Induced Noise and Vibration Issues and Aspects*, DOI 10.1007/978-3-319-09713-8_12

1 Introduction

Structures excited by the turbulent boundary layer (TBL) are very common in practical applications. Car, airplanes, trains, and submarines may be excited by pressure fluctuations due to the turbulent flow induced by their motions. In order to reduce the noise radiated from these structures, it is important to understand at the design stage how the structure reacts to the TBL excitation. It is then necessary to develop numerical tools allowing predicting the vibration or the radiated pressure from the structure excited by the turbulent flow. Usually, the calculation process is decomposed in 3 steps:

1. A stationary hydrodynamic model is used to estimation the TBL parameters over the surface of the structure from its geometry and the flow conditions;
2. The spectrum of the wall pressure fluctuations is evaluated from the TBL parameters estimated in the previous step and by using one of the models proposed in the literature. Some of them are expressed in the space—frequency domain (like the famous Corcos model [1]) whereas as others are expressed in the wavenumber—frequency domain (like the no less famous Chase model [2]); Discussion about different models and comparison with experiment can be found in [3, 4] for the frequency auto spectrum and in [5, 6] for the normalized wavenumber cross spectrum;
3. The last step consists in using a vibro-acoustic model to estimate the response of the structure to the pressure fluctuations. The choice of the model depends on the frequency range of interest:

    - For the low frequencies, deterministic models considering harmonic excitations are generally considered. For example, it can be a standard Finite Element Model (FEM) for a structural problem or FEM coupled with a Boundary Element Model (BEM) for an acoustic radiation problem. The coupling between the statistical model used to describe the wall pressure fluctuations and the deterministic vibroacoustic model constitute a difficulty in the calculation process described above (i.e. the transition from step 2 to step 3). This topic is specifically addressed in the first part of this paper. Five approaches will be proposed and discussed in Sect. 3 after having recalled the mathematical formulation of the problem in Sect. 2.
    - For high frequencies, the Statistical Energy Analysis (SEA) method [7] is generally used to represent the vibro-acoustic behavior of complex structures. As the excitation is characterized in SEA by its time-averaged injected power for each frequency band, it is necessary to evaluate this quantity when considering the TBL excitation. We propose and discuss in Sect. 4 a formula allowing estimating the injected power from the wall pressure spectrum expressed in the wavenumber-frequency space. A methodology is also proposed to take the spatial variations of the TBL parameters into account.

2 Vibrating Structures Excited by Random Pressure Fluctuations

2.1 Presentation of the Problem

Let us consider a baffle panel of surface S_p excited by a TBL as shown in Fig. 1. Three assumptions are considered:

- The TBL is assumed to be fully developed, stationary, and homogeneous over S_p;
- The plate and the boundary layer are supposed weakly coupled. It is then supposed that the vibration of the plate does not modify the TBL wall pressure excitation. Spectra of the wall pressures over a rigid surface can then be considered;
- It is assumed that the propagation of the acoustic waves into the fluid is not affected by the turbulent flow. Moreover, for the marine applications (i.e. low Mach number), we could also neglect the convective effect on the acoustic wave propagation.

The marine test case considered for the numerical application is composed of a thin rectangular plate simply supported along its four edges and immersed in water on one-side. The flow direction is parallel to the longest edges of the plate (i.e. about x-axis). Numerical values of the physical parameters considered for this test case are given on Table 1.

The parameters characterizing the turbulent boundary layer are supposed to be known: U_∞ is the flow velocity, U_c, the convection velocity, δ is the boundary layer thickness, and τ_w the wall shear stress. From these parameters and the wall pressure models proposed in the literature [2–5], we can define the spectrum of the wall pressure fluctuations acting on the plate. The auto spectrum density of the wall pressure $S_{pp}(\omega)$ is evaluated here considering Goody's model [8] whereas the normalised cross spectrum density is evaluated using the Corcos's model [2]. The later is considered for it simplicity because it provides an analytical expression of the cross spectrum both in the space-frequency domain $\bar{\phi}_{pp}(\zeta, \omega)$ and in the wavenumber-frequency domain $\bar{\phi}_{pp}(k, \omega)$, both.

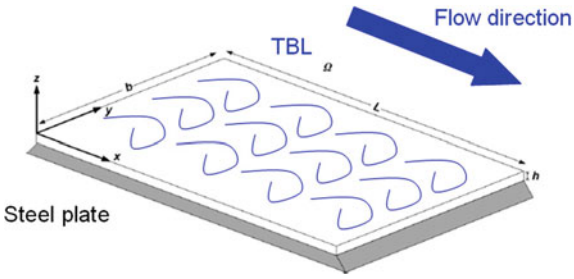

Fig. 1 Baffled simply supported plate excited by a homogeneous and stationary TBL

Table 1 Physical parameters of the marine test case

Parameters	Numerical value
Flow velocity	U_∞ = 7 m/s
Convection velocity	U_c = 5 m/s
Boundary layer thickness	δ = 9.1 cm
Wall shear stress	τ_w = 2.52 Pa
Corcos' parameters	α = 0.11; β = 0.77
Panel thickness	h = 1 mm
Panel length in the streamwise direction	L = 0.455 m
Panel length in the crosswise direction	b = 0.375 m
Panel Young's modulus	$E = 2.1 \times 10^{11}$ Pa
Panel Poisson's ratio	ν = 0.3
Panel mass density	ρ = 7,800 kg/m^3
Panel damping loss factor	η = 0.01
Fluid sound speed	c_0 = 1,500 m/s
Fluid mass density	ρ_0 = 1,000 kg/m^3

The spectrum of the wall pressure fluctuations is then given by

- in the physical space $\zeta = (\zeta_x, \zeta_y)$ (i.e. spatial separation):

$$S_{pp}^{\mathrm{TBL}}(\zeta, \omega) = S_{pp}(\omega)\bar{\phi}_{pp}(\zeta, \omega), \text{ and,} \tag{1}$$

- in the wavenumber space $k = (k_x, k_y)$:

$$\phi_{pp}^{\mathrm{TBL}}(k, \omega) = S_{pp}(\omega)\bar{\phi}_{pp}(k, \omega). \tag{2}$$

The frequency band of interest is fixed here to [10 Hz–1 kHz] and is above the hydrodynamic coincidence frequency. It results that the wavelength associated to the convection velocity $\lambda_c = 2\pi U_c/\omega$ is always smaller than the flexural wavelength of the plate.

The objective of the present paper is to estimate the panel response induced by the wall pressure fluctuation defined by its spectrum. In the next section, we give the outlines of the formulation which is described in details in the literature [9–11].

2.2 Mathematical Formulation

$p_b(x, t)$ represents the wall-pressure fluctuations due to the TBL on the plate at point x as a function of time t. The plate velocity at point x due to wall-pressure fluctuations, $v(x, t)$ can be expressed as the convolution product

$$v(x,t) = \int_{S_p} \int_{-\infty}^{+\infty} h_v(x,\tilde{x},t-\tau) p_b(\tilde{x},\tau) d\tau d\tilde{x}, \tag{3}$$

where $h_v(x,\tilde{x},t)$ is the velocity impulse response at point x for a normal unit force at point $\tilde{x}$. The improper integral corresponds to the convolution product between the impulse response $h_v(x,\tilde{x},t)$ and the force $p_b(\tilde{x},\tau)d\tilde{x}$ exerted on an elementary surface $d\tilde{x}$ and it gives the plate velocity at point x due to this force (for a time-invariant system). The surface integral over S_p corresponds to the summation of the effect of the elementary forces over the plate surface and it gives $v(x,t)$ (based on the principle of superposition for a linear system).

As the turbulent flow produces random fluctuations, the plate response is characterised by the auto-correlation function of the velocity, R_{vv}. Supposing that the process is stationary and ergodic (i.e. expectation replaced by the limit of a time average), R_{vv} can be written as:

$$R_{vv}(x,t) = \lim_{T\to\infty} \frac{1}{T} \int_{-T/2}^{T/2} v(x,\tau) v(x,t+\tau) d\tau. \tag{4}$$

The Auto Spectrum Density (ASD) of the velocity at point x is defined as the time Fourier transform of R_{vv}:

$$S_{vv}(x,\omega) = \int_{-\infty}^{+\infty} R_{vv}(x,t) e^{-j\omega t} dt, \ \forall \omega \in \mathbb{R}. \tag{5}$$

The same definition is used for the ASD of the wall-pressure fluctuations, $S_{pp}^{CLT}(\zeta,\omega)$.

Note that:

- the Fourier transform $\tilde{f}(\omega)$ of a function $f(t)$, is defined as $\tilde{f}(\omega) = \int_{-\infty}^{\infty} f(t) e^{-j\omega t} dt$ whereas others conventions can be used (for example $\tilde{f}(\omega) = \frac{1}{2\pi}\int_{-\infty}^{\infty} f(t) e^{-j\omega t} dt$). A special attention should be given on this point when the ASD of the wall-pressure fluctuations is extracted of the literature;
- Moreover, the $S_{pp}^{CLT}(\zeta,\omega)$ is here a double-sided spectrum and is a function of the angular frequency ω. The relation with a single-sided spectrum $\bar{S}_{pp}^{CLT}(\zeta,f)$ expressed as a function of only the positive frequency f is $S_{PP}^{CLT}(\zeta,\omega) = (4\pi)^{-1}\bar{S}_{pp}^{CLT}(\zeta,f)$.

Introducing (3) in (4), and the result in (5), we obtain after some manipulations of integrals:

$$S_{vv}(x,\omega) = \int_{S_p}\int_{S_p} H_v(x,\tilde{x},\omega) S_{pp}^{\mathrm{TBL}}\left(\tilde{x}-\tilde{\tilde{x}},\omega\right) H_v\left(x,\tilde{\tilde{x}},\omega\right) d\tilde{x} d\tilde{\tilde{x}}, \tag{6}$$

where $H_v(x,\tilde{x},\omega) = \int_{-\infty}^{+\infty} h_v(x,\tilde{x},t) e^{-j\omega t} dt$ is the Frequency Response Function (FRF) in velocity at point x for a normal force at point $\tilde{x}$.

In the same manner, we can obtain the ASD of the radiated pressure at point z into the fluid

$$S_{pp}(z,\omega) = \int_{S_p}\int_{S_p} H_p(z,\tilde{x},\omega) S_{pp}^{\mathrm{TBL}}\left(\tilde{x}-\tilde{\tilde{x}},\omega\right) H_p\left(z,\tilde{\tilde{x}},\omega\right) d\tilde{x} d\tilde{\tilde{x}}, \tag{7}$$

where $H_p(z,\tilde{x},\omega)$ is the Frequency Response Function (FRF) in pressure at point z for a normal force at point $\tilde{x}$.

These two equations are the starting point of the following techniques for coupling a wall pressure model with a deterministic vibroacoustic model. In the next section, five different techniques are presented to estimate the vibration response of the panel from (6). These techniques are also applicable to estimate the radiated pressure into the fluid from (7).

3 Different Approaches to Couple a Stochastic Wall Pressure Field to a Deterministic Vibroacoustic Model

3.1 Preamble: Calculation of Frequency Response Functions

Different vibroacoustic models can be used to estimate the Frequency Response Functions (FRF) of complex panels radiated into a fluid:

- FEM using Perfectly Matched Layers (PMLs) [12];
- FEM coupled with BEM [13];
- FEM coupled with Infinite Elements [14];
- Transfer Matrix Method (TMM) for infinite multi-layers panels [15];
- Etc…

In these models, different types of harmonic excitations can be considered:

- A normal point force as illustrated on Fig. 2 for estimating a point to point FRF;
- A wall plane wave excitation;
- A specified pressure field over the panel surface.
- Etc…

Basically, for an angular frequency ω, the equations of motions of the vibroacoustic problem can be written in the matrix form:

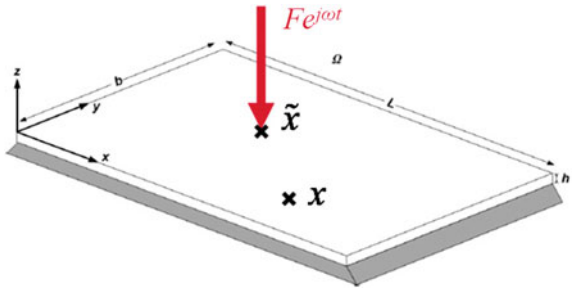

Fig. 2 Illustration of the problem for evaluating the FRF between point x and $\tilde{x}$: $H_{vv}(x, \tilde{x}, \omega) = V_x/F$

$$\mathrm{Dx} = \mathrm{F}, \tag{8}$$

where D is the dynamic stiffness matrix; x, the response vector; and F, the force vector of the considered load case.

The response vector is obtained by inverting the dynamic stiffness matrix:

$$\mathrm{x} = \mathrm{D}^{-1}\mathrm{F}. \tag{9}$$

The FRF can then been determined by extracting the appropriate information in the response vector. In order to simulate the effect of the TBL excitation, many FRFs should be calculated with the vibroacoustic model, and consequently, many load cases should be considered for the process described above [i.e. Eqs. (8) and (9)]. The management of multi load cases is then an important issue when dealing with TBL excitation. For example, it is generally more efficient to multiply D^{-1} by a force matrix containing the different load cases (i.e. matrix–matrix product) than to achieve a loop over the different load cases and to multiply D^{-1} by the force vector of each considered load case (i.e. loop + matrix − vector product). Moreover, in some situations, for example when using of commercial software, it is not always possible to have this optimal management of the multi load cases. This is why in the following, we will not only indicate the computing time observed on the present test case, but we also indicate the number of considered load cases.

For this present test case, the FRFs have been evaluated using an in-house code based on the PTF (Path Transfer Function) approach [16–18]. It allows us to have an optimal management of the multi load case under the MATLAB environment. This substructuring method consists in decomposing our problem in two parts: the panel and the semi-infinite fluid. The coupling surface is divided into patches which sizes depend on the considered wavelengths. Each part is characterised separately by PTFs (i.e. Path mobilities for the panel using the modal expansion method, path impedances for the fluid using the Rayleigh integral). Writing the continuity conditions at the coupling interface allows us to assemble the two parts. The particularity of the present model compared to [17, 18] is that the fluid added mass effect is

taken into account through the "wet modal frequencies" (which are estimated by assuming the fluid incompressible) instead of using the imaginary part of the acoustic impedance of the fluid domain. This permits to overcome the convergence issue evoked in [18] concerning the patch size criterion. Here, a patch size lower than half the flexural wavelength gives results with good numerical convergence. The numerical process based on the PTF approach has been validated for the test case considered by comparison with results published in the literature [19]. We do not describe more in details these calculations which are out of the scope of the present paper.

3.2 The Spatial Method

The first method for coupling the wall pressure spectrum and the FRFs calculated with a vibroacoustic model is simply based on a regular spatial discretization of the panel surface as shown on Fig. 3. Equation (6) becomes:

$$S_{vv}(x,\omega) = \sum_{i=1}^{\Theta}\sum_{j=1}^{\Theta} H_v(x,x_i,\omega) S_{pp}^{\mathrm{TBL}}\left(x_i - x_j,\omega\right) H_v\left(x,x_j,\omega\right)\delta x_i \delta x_j, \tag{10}$$

where Θ is the number of discrete points and δx_i is the elementary surface attributed at the discrete point i.

Equation (10) can be rewritten in the matrix form:

$$S_{vv} = {}^t\mathrm{H}\mathrm{S}_{pp}^{\mathrm{TBL}}\mathrm{H}, \tag{11}$$

with

$$\mathrm{S}_{pp}^{\mathrm{TBL}} = \begin{bmatrix} \ddots & \vdots & \iddots \\ \cdots & S_{pp}^{\mathrm{TBL}}\left(x_i - x_j,\omega\right) & \cdots \\ \iddots & \vdots & \ddots \end{bmatrix}_{\Theta\times\Theta}, \quad \mathrm{H} = \begin{bmatrix} \vdots \\ H_v(x,x_i,\omega)\delta x_i \\ \vdots \end{bmatrix}_{\Theta\times 1}. \tag{12}$$

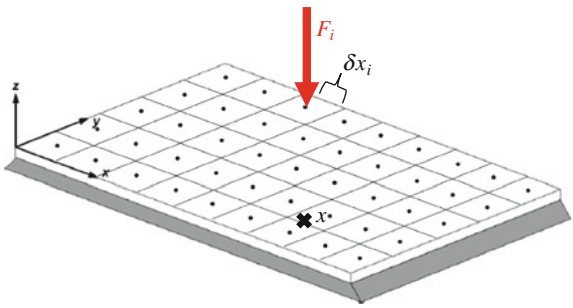

Fig. 3 Illustration of the spatial discretization of the panel surface

The point-to-point FRFs, $H_v(x, x_i, \omega)$, $\forall i \in [\![1, \Theta]\!]$, should be evaluated using the vibroacoustic model. The number of load cases corresponds to the number of discrete points, Θ.

A key parameter of this method is the spatial resolution of the discretisation. Results for the test case are plotted in Fig. 4 with different resolutions given as a function on the convective wavelength λ_c (which depends on the frequency). The coarser mesh (i.e. $\delta = \lambda_c$) gives poor results excepted at low frequency. It does not allow representing correctly the convective part of the pressure fluctuations. A spatial resolution corresponding to one third of the convective wavelength seems to be a good compromise between the results accuracy and the computing times. Even if the spanwise turbulence wall pressure correlation length of the Corcos model is lower than the convective wavelength (and the streamwise correlation length), a parametric survey shows us that the use of the same criterion for the spatial resolution in the spanwise direction than in the streamwise direction gives relevant results.

We emphasize that the calculation process [based on the matrix form (11)] requires high memory capacity, in particular to store the wall pressure CSD matrix S_{pp}^{TBL}. This is why the calculations have not been performed above 500 Hz with our computer (although 1 kHz was initially expected).

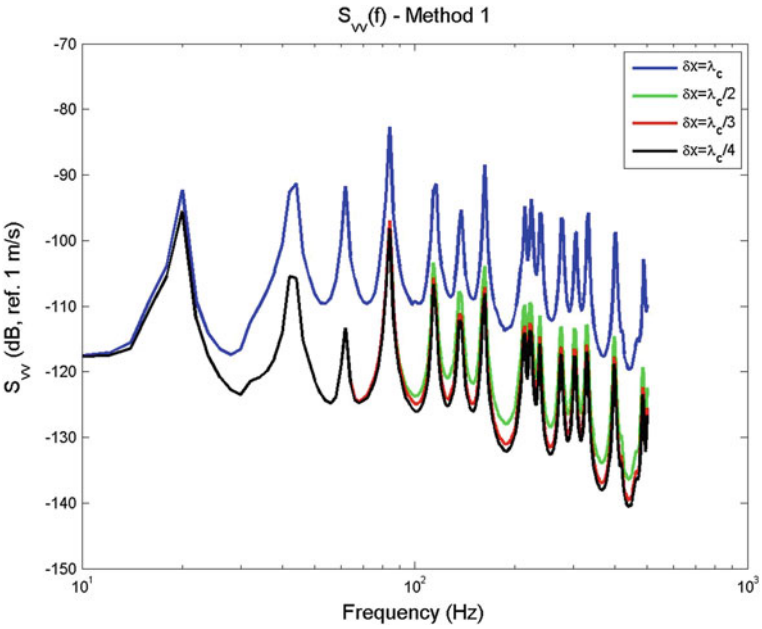

Fig. 4 Velocity ASD at point $x = (0.05, 0.18)$ for different spatial resolutions: *blue* $\delta = \lambda_c$; *green* $\delta = \lambda_c/2$; *red* $\delta = \lambda_c/3$; *black* $\delta = \lambda_c/4$

3.3 The Choslesky Method

The second method is based on a Choslesky decomposition of the wall pressure CSD matrix $\mathrm{S}_{pp}^{\mathrm{TBL}}$ [20, 21]:

$$\mathrm{S}_{pp}^{\mathrm{TBL}}(\omega) = \begin{bmatrix} \ddots & \vdots & \iddots \\ \cdots & S_{pp}^{\mathrm{TBL}}(x_i - x_j, \omega) & \cdots \\ \iddots & \vdots & \ddots \end{bmatrix} = \mathrm{L}(\omega)\mathrm{L}^T(\omega), \tag{13}$$

where $\mathbf{L}(\omega)$ is a lower-triangular matrix of dimensions $\Theta \times \Theta$ and superscript T indicates the transpose of the matrix.

In a first step, the method consists in achieving different realizations of the stochastic field characterized by $\mathrm{S}_{pp}^{\mathrm{TBL}}(\omega)$. The wall pressure vector of the kth realization [21], p^k is given by,

$$p^k(\omega) = L(\omega)e^{j\varphi^k}, \tag{14}$$

where φ^k is a phase vector of Θ random values uniformly distributed in $[0, 2\pi]$.

So, an ensemble average over a set of realizations of the pressure field approximates the wall pressure CSD matrix:

$$\mathrm{S}_{pp}^{\mathrm{TBL}}(\omega) \approx E\left[p^k(\omega)\bar{p}^k(\omega)\right], \tag{15}$$

where the bar over the complex value indicates the complex conjugate.

In a second step, the vibroacoustic model is used to estimate $v^k(x, \omega)$, the panel velocity at point x when the panel is excited by the pressure field, $p^k(\omega)$. This calculation is achieved for a given number of realizations, K. The number of load cases considered in the vibroacoustic simulations corresponds then to the number of realization.

Finally, the ASD of the velocity at point x is estimated by an ensemble average of the velocity responses, $v^k(x, \omega)$:

$$S_{vv}(x, \omega) \approx E\left[v^k(x, \omega)\bar{v}^k(x, \omega)\right]. \tag{16}$$

We illustrate this approach on the present test case. The velocity responses $v^k(x, \omega)$ of 20 realizations are plotted in grey in Fig. 5. A large dispersion of these responses can be observed. The ensemble average over these 20 realizations [Eq. (16)] is plotted with a black curve on Fig. 5 and compared with the result of the first method on Fig. 6. We can observe a good agreement between the two calculations even when only 20 realizations have been considered. With this approach, the number of load cases is then relatively small.

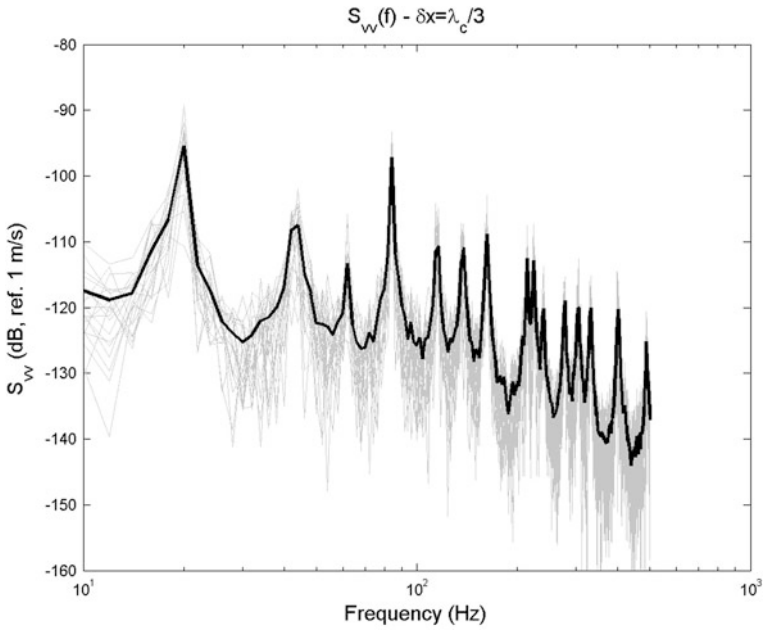

Fig. 5 Velocity ASD at point x = (0.05, 0.18). *Grey* results of 20 realizations; *black* average over the 20 realizations

3.4 The Wavenumber Method

The third method is based on a formulation in the wavenumber space of Eq. (6). Let us consider the space Fourier transform of the wall pressure spectrum, $\phi_{pp}^{\mathrm{TBL}}(k,\omega)$. With our definition of the Fourier transform, it is related to the wall pressure spectrum in the physical space $S_{pp}^{\mathrm{TBL}}\left(\tilde{x}-\tilde{\tilde{x}},\omega\right)$ by

$$S_{pp}^{\mathrm{TBL}}\left(\tilde{x}-\tilde{\tilde{x}},\omega\right)=\frac{1}{4\pi^2}\int_{-\infty}^{+\infty}\phi_{pp}^{\mathrm{TBL}}(k,\omega)e^{\mathrm{j}k\left(\tilde{x}-\tilde{\tilde{x}}\right)}dk. \tag{17}$$

Introducing Eq. (17) in Eq. (6) gives

$$S_{vv}(x,\omega)=\frac{1}{4\pi^2}\int_{-\infty}^{+\infty}\phi_{pp}^{\mathrm{TBL}}(k,\omega)\left|H_v(x,k,\omega)\right|^2dk, \tag{18}$$

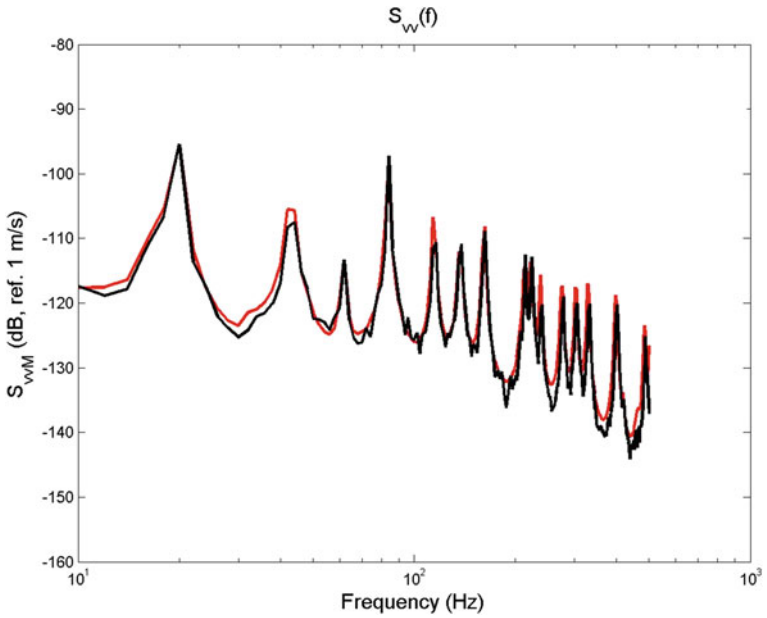

Fig. 6 Comparison of the results of method 1 (*red*) and method 2 (*black*)

with

$$H_v(x,k,\omega) = \int_{S_p} H_v(x,\tilde{x},\omega)e^{jk\tilde{x}}d\tilde{x}. \tag{19}$$

$H_v(x,k,\omega)$ is generally called the sensitivity function [22]. The interpretation of Eq. (19) indicates that this quantity corresponds to the velocity at point x when the panel is excited by an unit wall plane wave with wavevector k (i.e. by a wall pressure field e^{jkx}, $\forall x \in S_p$).

We emphasize that theses wall plane waves can be generated by travelling acoustic plane waves only for wavenumbers k inside the acoustic domain (i.e. $|k| \leq k_0$, with k_0, the acoustic wavenumber). For wavenumbers inside the subsonic domain (i.e. $|k| > k_0$), the acoustic plane waves are evanescent and it is then more complex to generate them physically. The Source Scanning Technique proposed in [23] is one solution. From a numerical point of view, this problem disappears. The pressure field of this excitation can be directly applied as the panel loading. When using a numerical vibroacoustic model (like FEM, BEM, etc.), it is however necessary to check that the spatial discretization of the model allows to represent the spatial variation of this pressure field.

The third method proposed on this paper is based on a truncation and a regular discretization of the wavenumber space k. We suppose that the discrete space is composed of I points which are noted k_i, $\forall i \in [\![1, I]\!]$. The ASD of the velocity at point x can then be approximated by

$$S_{vv}(x,\omega) \approx \frac{1}{4\pi^2}\sum_{i=1}^{I} \phi_{pp}^{\mathrm{TBL}}(k_i,\omega)|H_v(x,k_i,\omega)|^2 \Delta k_i, \tag{20}$$

where Δk_i is the elementary surface in the wavenumber domain attributed to the discrete wavenumber k_i.

The truncation and the discretisation of the wavenumber space should be done carefully in order to avoid the loss of information:

- the wavenumber resolutions in the two directions should be defined such as to permit a correct representation of the spatial variations in the wavenumber space of the sensitivity function and the wall pressure spectrum. For the present test case, an analytical calculation of the sensitivity function for an invacuo panel gives us an order of magnitude of these spatial variations (inversely proportional to the panel lengths). The wavenumber resolutions are fixed to 1 rad/m, independently of the frequency. For a more complex panel, a trial and error process would be necessary to fix these parameters;
- the cut-off wavenumbers in the two directions should be defined such as the main contributions of the integrant of (18) are well taken into account. This point is illustrated on Fig. 7 for the present test case at a given frequency. The highest values of the sensitivity functions are obtained for wavenumbers close to k_f^{wet}, the natural flexural wavenumber of an equivalent infinite plate taking the fluid added mass effect into account. On another hand, the wall pressure spectrum exhibits the highest values for wavenumbers close to the convective wavenumber, k_c. In theory, the cut-off wavenumber should be defined in the streamwise direction by $\bar{k}_x = \kappa_x \max\left[k_f^{\mathrm{wet}}, k_c\right]$ and in the crosswise direction by $\bar{k}_y = \kappa_y k_f^{\mathrm{wet}}$ where κ_x and κ_y are margin coefficient. As the considered frequency is well above the hydrodynamic coincidence frequency, we have $k_f^{\mathrm{wet}} \ll k_c$ and $\bar{k}_x = \kappa_x k_c$. This last criterion can lead to huge computing costs (because the spatial discretisation of the vibroacoustic model should be able to describe the "small" wavelength $2\pi/\bar{k}_x$). However, it is well known [24] that in many cases, the structure plays a role of filtering of the excitation which is dominant. This is illustrated on Fig. 7c where the product of the sensitivity function with the wall pressure spectrum [i.e. integrant of Eq. (18)] has been plotted. It can be observed that the contribution of the convective domain is negligible. Then, for this case, the cut-off wavenumber in the streamwise direction can be reduced to $\bar{k}_x = \kappa_x k_f^{\mathrm{wet}}$. This permits to save huge computing times. It should be emphasized that this restriction is not always valid. In particular, it depends on the frequency (compared to the hydrodynamic frequency), on the considered wall pressure model (see [25]), and the boundary conditions of the panel (see [26]). Here again, a trial and error process could be necessary at certain frequencies to fix the cut-off wavenumber;

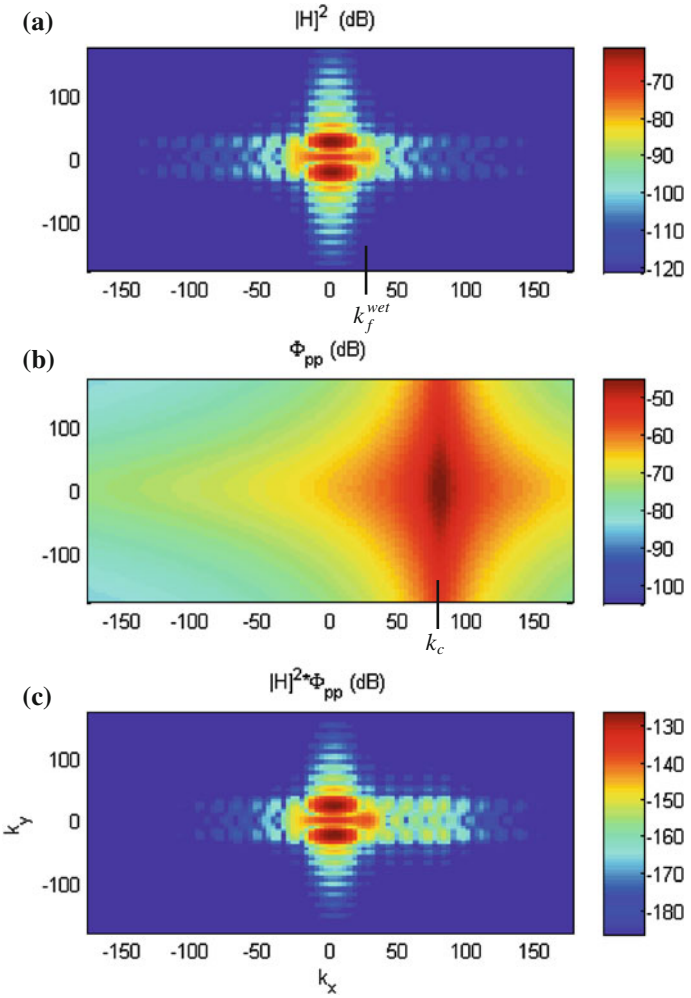

Fig. 7 Different quantities in the wavenumber space $k = (k_x, k_y)$: **a** the sensitivity function at point x, $H_v(x, k, \omega)$; **b** the wall pressure spectrum, $\phi_{pp}^{\mathrm{TBL}}(k, \omega)$; **c** the product between the sensitivity function and the wall pressure spectrum, $\phi_{pp}^{\mathrm{TBL}}(k, \omega)|H_v(x, k, \omega)|^2$. Results presented at 100 Hz

With this approach, the number of load cases corresponds to the number of wall plane waves considered for the calculation of the sensitivity functions, $H_v(x, k, \omega)$.

The present method respecting the previous criteria for the wavenumber resolutions and the cut-off wavenumbers is compared with the spatial method in Fig. 8. We can observe that the spatial method gives results slightly higher than the wavenumber method (excepted for the first peaks). This can be attributed to the

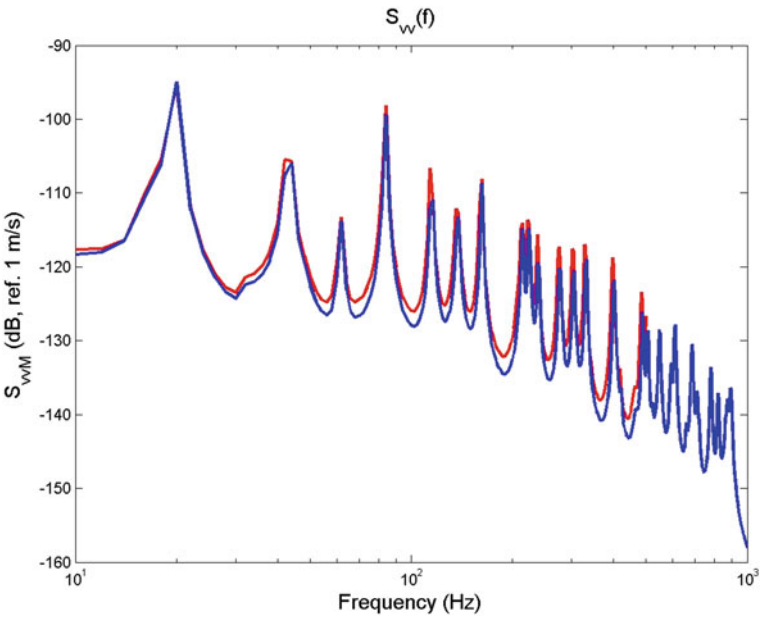

Fig. 8 Velocity ASD at point x = (0.05, 0.18). Comparison of the results of method 1 (*red*) and method 3 (*blue*)

spatial resolutions of the first method (i.e. $\delta = \lambda_c/4$) which is not sufficiently small to ensure a full convergence of the method.

Contrary to the spatial and Cholesky methods, the wavenumber method allows us to obtain results up to 1 kHz. This is mainly due to the fact that the convective ridge which can be supposed negligible is not described with this method when using appropriate cut-off wavenumbers.

3.5 The Reciprocity Method

This fourth approach has been proposed in [11] for predicting the noise radiated by stiffened structures excited by TBL. It is based on a reciprocity principle which gives a second interpretation of the sensitivity functions. Indeed, the Lyamshev reciprocity principle [27] for vibro-acoustic problems indicates that the ratio of the normal velocity of the plate at point x over the applied normal force at point $\tilde{x}$ is equal to the ratio of the normal velocity of the plate at point $\tilde{x}$ over the normal force applied at point x. With the present notation, we can write:

$$H_v(x,\tilde{x},\omega) = H_v(\tilde{x},x,\omega). \tag{21}$$

This expression can be injected in the definition of the sensitivity function [i.e. Eq. (19)] that allows us writing

$$H_v(x,-k,\omega) = \int_{S_p} H_v(\tilde{x},x,\omega)e^{-jk\tilde{x}}d\tilde{x}. \tag{22}$$

One recall that $H_v(\tilde{x},x,\omega)$ represents the velocity response at point $\tilde{x}$ when the panel is excited at point x. Then, $H_v(x,-k,\omega)$ can be interpreted as the spatial Fourier transform of the velocity response of the panel excited at point x. Consequently, the power spectrum density of the velocity of the plate at point x excited by the TBL can be calculated with Eq. (20) on the basis of the response of the plate excited by a normal force at point x and expressed in the wavenumber space by a discrete spatial Fourier transform. That is to say that the plate response at a given point due to TBL can be estimated from the vibratory field of the plate excited by a point force at this same point.

We can emphasize that this technique remains available even if the point of observation is into the fluid domain (for example for dealing with transmission loss problem). In this case, the radiated pressure at a point z by the TBL-excited panel would be estimated from the velocity field of the panel excited by an acoustic monopole located at point z and having unit volume flow rate [11].

The main advantage of this approach is that the number of load case is very small in general because it corresponds to the number of receiving points for which the response to the TBL excitation should be estimated. As this excitation is spatially distributed, it is generally not necessary to consider a large number of receiving points, the stochastic vibratory field being relatively homogeneous.

We compare the sensitivity functions obtained with these two interpretations on Fig. 9. Of course, the results are very similar. The wavenumber resolutions differ as the ones of the reciprocity method depends directly on the panel dimensions (as a consequence of the discrete spatial Fourier transform). The comparison of the wavenumber and reciprocity methods on Fig. 10 shows a good agreement. The slight differences can be attributed to the different wavenumber resolutions.

We can emphasize that this method requires few load cases but it requires evaluating the spatial distributions of the vibratory field in order to perform the spatial Fourier transform. When the vibratory field is evaluated from a numerical model (like the PTF approach used in the present paper), this task can be relatively time consuming and can reduce the efficiency of this approach. At its origin, this approach has been developed for dealing with stiffened structures like plate or shell stiffened in 1 direction or in 2 orthogonal directions [11]. For these cases, it is possible to calculate analytically the sensitivity functions thanks to the reciprocity principle described in this section. The computing times are then very short.

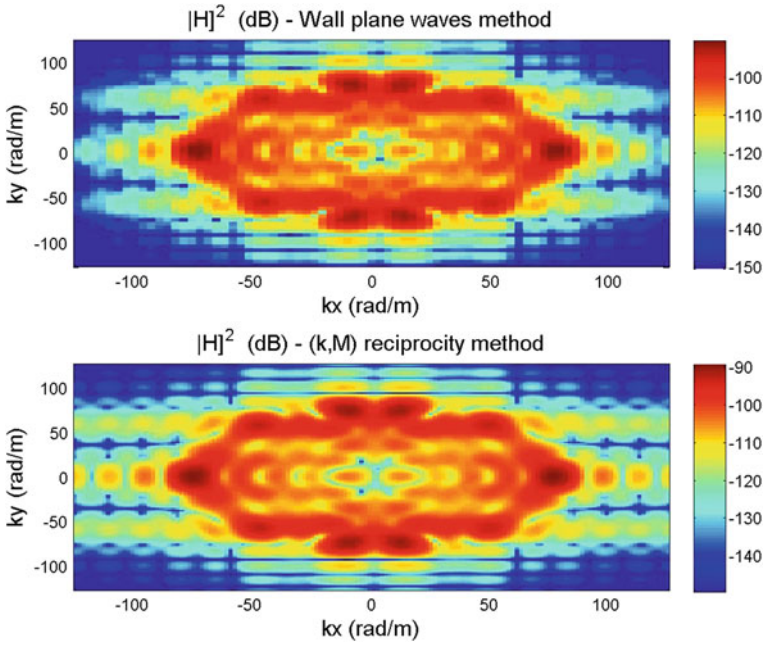

Fig. 9 Sensitivity function at point x = (0.05, 0.18) in function of the wavevector $k = (k_x, k_y)$. Results at 1 kHz. Two calculations: *upper*, with Eq. (19) (i.e. direct interpretation); *lower*, with Eq. (22) (i.e. using the reciprocity principle)

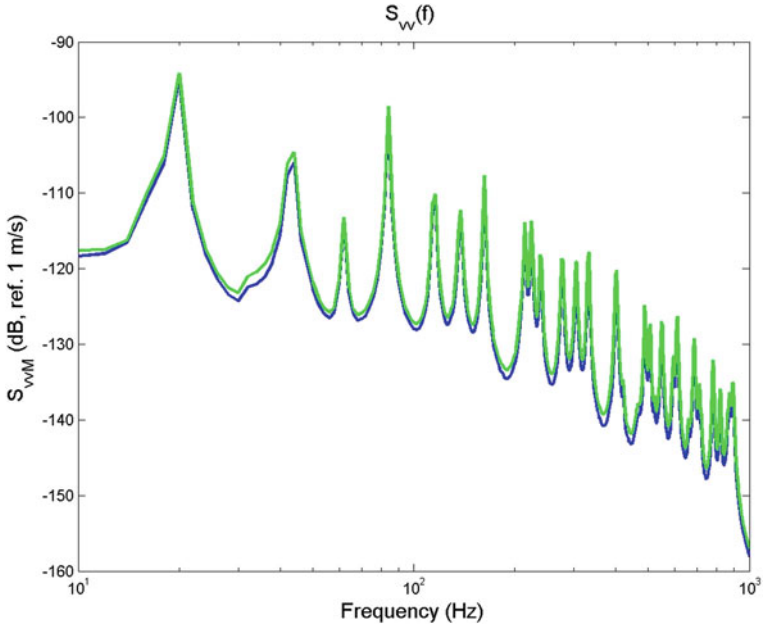

Fig. 10 Velocity ASD at point x = (0.05, 0.18). Comparison of the results of method 3 (*blue*) and method 4 (*green*)

3.6 Method Based on the Sampling of Uncorrelated Wall Plane Waves

The last of the five methods presented in this paper has been presented recently in [28]. It has some similarities with the method 2 (Sect. 3.3). But, contrary to the latter, it does not require a Cholesky decomposition (which can be time consuming).

Basically, it consists in rewriting Eq. (20) in the following form:

$$S_{vv}(x,\omega) \approx \sum_{i=1}^{I} S_{A_iA_i}(\omega)|H_v(x,k_i,\omega)|^2, \tag{23}$$

with

$$S_{A_iA_i}(\omega) = \frac{\phi_{pp}^{\mathrm{TBL}}(k_i,\omega)\Delta k_i}{4\pi^2}. \tag{24}$$

This expression can be interpreted as the panel response to a set of uncorrelated wall plane waves of stochastic amplitudes A_i, $i \in [\![1, I]\!]$. $S_{A_iA_i}(\omega)$ represents the ASD of the amplitude of the ith waves. These wall plane waves are uncorrelated because Eq. (23) corresponds to the case where $S_{A_iA_j}(\omega) = 0$, $\forall i \neq j$ (see [23] for details).

This interpretation is similar to the one generally considered for describing an acoustic diffuse field: a set of uncorrelated acoustic waves of equiprobable incident angles and equal intensities. In the present case with the TBL excitation, the waves are not limited to the acoustic domain and their amplitudes are not constant; they depend on the wall pressure fluctuations, $\phi_{pp}^{\mathrm{TBL}}(k_i,\omega)$ from Eq. (24).

From this interpretation, we can define the wall pressure field of the kth realization, $p^k(x_i,\omega)$ by,

$$p^k(x_i,\omega) = \sum_{i=1}^{I} \sqrt{S_{A_iA_i}(\omega)}e^{j\varphi_i^k}e^{jkx_i}, \tag{25}$$

where φ_i^k, $\forall i \in [\![1, I]\!]$, are random phase values uniformly distributed in $[0, 2\pi]$.

As for the method 2, the panel velocity at point x when the panel is excited by the pressure field, $p^k(\omega)$ is then estimated by using the vibroacoustic model. This process is repeated for a given number of realizations, K; and, finally, the ASD of the velocity at point x is estimated by an ensemble average of the velocity responses, $v^k(x,\omega)$ [see Eq. (16)].

In Fig. 11, the velocity responses of 20 realizations are plotted in grey and the ensemble average over these 20 realizations is plotted in black. We can observe that this figure is similar to Fig. 5 related to the method 2, excepted that the calculation is achieved up to 1 kHz. The advantages of the present method compared to the

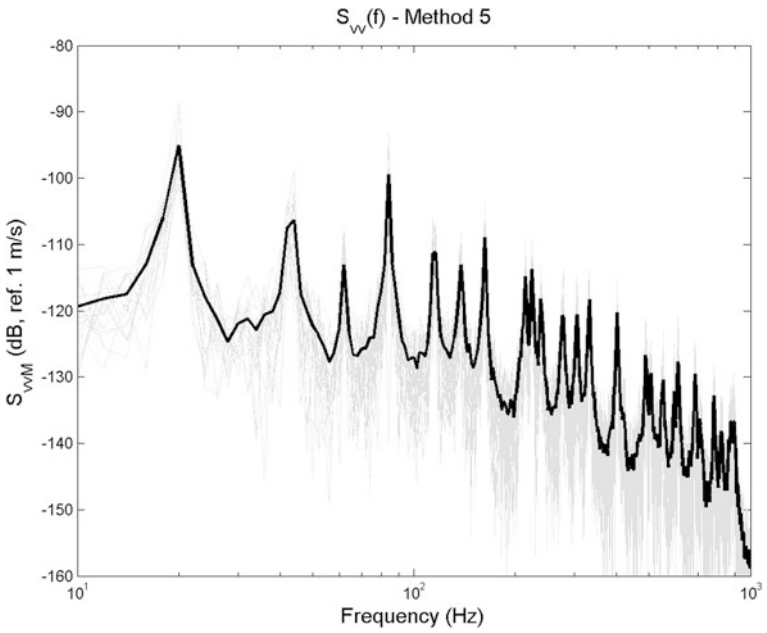

Fig. 11 Velocity ASD at point $x = (0.05, 0.18)$. *Grey* results of 20 realizations; *black* average over the 20 realizations

method 2 are: (a), it is not necessary to use a Cholesky decomposition to define the wall pressure field of each realization. Equation (25) with (24) can be applied directly from the wall pressure spectrum expressed in the frequency-wavenumber space (with a Corcos or a Chase model for example); (b), the use of adapted cut-off wavenumbers permits to neglect easily the effect of the convective ridge and then to save computing time.

The good agreement between the results of method 3 and 5 on Fig. 12 allows us validating the present approach.

3.7 Synthesis

Five methods for coupling a TBL wall pressure model with a deterministic vibro-acoustic model have been presented:

- The first two methods are adapted for a wall pressure spectrum expressed in the physical space (like given by the Corcos model); the spatial resolution criterion which permits to describe correctly the convective ridge requires a very fine discretization of the panel surface and it can limit these methods to low

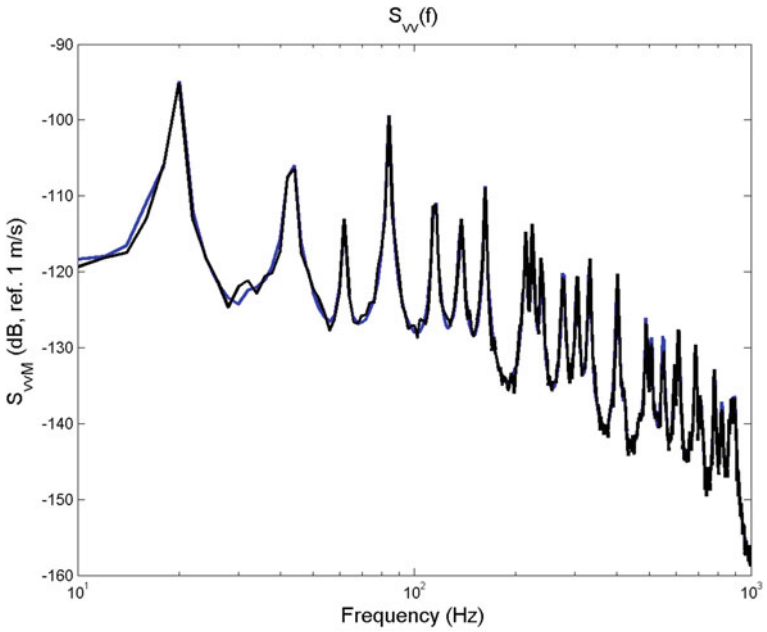

Fig. 12 Comparison of the results of method 3 (*blue*) and method 5 (*black*)

frequencies and/or to small panels. We have noticed that if this criterion is not respected, these two methods overestimate significantly the vibratory field;

- The three other methods are adapted for a wall pressure spectrum expressed in the wavenumber space. In some situations (e.g. for frequencies well above the hydrodynamic frequency), the effect of the convective ridge can be neglected which enables to reduce the cut-off wavenumber (with a criterion based on the panel characteristics and not on the TBL ones). It permits to save computing time. Thanks to that, a higher frequency range has been reached by comparison with the spatial methods. It should however be emphasized that if the wall pressure spectrum in the physical space was filtered by a low pass filter in order to suppress the convective peak corresponding to the small spatial separations, the spatial methods would certainly have a similar efficiency than the wavenumber methods.

As an indication, we give on Table 2 the number of load cases and the CPU time per frequency observed on the present test case for the 5 methods. We should emphasize that these computing times do not represent strictly the efficiency of each method; they depend strongly on the calculation algorithm (that we try to optimize), the computing environment (MATLAB for us), the management of the input/output of the vibroacoustic code (use of PTF in-house code). Anyway, the method based on the realizations of uncorrelated wall plane waves gave us smaller computing time. The reciprocity method is the one which necessitates the lowest number of

Table 2 Synthesis of the number of load cases and the computing times

Method	Spatial	Cholesky	Wavenumber	Reciprocity	Uncorrelated waves
Number of load cases	27,300	20	10,000	1	20
CPU time/frequency (s)	5.8	16.4	2.5	2.3	1.9

load case. It could be the most efficient if the management of the input/output with the vibroacoustic code would not be optimal.

The presented results and the discussion focus on the vibratory response of the panel. Of course, all the methods described in this paper can be used to evaluate the radiated pressure from the panel excited by TBL (for dealing with transmission loss problem for example). Moreover, they can be applied to more complex structures than the rectangular thin plate considered for illustration.

4 High Frequency Modelling

4.1 Statistical Energy Analysis

Statistical energy analysis (SEA) allows the vibro-acoustic behaviour of complex structures in high-frequency range to be predicted [7, 29]. The method is based on a fundamental relationship relating the power flow exchanged by two-coupled subsystems to their total subsystem energies by the coupling loss factor (CLF).

Basically, SEA consists in decomposing the global subsystem in different subsystems as illustrated in Fig. 13 for a Sonar self noise issue on a ship. This substructuring should be done in order to fulfil several conditions [30–33]. In particular, each subsystem should exhibit several (many) modes in the frequency band of interest and the couplings between subsystems should be weak [31]. For the case presented in Fig. 13, the coupling between the dome and the Sonar cavity filled

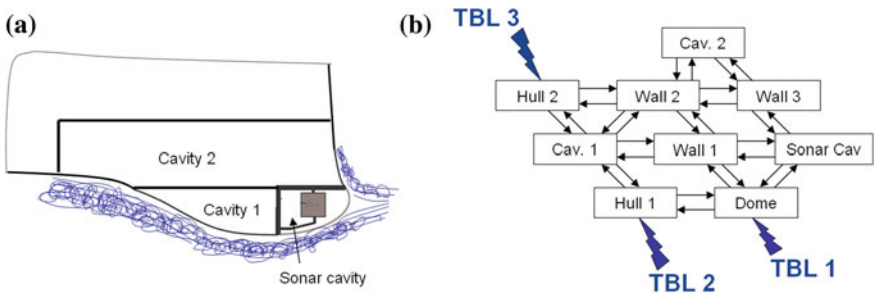

Fig. 13 **a** Illustration of the self noise issue on the bow of an anti-submarine warfare surface ship; **b** SEA model describing the energy sharing between subsystems

of water may be a problem because it does not respect strictly the weak coupling assumption [34]. In this case, SEA can be seen as a first approximate model which is valuable for practical studies [35].

In a second step, SEA consists in writing the power balance for stationary motion in each subsystem using the fundamental SEA relation to evaluate the power flows. It produces a linear equation system where the unknowns are the total energies of subsystems. Then, the difficulty in applying SEA is not due to solving complicated equations, but in evaluating the SEA input parameters such as the damping loss factors, the coupling loss factors [36] and the injected power [37–39].

In this section, we focus the discussion on the evaluation of the injected power when the SEA subsystem is excited by a TBL. For the illustration case of Fig. 13, it consists in estimating the injected power by the turbulent flow in three subsystems (i.e. the Sonar dome and the two parts of the hull) for each frequency band (typically, third octave bands).

We suppose that the TBL parameters characterizing the turbulent flow have been obtained from a hydrodynamic code and an appropriate model allows us describing the spectrum of the wall pressure fluctuations.

Before going into the details about the injected power calculation, it is necessary to make a break on two points:

- First, it should be remembered that the injected power depends not only on the excitation, but also on the receiving structure. If the structure was infinitely rigid, the injected power would be null. In the case of SEA model for which the global system has been decomposed in weakly coupled subsystems, one can suppose that the injected power in a given subsystem can be evaluated by neglecting the couplings with the others subsystems. This assumption is valid if the weak coupling condition is well respected with the others subsystems;
- The calculation of the injected power should be performed in the framework of SEA hypothesis. That is to say that the frequency is relatively high, the excited structure presents many modes, and the different SEA quantities (especially the injected power) are time-averaged for a considered frequency band. Under these hypotheses, it may be reasonable to evaluate the injected power in a complex structure from the one in an equivalent academic structure [7]. Generally, this latter is a rectangular thin plate. It could be surprising at the first sight to "replace" a complex structure like the Sonar dome by a thin plate. However, it is well-know that in the high frequencies, the effects of curvature of the dome and of the boundary conditions on its vibratory behaviour can be neglected. If the dome is made of an isotropic material and of constant thickness, a thin plate can then be reasonably considered to evaluate SEA parameters like the modal density or the injected power. For more complex structures like the stiffness hull of the ship, the thin plate alone is probably not sufficient to represent correctly the behaviour at high frequencies. In particular, the propagation of the Bloch-Floquet waves due to the periodic stiffeners would not be described. This aspect of approximation is part of the difficulties in applying SEA to manufactured structures and is also part of the expertise of the SEA specialists.

Anyway, in this paper, we have decided to focus our attention on the estimation of the power injected by the TBL in an equivalent thin plate.

4.2 Estimation of the Time-Average Injected Power

Let us consider a thin plate subjected to a TBL excitation. The plate is made of an isotropic elastic material and has a constant thickness. *M, D, h,* η_s are, respectively, the mass per unit area, the flexural rigidity, the thickness, and the damping loss factor of the plate. The TBL is fully developed, stationary and homogeneous. We consider a frequency band of angular bandwidth $\Delta\Omega$ and of central angular frequency Ω which is well above the hydrodynamic coincidence angular frequency.

The energy balance equation consists in writing that the injected power by the TBL is dissipated by the plate. The time average of the injected power in the considered frequency band, Π_{inj} can then be evaluated from

$$\Pi_{\text{inj}} \approx \Omega \eta_s M \langle V^2 \rangle, \tag{26}$$

where $\langle V^2 \rangle$ is the time and space average of the quadratic velocity of the plate.

In the high frequencies, the shape of the plate and the type of boundary conditions do not influence the SEA parameters [7]. Then, a rectangular simply-supported plate was considered in [24, 37] for evaluating $\langle V^2 \rangle$ from a modal expansion. An alternative consists in considering an infinite plate (which is excited by a 'fictive' homogeneous CLT) and in evaluating $\langle V^2 \rangle$ for a given area, S_p of the plate. This "equivalence" of vibratory behaviour in the high frequencies between a finite structure and an infinite one is often used in SEA. For its simplicity in the mathematical developments, we adopt it in the present paper.

As the infinite plate is theoretically excited by a homogeneous CLT, the vibratory field is assumed to be spatially homogeneous. The ASD of the velocity at a given point x is independent of the point position:

$$S_{vv}(x, \omega) = S_{vv}(\omega), \ \forall x \in S_p. \tag{27}$$

The time and space average of the quadratic velocity of the plate is obtained from

$$\langle V^2 \rangle = \frac{1}{2\pi} \int_{\Omega - \Delta\Omega/2}^{\Omega + \Delta\Omega/2} S_{vv}(\omega) d\omega. \tag{28}$$

The wavenumber formulation of Sect. 3.4 allows us writing the ASD of the velocity

$$S_{vv}(\omega) = \frac{1}{4\pi^2} \int_{-\infty}^{\infty} \int_{-\infty}^{\infty} \phi_{pp}^{\mathrm{TBL}}(k_x, k_y, \omega) \left| H_v(k_x, k_y, \omega) \right|^2 dk_x dk_y, \tag{29}$$

where k_x, k_y are wavenumbers in the streamwise and spanwise directions, respectively.

The sensitivity functions, $H_v(k_x, k_y, \omega)$ can be calculated using the reciprocity principle described in Sect. 3.5. It corresponds to the transversal velocities of the plate expressed in the wavenumber space when the plate is excited by a normal point force at an arbitrary point. (We chose the coordinate origin for convenience.) Considering the Kirchhoff-Love's dynamic plate equation, we obtain:

$$H_v(k_x, k_y, \omega) = \frac{j\omega}{D\left[(1 + j\eta_s)\left(k_x^2 + k_y^2\right)^2 - k_f^4\right]}, \tag{30}$$

with $k_f = \omega^{1/2} \left(\frac{M}{D}\right)^{1/4}$, the natural flexural wavenumber of the plate.

We can notice that these sensitivity functions have the most important magnitudes for wavenumbers close to the flexural wavenumber (i.e. when $\sqrt{k_x^2 + k_y^2} \approx k_f$) and their magnitudes decrease quickly when the wavenumbers deviate from these values (see example Fig. 14a). On the contrary, the wall pressure spectrum varies relatively slowly in the subconvective wavenumber domain (see Fig. 14b). Then, the more significant contributions of the integrand of (29) correspond to the wavenumbers close to the flexural wavenumber (taking account that the convective ridge can be neglected seeing that the frequency band of interest is well above the hydrodynamic coincidence frequency). Supposing moreover that the wall pressure spectrum is relatively flat for wavenumbers close to the flexural wavenumber, we can write:

$$S_{vv}(\omega) \approx \frac{\phi_{pp}^{\mathrm{TBL}}(k_f, 0, \omega)}{4\pi^2} \int_{-\infty}^{\infty} \int_{-\infty}^{\infty} \left| H_v(k_x, k_y, \omega) \right|^2 dk_x dk_y, \tag{31}$$

This approximation is illustrated in Fig. 14c by comparing $\phi_{pp}^{\mathrm{TBL}}(k_x, k_y, \omega) \left| H_v(k_x, k_y, \omega) \right|^2$ (full line) with $\phi_{pp}^{\mathrm{TBL}}(k_f, 0, \omega) \left| H_v(k_x, k_y, \omega) \right|^2$ (dashed line); as discussed in Sect. 3.4, it should be emphasized that this restriction is not always valid. The validity of this approximation depends on the frequency (compared to the hydrodynamic frequency), on the considered wall pressure model, and the boundary conditions of the panel. In the 'high' frequency, it is generally well respected.

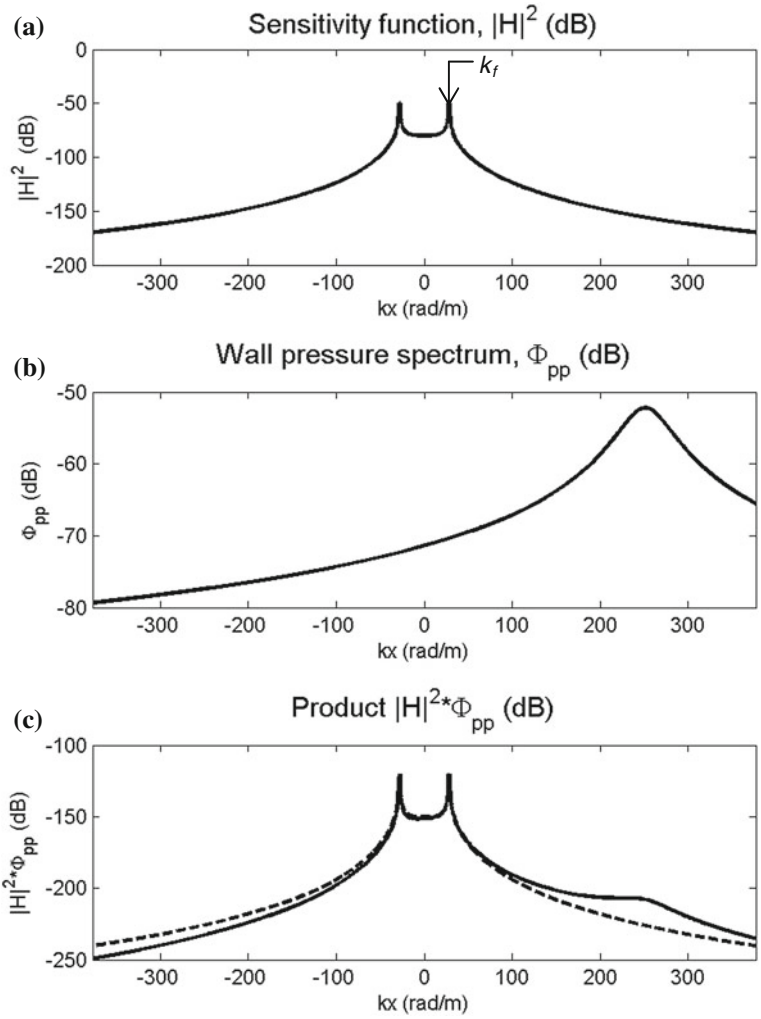

Fig. 14 **a** Sensitivity function for an infinite steel 1 mm-thick plate; **b** corcos wall pressure spectrum; **c** product between the sensitivity function and the wall pressure spectrum: *full* without approximation; *dotted* with the approximation used in Eq. (31). Results at 200 Hz for $k_y = 0$ rad/m

The integral of this expression can be approximated by

$$\int_{-\infty}^{\infty}\int_{-\infty}^{\infty} \left|H_v\left(k_x, k_y, \omega\right)\right|^2 dk_x dk_y \approx \frac{\omega^2}{8D^2\eta_s k_f^6}. \tag{32}$$

Introducing Eqs. (28, 31, 32) in Eq. (26) and supposing that $\Delta\Omega \ll \Omega$ (and then $\omega \approx \Omega$), we obtain an estimation of the injected power by the TBL in the plate:

$$\Pi_{\text{inj}} \approx \frac{S}{4\sqrt{MD}} \phi_{pp}^{\text{TBL}}\left(k_f, 0, \Omega\right) \Delta\Omega. \tag{33}$$

An expression which differs only by a $(2\pi)^3$ factor was obtained in [37] considering a simply supported plate and a modal calculation. This factor is only due to the difference of definition of the space-time Fourier transforms between the two papers.

We notice that this power is independent from the plate damping. This may have consequences for vibration and noise control. As it can be expected, it is also proportional to the area excited by the turbulent flow.

Different approximations have been made to obtain this formula. In particular, the frequencies should be well higher than the hydrodynamic coincidence frequency and the wall pressure spectrum should be considered relatively flat in the wavenumber region concerned by the plate characteristic wavenumbers (i.e. flexural wavenumber). Comparison in [37] with an "exact calculation" for a present test case and considering the Corcos model showed that the discrepancies were very small in the frequency domain for which the SEA can be applied. For aeronautical application, the calculation of the injected power proposed in Refs. [38, 39] can be more accurate for frequencies lower than or close to the aerodynamic coincidence frequency.

Expression (33) has been obtained considering a flat plate and it may give a fair approximation of the injected power in subsystems composed of sheets having a high radius of curvature, roughly constant thickness and made of isotropic material. For stiffened structures like the ship hull, it could be seen as a first approximation. A more accurate prediction could be obtained by considering the sensitivity functions of a periodically stiffened plate [11]. In this way, it would be difficult to obtain an analytical expression of the injected power but a numerical process could be developed. SEA results could be compared to the approach proposed in [40–42] to estimating broadband levels of acoustic power radiated due to rib/panel interaction under TBL-like excitation.

4.3 A Methodology for Taking into Account the Spatial Variation of the TBL Parameters

Hydrodynamic codes [37] permit to estimate spatial variations of the TBL parameters due to static pressure gradients or development of the TBL. An illustration is given on Fig. 15 for the bow of an Anti-Submarine Warfare surface ship. The TBL parameters can then vary on the surface of a given SEA subsystem (for example the Sonar dome of the ship). This can be an issue for evaluating the SEA injected power. However, if these variations are relatively slow compared to the wavelengths of the flexural motions, a numerical process taking these variations into account can be proposed. Indeed, we have noticed previously that the

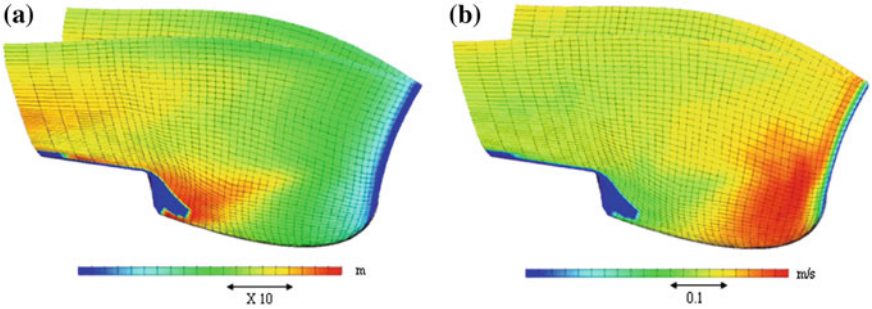

Fig. 15 Illustration of hydrodynamic calculation of the TBL parameters for the front of a ship [37]: **a** boundary layer thickness; **b** hydrodynamic friction velocity

relation (33) has been obtained independently of the boundary conditions of the panel and it remains valid as long as many wavelengths are contained along each edge of the panel. Then, it can be use to evaluate the injected power in a part of a subsystem for which TBL parameters does not vary significantly.

The process consists in dividing the subsystem surface (excited by TBL) in K patches having roughly constant TBL parameters. For each patch k of surface S^k, we can evaluate the injected power per unit area, π_{inj}^k:

$$\pi_{\text{inj}}^k = \frac{1}{4\sqrt{MD}} \phi_{pp,k}^{\text{TBL}}\left(k_f, 0, \Omega\right) \Delta\Omega,\ k \in [\![1, K]\!], \tag{34}$$

where $\phi_{pp,k}^{\text{TBL}}$ is the wall pressure spectrum depending on the TBL parameters on the kth patch.

An approximation of the injected power can then be obtained from

$$\Pi_{\text{inj}} \approx \sum_{k=1}^{K} \pi_{\text{inj}}^k S^k. \tag{35}$$

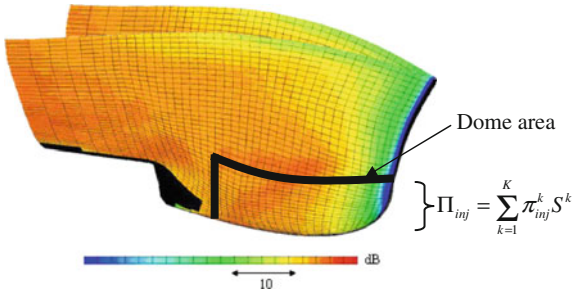

Fig. 16 Values of the injected power by unit area obtained from the TBL parameters of Fig. 15 [37]

An illustration of this process is given on Fig. 16. The injected power in the Sonar dome is evaluated by integrating over the dome surface the injected power by unit area. The latter has been calculated from the parameters of Fig. 15 and it exhibits significant spatial variations. This highlights the importance to taken the TBL parameters into account.

5 Conclusions

This paper is focused on the coupling between TBL excitations and vibro-acoustic models. In the low frequency range, different techniques have been presented to make the relationship between the stochastic excitation and the deterministic model. The efficiency of these techniques in terms of computation time depends on various parameters such that the choice of the wall pressure models (in spatial or wave-number form), the values of the physical parameters of the considered case, the efficiency of the vibro-acoustic code (in particular, its ability to manage multi-load cases), etc. For the marine test considered in this paper, the method consisting in the realizations of uncorrelated wall plane waves was found to be the fastest one. This method is easy to implement and it requires a small number of vibro-acoustic calculations (i.e. the number of load cases is equal to the number of realization). These methods offer a large possibility for coupling the wall pressure spectrum of the CLT excitation with the transfer functions describing the vibro-acoustic behaviour of the considered structure. In the future a more detailed study of the influence of the spatial variations of the TBL parameters should be undertaken.

In the high frequency range, a formulation of the injected power in a SEA subsystem subjected to a TBL excitation has been proposed as a function of the wall pressure spectrum expressed in the frequency-wavenumber space. It has been obtained considering an infinite flat plate and several assumptions which are generally valid for high frequencies. Investigations should be performed in the future to extend these developments to more complex cases such as the stiffened structures frequently met in industrial applications.

References

1. G.M. Corcos, Resolution of pressure in Turbulence. J. Acoust. Soc. Am. **35**(2), 192–199 (1963)
2. D.M. Chase, The character of the turbulent wall pressure spectrum at subconvective wavenumbers and a suggested comprehensive model. J. Sound Vib. **112**(1), 125–147 (1987)
3. Y. Hwang, W. Bonness, S. Hambric, Comparison of semi-empirical models for tuburlent boundary layer wall pressure spectra. J. Sound Vib. **319**(1), 199–217 (2009)
4. Y. Rozenberg, G. Robert, S. Moreau, Wall-pressure spectral model including the adverse pressure gradient effects. AIAA J. **50**(10), 2168–2179 (2012)

5. W. Bonness, D. Capone, S. Hambric, Low-wavenumber turbulent boundary layer wall-pressure measurements from vibration data on a cylinder in pipe flow. J. Sound Vib. **329**(20), 4166–4180 (2010)
6. W.R. Graham, A comparison of models for the wavenumber-frequency spectrum of turbulent boundary layer pressures. J. Sound Vib. **206**(4), 541–565 (1997)
7. R.H. Lyon, R.G. Dejong, *Theory and Application of Statistical Energy Analysis*, 2nd edn. (Butterworth-Heinemann, Boston, 1995), p. 277
8. M. Goody, Empirical spectral model of surface pressure fluctuations. AIAA J. **42**, 1788–1794 (2004)
9. W.A. Strawderman, Wavevector-Frequency Analysis with Applications to Acoustics, Naval Underwater Systems Center, Technical Report, NUSC 8209 (1988)
10. C. Maury, P. Gardonio, S.J. Elliott, A wavenumber approach to modelling the response of a randomly excited panel, part I : general theory. J. Sound Vib. **252**, 83–113 (2002)
11. L. Maxit, V. Denis, Prediction of flow induced sound and vibration of periodically stiffened plates. J. Acoust. Soc. Am. **133**(1), 146–160 (2013)
12. I. Harari, M. Slavutin, E. Turkel, Analytical and numerical Studies of a finite element PML for the Helmholtz equation. J. Comput. Acoust. **8**, 121–137 (2000)
13. P. Bettess, Infinite elements. Int. J. Num. Meth. Eng. **11**, 53–64 (1977)
14. D.W. Herrin, T.W. Wu, A.F. Seybert, Boundary Element Modelling, *Handbook of noise and vibration control*, Paper 8, ed. by M.J. Crocker (John Wiley and Sons, Inc., New York, 2007), pp. 116–127
15. M. Abid, M.S. Abbes, J.D. Chazot, L. Hammemi, L. Hammemi, M. Haddar, Acoustic response of a multilayer panel with viscoelastic material. Int. J. Acoust. Vib. **17**, 82–89 (2012)
16. M. Ouisse, L. Maxit, C. Cacciolati, J.L. Guyader, Patch transfer functions as a tool to couple linear acoustic problems. J. Vib. Acoust. (ASME) **127**, 458–466 (2005)
17. M. Aucejo, L. Maxit, N. Totaro, J.L. Guyader, Convergence acceleration using residual shapes technique when solving structure-acoustic coupling with patch transfer functions method. Comput. Struct. **88**, 728–736 (2010)
18. L. Maxit, M. Aucejo, J.L. Guyader, Improving the patch transfer function approach for fluid-structure modelling in heavy fluid. J. Vib. Acoust. ASME **134**, 1–14 (2012)
19. A. Berry, A new formulation for the vibrations and sound radiation of fluid-loaded plates with elastic boundary conditions. J. Acoust. Soc. Am. **96**(2), 889–901 (1994)
20. ACTRAN 12.2 User's Guide. Vol. 1: Installation, operations, theory and utilities. Chap. 20: Random excitation. Free Field Technologies SA, Belgium (2012)
21. L.E. Wittig, A.K. Sinha, Simulation of multicorrelated random processes using the FFT algorithm. J. Acoust. Soc. Am. **58**, 630–634 (1975)
22. F. Birgersson, N.S. Ferguson, S. Finnveden, Application of the spectral finite element method to turbulent boundary layer induced vibration of plates. J. Sound Vib. **259**(4), 873–891 (2003)
23. M. Aucejo, L. Maxit, J.-L. Guyader, Experimental simulation of turbulent boundary layer induced vibrations by using a synthetic array. J. Sound Vib. **331**(16), 3824–3843 (2012)
24. W.K. Blake, Mechanics of flow-induced sound and vibration. Vol. I: General concept and elementary sources. Vol. II: Complex flow-structure interaction. Orlando, Florida, Academic press, Inc. (1986)
25. A.O. Borisyuk, V.T. Grinchenko, Vibration and noise generation by elastic elements excited by a turbulent flow. J. Sound Vib. **204**(2), 213–237 (1996)
26. S. Hambric, Y. Hwang, W. Bonness, Vibrations of plates with clamped and free edges excited by low-speed turbulent boundary layer flow. J. Fluids Struct. **19**, 93–110 (2004)
27. F. Fahy, Some applications of the reciprocity principle in experimental vibroacoustics. Acoust. Phys. **49**, 262–277 (2003)
28. M. Berton, L. Maxit, D. Juvé, C. Audoly, Prediction of flow-induced sound and vibration: on different methods for introducing the TBL excitation in the vibroacoustic model, in *Proceedings of Acoustics2013,* New Delhi, India, November 2013
29. F. Fahy, Statistical energy analysis: a critical overview. Phil. Trans. R. Soc. Lond. A **34**, 431–447 (1994)

30. A. Le Bot, Derivation of statistical energy analysis from radiative exchanges. Journal of Sound and Vibration **300**(3), 763–779 (2007)
31. A. Le Bot, V. Cotoni, Validity diagrams of statistical energy analysis. J. Sound Vib. **329**(2), 221–235 (2010)
32. T. Lafont, N. Totaro, A. Le Bot, Review of statistical energy analysis hypotheses in vibroacoustics. Proc. R. Soc. A **470**, 20130515 (2013)
33. A. Culla, A. Sestieri, Is it possible to treat confidentially SEA the wolf in sheep's clothing? Mech. Syst. Signal Process. **20**, 1372–1399 (2006)
34. L. Maxit, J.-L. Guyader, Estimation of SEA coupling loss factors using a dual formulation and FEM modal information. Part I: theory. J. Sound Vib. **239**(5), 907–930 (2001)
35. L. Maxit, Analysis of the modal energy distribution of an excited vibrating panel coupled with a heavy fluid cavity by a dual modal formulation. J. Sound Vib. **332**(25), 6703–6724 (2013)
36. C. Audoly, S. Beretti, Prediction of Turbulent Flow Noise Inside an Acoustic Sounder Cavity, in *Proceedings of Euromech*. Cargèse, France, April 1999
37. L. Maxit, C. Audoly, Hydrodynamic Noise Prediction Inside a Sonar Dome: Estimation of Injected Power from the Wavenumber—Frequency Spectrum of The Turbulent Wall Pressure, in *Proceedings of NOVEM 2005*, St Raphael, France, Apr 2005
38. N. Totaro, J.L. Guyader, Model of frequency averaged injected power into a plate excited by a turbulent boundary layer. Acta Acust. United Acust. **89**, 647–657 (2003)
39. N. Totaro, G. Robert, J.L. Guyader, Frequency averaged injected power under boundary layer excitation: an experimental validation. Acta Acust. United Acust. **94**, 534–547 (2008)
40. M.L. Rumerman, Estimation of broadband acoustic power due to rib forces on a reinforced panel under turbulent boundary layer-like pressure excitation. I. Derivations using strong model. J. Acoust. Soc. Am. **109**, 563–575 (2001)
41. M.L. Rumerman, Estimation of broadband acoustic power due to rib forces on a reinforced panel under turbulent boundary layer-like pressure excitation. II. Applicability and validation. J. Acoust. Soc. Am. **109**, 576–582 (2001)
42. M.L. Rumerman, Estimation of broadband acoustic power radiated from a turbulent boundary layer-driven reinforced finite plate section due to rib and boundary forces. J. Acoust. Soc. Am. **111**, 1274–1284 (2001)

Dimensionless Representations of the Interaction Between Turbulent Boundary Layer and Elastic Plates

Elena Ciappi, Sergio De Rosa and Francesco Franco

Abstract The study of the interaction between elastic structures and turbulent boundary layer still presents some uncertainties. This is true even assuming a one-way coupling and stationary turbulent boundary layer (TBL) over smooth and flat plates in subsonic flow. The reasons are mainly related to (i) the limitation for the direct numerical simulations of Reynolds number value of the Navier-Stokes equations, (ii) the high frequency structural and acoustic numerical and modelling difficulties and (iii) the lack of experimental data representative of all frequency-wavenumber pressure fluctuation regions, needed for the direct validation of the semi-empirical pressure models. In fact, when the pressure convective terms are the dominant sources of vibrations and radiated noise, consolidated and almost case independent formulations exist; on the contrary, when the subconvective terms are of concern, the definition of models seems to be strongly dependent on the flow conditions and the characteristics of the fluid-structure interaction. In order to find a general procedure for the estimation of the response of elastic thin panels to TBL excitation, some scaling laws derived using dimensional analysis and energetic considerations are proposed. These dimensionless relations contain a combination of both flow and structural parameters yielding to simple analytical expressions relating a dimensionless structural response metric and a dimensionless frequency. The found scaling expressions are validated with wall pressure fluctuations and vibrational response data acquired in wind tunnels and towing tank for the case of thin flat plates made of homogeneous isotropic and composite materials.

E. Ciappi (✉)
CNR-INSEAN, Marine Technology Research Institute, National Research Council of Italy, Via di Vallerano 139, Rome, Italy
e-mail: elena.ciappi@cnr.it

S. De Rosa · F. Franco
Department of Industrial Engineering, Aerospace Section, University of Naples Federico II, Naples, Italy

E. Ciappi et al. (eds.), *Flinovia - Flow Induced Noise and Vibration Issues and Aspects*, DOI 10.1007/978-3-319-09713-8_13

1 Introduction

Turbulent boundary layer (TBL), inducing vibrations of elastic structures, is one of the major noise sources in naval, aerospace, and automotive engineering.

The characterization of wall pressure fluctuations (WPF) is usually addressed theoretically and experimentally by the definition of scaling laws for the power spectral density (PSD) [1–4] and of semi-empirical models for the cross spectral density (CSD) [5–7]. The identification of the scaling laws permits to make pressure spectra independent of the test conditions and extrapolate data at full scale from low Reynolds number laboratory experiments. The CSD models are supposed to be valid only under the hypotheses of 2D fully developed TBL with zero pressure gradient acting on a flat plate and contain empirical parameters most likely derived from experimental data. Unfortunately, these parameters are not always universal but necessitate dedicated experimental campaigns to be defined [8–10].

Besides, being time demanding and expensive, a model scale experiment for this kind of measurements would only provide a partial information about the physics of the problem. In fact, standard experimental set-up and data analyses for WPF characterization, that make use of a spatial domain comparison between measured CSD spectra and theoretical models can only capture the convective character of the TBL. Only direct measurements of the wavenumber-frequency spectra or experimental setup specifically designed to measure the longer wavelengths can provide information about the subconvective domain. However, with respect to the large amount of WPF experimental data only relatively few regard this range. A summary of available data can be found in [1, 2, 11].

For these reasons, the definition of a predictive model able to represent correctly the spatial variation of the wall pressure field, in all the frequency and wave-number ranges, is still a research topic.

Some considerations can be found in [8, 9, 11] on the basis of the comparison between numerical and experimental structural response data.

Moreover, with specific reference to underwater applications, some simplified expressions for the representation of the low wavenumber domain have been proposed in the last 30 years [1, 6, 12]. Recently Bonness et al. [11], using the wavenumber white hypothesis and vibration measurements of a cylinder in pipe flow identified the surface pressure level in the low wavenumber domain.

In recent years, aided by the increase of the computing power, a number of numerical studies have been performed. Direct numerical simulations (DNS) of the Navier-Stokes equations are generally limited to problems in which the local Reynolds number, based on the momentum thickness, is of the order of 300 [13, 14]. A significant reduction of the computational time can be certainly obtained using Reynolds Average Navier Stokes (RANS) simulations [15, 16]. In particular

in [16] an original stochastic model for the representation of the space-time wall pressure spectrum that used statistical data obtained from RANS calculations is proposed. The values of Re_ϑ are in this case between 1,400 and 8,000.

On the other hand, the numerical solution of the structural equations, especially when dealing with complex structures such as an aircraft fuselage or a ship hull, deserves some attention. When the structural wavelengths are small compared to the typical dimension of the problem, i.e. at high frequency, energy methods such as the Statistical Energy Analysis [17], can be used. However, the definition of the input power, starting from a general model for the pressure cross spectral density, not using the separation of variables, can be rather complicated and computationally demanding as the standard modal solution utilized in most of the low and mid frequency analyses. Interesting developments are in [18, 19] and those findings are here fruitfully used.

The problem of the computational cost versus the frequency bandwidth of interest and the proposition of new efficient numerical and theoretical algorithms is also addressed in several recent works [8, 20–23].

It is clear that the possibility to identify analytical relations for the structural response on the basis of few dimensionless parameters can drastically reduce the computational time. Several theoretical analyses, physical considerations and analytical formula can be found in [1] and in some pioneer works cited herein.

More recently [24], some scaling laws, for the structural response of flat thin panel excited by a stationary TBL in subsonic and zero pressure gradient flow conditions, have been proposed and partially validated using available experimental data acquired in wind tunnels and towing tank. In that work, it is shown that the proposed scaling, simply obtained from dimensional analysis, is able to determine, at least for a certain class of problems, a unique representation of the plate response independent of the particular flow conditions or structural properties.

Moreover, the functional relations between the physical parameters are discussed and analytical expressions for the dimensionless plate response versus dimensionless frequency are also identified. In the same paper, the possibility to derive similar dimensionless dependences, starting from the energy based approach proposed in [18], have been discussed too.

In this work, some new considerations about the definition and the validity of these dimensionless forms are presented and discussed using new data sets. This is aimed at extending the range of variations of Mach and Reynolds number values with respect to previous studies. Furthermore, the possibility to apply the same scaling to the response of panels made of composite materials is here discussed with the help of data acquired in wind tunnel on composite panels with different lay-ups. The results for the experimental data set, herein considered, have shown that the approach is feasible and can provide interesting comparison metrics for this class of problems.

2 Structural Response Analysis

2.1 Definition of the Problem and of the Fundamental Hypotheses

The mechanical system under study is a thin, flat, homogeneous plate with no pre-stress (negligible pressurization and edge loadings), where only flexural waves are considered. The plate is mounted on an ideally infinite rigid baffle flush with the flow, and it is considered belonging to a xy plane. The flexural out-of-plane displacements, named $w(x, y, t)$, are along the z axis, while the flow is along the x direction. The side lengths are a and b, in stream-wise and cross-stream direction, respectively.

The plate is exposed on one side to a stationary TBL in an almost zero pressure gradient and subsonic flow.

Moreover, a one-way coupling between the structure and the fluid is assumed, i.e. the elastic deformation does not affect the fluid dynamic field.

2.2 Mathematical Formulation Through the Modal Approach

The displacement cross spectral density between any arbitrary couple of points belonging to the plate, $A(x_A, y_A)$ and $B(x_B, y_B)$, due to an assigned stochastic distributed excitation, can be found with the following modal expansion as given in [25] and discussed in [20, 23]:

$$S_w = \sum_{j=1}^{\infty}\sum_{k=1}^{\infty}\left[\frac{\psi_j(x_A,y_A)\psi_k(x_B,y_B)}{L_j^*(\omega)L_k(\omega)}\right]\cdot\left[\frac{S_p(\omega)(ab)^2}{\gamma_j\gamma_k}\right]A_{Q_jQ_k}(\omega) \tag{1}$$

with

$$\begin{aligned} A_{Q_jQ_k}(\omega) &= \int_0^a\int_0^a\int_0^b\int_0^b\left[\frac{X_{pp}(x,y,x',y',\omega)}{S_p(\omega)(ab)^2}\psi_j(x,y)\psi_k(x',y')\right]dy\,dy'dx\,dx' \\ \gamma_j &= \int_0^a\int_0^b\psi_j^2(x,y)dy\,dx;\; L_j(\omega) = \rho_s h\left[\omega_j^2 - \omega^2 + i\eta\omega_j^2\right] \end{aligned} \tag{2}$$

The symbol ψ_i denotes the *ith* mode shape, and ω_i the *ith* natural radian frequency. The integrals defined by the symbol A_{QjQk} are well known also as the acceptances: *joint acceptance* for $j = k$, or *cross acceptance* for $j \neq k$. The formulation contained in the Eqs. (1) and (2) can be applied to any structural operator

once assumed its modal base. This can be in continuous or discrete coordinates, thus moving the problem to the finite element approach which is the standard for the structural modelling.

In the present analysis, the fluid effects on the dynamic response of the plate can be taken into account by introducing the wetted natural frequencies and mode shapes. This information requires the evaluation of the added mass due to the fluid, which is generally negligible in air, but induces significant modifications in the modal parameters for heavy fluid like water.

From the analysis of the first of Eq. (2), it is evident that the quality of the predictions is strictly related to the spatial characterization of wall pressure fluctuations expressed in terms of its cross-spectral density function X_{PP}.

2.3 Mathematical Formulation Through Dimensional Analysis

In order to find a general and case independent representation for the structural response to TBL excitation an approach based on dimensional analysis is here used. Within the present analysis, the power spectral density of the plate displacement S_w is considered as the output variable.

The cross spectral density of wall pressure fluctuations X_{pp} can be written in general form as the product of the power spectral density S_P in a reference point and a spatial correlation function Γ between two points, whose distance is ξ_x and ξ_y in stream-wise and cross-stream direction, respectively, as shown in the following equation:

$$X_{pp}(\xi_{x,}\xi_{y,},\omega) = S_p(\omega)\Gamma(\xi_{x,}\xi_{y,},\omega) \tag{3}$$

Both terms of the right hand side of Eq. (3) are in general complex functions of flow parameters. In particular, the single point spectral density depends on the boundary layer characteristic lengths δ, δ^*, on the characteristic velocities U and u_τ and on flow properties namely ρ_f and ν.

According to the scaling laws provided by several authors [1–3] and on the derived analytical formulation [4], the role of δ and δ^* is equivalent thus, only δ is retained for the dimensional analysis.

The semi-empirical models, available in the scientific literature to represent the function Γ, suggest different functional dependences on flow parameters. The most popular of them is the Corcos model [5], which considers the dependence on the convection velocity U_c, only, whereas more sophisticated models [6, 7] include also the dependence on δ and u_τ. Thus, Eq. (3) can be rewritten in a more general form as:

$$X_{pp} = S_p\left(\omega, \delta, U, u_\tau, \rho_f, \nu\right)\Gamma\left(\xi_x, \xi_y, \omega, \delta, U_c, u_\tau\right) \tag{4}$$

In view of a dimensional analysis related to the evaluation of the structural response, it is convenient to consider directly as one of the dimensional parameter the power spectral density of wall pressure fluctuations. In this case the dependence on ρ_f and ν, appearing only in the first term of Eq. (4), is not considered explicitly. The same considerations hold for U.

Under the above assumptions, the plate response to the pressure field induced by a turbulent boundary layer, according to Eq. (1), can be represented as a generic function f depending on both the following dimensional fluid dynamic and structural variables:

$$f\left(S_w, S_p, \omega, \delta, U_c, u_\tau, \rho_s, E, \eta, h, a, b, \xi_x, \xi_y\right) = 0 \tag{5}$$

where ρ_s is the material density, E the Young modulus, η is the total damping coefficient (sum of the material and of the aero/hydrodynamic damping) and h, a, b are the plate thickness, length and width, respectively. In Eq. (5) there are 14 dimensional parameters thus, according to the Buckingham theorem [26], there are 11 dimensionless parameters governing the problem. The identification of these last is not unique but one of the admissible sets is given by:

$$\frac{S_w U_c}{h^3};\ \rho_s\sqrt{\frac{U_c^3 h}{S_p}};\ E\sqrt{\frac{h}{S_p U_c}};\ \frac{\omega h}{U_c};\ \frac{u_\tau}{U_c};\ \frac{a}{h};\ \frac{b}{h};\ \frac{\delta}{h};\ \frac{\xi_x}{h};\ \frac{\xi_y}{h};\ \eta$$

Then, the power spectral density of the plate displacement can be rewritten in the following form:

$$S_w = \frac{h^3}{U_c}\, g\left(\rho_s\sqrt{\frac{U_c^3 h}{S_p}}, E\sqrt{\frac{h}{S_p U_c}}, \frac{\omega h}{U_c}, \frac{u_\tau}{U_c}, \frac{a}{h}, \frac{b}{h}, \frac{\delta}{h}, \frac{\xi_x}{h}, \frac{\xi_y}{h}, \eta\right) \tag{6}$$

In [24], a deep analysis on the physical meaning of the dimensionless parameters aimed at establishing their relevance with respect to the conditions under study is performed. The conclusions are briefly summarized hereafter:

- in the present analysis only thin plates are considered therefore the value of a/h and b/h can be assumed definitely large;
- the dimensionless parameter δ/h indicates the fluid-structure degree of coupling for conventional plates (the case of thick flexible plates is excluded a priori). Consistent numerical values of δ and h for the present test cases indicate that their ratio is always much greater than 1. This is coherent with the hypothesis of one-way coupling;
- if it is assumed that the major contribution to the plate response is due to diagonal terms of the cross-spectral density matrix, ξ_x/h and ξ_y/h can be neglected;

- although the ratio u_τ/U_c for an equilibrium boundary layer over a flat plate is a function of the Reynolds number [27], its variation is small and can be considered of minor importance;
- for the considered plates damping coefficient values are approximately the same thus, as a first approximation, η is neglected.

From the analysis of the remaining parameters it is straightforward to define a dimensionless frequency:

$$\omega^* = \frac{\omega h}{U_c} \tag{7}$$

A useful reading of this parameter can be suggested by introducing the coincidence frequency ω_c and the longitudinal structural wave speed c_L whose expressions are:

$$\omega_c = U_c^2 \sqrt{\frac{\rho_s h}{D}} \quad \text{with} \quad D = \frac{Eh^3}{12(1-\nu^2)}, c_L = \sqrt{\frac{E}{\rho_s(1-\nu^2)}}$$

Equation (7) can be rewritten in the following way:

$$\omega^* \propto \frac{\omega}{\omega_c}\frac{U_c}{c_L} \tag{8}$$

showing that the proposed reduced frequency relates to both the ratio of the actual and coincidence frequencies and the ratio between the flow and the structural waves velocities.

The last two dimensionless parameters that seem important for the present problem are those involving the pressure power spectral density.

Without any further considerations on the physics of the problem, the plate response can be dependent on one of them or on a combination of the two. Nevertheless, in order to make the plate response independent of the input it seems convenient to consider the ratio S_w/S_p as done already in [8].

In [24] it was shown that, it is possible to define three functional dependences for the spectral density functions related to the plate displacement, by evidencing also a generic function, g, of the dimensionless frequency ω^*. Since in the same work has been already demonstrated that one of them does not produce a satisfactory data collapse only the other two are here considered, their expression is:

$$S_w = \frac{h^3}{U_c}\left(E\sqrt{\frac{h}{S_p U_c}}\right)^{-2} g(\omega^*); \tag{9}$$

$$S_w = \frac{h^3}{U_c}\left(\rho_s E\sqrt{\frac{h}{S_p U_c}}\sqrt{\frac{U_c^3 h}{S_p}}\right)^{-1} g(\omega^*); \tag{10}$$

Accordingly, it is possible to define two dimensionless displacement functions of the dimensionless frequency ω^* only:

$$\frac{S_w}{S_p}\left(\frac{E}{h}\right)^2 = \frac{S_w}{S_p}\left(\frac{\rho_s}{h}\right)^2 c_L^4 = g_{\mathrm{I}}(\omega^*) \tag{11}$$

$$\frac{S_w}{S_p}\left(\frac{U_c}{h}\right)^2 \rho_s E = \frac{S_w}{S_p}\left(\frac{\rho_s}{h}\right)^2 U_c^2 c_L^2 = g_{\mathrm{II}}(\omega^*) \tag{12}$$

The capability of the above relations to produce a data collapse and the functional dependence on the dimensionless frequency is investigated using available experimental data.

2.4 Energy Formulation

In this section, some literature results, obtained using an energetic formulation, are considered to identify the characteristic parameters governing the plate response to TBL and to provide a theoretical comparison with the forms derived using dimensional analysis.

The development of an energy model for the plate response needs a correct representation of the power input for a TBL excitation that can be rather difficult and time consuming. This issue is addressed in [18] by using, as fundamental relationship, the modal response expressed by Eq. (1). Specifically, the main TBL models, due to Corcos, Corcos with Davies approximation, Efimstov and Blake, are investigated. In [18] the following representation for the power input P_{IN} is adopted:

$$P_{\mathrm{IN}}(\omega) \propto S_p(\omega)\frac{ab}{2\rho_S h}\frac{U_c^2}{\omega^2}\sqrt{\frac{\rho_s h}{D}} \cdot \Phi(a, b, U_c, \omega, c_L, u_\tau, \delta) \tag{13}$$

where Φ is a dimensionless function representing the average value of the joint acceptance integral in wavenumber space. This term depends on the selected model for the TBL excitation, on plate geometry and on boundary conditions. In the above representations the functional dependence is the more general with respect to different TBL models [see also Eqs. (1) and (4)]. Recalling that P_{IN} has the following general expressions:

$$P_{\mathrm{IN}}(\omega) = \eta\omega^3 ab\rho_S h S_{w,\mathrm{mean}} \tag{14}$$

where $S_{w,\text{mean}}$ denotes the mean displacement response, it is straightforward to get that:

$$\frac{S_{w,\text{mean}}(\omega)}{S_p(\omega)}\left[\left(\frac{h^2}{\rho_S^2 c_L U_c^3}\right)\frac{1}{\eta}\right]^{-1} \propto \left(\frac{U_c}{\omega h}\right)^5 \cdot \Phi(a, b, U_c, \omega, c_L, u_\tau, \delta). \tag{15}$$

Therefore, a dimensionless response is again obtained and it evidences the same groups highlighted in the previous section with a classical dimensional analysis, Eqs. (11, 12). According to the present result, the dependence is with the fifth power of the reciprocal of the dimensionless frequency. All the remaining dependences are left in the Φ function in which they can be attributed specifically to the difference among the TBL models, the boundary conditions, etc.

However, without any loss of generality, it is possible to state that, as far as frequency increases, i.e. for $\omega \gg \omega_c$ function Φ tends to a constant value [see also (18)] therefore a new dimensionless panel response is easily defined in the form:

$$\frac{S_{w,\text{mean}}(\omega)}{S_p(\omega)}\left(\frac{\eta\rho_S^2 c_L U_c^3}{h^2}\right) = g_{\text{IV}}(\omega^*) = (\omega^*)^{-5} \quad \omega^* \gg \frac{U_c}{c_L} \tag{16}$$

Moreover, in Totaro [18] it is shown that, if the Corcos model with the Davies approximation [28] is adopted and if the expression for the injected power is frequency averaged, function Φ is independent of plate dimensions and boundary conditions but is dependent on the ratio ω/ω_c only. Therefore it is possible to define a new dimensionless response as:

$$g_{\text{V}} = (\omega^*)^{-5}\Phi\left(\omega^* \frac{c_L}{U_c}\right), \quad \omega^* \gg \omega^*_{\text{lim}} = \frac{\pi h}{\min(a, b)} \tag{17}$$

It can easily be seen that if a dependence on the velocity ratio is assumed in the form: $\left(\frac{c_L}{U_c}\right)^{-1}$, Eq. (17) returns Eq. (12) but multiplied by η, i.e.:

$$g_{\text{V}}(\omega^*) = g_{\text{II}}(\omega^*)\,\eta \tag{18}$$

Equation (18), although obtained forcing a functional dependence on the basis of the results attained by dimensional analysis, indicates a rigorous way to introduce the dependence on damping in the dimensionless panel response.

3 Experimental Data Sets

The five experimental data sets, considered for this analysis, concern steady turbulent boundary layers in almost zero pressure gradient and subsonic flow acting on thin flat plates.

Among the large amount of data available in the literature, on wall pressure fluctuations and induced structural vibrations, these experimental setups are the few ones able to provide, for each test case, information on both quantities acquired in the same facility and with the same setup. This aspect is fundamental for the validation of the proposed scaling procedure. However, the two measures are never performed simultaneously in fact, wall pressure fluctuations are typically acquired using sensor arrays flush mounted on thick rigid plates.

The first two sets of data are extracted from a database containing measurements of wall pressure fluctuations and structural response acquired in a towing tank. The first one is relative to an experimental campaign performed on a catamaran model [9]. Two PVC plates 3 and 2.5 mm thick, respectively, in the following named P1a and P1b have been inserted in the bottom of the hull in correspondence of the stern region to detect vibrations; measurements are performed for model speeds of 3.3 and 5.3 m/s, respectively. A complete description of this experimental campaign can be found in [9].

The second set of data belongs to an experimental setup designed to measure wall pressure fluctuations and the response of elastic portions of a scaled bulbous model of a surface ship. The considered data regard a particular section where the flow reaches stationary conditions and where pressure gradient effects, due both to water surface deformation and to structural curvature, can be neglected. The elastic element inserted in the model is a PVC 3.3 mm thick plate, hereinafter called P2. The model velocity in this case ranges between 3.6 and 6.36 m/s. A more detailed description of this experimental campaign can be found in [10, 29].

The other three sets of data instead are obtained from measurements performed in aerodynamic tunnels.

The former is due to Finnveden et al. [8], it consists of a 1.6 mm aluminum plate, below named P3, exposed to flow velocities of 80, 100 and 120 m/s, respectively. The second is part of the experimental campaign performed by Totaro et al. [19] on four different plates of different geometries and materials. The data considered for this analysis regard the 1 mm thick PVC plate, indicated as P4, for flow velocities equal to 35 and 50 m/s, respectively.

The latter data set is obtained from an experimental campaign performed in a transonic wind tunnel [30, 31] over a 1.6 mm thick aluminum plate and two composite panels with similar layup except for a viscoelastic layer, at different Mach numbers ranging between 0.45 and 0.8. Data, here considered, are relative to Mach = 0.6 selected, among the available ones, to ensure that flow is stationary and still subsonic. These last three panels are hereafter called P5, C1 and C2.

Table 1 lists the principal mean flow TBL parameters of the 11 experimental test cases whereas Table 2 presents the principal characteristics of the plates made of isotropic homogeneous materials.

Tables 3 and 4 report the geometrical and material characteristics of the composite panels and of the single layers, respectively.

In Fig. 1 the range of variation of the dimensionless frequency for each data set is depicted. As expected, the wind tunnel and the towing tank setups are divided into two distinct groups even if an overlap region exists for $0.07 < \omega^* < 0.52$.

Table 1 TBL mean flow parameters

Fluid	Plate	U (m/s)	δ (mm)	u_τ (m/s)	U_c (m/s)
Water	P1a, P1b	3.3	120	0.11	0.70 U
		5.3	113	0.163	0.70 U
	P2	3.64	51	0.102	0.65 U
		5.45	49.7	0.147	0.65 U
		6.36	48	0.171	0.65 U
Air	P3	80	50	2.6	0.75 U
		100	50	3.1	0.75 U
		120	53	3.7	0.75 U
	P4	35	55	1.4	0.62 U
		50	85	1.96	0.62 U
	P5, C1, C2	204	54.8	8.72	0.6 U

Table 2 Panels geometrical characteristics and material properties

	P1a	P1b	P2	P3	P4	P5
Material	PVC	PVC	PVC	Aluminum	PVC	Aluminum
Density (Kg/m^3)	1,190	1,190	1,190	2,700	1,400	2,700
Young's modulus (GPa)	3.2	3.2	3.2	71	4.5	70
Thickness (mm)	3.0	2.5	3.3	1.6	1.0	1.6
η	0.02	0.02	0.02	0.005	0.018	0.01

Table 3 Composite panels characteristics

Panel	Lay-up	h (mm)	η
C1	0F/45/90/-45/0/45/-45/0/-45/90/45/0F-IWWF	2.37	0.01
C2	0F/45/90/-45/0/45/VEM/-45/0/-45/90/45/0F-IWWF	2.52	0.04–0.02

F fabric layer
IWWF inter-woven wire fabric for lightning strike protection
VEM visco-elastic material

Table 4 Properties of the layers

Layer type	ρ_s (kg/m^3)	h_L (mm)	E_1 (GPa)	E_2 (GPa)	ν_{12}	G_{12} (GPa)
Unidirectional	1,550	0.193	142	7.79	0.34	4.00
Fabric	1,531	0.220	65.2	65.2	0.05	3.86
Fabric-IWWF	1,909	0.220	65.2	65.2	0.05	3.86

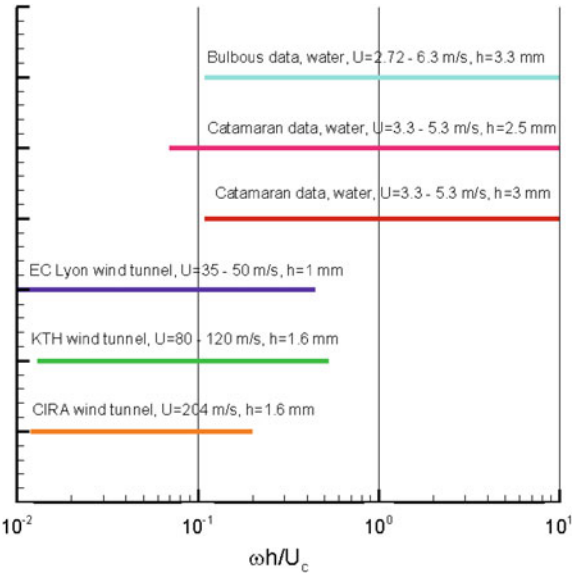

Fig. 1 Range of variation of dimensionless frequency

As a final note, it is important to underline that the experimental power spectral densities of the plate responses here used are representative of their spatial mean, calculated using acceleration/velocity signals acquired in different points over the plate surface. In a similar way, the power spectral density of WPF considered for the present analysis is, for each setup, the mean value over all the available pressure sensors.

Figure 2 shows the ratio between the PSD of the plate acceleration and that of WPF for the 13 data sets. Again, due to the difference among test conditions the

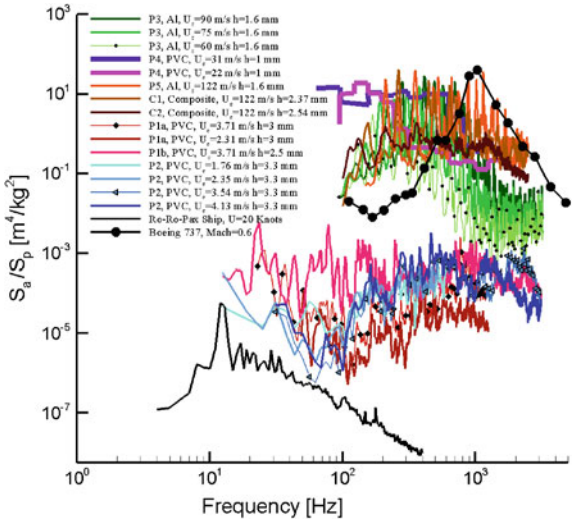

Fig. 2 Dimensional panel responses

plate responses exhibited different amplitudes and different shapes. This is particularly evident in the low-mid frequency range, 10–10^3 Hz. In this region, the significant gap in the curve levels is related to the different fluid and flow velocities and to the different values assumed by the ratio between the structural and the aero/fluid-dynamic wavenumbers. In particular for the aerodynamic case (Plates P3, P4, P5, C1 and C2), the structural responses are dominated by the convective components of the pressure field for a large part of the low-mid frequency range. On the contrary, coincidence frequencies for P1a, P1b and P2 are below 1 Hz. As a consequence of this, the spectrum amplitude does not display a distinct maximum and structures receive energy mainly from the sub-convective component of the pressure field. The same Figure displays a curve relative to flight data acquired on a Boeing 737 [32] and full scale data measured during an experimental campaign performed on a Ro-Ro-Pax ship [33]. Although not directly useful to validate the present approach, due to the lack of information about flow parameters and structural details, they can give interesting insights about the significance of the available model scale data in terms of frequency range and spectra amplitude.

4 Application of the Scaling Laws

4.1 Summary

It is useful to summarise here the proposed scaling laws in order to facilitate the reading of the results discussed in the next section. The names are selected to evidence the main contributions to the functional dependence (see Table 5).

The structural law involves only parameters, which can be related to the knowledge of the material and the plate characteristics. The aeroelastic law is defined by the presence of the ratio (at the second power) between the convective speed and the thickness of the plate, thus linking to the aeroelastic dimensionless reduced frequency, $\omega h/U_c$. The last two laws are related to the energy distribution, being derived inside an approach useful for the high frequency range where the structural elastic domain behaves as a waveguide. The only difference is in the approximation used in defining the power input into the system.

Table 5 Summary of the proposed scaling laws

Equation	Scaling law	Name
(11)	$\frac{S_w}{S_p}\left(\frac{E}{h}\right)^2 = g_{\mathrm{I}}(\omega^*)$	Structural
(12)	$\frac{S_w}{S_p}\left(\frac{U_c}{h}\right)^2 \rho_s E = g_{\mathrm{II}}(\omega^*)$	Aeroelastic
(16)	$\frac{S_{w,\mathrm{mean}}(\omega)}{S_p(\omega)}\left(\frac{\eta \rho_s^2 c_L U_c^3}{h^2}\right) = g_{\mathrm{IV}}(\omega^*)$	Energy-I
(18)	$g_{\mathrm{V}} = \eta g_{\mathrm{II}}(\omega^*)$	Energy-II

4.2 Homogeneous Panels

The first non-dimensional quantity, defined by Eq. (11), is represented in Fig. 3 to check its ability to provide a scaling of the 11 data sets relative to the homogeneous panels. The results clearly indicate an excellent collapse of the three curves relative to P3 whereas the curves relative to P4 show the same trend in a similar non-dimensional frequency range and a complete superposition with the previous ones. Moreover, P5 shows a similar trend and a satisfactory superposition with P3 and P4 data. Finally, curves relative to P1a, P1b and P2 exhibit a good collapse both among themselves and with the aeronautical ones for values of the dimensionless frequency corresponding to the overlap region (see Fig. 1). The slight data dispersion, visible in this last frequency range, can be in large part attributed to the presence of noise in the acceleration signals.

In [24] three distinct regions for the panel response have been identified, the functional relations between dimensionless frequency and dimensionless response are obtained with linear regression curves (in logarithmic scale), well approximated by the simple relations:

$$S_w^* = \begin{cases} 4 \times 10^8 (\omega^*)^{-4} \omega^* < 0.07 \\ 1 \times 10^8 (\omega^*)^{-8} 0.07 < \omega^* < 0.21 \\ 2 \times 10^7 (\omega^*)^{-3} \omega^* > 0.21 \end{cases}$$

drawn for comparison in Fig. 3, along with the experimental measurements.

On the contrary, the capability of Eq. (12) to provide a good data collapse is analyzed in Fig. 4. In this case the superposition among all curves acquired in wind tunnels is excellent moreover, it seems that in the overlap frequency range data spreading is a little reduced with respect to the results shown in Fig. 3.

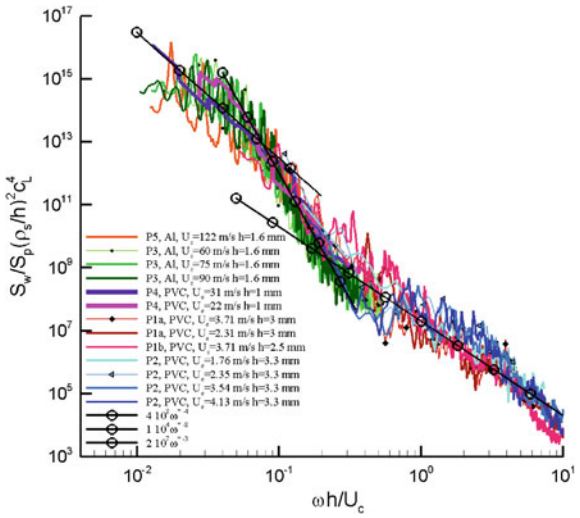

Fig. 3 Dimensionless panel response Eq. (11), homogeneous materials

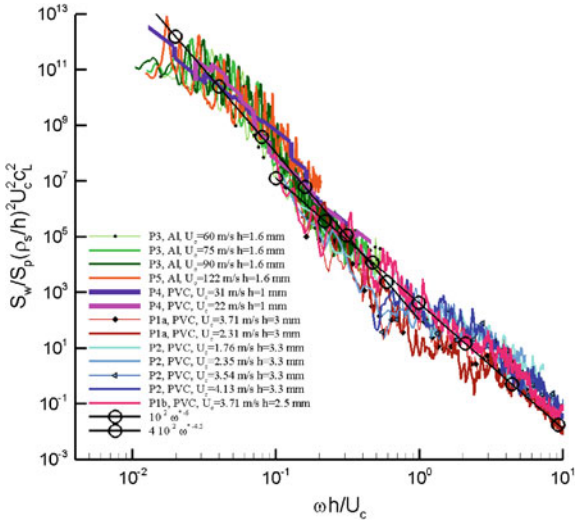

Fig. 4 Dimensionless panel response Eq. (12), homogeneous materials

By the inspection of Fig. 4 it is possible to identify at least two distinct regions for the plate dimensionless response. Using a linear regression curve, the two regions can be represented by the following expressions:

$$S_w^* = \begin{cases} 1 \times 10^2(\omega^*)^{-6} & \omega^* < 0.35 \\ 4 \times 10^2(\omega^*)^{-4.5} & \omega^* > 0.35 \end{cases} \tag{19}$$

At this time it is interesting to analyze the behavior of Eq. (16) when applied to the same data sets. The result is shown in Fig. 5 along with the curve ω^{*-5} obtained

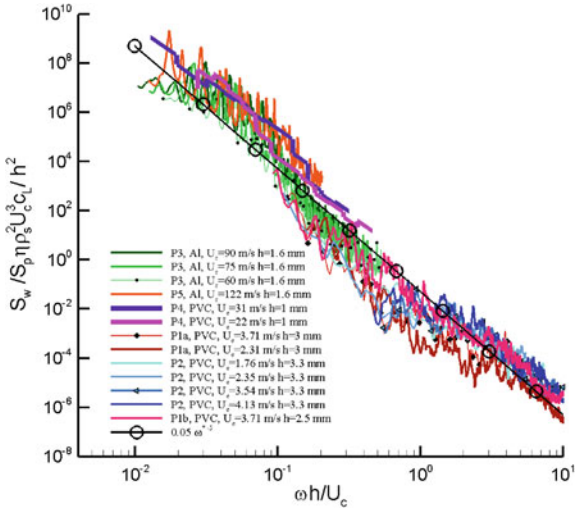

Fig. 5 Dimensionless panel response Eq. (16), homogeneous materials

analytically using the energy approach. Although data collapse is not as good as in the previous cases the energetic formulation gives a rather good approximation of the structural response. In particular, the law directly provided by the expression of the power input seems to give a good description, as expected, for sufficient high values of the dimensionless frequency i.e. well above the convective region.

4.3 Composite Panels

The application of the dimensionless relations to composite panels, if the c_L value is not available from complementary analyses, needs the definition of an equivalent Young modulus i.e. of the value E of an equivalent panel with same dimensions but made of a homogeneous isotropic material. The definition of this equivalence can be done on the basis of different principles. Here a dynamic equivalence is applied by equating the first natural frequencies of the two panels, assuming simply supported boundary conditions, same side lengths and mass. The variation of E, when considering the first 10 modes is small, its mean value for both panels C1 and C2 is equal to 43.5 GPa.

The results obtained applying Eqs. (11), (12) and (16) to the composite panels are displayed in Figs. 6, 7 and 8, respectively. In particular, by the inspection of Fig. 6 it is evident that C1 and C2 are well overlapped to P5 suggesting that the equivalence has been correctly formulated. However, a quite significant dispersion of data at low frequency is more clearly visible. On the contrary, Fig. 7 shows an excellent collapse of all data sets. Again, the best fit is obtained with Eq. (19).

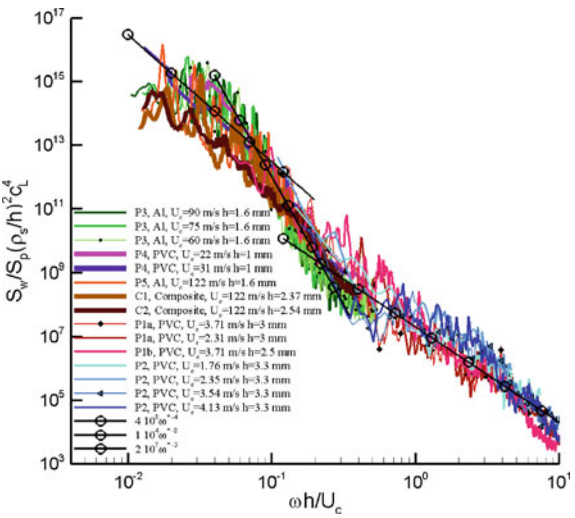

Fig. 6 Dimensionless panel response Eq. (11), homogeneous and composite materials

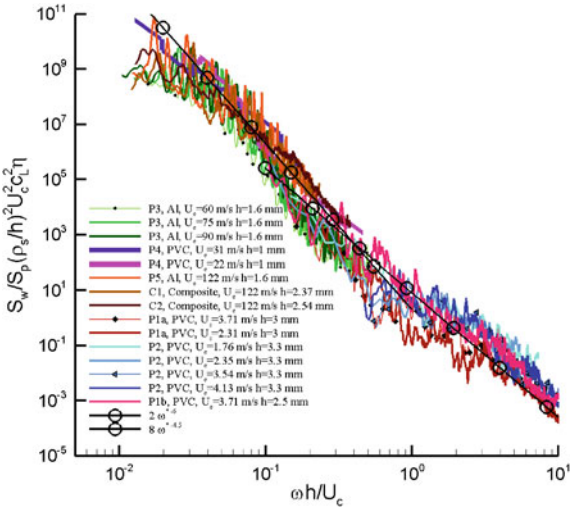

Fig. 7 Dimensionless panel response Eq. (12), homogeneous and composite materials

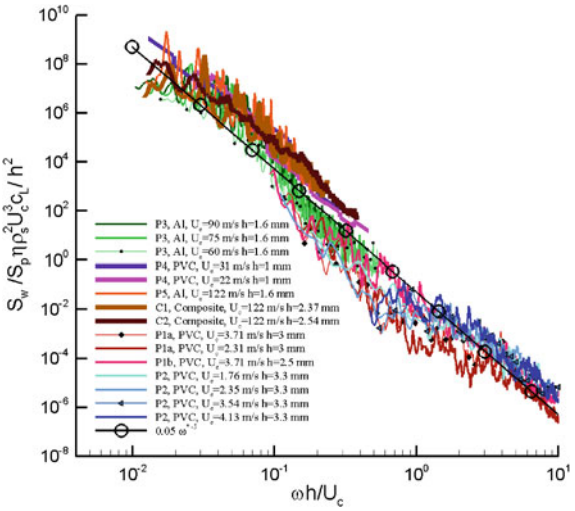

Fig. 8 Dimensionless panel response Eq. (16), homogeneous and composite materials

Finally, the application of g_{IV} provides, as in Fig. 5, a satisfactory but not excellent collapse of data. In particular, the high frequency part of the composite response curves is not perfectly superimposed nor to wind tunnel neither to towing tank data.

As a final note, it is interesting to analyse the form provided by Eq. (18) where structural damping is included in the expression of the dimensionless response. The result is displayed in Fig. 9 where a very good scaling, of the same quality as the one provided by g_{II}, is evident.

It has to be noted that, for the available data sets, the variation of η is not so significant since the extreme values are that of P3 equal to 0.5 % and that of C2

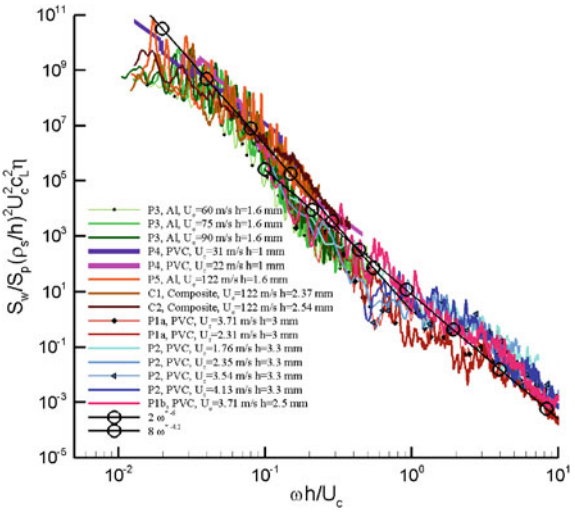

Fig. 9 Dimensionless panel response Eq. (18), homogeneous and composite materials

where the presence of the viscoelastic layer returns a damping coefficient varying with frequency between 4 and 2 %. For the sake of precision the higher value is used here to obtain the curve displayed in Fig. 9. In particular, the results obtained with data acquired in high Mach number flow conditions (panels P5, C1 and C2), indicate that the use of g_{I} has a less efficacy at providing a good scaling for the low frequency range. Moreover it is not negligible that similar functional dependences as those provided by g_{II} have been already obtained starting from theoretical formulations based on energy methods.

Recalling Eq. (19), it can be assumed that the different dimensionless frequency regions identified in Figs. 4 and 7 are representative of the response around the convective region and a little above i.e. for $\omega \geq \omega_c$ and of the response of the panel for $\omega \gg \omega_c$, respectively.

The knowledge of the data for the material has been here limited to the longitudinal waves propagation speed and to the Young modulus. This last has been obtained with the described equivalence. A more detailed analysis can be performed by using the spectral finite element approach [34] that is just aimed at the simulation of the material rather than the structure. This approach is fundamental when dealing with complicated assembly of materials and configurations and can provide the required parameters for the dimensionless representation.

5 Conclusions

In this work some scaling laws derived from the sole application of dimensional analysis are proposed and validated on the basis of a quite large amount of experimental data acquired both in wind tunnels and in the towing tank. These data

allow a considerable variation of the identified dimensionless parameters. In particular, with respect to previous applications, scaling laws have been successfully applied to high Mach number data and to response curves relative to composite panels, leading to more robust conclusions about the effectiveness of the dimensionless forms.

In particular it has been shown that the dimensionless expression that take into account for the fluid structural coupling here named as aeroelastic formulation, seems to be the most adequate at providing data collapse in the whole frequency range. Consequently, analytical expressions have been identified to represent the trend of the dimensionless response curves vs dimensionless frequency in the logarithmic plane. It is worthwhile to recall that this expression found a strong theoretical basis in some relations that can be obtained following energetic considerations.

The application of the scaling laws to the response curves of ribbed panels typical of aeronautical and naval structures and to different kind of composite materials can widen the significance of the proposed approach.

References

1. W.K. Blake, *Mechanics of Flow-Induced Sound and Vibrations* (Academic Press Inc., New York, 1986)
2. M.K. Bull, Wall pressure fluctuations beneath turbulent boundary layers: some reflections on forty years of research. J. Sound Vib. **190**, 299–315 (1996)
3. W.L. Keith, D.A. Hurdis, B.M. Abraham, A comparison of turbulent boundary layer wall-pressure spectra. J. Fluids Eng. **114**, 338–347 (1992)
4. M. Goody, Empirical spectral model of surface pressure fluctuations. AIAA J. **42**, 1788–1794 (2004)
5. G.M. Corcos, The structure of the turbulent pressure field in boundary-layer flows. J. Fluid Mech. **18**, 353–379 (1964)
6. D.M. Chase, Modelling the wavevector-frequency spectrum of turbulent boundary layer wall pressure. J. Sound Vib. **70**, 29–67 (1980)
7. B.M. Efimtsov, Characteristics of the field of turbulent wall pressure fluctuations at large Reynolds numbers. Sov. Phisics-Acoust. **28**, 289–292 (1982)
8. S. Finnveden, F. Birgersson, U. Ross, T. Kremer, A model for wall pressure correlation for prediction of turbulence-induced vibration. J. Fluids Struct. **20**, 1127–1143 (2005)
9. E. Ciappi, F. Magionesi, S. De Rosa, F. Franco, Hydrodynamic and hydroelastic analyses of a plate excited by the turbulent boundary layer. J. Fluids Struct. **25**, 321–342 (2009)
10. F. Magionesi, E. Ciappi, R. Camussi, T. Pagliaroli, A. Di Mascio, B. Imperatore, A. Marino, Measurement and modeling of turbulent boundary layer excitation for naval and aeronautical applications. Proceedings of NOVEM2012 Conference Noise and Vibration: Emerging Methods, Sorrento, 01–04 Apr 2012, ISBN: 9788890648403
11. W.K. Bonness, D.E. Capone, S.A. Hambric, Low-wavenumber turbulent boundary layer wall-pressure measurements from vibration data on a cylinder in pipe flow. J. Sound Vib. **329**, 4166–4180 (2010)
12. M.S. Howe, Surface pressures and sound produced by turbulent flow over smooth and rough walls. J. Acoust. Soc. Am. **90**, 1041–1047 (1991)
13. H. Choi, P. Moin, On the space-time characteristics of wall pressure fluctuations. Phys. Fluids A **2**, 1450–1460 (1990)

14. P.A. Chang, U. Piomelli, W.K. Blake, Relationship between wall pressure and velocity-field sources. Phys. Fluids A **11**, 3434–3448 (1999)
15. Y.T. Lee, W.K. Blake, T.M. Farabee, Modeling of wall pressure fluctuations based on time mean flow field. J. Fluids Eng. **127**, 233–240 (2005)
16. L.J. Peltier, S.A. Hambric, Estimating turbulent-boundary-layer wall-pressure spectra from CFD RANS solutions. J. Fluids Struct. **23**, 920–937 (2007)
17. R.H. Lyon, R.G. De Jong, *Theory and Application of Statistical Energy Analysis* (Butterworth-Heinemann, London, 1995)
18. N. Totaro, Caracterisation de sources aerodynamiques et sous-structuration pour la method SEA. Ph.D. thesis. INSA, Lyon, France, 04 ISAL 010 (2004)
19. N. Totaro, G. Robert, J.L. Guyader, Frequency averaged injected power under boundary layer excitation: an experimental validation. Acta Acustica **94**, 534–547 (2008)
20. S. De Rosa, F. Franco, Exact and numerical responses of a plate under a turbulent boundary layer excitation. J. Fluids Struct. **24**, 212–230 (2008)
21. C. Hong, K.K. Shin, Modelling of wall pressure fluctuations for finite element structural analysis. J. Sound Vib. **329**, 1673–1685 (2010)
22. M.N. Ichchou, B. Hiverniau, B. Troclet, Equivalent 'rain on the roof' loads for random spatially correlated excitations in the mid frequency range. J. Sound Vib. **322**, 926–940 (2009)
23. F. Franco, S. De Rosa, E. Ciappi, Numerical approximations on the predictive responses of plates under stochastic and convective loads. J. Fluids Struct. **42**, 296–312 (2013)
24. E. Ciappi, F. Magionesi, S. De Rosa, F. Franco, Analysis of the scaling laws for the turbulence driven panel responses. J. Fluids Struct. **32**, 90–103 (2012)
25. I. Elishakoff, *Probabilistic Methods in the Theory of Structures* (Wiley, New York, 1983)
26. E. Buckingham, On physically similar systems; illustrations of the use of dimensional equations. Phys. Rev. **4**, 345–376 (1914)
27. H. Schlichting, *Boundary Layer Theory* (McGraw-Hill, New York, 1978)
28. H.G. Davies, Sound from turbulent-boundary-layer-excited panels. J. Acoust. Soc. Am. **49**, 878–889 (1971)
29. F. Magionesi, E. Ciappi, Characterisation of the response of a curved elastic shell to turbulent boundary layer. 7th International Symposium on Fluid-Structure Interactions, Flow-Sound Interactions, and Flow-Induced Vibration and Noise, Montreal, Canada (2010)
30. R. Camussi, T. Pagliaroli, E. Ciappi, F. Magionesi, B. Imperatore, A. Marino, Wind tunnel measurements of pressure fluctuations and structural response induced by the turbulent boundary layer at high Mach number. Part 1: velocity and pressure field characterisation. Proceedings of NOVEM2012 Conference Noise and Vibration: Emerging Methods, Sorrento 01–04 Apr 2012 ISBN: 9788890648403
31. S. De Rosa, F. Franco, E. Ciappi, F. Magionesi, V. Quaranta, P. Vitiello, M. Di Giulio, Wind tunnel measurements of pressure fluctuations and structural response induced by the turbulent boundary layer at high Mach number. Part 2: comparisons between experimental and numerical data for the structural response. Proceedings of NOVEM2012 Conference Noise and Vibration: Emerging Methods, Sorrento 01–04 Apr 2012 ISBN: 9788890648403
32. J.F. Wilby, F.L. Gloyna, Vibration measurements of an airplane fuselage structure II jet noise excitation. J. Sound Vib. **23**, 467–486 (1972)
33. E. Ciappi, F. Magionesi, D.D'. Orazio, M. Bassetti, J.M. Fernández Hernando, Measurements and modelling of turbulent boundary layer excitation and induced structural response on a ship: Part II full scale structural response. Proceedings of INTERNOISE 2012, New York, USA, Aug 2012
34. E. Barbieri, A. Cammarano, S. De Rosa, F. Franco, Waveguides of a composite plate by using the spectral finite element approach. J. Vib. Control **19**, 1674–1689 (2009)

The Method of the Pseudo Equivalent Deterministic Excitations ($PEDE_M$) to Bound the Random Response

Sergio De Rosa, Francesco Franco and Elena Ciappi

Abstract The analysis of the response of a stochastic system, through a discrete coordinate set, can become computationally challenging, even when using a full modal representation. Nevertheless, many dynamic load cases, in engineering applications, have stochastic behaviour as the wall pressure fluctuations due to the turbulent boundary layer. In this work, a new method is proposed: it is named as frequency Modulated Pseudo Equivalent Deterministic Excitation, $PEDE_M$, and it is based on the Pseudo Excitation Method, PEM. This latter can be considered as an exact representation since it uses a modal decomposition of the cross-spectral density matrix of the excitation; the extraction of the eigensolutions of the load matrix, at each frequency step, is a computational disadvantage. $PEDE_M$ overcomes this issue by introducing some approximations based on the analysis of the eigensolutions of the dynamic load matrix versus frequency. Mainly, two different approximations are proposed with reference to extreme frequency ranges (low and high) wherein the dynamic matrix of a random and convective load has different characteristics. A criterion to identify these frequency ranges is proposed versus a dimensionless representation of the frequency. Moreover, it is shown that the proposed approximations represent the bounding curves of the response for the whole frequency range. Fruitful comparisons with a full stochastic approach is discussed. The proposed approximations combine a good accuracy and represen-

S. De Rosa (✉) · F. Franco
Pasta-Lab, Department of Industrial Engineering, Aerospace Section, Università Degli Studi Di Napoli "Federico II", Via Claudio 21, 80125 Naples, Italy
e-mail: sergio.derosa@unina.it
URL: http://www.pastalab.unina.it

F. Franco
e-mail: francesco.franco@unina.it

E. Ciappi
CNR-INSEAN, Marine Technology Research Institute, National Research Council of Italy, Via di Vallerano 139, Rome, Italy
e-mail: elena.ciappi@cnr.it
URL: http://www.insean.cnr.it

E. Ciappi et al. (eds.), *Flinovia - Flow Induced Noise and Vibration Issues and Aspects*, DOI 10.1007/978-3-319-09713-8_14

tation of the stochastic system together with a significant reduction of the computational costs if compared to a full stochastic response or a PEM solution. The method is applied over two simple configurations (a chain of oscillators and two flexural plates) but the possible extensions to more complex cases are motivated by the quality of these preliminary results.

1 Introduction

The problem of the response of engineering structures can be separated in the analysis of the type of excitation and the possibility to represent the system response characteristics.

A large part of the loads are time-variant and have a random behaviour and thus this pre-requisite knowledge can rule the quality of the obtained predictions. At the same time, it is rather common to analyse the structural response in discrete coordinate since this approach is central for a large part of numerical disciplines such as the finite element approach (FEA), a standard for the engineering field [1–3]. The analysis of the building response under earthquake and the vibration of a vehicle induced by roughness of road surface are classical example of random vibrations.

Even if this field is rather well-known, the practical applications are often limited by computational costs which severely rule the engineering needs of stability, robustness and quickness in getting the results. This is due to the degrees of freedom needed for the simulation of the given system, as in FEA, and/or to the mathematical operations needed for the treatment of the stochastic variables.

This paper is just centred on the analysis of the random response of systems represented in discrete coordinates excited by a random and convective load due to the turbulent wall pressure fluctuations. This kind of load well reproduces the high level of complexity of a generic random and convective excitation; in fact, several types of real loads can be considered as a derivation of this case. This holds for frequency domain random response under stationary excitations.

A formulation in discrete coordinates of such random response involves many matrix operations and often a solution based on a modal approach is pursued [1]. In this case, the expansion on modes and natural frequencies can use only few terms if a low degree of overlap exists in the first low frequency region. All required operators are expanded by using the structural in vacuum and undamped mode shapes and natural frequencies. Nevertheless, some improvements can be performed by accounting also for aeroelastic interactions and/or by using complex modal basis which can be an important aspect when the stochastic load has convective characteristics [4, 5].

In the present work, Corcos model is considered as a stochastic dynamic load simulating a one- or two-dimensional distribution of turbulent wall pressure fluctuations [6, 7]. The aim here is the development of a numerical procedure that,

under some approximations, allows a reduction of the computational cost in a discrete coordinates framework. It must be stated that many other turbulent boundary layer (TBL) models exist in literature [8–11] but their analysis is out of the scope of the present work.

The problem of the structural response under a TBL excitation is addressed in many works [12–14]. For such a problem, the transformation of the pressure distribution into discrete locations is one of the most critical points and it can be computationally expensive for the desired level of numerical accuracy. Then, the use of consistent formulation in the finite element scheme can be sometimes unfeasible as frequency increases [15]. A spatially equivalent approximation of the load matrix is suggested in recent works in order to simplify the numerical algorithms in the high frequency bands [16–18].

In other approaches, deterministic solution schemes have been proposed to afford a stochastic problem [19–23]. These last represent the core references for the present applications. In particular, the pseudo excitation method, PEM, is the kernel of the present derivations and it has been proposed by Lin [19–23], since 1985. The work in [19], although in Chinese, is accredited to be the reference paper for PEM definition. PEM can be considered as an exact representation, a good summary is in [2] where a detailed discussion about the computational advantages can be also found in comparison with a full stochastic response (FSR). FSR is here used as reference too. Recently, PEM has been also applied to the coupled structural-acoustic systems under random excitations [24].

As shown later, PEM decomposes the cross-spectral density matrix of the excitation that, although much more efficient than FSR, requires the analysis of the eigensolutions of the load matrix at each frequency step. Thus, even if more useful than the FSR approach, this eigenanalysis can be computationally expensive.

In this paper, a frequency modulated pseudo equivalent deterministic excitation, PEDE_M, is proposed and its derivation is based on the PEM.

PEDE_M is always applied inside a deterministic solution scheme but tries to overcome the disadvantages of the extraction of the eigensolutions at each frequency step. In fact, the solution approach uses the different approximations for the load matrix as derived in the extreme frequency range where a dimensionless frequency assumes very low and very high values. Specifically, these approximations derive from the careful analysis of the evolution of the eigensolutions of the load matrix. Clearly, a criterion is also proposed to identify the three (*low*, *mid*, *high*) frequency ranges. It is expressed in terms of the cited dimensionless frequency.

PEDE_M is applied here to two-test cases both containing the relevant features of the specific random response problem: a chain of 1D oscillators and a flexural plate. They are analysed in order to discuss the robustness of the numerical solution scheme by comparing the PEDE_M results with those obtained with a full stochastic solution.

The attention is totally devoted on the analysis of the possible *bounding curves* derived by the PEDE_M approach for the stochastic response of systems in discrete coordinates. The turbulent boundary layer model (TBL) used for the analysis of a random and convective load is invoked to simulate a complicated distribution of the

coherence and correlation lengths; nevertheless, it is very similar to many real situations.

After these introductory notes, Sect. 2 shortly presents the exact approaches; i.e. the full stochastic response through the modal approach and PEM. An analysis of the characteristics of the eigensolutions of the excitation matrix is in Sect. 3 and it introduces the frequency modulated pseudo-equivalent deterministic excitation, detailed in Sect. 4. The numerical test-cases are discussed through system eigensolutions and forced responses in Sect. 5 and the concluding remarks are reported in Sect. 6.

A final note about the lexicon herein used: the word *limits* is used for describing the frequency ranges in which the solutions is presented and discussed; the terms *bounds* or *bounding curves* is invoked for defining the intervals in which the response can be represented.

2 Exact Approaches

This section presents the two announced methods for the analysis of the stochastic response. They are related to stationary excitations in the frequency domain.

It has to be highlighted that the structural system model is a linear one, assembled in discrete coordinates by using its eigensolutions, eigenvectors (mode shapes) and eigenvalues (natural frequencies).

2.1 Full Stochastic Response (FSR) Through Modal Approach

The formulation for getting the stochastic response of a system composed by NG discrete coordinates, is here reported [1]:

$$\mathbf{S_{WW}}(\boldsymbol{\omega}) = \mathbf{V}\,\mathbf{H}^{*}(\boldsymbol{\omega})\,\mathbf{V}^{T}\,\mathbf{S_{FF}}(\boldsymbol{\omega})\,\mathbf{V}\,\mathbf{H}(\boldsymbol{\omega})\,\mathbf{V}^{T} \tag{1}$$

where the symbols denote:

- $\boldsymbol{\omega}$, the circular excitation frequency;
- $\mathbf{S_{WW}}$, the output hermitian cross-spectral density matrix;
- $\mathbf{H}$, the complex diagonal matrix of the modal mobilities, H_i; the ith transfer function with reference to a constant damping value, η: $H_i(\omega) = \left(\omega_i^2 - \omega^2 + j\omega_i^2\eta\right)^{-1}$, being ω_i, the ith system natural frequency and j the imaginary unit;
- $\mathbf{V}$, the real matrix of the structural system eigenvectors;
- $\mathbf{S_{FF}}$, the hermitian cross-spectral density matrix of the input load.

The superscripts T and $*$ denote respectively the transposition and conjugation of the matrix.

The generic output cross-spectral density matrix, $\mathbf{S_{WW}}$, is thus obtained through the multiplication of several matrices for each excitation frequency: the frequency dependent operations lead to an unacceptable computational cost, even if the number of modes, NM, is lower than the degrees of freedom, NG. This topic is addressed in [15].

2.2 Pseudo Excitation Method (PEM)

PEM uses the eigenvalues and eigenvectors of the load matrix, $\mathbf{S_{FF}}$, to decompose the random response in addition to the system ones. A summary is here given from [23].

2.2.1 Summary

A linear system is considered under a zero-mean stationary random excitation with a given power spectral density, $S_{FF}(\omega)$.

Two generic time responses, $q(t)$ and $y(t)$, can be considered as system outputs. Their auto and cross spectral densities, S_{QQ}, S_{YY} and S_{QY}, can be obtained by using PEM. In fact, the excitation function, $f(t)$, can be replaced by a sinusoidal excitation; here the symbol $\hat{f}$ denotes the pseudo equivalent term:

$$\hat{f}(t) = \sqrt{S_{FF}(\omega)}\exp(j\omega t) \tag{2}$$

By invoking the frequency response transfer function, $H_q(\omega)$ and $H_y(\omega)$, one gets:

$$\hat{q}(t) = \sqrt{S_{FF}(\omega)}H_q(\omega)\exp(j\omega t) \tag{3}$$

$$\hat{y}(t) = \sqrt{S_{FF}(\omega)}H_y(\omega)\exp(j\omega t) \tag{4}$$

The auto and cross power spectral densities can be easily obtained:

$$\hat{q}^*(t)\,\hat{q}(t) = S_{QQ}(\omega) \tag{5}$$

$$\hat{q}^*(t)\,\hat{y}(t) = S_{QY}(\omega) \tag{6}$$

$$\hat{y}^*(t)\,\hat{y}(t) = S_{YY}(\omega) \tag{7}$$

If $\hat{\mathbf{q}}$ and $\hat{\mathbf{y}}$ are now two vector responses:

$$\hat{\mathbf{q}}^* \, \hat{\mathbf{q}}^T = \mathbf{S_{QQ}} \tag{8}$$

$$\hat{\mathbf{q}}^* \, \hat{\mathbf{y}}^T = \mathbf{S_{QY}} \tag{9}$$

$$\hat{\mathbf{y}}^* \, \hat{\mathbf{y}}^T = \mathbf{S_{YY}} \tag{10}$$

PEM allows evaluations of auto and cross spectral densities of two selected random responses by using the corresponding pseudo harmonic responses, that is the response to the equivalent sinusoidal excitation as in Eq. (2).

An immediate choice for the formation of the pseudo excitation vectors is to invoke the modal decomposition of the load matrix. For a square hermitian NG matrix of rank NR:

$$\mathbf{S_{FF}}(\omega) = \sum_{i}^{\mathrm{NR}} d_i(\omega) \, \mathbf{Z}^{<i>} \, \mathbf{Z}^{<i>\,T}, \quad \mathrm{NR} \leq \mathrm{NG} \tag{11}$$

$d_i(\omega)$ is the real ith eigenvalue and $\mathbf{Z}^{<i>}$ denotes the ith complex column of the eigenvector matrix $\mathbf{Z}$.

The system response can be written as follows:

$$\mathbf{S_{WW}}(\omega) = \sum_{i}^{\mathrm{NG}} \mathbf{w}^*(\omega, i) \, \mathbf{w}^T(\omega, i) \tag{12}$$

$$\mathbf{w}(\omega, i) = \mathbf{V} \, \mathbf{H}(\omega) \, \mathbf{V}^T \mathbf{Z}^{<i>} \sqrt{d_i(\omega)} \tag{13}$$

As stated before, PEM involves a decomposition of the load matrix and thus it converges to the exact response, see Eq. (1), if all the eigensolutions are used.

Thus, the spectral density of a structural response, $\mathbf{S_{WW}}(\omega)$, to an input spectral density, $\mathbf{S_{FF}}(\omega)$, can be obtained by subjecting it to a series of pseudo excitations, covering the frequency range of interest.

It has to be underlined that

- in FSR, Eq. (1), the same structural eigensolutions, $\mathbf{V}$ and ω_i, are used to decompose both the load and the structural matrices.
- In PEM, Eqs. (12) and (13), two eigensolutions sets are used: the first is related to the load matrix, $\mathbf{Z}$ and d_i, and the second belongs to the structural matrices, $\mathbf{V}$ and ω_i.

Moving from the last consideration, the approximation proposed in this work eliminates the evaluation of the load matrix eigensolutions under some circumstances.

3 Characteristics of the Eigensolutions of Excitation Matrix

Before proceeding at defining the new method, some considerations about the eigensolutions of the load matrix are needed. For the sake of completeness, it must be cited an interesting analysis of the excitation wave-types and their adequacy to represent the physical cases [16].

The attention is focused on a specific excitation field; i.e. the random and convective load produced by turbulent boundary layer wall pressure distribution. This pressure input can be represented in a simple 1D domain, according to [6], as a load matrix whose generic member in 1D case is (the subscript **FF** is omitted):

$$S_{i,j}(\omega) = A(\omega) \exp\left[-\alpha_x \frac{\omega|x_i - x_j|}{U_c}\right] \exp\left[j\frac{\omega(x_i - x_j)}{U_c}\right] \tag{14}$$

being x the coordinates of the two control points and U_c the convective flow speed; this U_c is generally a constant fraction of the undisturbed one, U. The symbol α_x denotes a correlation coefficient, since the term $\frac{U_c}{\omega\alpha_x}$ can be easily read as a correlation distance.

For the sake of simplicity, the autospectral function $A(\omega)$ in all this work is considered as unit value, $A(\omega) = 1$. This work hypothesis does not influence the whole development.

For a problem formulated according to following expressions Δ can be defined as a measure of the mesh size used to sample the spatial distribution of the excitation. Thus, it is useful to introduce a dimensionless frequency, κ, in which the excitation frequency, the convective flow speed and the spatial distribution of the control points are included, being Δ the minimum distance among two different control points:

$$\kappa(\omega, U_c, \Delta) = \frac{\omega\Delta}{U_c} \tag{15}$$

Now, it is useful to report the trivial eigensolutions, (λ and $\mathbf{Z}$) of two particular square matrices of NG order, the identity, $\mathbf{I}$, and the unity, $\mathbf{1}$, ones.

The (m, n)th member of the first is defined as follows:

$$I_{m,n} = \delta_{m,n} \tag{16}$$

where δ is the Kronecker operator. Its NG eigenvalues, named λ, are identical and they are all unitary, being solution of $(\lambda - 1)^{\mathrm{NG}} = 0$. The jth eigenvector is composed by null values with the only exception of jth element:

$$\mathbf{Z}^{(j)^T} = \gamma\{0 \ldots 1 \ldots 0\} \tag{17}$$

being γ the constant used for the required normalisation.

The (m,n)th member of the **1** is defined as follows:

$$1_{m,n} = 1 \tag{18}$$

The equation for λ is $\lambda^{\mathrm{NG}-1}(\lambda - \mathrm{NG}) = 0$ thus the only non null eigenvalue of **1** has the value of NG; its associated eigenvector is:

$$\mathbf{Z}^{(j)^T} = \gamma\{1\ 1\ 1 \ldots 1\} \tag{19}$$

Two limit matrices are thus evidenced. One holds in the *low* frequency range, $\kappa \to 0$:

$$\lim_{\kappa \to 0} \mathbf{S_{FF}} = \mathbf{1}; \tag{20}$$

the other one in the *high* frequency range, $\kappa \to \infty$:

$$\lim_{\kappa \to \infty} \mathbf{S_{FF}} = \mathbf{I} \tag{21}$$

The above mentioned properties, in terms of eigensolutions, are used in the next section.

4 Frequency Modulated Pseudo Equivalent Deterministic Excitation (PEDE$_M$)

PEDE$_M$ derives directly from PEM, but it avoids the computational penalty related to the extraction of the load matrix eigensolutions at each frequency step of the solution range. Equations (12) and (13) are used but they are approximated according to following expressions:

$$\mathbf{S_{WW}}(\omega) = \sum_{i}^{\mathrm{NG}} \mathbf{r}^*(\omega, i)\ \mathbf{r}^T(\omega, i) \tag{22}$$

$$\mathbf{r}(\omega, i) = \mathbf{V}\ \mathbf{H}(\omega)\ \mathbf{V}^T \sqrt{\mathbf{S_{FF}}^{(i)}(\omega)} \tag{23}$$

The ith eigensolution of the load matrix have been substituted with the (i)th column of the same matrix.

The discussion on the proposed approximation can start by investigating the variation of the eigenvalues as function of the dimensionless frequency, Fig. 1.

The present TBL model reduces to a normal incident wave as $\kappa \to 0$; in fact, in this limit condition the pressure field is fully correlated. Therefore, in the low frequency range the $\mathbf{S_{FF}}$ matrix can be approximated by the **1** matrix. The output

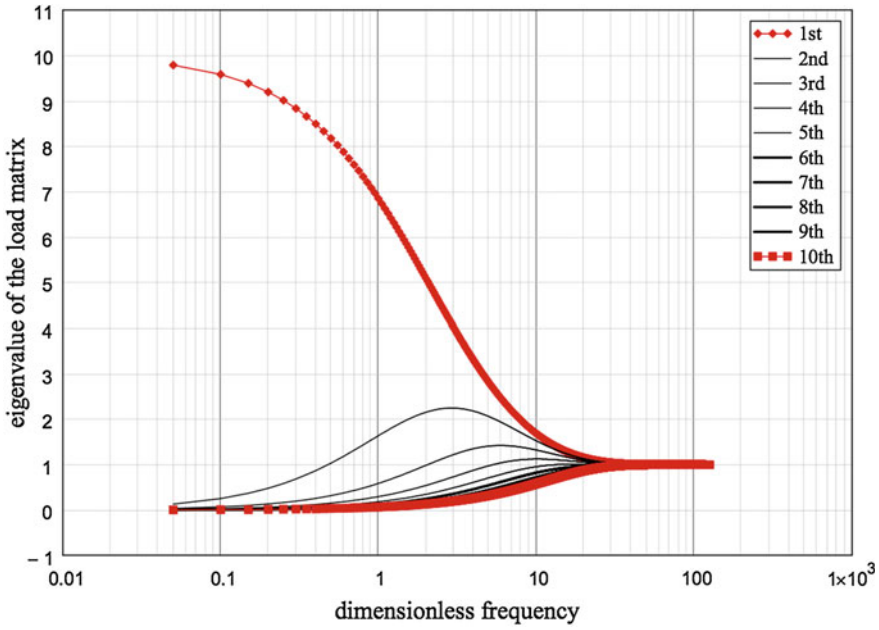

Fig. 1 Eigenvalues for a 1D TBL load matrix with 10° of freedom, Eq. (14). The *red curves* represent the first and last eigenvalues; the symbols are the *diamond* and *square*, respectively

cross-spectral matrix can be built using Eqs. (12) and (13) where the only non null eigenvalue is equal to NG and the associated eigenvector is given by Eq. (19). This range will be named as *low* frequency range and Eqs. (22) and (23) can fruitfully applied. The superscript *low* will be used. It is thus useful to write again the Eq. (22) by using the (*low*) apex:

$$\mathbf{S_{WW}}^{(low)}(\boldsymbol{\omega}) = \sum_{i}^{\mathrm{NG}} \mathbf{r}^{*}(\boldsymbol{\omega}, i)\, \mathbf{r}^{T}(\boldsymbol{\omega}, i) \tag{24}$$

Nevertheless, any TBL field can be represented as a totally uncorrelated pressure field as $\kappa \to \infty$. Therefore, the $\mathbf{S_{FF}}$ matrix in the high frequency range can be approximated by the $\mathbf{I}$ matrix. The output cross-spectral matrix can be built, again, using Eqs. (12) and (13) where the eigenvalues are all equal to 1 and the associated eigenvectors have the form in Eq. (17). This range is named as *high* frequency range and it is very easy to check that a useful relationship exists and this will be specified in the section related to the plate results.

PEM, Eqs. (12) and (13), can be related to great computational savings if compared with the FSR, Eq. (1), requiring only a given set of the eigensolutions of the load matrix. Consequently, the PEDE_M can have the same computational

Table 1 Definition of the dimensionless frequency limits—1D

	Low	Mid	High
κ	$\kappa < \alpha_x$	$\alpha_x < \kappa < \alpha_x^{-1}$	$\kappa > \alpha_x^{-1}$

advantages in the low and high frequency ranges. Thus, it remains to verify when and how PEDE_M can be applied with specific attention to the mid-frequency range.

The frequency ranges are better identified through the dimensionless frequency, κ. In fact, the rate of spatial correlation of the pressure field is a function of the frequency, the convective flow speed, the correlation parameter, α_x, and, obviously, the spatial sampling distance, Δ. As consequence, the following are the proposed criteria for the three frequency ranges (Table 1).

Bounding curves (max–min) for the response are defined in terms of a power of NG. This point is specifically addressed in the section concerning the flexural plates. In PEM sense, this interval is the maximum evolution of the eigenvalues in the whole frequency range. The missing knowledge about the evolution of the eigenvalues generates an interval of the response measured by a power of NG. It is expected that this interval is very important in the *mid* frequency range where both the approximations are expected to be not adequate and they can be interpreted only as *bounding curves*.

A final point is that the relative position of the load matrix eigenvalues and the structural ones has to be taken into account. To this aim the possible occurrences are summarised in the sketch proposed in Fig. 2. There the thick double-arrowed red segments identify the frequency ranges between the first and last structural natural frequencies so that each situation is measured on the dimensionless frequency axis.

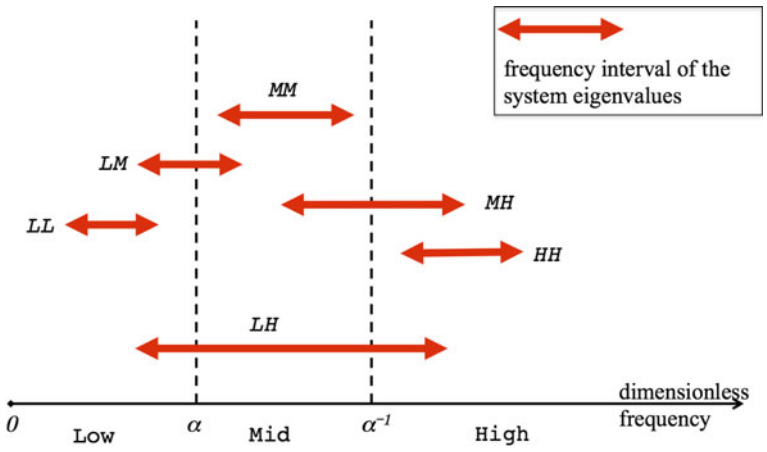

Fig. 2 Sketch of the possible locations of the structural eigenvalues as measured on the dimensionless frequency axis

As stated before, the attention is here concentrated on the *bounding curves* derived from $PEDE_M$ and thus the $\mathbf{S_{WW}}^{(low)}$ and $\mathbf{S_{WW}}^{(high)}$ will be directly compared with the FSR results in order to evaluate if they represent the interval of the response between the minimum and maximum values for each excitation frequency.

It is expected that the $PEDE_M$ bounding solutions, defined as *low* and *high*, may give origin to different accuracy of the response results in the different frequency ranges.

It has to be eventually underlined that the proposed $PEDE_M$ solutions are associated to cheaper computational costs than the PEM ones avoiding at all the extraction of the eigensolutions. Furthermore, the *high* frequency one requires only a multiplication of the *low* one for the factor NG.

5 Test-Cases

This section is fully devoted to the analysis of the two selected test-cases.

The first involves a 1D system represented by a chain of 10 mass-spring oscillators; the second concerns the response of two rectangular flexural plates both made of homogeneous material.

5.1 A Chain of Oscillators

5.1.1 Main Data

The system is represented by a chain of 10 (mass-spring) oscillators equally spaced ($\Delta = 20$ cm) along a given x axis; they can move only along this one and thus NG = 10. The system is fixed at one edge and free at the other end (Fig. 3).

The mass values are (kg): 1, 5, 3, 3, 5, 1, 2, 3, 5, and 0.1; the stiffness ones (Pa m): 1, 0.2, 4, 0.5, 0.3, 1, 0.5, 6, 0.3, 0.33.

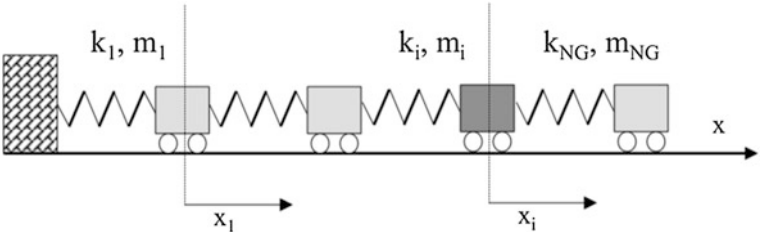

Fig. 3 Chain of mass-spring oscillators

Table 2 Summary of the results: $U = 80$ m/s, $\alpha_x = 0.13$, $\eta = 0.01$

Γ	Figure	Range (Fig. 2)
10^{-3}	4	LL
10^{-1}	5	LM
10^{1}	6	MM
10^{3}	7	MH
10^{5}	8	HH
10^{7}	9	HH

A damping value, η, is introduced by multiplying directly the stiffness matrix for the term $(1 + j\,\eta)$. For the present evaluations it has been fixed at a constant value, $\eta = 0.03$..

It has to be remarked that the elements of the load matrix are represented by functions in which the auto-spectra are unit values.

In order to study this system, as function of the dimensionless frequency, the original stiffness matrix has been multiplied by a coefficient Γ to allow an easy variation of structural natural frequencies. For the given values of Γ, the natural frequencies of the chain of the oscillators move to higher or lower values with respect to the original ones, obtained with $\Gamma = 1$. The role of the relative location of the eigenvalues of the structural matrix and of the load one on the system response can be thus analysed (Fig. 2).

Table 2 reports the values of Γ and the correlation coefficient, α_x. A more complete investigations of the frequency ranges can be found also in [25].

5.1.2 Analysis of the Response

The response of the system in different conditions are herein analysed. They consist of the sum of velocity autospectra, that is the sum of the elements on the diagonal of the output matrix.

Each of them is evaluated at 275 frequencies equally spaced between the first and last system natural frequencies. Furthermore, in each graph, the limits of low frequency, α_x, and high frequency, α_x^{-1}, are always reported as vertical red dashed lines. In this way, it is simple to evaluate where the 10 natural frequencies are located with reference to the specific ranges as in Fig. 2. It has to be remarked also that the value of $\alpha_x = 0.13$ is unchanged in the present evaluations; its reciprocal is constant too, $\alpha_x^{-1} = 7.7$.

In each figure, from Figs. 4 to 9, the thick red line is the FSR solution and the continuous and dashed black lines are the low and high PEDE_M bounding curves, respectively.

Figure 4 presents the response results in the LL frequency range and the agreement is perfect between FSR and the *low* approximation, as expected. In fact, in this frequency range, the load matrix can be well confused with the **1** one.

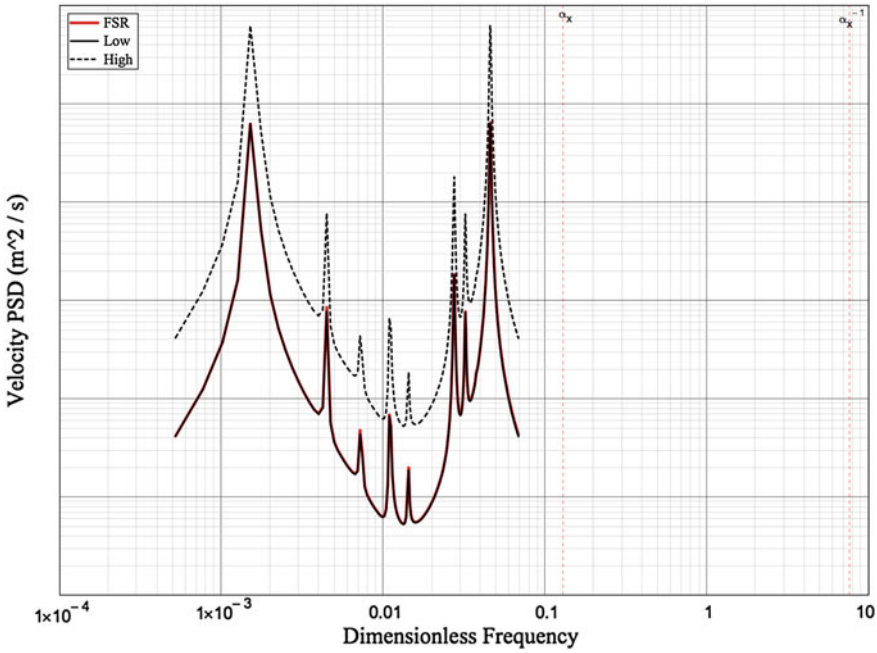

Fig. 4 Response of the chain of oscillators: velocity (PSD) $(m^2\ s^{-1})$ versus dimensionless frequency; LL range

In Fig. 5, being in the LM range, the situation is still acceptable even if some differences start appearing. In the MM range, Fig. 6, both the approximations well bound the FSR response which migrates from one to another for increasing excitation frequency. This behaviour is much more evident in Figs. 7 and 8.

In the last frequency range, HH, Fig. 9 the response is dominated by the uncorrelated field, thus by a load matrix which can be well represented by the **I** one. On the contrary, in Fig. 8, which refers to the HH range too, the first natural frequency is close to the high frequency limit and therefore, there is an effect of the mid-frequency behaviour.

With these parameters, a LH case is not discussed since it is presented for the flexural plates in the next section.

5.2 Flexural Plates

Two plates are considered here and they come from research projects in which the results have been compared to experimental measurements performed in wind tunnel facilities. In the present work, the comparisons with the experimental data for validation purposes, are not be shown, while the applicability of the proposed

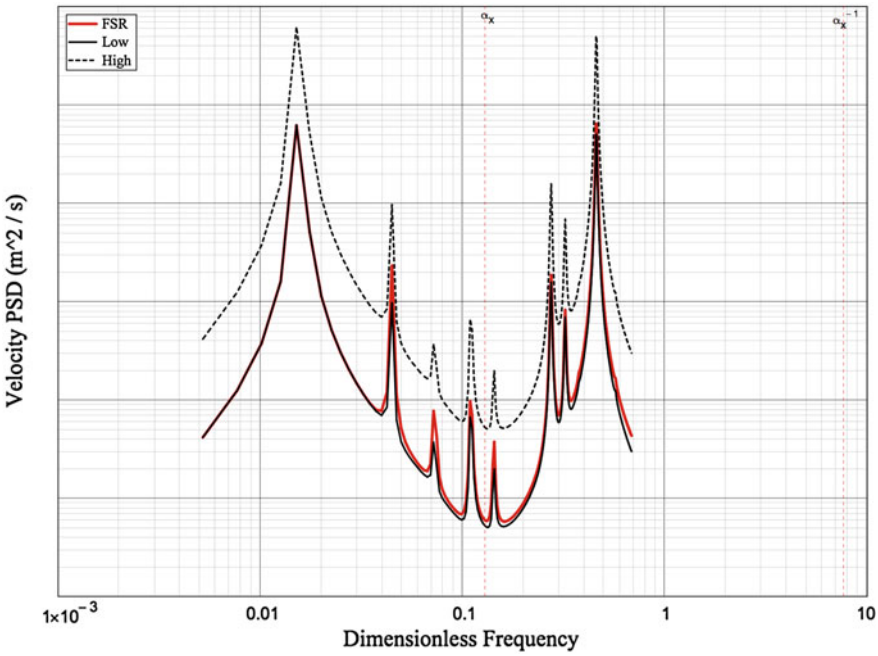

Fig. 5 Response of the chain of oscillators: velocity (PSD) ($m^2\ s^{-1}$) versus dimensionless frequency; LM range

approach is discussed. Nevertheless, it can be underlined that the following analytical results have been verified with the above mentioned experimental data and full stochastic results in discrete coordinates [14, 15].

The models refer to plates lying in a generic xy plane, being x the direction of undisturbed flow, U.

Herein, the simulations always concern a Corcos type load. In terms of matrix, Eq. (14) becomes now:

$$S_{i,j}(\omega) = A(\omega) \exp\left[-\frac{|x_i - x_j|}{L_x(\omega)}\right] \exp\left[-\frac{|y_i - y_j|}{L_y(\omega)}\right] \exp\left[j\frac{\omega(x_i - x_j)}{U_c}\right] \tag{25}$$

being x and y the coordinates of the two control points; L_x and L_y denote the correlation lengths; U_c is the convective flow speed, and it is assumed a fixed percentage of the undisturbed one, $U_c = 0.8U$. The correlation distances are the following:

$$L_x(\omega) = \frac{U_c}{\omega\alpha_x};\ \ L_y(\omega) = \frac{U_c}{\omega\alpha_y}. \tag{26}$$

α_x and α_y are the stream- and cross-wise correlation parameters, respectively.

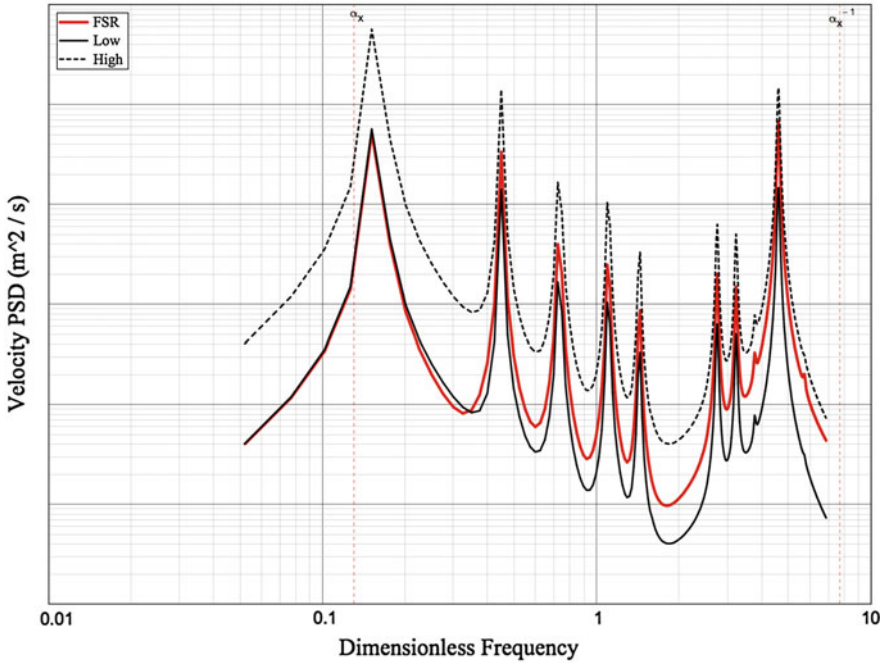

Fig. 6 Response of the chain of oscillators: velocity (PSD) $(\mathrm{m}^2\ \mathrm{s}^{-1})$ versus dimensionless frequency; MM range

The numerical results are carried out with the following set of parameters: $\alpha_x = 0.12$ and $\alpha_y = 0.7$.

The quantity R defines a dimensionless metric for the plate response:

$$R(\omega) = \frac{\omega^4(\rho\ h)^2}{A(\omega)} S_{WW} \tag{27}$$

This metric is used to discuss the results. In this way, the structural response does not depend on the power spectral density of the wall pressure fluctuations, which is only a multiplicative factor. The numerator is a measure of the vibrational energy of the plate.

For both the plates the evolutions of the eigenvalues are very similar to the content of Fig. 1. Thus, the previous considerations still hold, and also the representation in terms of dimensionless frequency ranges as in Fig. 2.

The definition of the dimensionless frequency ranges is not trivial in the 2D case; thus, for the sake of simplicity, the same definition adopted in the 1D test has been used also for the plate, by using only α_x. This definition will be one of the points to be addressed in the near future.

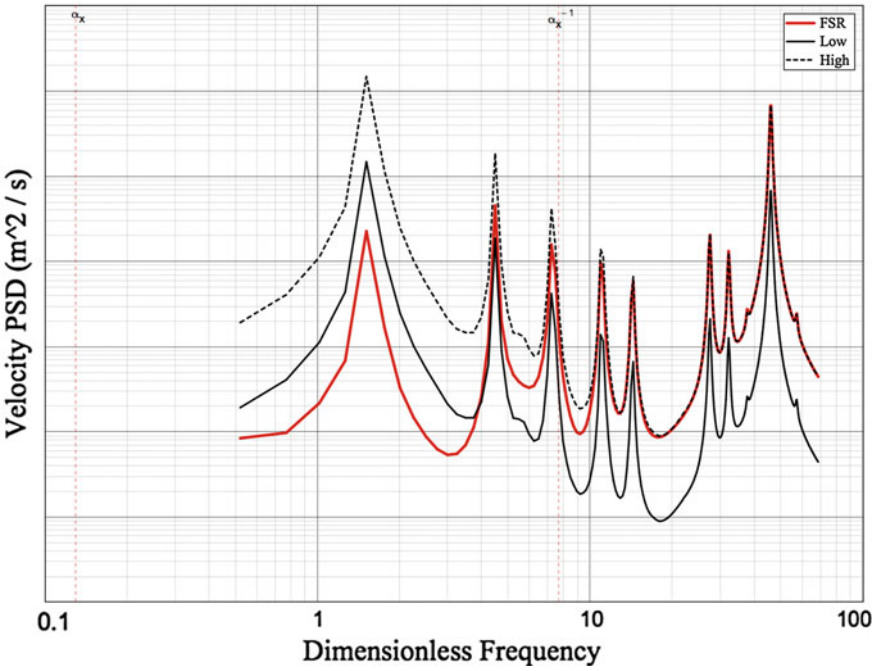

Fig. 7 Response of the oscillators: velocity (PSD) ($m^2\ s^{-1}$) versus dimensionless frequency; MH range

The bounds of the structural response can be specified by using a factor $\sqrt{\text{NG}}$ to define the interval according to the PEDE_M framework. In fact, it is easy to show that:

$$\mathbf{S_{WW}}^{(high)}(\boldsymbol{\omega}) = \sqrt{\text{NG}}\,\mathbf{S_{WW}}^{(low)}(\boldsymbol{\omega}) \tag{28}$$

5.2.1 KTH Plate

The flexural plate discussed here is made of aluminium and is 1.6 mm thick; the area is 768×328 mm^2, being the longest side in the stream-wise direction. The plate is simply supported along its edges and a finite element model has been assembled to obtain natural frequencies and mode shapes, in order to build a reference solution according with Eq. (1).

The plate belongs to a series of test performed in the wind-tunnel facility at KTH in Stockholm, during the EU project ENABLE [13].

It has to be noted that for such kind of problems, that is simulation of the stochastic response in discrete coordinates, another problem adds complexity to the solution; in fact, the discretization of the joint acceptance integral and its solution are based on both the number of degrees of freedom (sampling of the aerodynamic wavelength) and the integration type [15].

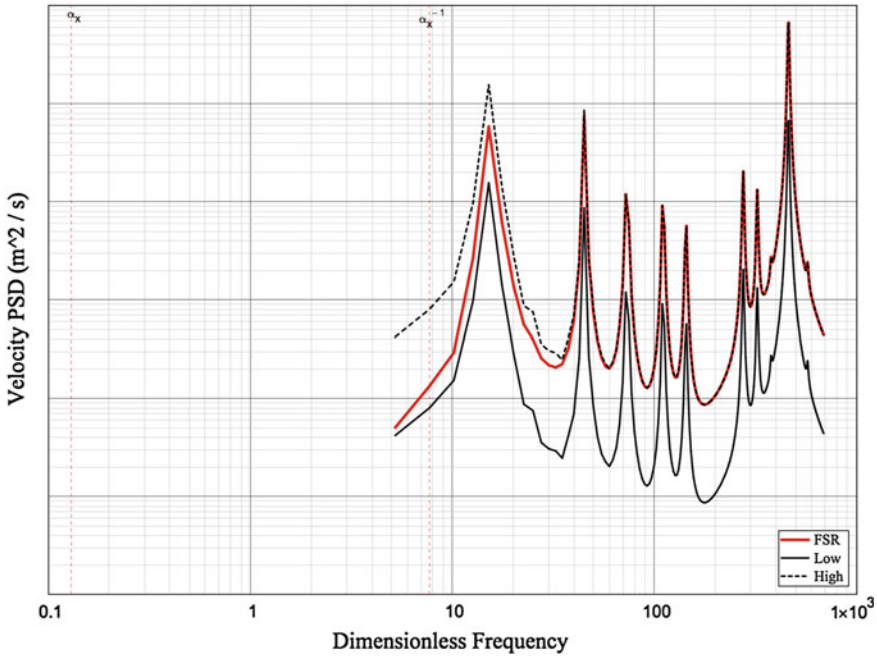

Fig. 8 Response of the chain of oscillators: velocity (PSD) $(m^2\ s^{-1})$ versus dimensionless frequency; HH range

In Fig. 10, the analytical solution of the plate response is reported together with the bounding curves provided by the PEDE$_M$ method. The considerations made for the chain of oscillators hold also in this 2D case.

Figure 11 presents on the same chart the analytical response, the full stochastic one with the modes obtained by the finite element model and the PEDE$_M$ high frequency solution with the spatial equivalence suggested in [16].

The spatial equivalence approximates the load matrix with a particular diagonal one. This approximation is more and more valid as frequency increases because the wall pressure field becomes spatially uncorrelated. The spatial equivalence approximation determines the expression of each term of the matrix diagonal and they are function of frequency and wall pressure field coefficients. The knowledge of this term allows an easy evaluation of the load matrix eigensolutions and, therefore, a direct application of the PEDE$_M$ approach.

The structural mesh has been designed to work up to 18,000 Hz but the aliasing problem for the aerodynamic load limits this maximum frequency at 1,350 Hz. The finite element mesh is 101×43 nodes, so that $\Delta = 7.7$ mm. As consequence, for $U_c = 40$ m/s, the low frequency limit is around 100 Hz; the high one is around 1,200 Hz.

A summary is also given in Fig. 12 where the flow speed is only changed. The increased flow-speed simplifies the response calculations because the aliasing

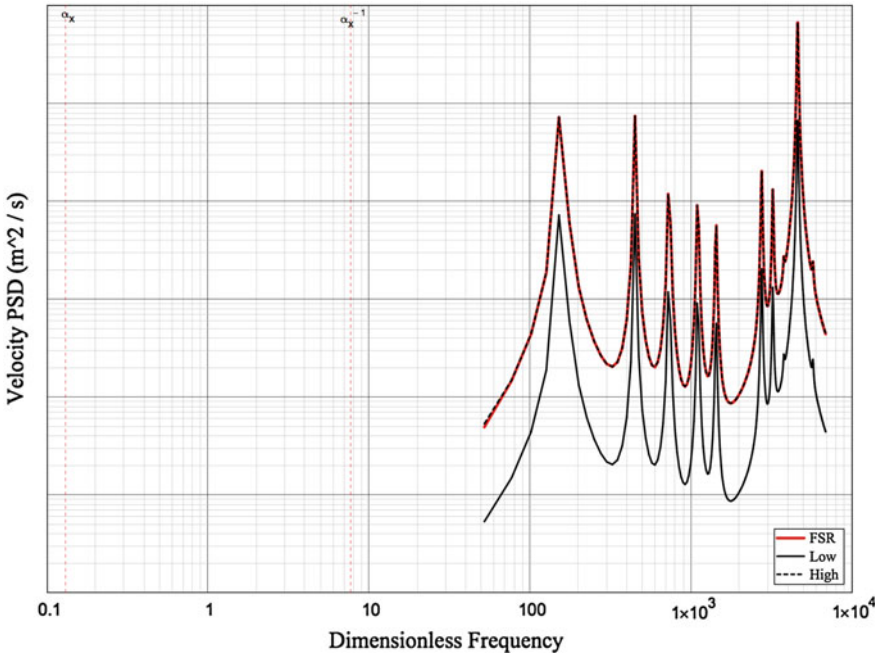

Fig. 9 Response of the chain of oscillators: velocity (PSD) $(m^2\ s^{-1})$ versus dimensionless frequency; HH range

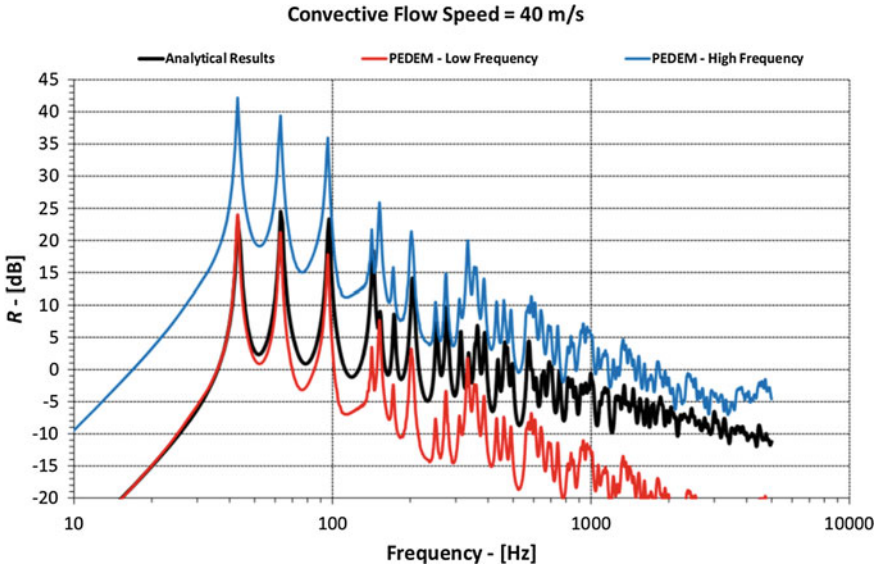

Fig. 10 Response of the KTH flexural plate: metric *R* (dB) versus frequency (Hz)

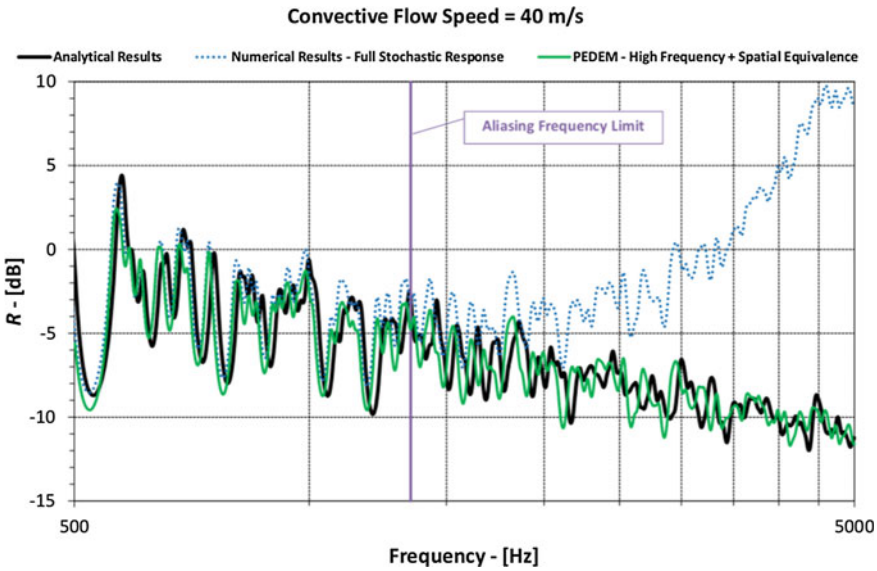

Fig. 11 Response of the KTH flexural plate: metric R (dB) versus frequency (Hz)

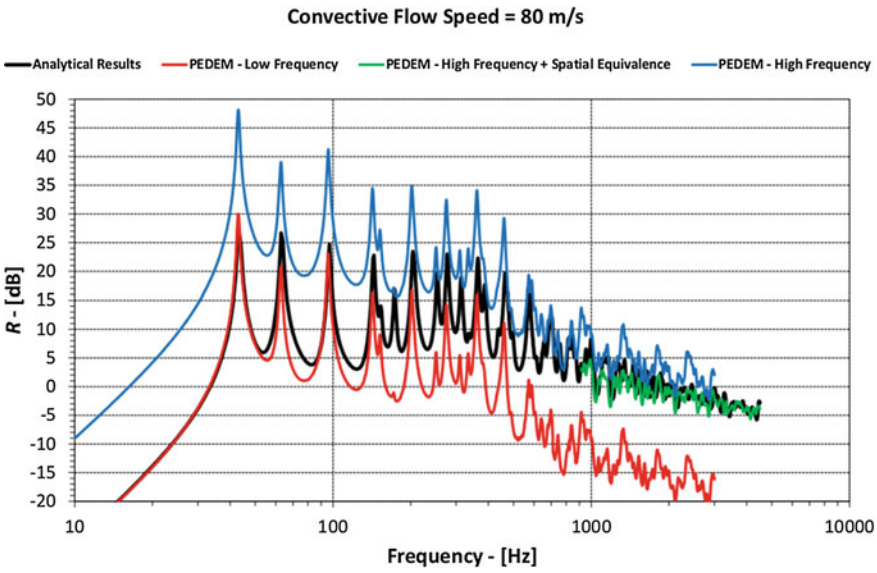

Fig. 12 Response of the KTH flexural plate: metric R (dB) versus frequency (Hz)

frequency limit is around 2,700 Hz. In fact, the PEDE_M results show a better convergence to the analytical ones as frequency increases.

For $U_c = 80$ m/s, the low frequency limit is around 200 Hz; the high one is around 2,400 Hz.

5.2.2 AMACA Plate

The second investigated plate is still made of aluminium and has the same thickness of the KTH one, 1.6 mm; the area is 420×320 mm^2. It is simply supported along its edges and a finite element model has been assembled to obtain natural frequencies and mode shapes, in order to build a reference solution according with Eq. (1). The finite element mesh is 57×42 nodes, so that $\Delta = 8$ mm. As consequence, for $U_c = 136$ m/s, the low frequency limit is around 350 Hz; the high one is around $4,000$ Hz.

This plate is one of the test-articles used in a research project managed by ALENIA/Aermacchi during three years 2008–2010. Homogeneous and composite materials plates have been tested in the CIRA transonic wind-tunnel at several Mach numbers and with different conditions of the boundary layer [26, 27].

By looking at the content of Fig. 13, all the previous considerations remain valid: the PEDE_M bounding curves allow confining the response without any information about the eigenvalues of the load matrix.

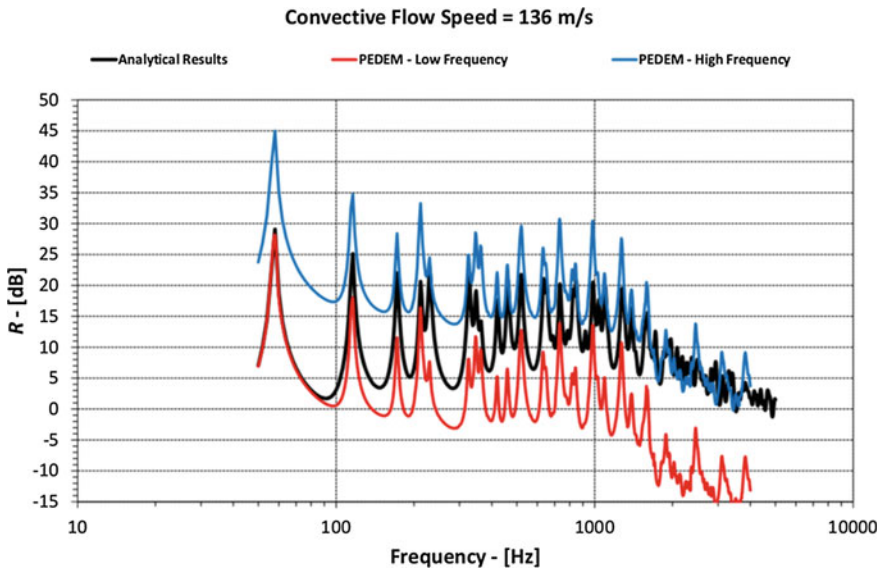

Fig. 13 Response of the AMACA flexural plate: metric R (dB) versus frequency (Hz)

6 Concluding Remarks

A newly defined technique named PEDE$_M$ is here used to define bounding curves for the analysis of the stochastic response of linear operators in discrete coordinates. This is accomplished by using a set of pseudo equivalent deterministic forces. The method is based on PEM, pseudo excitation method, but it avoids the analysis of the eigensolutions of the cross-spectral load matrix.

The two test cases are very simple and concern a chain of mass-spring oscillators and a flexural plate; both are excited with a pressure distribution as generated by a turbulent boundary layer.

The results shown that the curves generated in PEDE$_M$ as approximations of the PEM theory are (i) computationally cheap avoiding the extraction of the load matrix eigenvalues and (ii) well bound the exact responses used as references. The analyses are carried out in all the dimensionless frequency ranges by using the asymptotic forms assumed by the load matrix.

Investigations on more realistic configurations are needed but the actual results are very satisfactory.

Nevertheless, it is shown that the low and high frequency PEDE$_M$ approximations are in agreement with the reference curves in the analogous frequency ranges. Therefore, the defined bounds can be used only in the mid frequency range where the eigensolutions of the load matrix strongly vary versus frequency. A detailed analysis of the load matrix eigensolutions could improve the quality of the results and narrow the response bounds. It can be one of the first topics to be addressed.

References

1. I. Elishakoff, Probabilistic Methods in the Theory of Structures. Wiley Interscience, New York, 2nd edition (Dover Publications, Mineola, New York, 1999)
2. W. X. Zhong, Duality system in applied and optimal control. (Kluwer Academic Publishers 2004), ISBN: 1-4020-7880-3
3. W.S. Cho To, Stochastic Structural Dynamics: Application of Finite Element Methods (Wiley, New York, 2013), ISBN: 978-1-118-34235-0
4. F. Sgard, N. Atalla, J. Nicolas, Coupled FEM-BEM approach for mean flow effects on vibro-acoustic behaviour of planar structures. AIAA J. Aircr. **32**(12), 2351–2358 (1994)
5. P. Vitiello, S. De Rosa, F. Franco, Convected field analysis of flat panels response to turbulent boundary layer induced excitation. Aerosp. Sci. Technol. **12**, 91–104 (2008)
6. G.M. Corcos, The structure of the turbulent pressure field in boundary-layer flows. J. Fluid Mech. **18**, 353–379 (1964)
7. G.M. Corcos, Resolution of pressure in turbulence. J. Acoust. Soc. Amer. **35**, 192–199 (1963)
8. W.R. Graham, A comparison of models for the wavenumber frequency spectrum of turbulent boundary layer pressures. J. Sound Vib. **206**(4), 541–565 (1997)
9. B.M. Efimtsov, Characteristics of the field of turbulent wall pressure fluctuations at large Reynolds numbers. Soviet Phisics-Acoust. **28**(4), 289–292 (1982)
10. D.M. Chase, Modelling the wavevector-frequency spectrum of turbulent boundary layer wall pressure. J. Sound Vib. **70**(1), 29–67 (1980)

11. E. Ciappi, F. Magionesi, S. De Rosa, F. Franco, Hydrodynamic and hydroelastic analyses of a plate excited by the turbulent boundary layer. J. Fluids Struct. **25**, 321–342 (2009)
12. S.A. Hambric, Y.F. Hwang, W.K. Bonness, Vibrations of plates with clamped and free edges excited by low-speed turbulent boundary layer flow. J. Fluids Struct. **19**, 93–110 (2004)
13. S. Finnveden, U. Birgersson, U. Ross, T. Kremer, A model of wall pressure correlation for prediction of turbulence-induced vibration. J. Fluids Struct. **20**, 1127–1143 (2005)
14. S. De Rosa, F. Franco, Exact and numerical responses of a plate under a turbulent boundary layer excitation. J. Fluids Struct. **24**, 212–230 (2008)
15. F. Franco, S. De Rosa, E. Ciappi, Numerical approximations on the predictive responses of plates under stochastic and convective loads. J. Fluids Struct. **42**, 296–312 (2013)
16. M.N. Ichchou, B. Hiverniau, B. Troclet, Equivalent rain on the roof loads for random spatially correlated excitations in the mid frequency range. J. Sound Vib. **322**, 926–940 (2009)
17. C. Hong, C.K.K. Shin, Modelling of wall pressure fluctuations for finite element structural analysis. J. Sound Vib. **329**, 1673–1685 (2010)
18. O. Collery, J.-L. Guyader, Solving the vibroacoustic equations of plates by minimization of error on a sample of observation points. J. Acoust. Soc. Amer. **127**(3), 1347–1356 (2010)
19. J. Lin. A deterministic algorithm of stochastic seismic response. Chin. J. Earthq. Eng. **5**, 89–93, (1985) (in Chinese)
20. L. Jiahao, Z. Wenshou, L. Jianjun, Structural responses to arbitrarily coherent stationary random excitations. Comput. Struct. **50**(5), 629–633 (1994)
21. Y.L. Xu, W.S. Zhang, J.M. Ko, J.H. Lin, Pseudo-excitation method for vibration analysis of wind-excited structures. J. Wind Eng. Ind. Aerodyn. **83**, 443–454 (1999)
22. J. Lin, Y. Zhao, Y. Zhang. Accurate and highly efficient algorithms for structural stationary/non-stationary random response. Comput. Methods Appl. Engr. **191**, 103–111 (2001)
23. J.H. Lin, Y.H. Zhang, Y. Zhao, Pseudo excitation method and some recent developments. Procedia Eng. **14**, 2453–2458 (2011)
24. G. Zhao, G. Chen, Z. Kang, An iterative algorithm for analysis of coupled structural-acoustic systema subject to random excitations. Acta. Mech. Sin. **28**, 458–467 (2012)
25. S. De Rosa, F. Franco and E. Ciappi. The stochastic response of a linear system through equivalent deterministic forces, in EURODYN2014, IX International Conference on Structural Dynamics, Porto, Portugal, 30 June 2014
26. F. Magionesi, E. Ciappi, R. Camussi, T. Pagliaroli, A. Di Mascio, B. Imperatore, A.Marino. Measurement and modeling of turbulent boundary layer excitation for naval and aeronautical applications, in *Proceedings of NOVEM2012 Conference â€œNoise and Vibration: Emerging Methods*, Sorrento 1–4 April 2012, ISBN: 9788890648403
27. S. De Rosa, F. Franco, E. Ciappi, F. Magionesi, V. Quaranta, P. Vitiello, M. Di Giulio. Wind tunnel measurements of pressure fluctuations and structural response induced by the turbulent boundary layer at high Mach number. Part 2: comparisons between experimental and numerical data for the structural response, in *Proceedings of NOVEM2012 Conference Noise and Vibration: Emerging Methods*, Sorrento 1–4 April 2012, ISBN: 9788890648403

A Numerical Methodology for Resolving Aeroacoustic-Structural Response of Flexible Panel

Randolph C.K. Leung, Harris K.H. Fan and Garret C.Y. Lam

Abstract Fluid-structure interaction problem is relevant to the quieting design of flow ducts found in many aeronautic and automotive engineering systems where the thin duct wall panels are directly in contact with a flowing fluid. A change in the flow unsteadiness, and/or in the duct geometry, generates an acoustic wave which may propagate back to the source region and modifies the flow process generating it (i.e. an aeroacoustic process). The unsteady pressure arising from the aeroacoustic processes may excite the flexible panel to vibrate which may in turn modify the source aeroacoustic processes. Evidently there is a strong coupling between the aeroacoustics of the fluid and the structural dynamics of the panel in this scenario. It is necessary to get a thorough understanding of the nonlinear aeroacoustic-structural coupling in the design of effective flow duct noise control. Otherwise, an effective control developed with only one media (fluid or panel) in the consideration may be completely counteracted by the dynamics occurring in another media through the nonlinear coupling. The present paper reports an attempt in developing a time-domain numerical methodology which is able to calculate the nonlinear fluid-structure interaction experienced by a flexible panel in a flow duct and its aeroacoustic-structural response correctly. The developed methodology is firstly verified able to capture the acoustic-structural interaction in the absence of flow where the numerical results agree with theory very well. A uniform mean flow is then allowed to pass through the duct so as to impose an aeroacoustic-structural interaction on the flexible panel. As a result, the nonlinear coupling between the flow aeroacoustics and panel structural dynamics are found completely different from the case without mean flow. A discussion of the new physical behaviors found is given.

R.C.K. Leung (✉) · H.K.H. Fan · G.C.Y. Lam
Department of Mechanical Engineering, The Hong Kong Polytechnic University, Hung Hom, Kowloon, Hong Kong
e-mail: mmrleung@polyu.edu.hk

H.K.H. Fan
e-mail: mr.harrisfan@connect.polyu.hk

G.C.Y. Lam
e-mail: garret.lam.hk@connect.polyu.hk

E. Ciappi et al. (eds.), *Flinovia - Flow Induced Noise and Vibration Issues and Aspects*, DOI 10.1007/978-3-319-09713-8_15

1 Introduction

The accurate prediction of noise generation by flow induced vibration is an important and challenging task in many engineering problems. It is a major consideration in the quieting design of many applications that involve unsteady flow and flexible structures, such as those found in aircraft, automotive and ventilation systems. For example, people staying indoor are always annoyed by the noise radiation from air-conditioning or ventilation systems. The noise generated by the operations of air-moving machines, or by the turbulent flows in ducts, propagates through the ductworks and radiates from the duct outlets. Besides, the duct walls are commonly constructed from thin metal sheets. They are easily set to vibrate by both turbulent flows and noise. The vibration will generate additional noise to both inside and outside of the ducts [8] which causes more annoyance to people. Usually in such kind of problem, a complex interaction between the flow dynamics, acoustics and structural dynamics is involved. The three dynamical processes affect each other in a coupled manner and the final noise generation is very complicated.

Researchers have attempted different approaches to the study of the dynamics of flow-acoustics-structure interaction problem. Some of them favour their focus on the interaction between flow and structure over the acoustic aspects. Carpenter and Garrad [3] developed a simple model for flow over a compliant surface supported on an elastic foundation for the investigation of different types of flow-induced surface instabilities. Lucey [19] studied the wave-bearing behaviour of a finite flexible plate in a uniform flow. He found that it is possible for the plate to respond at frequencies other than that of the driver in the presence of flow. He assumed an incompressible flow in his study so the relevant acoustic field cannot be resolved. On the other hand, some researchers studied the interaction between an acoustic wave and a vibrating structure. Frendi et al. [10] compared two coupling models of acoustic-structural interaction. He found that the "decoupled model" is more accurate in predicting the panel response and acoustic radiation, and need lower computational cost. Huang [12] studied an idea of duct noise control by installing a flexible panel in an otherwise rigid duct, and provided theoretical solutions of this acoustic-structural interaction problem in frequency domain.

Other researchers are interested in studying the acoustic radiation driven by a fluid-structure interaction. Clark and Frampton [6] demonstrated the importance of including aeroelastic coupling in modelling the structural acoustic response for interior noise control on modern aircraft. Schäfer et al. [21] attempted to solve the fluid-acoustic-structure interaction of a flow past a thin flexible structure fully. They solved the fluid-structure interaction through a numerical coupling of the solutions from a fluid dynamic solver and a structural dynamic solver, and then determined the resultant acoustic field by adding the contributions from the fluid dynamic and structural dynamic solutions. In that way, the acoustic solution was simply treated as a consequence to the fluid-structure interaction but the effect of the acoustics on fluid-structure interaction was omitted.

All the aforementioned studies reveal that the three elemental dynamical processes (i.e. acoustics, flow and structural dynamics) are equally important in literally all fluid-acoustics-structure interaction problems but the current state of effort in resolving their highly coupled interactions is still far from satisfactory. It remains in a stage in which the coupled interaction between any two dynamics (e.g. fluid and structure) are calculated and the solution thus obtained is used to deduce the remaining dynamical process as an effect. In some situations, such effect may be fed back to significantly modify the interactions creating it but the determination of this feed-back process is always lacking. Furthermore, the current approaches usually involve the use of three different solvers for each dynamics. Pairwise dynamical coupling relies on extensive data exchange of three data sets for the calculation of complete interaction. That way would inevitably lead to prohibitively high demands in computational resources, high programming difficulties as well as severe numerical errors arising from data extrapolation involved during the exchanges.

In this light, the goal of the present study is to develop a simple yet accurate numerical methodology that fully accounts for the nonlinear fluid-acoustics-structure interaction encountered in real applications. The development takes the view that typically a fluid-acoustics-structure interaction problem occurs within a domain composed of a compressible fluid and a flexible structure. It is logical to take an approach that calculates the fluid dynamical processes entirely (i.e. fluid dynamics and acoustics) as well as the structural dynamics, and then resolves their coupled interaction. It is more appropriate to describe the fluid-acoustics-structure interaction problem as a aeroacoustic-structural interaction problem. Here we report the formulation of the numerical methodology and demonstrate its capability by solving the aeroacoustic-structural response of a canonical problem that involves an excited panel in a duct carrying a flow.

2 Problem of Interest

Recently Huang [12] has proposed a concept for low-frequency duct noise control making use of a finite length tensioned flexible panel flush-mounted in an infinite rigid flow duct (Fig. 1). When a plane acoustic wave is propagating through the duct, the panel responds to vibrate and the local distension in the vicinity of the panel thus created renders a local wave propagation speed far less than its isentropic value. The mismatch in the wave speed there leads to reflection and scattering of acoustic wave at the edges of the panel. The extent of reflection and scattering depends on the acoustic-structural interaction occurring with the vibrating panel which eventually results in creates passbands and stopbands for the acoustic transmission.

We select the cases Huang [12] attempted for the demonstration of the developed numerical methodology. He presented a detailed linear analysis in frequency domain

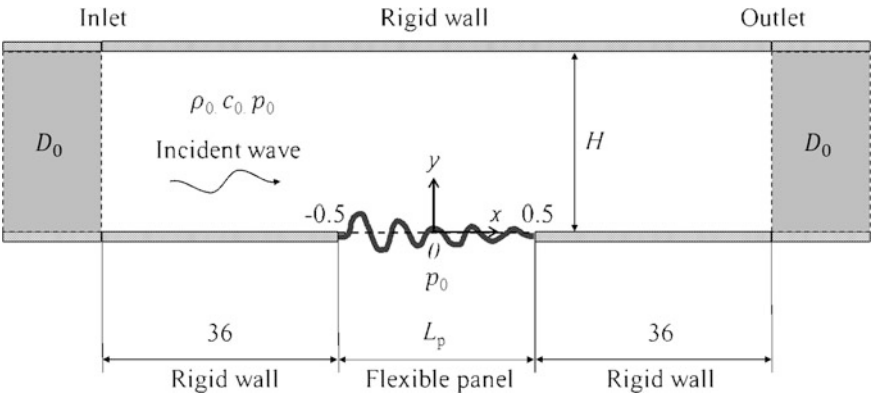

Fig. 1 Schematic configuration of the problem

on how various panel parameters (e.g. length, stiffness, structural damping, etc.) influence the acoustic-structural interaction and subsequent transmission loss in the absence of mean flow. His results of the analysis are complete and provide a set of good reference for validating and verifying of the calculation. It is worthwhile to note that Huang and his co-workers [12, 13] have later extended the concept to develop the so-called drum-like silencer configuration by appending a side-branch cavity to the flexible panel. The fluid inside cavity provides additional elastic stiffness to the vibrating panel. In the present paper, the duct side-branch is excluded.

3 Formulation of Numerical Methodology

Schäfer et al. [21] calculated the acoustic field generated from the interaction of a thin flexible panel with a turbulent flow in a semi-open domain in time-domain. They first solved the fluid-structure interaction by coupling, through a parallel data-exchange interface, the solutions obtained from an finite-volume incompressible large-eddy simulation (LES) flow solver and an finite-element structural mechanics solver. Then they summed up the acoustic waves generated respectively from the unsteady flow solution and the panel structural solution using an finite-element acoustic solver. The total acoustic wave is allowed to propagate freely away from the panel. The effect of acoustic wave on the fluid-structure interaction is essentially excluded in the calculation. Such kind of hybrid approach is not appropriate for the present problem of interest. It is because in a flow duct the generated acoustic waves are reflected by the duct walls and mixed with the flow fluctuations. The overall fluctuations may propagate back to the source region and alter the unsteady

flow dynamics and the panel structural vibration there. On the other hand, coupling approach described in [21] involves three channels for data exchange with three solvers. It involves many extrapolations of flow and panel vibration data which inevitably leads to substantial loss of useful dynamic data especially those with high-frequencies. Considering all these weaknesses of the hybrid approach, it is proposed to adopt a formulation which tries to maintain the accuracy of individual solvers yet keep the number of data exchange during coupling to minimal.

In order to obtain accurate time-domain solution of the aeroacoustic-structural response of the in-duct flexible panel exposed to flow and acoustic wave, there are three key elements in the numerical methodology. They are (i) the modeling of aeroacoustics of the fluid, (ii) the prediction of the dynamic response of the panel, and (iii) correct coupling strategy for the nonlinear interplay between the fluid aeroacoustics and panel structural dynamics. All of these elements must be included in the formulation of the numerical solver and each one of them must be selected according to the specific configuration considered.

3.1 Aeroacoustic Model

Acoustic motion is just a kind of unsteady flow motions that a fluid medium supports [7]. It is logical to adopt a numerical model for the fluid medium which allows simultaneous calculation of both the acoustic field and the unsteady flow generating it. Otherwise, the inherent nonlinear interaction between these two fields cannot be properly accounted for in the calculation. This capability is particularly important in calculating the present aeroacoustic problem because the acoustic fluctuations experience multiple reflections and scattering inside the duct which may propagate back and alter the unsteady flow dynamics and the panel structural vibration there. This capability is completely missing in the hybrid aeroacoustic models in which the flow solution is used to drive the acoustic field. As such, we adopt an aeroacoustic model based on direct aeroacoustic simulation (DAS) approach [17, 18] in the present study.

The aeroacoustic problem is governed by the two-dimensional compressible Navier-Stokes equations together with ideal gas law for calorically perfect gas. The normalized Navier-Stokes equations without source can be written in the strong conservation form as,

$$\frac{\partial \boldsymbol{U}}{\partial t} + \frac{\partial (\boldsymbol{F} - \boldsymbol{F}_v)}{\partial x} + \frac{\partial (\boldsymbol{G} - \boldsymbol{G}_v)}{\partial y} = 0, \tag{1}$$

where

$$\boldsymbol{U} = \begin{bmatrix} \rho \\ \rho u \\ \rho v \\ \rho E \end{bmatrix}, \quad \boldsymbol{F} = \begin{bmatrix} \rho u \\ \rho u^2 + p \\ \rho uv \\ (\rho E + p)u \end{bmatrix}, \quad \boldsymbol{G} = \begin{bmatrix} \rho v \\ \rho uv \\ \rho v^2 + p \\ (\rho E + p)v \end{bmatrix},$$

$$\boldsymbol{F}_v = \frac{1}{Re} \begin{bmatrix} 0 \\ \tau_{xx} \\ \tau_{xy} \\ \tau_{xx}u + \tau_{xy}v - q_x \end{bmatrix}, \quad \boldsymbol{G}_v = \frac{1}{Re} \begin{bmatrix} 0 \\ \tau_{xy} \\ \tau_{yy} \\ \tau_{xy}u + \tau_{yy}v - q_y \end{bmatrix},$$

ρ is the density of fluid, u and v are the velocities in x and y direction respectively, t is the time, normal and shear stress $\tau_{xx} = (2/3)\mu(2\partial u/\partial x - \partial v/\partial y)$, $\tau_{xy} = \mu(2\partial u/\partial y + \partial v/\partial x)$, $\tau_{yy} = (2/3)\mu(2\partial v/\partial y - \partial u/\partial x)$, total energy $E = p/\rho(\gamma - 1) + (u^2 + v^2)/2$, pressure $p = \rho T/\gamma M^2$, heat flux $q_x = [\mu/(\gamma - 1)PrM^2](\partial T/\partial x)$ $q_y = [\mu/(\gamma - 1)PrM^2](\partial T/\partial y)$, the specific heat ratio $\gamma = 1.4$, Mach number $M = \hat{u}_0/\hat{c}_0$ where $\hat{u}_0$ is the duct mean flow velocity, $\hat{c}_0 = \sqrt{\gamma \hat{R}\hat{T}_0}$, the specific gas constant for air $\hat{R} = 287.058\text{J}/(\text{kg} \cdot K)$, Reynolds number $Re = \hat{\rho}_0 \hat{c}_0 \hat{L}_p/\hat{\mu}_0$, and Prandtl number $Pr = \hat{c}_{p,0}\hat{\mu}_0/\hat{k}_0 = 0.71$.

The DAS solver must be able to accurately calculate the acoustic and flow fluctuations, which exhibit large disparity in their energy and length scales. This poses a strict requirement to the solver of being low dissipation and highly accurate. Conventionally, high order explicit finite difference schemes such as Bogey [2] are adopted in DAS. Recently, the conservation element and solution element (CE/SE) method [5] has been proven to be a viable alternative [18]. This numerical scheme takes an entirely different approach and concept from conventional schemes (e.g., finite-difference). Its numerical framework relies solely on strict conservation of physical laws and emphasis on the unified treatment in both space and time. Lam et al. [18] showed that CE/SE method is capable of resolving the low Mach number interactions between the unsteady flow and acoustic field accurately by calculating the benchmark aeroacoustic problems with increasing complexity. Therefore, the CE/SE based the DAS solver is adopted as the aeroacoustic model in the present study. In this paper, the formulation of the CE/SE method is not given. Its details can be referred to the works of Lam [16].

3.2 Structural Dynamic Model

The dynamic response of the flexible panel can be modeled with the nonlinear Von Karman's theory for isotropic rectangular elastic plate on Kelvin foundation. The panel is assumed to be of uniform small thickness h_p and initially flat. In the theory

the normal displacements of the vibrating panel can reach the order of h_p but the tangential displacements can still be assumed to be negligibly small. Using the same set of reference parameters adopted in the aeroacoustic model, the normalized governing equation for panel displacement $w = \hat{w}/\hat{L}_p = w(x,z)$, where z is the direction pointing out of paper in Fig. 1, can be written as,

$$D\nabla^4 w - \mathscr{L}\left(T_x, T_y, T_{xy}, w\right) + \rho_p h_p \frac{\partial^2 w}{\partial t^2} + C\frac{\partial w}{\partial t} + Kw = p_{ex}, \tag{2}$$

where $\mathscr{L}\left(T_x, T_y, T_{xy}, w\right) = T_x[\partial^2 w/\partial x^2] + T_y[\partial^2 w/\partial y^2] - 2T_{xy}[\partial^2 w/(\partial x \partial y)]$, $D = \hat{D}\hat{L}_p^4/(\hat{\rho}_0 \hat{u}_0^2)$ is the flexural rigidity of panel, $\rho_p = \hat{\rho}_p/\hat{\rho}_0$ is the density of panel, $h_p = \hat{h}_p/\hat{L}_p$ is thickness of panel, $C = \hat{C}/(\hat{\rho}_0 \hat{c}_0)$ is the structural damping coefficient, $K_p = \hat{K}_p\hat{L}_p/(\hat{\rho}_0\hat{c}_0)$ is the stiffness of foundation, $p_{ex} = \hat{p}_{ex}/(\hat{\rho}_0\hat{c}_0^2)$ is the net pressure exerted on the panel surface, $T_x = \hat{T}_x/(\hat{\rho}_0\hat{c}_0^2\hat{L}_p)$, $T_y = \hat{T}_y/(\hat{\rho}_0\hat{c}_0^2\hat{L}_p)$ and $T_{xy} = \hat{T}_{xy}/(\hat{\rho}_0\hat{c}_0^2\hat{L}_p)$ are the axial stress resultants, and $\nabla^4 = \partial^4/\partial x^4 + 2\left[\partial^4/(\partial x^2 \partial y^2)\right] + \partial^4/\partial y^4$ is the biharmonic operator.

In his analysis [12], Huang used a membrane model for the structural dynamics of the flexible panel. In order to ensure a consistent comparison with his analytical results, we need to simplify Eq. (2) for the calculation. A membrane can be considered as a very thin (with thickness/span <1/50) elastic panel with no appreciable flexural resistance so $D = 0$. The panel exterior is freely exposed to ambient air so $K = 0$. It is further assumed that in-plane shear stress can be ignored because the sideways motion at every point on the membrane is negligible. Consequently the tension is effectively uniform across the panel thickness. With all these assumptions made, the membrane model can describe the thin panel dynamics with small displacements (i.e. $\hat{w}/\hat{h}_p \leq 0.2$) [4, 20, 23]. For the present study, we further assume no variations of the panel dynamics in z-direction so that the panel behaves more or less a quasi one-dimensional flexible beam along x-direction. Therefore, $w = w(x)$, $\mathscr{L}\left(T_x, T_y, T_{xy}, w\right) = \mathscr{L}(T_x, w) = T_x[\partial^2 w/\partial x^2]$, and the panel structural dynamic equation to be solved becomes

$$\rho_p h_p \frac{\partial^2 w}{\partial t^2} + C\frac{\partial w}{\partial t} - T_x \frac{\partial^2 w}{\partial x^2} = p_{ex}. \tag{3}$$

Note that in this equation the net external pressure should be interpreted as pressure difference across the panel, i.e. $p_{ex} = p_0 - p$ (Fig. 1).

The panel dynamic equation is solved using the standard finite-difference procedures. The panel is initially discretized into a series of connect linear meshes of size Δx. All panel mesh points are located below the row of CE/SE solution points just next to boundary of fluid domain (Fig. 2). All spatial derivatives of the panel displacement are approximated using second-order central differences [11] as follows,

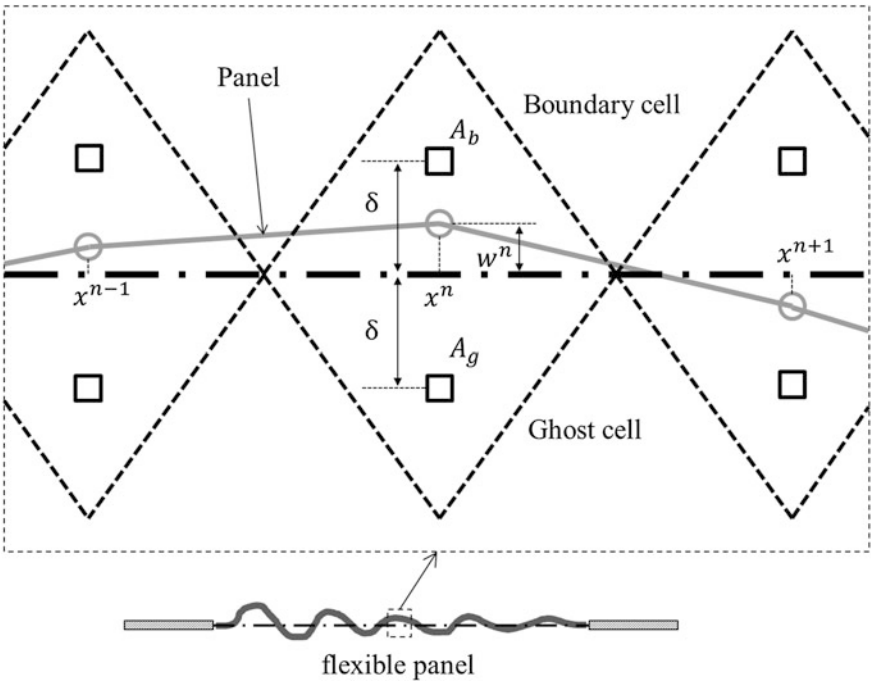

Fig. 2 Meshes at fluid-panel interface. *Dashed line* undeflected panel position. *Square* solution points of boundary cells and ghost cells of CE/SE mesh. *Circle* panel mesh points

$$\frac{\partial w^{n,j}}{\partial x} = w_x^{n,j} = \frac{1}{2\Delta x}\left(w^{n+1,j} - w^{n-1,j}\right), \tag{4}$$

$$\frac{\partial^2 w^{n,j}}{\partial x^2} = w_{xx}^{n,j} = \frac{1}{\Delta x^2}\left(w^{n+1,j} - 2w^{n,j} + w^{n-1,j}\right), \tag{5}$$

where the superscripts j and n indicate the j-th time step and n-th panel mesh point respectively. The second-order spatial derivatives at the two panel edges are given by $w_{xx}^{1,j} = \left(-4w^{1,j} + \frac{4}{3}w^{2,j}\right)/\Delta x^2$ and $w_{xx}^{N,j} = \left(-4w^{N,j} + \frac{4}{3}w^{N-1,j}\right)/\Delta x^2$. The time derivatives are calculated using the following approximations, with time step size Δt,

$$\frac{\partial w^{n,j}}{\partial t} = \dot{w}^{n,j} = \frac{1}{2\Delta t}\left(w^{n,j+1} - w^{n,j-1}\right), \tag{6}$$

$$\frac{\partial^2 w^{n,j}}{\partial t^2} = \ddot{w}^{n,j} = \frac{1}{\Delta t^2}\left(w^{n,j+1} - 2w^{n,j} + w^{n,j-1}\right), \tag{7}$$

Substituting all these approximations to Eq. (3), the panel displacement is approximated as

$$w^{n,j+1} = \frac{Cw^{n,j-1}\Delta t - 2\rho_p h_p(w^{n,j-1} - 2w^{n,j}) + 2p\Delta t^2 + 2T_x w_{xx}^{n,j}\Delta t^2}{2\rho_p h_p + C\Delta t}. \quad (8)$$

Therefore, after each time step the dynamics of all panel mesh points $\boldsymbol{W} = [w, \dot{w}, \ddot{w}]^T$ are readily available.

3.3 Boundary Condition

The boundary conditions for the duct fluid domain are prescribed as follows. Isothermal condition $T_p = T_0$ is specified on all solid surfaces. Slip boundary condition is applied to all rigid surfaces. For the fluid boundary in contact with the vibrating panel, the tangency condition $(v - \dot{w}) = 0$ and the normal pressure gradient condition $\partial p/\partial y = \rho\,\ddot{w}$ are required to satisfy. Pinned conditions are prescribed at both edges for the flexible panel where the displacement and bending moment are set to zero, i.e. $w^{1,j} = w^{N,j} = w_{xx}^{1,j} = w_{xx}^{N,j} = 0$.

At each time step the fluid domain is deformed by the calculated panel displacement. Usually remeshing (e.g. in So et al. [22]) is applied to the deformed fluid domain so as to eliminate any highly strained mesh where the solution is underresolved. Otherwise the solution accuracy will be seriously deteriorated. In the remeshing procedure all mesh points in the fluid domain are updated so heavy computational resources are required. For the present problem, recognizing the characteristic feature in CE/SE method on how the flow solution is calculated at solution points [16] and the fact that panel displacements are very small compared to panel thickness [12], we can account for the effect of deformation of fluid domain with a much simpler technique that is derived in the spirit of immersed element boundary method [9].

A brief of this simplified technique is given here with the help of the description of the computational domain around a panel mesh point x^n illustrated in Fig. 2. In CE/SE method the solution points are not laid on the physical fluid domain boundary. The flow conditions at the boundary there are manifested by placing a mirror ghost cell behind the boundary (e.g. A_g). Appropriate flow variables are then specified at the ghost cell such that the desired flow conditions at the true panel position are implicitly given by interpolation with the boundary and ghost cells. For the rigid duct boundaries, we set the ghost point transverse velocity $v_g = -v_b$ for enforcing slip boundary condition. For the vibrating panel surface, we assume that its displacement is smaller than the offset δ of solution point A_b and its velocity in y-direction v_g can be approximated as

$$v_g = \dot{w}^n + \frac{\delta + w^n}{\delta - w^n}(\dot{w}^n - v_b). \tag{9}$$

All the flow variables other than v_g in the ghost cell are set according to the slip boundary condition procedure of Lam et al. [18]. Certainly we need to pay attention whether our assumption is valid during the course of calculations. For a large displacement (i.e. $w > \delta$), the tangential panel velocity becomes significant and the panel vibration starts to exhibit nonlinear behaviors. In this situation a more elaborated panel structural dynamic model together with a proper remeshing procedure must be used. In all the calculations reported here we found $w/\delta < 68\ \%$ consistently. This observation indicates that our proposed simplified technique works well for the present problem.

3.4 Fluid-Panel Coupling Scheme

When an unsteady flow and an acoustic wave are passing over the flexible panel, the flow pressure fluctuations acting on the panel will force to vibrate. The vibrating panel then modifies the boundary condition of the aeroacoustic flow which has to change as a consequence. The aeroacoustic field and the panel structural response are coupled to each other through the tangency boundary condition (effect of structural response on the unsteady flow) and the normal pressure gradient condition (effect of flow unsteadiness on the structural response). Both physical conditions respectively ensure the continuity of velocity and momentum at the fluid-panel interface in the solution of the problem. Therefore, an coupling scheme that allows seamless coupling of both effects is necessary for the accurate prediction of the flow-panel interaction involved. In addition to achieving the required numerical accuracy, we also want a scheme that is efficient and does not invoke too heavy computational resource requirement for marching the solution. We attempted two schemes for coupling in the present study.

The first scheme we attempted follows the idea of Jaiman et al. [15] which is schematically illustrated in Fig. 3. In this scheme, the panel structural dynamic solution $\boldsymbol{W}_{j-1}$ available at the end of the $(j-1)$-th time step is treated as the boundary condition of the fluid domain in contact with the panel for the solver of aeroacoustic model for calculating the new aeroacoustic solution at the j-th time step, i.e. the $\boldsymbol{U}_j$. Then the new panel structural response $\boldsymbol{W}_j$ is evaluated by solving Eq. (3) with its forcing term, i.e. p_{ex}, constructed from the aeroacoustic solution $\boldsymbol{U}_j$. Both $\boldsymbol{U}_j$ and W_j available at the end of the j-th time step are then used as the initial solutions for the $(j+1)$-th time step and the solution of the problem marches in time afterwards. As such in each time step the update of the panel structural response appears to lag that of aeroacoustic solution. This feature leads to the enforcement of the tangency condition and the normal pressure gradient condition in a staggered manner. Thus the communication between the two solutions is

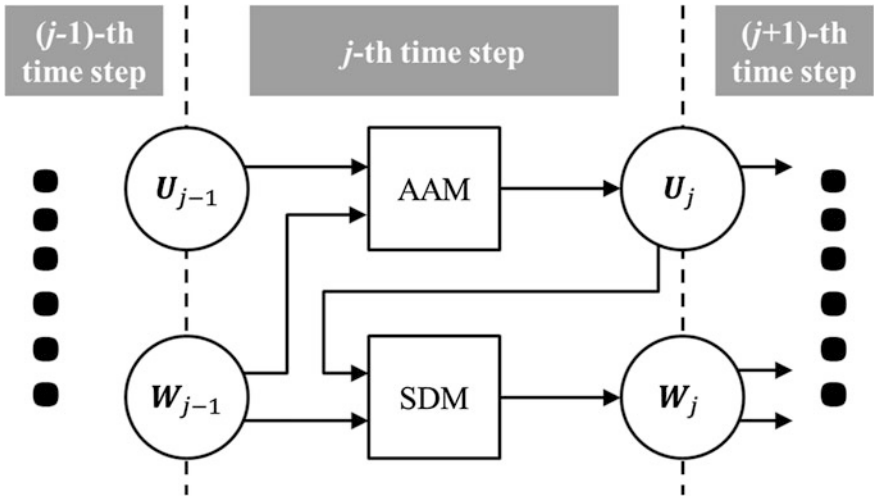

Fig. 3 Calculation procedure of the staggered coupling scheme. *AAM* aeroacoustical model; *SDM* structural dynamic model

literally one-way so the scheme can be considered to resolve the fluid-panel interaction in a loose coupling sense. The numerical error arising from the delay between the updates of aeroacoustic and structural dynamic solutions can be effectively suppressed with the reduced time step size [15]. Since a small time step size is always needed for the present explicit CE/SE aeroacoustic solver [18], especially in the case with a low Mach number flow, the scheme appears to be a reasonable choice for solving the present problem.

Another more elaborated scheme we attempted for calculating the fluid-panel coupling follows the idea of Jadic et al. [14] which emphasizes more on the two-way coupling between the aeroacoustic and structural dynamic solutions (Fig. 4). In the calculation at the j-th time step, initial solution estimates, $\boldsymbol{U}_{ie}$ and $\boldsymbol{W}_{ie}$ are firstly evaluated in the same way as described in the loose coupling scheme. The initial estimates are then put into a predictor-corrector procedure in which the errors in the satisfaction of both tangency and normal pressure gradient conditions are minimized in an iterative manner. Essentially, an aeroacoustic solution estimate $\boldsymbol{U}_{k+1}$ is obtained with an predicted boundary condition $\lambda \boldsymbol{W}_k + (1-\lambda)\boldsymbol{W}_{k-1}$, where λ is the relaxation factor [1]. Then the estimated $\boldsymbol{W}_{k+1}$ is obtained with an predicted forcing from $\lambda U_{k+1} + (1-\lambda)U_k$. If the relative errors between the solutions at iterations k and $k+1$ at all panel mesh points is less than the prescribed precision ε, then the final solutions $\boldsymbol{U}_j = \boldsymbol{U}_{k+1}$ and $\boldsymbol{W}_j = \boldsymbol{W}_{k+1}$ are marched forward to next time step; otherwise the iteration continues until the precision requirement is reached. Since the effects of aeroacoustics on the panel structural dynamics and its vice versa are accounted for in the solution in equal footing, the procedure described leads to a more tightly coupled scheme for resolving the fluid-panel interaction. Nevertheless

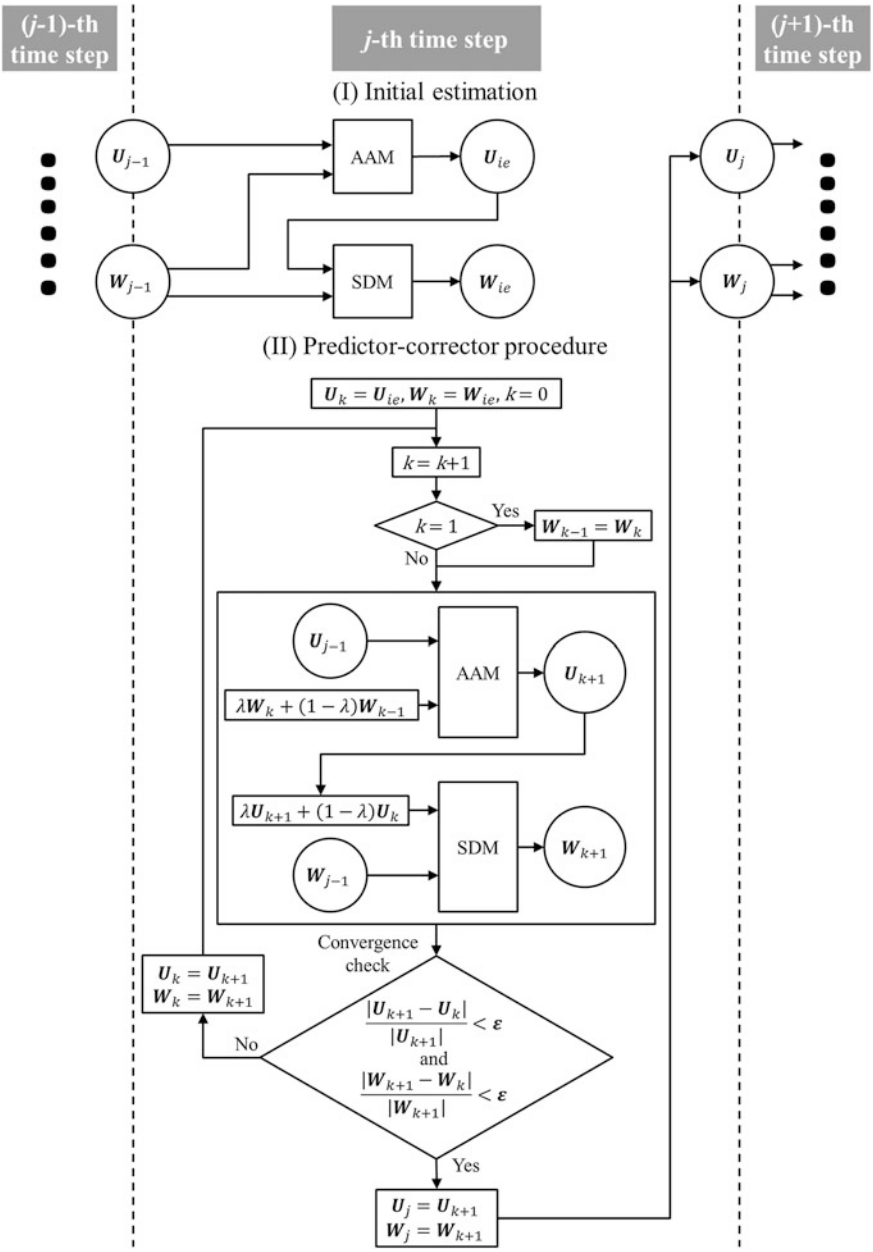

Fig. 4 Calculation procedure of the iterative coupling scheme. *AAM* aeroacoustical model; *SDM* structural dynamic model

the computational resources incurred is heavier. In all the calculations reported in the later sections, λ is set equal to 0.5 whereas the precision requirement ε is prescribed to 10^{-10}. The number of iterations in each time step is around 20.

4 Results and Discussions

Although the numerical methodology developed aims to resolve the nonlinear aeroacoustic-structural interaction between a flexible panel and an incident acoustic wave in the presence of flow, it would be informative to assess how accurate the developed methodology resolves the acoustic-structural response of the panel without flow first. We then proceed to include uniform flows for the study of its capability of resolving the aeroacoustic-structural interaction. We use the same physical parameters as in Huang [12]: duct width $\hat{h} = 100\,\text{mm}$, panel length $\hat{L}_p$ can be changed, density of panel $\hat{\rho}_p = 1000\,\text{kg/m}^3$ (close to rubber), thickness of panel $\hat{h}_p = 0.05\,\text{mm}$, tensile force $\hat{T}_x = 58.0601\,\text{N/m}$ and frequency of incident wave $\hat{f} = 340\,\text{Hz}$.

The present computational domain for Huang's problem is detailed in Fig. 1. In solving the problem, we normalize all the flow and structural variables with the reference parameters, namely, length = panel length $\hat{L}_p$, velocity $= \hat{c}_0 = 340\,\text{m/s}$, time $\hat{t}_0 = \hat{L}_p/\hat{c}_0$, density $= \hat{\rho}_0 = 1.225\,\text{kg/m}^3$, and pressure $\hat{\rho}_0\hat{c}_0^2$. Here the variables with a caret "^" denote the quantities with dimensions and subscript "0" means the fluid property in stationary ambient. The duct sections upstream and downstream of the flexible panel is set 36 times of the panel length for ensuring sufficient space for the generated acoustic wave to propagate. In order to avoid the contamination of any erroneous waves reflected from the physical duct inlet and outlet, numerical anechoic termination (D_0 in Fig. 1) proposed by Lam et al. [17] is attached to the inlet and outlet. It acts to absorb leaving acoustic waves scattered from the vibrating panel. The chosen physical parameter gives $Re = 10^{12}$. Thus the fluid viscosity effect is effectively suppressed and the flow in the calculation is essentially inviscid.

Different meshing on the fluid domain and the panel was attempted for convergence study of the proposed methodology. The mesh used in the calculations for the forthcoming discussions is the largest one that exhibits convergent results. It is defined as follows. The panel mesh size is set to $\Delta x = 0.002$ uniformly. The fluid region above the panel follows the same mesh size along x-direction. The mesh size is smoothly increased to $\Delta x = 0.05$ from the panel edges to the duct interior upstream and downstream of the panel over approximately a panel length beyond which Δx remains constant on going towards the duct inlet and outlet. A uniform mesh distribution $\Delta y = H/50$ is taken along y-direction in all cases.

4.1 Acoustic-Structural Response

As mentioned earlier, the acoustically excited vibration of the flexible panel is able to reflect and scatter the incident acoustic waves. As a result the pressure of the acoustic wave propagating to duct section downstream of the panel is reduced. The reduction of the acoustic pressure is described by the transmission loss TL defined as

$$\mathrm{TL} = 20\log_{10}\left(\frac{(p_{\mathrm{downstream}})_{rms}}{(p_{\mathrm{incident}})_{rms}}\right), \tag{10}$$

where subscript *rms* means the root-mean-squared value. We calculate the TL with different panel lengths $L_p/H = 4.3$, 6 and 8 using both staggered and iterative fluid-panel coupling schemes. No structural damping is assumed. Since the panel length is chosen as the reference length, here we calculate the effects of L_p/H variation through modifying the value of duct width H. This is different from the notation adopted in the theory where H is fixed but L_p varies. A comparison of the numerical TL with the corresponding theoretical values is given in Table 1. The difference $\Delta\mathrm{TL} = \mathrm{TL}_{\mathrm{numerical}} - \mathrm{TL}_{\mathrm{theoretical}}$ is also provided. In general ΔTL reduces as L_p/H increases. The iterative fluid-panel coupling scheme appears to perform better than the staggered scheme for all cases attempted. The difference in the numerical result is particularly pronounced for a short panel ($L_p/H = 4.3$) where the $\Delta\mathrm{TL} = 2.2$ db for staggered scheme but $\Delta\mathrm{TL} = 0.9$ db for the iterative scheme. All these observations reveal that the iterative coupling scheme is more superior in capturing the fluid-panel interaction. Furthermore a careful check shows that additional time spent in iterative scheme takes approximately 30 % of that used in the staggered scheme. Having compared with the pros and cons of the scheme, we decide to employ the iterative scheme for all subsequent calculations.

A more elaborated assessment of the numerical methodology with iterative scheme is illustrated in Fig. 5. In this figure the numerical results with panel structural damping are also included. In Huang's frequency-domain analysis [12], the damping coefficient taken for the n-th structural vibration mode is estimated as

$$C = \frac{n\rho_p h_p \bar{C}}{L_p}\sqrt{\frac{T_x}{\rho_p h_p}}, \tag{11}$$

Table 1 Transmission loss TL at various L_p/H

	L_p/H		
	4.3	6	8
Theoretical results	2.1	2.1	15.0
Staggered scheme	4.4 (2.2)	1.1 (−1.0)	14.2 (−0.8)
Iterative scheme	3.0 (0.9)	1.3 (−0.8)	14.7 (−0.3)

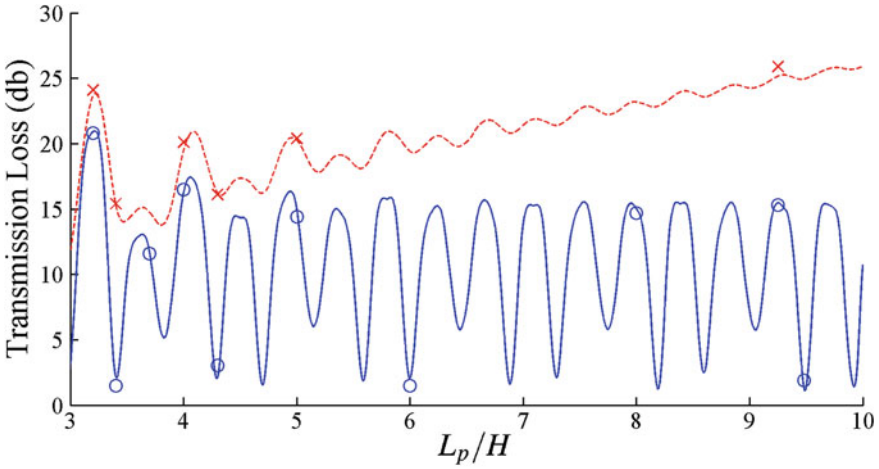

	L_p/H									
	3.2	3.4	3.7	4	4.3	5	6	8	9.25	9.48
Without structural damping	-0.1	-0.7	0.0	0.3	0.9	-0.6	-0.5	-0.3	-0.2	0.6
With structural damping	0.5	0.1		0.6	-0.1	0.1			0.8	

Fig. 5 Variation of transmission loss TL with panel length L_p/H. *Line* theoretical result with undamped panel [12]; *dashed lin*e theoretical result with damped panel; *circle* numerical result with undamped panel; *cross* numerical result with damped panel. The table shows ΔTL at all cases

where n is the mode number and $\bar{C}$ is a function of material property. For the present time domain analysis, we choose n corresponding to the dominant mode of vibration of undamped panel vibration and $\bar{C} = 0.2$. A summary of the ΔTL in the figure shows that the largest deviation observed is less than 1 db. It indicates that the present numerical solver is able to capture the acoustic-structural interaction accurately.

We can better understand the mechanism of transmission loss through the study of the temporal evolution of the acoustic pressure fluctuations. Take the time-stationary solution for the case with $L_p/H = 3.2$ as an example which gives high TL = 20.9 in undamped case. Figure 6 illustrates the snapshots of acoustic pressure fluctuations within one period of the acoustic excitation. Figure 6a shows the total acoustic pressure fluctuations p'. Strong acoustic-structural interaction is evident around in the vicinity of the vibrating panel. Figure 6b shows the propagation of pressure fluctuations p'_{incident} of the incident wave when the flexible panel is absent.

In response to the incident excitation the flexible panel re-radiates an acoustic wave $p'_{\text{re-radiated}} = p' - p'_{\text{incident}}$ to both upstream and downstream directions.

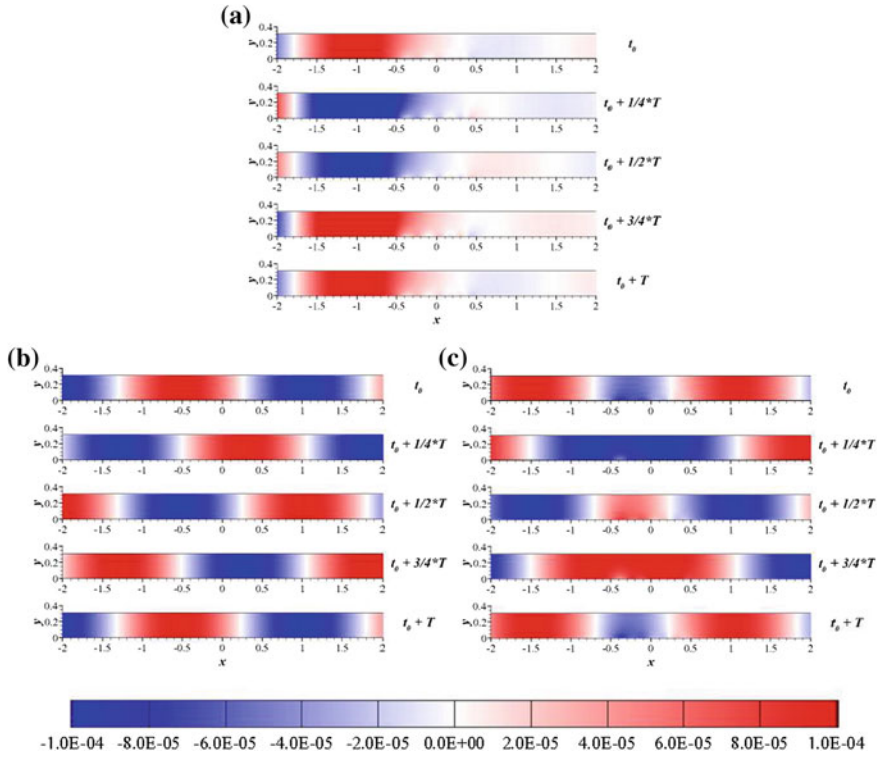

Fig. 6 Snapshots of acoustic pressure fluctuations in one period of incident excitation ($L_p/H = 3.2$). t_0 is beginning moment. T is the period of the incident wave. **a** Total acoustic pressure p', **b** incident acoustic wave p'_{incident}, **c** re-radiated wave $p'_{\text{re-radiated}}$

Upstream of the panel, the re-radiated wave interferes constructively with the incident wave which results in a strong standing wave is created in duct section upstream of the panel (Fig. 6a). Downstream of the panel, the re-radiated wave and the incident wave maintains almost out-of-phase so an effective cancellation is resulted (Fig. 7). This explains why only a weak resultant acoustic wave can be observed in the duct downstream (Fig. 6a) and high TL prevails in this case.

The calculated panel structural response for $L_p/H = 5$ and $C = 0$ is illustrated in Fig. 8. In Fig. 8a the panel velocity distribution is obtained from taking the mean value over one forcing period. In Fig. 8b the modal amplitudes are obtained from performing a spatial fast Fourier transform on the panel velocity. Both figures are normalized by the strongest observed value $x = -0.41$. Evidently that the numerical panel responses agree well with the theoretical prediction. The panel vibration is dominated by in a narrowband with the 12-th axial mode as the peak (Fig. 8a). Consequently 12 vibration peaks are evident along the panel (Fig. 8b) where the strongest vibration occurs at the second peak close the leading edge of the panel. From a closer look in the same figure we can see that the present

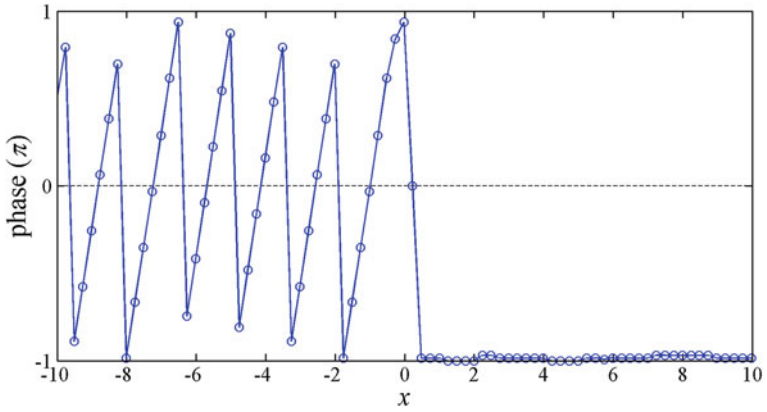

Fig. 7 Variation of the phase difference of between incident wave and re-radiated wave along the duct $(L_p/H = 3.2)$

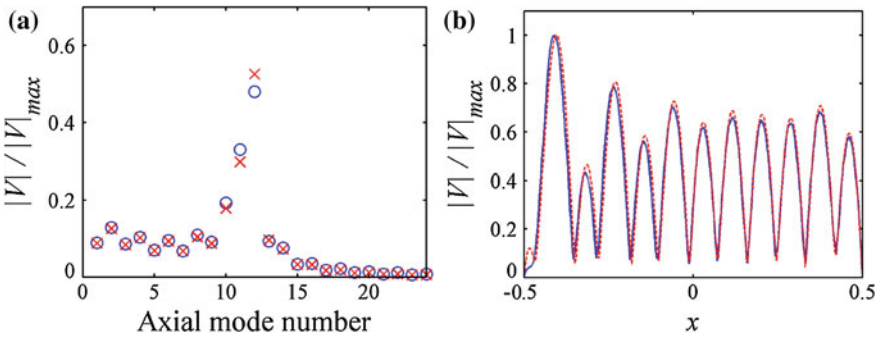

Fig. 8 Panel structural response of case $(L_p/H = 5)$. **a** Panel modal vibrating velocity amplitude. *Circle* theoretical result; *cross* numerical result. **b** Panel vibrating velocity amplitude along the panel. *Line* theoretical result; *dashed line* numerical result

time-domain calculation succeeds to calculate all the peaks but the linear frequency-domain theory fails to predict the first peak at $x = -0.48$, which is in fact very weak. This observation reveals that the strong ability of the present numerical methodology in capturing the nonlinearity of the fluid-panel interaction no matter how weak they are. The panel structural responses of cases with strong (TL = 20.8) and with weak transmission loss (TL = 3.0) are compared in Fig. 9. They occur with $L_p/H = 3.2$ and $L_p/H = 4.3$ respectively. Again structural damping is not included in the calculations. There is a distinct difference observed. In high TL case the dominant vibration mainly occurs in a narrowband of vibration modes (the 6-th to the 8-th modes) in the present. Same observation prevails in the case with $L_p/H = 5$. However, in low TL case, the panel vibration is dominated by a single peak (the 10-th mode). These observations suggest that as the modal content of the

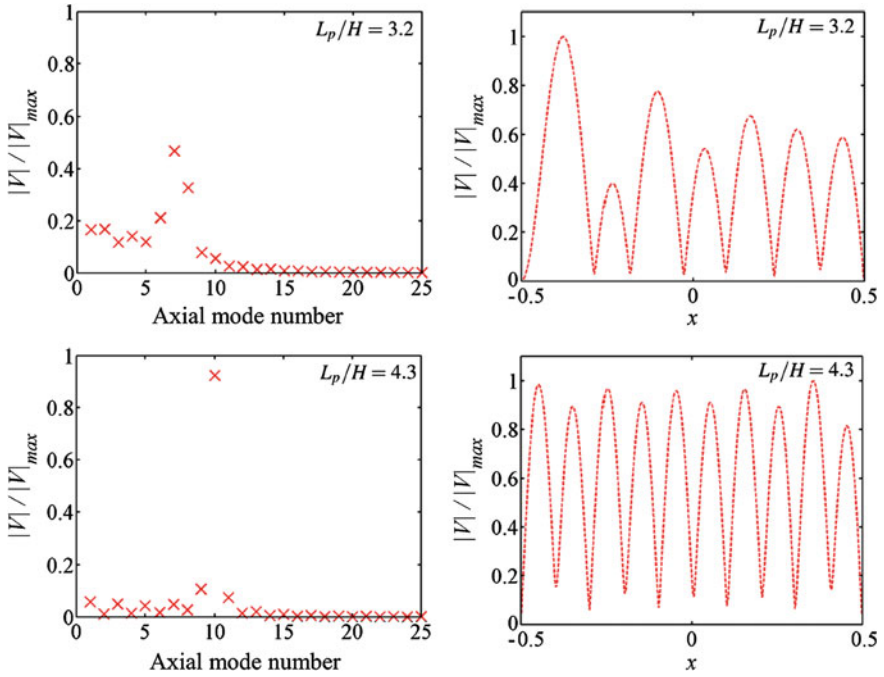

Fig. 9 Structural responses with high and low TL. *Left column* panel modal velocity amplitude; *right column* modal velocity along the panel

vibrating panel gets richer, the associated distension created by the fluid-panel interaction becomes richer and more prominent. That will increase the mismatch of the phases between the vibrating panel and the incident acoustic wave and lead to a more severe change in the impedance above the panel. Consequently more acoustical energy can be reflected so the TL becomes high. On the other hand, as there is only a single mode prevailing the in the panel vibration, the associated change in the impedance will be much limited. Only a very limited amount of reflection is possible so the TL becomes very small.

4.2 Aeroacoustic-Structural Response

To demonstrate the ability of the proposed methodology to capture full aeroacoustic-structure interaction of the panel, we select the panel with $L_p/H = 3.2$ and $C = 0$ and impose an uniform mean flow with velocity $\hat{u}_0$ in the same direction of the incident acoustic wave in the duct. The Mach numbers attempted are $M = 0.1$, 0.5 and 0.8. The transmission loss calculated is illustrated in Fig. 10. In general, the mean flow acts to suppress the transmission loss of the flexible panel. The reduction of transmission loss gives a nonlinear trend with the mean flow velocity.

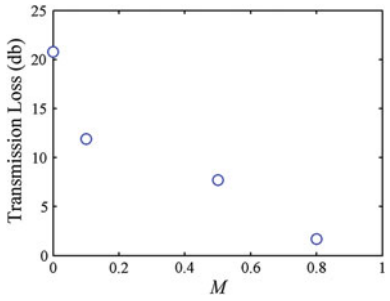

Fig. 10 Variation of TL with mean flow Mach number for undamped panel ($L_p/H = 3.2$)

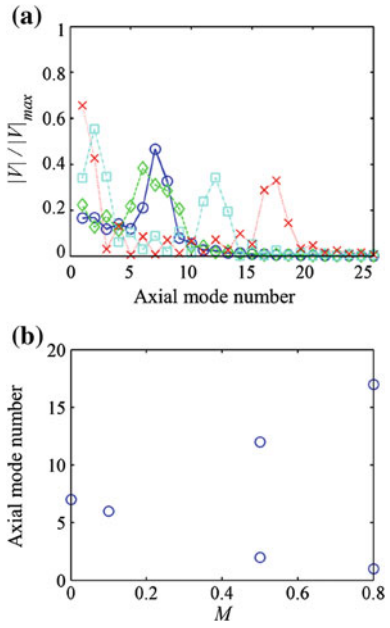

Fig. 11 Panel vibration with $L_p/H = 3.2$. **a** Modal velocity along the panel, *circle*, $M = 0$; *diamond*, $M = 0.1$; *square*, $M = 0.5$; *cross*, $M = 0.8$. **b** Modal peaks

Figure 11 shows the modal distribution of the panel vibration at all values of M attempted. In the absence of the mean flow (i.e. $M = 0$), the panel vibration lies within a narrowband of axial mode number (Fig. 11a). When M is increased slightly to 0.1, broadening of the bandwidth is observed and the modal amplitudes reduce. Such change in the panel vibration, however, results in a significant reduction of 9 db in the transmission loss. When M is increased further to 0.5, the modal distribution changes from a unimodal one to a bimodal one with the stronger vibration prevailing at lower mode number. The separation and the amplitude difference between the two arms of bimodal distribution increases at a higher $M = 0.8$. In order to get a clearer picture of the changes mentioned, it would be informative to observe the panel flexural wave behaviours closely. Figure 12 shows the snapshots of panel displacements. It is interesting to observe that at this Mach number the two modal

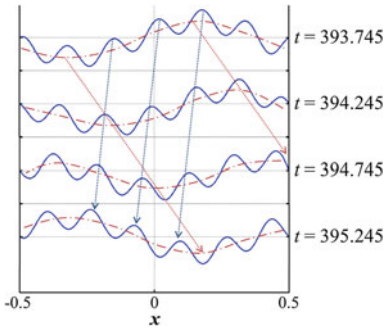

Fig. 12 Snapshots of panel vibration with $L_p/H = 3.2$ and $M = 0.5$

peaks observed in Fig. 11 in fact correspond to two flexural waves. The longer wavelength one (at the second mode) is propagating along the incident wave direction. On the contrary the shorter wavelength one (at the 12-th mode) is propagating opposite to the incident wave direction. Certainly these two kinds of flexural wave propagation will create two different kinds of fluid-panel interactions but their overall effect is counterproductive. This phenomenon has never been observed before, so a more detailed analysis is needed.

5 Concluding Remarks

We have presented the development of a numerical methodology for the time-domain prediction of aeroacoustic-structural response of a flexible panel exposed to an incident acoustic wave in a flow duct. The methodology aims to correctly resolve the nonlinear coupling of the acoustics, fluid dynamics as well as structural dynamics simultaneously. Previous numerical attempts have relied on the approach in which the physical processes are individually solved and their solutions are communicated through three numerical interfaces for resolving the overall interaction. That way would lead to an increase in the errors in resolving the coupling due to frequent extrapolation of solutions from one dynamics solver to another. Such errors may be effectively reduced at the expense of prohibitively large demand in the computational resources. In the present approach, we solve the entire problems with solvers in two domains, namely the fluid domain and the flexible panel, with a single coupling procedure. In the fluid domain, we adopt a numerical solver based on the direct aeroacoustic simulation (DAS) approach which has been proven to be able to accurately solve the scale-disparate fluid dynamics and acoustics, as well as their interactions, simultaneously. We solve the structural dynamics of the flexible panel using a standard finite-difference scheme. Both staggered and iterative procedures are evaluated for coupling the aeroacoustic and structural solutions for resolving the fluid-panel interaction. We first calculate the acoustic-structural responses of a flexible panels with different length in the absence of flow and compared the numerical results with the predictions with existing

theory. The numerical results are consistent with the theory. The maximum error in the calculation transmission loss is less than 1 db. This shows that the present numerical methodology is able to capture all the key acoustic and structural dynamic processes arising from the interaction. The comparison also shows that the iterative procedure gives much less error with a mild increase in the computational resources. We then include uniform mean flows of different Mach numbers into the problem. The numerical results show that the presence of mean flow changes the acoustic and panel structural responses entirely. The responses are completely different from those in no flow case. Consequently the transmission loss decreases rapidly with an increasing flow velocity. All the observations highlight the mean flow plays an important role in determining the nonlinear aeroacoustic-structural interaction.

Acknowledgements The authors gratefully acknowledge the supports given by the Research Grants Council of Hong Kong SAR Government under Grant Nos. PolyU 5230/09E and PolyU 5199/11E.

References

1. D.A. Anderson, J.C. Tannehill, R.H. Pletcher, *Computational Fluid Mechanics and Heat Transfer*, 2nd edn. (McGraw-Hill, New York, 1984), pp. 156–157
2. C. Bogey, A family of low dispersive and low dissipative explicit schemes for flow and noise computations. J. Comput. Phys. **194**, 194–214 (2004)
3. P.W. Carpenter, A.D. Garrad, The hydrodynamic stability of flow over Kramer-type compliant surfaces. Part 2. Flow-induced surface instabilities. J. Fluid Mech. **170**, 199–232 (1986)
4. S. Chakraverty, *Vibration of Plates* (CRC Press, Boca Raton, 2009), pp. 21–22
5. S.C. Chang, The method of space-time conservation element and solution element–a new approach for solving the Navier-Stokes and Euler equations. J. Comput. Phys. **119**, 295–324 (1995)
6. R.L. Clark, K.D. Frampton, Aeroelastic structural acoustic coupling: implications on the control of turbulent boundary-layer noise transmission. J. Acoust. Soc. Am. **102**(3), 1639–1647 (1997)
7. D.G. Crighton, Acoustics as a branch of fluid mechanics. J. Fluid Mech. **106**, 261–298 (1981)
8. A. Cummings, Sound transmission through duct walls. J. Sound Vib. **239**, 731–765 (2001)
9. M. De' Michieli Vitturi, T. Esposti Ongaro, A. Neri, M.V. Salvetti, F. Beux, An immersed boundary method for compressible multiphase flows: application to the dynamics of pyroclastic density currents. Comput. Geosci. **11,** 183–198 (2007). doi:10.1007/s10596-007-9047-9
10. A. Frendi, L. Maestrello, L. Ting, An efficient model for coupling structural vibrations with acoustic radiation. J. Sound Vib. **182**(5), 741–757 (1995)
11. S.I. Hayek, *Advanced Mathematical Methods in Science and Engineering*, 2nd edn. (CRC Press, Boca Raton, 2011), p. 599
12. L. Huang, A theoretical study of duct noise control by flexible panels. J. Acoust. Soc. Am. **106** (4), 1801–1809 (1999)
13. L. Huang, Y.S. Choy, R.M.C. So, T.L. Chong, Experimental study of sound propagation in a flexible duct. L. J. Acoust. Soc. Am. **118**(2), 624–631 (2000)
14. I. Jadic, R.M.C. So, M.P. Mignolet, Analysis of fluid-structure interactions using a time-marching technique. J. Fluid Struct. **12**, 631–654 (1998)

15. R. Jaiman, P. Geubelle, E. Loth, X. Jiao, Combined interface boundary condition method for unsteady fluid-structure interaction. Comput. Methods Appl. Mech. Engrg. **200**, 27–39 (2011)
16. G.C.Y. Lam, Aeroacoustics of merging flows at duct junctions. Dissertation, Department of Building Services Engineering, The Hong Kong Polytechnic University, Hong Kong, 2011
17. G.C.Y. Lam, R.C.K. Leung, S.K. Tang, Aeroacoustics of T-junction merging flow. J. Acoust. Soc. Am. **133**, 697–708 (2013)
18. G.C.Y. Lam, R.C.K. Leung, S.K. Tang, K.H. Seid, Validation of CE/SE scheme for low mach number direct aeroacoustic simulation. Int. J. Nonlin. Sci. Num. **15**(2), 157–169 (2014)
19. A.D. Lucey, The excitation of waves on a flexible panel in a uniform flow. Philos. T Roy. Soc. A **356**(1749), 2999–3039 (1998)
20. J.S. Rao, *Dynamics of Plates* (Narosa Publishing House, New Delhi, 1999), p. 227
21. F. Schäfer, S. Müller, T. Uffinger, S. Becker, J. Grabinger, M. Kaltenbacher, Fluid-structure-acoustic interaction of the flow past a thin flexible structure. AIAA J. **48**(4), 738–748 (2010)
22. R.M.C. So, Y. Liu, Y.G. Lai, Mesh shape preservation for flow-induced vibration problems. J. Fluids Struct. **18**(3–4), 287–304 (2003)
23. R. Szilard, *Theories and Applications of Plate Analysis* (Wiley, Hoboken, 2004), pp. 57–60

Calculating Structural Vibration and Stress from Turbulent Flow Induced Forces

Stephen A. Hambric, Matthew Shaw, Robert L. Campbell and Stephen C. Conlon

Abstract This paper summarizes computational procedures for assessing structural vibration and stress induced by turbulent flow excitation. The overall process is described, including commonly used empirical models for wall pressure fluctuations from turbulent boundary layers, impinging jets, and separated flows. A tutorial on how to assess potential structural damage caused by excessive tensile/compressive loading is given, including how to account for combined mean and cyclic stresses. An example of a beam driven by a turbulent shear layer emanating from a nozzle is given, showing calculations made in the time and frequency domains.

1 Introduction

Fluctuating pressures in high-speed complex fluid flow can excite structures into vibration so severe that fatigue cracking or material yielding can occur [13, 18, 19]. In 2011, a panel on the top of a Boeing 737 fuselage failed during flight (see Fig. 1), causing the grounding of several planes until the cause of the failure, fatigue cracking in the Aluminum underskin of the panel joints, was determined and corrected. In 2004, large sections of metal separated from steam dryers in two boiling water reactors [11]. The cause was acoustically induced fatigue cracking and eventual crack propagation and failure. Although these sorts of flow-induced stress failures occur periodically in many industries, most of the open literature focuses on the forcing functions and/or vibration and noise, but does not often address alternating stresses and fatigue failure. This paper summarizes the overall flow-induced stress analysis process, and provides a brief tutorial on methods for assessing the likelihood of structural failure. Additional references are provided which include more detail.

S.A. Hambric (✉) · M. Shaw · R.L. Campbell · S.C. Conlon
Applied Research Lab, Penn State University, PO Box 30, State College, PA 16804, USA
e-mail: sah19@arl.psu.edu

E. Ciappi et al. (eds.), *Flinovia - Flow Induced Noise and Vibration Issues and Aspects*, DOI 10.1007/978-3-319-09713-8_16

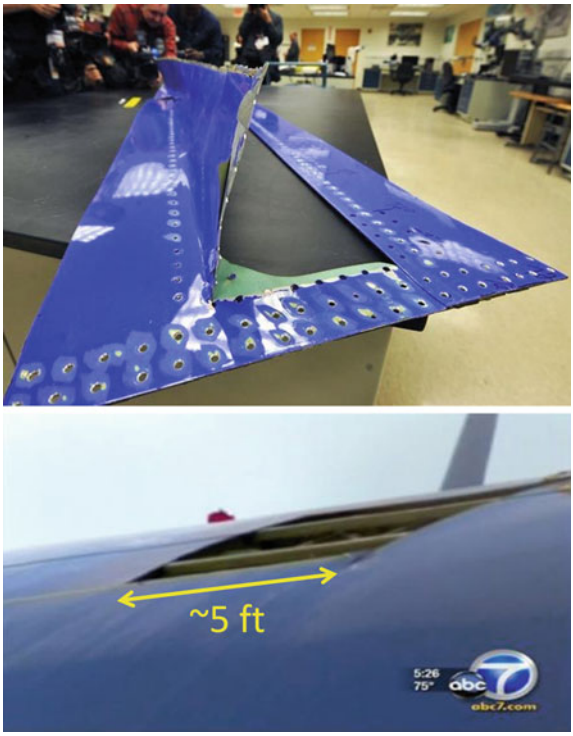

Fig. 1 Photographs of Boeing 737 fatigue failure in 2011 (from public news reports)

Analyzing the fluctuating stresses within flow-excited structures requires several steps, each of which must be executed with great care to ensure accurate calculations. They are:

1. determining the mean and fluctuating surface pressure distribution beneath the fluid flow field;
2. mapping the pressures onto a vibro-acoustic model of the underlying structure;
3. computing the structural vibration response, along with the strain and stress response, and
4. analyzing the stress results to determine if yielding or fatigue failure might occur.

In this paper, we survey some of the computational techniques used to perform these analyses.

2 Fluctuating Pressures

There are many examples of turbulent fluid flows which can cause excessive vibration and stress in structures, including:

- high speed, but subsonic turbulent boundary layer (TBL) flow over aircraft;
- separated and reattached flow over launch vehicles ascending into orbit;
- jet discharge flow impinging on runways beneath STOVL aircraft; and
- flow instabilities caused by vortices shed from structures, like turbomachinery blades.

These and other complex flow fields are often extremely difficult to characterize quantitatively, comprised of partially correlated random velocity events over space and time. Measurements are usually limited to a fixed number of sensors which are insufficient to fully define the pressure amplitudes and correlation distributions. However, for some of the more simplified flows, like TBLs over large structures, empirical models have been developed to approximate the important features of the pressure fluctuations [12]. In cases like these, a stationary ergodic wall pressure signal is common, and frequency-domain representations may be applied to the driven structures, with averaged spectral response may be computed. For the more complex flows with less available data, Computational Fluid Dynamics (CFD) time-accurate modeling is often attempted to estimate the loading, supported by limited experimental validation data. Figure 2 is an example of a flow field at an instant in time computed using CFD Large Eddy Simulation (LES) methods. The velocity fluctuations become more pronounced as the flow progresses downstream. Turbulent eddies pulsate and collide with each other, with the pressure disturbances propagating eventually to the underlying wall surface.

Relative to unsteady forcing function modelling, TBL flow is perhaps the best understood of all turbulent flows. Flow attached to a surface becomes turbulent above a critical speed U, usually nondimensionalized against size D and viscosity v as a Reynolds Number (UD/v). When this happens, the flow cannot sustain the velocity gradients in the boundary layer profile and turbulent eddies form. The eddies don't last long, dissipating into smaller and smaller eddies until their energy is eventually dissipated by viscous effects. As they propagate and pulsate, however,

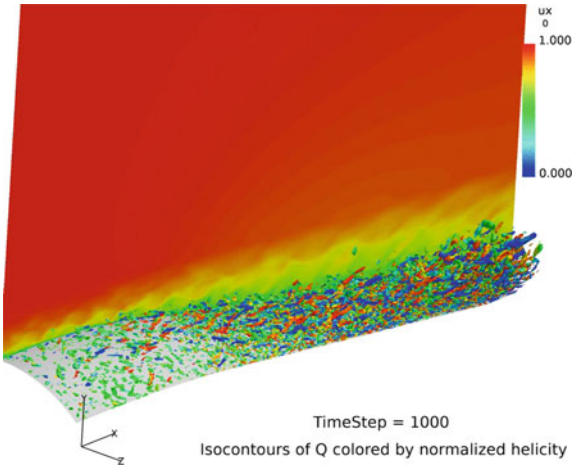

Fig. 2 Example of flow field over a curved surface (flow moves from *left* to *right*) at an instant in time computed using CFD LES methodology, courtesy of ARL/Penn State Computational Mechanics Division

they generate pressure fluctuations on the underlying surface. The net pressure fluctuations are a superposition of the pulsations from all of the eddies passing by above the surface.

Since the turbulent eddies are short lived events, the distribution of pressure fluctuations over the surface is only partially correlated, both over space and time. Many investigators have measured these pressures, in the form of amplitudes, spatial and time correlation, and effective convection velocity. A recent set of measurements on an operating small aircraft provides new insights into these quantities [16]. The convection velocity varies with frequency and separation distance, since different eddy sizes dominate the wall pressures at different frequencies.

Although TBL pressure fields are extremely complicated, their frequency spectra may be approximated with empirical models. Many models have been suggested [12], and usually subdivide the wall pressures into autospectrum and cross-spectrum components. The autospectrum, not surprisingly, is proportional to flow speed and fluid density. An RMS wall pressure is estimated (proportional to $Q = \frac{1}{2}\rho U^2$), and the energy is distributed over frequency according to an empirically assumed distribution. For example, TBL flow RMS wall pressures typically vary from 0.005 to 0.02Q, whereas separated and reattached flow wall pressures are much higher, about 0.1Q. The cross-spectrum depends on the effective convection velocity, and empirically determined decay coefficients which represent the spatial breadths of the wall pressure correlations. The models are all effectively curve fits to measured data, and are routinely used in TBL-induced vibration and noise studies.

Although TBL flow is often investigated in the literature, it is actually quite benign when compared to other more powerful excitation types. In particular, the TBL literature almost always assumes the wall pressure statistics are homogenous (invariant of position), and the static pressure is constant. In many cases, such as flow over airfoil noses, the flow is affected by a static pressure gradient, which distorts the shape of the boundary layer. This distortion affects the production of turbulent eddies, and their shapes and propagation speeds and directions. Adverse pressure gradients lead to stronger large turbulent eddies, and increased low frequency wall pressure spectra [17].

Even stronger wall pressures are caused by flow separated from a body which reattaches farther downstream. The separated flow contains large, highly energetic vortices which impinge on the reattached region strongly, leading to very high low frequency excitation. The impinging pressures are also more highly correlated over space, which also increases effective structural excitation [6].

Jets emanating from nozzles can generate strong pressure pulsations on downstream surfaces. Impinging jets [1], like those discharging from Vertical Take Off and Landing (VTOL) aircraft and striking runways, have been known to cause significant structural damage. Measurements of the pressure spectra, as well as the spatial correlations of the wall pressures [21] are available, and empirical models have been suggested to simulate them [9]. Jets also generate strong wall pressures when propagating or ‘washing’ over a surface. Measurements show a complex variation in wall pressures and surface correlations with jet speed variation [5]. When the jets become supersonic, shock cells form in the flow, further complicating

the quantification of wall pressures as turbulent eddies are scattered when interacting with the sudden impedance discontinuities near the shock cells.

While empirical models are often used to simulate the surface loading caused by these and other turbulent flow sources, time-accurate CFD techniques like LES are being used more frequently to model more complex flows not well suited to simplified models. Massively parallel computer clusters allow model sizes previously unimaginable to be analyzed at Reynolds Numbers of practical interest and over time spans sufficiently long to compute reasonably accurate wall pressure statistics. When time-accurate CFD solutions are available, the entire surface pressure field may be stored and applied to a structural model, either in the native time domain, or transformed into the frequency domain.

3 Mapping Pressures to Structural Models

While it may seem trivial to apply computed pressure loads to structural models, this step is often prone to errors. Of course, empirical models may be easily exercised to generate wall pressures and cross-correlations over any grid of points. However, computational flow models nearly always use different spatial discretization resolution than structural models. Careful planning is therefore required to ensure a common subset of mesh points is used for both the fluid and structural models. If common points are not used, the pressure field must be interpolated onto the different discretization in the structural model. Interpolation must be performed with great care to avoid adding bias errors to the final structural loading. Finally, CFD models are usually exercised at much smaller time steps than are required for a structural vibration analysis. The finer time step resolution is required to ensure converged flow solutions. Resampling the pressure time histories with a larger time step will reduce structural analysis computational times considerably.

4 Computing Structural Vibration and Stress Response

The most common approach used to analyze the vibrations of structures excited by time-varying pressure fluctuations is modal expansion [4, 10]. The response is modeled as a series summation of modal amplitudes, where each mode responds differently to the pressure field. A given modal response, often referred to as a joint acceptance [22], is simply the integrated product of the pressure distribution and a given mode shape. The more closely the pressure distribution and mode shape aligns, the higher the modal response.

The modal responses and resulting vibrations may be computed in either the time or frequency domains. However, frequency domain calculations require the pressure loading to be stationary and ergodic to compute meaningful response spectra. For pressure fields influenced by sporadic, non-stationary events, a time-

domain calculation may be required to ensure that peak loading and response is accurately captured.

For stiff, lightweight structures or structures immersed in water, acoustic models of the radiation resistance of any internal or external fluid must be applied to the structural surface. The resistance adds significant damping to the structural vibrations at and around the acoustic coincidence frequencies. Reactances can also be important, adding stiffness or mass to lightweight structures, shifting resonance frequencies. Boundary element modeling is commonly used to compute these resistances and reactances.

Stresses may be calculated by post-processing the vibration fields, taking spatial derivatives to compute strains, which are then combined with stress-strain material relationships to compute stress tensors. The derivatives, however, are often inaccurate for regions with strong spatial gradients. A more accurate approach is to precompute converged stress 'mode shapes', which may be combined with the modal amplitudes to compute stresses. Both static and alternating stresses are required to assess whether a structure may fail.

An example of a flow-excited structural stress response calculation is given here. Consider a beam downstream of a nozzle, as shown in Fig. 3. High internal pressure drives air flow out of the nozzle. A turbulent shear layer forms on the outer surface of the nozzle, and propagates downstream, expanding and diffusing. As the turbulence propagates, velocity fluctuations combine to generate impinging pressures on the beam surface. The beam, constrained on its ends with simple supports, has the following dimensions and material properties:

Length	1.103 m
Cross-sectional area	$4e^{-4}$ m^2
Density	2,700 kg/m^3
Young's modulus	70 GPa
Loss factor	0.01

The turbulent shear layer is computed using an inviscid Large Eddy Simulation (LES) CFD computer program. The simulation generated 0.4 s of results with a

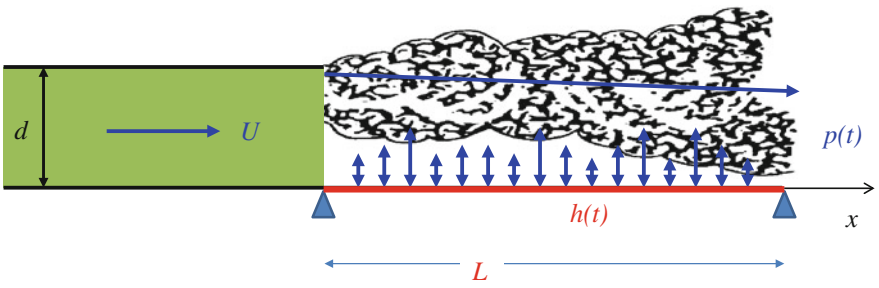

Fig. 3 Turbulent nozzle discharge flow with wall pressure fluctuations applied to beam surface

"sample rate" of 5,000 Hz. Figure 4 shows the wall surface pressure variation with time. The propagating shear layer is clearly visible in the contours, which show an alternating wave convecting downstream. The total pressure (mean + alternating) is always positive, indicating a static component that pushes downward on the beam. The static component is mostly due to atmospheric pressure, and partly to the steady flow. Figure 5 shows a Fourier Transform of the wall pressure time histories. Most of the excitation is at low frequencies, and becomes stronger as the flow propagates downstream.

Figure 6 shows the first three mode shapes of the beam, which vibrate with the highest amplitudes. Displacement and stress (stress on the outer beam fibers, with positive stresses implying tension) are shown. Displacement spectra computed from both frequency domain and time domain approaches are compared in Fig. 7. The peak responses match well, particularly for the low order modes. Figure 8 shows the static beam deflection, and Fig. 9 shows spectra of the tensile stresses computed at $x/L = 0.15$.

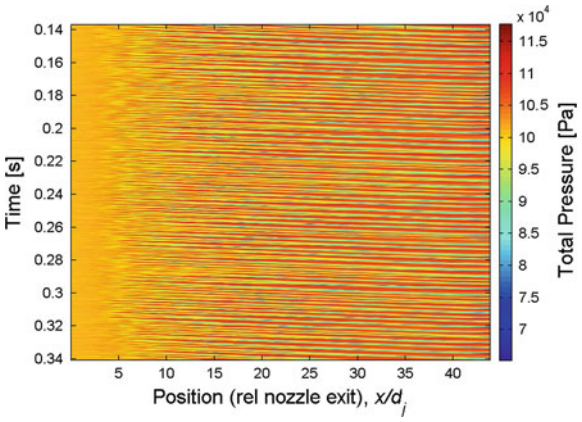

Fig. 4 Wall pressure (including atmospheric) as a function of distance (x-axis) and time (y-axis). Distance (x) is normalized by nozzle height (d)

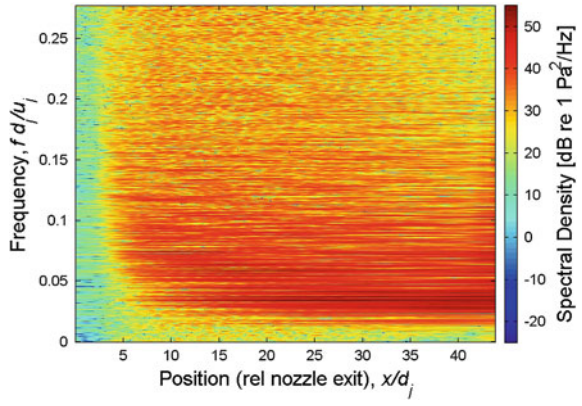

Fig. 5 Wall pressure as a function of distance (x-axis) and frequency (y-axis). Position is normalized by nozzle height (d). Frequency is normalized by nozzle height (d) and mean flow velocity (u)

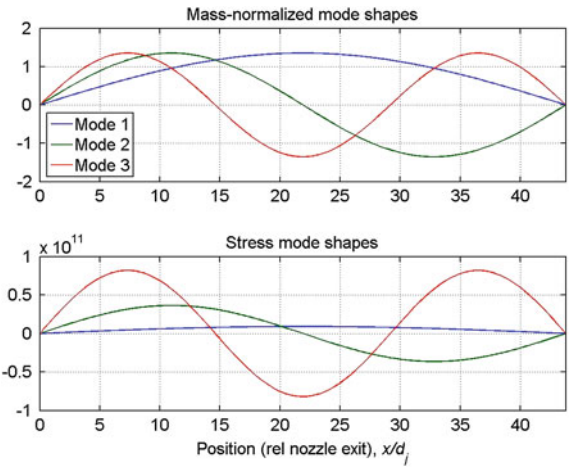

Fig. 6 Fundamental simply supported beam mode shapes, displacement (*top*) and tensile stresses on outer fibers of cross section (*bottom*)

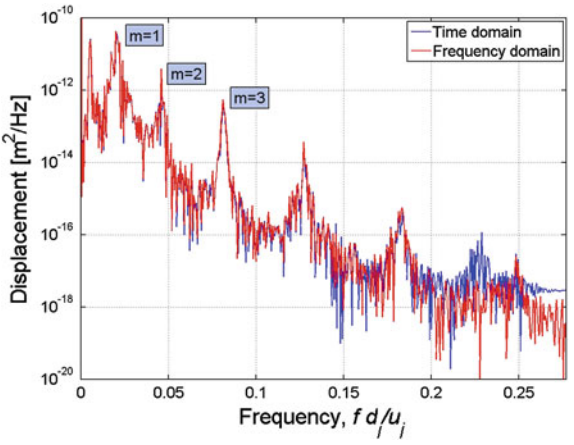

Fig. 7 Displacement spectra computed using time- and frequency-domain methods at $x/L = 0.15$. The first three beam mode orders are indicated. The lowest peak below 100 Hz is a tone in the CFD computed wall pressures

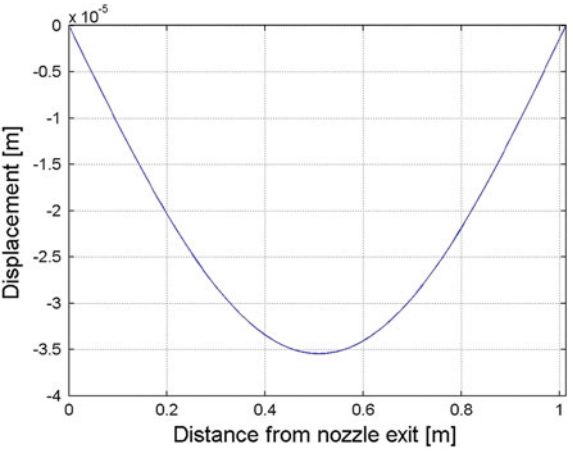

Fig. 8 Mean (static) beam displacement distribution

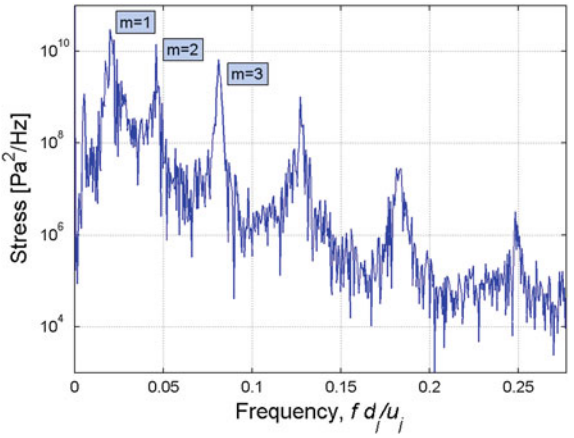

Fig. 9 Tensile stress spectrum computed at $x/L = 0.15$

5 Post-processing of Stresses

The resulting stresses, whether computed in the time or frequency domain, are examined using various techniques to determine the likelihood of failure. It is important to include both the fluctuating, as well as the static (or mean) components of the stress in these assessments. Figure 10 shows a notional time history of stress. The structural material is damaged only when total (mean + time-varying) stress exceeds its limits. Yielding, which is rare, is more readily assessed. Peak stress is compared to a material's yield limit. Fatigue failure, however, is much more difficult to determine considering the uncertainties involved in the assessment.

There are simple and complicated ways to assess structural fatigue failure. The simplest is to plot static and alternating stresses on a Goodman diagram [8], as shown in Fig. 11. In a Goodman diagram, the x-axis represents static stress, with tensile stresses positive, and compressive stresses negative. Only tensile stresses can induce cracking, so we only consider the right side of the diagram. The y-axis represents alternating stress. The ultimate stress limit of the material is plotted on the static stress axis, and the endurance stress limit (more on this soon) is plotted on

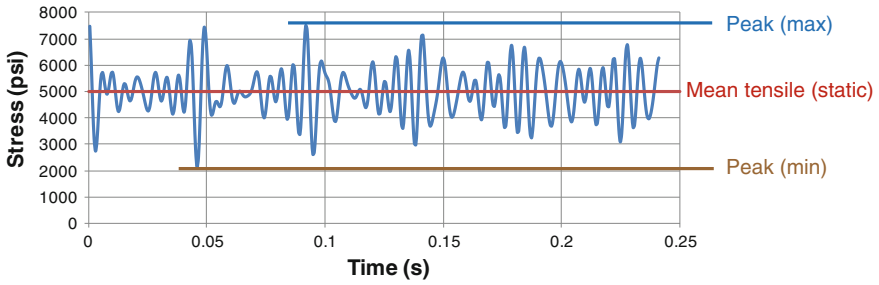

Fig. 10 Notional time history of stress which includes a mean (static) component

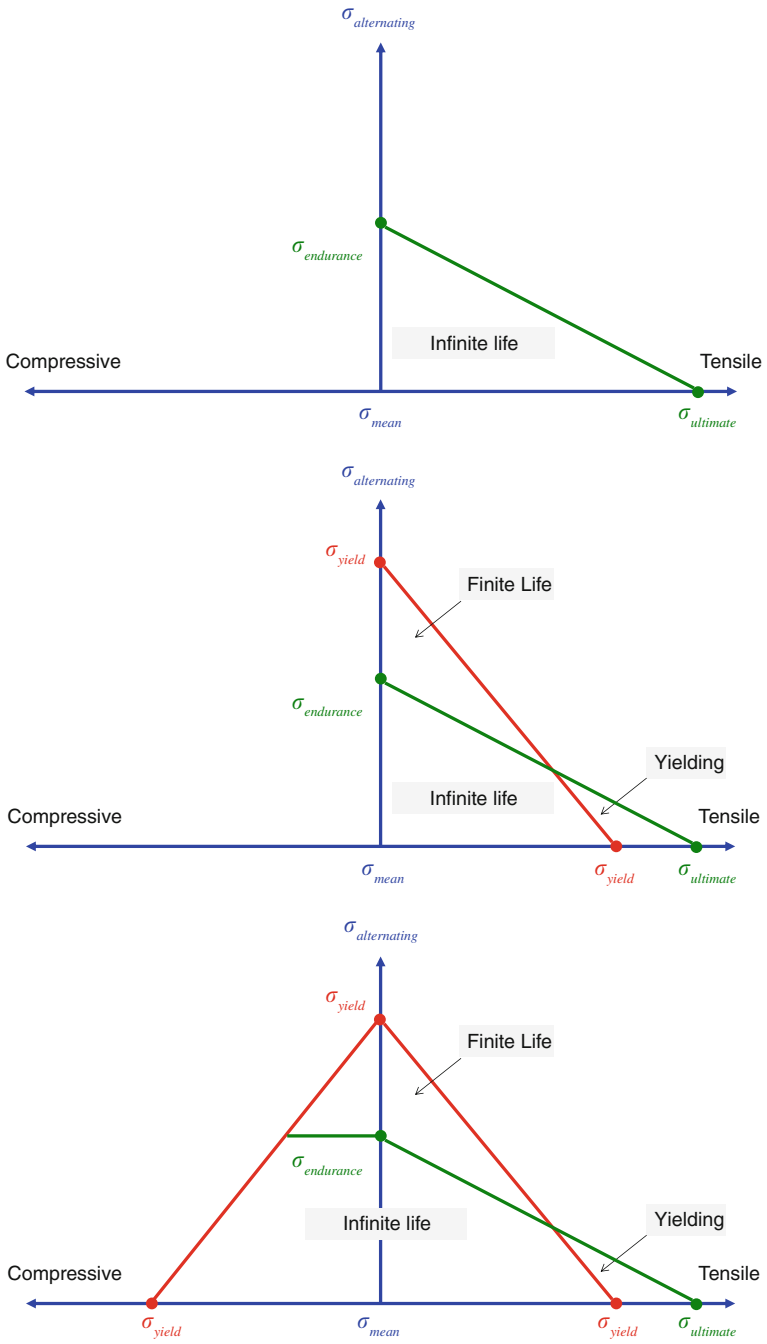

Fig. 11 Goodman diagrams based on [8]. *Top* basic diagram, *Middle* modified diagram, *Bottom* modified diagram including compressive terms

the alternating stress axis. A straight line connects the two points. Any stress state inside the lower triangle of the diagram is acceptable for infinite life. Note that the allowable alternating stress decreases as static stress increases.

A modified Goodman diagram includes the material yield stress limits, plotted as points on both the static and alternating stress axes. Another straight line joins these points, forming two new triangles. The one on the upper left represents finite structural life, where a structure will crack after a certain number of stress cycles. Finally, the diagram may be extended to the compressive quadrant, but the endurance limit does not apply for compressive stresses.

To determine fatigue life for a structure, material test data are used. Figure 12 shows an adaptation of a typical design fatigue curve for Austenitic Steels and Aluminum. Samples of material are tested in a lab, usually with alternating uniaxial loading applied, until enough material damage accumulates and cracking is observed. Samples are tested under zero mean load, and also with the presence of mean stresses, mainly to represent any residual stresses that may be present in a material that has not been 'stress-relieved' (heated and allowed to relax for a set period of time until all residual stresses are minimized), or for materials which are welded (where the welding induces residual deformation and stress).

In a fatigue curve, the alternating stress value is usually plotted on the y axis, and the number of stress cycles plotted on the x axis. For a sinusoidal stress of a given magnitude, the number of cycles to failure may be either inferred graphically, or computed using a curve fit to the data. Figure 12 shows a commonly used empirical model for the low cycle count region of the fatigue curve. At very low cycle counts (less than about 10^5) where stresses are high, fatigue is called 'low cycle', and above about 10^5 cycles, where stresses are lower, 'high cycle'. Constants for the magnitude and exponential are determined and fatigue life may be estimated directly from the formula. Fatigue curves are only the means of many statistical samples, however, so that the actual number of cycles to failure may be somewhat

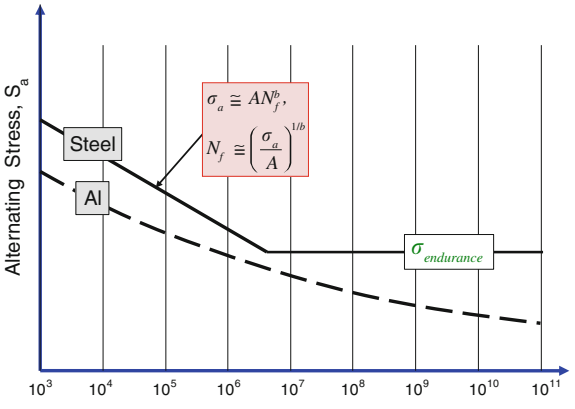

Fig. 12 Approximate fatigue life curve for austenitic steels, adapted from [2], and Aluminum. Note that there is no upper asymptotic limit for Aluminum

lower or higher depending on material quality. Obviously, the higher the alternating stress, the fewer cycles required to induce cracking. For some materials, like steel, there is an upper bound, or endurance limit. These materials should never crack if the alternating stresses are below this limit. For Aluminum, however, there is no upper endurance limit.

For structures that experience nonzero mean stresses, approximations of the total effective alternating stress are often made. The simplest model for determining equivalent completely reversed stress amplitude σ_{ar} is from Smith-Watson-Topper [7, 20], where a geometric mean of stress amplitude σ_a (half of the range between minimum peak and maximum peak stresses) and peak stress ($\sigma_{\max}$) is computed:

$$\sigma_{ar} \cong (\sigma_a \sigma_{\max})^{1/2}.$$

For stresses which include many peak frequencies, like the example in Fig. 9, linear summations of stress cycles are used to estimate damage. The well-known Palmgren Miner linear cumulative damage hypothesis [14, 15] is often used, and summarized in Fig. 13. The hypothesis assumes that all alternating stress amplitudes contribute equally to cumulative stress, so that:

$$E[\text{Damage}] = \sum \frac{n_i}{N_{f_i}} = \frac{n_1}{N_{f_1}} + \frac{n_2}{N_{f_2}} + \frac{n_3}{N_{f_3}} + \cdots$$

where n_i are the number of cycles corresponding to stress amplitude σ_i and its respective limit N_i. If the final result is greater than 1, there is more than a 50 % chance that fatigue cracking will initate.

It is often not straightforward to extract the number of cycles for a given stress amplitude from a stress time history. The most popular approach is called Rainflow Analysis, where a time history is post-processed to sort various stress events into a histogram [3]. The estimated cumulative damage is then based on summing all of these events and applying them using the Palmgren-Miner rule and a material fatigue life curve.

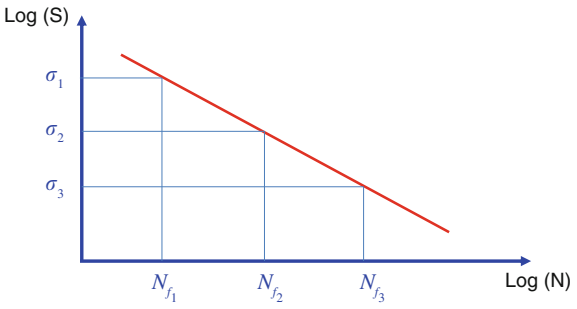

Fig. 13 Palmgren-Miner linear cumulative damage hypothesis

6 Summary and Conclusions

This paper summarizes the full process of computing structural vibrations, stresses, and potential material damage in flow-excited structures. Methods for estimating flow-induced surface pressures, analyzing structural response, and post-processing resulting stress calculations to assess damage probability are discussed. Examples from the open literature are cited, providing a survey of papers useful to the community.

The discussion on stress post-processing and damage assessment presents only the basics of this complex field. There are many more advanced fatigue assessment approaches available, which address the order of stress events (high amplitude stress events which occur early during a structure's life very likely have a larger impact on damage accumulation than those which occur later in life) and other complicated effects, such as non-uniaxial stresses in complex structural shapes. Also, once fatigue cracking initiates, how the crack continues to grow and propagate requires much more complicated analyses. Entire journals are devoted to fatigue analysis and crack behavior, and the reader is encouraged to pursue these if a more rigorous fatigue and/or cracking propagation treatment is desired. However, the bulk of the stress community uses the simple models and rules presented here. If a structure can be designed conservatively so that cracking never initiates, crack propagation assessments are, of course, not necessary.

Acknowledgments The authors acknowledge Michael Lurie and Dr. Phil Morris for the notional wall pressure CFD LES calculations used to demonstrate the structural vibration and stress calculation procedures. The authors also gratefully acknowledge Pratt and Whitney for their sponsorship of some of this work under the Penn State/Pratt and Whitney Center of Excellence.

References

1. F.S. Alvi, Experimental and computational investigation of supersonic impinging jets. AIAA J. **40**(4) (2002)
2. ASME Boiler and Pressure Vessel Code, Section III, Division 1, Subsection NG, 2010
3. ASTM E-1049, Standard practices for cycle counting in fatigue analysis
4. R. Blevins, An approximate method for sonic fatigue analysis of plates and shells. J. Sound Vib. **129**(1), 51–71 (1989)
5. P. Bremner et al., *Validation of methods to predict vibration of a panel in the near field of a hot supersonic rocket plume. 17th AIAA/CEAS Aeroacoustics Conference* (Portland, Oregon, 2011)
6. T.A. Brungart, G.C. Lauchle, S. Deutsch, E.T. Riggs, Wall pressure fluctuations induced by separated/reattached channel flow. J. Sound Vib. **251**(3), 558–577 (2002)
7. N.W. Dowling, Mean stress effects in stress-life and strain-life fatigue F2004/51, SAE 2004
8. J. Goodman, Mechanics applied to engineering, Longman, Green, and Company, London 1899
9. A. Foley, M. Howe, T. Brungart, Spectrum of the sound produced by a jet impinging on the gas-water interface of a supercavity. J. Sound Vib. **329**, 415–424 (2010)

10. S. Hambric et al., *Simulating the vibro-acoustic power of fluid-loaded structures excited by randomly distributed fluctuating forces* (St. Rafael, France, 2005)
11. S. Hambric et al., in *Acoustic loading on BWR steam dryers caused by valve singing*. 9th NRC/ASME Symposium on Valves, Pumps, and Inservice Testing, Washington DC, 2006
12. Y.F. Hwang, W.K. Bonness, S.A. Hambric, Comparison of semi-empirical models for turbulent boundary layer wall pressure spectra. J. Sound Vib. **319**, 199–217 (2009)
13. J. Miles, On structural fatigue under random loading. J. Aeronaut. Sci. (1954)
14. M.A. Miner, Cumulative damage in fatigue. J. Appl. Mech. **12**, A159–A164 (1945)
15. A. Palmgren, *Die Lebensdauer von Kugellagern* (The service life of ball bearings). Zeitschrift des Vereines Deutscher Ingenieure **68**(14) (1924)
16. D. Palumbo, Determining correlation and coherence lengths in turbulent boundary layer flight data. J. Sound Vib. **331**, 3721–3737 (2012)
17. L.J. Peltier, S.A. Hambric, Estimating turbulent boundary layer wall pressure spectra from CFD RANS solutions. J. Fl. Str. **23**, 920–937 (2007)
18. A. Powell, On the fatigue failure of structures due to vibrations excited by random pressure fields. J. Acoust. Soc. Am. **30**(12) 1958
19. P. Rabbe, L. Anquez, *Fatigue of Materials and Structures: Fundamentals* (Wiley, New York 2013)
20. K. Smith, P. Watson, T. Topper, A stress-strain function for the fatigue of metals. J. Mater. ASTM **5**(4), 767–778 (1970)
21. D. Strong, T. Siddon, W. Chu, Pressure fluctuations on a flat plate with oblique jet impingement. NASA CR-839 (1967)
22. J.F. Wilby, The response of simple panels to turbulent boundary layer excitation. Technical Report AFFDL-TR-67-70 (1967)

Appendix
Vortex Shedding from a Two-Dimensional Hydrofoil at High Reynolds Number

Professor Steven L. Ceccio
Chair, Naval Architecture and Marine Engineering
Mechanical Engineering
University of Michigan
Ann Arbor, Michigan 48109

Abstract Prediction of lifting surface performance (such as lift, drag, vibration, and hydroacoustic noise) requires an understanding of the separated turbulent flow at the surface's trailing edge. In this region, the boundary layers that separate from the suction and pressure side of the lifting surface may interact to form a structured near wake composed of vortical structures having a quasi-periodic geometrical arrangement (a condition commonly called vortex shedding). When it occurs, this type of structured near wake often leads to unwanted tonal hydroacoustic noise. However, vortex shedding is difficult to predict, and it does not follow any simple scaling based on Reynolds number. This presentation describes results from an experimental effort to identify and measure the major flow features in the near-wake of a hydrofoil at chord-based Reynolds numbers as high as those of full-scale ship propellers and heavy lift aircraft wings ($\sim$50 million). The experiments were conducted at the US Navy's William B. Morgan Large Cavitation Channel with a two-dimensional, test-section-spanning hydrofoil (2.13 m chord, 3.05 m span, 60 metric tons of lift). Two trailing edge shapes were investigated. Measurements include hydrofoil vibration, time-averaged and unsteady surface pressures, and LDV- and PIV—determined flow velocities. When taken together, the measured results suggest that the relative strength of vortex shedding can be assessed from the trailing-edge geometry and the time-averaged shear rate in the foil's boundary layers at its trailing edge (Figs. A.1 and A.2).

E. Ciappi et al. (eds.), *Flinovia - Flow Induced Noise and Vibration Issues and Aspects*, DOI 10.1007/978-3-319-09713-8

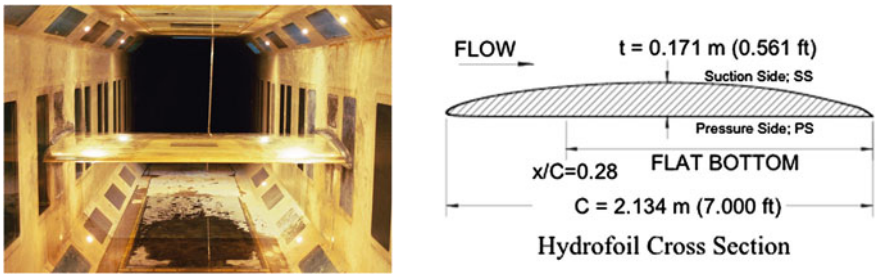

Fig. A.1 The HIFOIL mounted in the test section of the Large Cavitation Channel (*left*) and a schematic of the HIFOIL cross-section (*right*)

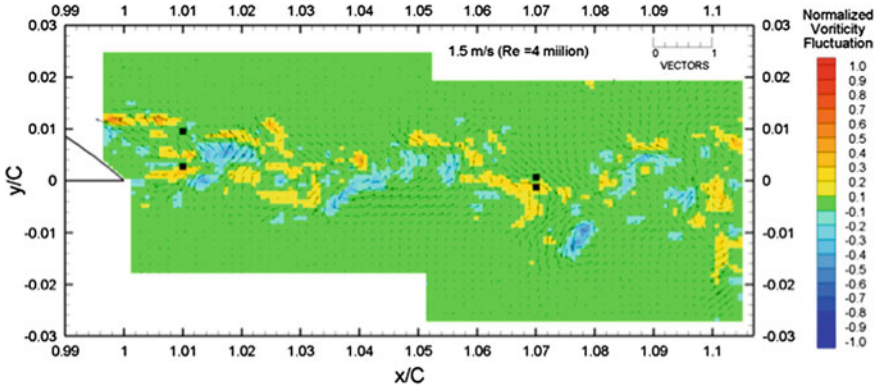

Fig. A.2 Instantaneous contour of normalized instantaneous vorticity fluctuation and vector field of normalized instantaneous velocity fluctuations in the near wake of the HIFOIL for the baseline trailing edge at 1.5 m/s ($\mathbf{Re_C}$ = 4 Million)

References

D. Bourgoyne, J. Hamel, S.L. Ceccio, D.R. Dowling, Time-averaged flow over a hydrofoil at high reynolds number. J. Fluid Mech. **496**, 365–404 (2003)

D. Bourgoyne, S.L. Ceccio, D.R. Dowling, Dynamic flow over a hydrofoil at high reynolds number. J. Fluid Mech. **531**, 293–324 (2005)

K.G. Sabra, E.S. Winkel, D.A. Bourgoyne, B.R. Elbing, S.L. Ceccio, M. Perlin, D.R. Dowling, On using cross correlations of turbulent flow-induced ambient vibrations to estimate the structural impulse response. Application to structural health monitoring. J. Acoust. Soc. Am. **121**(4), 1987–1995 (2007)